Society of Structural Engineers, Sri Lanka

Proceedings of Annual Sessions 2025

On 19th August 2025

Cinnamon Grand Hotel, Colombo

Sole Sponsor

TOKYO CEMENT GROUP

Society of Structural Engineers - Sri Lanka

Proceedings

of

ANNUAL SESSIONS - 2025

held on

19th August 2025

at

Cinnamon Grand Hotel

Colombo

This Proceedings comprises of papers presented at the 15th Annual Sessions organised by the Society of Structural Engineers - Sri Lanka, held on 19th of August 2025 at Cinnamon Grand Hotel, Colombo.

The views and the findings in the papers are those of the respective authors and are not meant to reflect those of the Society of Structural Engineers - Sri Lanka.

Edited & Page Setup by:

Eng. (Dr.) A.M.L.N. Gunathilaka

Eng. K.A.B.P. Kuruppu

Eng. A.M.D. Rathnayaka

Cover Page Designed by:

Eng. K.A.B.P. Kuruppu

Published by:

Society of Structural Engineers - Sri Lanka
Room No. 222, 2nd Floor
Institution of Engineers Building
120/15, Wijerama Mawatha
Colombo 00700
Tel/Fax: 011 2698726
e-mail: ssesl@sltnet.lk

ISBN 978-624-6028-12-1

August 2025

PRESIDENT'S MESSAGE

As we prepare for the Annual Session-2025 of the Society of Structural Engineers Sri Lanka(SSESL), I am filled with a sense of pride and optimism. Taking place on 19 th August 2025 at the Oak Room, Cinnamon Grand Colombo, this event is more than a gathering — it's a collective commitment to the future of Structural Engineering.

The Annual Session is a cornerstone in SSESL's calendar, serving as a premier forum where practicing engineers, researchers, and academics converge to share knowledge, present research, and explore advancements in Structural Engineering and related disciplines. It is this exchange of ideas and experiences that strengthens our profession and fosters innovation across industry.

This year's event is enriched by two distinguished keynote addresses.

We are honoured to welcome Prof. Pennung Warnitchai, Professor of Structural Engineering, Sirindhorn International Institute of Technology, Thailand who will deliver a lecture on "Impact of the M7.7 Manday Earthquake on High Rise buildings with Long Natural Periods in Bangkok. We are also privileged to hear from Prof. Nawarathnarajah Sathiparan, of Department of Civil Engineering, University of Jaffna, Sri Lanka, presenting on "Supplementary Cementitious Materials (SCMs) in Pervious Oxide effect and Machine Learning Insight."

I take this opportunity to sincerely thank all authors, presenters, panel members, and moderators for their valuable contributions. Your work brings academic excellence and practical relevance to this event.

I also wish to extend my deep appreciation to the Organizing Committee — Eng. (Prof.) Anura Nanayakkara, Eng. (Dr.) Nadira Gunathilaka and Eng. Bandhuka Kuruppu — for their outstanding efforts in curating this session with professionalism and dedication.

We are especially grateful to our Principal Sponsor, Tokyo Cement Group, whose generous support has been instrumental in making this event a success.

My sincere thanks also go to our resolute secretariat team, Hashan and Dilki, for their hard work behind the scenes.

In addition, I would like to acknowledge the management and staff of Cinnamon Grand Colombo, whose excellent arrangements and consistent hospitality have supported us over the past decade.

As we come together for this important occasion, let us continue to build on our legacy one that reflects excellence in research, strength in collaboration, and a shared vision for the future of Structural Engineering.

Eng. R M A Senarath

BSc. Eng. (Hons), C.Eng, MICE, MIE(SL), FSSE(SL), MConsE(SL)

President (2025)
Society of Structural Engineers, Sri Lanka

SOCIETY OF STRUCTURAL ENGINEERS

SRI LANKA

SOCIETY OF STRUCTURAL ENGINEERS - SRI LANKA
EXECUTIVE COMMITTEE - 2025

Eng. R.M.A. Senerath	- President
Eng. (Mrs) T.J. Jayasundara	- Immediate Past President
Eng. N. Abeysuriya	- Past President
Eng. A. S. B. Edirisinghe	- Vice President
Eng. D.T. Rajasekaran	- Honorary Secretary
Eng. R.S.K. Thrimavithana	- Treasurer
Eng. (Prof.) S. M. A. Nanayakkara	- Editor
Eng. G. Ramawickrama	- Public Relation Officer
Eng. S. S. A. Kalugaldeniya	- Assistant Secretary
Eng. (Dr.) A. M. L. N. Gunathilaka	- Assistant Treasurer
Eng. K. P. M. D. D. N. Ferdinando	- Assistant Editor
Eng. L. Gunawickrema	- Committee Member
Eng. (Mrs.) A. D. S. Gunawardana	- Committee Member
Eng. M. Gamage	- Committee Member
Eng. (Dr) P. D. Dharmaratne	- Committee Member
Eng. A. R. M. D. N. B. Ranasinghe	- Committee Member
Eng. K.A.B.P. Kuruppu	- Committee Member

REPRESENTATIVES FROM UNIVERSITIES

Eng, (Prof.) (Mrs.) Chintha Jayasinghe	- University of Moratuwa
Eng, (Dr.) Udaya Dissanayaka	- University of Peradeniya
Eng. (Prof.) G. S. Y. De Silva	- University of Ruhuna
Eng. (Prof.) K. M. C. Konthesinghe	- University of J'Pura
Eng. (Dr.) B. Janarthanan	- University of Jaffna
Eng. (Dr.) T. Jeyakaran	- University of South Eastern
Lt. Col. O. M. R. Priyantha	- General Sir John Kotelawala Defense University

COMMITTEES OF ANNUAL SESSIONS – 2025

Organising Committee

Eng. (Prof.) S. M. A. Nanayakkara	-	Chairperson
Eng. (Dr.) A. M. L. N. Gunathilaka	-	Committee Member
Eng. K. A. B. P. Kuruppu	-	Committee Member

Selection Committee for the Best Paper Award

Eng. (Prof.) Priyan Dias

Eng. (Dr.) (Mrs.) Premini Hettiarachchi

Eng. A. S. B. Edirisinghe

Presentation Evaluation Committee

Eng. D.T. Rajasekaran

Eng. K. A. B. P. Kuruppu

Panel of Reviewers

Eng. (Dr.) (Mrs.) Premini Hettiarachchi
Eng. (Dr.) Chathura Rajapaksha
Eng. (Dr.) Gobithas Tharmarajah
Eng. (Dr.) Hasitha Damruwan
Eng. (Dr.) Isuru Wijewardana
Eng. (Dr.) K. Baskaran
Eng. (Prof.) Navaratnarajah Sakthiparan
Eng. (Prof.) Hiran Yapa
Eng. (Dr.) Pasindu Weerasingha
Eng. (Mrs.) Tharangika Jayasundara
Eng. K.L.S. Sahabandu
Eng. N. Abeysuriya
Eng. A. S. B. Edirisinghe
Eng. S. S. A. Kalugaldeniya
Eng. (Dr.) Sumudu Herath
Eng. (Dr.) Irindu Upasiri
Eng. (Prof.) Sudhira de Silva
Eng. Buddhika Edirisooriya
Eng. (Prof.) Chaminda Konthesinghe
Eng. (Prof.) Chinthaka Mallikaarchcchi
Eng. (Prof.) Kushan Wijesundara
Eng. Neomal Ferdinando

SOCIETY OF STRUCTURAL ENGINEERS, SRI LANKA

15th Annual Sessions

on 19th August 2025 at Cinnamon Grand Hotel, Colombo

PROGRAMME

08:30 - 09:00 Registration of Participants

09:00 - 09:05 National Anthem

09:05 - 09:15 Lighting of Oil Lamp

09:15 - 09:20 Welcome Address - Eng. Anuruddha Edirisinghe, Vice President – SSESL

Morning Session Chair - Eng. (Prof.) Kushan Wijesundara

09:20 - 09:30 Sponsor's Presentation 1

09:30 - 10:15 **Keynote Address – The Impact of the M7.7 Mandalay Earthquake on High-Rise Buildings with Long Natural Periods in Bangkok**
by Prof. Pennung Warnitchai

Department of Civil and Infrastructure Engineering (CIE)
Asian Institute of Technology, Thailand

10:15 – 10:30 Question Time – Keynote Address

10:30 – 10:45 **Structural Analysis of Pier and Capping Beam Systems during segmental construction and service stages of Balanced Cantilever Bridges - A Case Study**

M.S.S Haakeel, T. Ramachandran and, M.A.R.M.A Jabbar

10:45 – 11.00 **AI-Powered Integrity Assessment of Pre-Stressed Concrete Girders: Automated Damage Detection After Impact Events**

R.A. Dihan, S.V. Pinnalanda, D.M.A.A.G.B. Dissanayake, A.J. Dammika and, C.S. Bandara

11:00 – 11.15 **Experimental and Numerical Investigation of Shear-Deficient Reinforced Concrete Beams Strengthened with Ultra-High Performance Fiber Reinforced Concrete (UHPFRC) Jackets**

S. Wijesundara, I Abeykoon, S. Bandara and, K. Wijesundara

11:15 – 11.30 **Numerical Analysis of Web Crippling in Web Rib-stiffened Lipped Channel (WRLC) Beams with Perforations**

W.K.V.J.B. Kulsooriya, H.M.S.T. Herath and, D.P.P. Meddage

11:30 – 11.45 **Optimization of UHPFRC-Strengthened Square Bridge Piers for Enhanced Impact Resistance**

R. Thulakshan, N.T. Vandabona and, P.L.N. Fernando

11:45 – 12.00 **Review and Modelling of Effects of Corrosion in Dapped End Connections**

T. Ariyarathnam, H.G.H. Damruwan and, C. Rajapakse

12:00 – 12:30 Discussion of Papers

12:30 – 13:35 Lunch Break

Evening Session Chair - Eng. (Mrs.) Tharangika Jayasundara

13:35 – 13:45 Sponsor's Presentation 2

13:45 – 14:30 **Keynote Address - Supplementary Cementitious Materials (SCMs) in Pervious Concrete, Oxide Effect, and Machine Learning Insight**

by Prof. Navarathnarajah Sathiparan

Department of Civil Engineering,
University of Jaffna, Sri Lanka

14:30 – 14:45 **Investigating the Possibility of Partially Replacing Cement by Corn Cob Ash and Quicklime in Non-rectangular Interlocking Paving Blocks**

K.R.S.B Abeywardane and, A.M.L.N. Gunathilaka

14:45 – 15.00 **Assessment of Durability of Concrete Carrying Blended Sea Sand and Manufactured Sand**

H.M.S.A. Koswaththa, P.R.P.U.B. Abeyratne, H.A.D. S. Buddika and, H.D. Yapa

15:00 – 15:15 **Feasibility Assessment of using Recycled Plastic as a complete replacement for Coarse Aggregates in Structural Lightweight Concrete**

T. Abirami, C.S. Bandara, H.D. Yapa and, P.B.R. Dissanayake

15:15 – 15:30 **Study on Methods of Testing Tensile Strength of Concrete**

Z.R. Dole and, K. Baskaran

15:30 – 15:45 **Design and application of a small-scale test method for façade fire testing**

W.C.V. Fernando, R.S.S. Ranasinghe and, T.G.P.L. Weerasekera

15:45 – 16:00 **Review on the Effect of Moss Growth in Structures - Positive and Negative Impacts**

L.R. Irudhayaraj, I.R. Upasiri and, A. Amarasinghe

16:00 – 16:15 **Soil Engineering Based Characterization of Ceramic Clays in Sri Lanka**

B.G.N.M.S. Kumara, H.G.S. Mayuranga, A.G. Jayasinghe and, G.I.P. De Silva

16.15 – 16.45 Discussion of Papers

16.45 – 16.50 Vote of Thanks

16:50 onwards Afternoon Tea

CONTENTS

KEYNOTE 1:

The impact of the M7.7 Mandalay earthquake on high-rise buildings with long natural periods in Bangkok

Prof. Pennung Warnitchai

Professor of Structural Engineering,

Department of Civil and Infrastructure Engineering (CIE),

Asian Institute of Technology,

Thailand.

About the Keynote Speaker

Pennung Warnitchai received his doctoral degree in Civil Engineering from the University of Tokyo in 1990 and is currently Professor of Structural Engineering at the Asian Institute of Technology (AIT). He has been actively involved in research and practice in the fields of structural dynamics, earthquake engineering, wind effects on structures, bridge engineering and disaster management. Since 2002, he has been leading a long-term research program on "Mitigation of Earthquake Risk in Thailand" funded by the Thai Research Fund and later by the National Research Council of Thailand. More than 30 researchers from ten universities and three government agencies in Thailand have participated in this program. In the professional organizations, he was the chairman of the chapter on the effects of earthquakes and wind loads at the Engineering Institute of Thailand (EIT) from 2002 to 2016. He led a team of experts and professional engineers to develop the first official seismic design standard for buildings and structures in Thailand in 2009. Several of his research team's findings, such as new design spectra for long-period ground motions in the Bangkok basin and a new method for analyzing the seismic response of tall buildings, were translated into code of practice in this seismic standard. He is also currently Thailand's national delegate to the International Association for Earthquake Engineering (IAEE) and founding director of the Earthquake Research Center of Thailand (EARTH).

The Impact of the M7.7 Mandalay Earthquake on High-Rise Buildings with Long Natural Periods in Bangkok

P. Warnitchai

Abstract

Bangkok, the capital of Thailand, was significantly affected by the M7.7 Mandalay earthquake, even though it is located about 1000 km from the earthquake epicenter. The city lies on a large, 800 m deep soil basin, which can strongly amplify long-period ground motions. A large number of high-rise buildings with long natural periods were strongly shaken by the resonance effect of these amplified ground motions, causing great panic among building occupants. Several hundred of these buildings suffered minor to severe damage to non-structural components (e.g. partition walls, ceilings, elevators), about ten of them suffered significant damage in structural walls (concrete crushing and buckling of reinforcing bars), and one 30-storey building collapsed completely. This event is the most severe earthquake Bangkok has ever experienced in modern times. Bangkok is indeed prepared for the effects of such distant large earthquakes, as high-rise buildings have been designed and built since 2007 to withstand the expected long-period ground motions. The design spectrum was determined based on a comprehensive study of basin amplification and a probabilistic seismic hazard assessment. During this earthquake, ground motions were recorded at five seismic stations in Bangkok. Although the spectral accelerations of these recorded motions are lower than those of the design-basis earthquake, their impact on high-rise buildings appears to be disproportionately high. Subsequently, an investigation was conducted using the acceleration records at rooftop of two high-rise buildings and the time histories of lateral roof displacements of several high-rise buildings obtained from video clips using a pixel tracking technique. The result shows that the critical damping ratio of the fundamental vibration modes of these buildings is much lower than expected; it is about 1% instead of 2.5%--the value recommended by the Tall Buildings Initiative and adopted by the Thai national standard for earthquake-resistant design. This finding could explain the higher-than-expected impact on high-rise buildings in Bangkok from the distant large earthquake. It could also mean that the seismic design criteria for Bangkok will need to be significantly adjusted in the near future. It also suggests an effective method to suppress the seismic response: increasing the damping level by installing energy-absorbing devices in high-rise buildings.

The slides of Prof. Pennung's presentation are attached as an annex to the proceedings.

KEYNOTE 2:

Supplementary Cementitious Materials (SCMs) in Pervious Concrete, Oxide Effect, and Machine Learning Insight

Prof. Navarathnarajah Sathiparan

Professor of Civil Engineering,

Department of Civil Engineering,

University of Jaffna,

Sri Lanka.

About the Keynote Speaker

Prof. *Navarathnarajah* Sathiparan completed his undergraduate studies at the University of Moratuwa, followed by a Master of Engineering and Ph.D. from the University of Tokyo. He is a leading expert in the field of structural engineering, with a focus on seismic retrofitting of masonry structures, sustainable materials, pervious concrete design and modelling, and the application of machine learning for predicting the properties of construction materials. With over 150 peer-reviewed journal articles and conference proceedings published, Prof. Sathiparan has made significant contributions to advancing the understanding of construction material behaviour and structural resilience. His research integrates innovative materials and advanced modelling techniques to enhance the performance of infrastructure. Prof. Sathiparan is also recognized for his academic excellence, having been included in the prestigious Stanford/Elsevier's Top 2% Scientist Rankings in 2023. His work continues to shape the direction of research in sustainable construction practices and the application of AI in engineering.

Supplementary Cementitious Materials (SCMs) in Pervious Concrete, Oxide Effect, and Machine Learning Insight

N Sathiparan[1]

Abstract

This study investigates a synergistic approach to designing sustainable pervious concrete by integrating Supplementary Cementitious Materials (SCMs) with Machine Learning (ML). Pervious concrete offers an elegant solution to urban stormwater management, but achieving a critical balance between high permeability and adequate compressive strength remains a challenge. The research demonstrates how the strategic use of SCMs, guided by their "oxide effect" and pozzolanic reactions, can significantly enhance the material's mechanical and durability properties while reducing its carbon footprint. Furthermore, the study examines the transformative potential of ML models to accurately predict key properties, such as compressive strength and permeability. This predictive capability circumvents the traditional, time-consuming, and resource-intensive trial-and-error process, enabling the efficient optimization of mix designs. The findings suggest that combining SCMs with ML provides a robust framework for developing durable, cost-effective, and environmentally friendly pervious concrete, paving the way for more sustainable construction practices.

1. Introduction

Pervious concrete, a unique and environmentally beneficial construction material, has gained significant attention for its ability to manage stormwater runoff, replenish groundwater, and mitigate urban heat island effects. Unlike conventional concrete, pervious concrete is designed with a high void content, allowing water to infiltrate directly through its structure. This characteristic, while advantageous for hydrological management, presents a critical challenge: striking an optimal balance between sufficient permeability and adequate compressive strength to ensure structural integrity [1]. The inherent trade-off necessitates innovative approaches to mix design, with Supplementary Cementitious Materials (SCMs) emerging as a cornerstone for enhancing the performance of pervious concrete. This paper explores the fundamental aspects of pervious concrete, including the critical factors that influence its properties, the subtle yet profound "oxide effect" of SCMs, and the transformative potential of Machine Learning (ML) in optimizing its design and predicting its behavior [2].

1.1 Applications and the strength-permeability balance

Pervious concrete finds diverse applications in sustainable urban development, including parking lots, sidewalks, low-volume roads, residential streets, and sports courts. Its primary function is to facilitate stormwater infiltration, thereby reducing the burden on conventional drainage systems, preventing localized flooding, and minimizing the runoff of pollutants into natural water bodies. The defining characteristic of pervious concrete is its interconnected void structure, typically ranging from 15% to 35% of the total volume [3]. This porosity directly dictates its permeability, allowing water to pass through at rates significantly higher than traditional concrete. However, this high void content inherently compromises its compressive strength. A delicate balance must be struck: sufficient strength to withstand anticipated loads without compromising the required permeability. For most applications, a compressive strength between 2.8 MPa and 28 MPa is acceptable, depending on traffic intensity and structural demands, while permeability rates often exceed 100 mm/hour [4].

1.2 Requirement of cement and role of SCMs

In pervious concrete, cement acts as the primary binder, forming a thin paste that coats the coarse aggregate particles and creates the skeletal structure. Due to the limited fine aggregate content or its complete absence, the cement paste plays an even more crucial role in binding the coarse aggregates together. However, relying solely on Portland cement can lead to several issues:

- Environmental impact: Cement production is energy-intensive and a significant contributor to CO_2 emissions.
- Increased drying shrinkage: High cement content can lead to more significant shrinkage.
- Higher heat of hydration: Can cause thermal cracking, especially in thicker sections.

This is where Supplementary Cementitious Materials (SCMs) become indispensable. SCMs are finely divided materials that, when used in conjunction with Portland cement, contribute to the properties of hardened concrete through hydraulic or pozzolanic activity, or both. Possible embodied energy and CO_2 emission reduction by using SCMs as cement replacement in pervious concrete is illustrated in Figure 1. The role of SCMs in pervious concrete is multifaceted:

- Enhanced strength: SCMs react with calcium hydroxide ($Ca(OH)_2$), a byproduct of cement hydration, to form additional calcium silicate hydrate (C-S-H) gel, which is the primary source of concrete strength. This pozzolanic reaction densifies the paste-aggregate interface and fills larger pores, leading to improved strength [5].

[1] Department of Civil Engineering, University of Jaffna.
(e-mail: sakthi@eng.jfn.ac.lk)

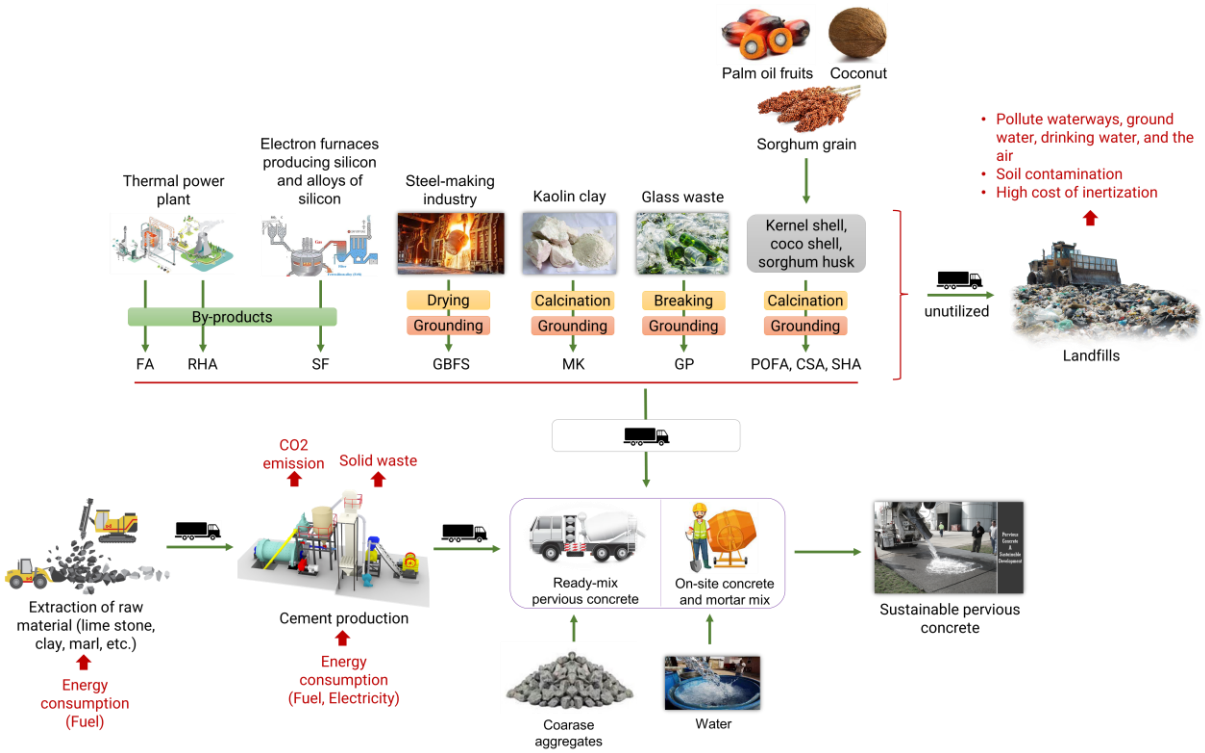

Figure 1: Possible embodied energy and CO_2 emission reduction by using SCMs as cement replacement in pervious concrete [2]

- Refined pore structure: By filling micro-pores and reducing the size of larger pores, SCMs can optimize the void structure, potentially improving strength without significantly compromising permeability.
- Improved durability: SCMs enhance resistance to sulfate attack, alkali-silica reaction (ASR), and chloride ingress, extending the service life of pervious concrete.
- Reduced permeability (of the paste): While pervious concrete needs overall high Permeability, SCMs can reduce the permeability of the cement paste itself, leading to a more durable and less susceptible binder.
- Environmental benefits: Utilizing industrial byproducts as SCMs reduces waste in landfills and lowers the carbon footprint associated with cement production.

1.3 Factors affecting compressive strength and permeability of pervious concrete

The performance of pervious concrete is highly sensitive to its mix design and construction parameters. Understanding these factors is crucial for achieving the desired balance of strength and permeability.

- Aggregate size and gradation: The size and gradation of coarse aggregates are perhaps the most critical factors. Pervious concrete typically uses single-sized or narrowly graded coarse aggregates (e.g., 9.5 mm to 19 mm). Larger aggregate sizes generally lead to higher void content and thus higher permeability but lower compressive strength due to fewer contact points between aggregates and a thinner paste coating. Smaller aggregate sizes result in lower void content, lower permeability, and generally higher compressive strength due to more aggregate contact points and a denser packing.
- Aggregate-to-binder (Agg/B) ratio: The aggregate-to-binder ratio dictates the amount of paste available to coat the aggregates. A higher Agg/B ratio means less paste, leading to higher void content and higher permeability, but potentially lower strength if there is not enough paste to adequately bind the aggregates. A lower Agg/B ratio implies more paste, which can fill more voids, leading to lower permeability and potentially higher strength; however, it also risks clogging the pore structure if excessive.
- Compaction: Compaction is vital for achieving the desired density and strength without excessively reducing permeability. Insufficient compaction leads to very high void content, resulting in low strength and a fragile structure. Excessive compaction can crush the aggregates, significantly reduce the void content, and drastically lower permeability, thereby defeating the purpose of pervious concrete. Optimal compaction ensures adequate bonding between aggregates while maintaining interconnected voids.
- Water-to-cement (W/C) ratio: The W/C ratio influences the workability of the fresh paste and the strength of the hardened paste. A lower W/C ratio generally leads to higher compressive strength due to a denser cement paste, but can reduce workability, making proper coating of aggregates difficult. A higher W/C ratio increases workability but reduces the strength of the cement paste, leading to lower overall strength. For pervious concrete, a very low W/C ratio (typically 0.28 to 0.33) is often used to ensure a stiff, non-slumping mix that adheres well to the aggregates without flowing into and blocking the voids.

1.4 Importance of prediction of compressive strength of pervious concrete

Predicting the compressive strength and permeability of pervious concrete is essential for several key reasons. Compressive strength ensures that concrete can withstand the load and pressure it faces and it is vital in determining the right mix design for concrete in various construction applications, ensuring it performs as required. Accurate predictions help optimize material usage, reducing waste and ensuring both strength and drainage without compromising the concrete's structural integrity. This leads to cost-efficient construction practices by avoiding the use of overly strong or inadequate concrete. Predicting compressive strength ensures that the concrete mix meets the required specifications without excess material, saving costs in the long run. Pervious concrete offers environmental benefits, such as reducing surface runoff and improving groundwater recharge. By predicting the permeability, engineers can ensure that the concrete functions as intended, contributing to sustainability efforts and environmental protection. Furthermore, these predictions support the development of safer, more durable designs, especially in high-traffic or flood-prone areas, ensuring the structures are both resilient and safe. In addition, predictive methods help construction projects comply with regulatory standards regarding concrete strength and permeability, preventing potential legal issues. They also allow for long-term performance monitoring, enabling early detection of any potential issues before they lead to significant damage.

1.5 The Oxide effect in SCMs

The beneficial effects of SCMs in concrete, particularly in pervious concrete, are intrinsically linked to their chemical composition, specifically the presence and reactivity of various oxides. Range of chemical composition of supplementary cementitious materials varies as shown in Figure 2. The "oxide effect" refers to how the proportions of key oxides, such as silicon dioxide (SiO_2), aluminum oxide (Al_2O_3), iron oxide (Fe_2O_3), and calcium oxide (CaO), in SCMs influence their pozzolanic or hydraulic activity and, consequently, the properties of the concrete.

- Calcium Oxide (CaO): The CaO content in SCMs (especially in GGBS and some fly ashes) determines their hydraulic potential. SCMs with higher CaO content can exhibit self-cementitious properties or accelerate the hydration of Portland cement, thereby contributing to early strength development. The CaO/SiO_2 ratio in SCMs is a significant indicator of their reactivity and the type of C-S-H gel formed.
- Silicon Dioxide (SiO_2): This is the primary component responsible for the pozzolanic reaction. Reactive silica in SCMs (e.g., fly ash, silica fume, metakaolin, RHA) reacts with the calcium hydroxide ($Ca(OH)_2$) released during cement hydration to form additional C-S-H gel. A higher content of amorphous and reactive SiO_2 generally leads to greater strength development and pore refinement. Silica fume, for instance, is almost pure amorphous silica, making it highly reactive.

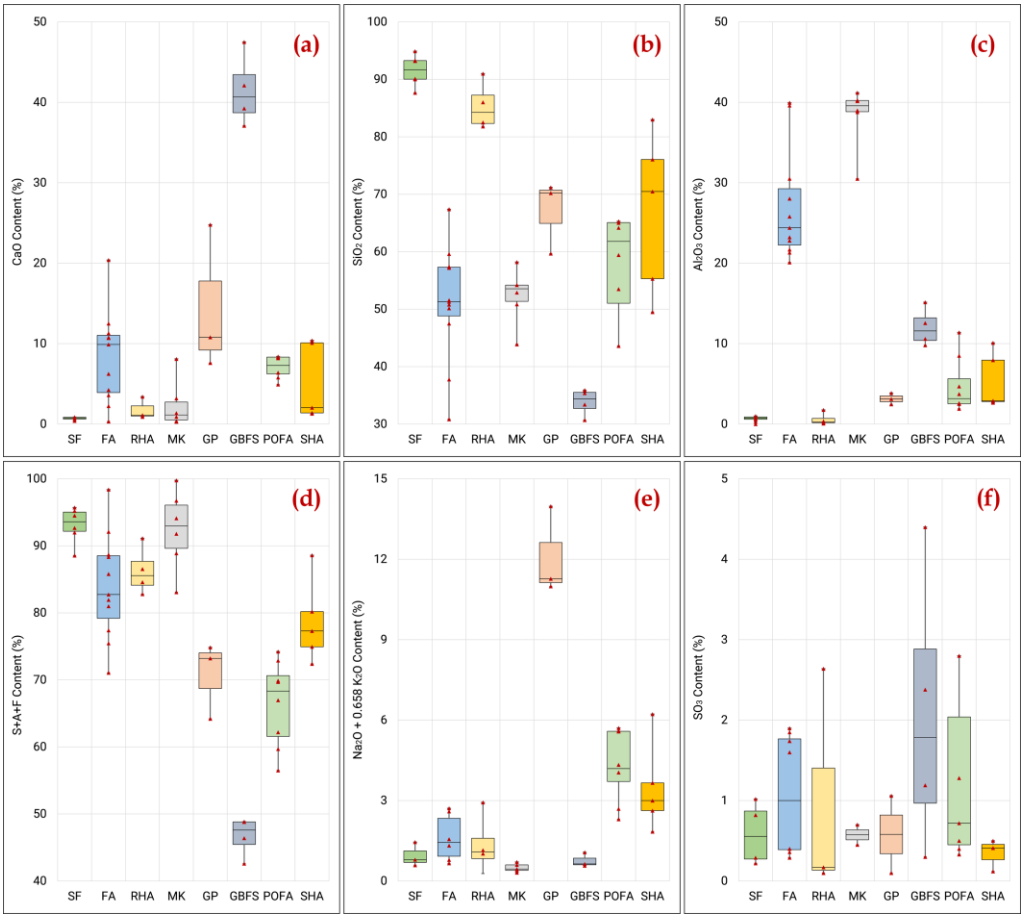

Figure 2: Range of chemical composition of supplementary cementitious materials [2]

- Aluminum Oxide (Al_2O_3): Alumina contributes to the formation of calcium aluminate hydrate (CAH) and contributes to the early strength development, especially in the presence of sulfates. In SCMs like fly ash and GGBS, Al_2O_3 can participate in complex reactions that modify the C-S-H structure, influencing both strength and durability.
- Iron Oxide (Fe_2O_3): While less reactive than SiO_2 and Al_2O_3, iron oxide can also contribute to the pozzolanic reaction to a lesser extent. Its presence can influence the color of the concrete, but generally has a minor direct impact on strength compared to silica and alumina.

The synergistic interaction of these oxides dictates the overall reactivity of an SCM. For example, a high SiO_2 content ensures good long-term strength development, while an optimal balance with Al_2O_3 and CaO can improve early strength and overall microstructure. Understanding the oxide effect enables a more informed selection and proportioning of SCMs to achieve specific performance targets in pervious concrete, thereby optimizing the strength-permeability balance and enhancing durability.

1.6 Machine learning insight for pervious concrete optimization

The complex interplay of mix design parameters, SCM types, and the "oxide effect" makes traditional empirical methods for pervious concrete mix design challenging and time-consuming. This is where ML offers a decisive paradigm shift. ML algorithms can identify intricate, non-linear relationships within large datasets, enabling more accurate predictions and optimization. ML models (e.g., Artificial Neural Networks (ANN), Support Vector regression (SVM), K-Nearest Neighbors (KNN), Decision Tree, eXtreme Gradient Boosting (XGB)) can be trained on experimental data to predict key properties like compressive strength and permeability based on input parameters such as: aggregate size, Agg/B ratio, W/C ratio, compaction effort, curing days, SCM type and dosage and chemical composition (oxide percentages) of SCMs. the architecture of the ML models is shown in Figure 3.

By inputting mix design parameters, engineers can quickly estimate the expected performance, significantly reducing the need for extensive trial mixes. ML algorithms, particularly optimization techniques coupled with predictive models, can be used to identify optimal mix proportions that satisfy multiple performance criteria simultaneously (e.g., maximizing permeability while maintaining a minimum compressive strength). This allows for data-driven, efficient design of pervious concrete for specific applications. ML models can quantify the relative importance of different input features on the output properties. This can reveal which factors (e.g., aggregate size vs. SCM type) have the most significant impact on strength or permeability, guiding future research and practical mix design decisions. The integration of ML into pervious concrete research and practice promises to accelerate material development, enhance performance predictability, reduce costs, and promote the broader adoption of this sustainable material.

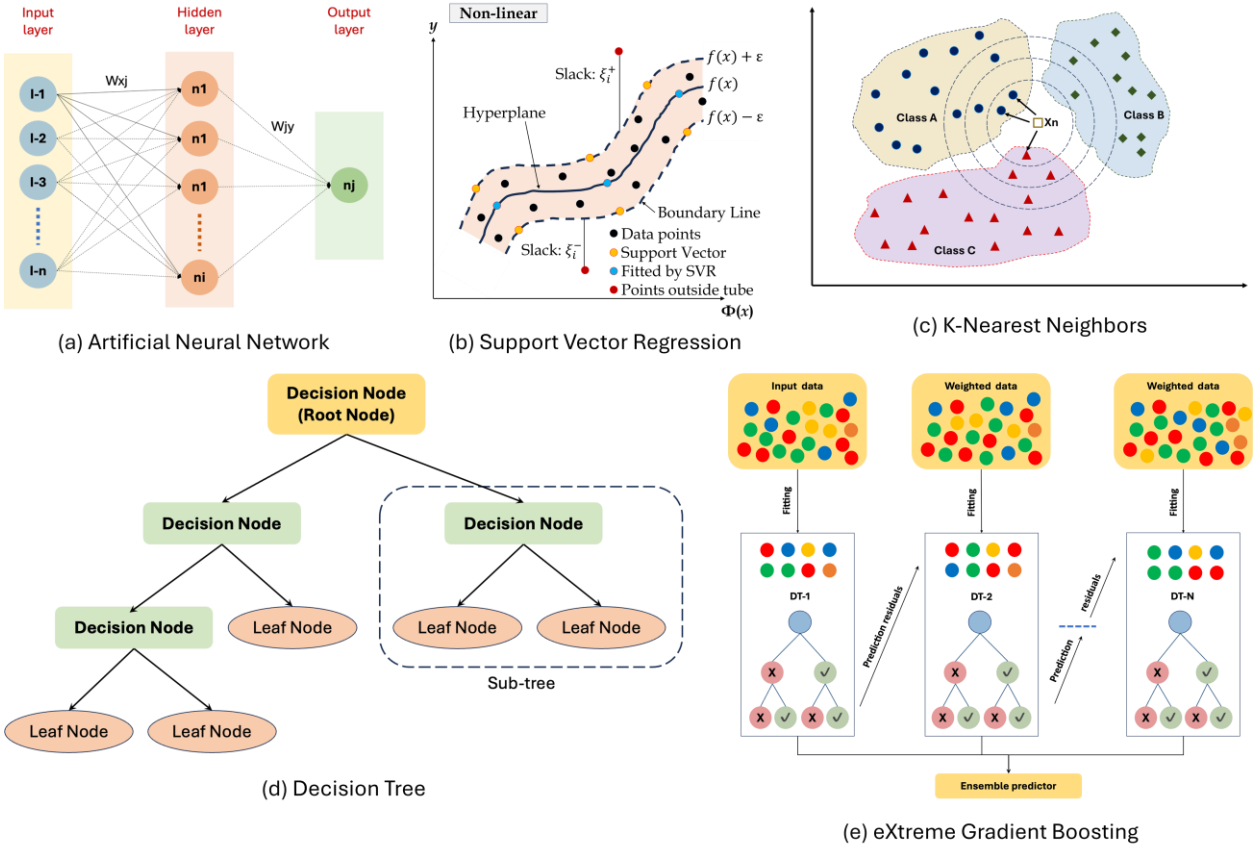

(a) Artificial Neural Network (b) Support Vector Regression (c) K-Nearest Neighbors

(d) Decision Tree (e) eXtreme Gradient Boosting

Figure 3: Standard machine learning models are used for the prediction of properties of pervious concrete [6]

2. Methodology

Figure 4 outlines a framework for analyzing the compressive strength of pervious concrete. The methodology includes data cleaning, dataset preparation, split into 70% training and 30% testing for ML models.

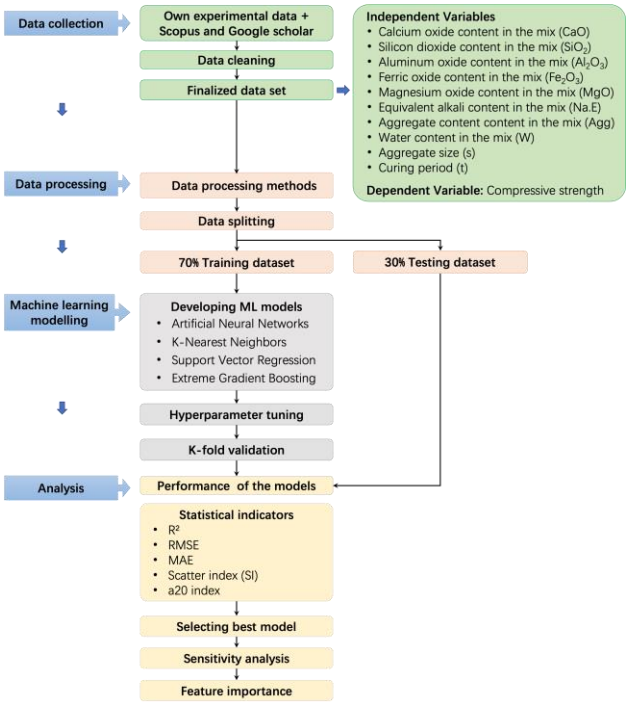

Figure 4: Methodology flowchart for machine learning model

2.1 Data Collection

The dataset used in this study was derived from the authors' previous research, which examined pervious concrete compositions, particularly those incorporating various Supplementary Cementitious Materials (SCMs). The dataset was obtained through a systematic literature review, conducted following the PRISMA methodology, to ensure comprehensive coverage of relevant studies. A total of 659 observations were collected from our experiments and published articles, meeting the criteria of providing detailed information on the chemical compositions of SCMs and their corresponding mix designs. These studies were carefully selected based on their relevance to hydration processes and microstructural formation in pervious concrete. Key input variables included the chemical compositions of calcium oxide (CaO), silicon dioxide (SiO_2), ferric oxide (Fe_2O_3), aluminum oxide (Al_2O_3), magnesium oxide (MgO), equivalent alkali content, aggregate content, water content, aggregate size, and curing period. The final dataset is robust enough to serve as the foundation for developing predictive models to estimate compressive strength in pervious concrete mixtures.

2.2 Machine Learning Algorithms

Several ML models were evaluated for their ability to predict compressive strength: Artificial Neural Network (ANN: Chosen for its ability to model complex, non-linear relationships between inputs and outputs. ANN learns intricate patterns in the data and is flexible in adapting to more data over time), K-Nearest Neighbors (KNN: A simpler, distance-based model that relies on the similarity between data points. Although compelling for capturing local patterns, it can struggle with high-dimensional data), Support Vector Regression (SVR: Effective for capturing complex relationships, especially when data is high-dimensional, using kernel functions for non-linear transformations), and Extreme Gradient Boosting (XGB: A tree-based model that uses boosting to improve performance iteratively by minimizing residuals from previous iterations). These models were selected for their distinct strengths in handling complex data and their applicability to predicting compressive strength in concrete materials.

2.3 Performance Indicators

The performance of each model was assessed using the following metrics: Coefficient of Determination (R^2: Measures the proportion of variance explained by the model. An R^2 closer to 1 indicates a better fit), Root Mean Square Error (RMSE: Measures the average deviation between predicted and actual values. Lower RMSE indicates better model performance), Mean Absolute Error (MAE: Provides the average absolute difference between predictions and actual outcomes), Scatter Index (SI: Measures the dispersion of errors, with lower values indicating better performance), and a20-Index: Represents the proportion of predictions falling within 20% of the actual values)

2.4 Hyperparameter Tuning

Hyperparameters for each ML model were fine-tuned to optimize performance. For instance, ANN: Activation functions (TanH, Gaussian) and layer configurations were explored to enhance training, SVR: Kernel type and cost parameters were adjusted to control the complexity of the model, and XGB: Hyperparameters like tree depth, subsample size, and learning rate were tuned to improve the model's accuracy.

2,5 K-Fold Validation

The K-fold validation method was used to assess the generalization capability of the models. The dataset was divided into K subsets, with one subset used for testing and the remaining for training. The results were averaged to evaluate model performance across different folds. This helped to identify overfitting or underfitting issues and ensure that the models perform consistently on new, unseen data.

3. Results and Discussion

3.1 Performance of the models

The performance of various ML models – ANN, KNN, SVR, and XGB – was evaluated to predict the compressive strength of pervious concrete. The models were trained on raw data, and their predictive capabilities were assessed using several key performance indicators on both the training and testing datasets. As shown in Figure 5, all four models demonstrated a high degree of accuracy, with R^2 values ranging from 0.88 to 0.99 on the training data and 0.75 to 0.92 on the testing data. A high R^2 value (closer to 1) indicates that the model can explain a large proportion of the variance in the observed data.

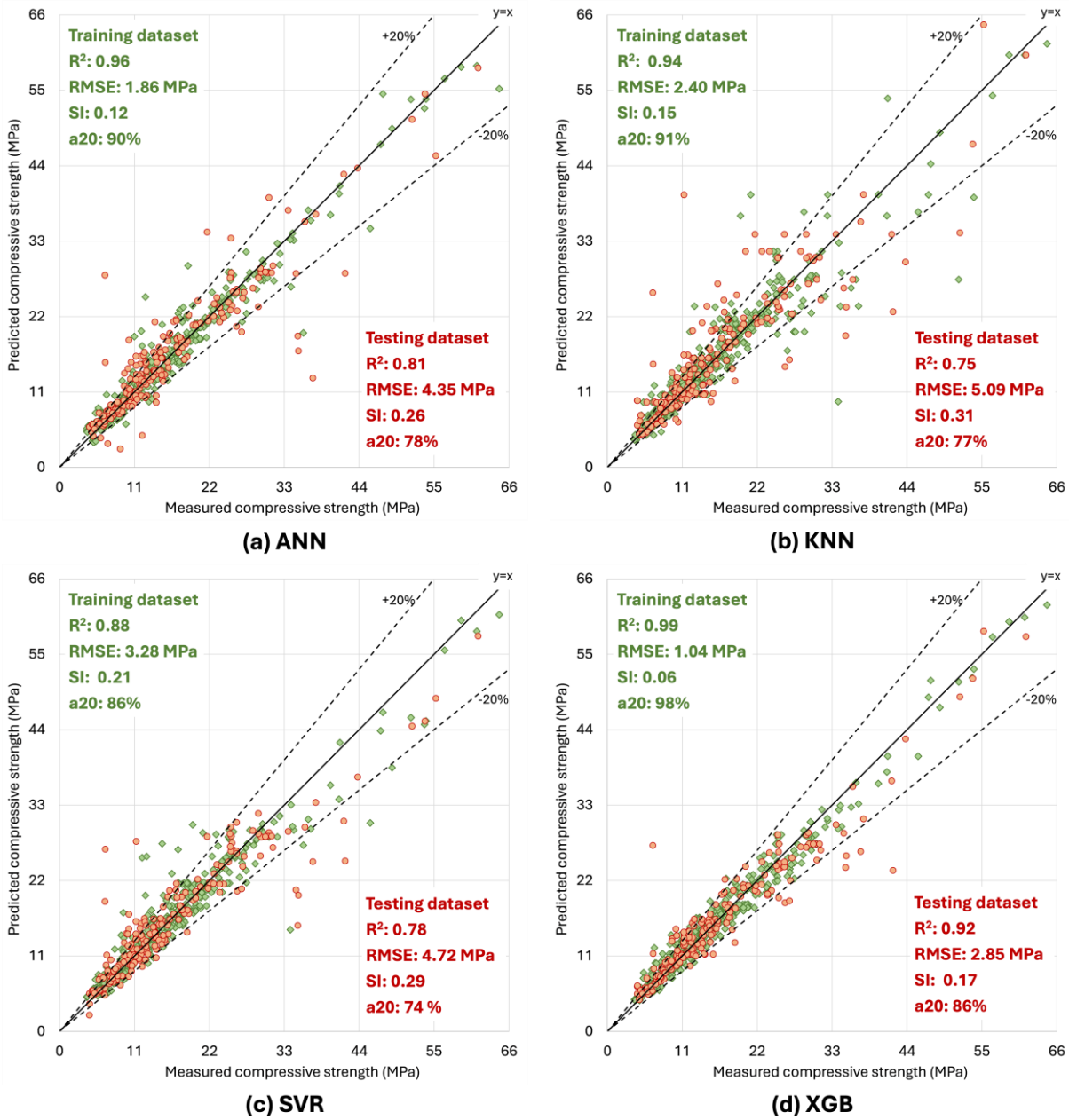

Figure 5: Predicted and actual compressive strength using various machine learning models (a) ANN, (b) KNN, (c) SVR, and (d) XGB

XGB emerged as the best-performing model, exhibiting the highest R^2 of 0.99 on the training set and 0.92 on the test set. It also had the lowest RMSE of 1.04 MPa and the lowest Scatter Index (SI) of 0.06 on the training data, with similarly superior performance on the test data (RMSE: 2.85 MPa, SI: 0.17). This indicates that the XGBoost model not only fitted the training data exceptionally well but also generalized effectively to unseen data, making it a robust predictive tool for the compressive strength of pervious concrete. Its high a20-index of 86% on the test set further confirms its reliability, meaning that 86% of its predictions were within a 20% error margin of the actual values. The superior performance of tree-based ensemble methods, such as XGB, is often attributed to their ability to capture complex, non-linear relationships and interactions between input variables.

ANN also performed very well, securing the second-highest R^2 on both the training (0.96) and test (0.81) sets. Its low RMSE and SI values suggest strong predictive accuracy. However, there is a more significant drop in its R^2 from the training to the test set (from 0.96 to 0.81) compared to XGB, indicating a slight tendency towards overfitting, though its generalization ability remains strong. KNN demonstrated a respectable performance, with a training R^2 of 0.94 and a test R^2 of 0.75. However, its higher RMSE and SI values compared to ANN and XGB suggest that its predictions were less accurate, with larger average errors. SVR, although still a viable model, demonstrated the lowest performance among the four, with a training R^2 of 0.88 and a test R^2 of 0.78. Its higher RMSE and SI on both datasets indicate a greater discrepancy between its predictions and the actual values, making it the least precise model in this comparison.

The results demonstrate that ML models are highly effective tools for predicting the compressive strength of pervious concrete. The use of advanced ensemble methods,

such as XGBoost, offers an exceptionally accurate and reliable approach, surpassing other models in both fitting and generalization performance. The high R^2 values for all models on the test data, with a minimum of 0.75, highlight their potential for practical application in mix design and quality control. This approach not only saves time and resources associated with physical testing but also provides a deeper understanding of how various input parameters influence the final properties of the material.

3.2 Sensitivity analysis

SHAP (SHapley Additive exPlanations) analysis provides valuable insights into the factors that influence concrete's compressive strength. It assigns SHAP values to each parameter, allowing a detailed understanding of their contributions and plot in Figures 6 and 7. The curing period also plays a critical role in increasing compressive strength. Longer curing times correspond to higher strength, as more complete hydration occurs, resulting in a denser microstructure. However, insufficient curing, leading to premature drying, negatively affects hydration, as indicated by negative SHAP values, highlighting the importance of proper curing practices for optimal concrete performance. The analysis of water content reveals a more complex relationship with compressive strength. While adequate water levels support the hydration process, a water content exceeding the optimal ratio dilutes the cement paste, reducing its density and strength. Thus, achieving a balanced water-to-cement ratio is essential for maximizing compressive strength. The dual trend observed in water content emphasizes the need for precise control during mixing. The size of aggregates generally contributes positively to compressive strength. Larger aggregates reduce voids in the mix, improving the concrete's load-bearing capacity. However, very large aggregates can reduce workability and bonding, which may negatively impact strength. Thus, selecting the appropriate aggregate size is crucial for achieving a balance between strength and workability. In contrast, aggregate content has the least influence on compressive strength, with its contribution being overshadowed by other factors, such as Al_2O_3 content and curing time. Despite this, the right mix of aggregates is still essential for achieving the desired strength characteristics.

Al_2O_3 content stands out as a significant positive contributor to compressive strength. The analysis indicates that increases in Al_2O_3 concentration enhance the concrete's ability to form stable bonds during hydration, likely due to its role in pozzolanic reactions. This finding is consistent with the existing literature, which highlights the importance of alumina in promoting the formation of calcium-aluminate hydrates, a crucial step in strength development. MgO content shows a positive correlation with compressive strength at moderate levels, contributing to the formation of additional hydration products. However, excessive MgO content can cause unsoundness, which affects the concrete's quality, indicating the importance of carefully managing MgO incorporation in the mix. The analysis of equivalent Na_2O reveals that while higher levels improve workability, excessive Na_2O has a negative impact on long-term strength. Similarly, Fe_2O_3 exhibits a generally adverse effect on compressive strength at higher concentrations due to the formation of weaker phases in the concrete matrix. Lastly, SiO_2 and CaO exhibit complex relationships with compressive strength. SiO_2 has a positive impact at lower concentrations, but its effect diminishes as levels rise, potentially due to reduced reactivity in hydration. In contrast, CaO consistently enhances compressive strength, underscoring its crucial role in improving the cementitious properties of the mix. Overall, the SHAP analysis reveals that factors such as Al_2O_3 content, curing period, and water content are critical drivers of compressive strength. Understanding the influence of these parameters enables the formulation of more effective concrete mixes, enhancing both structural performance and durability.

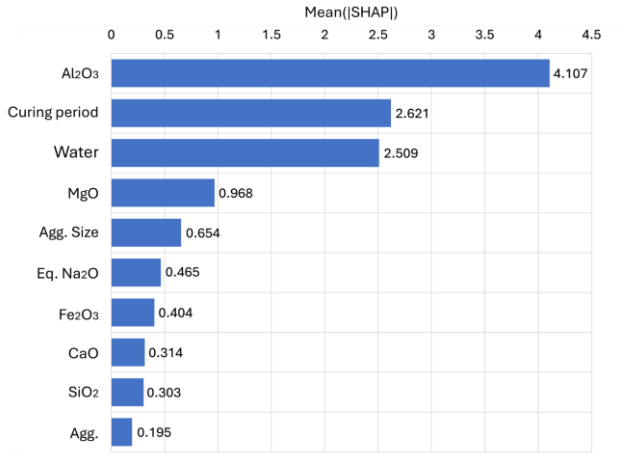

Figure 6: Mean SHAP plot for output of XGB model with raw data

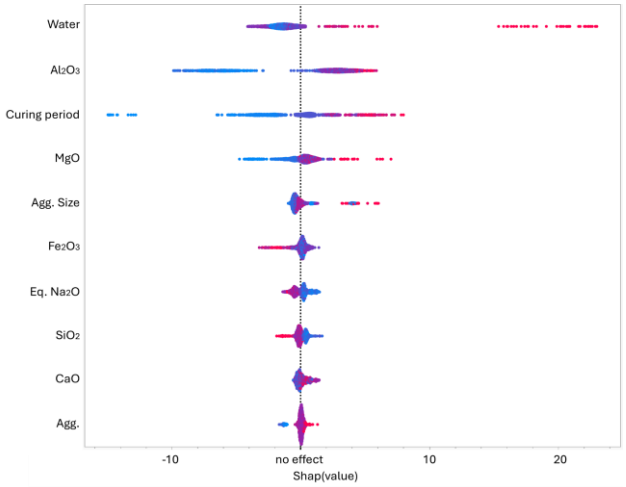

Figure 7: Summary SHAP plot for the output of the XGB model with raw data

3.3 Feature importance

The feature importance analysis for predicting compressive strength is shown in Table 1 and provides valuable insights into the impact of various parameters on model performance. Using the XGB model with the raw dataset, the model demonstrated strong predictive capability, achieving high accuracy during training and testing, with low prediction errors.

Table 1. Performance indicators for the XGB model with one input variable left out

Removed parameter	Train				Test				Rank
	R^2	RMSE (MPa)	SI	a20 (%)	R^2	RMSE (MPa)	SI	a20 (%)	
None	0.99	1.04	0.06	98	0.92	2.85	0.17	86	-
CaO	0.97	1.68	0.11	92	0.89	3.30	0.20	83	3
SiO_2	0.98	1.37	0.09	95	0.90	3.16	0.19	80	4
Al_2O_3	0.98	1.33	0.08	96	0.91	3.07	0.19	80	5
Fe_2O_3	0.99	1.13	0.07	98	0.91	3.11	0.19	86	8
MgO	0.98	1.25	0.08	96	0.91	3.02	0.18	85	9
Eq.Na_2O	0.97	1.51	0.09	94	0.91	3.10	0.19	83	6
Agg.	0.99	1.02	0.06	98	0.91	3.09	0.19	83	7
Water content	0.95	2.14	0.13	91	0.85	3.92	0.24	76	2
Agg.Size	0.98	1.28	0.08	97	0.92	2.83	0.17	86	10
Curing period	0.72	5.01	0.31	64	0.55	6.80	0.41	56	1

When parameters were removed one by one, notable changes in model performance were observed. For example, removing CaO resulted in a noticeable drop in both training and testing performance, accompanied by an increase in error metrics, underscoring the critical role of CaO in the model's accuracy. Similarly, removing SiO_2 resulted in a decrease in performance and an increase in error values, further underscoring the importance of this component. Al_2O_3 showed a slightly less severe impact but still contributed meaningfully to the model.

The removal of Fe_2O_3 had a negligible effect on training performance but significantly impacted testing accuracy, suggesting that Fe_2O_3 plays a role in improving the model's generalization to new data. Other parameters like MgO and Eq.Na_2O also showed performance declines when removed, indicating its moderate importance. Aggregate content had a slight impact on performance, emphasizing its relevance, though not as critical as the aforementioned parameters.

Water content proved to be highly significant, with its removal leading to a substantial increase in error metrics, indicating its essential role in accurate predictions. In contrast, aggregate size had the least influence on the model, suggesting that it is less critical than other parameters. Finally, the curing period had the most significant effect on the model's performance. Its removal caused drastic declines in all metrics, confirming its status as the most crucial parameter for predicting compressive strength.

3.4 Future research prospects

The future research directions in the paper are discussed as follows:

- Expansion of dataset diversity: Future research could benefit from expanding the dataset to include a broader range of supplementary cementitious materials (SCMs) and concrete formulations. Including more diverse materials and varying environmental conditions could help improve the generalizability of the models and further enhance the robustness of predictions.
- Optimized data processing techniques: Further research could investigate the optimization of data preprocessing, such as advanced feature extraction or dimensionality reduction methods, to enhance model performance. Exploring new data transformation methods could help mitigate data bias and improve predictive power.
- Consideration of long-term performance: Future studies could focus on investigating the long-term durability and performance of pervious concrete under varying environmental conditions. This includes assessing the impact of long-term exposure to weathering, chemical attacks, or mechanical stress on predictions of compressive strength.
- Development of predictive models for other pervious concrete properties: Expanding beyond compressive strength, future research could aim to predict other essential properties of concrete, such as permeability, durability, and resistance to cracking. Incorporating additional performance metrics into predictive models can provide more comprehensive solutions for optimizing concrete mix design.
- Integration with sustainable construction practices: Future work could also explore how the predictive models can be integrated with sustainable construction practices, including reducing the carbon footprint of concrete production, optimizing the use of recycled materials, and improving the environmental performance of concrete mixtures.

These directions aim to enhance existing models, broaden the scope of research, and ensure that predictive tools are more applicable to real-world construction scenarios.

4. Conclusion

Pervious concrete represents a critical innovation in sustainable civil engineering, offering an elegant solution to urban stormwater management and the environmental challenges posed by traditional construction materials. The core challenge of balancing high permeability with adequate compressive strength can be effectively addressed through the strategic incorporation of Supplementary Cementitious Materials (SCMs).

This paper has demonstrated the multifaceted role of SCMs, highlighting how they not only improve the mechanical and durability properties of pervious concrete through pozzolanic and hydraulic reactions but also significantly contribute to a reduced carbon footprint. The "oxide effect"—where the chemical composition of SCMs

dictates their reactivity—was identified as a key factor governing material performance. Furthermore, the paper underscored the transformative potential of ML in optimizing pervious concrete mix designs. By predicting properties like compressive strength and Permeability, ML models can circumvent the time-consuming and resource-intensive nature of traditional trial-and-error methods. This predictive capability is crucial for designing durable, safe, and cost-effective pervious concrete structures that meet both structural and environmental requirements.

References

[1] S.A. Ahmad, H.U. Ahmed, S.K. Rafiq, F.S. Jafer, K.O. Fqi, A comparative analysis of simulation approaches for predicting permeability and compressive strength in pervious concrete, Low-carbon Materials and Green Construction 2(1) (2024) 10.

[2] N. Sathiparan, D.H.H.P. Dassanayake, D.N. Subramaniam, Utilization of supplementary cementitious materials in pervious concrete: a review, International Journal of Environmental Science and Technology 21(6) (2024) 5883-5918.

[3] A. Ibrahim, E. Mahmoud, M. Yamin, V.C. Patibandla, Experimental study on Portland cement pervious concrete mechanical and hydrological properties, Construction and Building Materials 50 (2014) 524-529.

[4] V.V. Hung, S.-Y. Seo, H.-W. Kim, G.-C. Lee, Permeability and Strength of Pervious Concrete According to Aggregate Size and Blocking Material, Sustainability, (2021) 426.

[5] K. Moolchandani, Industrial byproducts in concrete: A state-of-the-art review, Next Materials 8 (2025) 100593.

[6] N. Sathiparan, P. Jeyananthan, D.N. Subramaniam, A machine learning approach to predicting pervious concrete properties: a review, Innovative Infrastructure Solutions 10(2) (2025) 55.

Structural Analysis of Pier and Capping Beam Systems During Segmental Construction and Service Stages of Balanced Cantilever Bridges-A Case Study

M S S Haakeel*[1], T Ramachandran [1], M A R M A Jabbar[1]

Abstract

Balanced cantilever construction involves the symmetrical placement of precast segments on both sides of a pier toward midspan, with a closure segment cast to complete the span once segments from the adjacent piers converge. This case study investigates the structural behavior of a two-span post-tensioned concrete box girder bridge, with each span of 30.0 m. The analysis focuses on the internal force response of the pier and capping beam system during both segmental construction and the service stages. The bridge pier consists of a stem that splits into two inclined columns forming a V-shape, which monolithically supports the capping beam. A finite element model developed in SAP2000 using shell and frame elements to evaluate internal force behavior. During the segmental construction stage, 3.0 m precast box girder segments were launched incrementally from the capping beam toward midspan, extending up to 15.0 m on one side and 12.0 m on the other to simulate a typical unbalanced condition. Load considerations included dead and live loads. The service stage analysis considered the complete two-span system under permanent dead loads, superimposed dead loads, and live loads applied over one span to represent critical loading on the central pier capping beam system. The results indicate that internal forces in the pier and capping beam system differ significantly between the segmental construction and service stages. Critical internal forces governing the design have been identified for each stage. During the service stage, the capping beam experiences longitudinal bending moments up to 10,775 kNm, necessitating appropriate reinforcement. The pier column axial force reaches 5,897 kN, with biaxial bending also accounted for to assess the column's bending capacity. Overturning moments during segmental construction generate substantial transverse effects that must be addressed in the design. Using both shell and frame element analysis approach provides accurate and reliable structural assessment.

Keywords: finite element, box girder, balance cantilever

1. Introduction

The balanced cantilever method is widely used in long-span bridge construction, particularly in locations where ground supports are impractical, such as deep valleys, rivers, and urban areas. This technique enables the erection of bridge superstructures without the need for extensive scaffolding [1]. This method involves the construction of symmetrical, either precast or cast-in-place (CIP), segments on both sides of piers, which helps to maintain balanced structural forces throughout each stage of the construction process [2, 3]. Segments are placed up to the midspan of both sides of the piers, while other segments are converged from the adjacent piers or abutments, and closure segments are then installed to complete the superstructure [4, 7]. Key advantages of the balanced cantilever method include reduced environmental impact, accelerated construction timelines, and enhanced adaptability to complex site geometries [5, 6]. However, despite these benefits, practical challenges can arise during the staged construction process. One of the drawbacks of the balanced cantilever method is the occurrence of intermediate imbalance during segmental construction when one side has an extra segment compared to the other, resulting in unbalanced internal forces within the pier and capping beam system. In some cases, these forces are more severe than those experienced under service conditions, especially in areas where girders connect to the capping beams. Temporary measures such as tendons, supports, or bracing are used to mitigate unbalanced forces during segmental construction. However, they do not fully eliminate internal forces but rather redistribute them within the pier and capping beam system. Recent advancements in finite element modeling, particularly with software such as SAP2000, allow for detailed simulation of construction staging, tendon stressing, and time-dependent effects. These tools provide valuable insights into how internal forces evolve throughout the construction and service stages [8]. Many studies on balanced cantilever bridges have investigated moment calculations, time-dependent effects, and tendon stressing, primarily focusing on the superstructure [6,9,10]. Furthermore, despite the crucial role of lateral forces induced by overturning moments during segmental construction stages, the internal forces within the pier and capping beam systems need to be analyzed stage-wise to achieve better design accuracy and performance assessment. On this basis, the aim of this case study is to examine the structural performance of the pier and capping beam system in a balanced cantilever bridge, focusing on critical internal forces during both segmental construction and service stages. This case study will initially involve manual computation of the overturning moment. Subsequently, the pier and capping beam system will be simulated during the segmental construction stage using shell elements within the finite element modeling framework. The analysis will focus on the development of lateral bending moments, axial membrane forces, and the distribution of overturning moments within the system. Additionally, the pier and capping beam system will be simulated again using frame elements to analyze the internal force distribution during the construction stage.

M.S.S Haakeel*[1], T. Ramachandran [1], M.A.R.M.A Jabbar[1]
[1] Road Development Authority, Bridge design division
Corresponding author: haakeels@gmail.com

Furthermore, the simulation will be extended to the service stage once the cantilever section is completed. This simulation will evaluate the internal forces after achieving full structural continuity, thereby providing insights into the structural performance under service conditions. Shell elements are used to assess lateral behavior, while frame elements capture global internal forces. Though employed for distinct purposes, these analyses together enhance the understanding of the structural response.

2. Methodology

2.1 Geometrical Configuration

A two-span bridge with a total length of 60.0 m was analyzed in this case study. The structure comprises three primary components: the pier, the capping beam, and the precast post-tensioned concrete box girder segments. Additionally, the substructure includes a pile cap and deep foundation system. Figure 1 illustrates the overall configuration of the pier, capping beam, box girder segments, pile cap, and pile foundation considered in this case study.

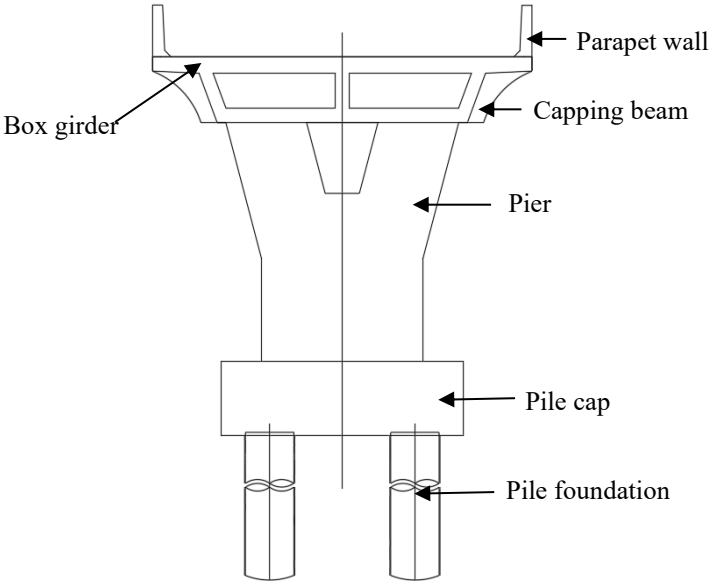

Figure 1: Configuration of pier, capping beam, concrete box girder segments, pile cap and pile foundation.

The pier consists of a stem that splits into two inclined columns, forming a V-shape to enhance structural stability, facilitate segmental launching and, improve aesthetics. The capping beam is monolithically cast above the pier columns and serves as the launching platform for the concrete box girder, which was aligned longitudinally with the capping beam. The dimensions of the capping beam were chosen to align with the concrete box girder facilitate tendon installation., while the pier dimensions were selected to accommodate the capping beam and meet the requirements of elevated highways. Further details of the pier and capping beam configuration are shown in Figure 2.

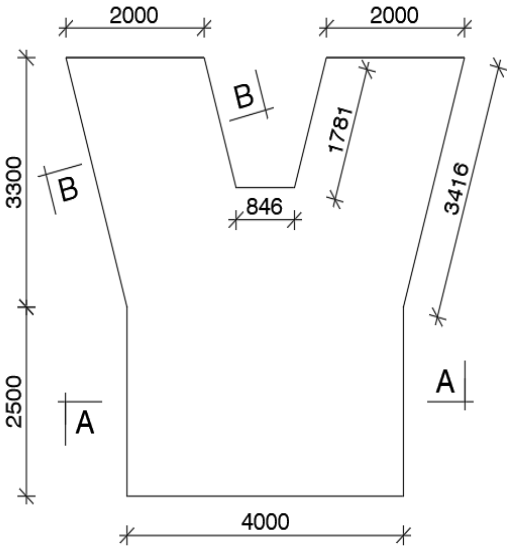

(a) Elevation of pier (mm).

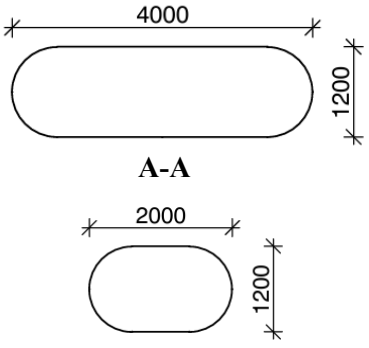

(b) Cross sections of pier (mm).

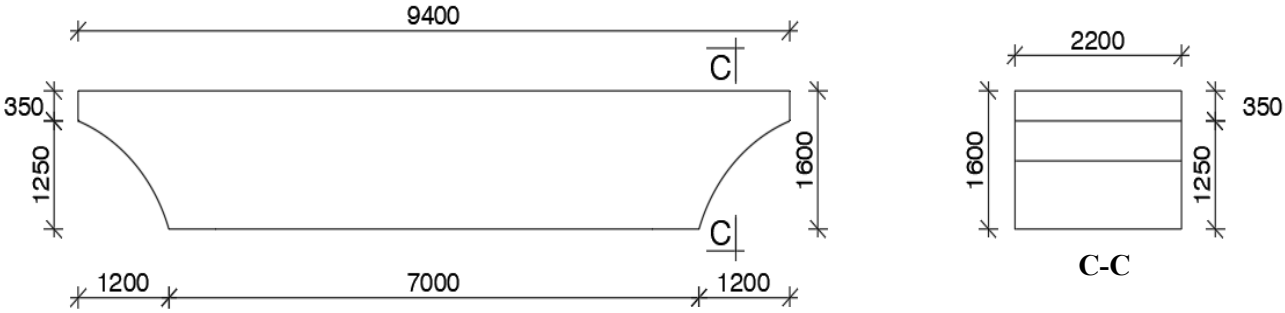

(C) Section of capping beam (mm).

Figure 2: Details of pier and capping beam.

The post-tensioned concrete box girder segment, presented in Figure 3, has a hollow cross-section optimized for both structural efficiency and ease of segmental erection. This section has top and bottom section moduli of Zt = 9.23E+07 m^3 and Zb = 1.39E+08 m^3, respectively, which are greater than the corresponding values required to transfer dead loads, service loads, and prestress eccentricity (Zt = 3.56E+07 m^3 and Zb = 5.68E+07 m^3, respectively), and this section was selected according to M. T. R. Jayasinghe *et al*. [16]. The segments are 3.0 m in length and symmetrically placed on either side of the pier, following the balanced cantilever construction sequence to simulate the construction process and structural behavior under various stages of loading.

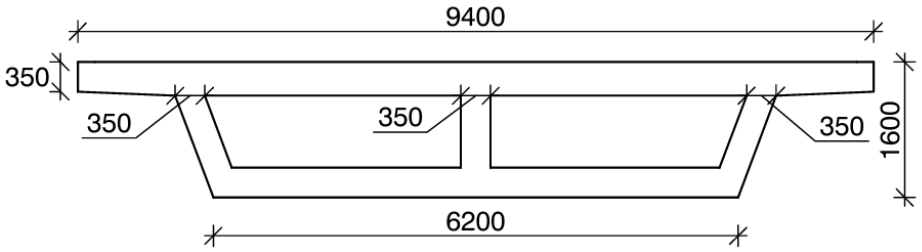

Figure 3: Details of post-tensioned concrete box girder segments (mm).

2.2 Materials

The pier, capping beam, piles, and pile cap were modeled using C40/50 grade concrete, while C50/60 grade concrete was used for the post-tensioned concrete box girders to meet higher flexural and shear demands. Concrete unit weight was 25kN/m^3. Assuming post-tensioning was implemented with 15.2 mm diameter, 7-wire super strands, each having a characteristic tensile strength of 1670 N/mm² to ensure effective force transmission and deflection control.

2.3 Numerical Simulation

In this case study, a numerical simulation was developed using SAP2000 to investigate the structural response of the pier and capping beam system during balanced cantilever bridge construction.

The first phase of analysis simulated the segmental construction stage, where precast segments were incrementally launched from the capping beam toward midspan on one side (15.0 m), while the opposite side remained one segment shorter (12.0 m) to replicate the practical challenges of balanced cantilever construction. The second phase represented the service stage, modeling the complete two-span bridge (each span 30.0 m) under operational loading conditions. Together, these analyses offer a comprehensive numerical evaluation of the pier and capping beam system's behavior from construction through long-term service performance (see Figure 4).

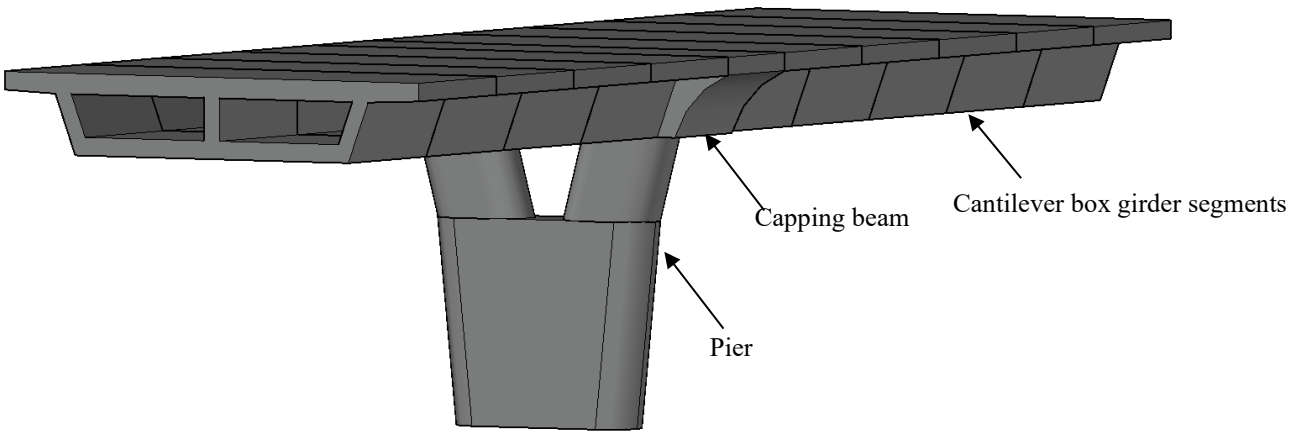

(a) Segmental construction stage simulation.

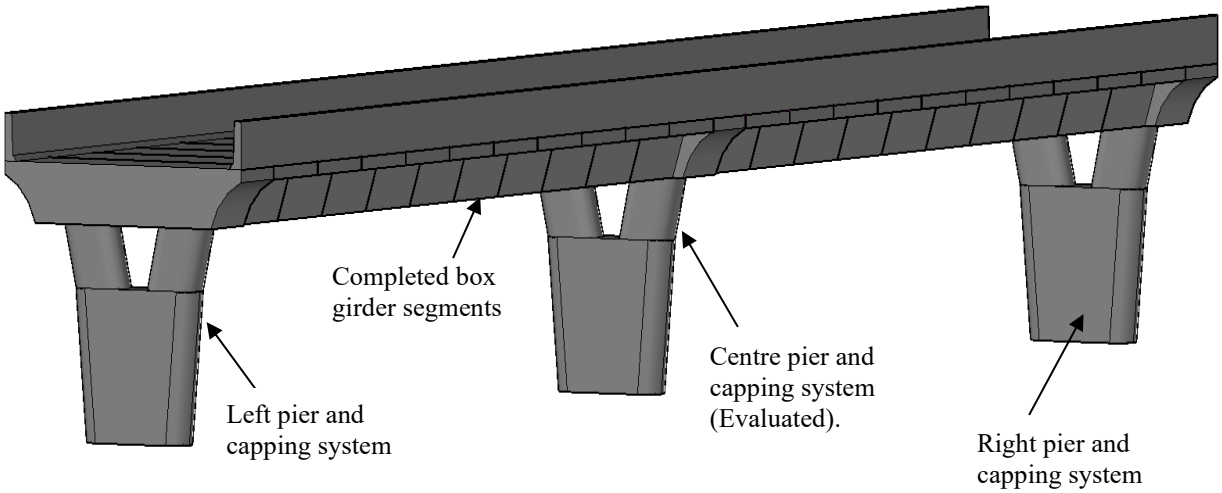

(b) Service stage simulation.

Figure 4: 3D model showing the arrangement of box girders, capping beam, and pier during both the segmental construction and service stages.

2.4 Meshing, boundary conditions, and frame element analysis

To capture the structural response induced by overturning moments during segmental construction, the pier and capping beam were modeled using thick shell elements in SAP2000, with thicknesses of 1.2 m and 2.2 m, respectively. The shell element analysis was essential for representing the lateral behavior caused by unbalanced cantilever loading, specifically five segments (15.0 m) on one side and four segments (12.0 m) on the other. This configuration induced a global overturning effect, which was captured as lateral out-of-plane bending moments and membrane axial forces within the shell model. However, shell elements do not provide sectional internal forces required for structural design, such as major and minor axis bending moments, shear forces, axial forces, and torsion within the pier and capping beam system.

To obtain these forces during both the segmental construction and service stages, the pier and capping beam were also modeled using frame elements, allowing for comprehensive analysis of global structural behavior. Care was taken to avoid duplication of stiffness or load effects; the shell and frame models were analyzed independently to fulfill different analytical objectives. Additionally, the pile cap (6.0 m × 6.0 m) was modeled as a thick shell element with a thickness of 1.8 m. A refined mesh was applied to ensure sufficient resolution for capturing localized effects, particularly within the pier and capping beam system. Figure 5 illustrates both the refined shell mesh and the frame element model of the pier and capping beam system. This combined modeling approach, with lateral behavior captured by thick shell elements induced by the overturning moment during the segmental construction stages, alongside bending moments, axial forces, torsion, and shear forces captured by frame elements during both stages, ensures a comprehensive and accurate representation of the pier and capping beam system behavior throughout stage-wise analysis.

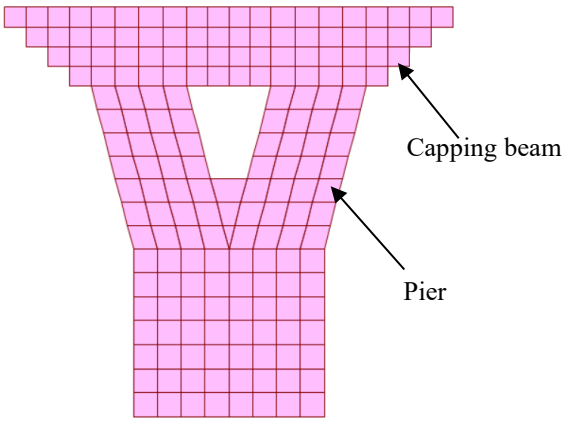

(a) Meshing of pier and capping beam system.

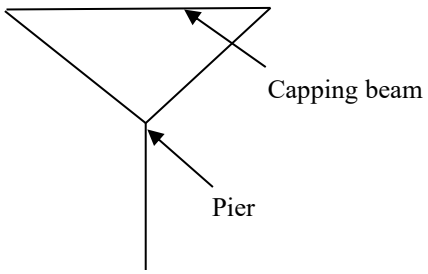

(b) Frame element analysis pier and capping system.

Figure 5: Mesh used in shell element and frame element model for pier and capping beam system.

The concrete box girders, transverse/cross beams, and pile foundations were modeled using frame elements to accurately capture the primary flexural and axial behavior of these components. The superstructure in the service stage was simulated as a grillage system, enabling efficient representation of the deck's load distribution characteristics. Transverse beams were introduced to channel the forces from the deck to the concrete box girder, ensuring realistic load transfer (see Figure 6). Proper nodal connectivity was maintained between all structural components to ensure continuous load transfer and structural integrity. The model incorporated four piles, each with a diameter of 1.2 m and a length of 24.0 m, representing the foundation system. Pile supports were modeled using lateral spring constraints (k_s) of 16,500 kN/m at 1.5 m intervals (Ls=1.5m), based on a subgrade modulus (k_h) of 11,000 kN/m²/m typical for dense sand, using Equation 1: $k_s=k_h \cdot L_s$. This simulates soil–structure interaction realistically. Vertical spring constants were taken as 10% of the lateral spring stiffness to represent vertical soil resistance. Fixed support conditions were assigned at the base of each pile to represent end restraint accurately.

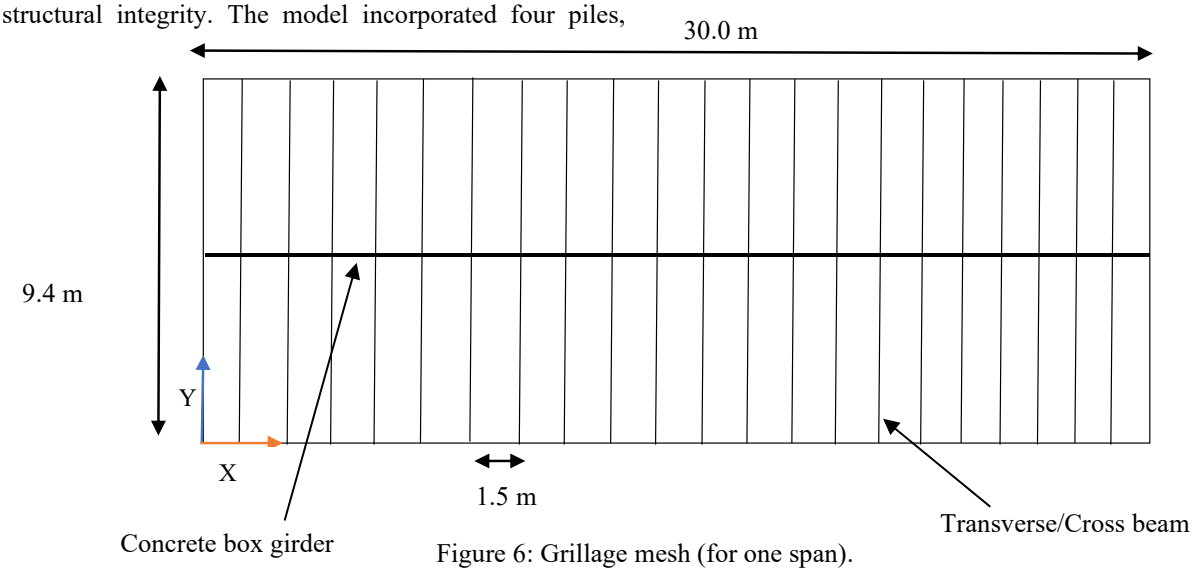

Figure 6: Grillage mesh (for one span).

2.5 Loading conditions

In segmental balanced cantilever bridge construction, structural analysis is performed in distinct stages to accurately capture the evolution of internal forces. Each stage involves a specific set of loads representing the actual conditions during segmental construction and in service. The segmental construction stage simulates the incremental launching of segments and includes the associated effects of dead loads, prestress actions, construction equipment actions, wind actions**,** and accidental actions**.** The service stage represents the completed bridge under full operational conditions, incorporating long-term effects such as dead loads, prestress actions, imposed traffic actions, wind loads, and accidental actions**.** The following Table 1 summarizes the applied load, relevant load combination and, corresponding Eurocode references for each stage of the analysis. The self-weight of all structural components was automatically computed by SAP2000. Superimposed loads included the parapet wall, which was modeled as a uniformly distributed load of 9.0 kN/m based on its estimated weight. Temporary equipment loads from the traveler were represented by a uniformly distributed load of 20.0 kN/m, reflecting the typical self-weight of the traveler used during segmental construction. According to Eurocode provisions [12], main variable traffic actions groups gr1a and gr2 are applied to represent traffic loading in the service stage. The traffic groups gr1a and gr2 are considered critical in the analysis, as manual calculations show that those govern the maximum internal forces in the pier, particularly influencing bending moments and axial forces at the pier and capping beam system. In the service stages, only one-span live loading is considered to capture the most severe unbalanced effects on the central pier and capping beam system. The variable loads, such as wind actions and accidental actions, were applied in accordance with Eurocode provisions in both stages [13,14]. To replicate the global effect of prestressing, external prestressing was applied. A total prestress force of 10,000 kN with a mean eccentricity of 1.5 m was derived from the Magnel diagram for post-tensioned box girders [15]. To replicate the bending effects induced by the eccentric prestress force, equivalent external prestress moments (Mp) were applied to the box girders, as determined using Equation 2.

$$M_p = P \cdot e \qquad \text{(Equation 2)}$$

where P is the prestressing force and e is the mean eccentricity of the tendon profile. As the primary objective of this study is to assess the internal forces in the pier and capping beam system during the segmental construction and service stages, the detailed nonlinear behavior of curved tendons and time-dependent effects such as creep and shrinkage were not modeled.

Accordingly, the use of external prestress moments (Mp) provides a valid and practical approximation of the global prestress effect in frame-based finite element models, in alignment with established structural mechanics principles.

Table 1: Applied loads and load combinations.

<table>
<tr><th></th><th>Notation</th><th>Load type</th><th>Load Combination (STR)
(Set B & Set C) [11].</th></tr>
<tr><td rowspan="5">Segmental construction stage</td><td>$G_{k,Pier}$</td><td>Pier self-weight</td><td rowspan="5">I= Set B ($\gamma_G G_{k,Pier}+\gamma_G G_{k,BGS}+\gamma_P P + \gamma_Q Q_{k,TE} + \gamma_Q \Psi_0 Q_{k,w}$)

II= SET C ($\gamma_G G_{k,Pier+}\gamma_G G_{k,BGS}+\gamma_P P + \gamma_Q Q_{k,TE} + \gamma_Q \Psi_0 Q_{k,w}$)</td></tr>
<tr><td>$G_{k,BGS}$</td><td>Box girder self-weight</td></tr>
<tr><td>P</td><td>Prestress actions</td></tr>
<tr><td>$Q_{k,\ TE}$</td><td>Temporary equipment actions (Travelers)</td></tr>
<tr><td>$Q_{k,\ w}$</td><td>Wind actions</td></tr>
<tr><td rowspan="8">Service stage (One-span live loading)</td><td>$G_{k,Pier}$</td><td>Pier self-weight</td><td rowspan="8">III= Set B ($\gamma_G G_{k,Pier}+\gamma_G G_{k,BGS}+\gamma_G G_{k,SID} + \gamma_P P + \gamma_Q Q_{k,gr1a} + \gamma_Q \Psi_0 Q_{k,w}$)

IV= SET C ($\gamma_G G_{k,Pier}+\gamma_G G_{k,BGS}+\gamma_G G_{k,SID} + \gamma_P P + \gamma_Q Q_{k,gr1a} + \gamma_Q \Psi_0 Q_{k,w}$)

V= Set B ($\gamma_G G_{k,Pier}+\gamma_G G_{k,BGS} +\gamma_G G_{k,SID} + \gamma_P P + \gamma_Q Q_{k,gr2} + \gamma_Q \Psi_0 Q_{k,w}$)

VI= SET C ($\gamma_G G_{k,Pier}+\gamma_G G_{k,BGS}+ \gamma_G G_{k,SID} +\gamma_P P + \gamma_Q Q_{k,\ gr2} + \gamma_Q \Psi_0 Q_{k,w}$)</td></tr>
<tr><td>$G_{k,BGS}$</td><td>Box girder self-weight</td></tr>
<tr><td>$G_{k,SID}$</td><td>Super Imposed Dead actions</td></tr>
<tr><td>P</td><td>Prestress actions</td></tr>
<tr><td>$Q_{k,\ gr1a}$</td><td>Vertical variable traffic actions (gr1a: Characteristic values of LM1)</td></tr>
<tr><td rowspan="2">$Q_{k,\ gr2}$</td><td>Vertical variable traffic actions (gr2: Frequent values of LM1)</td></tr>
<tr><td>Horizontal variable traffic actions (gr2: Braking and acceleration load)</td></tr>
<tr><td>$Q_{k,\ w}$</td><td>Wind actions</td></tr>
<tr><td colspan="4">Note:
The partial factors for each set are as follows:

SET B ($\gamma_{G,\ self\text{-}weight} = 1.35$, $\gamma_{G,\ Super\ imposed\ dead\ actions}=1.20$, $\gamma_P =1.35$, $\gamma_{Q,\ Temporary\ equipment\ actions} =1.35$, $\gamma_{Q,\ Wind} = 1.70$, $\gamma_{Q,\ gr1a,\ gr2} = 1.35$).

SET C ($\gamma_{G,\ self\text{-}weight} = 1.00$, $\gamma_{G,\ Super\ imposed\ dead\ actions}=1.00$, $\gamma_P =1.00$, $\gamma_{Q,\ Temporary\ equipment\ actions} =1.15$, $\gamma_{Q,\ Wind} = 1.45$, $\gamma_{Q,\ gr1a,\ gr2} = 1.15$).

The combination factors $\Psi 0$; for gr1a; 0.75 for gr2; 0, for $Q_{k,w}$ (Service stage) 0.60& $Q_{k,w}$ (During construction) 0.80, respectively.</td></tr>
</table>

3. Results and Discussion

3.1 Overturning bending moment due to imbalance

During segmental construction in the balanced cantilever method, imbalance occurs practically when one side temporarily has more segments than the other. This situation leads to an imbalance in the pier and capping beam system, resulting in an overturning bending moment. This moment is calculated using the equation provided by G. Lucko et al. [5]

$$\Delta M = 1/2.\ w \cdot (L_1^2 - L_2^2) \qquad \text{(Equation 3)}$$

In this equation, w is the weight per meter of one segment (170 kN/m). The lever arms L_1 and L_2 are considered based on the mid-span because the balanced cantilever method stops at mid-span in both directions. The temporary imbalance occurs when one side reaches the mid-span (five segments, total length of 15.0 m), while the other side is one segment short of the mid-span (four segments, total length of 12.0 m). Therefore, using the above Equation 3, the total overturning moment is calculated as 6,885 kNm. Figure 7 provides a schematic representation of this analysis.

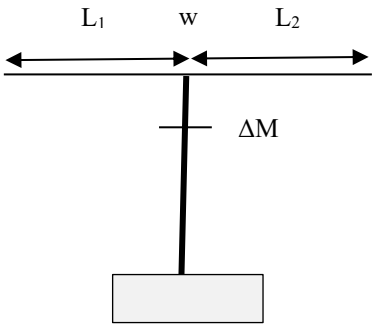

Figure 7: Overturning moment schematic presentation.

3.2 Overturning effects on pier and capping beam system

The lateral structural response of the pier–capping beam system under a global overturning moment was investigated using shell elements in SAP2000. To isolate the effects of overturning behavior, only the self-weight of the structure was considered in the shell element analysis, with no additional external loads applied. Shell elements were oriented such that the 1-direction aligned with the longitudinal axis of the capping beam (horizontal axis in the pier), while the 2-direction corresponded to the vertical axis (capping beam width or pier height).

The analysis specifically focused on the lateral out-of-plane bending moments (longitudinal moment M11 and transverse moment M22) and axial membrane forces (horizontal forces F11 and vertical forces F22). These internal forces reveal how the global overturning moment manifests as localized lateral actions in the structural system. The aim was not to directly equate the global overturning moment with the localized internal forces, but to examine the mechanism through which the global imbalance leads to lateral stresses within the shell element model. Figure 8 illustrates the distribution of lateral out-of-plane bending moments and axial membrane forces during the segmental construction stage, clearly highlighting critical regions through contour color gradients. From these zones, maximum moment and force values were extracted. Table 2 summarizes the lateral out-of-plane bending moments (M11, M22) and axial forces (F11, F22).

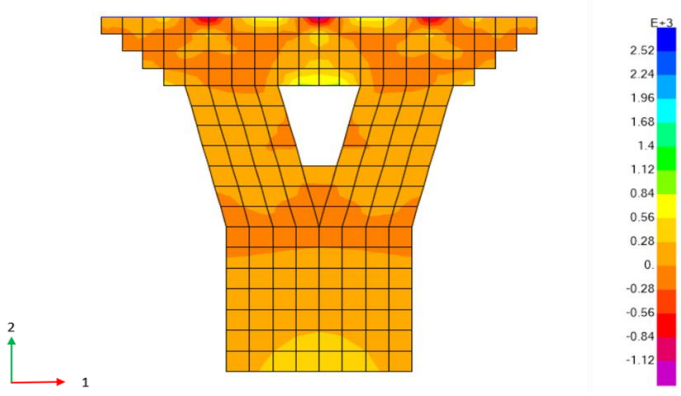

(a) Longitudinal bending moment (M11) under dead loads (self-weights only) during segmental construction stages (kNm).

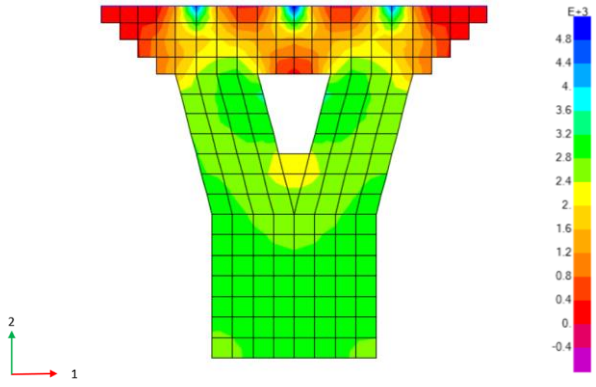

(b) Transverse bending moment (M22) under dead loads (self-weights only) during segmental construction stages (kNm).

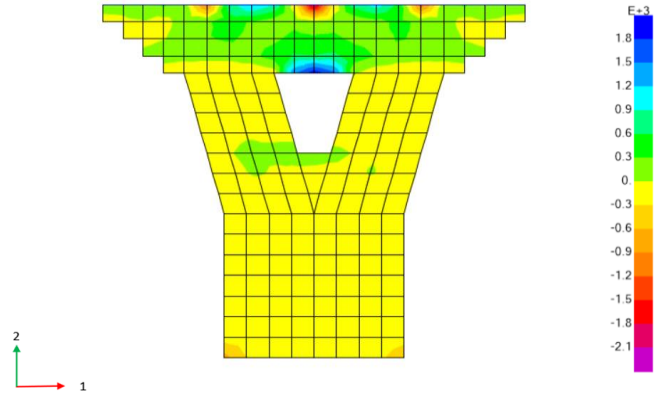

(c) Horizontal axial load (F11) under dead loads (self-weights only) during segmental construction stages (kNm).

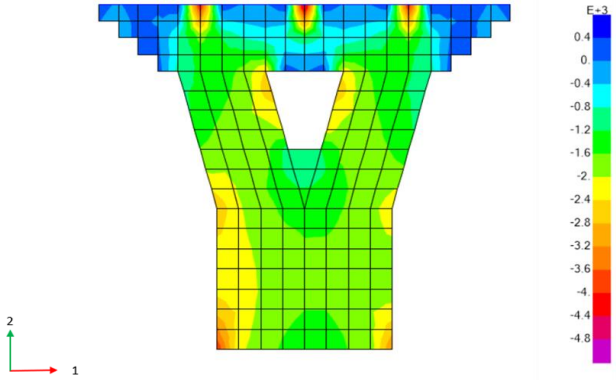

(d) Vertical axial load (F22) under dead loads (self-weights only) during segmental construction stages (kNm).

Figure 8: Lateral bending moments and membrane axial forces under dead loads (self -weight only) during segmental construction stages. (a-d)

Table 2: Lateral out-of-plane bending moments and axial membrane forces.

Stage	Structural Component	Applied Loads	M11 (kNm)	M22 (kNm)	F11 (kN)	F22 (kN)
Segmental construction stage	Capping beam	Self-weights only	627	2,553	1,149	3,045
	Pier		214	1,584	268	2,309

The overturning moment, computed as 6,885 kNm based on segmental imbalance using the cantilever method, is redistributed into localized internal actions throughout the shell model. Notably, even though only self-weight was applied, substantial transverse bending (M22) and axial force (F22) were observed. This highlights that the overturning moment alone, arising from segmental imbalance, induces significant lateral stresses in the pier and capping beam system. In the capping beam, maximum values of M22 and F22 reached 2,553 kNm and 3,045 kN, respectively. For the pier, M22 and F22 peaked at 1,584 kNm and 2,309 kN. By contrast, the longitudinal bending moment (M11) and horizontal axial force (F11) were markedly lower in both components, indicating that the overturning response is predominantly resisted by transverse stress resultants. Additionally, transverse shear forces and torsional stresses were found to be minimal, suggesting their limited role in resisting segmental imbalance. While the shell element model does not yield sectional forces in a Eurocode-compatible format for reinforcement design, it was instrumental in locating zones of high transverse stress concentration. These zones clearly visible in the contour plots occur at critical structural interfaces, specifically at the junctions between the capping beam and the box girders, and at the base of the pier. These regions warrant additional reinforcement consideration, supporting the engineering judgment behind the final design. The actual design was conducted using the frame element model, which provides explicit sectional forces for Eurocode-based detailing.

3.3 Internal forces analysis in the pier and capping beam system using frame elements.

Using the pier and capping beam system modeled as frame elements, the maximum internal forces, including major axis moment ($M_{Major\ axis}$), which represents bending about the primary axis; minor axis moment ($M_{Minor\ axis}$), which represents bending about the secondary axis; axial forces (F), shear forces (V), and torsional moments (T), were observed during segmental construction and service stages. Figure 9 illustrates the distribution of major axis bending moment ($M_{Major\ axis}$) along the length for Load Combination 1 during the segmental construction stage and Load Combination V during the service stage in the central pier and capping beam system, demonstrating how the results were obtained. The maximum values of the internal forces from each load combination were extracted. These values are summarized in Table 3. All internal forces follow the SAP2000 sign convention, where sagging moments and compressive forces are positive, while hogging moments and tensile forces are negative.

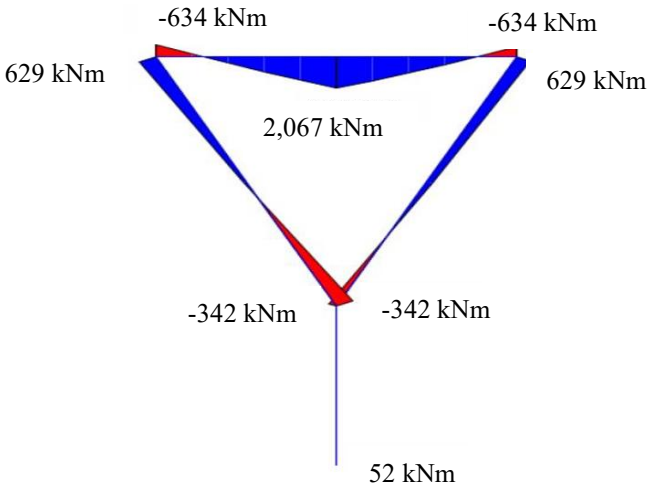

(a) Bending moment ($M_{Major\ axis}$) load combination I during segmental construction.

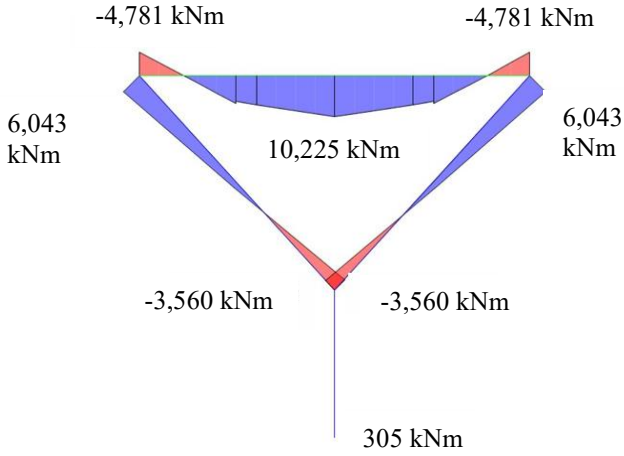

(b) Bending moment ($M_{Major\ axis}$) Load combination V in the service stage.

Figure 9: Bending moment ($M_{Major\ axis}$) for Load combination I during segmental construction stage and Load combination V during service stage.

Table 3: Internal Forces in both segmental construction and service stages.

Stages	Structural Component	Load Combination	$M_{Major\ axis}$ (kNm)	$M_{Minor\ axis}$ (kNm)	V (kN)	F (kN)	T (kNm)
Segmental construction stage	Capping beam	I	2,067	340	1,346	1,301	2,033
		II	1,531	252	997	964	1,506
	Maximum value		**2,067**	**340**	**1,346**	**1,301**	**2,033**
	Pier (columns)	I	630	5,317	381	3,603	2,204
		II	466	3,938	282	2,669	1,633
	Maximum value		**630**	**5,317**	**381**	**3,603**	**2,204**
Service stage	Capping beam	III	10,745	540	6,065	4,008	2,766
		IV	8,260	460	4,702	3,098	2,357
		V	10,225	409	5,776	3,822	2,079
		VI	7,817	349	4,445	2,940	1,771
	Maximum value		**10,775**	**540**	**6,065**	**4,008**	**2,766**
	Pier (columns)	III	6,373	1,451	1,673	5,897	645
		IV	4,929	1,236	1,288	5,137	550
		V	6,043	1,097	1,598	5,787	486
		VI	4,648	934	1,224	4,881	414
	Maximum value		**6,373**	**1,451**	**1,673**	**5,897**	**645**

Figure 10 shows a comparative assessment of internal forces in the capping beam and pier during both the segmental construction and service stages. The analysis reveals critical insights into their structural behavior, particularly the variation and interplay of bending, shear, torsion, and axial effects. The major axis bending moment ($M_{Major\ axis}$) in the capping beam increases significantly from 2,067 kNm during the segmental construction stage to 10,775 kNm under service loading. This substantial rise induces pronounced longitudinal tension at the soffit. The corresponding required steel area (As_{req}) required to carry the service stage moment is approximately 0.018m² [17].

According to Eurocode 2, the maximum allowable reinforcement ratio (As_{max}) for a concrete section is approximately 4% [17]. For a capping beam with a cross-sectional area of 2.2 m × 1.6 m, this yields a maximum permissible reinforcement area of approximately 0.141 m². Given that the required area of reinforcement to resist the design moment is only 0.018 m², it is evident that the necessary reinforcement can be accommodated without congestion or constructability issues. The shear force (V) increases markedly from 1,346 kN during the segmental construction stage to 6,065 kN in the service stage. This progression highlights the necessity for robust shear reinforcement, particularly near supports where maximum shear demand occurs. Closed stirrups or appropriately spaced shear ties must be detailed to prevent diagonal tension failure, especially under combined loading conditions with flexure and torsion. Torsional moments (T) in the capping beam, obtained from frame element analysis, increase from 2,033 kNm during the segmental construction stage to 2,766 kNm at the service stage. Due to the relatively large beam width of 2.2 m, torsional effects may be underestimated by the frame element model, which idealizes the beam as a one-dimensional element and cannot fully capture complex three-dimensional stress distributions.

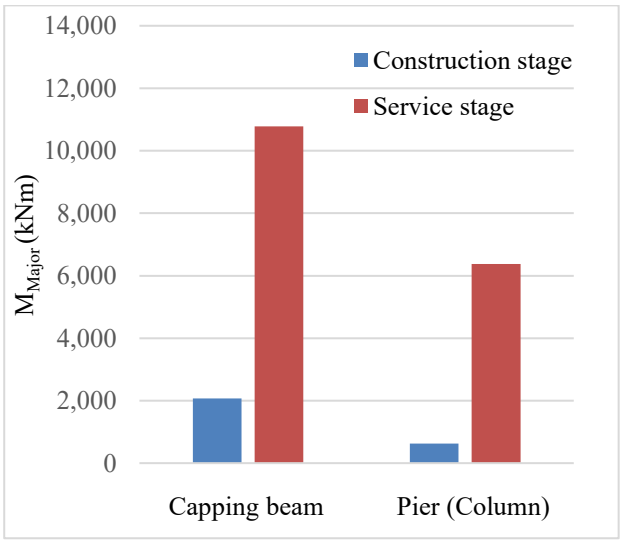

(a) Bending Moment ($M_{Major\ axis}$) (kNm).

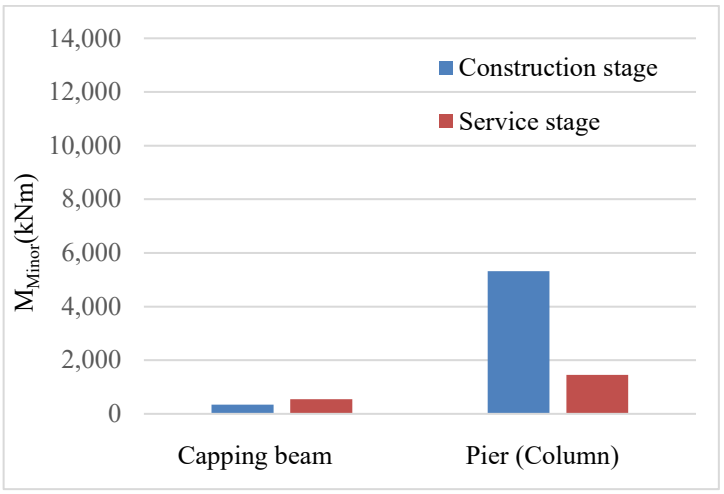

(b) Bending Moment ($M_{Minor\ axis}$) (kNm).

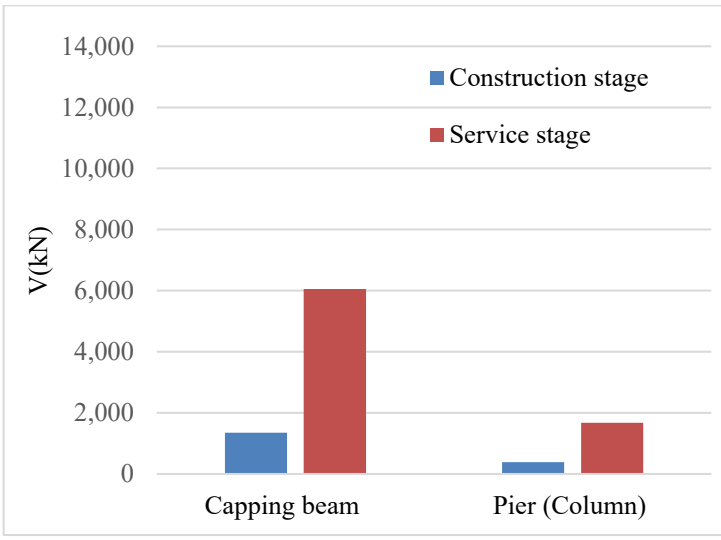

(c) Shear Force (V) (kN).

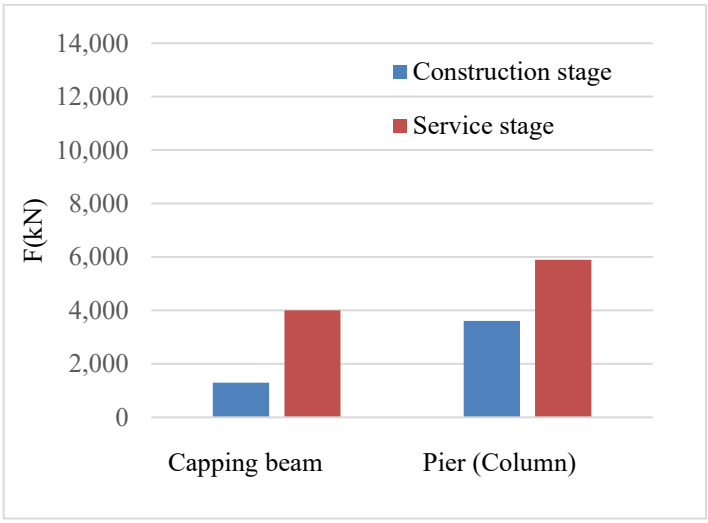

(d) Axial force (F) (kN).

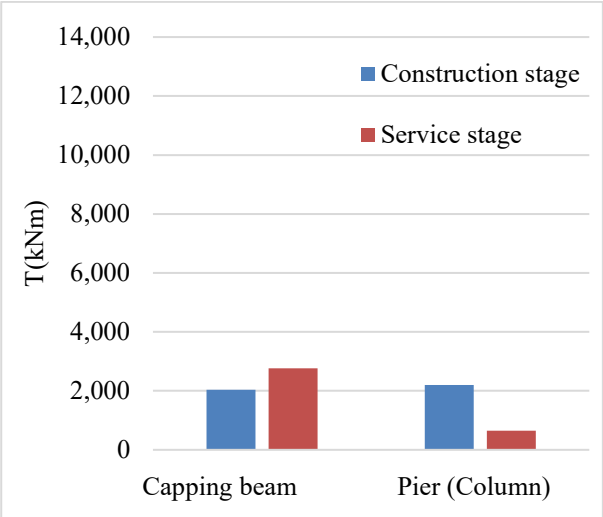

(e) Torsion Moment (T) (kNm).

Figure 10: Internal forces comparison during segmental construction and service stage.

The frame analysis also shows minor axis bending moments ($M_{Minor\ axis}$) increasing from 340 kNm to 540 kNm. Despite this increase, these remain secondary, with limited influence on reinforcement design, since longitudinal bending dominates and governs the required reinforcement layout. On the other hand, shell element analysis is not intended to provide exact design magnitudes but instead serves to identify critical zones of lateral effect across the beam. This analysis highlights regions where transverse effects, including torsion and bending across the width, become critical particularly during asymmetric segmental construction, which induces significant lateral deformation. These localized transverse effects, not fully captured by the frame model, indicate that additional transverse reinforcement may be required in specific regions of the capping beam to ensure structural adequacy and serviceability under combined loading conditions.

The axial compressive force (F) in the pier column increases from 3,603 kN during the segmental construction stage to 5,897 kN in the service stage, primarily due to the addition of superimposed and live loads. This increase in axial load governs the primary reinforcement requirement in the column section. However, in accordance with Eurocode 2 [17], the column must also be verified for biaxial bending resistance, as it is subjected to moments about both principal axes. During segmental construction, bending about the minor axis dominates ($M_{Minor\ axis}$), with a peak moment of 5,317 kNm arising from cantilever effects and lateral eccentricity. In the service stage, this minor axis moment ($M_{Minor\ axis}$) reduces significantly to 1,451 kNm as the structural system stabilizes. Conversely, the major axis moment ($M_{Major\ axis}$) increases from 629 kNm during construction to 6,373 kNm under one-span live loading in the service stage.

These values necessitate consideration of combined axial load and biaxial bending in the column design. The pier column has an oval cross-section, with a height of 1.2 m and a width of 2.0 m, and an effective length of 3.46 m. The calculated slenderness ratio is $\lambda = 11.53$, which is less than the limiting slenderness $\lambda_{lim} = 32.14$ as per Eurocode 2 [17], classifying the column as non-slender. Therefore, second-order effects may be neglected. The shear force (V) also increases markedly from 381 kN during construction to 1,673 kN in the service stage, particularly at the interface between the pier and the capping beam. This shear demand necessitates the provision of closed stirrups or shear ties to resist potential diagonal cracking.

Since different internal forces govern at different construction stages, the critical force whether axial, bending, shear, or torsion was identified at each stage to guide the design. This stage-specific approach ensures structural demands are properly addressed during both segmental construction and service phases. To enhance accuracy and safety, both shell (for lateral and distributed stress behavior) and frame (for global internal forces) analyses were used. This modeling strategy supports a robust design that accounts for three-dimensional effects and evolving load conditions.

4. Conclusion

The case study focused on the internal force analysis of the pier and capping beam system of the balance cantilever method during segmental construction and service stages. Based on the above results, it can be concluded that:

1. Internal forces in the pier and capping beam system vary significantly between the segmental construction stage and the service stage. For accurate design, the dominant internal forces at each stage must be identified and considered separately.

2. The capping beam is subjected to significant longitudinal bending moments during the service stage, primarily due to live load effects. Therefore, appropriate reinforcement must be provided to ensure serviceability.

3. The pier column design is governed by combined axial load and biaxial bending, with minor axis moment governing during segmental construction and major axis moment governing in the service stage.

4. Frame and shell analyses were conducted for distinct purposes rather than direct comparison. Frame elements capture global internal forces essential for design, while shell elements identify critical lateral effects and regions requiring additional reinforcement. Together, they enable a comprehensive and reliable structural assessment.

Acknowledgement

The authors would like to acknowledge the invaluable contributions of all the researchers involved in this study. Their dedication, expertise, and collaborative efforts have been instrumental in the successful completion of this research.

References

[1] W. Podolny and J. M. Muller, *Construction and Design of Prestressed Concrete Segmental Bridges*. New York, NY: John Wiley & Sons, Inc., 1982.

[2] A. G. Bishara and N. G. Papakonstantinou, "Analysis of Cast-in-Place Concrete Segmental Cantilever Bridges," *Journal of Structural Engineering, ASCE*, vol. 116, no. 5, pp. 1247-1268, 1990.

[3] G. Lucko, *Means and Methods Analysis of a Cast-In-Place Balanced Cantilever Segmental Bridge: The Wilson Creek Bridge Case Study*, M.S. thesis, Virginia Polytechnic Institute and State University, Blacksburg, VA, 1999.

[4] J. Mathivat, *The Cantilever Construction of Prestressed Concrete Bridges*. New York, NY: John Wiley & Sons, Inc., 1983.

[5] G. Lucko, J. M. de la Garza, and A. M. Asce, "Constructability Considerations for Balanced Cantilever Construction," *Practice Periodical on Structural Design and Construction*, vol. 8, no. 1, p. 47, 2003.

[6] H.-G. Kwak and J.-K. Son, "Determination of design moments in bridges constructed by balanced cantilever method," *Engineering Structures*, vol. 24, pp. 639-648, 2002.

[7] H.G. Kwak and J.K. Son, "Span ratios in bridges constructed using a balanced cantilever method," *Construction and Building Materials*, vol. 18, no. 10, pp. 767-779, Dec. 2004.

[8] S. Ates, "Numerical modelling of continuous concrete box girder bridges considering construction stages," *Applied Mathematical Modelling*, vol. 35, no. 8, pp. 3809-3822, Aug. 2011.

[9] R. Malm and H. Sundquist, "Time-dependent analyses of segmentally constructed balanced cantilever bridges," *Engineering Structures*, vol. 32, pp. 1038-1045, 2010.

[10] P. J. S. Cruz, A. R. Mari, and P. Roca, "Nonlinear time-dependent analysis of segmentally constructed bridges I: Control method," *Journal of Engineering Mechanics*, vol. 122, no. 6, pp. 489-494, 1996.

[11] Sri Lanka Standards Institution (SLSI), *National Annex to Eurocode: Basis of Structural Design*, NA to SLS EN 1990:2018, Colombo, Sri Lanka, 2018.

[12] Sri Lanka Standards Institution (SLSI), *National Annex to Eurocode: Actions on structures - Traffic loads on bridges*, NA to SLS EN 1991-2:2014, Colombo, Sri Lanka, 2014.

[13] Sri Lanka Standards Institution (SLSI), *National Annex to Eurocode: Actions on structures - Wind actions*, NA to SLS EN 1991-1-4:2019, Colombo, Sri Lanka, 2019.

[14] Sri Lanka Standards Institution (SLSI), *National Annex to Eurocode: Actions on structures - Accidental actions*, NA to SLS EN 1991-1-7:2006, Colombo, Sri Lanka, 2006.

[15] M. Virlogeux, "External prestressing for bridges: State-of-the-report," *PCI Journal*, vol. 40, no. 4, pp. 34-58, 1995.

[16] W. M. D. N. Ranasinghe and M. T. R. Jayasinghe, "A design method for prismatic prestressed continuous box girder bridges," in *Proceedings of the Research for Industry Conference*, Colombo, Sri Lanka, 1998.

[17] Sri Lanka Standards Institution (SLSI), *National Annex to Eurocode 2: Design of Concrete Structures – Part 1-1: General Rules and Rules for Buildings,* (NA to SLS EN 1992-1-1:2012), Colombo, Sri Lanka, 2012.

AI-Powered Integrity Assessment of Pre-Stressed Concrete Girders: Automated Damage Detection After Impact Events

R A Dihan[1*], S V Pinnalanda[1], D M A G B Dissanayake[1], A J Dammika[1], and C S Bandara[1]

Abstract

Pre-Stressed Concrete (PSC) girders are widely used in bridge construction due to their high strength and durability. However, during storage and transportation, these girders are vulnerable to accidental impacts, such as collisions with heavy vehicles, which may compromise their structural integrity. Traditional inspection methods rely on manual assessments, which are time consuming, subjective, and prone to human error. To address this challenge, this study presents an Artificial Intelligence (AI)-driven technique coupled with Finite Element (FE) modelling for automated damage detection and integrity assessment of PSC girders impacted during storage. The proposed technique utilizes Deep Learning (DL) models to analyze vibration data collected from both undamaged and damaged beam samples affected by vehicle impact at the site. By evaluating stiffness reduction, the AI model identifies cracks, deformations, and internal defects that may not be visible to the naked eye. The system is trained on a dataset developed using FE modelling techniques and validated with vibration data from pre-damaged and intact girders. This enables accurate classification and severity estimation of structural damage. Experimental validation demonstrates that the AI-FE hybrid approach significantly improves the reliability and efficiency of damage assessment on Shear Capacity Reduction (SCR) and Bending Moment Capacity Reduction (BMCR) compared to conventional visual inspections. The results confirm that the proposed method can accurately assess damage severity, predict failure risks, and support timely maintenance decisions with high AI accuracy of 89.95% and low Mean Squared Error (MSE) of 0.023 after 5-fold cross-validation-based training and validation. By implementing this AI-powered integrity assessment system, engineers and construction firms can ensure early detection of structural damage, preventing the use of compromised girders in critical infrastructure projects.

Keywords: Pre-Stressed Concrete (PSC) girders, Artificial Intelligence, Finite Element Modelling, Structural Health Monitoring, Impact Damage Assessment

1. Introduction

Pre-tensioned concrete girders serve as essential components in modern bridge construction, offering superior load-bearing capacity, durability, and resistance to cracking compared to conventional reinforced concrete elements, Wang *et al* [1] and Addepalli *et al* [2]. Their widespread application in infrastructure projects stems from their ability to withstand significant tensile forces introduced through pre-tensioning of embedded steel strands prior to concrete casting, Karthikeyan *et al* [3] and Burger *et al* [4]. Despite their structural advantages, these girders remain vulnerable to unintentional damage during manufacturing, transportation, and storage particularly impact damage from heavy machinery and vehicle collisions, Khandel *et al* [5] and Wang *et al* [6]. For instance, minor collisions with machinery can lead to surface cracking, which, although often visually detectable, may still reduce the overall stiffness of the girder. More moderate impacts can result in internal delamination, a type of localized stiffness loss that is difficult to detect without advanced non-destructive testing methods. Severe impacts may cause tendon debonding, leading to a substantial loss of pre-stress force, while impacts near the web region can induce web-shear cracks, reducing the girder's shear capacity both forms of damage are typically hidden from view. Additionally, collisions at mid-span may produce flexural cracks that compromise bending moment capacity, which are more likely to be visible. Some of these damage types are hidden or only partially visible, making their early detection challenging. Collectively, these damage mechanisms highlight the importance of inspection and structural health monitoring strategies to ensure the continued safety and reliability of PSC girders Venquiaruto *et al* [7] and Zhou *et al* [8].

Current inspection methods predominantly rely on manual visual assessment and rudimentary Non-Destructive Testing (NDT) techniques, both of which are labor-intensive, subjective, and limited in detecting internal damage Patel *et al* [9] and Torbali *et al* [10]. The increasing demand for efficient, accurate, and automated integrity evaluation in the precast industry has thus driven research toward intelligent damage detection systems Civera *et al* [11] and Liu *et al* [12]. Artificial Intelligence (AI), especially Deep Learning (DL) algorithms, has shown remarkable potential in revolutionizing Structural Health Monitoring (SHM) by automating damage classification, localization, and severity estimation with minimal human input Girmay *et al* [13] and Bader *et al* [14].

Among these intelligent methods, vibration-based damage identification has emerged as a particularly promising approach due to its sensitivity to structural changes such as stiffness degradation and crack propagation Zar *et al* [15] and Ren *et al* [16]. Unlike visual and surface-level techniques, vibration analysis offers a non-invasive means to detect internal or hidden damage by

[1] R A Dihan, S V Pinnalanda, D M A G B Dissanayake, A J Dammika, and C S Bandara: Department of Civil Engineering, Faculty of Engineering, University of Peradeniya, Sri Lanka. (e-mail: e18080@eng.pdn.ac.lk, samith2306@gmail.com, gihanashantha@gmail.com, dammikaaj@gmail.com, csbandara@eng.pdn.ac.lk)

interpreting shifts in dynamic response characteristics. When integrated with Finite Element (FE) modelling, AI systems can be trained using large-scale synthetic datasets that simulate diverse damage scenarios, enhancing model generalization while reducing dependency on costly real-world data collection Nath *et al* [17] and Lee *et al* [18]. This AI-FE integration also ensures consistency in feature representation and expands the diagnostic capability of DL networks to interpret complex structural behavior under various boundaries and loading conditions Ahmed *et al* [19] and Elharrouss *et al* [20].

This study introduces an AI-FE hybrid framework for the post-impact integrity assessment of PSC girders. The methodology employs a DL model trained on simulated vibration responses of girders with varying impact severities, crack positions, and damage modes Kim *et al* [21] and Jasmine *et al* [22]. Real-world experimental data collected from site-tested girder specimens both intact and impact-damaged are used for validation. The system focuses on evaluating Shear Capacity Reduction (SCR) and Bending Moment Capacity Reduction (BMCR), which are critical indicators of structural degradation in girder sections Furlong [23].

The integration of AI and FE modelling enables accurate detection of hidden damage, quantification of residual capacity, and prediction of failure mechanisms. The model demonstrates robust performance in distinguishing healthy girder from compromised girders Alkayem *et al* [24]. This innovation has the potential to transform inspection practices, enabling proactive maintenance and eliminating the risks associated with deploying damaged girders in critical infrastructure Singh *et al* [25].

2. Methodology

This study proposes a hybrid AI-FE framework for identifying, localizing, and assessing the severity of impact-induced damage in Pre-Stressed Concrete (PSC) girders by analyzing variations in their dynamic response. The focus is specifically on girders subjected to accidental impact events during storage and handling, due to collisions with heavy truck, as depicted in Fig. 1.

Figure 1: PSC girder stored on-site after impact by a truck.

While only minor surface damage was visually apparent on the impacted face, this research was undertaken to explore the possibility of internal damage such as microcracks or delamination that may remain undetected through conventional visual inspection but could critically compromise structural integrity. To address this, the proposed methodology integrates Finite Element (FE) modelling for simulating a wide range of damage scenarios with Deep Learning (DL) techniques to classify and quantify damage patterns and severities, as outlined in Fig. 2. The analysis is centered on two key vibration-based indicators: the Modal Assurance Criterion (MAC), used to detect deviations in mode shapes, and the Modal Frequency Shift (MFS), which tracks alterations in natural frequencies due to damage.

The approach begins with the systematic acquisition of vibration data from selected measurement points on both undamaged and impact-damaged girders at the storage site. This raw time domain vibration data is then processed using the Hilbert-Huang Transform (HHT) [25], and Fast Fourier Transform (FFT) to extract mode shapes and natural frequencies. These extracted features are converted to MAC and MFS, which serve as input variables to test the performance of a DL model for detecting and quantifying structural damage.

The DL model is trained and validated using a comprehensive dataset generated through FE modelling, which simulates a variety of impact damage scenarios differing in location and severity on the girder. This approach enhances the model's ability to generalize across different damage conditions and improves prediction accuracy.

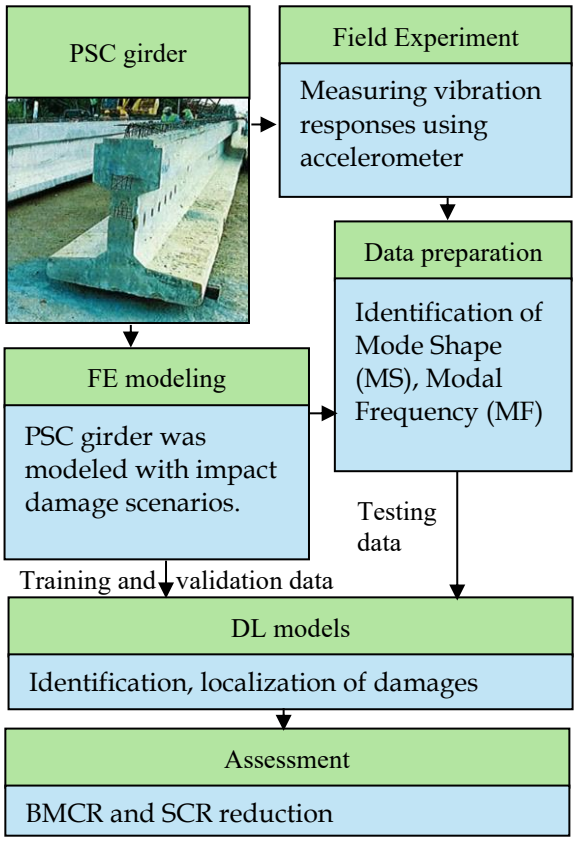

Figure 2: Flow chart of methodology.

2.1 Field Dynamic Testing of PSC Girder

The experimental setup involves collecting vibration data from a simply supported PSC girder (25 m long) as shown in Fig. 3. An impact hammer was used to excite the beam, while three strategically placed accelerometers (Guralp Fortis) along the girder connected to a dynamic data logger were used to capture its dynamic response, as shown in Fig. 4. Two sets of tests were conducted by changing the excitation point. That includes three tests (Test 1, Test 2 & Test 3) by giving excitation at quarter point of the beam (near to Accelerometer A1) and another three tests (Test 4, Test 5 & Test 6) by giving excitation at midpoint of the beam (near to Accelerometer A2).

(a) (b)

Figure 3: Experimental setup: (a) beam specimen, and (b) beam instrumented with accelerometers.

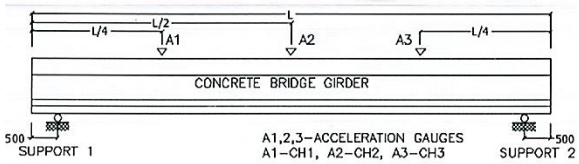

Figure 4: Accelerometer positions.

Four PSC girders were tested, including two undamaged reference girders and two impact-damaged specimens. For each girder, acceleration responses were recorded and analyzed in the frequency domain to capture dynamic behavior. These responses were processed to extract both mode shapes and modal frequencies. These measurements were taken at three critical locations CH1, CH2, and CH3 as illustrated in Figure 4.

2.2 FE Modelling of PSC Girder

In this study, a detailed 3D model of the girder was constructed using ABAQUS, utilizing tetrahedron solid element types to represent the girder's cross-section. To enhance the accuracy of the simulation results, the girder was divided into five distinct parts as shown in Fig. 5, allowing for a more refined analysis of its structural behavior.

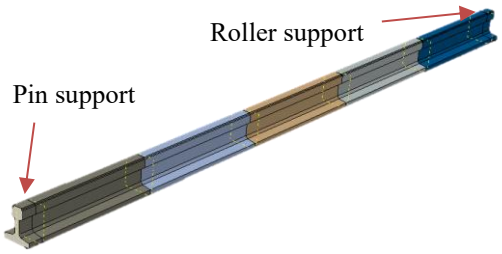

Figure 5: FE of the PSC girder divided into five segments for analysis.

The following Table 1 and Fig. 6 list the material properties and dimensions of the girder. The reinforcement and pre-stressed strands within the girder were modelled as distinct components using truss elements. To accurately simulate the interaction between these steel members and the surrounding concrete, an embedded region contact model was employed. For the pre-stressing tendons bars, a prestressing force of 1,252 N/mm² was applied to one strand out of a total of seven, following the establishment of the connection.

Table 1: Experimental material parameters.

Material property	**Girder**	**Reinforcement**	**Pre tensioned bar**
Material	Concrete	Steel	Steel
Elastic modulus (E/ GPa)	33.3	200	200
Poisson's ratio (υ)	0.2	0.3	0.3
Density (ρ/kgm-3)	2,447	7,800	7,800

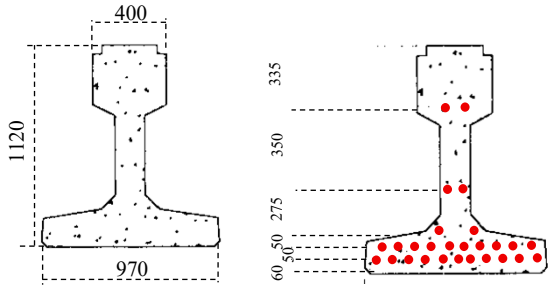

(a) (b)

Figure 6: Experimental beam dimensions: (a) cross sectional details and (b) strand details.

One end of the girder was assigned a pin support, restricting its translational Degrees of Freedom (DOF) in both the horizontal (x), (y) and vertical (z) directions, effectively preventing movement along the beam's length and height. At the opposite end, a roller support was applied, restraining only the vertical (z) translation while permitting horizontal and y direction movement and free rotation about the x-axis. This boundary condition setup, illustrated in Figure 4, represents the support conditions used in the FE model.

The recorded natural frequencies of the tested undamaged girder, presented in Table 2, represent the average values obtained from two undamaged girders. These frequencies were used to tune the FE model, ensuring that its dynamic response closely matches the actual behavior of the girder. In the tuning process, mesh refinement was applied to improve the convergence of the FE model's predicted natural frequencies to the experimentally recorded values as shown in Table 2. The final tuned model employed a mesh size of 5 mm.

Table 2: Experimental and FE-tuned modal frequencies of the undamaged girder.

Mode Type	**Experimental frequency (Hz)**	**FE tuned frequency (Hz)**
Lateral bending	2.115	2.115
1st Vertical bending	4.515	4.513
2nd Vertical bending	18.059	18.066

2.3 Damage Implementation in FE Model

To generate the modal parameters (natural frequencies and mode shapes) under various damage scenarios that required for the proposed DL model, damage is introduced into the FE model using a Damage Array (DA). This array incorporates two key parameters: damage size (d) and damage location (c), as defined in Eq. (1).

$$DA = [c, d] \tag{1}$$

To apply the selected DA as defined in Eq. (1), damage is introduced by reducing the elastic modulus within the specified damage region. This was implemented as a percentage reduction of the elastic modulus, denoted by λ_D. This reduction is governed by Eq. (2), as shown in Fig. 7, which modifies the original DA configuration. The updated DA, reflecting the effect of damage due to stiffness loss, is represented by Eq. (3). This approach enables a simulation of impact damage by capturing the influence of reduced material stiffness on the girder's dynamic behaviour.

$$\lambda_D = (1 - \alpha_D) \times 100 \tag{2}$$

where $\alpha_D = \frac{E_{damaged|\,concrete}}{E_{undamaged|\,concrete}}$ is the ratio between elastic modulus of damaged concrete ($E_{damaged|\,concrete}$) and elastic modulus of undamaged concrete ($E_{undamaged|\,concrete}$).

$$DA = [c, d, \lambda_D] \tag{3}$$

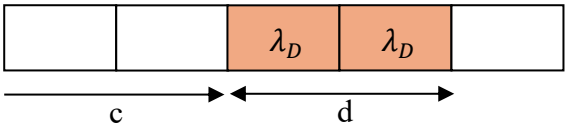

Figure 7: DA application on FE model.

A comprehensive set of damage scenarios is generated by varying the DA parameters namely damage location (c), damage size (d), and the damage severity factor (λ_D) within defined limits. These combinations, as outlined in Table 3, allow for systematic exploration of different damage configurations. A total of 900 distinct damage scenarios were generated by combining various values of the DA.

Table 3: Steps of Damage Array.

Indication parameter	**Range**
c	[0, 20] by 5 steps
d	[0, 25] by 5 steps
λ_D	(0, 30] by 1 steps

2.4 Data Generation

The time-domain data, obtained from the vibration response of the tested damaged girder, is transformed into the frequency domain along with the corresponding mode shapes and model frequencies to generate meaningful input features of Modal Frequency Shift (MFS) and Modal Assurance Criterion (MAC) for the DL models.

Modal Frequency Shift (MFS):

The MFS refers to the variation in modal frequency between the FE model (f_{FE}) and the experimental data (f_E) for a selected mode, expressed as a percentage. This shift is calculated using Eq. (4), which quantifies the difference in the frequencies obtained from the numerical simulation and the experimental measurements, providing insights into the accuracy of the FE model in representing the dynamic behaviour of the structure.

$$MFS = \frac{f_E - f_{FE}}{f_E} \tag{4}$$

Where f_{FE} is selected modal frequency of from the FE model and f_E is the corresponding experimental frequency.

Modal Assurance Criterion (MAC):

The MAC is a metric used to quantify the similarity between the mode shapes obtained from experimental data and those from a Finite Element (FE) model. It is calculated using the following Eq. (5):

.

$$MAC = \frac{\left(\phi_{FE}^T . \Phi_E\right)^2}{((\phi_{FE}^T . \Phi_{FE})\,(\phi_E^T . \Phi_E))} \tag{5}$$

Where Φ_{FE} is the mode shape vector from the finite element mode, Φ_E is the mode shape vector from experimental data and · represents the dot product.

Modal Shape Generation from Accelerometer Data:

The Hilbert-Huang Transform (HHT) is a method for analysing non-stationary and nonlinear time series data following Liu *et al* [26]. It consists of two main steps. The step 1 is Empirical Mode Decomposition (EMD) which decomposes the accelerometer time-series data $a_i(t)$ at location i into Intrinsic Mode Functions (IMFs) and a residual as in Eq. (6):

$$a_i(t) = \sum_{j=1}^{m} IMF_{i,j}(t) + R_i(t) \tag{6}$$

Where $IMF_{i,j}(t)$ are the intrinsic mode functions, $R_i(t)$ is the residual, and m is the number of IMFs.

Step 2 is Hilbert Spectral Analysis (HSA) which applies Hilbert Transform to each IMF to obtain the analytic signal $\widetilde{IMF_i}\ (t)$ as in Eq. (7):

$$\widetilde{IMF_i}\ (t) = IMF_{i,j}(t) + i.H\{IMF_{i,j}(t)\} \quad (7)$$

Where $H\{IMF_{i,j}(t)\}$ is the Hilbert Transform of $IMF_{i,j}(t)$. From this analytic signal, the instantaneous frequency $\omega_i(t)$ and amplitude $A_i(t)$ are derived. These quantities allow for a time-frequency representation of the original signal, providing a detailed insight into its dynamic characteristics.

The acceleration responses and corresponding frequency-domain representations for the four tested girders are shown in Fig. 8 to Fig. 11.

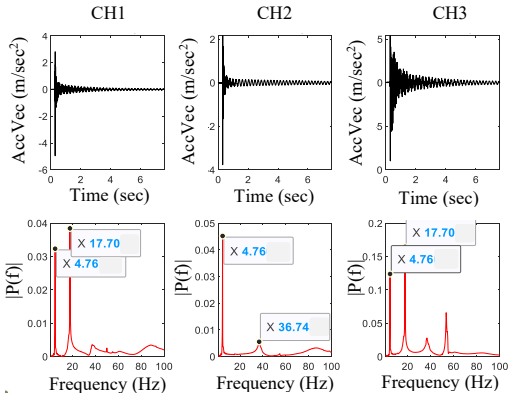

Figure 8: Variation of time and frequency domain response on damaged girder 1

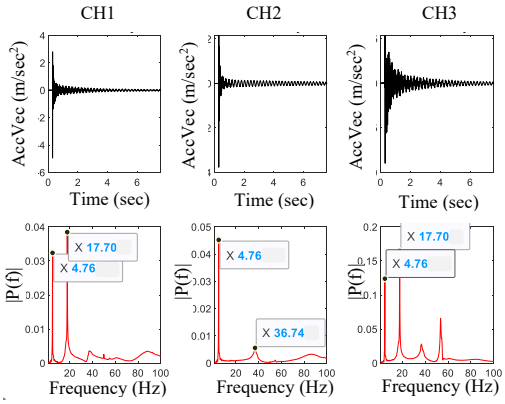

Figure 9: Variation of time and frequency domain response on damaged girder 2

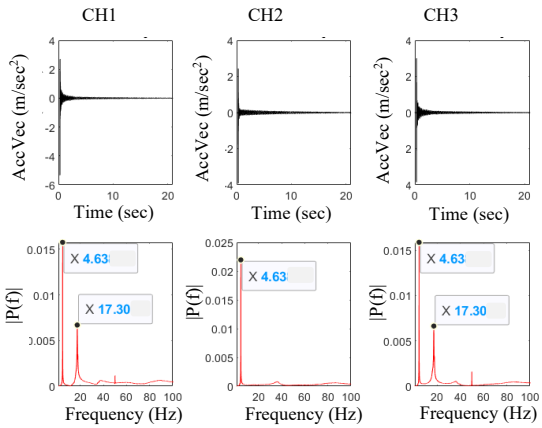

Figure 10: Variation of time and frequency domain

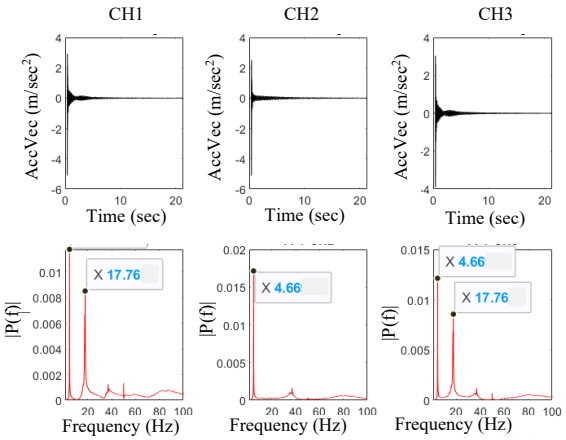

Figure 11: Variation of time and frequency domain response on undamaged girder 2

Bending Moment Capacity Reduction:

Bending Moment Capacity Reduction (BMCR) represents the decrease in bending moment capacity of an impact-damaged girder compared to an undamaged reference girder when subjected to a Uniformly Distributed Load (UDL) of approximately 100 kN/m^2 as per BS5400 Class 45 loading conditions, applied on the top surface Masrom *et al* [27]. This reduction is a critical indicator of how the structural integrity of the girder has been compromised due to localized damage. The BMCR is calculated using the relationship outlined in Eq. (8):

$$BMCR = (1 - M_d/M_u) \times 100\% \quad (8)$$

Where the $M_d = \int A\sigma_d(y) \cdot ydA$ is the bending moment capacity of the damaged girder, $M_u = \int A\sigma_u(y) \cdot ydA$ is the bending moment capacity of the undamaged girder, $\sigma_d(y)$ and $\sigma_u(y)$ are the stress distributions in the damaged and undamaged girders, respectively, at a given distance y from the neutral axis and A is the cross-sectional area of the girder.

Shear Capacity Reduction:

Shear Capacity Reduction (SCR) represents the decrease in shear resistance of an impact-damaged girder compared to an undamaged reference girder under a UDL of 100 kN/m^2 as per BS5400 Class 45 loading conditions, applied on the top surface. This reduction is a key

parameter in evaluating the ability of a girder to safely transfer shear forces across its cross-section, especially in the presence of localized damage such as cracking or material degradation. The SCR is calculated using the relationship outlined in Eq. (9):

$$SCR = (1 - V_d/V_u) \times 100\% \quad (9)$$

Where $V_d = \int A\tau_d(y)dA$ is the shear capacity of the damaged girder, and $V_u = \int A\tau_u(y)dA$ is the shear capacity of the undamaged girder. Here, $\tau_d(y)$ and $\tau_u(y)$ represent the shear stress distributions in the damaged and undamaged girders, respectively, over the cross-sectional area A. This formulation provides a quantitative assessment of the reduction in shear-carrying capacity due to impact, offering critical insight into the potential safety risks and the extent of structural degradation.

3. Results and Discussion

In this study, a DL model was employed to identify, localize, and assess the severity of impact-damaged girders. The model was trained and validated using dynamic characteristics generated from FE simulations under various damage scenarios. For testing and final damage assessment, experimentally identified dynamic parameters were utilized. This approach ensures that the DL model learns from a wide range of simulated conditions while being evaluated on real-world measurements. The overall DL network flow for impact damage assessment is illustrated in Fig. 12.

Damage Identification	Input	MFS
	Neurons	**Activation Function**
	256	Linear
	128	ReLU
	64	Linear
	2	Softmax
	Output	Damaged or not damaged

If damaged

Damage Localization	Input	MFS and MAC
	Neurons	**Activation Function**
	256	ReLU
	256	Tanh
	128	ReLU
	3	Softmax
	Output	$[c, d, \lambda_D]$

Severity Assessment	Input	DA
	Neurons	**Activation Function**
	128	Tanh
	64	Linear
	32	Tanh
	5	Linear
	Output	Severity levels

Figure 12: DL damage assessment architecture

The damage assessment architecture comprises three consecutive DL models dedicated to damage identification, localization, and severity assessment. Each of these models is developed using a Feedforward Neural Network (FNN) framework. For the damage identification stage, the model utilizes the variation in modal frequencies between the damaged and undamaged states. Specifically, the damaged modal frequencies, presented in Figure 13, are compared against the baseline undamaged frequencies shown in Fig. 14. However, the third peaks recorded in Fig. 10 and Fig. 11 in the CH3 FFT diagrams cannot be ignored, as they likely result from the excitation of an additional modal frequency. Nevertheless, since this study focuses only on comparing the first two excited modal frequencies, the third peak is excluded from the analysis. This comparison enables the model to effectively distinguish between healthy and damaged structural conditions.

To achieve optimal model performance, hyperparameter tuning was conducted by varying the number of hidden layers, neurons per layer, activation functions, and learning rates. A grid search approach combined with 5-fold cross-validation was employed to select the best configuration that minimized validation loss while maintaining high generalization capability. As a result, the optimal architecture of the damage identification model is presented in Table 4. This DL model achieved a high training accuracy of 98.82% and a validation accuracy of 89.95%, demonstrating its strong capability to generalize to unseen data. Additionally, the model attained a low MSE of 0.023, indicating precise prediction performance and reliable classification of damage presence based on modal frequency variations.

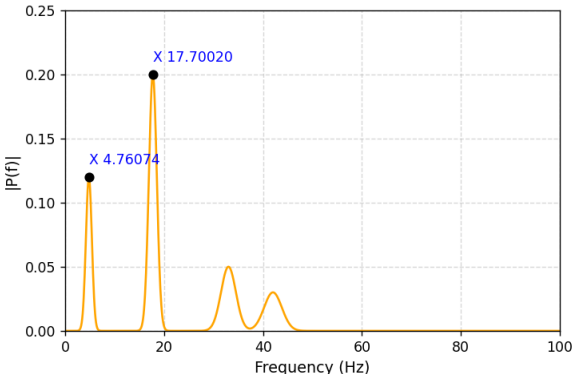

Figure 13: Impact damaged girder frequency domain variation

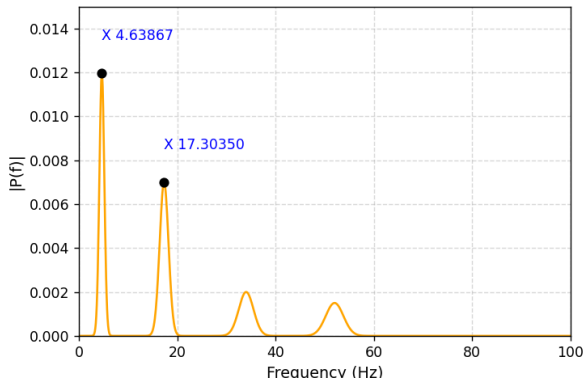

Figure 14: Undamaged girder frequency domain variation

Table 4: Damage identification optimal model architecture.

Input	[MFS1, MFS2]	
Category	Parameter	Value
Hyperparameter Grid Search	Optimizer	Adam
	Learning Rate	0.001
	Batch Size	64
	Epochs	250
	Data Split	0.2
	Cross-Validation	5-fold
	Layers	[256, 128, 64]
Loss and Evaluation Metrics	Loss Function	Mean Square Error (MSE)
	R^2 Score	0.88±0.0017
	MSE	0.023
	Best Validation Accuracy	89.95%
	Best Training Accuracy	98.82%
Output	[Damaged/Undamaged]	

The prediction accuracy of the DL model, as illustrated in the confusion matrix shown on Fig. 15, demonstrates excellent performance. Out of 900 training samples and 4 testing samples, the model accurately classified all instances, indicating strong generalization capability and reliable damage identification.

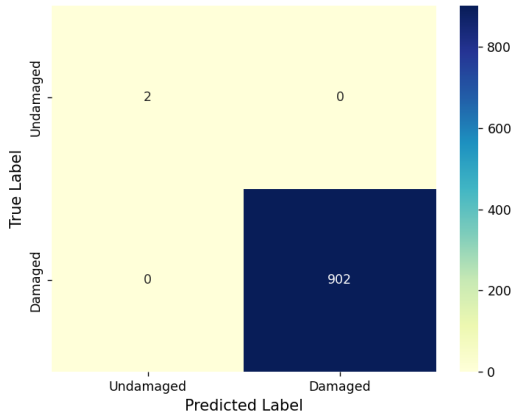

Figure 15: Confusion matrix of damage identification model

After successfully classifying the impact-damaged girders using the initial DL model designed for damage identification, the filtered output data was subsequently fed into a second stage model and FNN tailored for damage localization. This localization model plays a critical role in determining three key parameters associated with girder impact damage: the precise location of the damage denoted by c, the extent or size of the damage indicated by d, and the severity level of the damage quantified through the damage percentage λ_D.

In the early stages of model development, the input to the localization network consisted solely of MFS, extracted from the frequency domain. However, despite the theoretical relevance of MFS in detecting modal changes due to structural alterations, the use of MFS as the only input feature proved insufficient. Specifically, the model exhibited relatively low training and validation accuracies. A detailed analysis revealed that the limitations stemmed from the inability of MFS alone to capture and distinguish between symmetrical damage scenarios, which often produce similar frequency responses and thus confuse the network during learning. Moreover, the MFS value remained within a relatively low range, as illustrated in Fig. 16, further limiting the feature's effectiveness in discriminating damage locations.

To overcome this limitation, the model was retrained using a combination of MFS and MAC values as input features. This integrated approach significantly enhanced the model's performance, achieving nearly 100% accuracy in both training and validation phases. The comparison of training and validation accuracies between the MFS-only input and the combined MFS + MAC input is presented in Fig. 17. Fig. 18 presents a comparison of experimentally and numerically identified mode shapes using MAC values for two damaged girders relative to the undamaged experimental girder. Additionally, the comparison with the undamaged FE model outcome is included to demonstrate the accuracy of model tuning. This MAC comparison is essential, as it validates the effectiveness of incorporating MAC values for improving the fidelity of DL model.

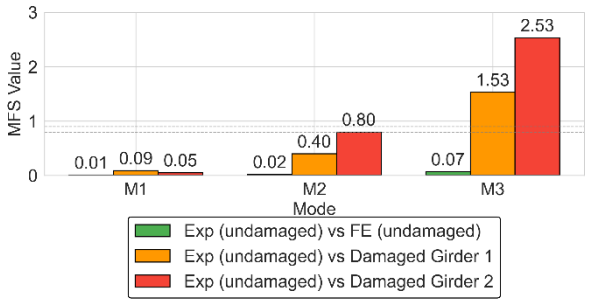

Figure 16: MFS comparison: undamaged vs. damaged girders

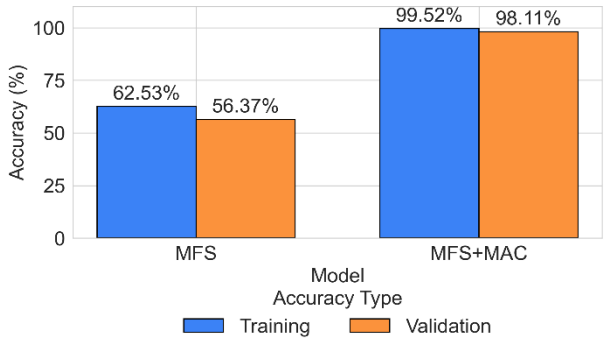

Figure 17: Training and validation accuracy of damage localization models

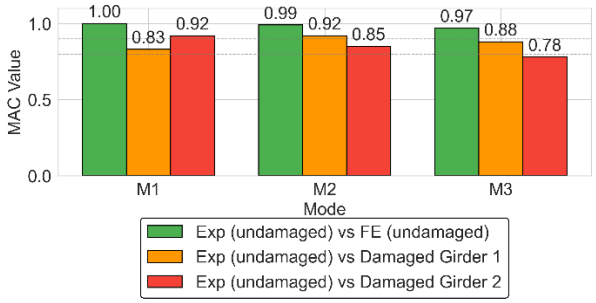

Figure 18: MAC comparison: undamaged vs. damaged girders

The optimal configuration of the damage localization model is presented in Table 5. This arrangement reflects the most effective combination of input features and model parameters that yielded the highest accuracy in identifying damage locations. Fig. 19 illustrates the accuracy achieved through 5-fold cross-validation for all tasks over epochs.

Table 5: Damage localization optimal model architecture.

Input	[MFS1, MFS2, MAC1, MAC2]	
Category	Parameter	Value
Hyperparameter Grid Search	Optimizer	Adam
	Learning Rate	0.001
	Batch Size	64
	Epochs	250
	Data Split	0.2
	Cross-Validation	5-fold
	Layers	[256, 256, 128]
Loss and Evaluation Metrics	Loss Function	Mean Square Error (MSE)
	R^2 Score	0.98±0.0017
	MSE	0.00132
	Best Validation Accuracy	98.11%
	Best Training Accuracy	99.52%
Output	$DA\ [c, d, \lambda_D]$	

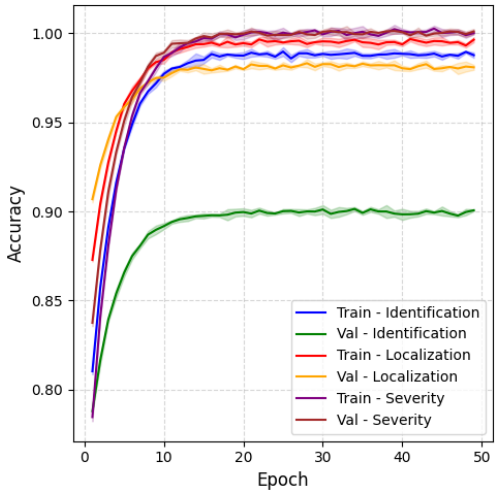

Figure 19: Training and validation accuracy (5-Fold) for damage identification, localization and severity

The identified damage distribution for the two impact-damaged girders is presented in Table 6. The results reveal that the damage is not widely distributed across the girders but is instead concentrated around the impact location. This localized damage pattern suggests that the impact did not cause significant structural spread. The estimated strength reduction in the concrete ranges between 5% and 10%, indicating relatively low levels of damage. However, the severity of the damage cannot be fully assessed based on strength reduction alone. A more comprehensive evaluation should be conducted using parameters such as BMCR and Shear SCR, which offer a more accurate representation of structural performance degradation.

Table 6: Impact damage distribution on girders.

Beam Index	**Damage Distribution**				
1	0	0	0	1.65	5.52
	c	15			
	d	10			
	λ_D	[1.65, 5.52]			
2	0	0	0.05	2.33	8.23
	c	10			
	d	15			
	λ_D	[0.05, 2.33, 6.23]			

In the last stage of this research, the variation of BMCR and SCR was calculated using DL model when the DA was identified using damage localization DL model. The distribution of BMCR and SCR variation over different damage location (c), damage size (d) and damage percentage (λ_D) shows in Fig. 20.

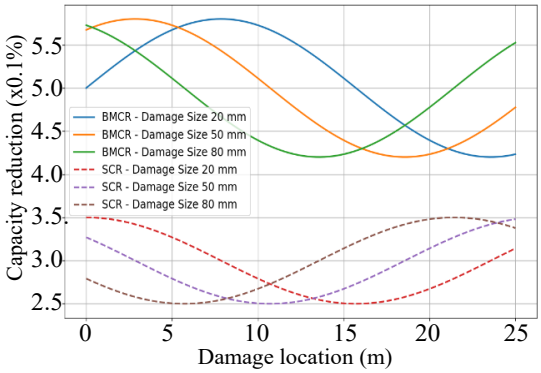

Figure 20: BMCR and SCR variation over damage location for 20% damage ($\boldsymbol{\lambda_D}$)

The developed FNN DL model for damage assessment achieved 100% accuracy in both training and validation phases, demonstrating its exceptional performance in identifying damage conditions from the input parameters. This high level of accuracy confirms that the model effectively learned the complex relationships between input features and the corresponding damage states. The optimal architecture of the FNN model, including the number of layers, neurons per layer, and activation functions used, is summarized in Table 7.

Table 7: Damage severity assessment optimal model architecture.

Input	$DA\ [c, d, \lambda_D]$	
Category	Parameter	Value
Hyperparameter Grid Search	Optimizer	Adam
	Learning Rate	0.001
	Batch Size	64
	Epochs	100
	Data Split	0.2
	Cross-Validation	5-fold
	Layers	[64, 64, 32]
Loss and Evaluation Metrics	Loss Function	Mean Square Error (MSE)
	R^2 Score	0.99±0.0001
	MSE	1E-8
	Best Validation Accuracy	100%
	Best Training Accuracy	100%
Output	[BMCR, SCR]	

The identified BMCR and SCR for the two impact-damaged girders, as determined by the damage severity assessment DL model, are presented in Table 8. These parameters provide critical insight into the structural response of the girders under impact conditions. The BMCR reflects the fundamental change in curvature behavior due to damage, while the SCR captures variations in strain-related curvature patterns. Together, they serve as reliable indicators for evaluating the severity and extent of the damage.

Table 8: Damage assessment criteria.

Beam Index	**Criteria name**	**Value (%)**
1	BMCR	0.83
	SCR	1.21
2	BMCR	1.01
	SCR	1.88

The results indicate that the two impact-damaged girders exhibit relatively low levels of damage, with a maximum variation of 2% in both the BMCR and SCR. Such minimal variations suggest that the structural integrity of the girders remains largely unaffected. The damage severity assessment DL model confirms that these variations fall within acceptable limits for minor damage, supporting the conclusion that the girders are still suitable for use in bridge construction. This highlights the effectiveness of the model in evaluating the usability of impact-damaged structural elements.

4. Conclusions

This study presents a comprehensive framework for evaluating impact-induced damage in concrete girders using a DL based methodology. Experimental validation was conducted on four girders, including two undamaged references and two impact-damaged specimens. Vibration data collected from critical locations, along with frequency domain features such as MFS and, were utilized for model development. The use of FE modeling further enhanced the data quality for training and validation, ensuring realistic simulation of structural behavior.

The DL framework consisted of three sequential stages: damage identification, localization, and severity assessment. The identification model, using MFS, achieved over 89% accuracy, while the localization model enhanced with MAC features reached over 95% accuracy. Severity assessment, based on BMCR and SCR, indicated that the damage was highly localized near the impact edge and relatively minor, with BMCR and SCR values below 2%. These results suggest that the girders retained most of their structural integrity despite localized damage. While the proposed approach shows promising results, it is important to note certain limitations. The DL models may be sensitive to noise in sensor data or to variations in mesh size used in the FE models, potentially affecting generalizability. Furthermore, explainability of the trained DL models critical for practical acceptance in engineering application was not explored in this work. These aspects will be addressed in future studies, focusing on model robustness under noisy conditions, mesh convergence studies, and integration of explainable AI techniques to enhance interpretability.

Overall, this study provides critical insights into the effectiveness of DL-based models for structural health monitoring. By combining dynamic response features such as MFS and MAC with a multi-stage DL framework, it becomes possible to accurately identify, localize, and quantify damage severity in concrete girders. These findings can be directly aligned with industrial quality control standards for precast bridge components and can be integrated into on-site inspection and acceptance procedures during storage, transportation, and installation phases to ensure compliance with safety and durability requirements.

References

[1] J. Wang and Y. J. Kim, “A state-of-the-art review of prestressed concrete tub girders for bridge structures,” *Journal of Infrastructure Preservation and Resilience*, vol. 3, no. 1, 2022.

[2] S. Addepalli and S. K. Ikkurthi, “Durability studies on prestressed concrete,” *Test Engineering and Management*, vol. 83, no. 1, pp. 15779, 2020.

[3] J. Karthikeyan and V. F. Praveen, “Long-term effects due to creep and shrinkage on prestressed concrete bridge girders using SCC,” *International Journal of Structural Engineering*, vol. 2, no. 4, pp. 390, 2011.

[4] H. Burger, T. Tepho, O. Fischer, and N. Schramm, “Performance assessment of existing prestressed concrete bridges utilizing distributed optical fiber sensors,” *CRC Press eBooks*, pp. 3134–3141, 2023.

[5] O. Khandel, M. Soliman, R. W. Floyd, and C. D. Murray, “Performance assessment of prestressed concrete bridge girders using fiber optic sensors and artificial neural networks,” *Structure and Infrastructure Engineering*, vol. 17, no. 5, pp. 605–619, 2020.

[6] S. Wang, P. Xia, K. Chen, F. Gong, H. Wang, Q. Wang, Y. Zhao, and W. Jin, “Prediction and optimization model of sustainable concrete properties using machine learning, deep learning and

swarm intelligence: A review," *Journal of Building Engineering*, vol. 80, pp. 108065, 2023.

[7] S. Venquiaruto, L. Bernardino da Silva, and D. C. C. Dal Molin, "Influence of preloading-induced microcracking on the durability of concrete produced with different types of cement," *Construction and Building Materials*, vol. 189, pp. 777–786, 2018.

[8] Z. Zhou, L. D. Wegner, and B. F. Sparling, "Structural health monitoring of precast concrete box girders using selected vibration-based damage detection methods," Advances in Civil Engineering, pp. 1–21, 2010.

[9] R. Patel, "A review on non-destructive testing (NDT) techniques: Advances, researches and applicability," *International Journal of Current Science Research and Review*, vol. 5, no. 4, 2022.

[10] M.E. Torbali, A. Zolotas, and N.P. Avdelidis, "A state-of-the-art review of non-destructive testing image fusion and critical insights on the inspection of aerospace composites towards sustainable maintenance repair operations," *Applied Sciences*, vol. 13, no. 4, p. 2732, 2023.

[11] M. Civera and C. Surace, "A comparative analysis of signal decomposition techniques for structural health monitoring on an experimental benchmark," *Sensors*, vol. 21, no. 5, p. 1825, 2021.

[12] N. Liu, Y. Ge, X. Bai, Z. Zhang, Y. Shangguan, and Y. Li, "Research on damage detection methods for concrete beams based on ground penetrating radar and convolutional neural networks," *Applied Sciences*, vol. 15, no. 4, pp. 1882–1882, 2025.

[13] M. A. Girmay, "Integrating AI in Structural Health Monitoring (SHM): A systematic review on advances, challenges, and future directions," i-manager's Journal on Structural Engineering, vol. 13, no. 3, pp. 43, 2024.

[14] A. Bader, A. Shtayat, and B. Al-Mistarehi, "Enhancing structural health monitoring with AI-ML algorithms: A focus on crack detection and prediction," *Asian Journal of Civil Engineering*, 2025.

[15] A. Zar, Z. Hussain, M. Akbar, T. Rabczuk, Z. Lin, S. Li, and B. Ahmed, "Towards vibration-based damage detection of civil engineering structures: overview, challenges, and future prospects," *International Journal of Mechanics and Materials in Design*, 2024.

[16] Y. Ren, O. Bareille, Z. Lin, and X.-R. Huang, "Review of damage detection techniques in vibration-based structural health monitoring," *International Journal of Dynamics and Control*, vol. 13, no. 3, 2025.

[17] D. Nath, Ankit, None, D. R. Neog, and S. S. Gautam, "Application of machine learning and deep learning in finite element analysis: A comprehensive review," *Archives of Computational Methods in Engineering*, 2024.

[18] Y. Lee, H. Kim, S. Min, and H. Yoon, "Structural damage detection using deep learning and FE model updating techniques," Scientific Reports, vol. 13, no. 1, 2023.

[19] S. F. Ahmed, S. Bin, M. Hassan, M. R. Rozbu, T. Ishtiak, N. Rafa, M. Mofijur, Ali, and A. H. Gandomi, "Deep learning modelling techniques: Current progress, applications, advantages, and challenges," *Artificial Intelligence Review*, vol. 56, no. 1, 2023.

[20] O. Elharrouss, Y. Akbari, N. Almaadeed, and S. Al-Maadeed, "Backbones-Review: Feature Extraction Networks for Deep Learning and Deep Reinforcement Learning Approaches," *arXiv*, Cornell University, 2022.

[21] J.-T. Kim, J.-H. Park, and B.-J. Lee, "Vibration-based damage monitoring in model plate-girder bridges under uncertain temperature conditions," *Engineering Structures*, vol. 29, no. 7, pp. 1354–1365, 2007.

[22] H. Jasmine, "Vibration Based Damage Detection Using Localized Crack-Type Damage Models and ANN," IOSR Journal of Mechanical and Civil Engineering (IOSR-JMCE), vol. 20, no. 2, pp. 50–66, 2023.

[23] R. Furlong, "Chapter 2 Design for Shear," accessed Jan. 28, 2025.

[24] N. F. Alkayem, M. Cao, Y. Zhang, M. Bayat, and Z. Su, "Structural damage detection using finite element model updating with evolutionary algorithms: A survey," Neural Computing and Applications, vol. 30, no. 2, pp. 389–411, 2017.

[25] V. Singh, A. Baral, R. Kumar, S. Tummala, M. Noori, S. V. Yadav, S. Kang, and W. Zhao, "A hybrid deep learning model for enhanced structural damage detection: Integrating ResNet50, GoogLeNet, and attention mechanisms," Sensors, vol. 24, no. 22, pp. 7249–7249, 2024.

[26] J. Liu, X. Wang, S. Yuan, and G. Li, "On Hilbert-Huang Transform approach for structural health monitoring," *Journal of Intelligent Material Systems and Structures*, vol. 17, no. 8-9, pp. 721–728, 2006.

[27] M. A. Masrom and L. D. Goh, "Comparative study of bridge traffic loadings between British standards and Eurocodes," in *AIP Conference Proceedings*, Langkawi, Malaysia, 2018.

Experimental and Numerical Investigation of Shear-Deficient Reinforced Concrete Beams Strengthened with Ultra-High Performance Fiber Reinforced Concrete (UHPFRC) Jackets

S. Wijesundara[1*], I. Abeykoon[1], S. Bandara[1], K. Wijesundara[1]
[1]Department of Civil Engineering, Faculty of Engineering, University of Peradeniya.
[*]sandaruw@eng.pdn.ac.lk

Abstract

This paper presents an experimental and numerical investigation of the performance of Ultra-High Performance Fiber Reinforced Concrete (UHPFRC) for retrofitting shear-deficient reinforced concrete (RC) deep beams. One control RC beam and one retrofitted beam were tested under three-point bending to assess structural enhancement due to retrofitting. Prior to UHPFRC application, the RC beam surface was roughened through chipping, followed by the application of a bonding agent to ensure proper adhesion. Two 40 mm-thick UHPFRC layers were cast on the vertical faces of the RC beam to improve its performance in shear. The experimental results revealed a significant improvement in structural behaviour due to retrofitting. Notably, the failure mode of the control beam transitioned from brittle shear to a more ductile flexure-dominated response in the retrofitted specimen. This transition was accompanied by more than a 100% increase in maximum load capacity and a significant improvement in deformation characteristics and overall stiffness. A detailed three-dimensional finite element (FE) model was developed to simulate the behaviour of the RC beams strengthened with UHPFRC. To accurately capture the interaction between the RC substrate and the UHPFRC overlay at the interface, a cohesive surface-based interface model was employed. This technique effectively captured the debonding behaviour of the UHPFRC jacket observed during testing. The numerical predictions closely aligned with experimental results in terms of load-deflection response and crack development, validating the accuracy and reliability of the FE model. These findings highlight the potential of UHPFRC retrofitting as a robust solution for strengthening shear-deficient RC deep beams.

Keywords: UHPFRC, Retrofitting, Shear-deficient, Shear Strengthening, Finite Element

1. Introduction

The premature degradation of reinforced concrete (RC) structures has emerged as a pressing challenge in modern civil engineering. Although designed for long service lives, many RC members face premature degradation due to several reasons, such as exposure to aggressive environmental conditions, like chloride attacks in coastal regions, carbonation in urban areas, freeze-thaw cycles, and chemical exposures [1,2]. Additionally, increasing live loads and evolving functional demands further compromise structural integrity, leading to a decline in load-bearing capacity and raising serious safety concerns [3].

Traditionally, the primary solution to this problem has been the demolition and reconstruction of damaged structures. However, this approach is too costly, time-consuming, environmentally detrimental, and often disrupts daily operations. In contrast, structural retrofitting has emerged as a more viable and sustainable alternative, aiming to restore or enhance the mechanical performance of deficient RC members while minimizing downtime and resource consumption.

Over the years, several retrofitting techniques have been developed and implemented in practice, including RC or steel jacketing [4–6], fiber-reinforced polymer (FRP) wrapping [7], external post-tensioning [8], and near-surface mounted (NSM) reinforcement [9]. However, each method presents specific limitations. RC jacketing increases member dimensions and dead load, which may adversely affect global structural behaviour [10]. Steel jacketing is susceptible to corrosion and fire hazards [11], while FRP systems often exhibit reduced performance under elevated temperatures and humid conditions, in addition to potential issues with surface preparation and long-term adhesion [12]. External prestressing and NSM systems also require meticulous execution and pose challenges related to long-term durability and maintenance.

In response to these limitations, Ultra High-Performance Fiber Reinforced Concrete (UHPFRC) has emerged as a highly promising retrofitting material. UHPFRC is characterized by a dense microstructure, high compressive strengths exceeding 120 MPa, and strain-hardening tensile behaviour facilitated by the inclusion of steel fibers [13,14]. These attributes offer exceptional ductility, tensile strength, crack resistance, and long-term durability in structural applications [15,16]. The application of UHPFRC as a retrofitting layer has proven to offer the dual advantage of enhanced performance and durability improvement without significantly altering the cross-sectional properties of the structural member.

[1] S. Wijesundara, I. Abeykoon, S. Bandara, and K. Wijesundara: Department of Civil Engineering, Faculty of Engineering, University of Peradeniya, Sri Lanka (e-mail: sandaruw@eng.pdn.ac.lk)

In recent years, a considerable body of experimental and numerical research has demonstrated the potential of UHPFRC in restoring and improving the flexural capacity of RC slender beams [17–21]. Various retrofitting configurations, such as T-sided (tension zone), C-sided (compression zone), 2-sided, and 3-sided (U-shaped), have been explored by several studies to optimize mechanical performance and compatibility with existing structures. Among these, 3-sided jacketing has shown superior flexural enhancement, primarily due to increased confinement and improved composite action [20,21]

While the use of UHPFRC in flexural strengthening applications has been extensively investigated, its potential for shear strengthening, particularly in RC deep beams, which are prone to brittle shear failure, remains underexplored. Unlike flexure failure, shear failure often occurs suddenly with limited warning, presenting a significant safety risk in deteriorated structures. This deficiency in existing literature and practice underscores the need for focused research into shear retrofitting solutions.

The present study investigates the effectiveness of UHPFRC as a retrofitting material for shear-deficient RC beams, with a focus on both experimental and numerical evaluation. By addressing this critical area of structural retrofitting, the current study aims to facilitate the practical implementation of UHPFRC as a reliable and efficient solution for enhancing the longevity of existing RC structures. Further, this study involved the development of a custom UHPFRC mix using locally available materials in Sri Lanka, with only the steel fibers being imported. This mix design approach is expected to ensure economic feasibility and promote the adoption of UHPFRC in the local industry.

2. UHPFRC Mix Preparation

The successful implementation of UHPFRC in real-world applications depends heavily on the selection of its constituent materials. In this study, particular emphasis was placed on optimizing material choice for cost-efficiency, availability, and technical performance to enhance the practical viability of UHPFRC in Sri Lanka.

2.1 Raw Materials

Cement: A locally available Type I OPC (42.5R) was used as a practical alternative to the typically recommended 52.5R grade, which is not widely available in the local market.

Fine aggregate: Processed River sand with particle size smaller than 600 µm was used to ensure proper particle packing and matrix density.

Microsilica: Microsilica conforming to ASTM C1240-14 with a high specific surface area of approximately 20000 m^2/kg was added to improve matrix densification and pozzolanic activity.

Superplasticizer: A polycarboxylate-based high-range water-reducing admixture was used to maintain workability at a low water-to-binder (w/b) ratio, meeting ASTM C494 and BS EN 934-2 standards.

Steel fibers: Microsteel fibers with hooked ends (13 mm long, 0.2 mm in diameter) and a tensile strength of 2800 MPa were used in the mix.

2.2 Mix Design

Table 1 presents the optimized UHPFRC mix design developed using a machine-learning model for compressive strength prediction [22]. The mix was tailored to achieve a target strength of 120 MPa while prioritizing economic viability and practical applicability within the local context.

Table 1: Optimized UHPFRC Mix Constituents

Constituent	Content/ (kg/m^3)
Cement	768
Fine Aggregate	1140
Microsilica	192
Superplasticizer	54
Water	154
Fiber	157

2.3 Mixing

A controlled, sequential mixing procedure was adopted throughout this research to ensure the homogeneity and quality of the UHPFRC. Initially, dry materials (cement, fine aggregate, and microsilica) were blended in a horizontal pan mixer for 2-3 minutes. Water and superplasticizer were then gradually introduced, and mixing continued for another 10-12 minutes until a uniform, flowable paste was achieved. Steel fibers were added last, dispersed slowly through a mesh over 3-5 minutes to prevent clumping and ensure uniform distribution.

2.4 Casting

Immediately after mixing, the fresh UHPFRC was cast into pre-prepared molds. For mechanical test specimens, casting was done in two layers, each compacted on a vibrating table. For retrofitting applications (beam jacketing), the UHPFRC was placed in layers and manually tampered with for proper surface distribution.

2.5 Curing

Curing was carried out in two phases. To minimize moisture loss, the specimens were promptly wrapped in polythene sheets following casting. After 24 hours, mechanical test specimens (cylinder and dog-bone specimens) were demolded and submerged in water until the designated testing age. Beam specimens were cured under wet gunny sacks with periodic rewetting to maintain surface moisture.

3. Material Property Assessment

The fresh and hardened properties of the developed UHPFRC mix were evaluated through a series of standardized tests to verify its mechanical performance and suitability for structural retrofitting. All tests were conducted in accordance with relevant international standards.

3.1 Flowability

Flowability of fresh UHPFRC was assessed using a flow table test following ASTM C1437 [23], with adaptations

from ASTM C1856/C1856M [24] and using equipment compliant with ASTM C230/C230M [25]. The measured flow diameter was 157 mm, indicating satisfactory workability for structural applications.

3.2 Compressive Strength

Compressive strength was determined through uniaxial compression tests on standard cylinders with dimensions of 100 mm in diameter and 200 mm in height. Casting and curing were done as per ASTM C31/C31M [26]. Testing was carried out using a 1000 kN capacity Universal Testing Machine (UTM) in accordance with ASTM C39/C39M [27], with load applied at a controlled rate of 0.2 MPa/s until failure. The UHPFRC mix achieved compressive strengths of 96.26 MPa at 7 days and 119.47 MPa at 28 days, closely matching the target strength of 120 MPa.

3.3 Splitting Tensile Strength

The splitting tensile strength was evaluated following ASTM C496 using the same cylindrical specimens. The tested specimens showed a splitting tensile strength of 9.91 MPa. Further, as illustrated in Figure 1, the failure patterns of the specimens revealed critical insights into the behaviour of fiber activation in the UHPFRC mix. The steel fibers exhibited prominent crack-bridging action, effectively delaying crack propagation and enhancing tensile resistance. Additionally, partial straightening and elongation of the hooked ends during pull-out were observed, indicating strong mechanical anchorage. This deformation behaviour reflects effective stress transfer across cracks, contributing to improved energy dissipation and enhanced post-cracking performance.

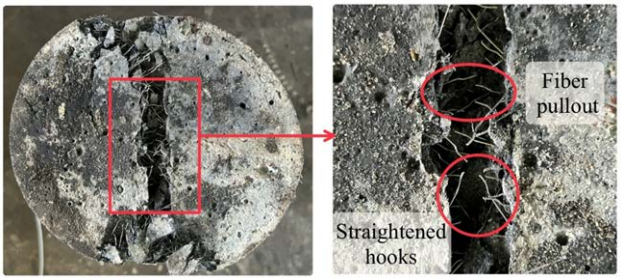

Figure 1: Failure Pattern of Splitting Tensile Test Specimens

3.4 Direct Tensile Strength

The direct tensile strength was assessed using dog-bone-shaped specimens, as shown in Figure 2. This particular geometry ensures a uniform stress distribution within the gauge section. To accommodate effective fiber dispersion and minimize matrix discontinuities, the cross-sectional dimensions were selected such that both the width and thickness exceeded at least twice the 13 mm fiber length. All specimen dimensions are detailed in Figure 3. The test yielded a direct tensile strength of 9.53 MPa, demonstrating the mix's high tensile capacity.

Figure 2: Dog-bone Specimens for Uniaxial Tensile Test

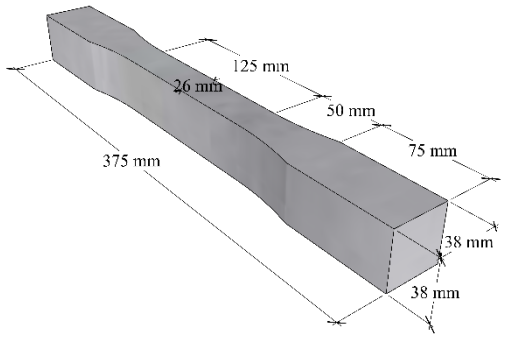

Figure 3: Dog-bone Specimen Dimensions

In addition to the material characterization of UHPFRC, uniaxial tensile tests were carried out on the reinforcing bars used in the beam specimens to accurately capture their mechanical properties. The yield and ultimate strength values obtained for the three types of reinforcement bars are summarized in Table 2.

Table 2: Properties of Steel Reinforcement Bars

Bar diameter/ (mm)	Yield Stress/ (MPa)	Ultimate Stress/ (MPa)
20	533.1	621.9
12	491.9	590.2
6	434.5	500.7

4. Experimental Investigation

4.1 Test Specimens

The experimental investigation was aimed at enhancing the shear capacity of RC deep beams through external strengthening using UHPFRC. To facilitate this, a shear-critical RC deep was specifically designed with an a/d ratio of 2.

The control beam (CB) served as the reference specimen, and its geometry, reinforcement layout, and details are presented in Figure 4. The concrete used in the control beam achieved an average compressive strength of 24.88 MPa and 31.62 MPa at 7 and 28 days, respectively, confirming the expected characteristics of normal-strength concrete used in typical structural applications.

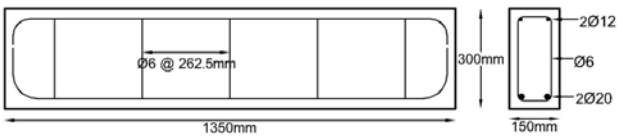

Figure 4: Geometry of the RC Beams

To evaluate the strengthening effect of UHPFRC, a retrofitted beam configuration (RE-40) was proposed. In this approach, 40 mm-thick UHPFRC layers were applied on both longitudinal faces of the existing RC beam as illustrated in Figure 5.

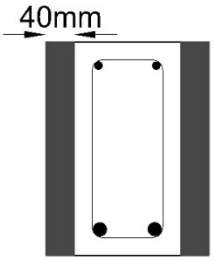

Figure 5: UHPFRC Strengthening Configuration

4.2 Interface Preparation

The quality of the interface between the normal concrete (NC) substrate and the UHPFRC overlay plays a pivotal role in ensuring effective composite action in retrofitting applications. In this study, a systematic surface preparation procedure was adopted to optimize bond performance. The concrete surface of the RC beams was roughened by mechanical abrasion to an approximate depth of 5 mm, as shown in Figure 6. Following that, all residual dust and debris were removed using pressurized air to ensure a clean surface. To minimize water absorption from the UHPFRC mix, the beams were wrapped with wet sacks 24 hours prior to overlay placement. Additionally, a commercial bonding agent was uniformly applied to the prepared surface 15 minutes before casting the UHPFRC layer.

Figure 6: Roughened RC Beam Surface

4.3 Test Setup

The experimental program utilized a three-point bending configuration to evaluate the structural response of RC deep beams under displacement-controlled loading. All beams were simply supported with a clear span of 1050 mm. Deflections of the beams were recorded at the midspan using Linear Variable Displacement Transducers (LVDTs). To monitor internal strain development, strain gauges were installed on selected stirrups and at the center of the longitudinal reinforcement on the tension face. The complete test and instrument setup is illustrated in Figure 7 and Figure 8.

Figure 7: Test Setup for Beam Tests

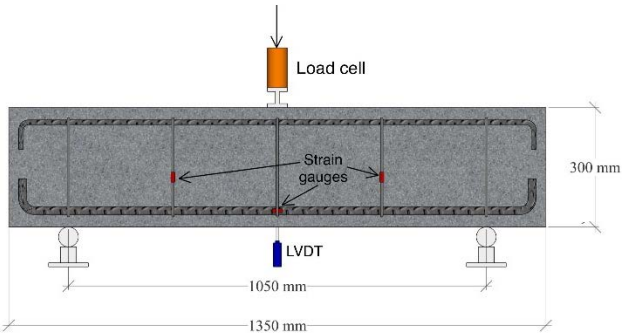

Figure 8: Instrument Setup

5. Experimental Results and Discussion

5.1 Failure Mechanisms

The control beam displayed a brittle shear failure mechanism. Initial flexure cracks were observed at a load of approximately 75 kN, followed by diagonal shear cracks at around 105 kN. At around 150 kN, a dominant shear crack started to propagate by combining multiple fine cracks. At this point, the primary diagonal crack widened to approximately 1.2 mm. The beam eventually attained its peak load of 185 kN, after which a major diagonal crack propagated, resulting in shear failure. The cracking pattern observed in the control beam is illustrated in Figure 9(a).

The strain responses shown in Figure 10, recorded from the strain gauges, further confirm the shear-dominant failure pattern as the data indicates yielding of one of the stirrups, which likely initiated the ultimate shear failure of the beam.

The strengthened beam demonstrated significantly improved performance overall. The first minor flexure crack occurred at 215 kN, indicating enhanced initial cracking resistance due to the UHPFRC confinement. As loading progressed, controlled crack propagation was observed, accompanied by audible fiber pullout. At approximately 370 kN, debonding of the UHPFRC overlay was noted along the top interface, forming a visible separation of about 0.5 mm. The beam reached its peak load of 376 kN and failed due to a dominant flexural crack. Inspection of the RC beam surface underneath revealed flexural cracks that were closely aligned with those in the UHPFRC layer, highlighting the effective composite action between the two materials during loading. Additionally, a prominent diagonal shear crack was observed, suggesting that once the interface bond

weakened, the underlying RC section was unable to resist the shear demand. 9 (b) shows the final crack pattern of the retrofitted beam.

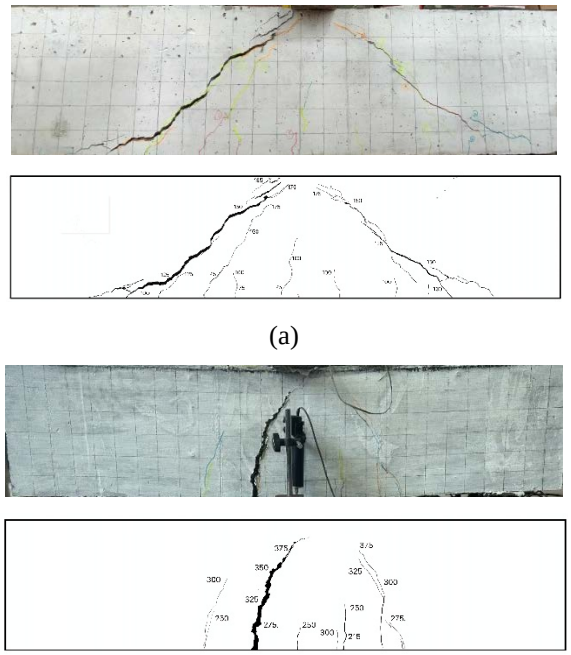

(a)

(b)

Figure 9: Final Crack Patterns of: (a) Control Beam; (b) Retrofitted Beam

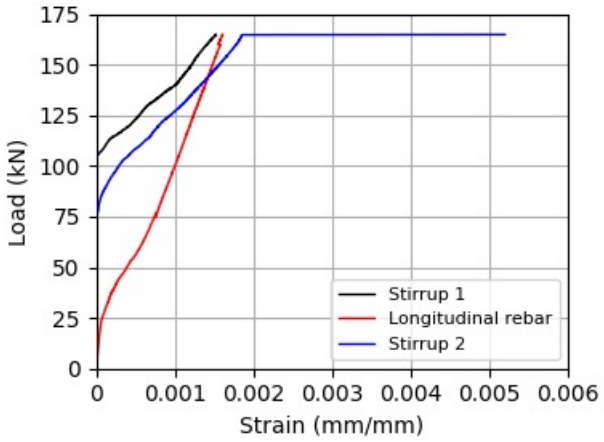

Figure 10: The Strain Responses of the Control Beam

5.2 Load – Displacement Behaviour

Figure 11 shows the load vs midspan deflection response of both the control beam and the retrofitted beam. The control beam reached a peak load of 185 kN at a midspan displacement of 4.96 mm, and the ultimate deflection was recorded as 6.22 mm.

In contrast, the retrofitted beam RE-40 exhibited significantly enhanced performance, achieving a peak load of 376 kN at 6.04 mm. Evidently, UHPFRC jacketing has contributed to a remarkable enhancement in load carrying capacity, with the peak load more than doubling that of the control beam. Additionally, the ultimate deflection reached 7.50 mm, indicating a notable enhancement in deformation capacity. These results clearly demonstrate the superior load resistance and energy dissipation capacity imparted by the UHPFRC layers in shear-critical RC beams.

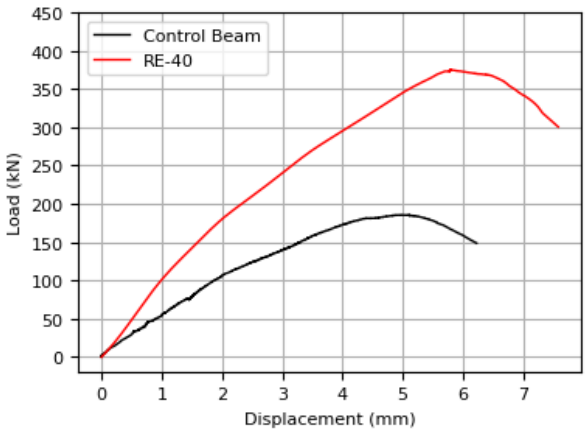

Figure 11: Load vs Mid-span Deflection of Beams

6. Numerical Investigation

6.1 Finite Element (FE) Modelling

For the numerical modeling of the test beams, the FE analysis software ABAQUS was employed in this study. Further, the nonlinear behaviour of concrete and UHPFRC was simulated using the Concrete Damage Plasticity (CDP) model. The CDP model is a continuum, plasticity-based damage model. It represents the inelastic response of concrete by integrating isotropic damaged elasticity with isotropic plasticity under both tension and compression. The model is based on the premise that concrete primarily fails through tensile cracking and compressive crushing mechanisms. These mechanisms are represented through scalar damage variables that degrade material stiffness.

Both concrete and UHPFRC were modeled using eight-node linear brick elements with reduced integration and hourglass control (C3D8R), and the longitudinal reinforcement and stirrups were modeled using two-node linear 3D elements (T3D2) that transmit only axial forces. To ensure accurate results without excessive computational cost, a mesh sensitivity analysis was conducted, varying mesh size from 15 mm to 50 mm. Based on convergence behaviour, an optimum mesh size of 25 mm and 30 mm was adopted for the control beam and retrofitted beam, respectively.

6.2 Material Behaviour and Constitutive Modeling

6.2.1 Concrete

To simulate the uniaxial compressive and tensile behaviour of concrete, the Carreira and Chu [28] model was adopted in this study due to its proven accuracy in capturing the nonlinear response of concrete. The stress-strain relationship of concrete in compression and tension is presented in Figure 12 and Figure 13 respectively. Further, the material properties defined for concrete in the FE model include a density of 2350 kg/m^3, an elastic modulus of 25 GPa, and a Poisson's ratio of 0.20.

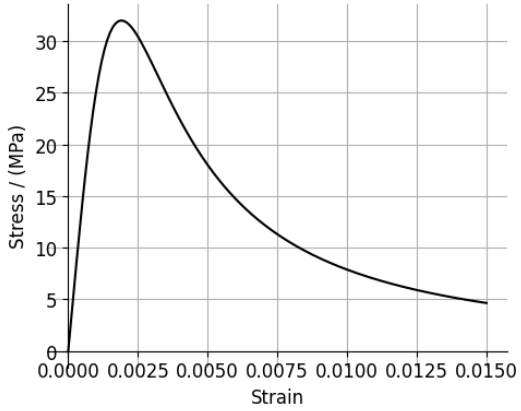

Figure 12: Stress-Strain Response of Concrete in Compression

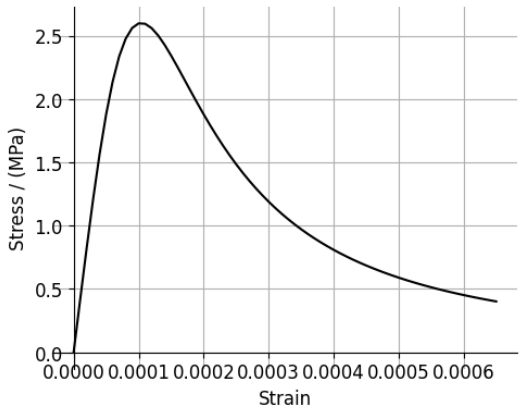

Figure 13: Stress-Strain Response of Concrete in Tension

The concept of damage factor is introduced to describe the stiffness degradation of concrete. The damage parameter for both compression and tension is derived in the current study as recommended by Mahmu et al. [29], and it is presented in Equation (1). σ represents the stress at a single instance, and σ_0 denotes the peak stress. Figures 14 and 15 show the variation of the damage parameter in compression and tension. This is considered to initiate upon reaching the peak strength.

$$d = 1 - \frac{\sigma}{\sigma_0} \quad (1)$$

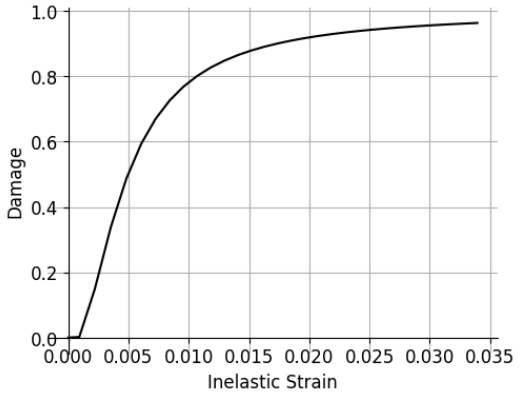

Figure 14: Variation of Damage Parameter for Concrete in Compression

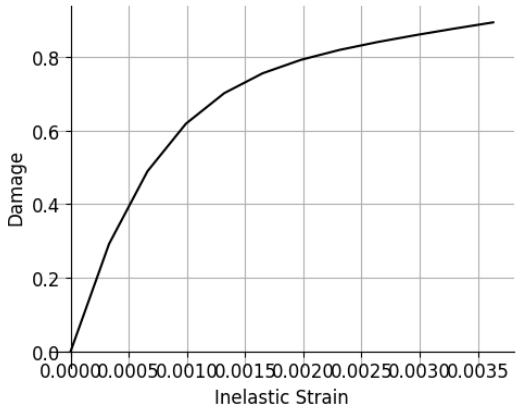

Figure 15: Variation of Damage Parameter for Concrete in Tension

6.2.2 UHPFRC

The uniaxial compressive behaviour of UHPFRC was modelled using a stress-strain relationship derived from empirical equations proposed by Lu et al. [30], which were later modified based on recommendations by Singh et al. [31] to better capture the distinct characteristics of UHPFRC, particularly its post-peak behaviour. This model effectively represents both the ascending and descending branches of the compressive response. The stress-strain relationship of UHPFRC in compression is shown in Figure 16. Further, the UHPFRC material properties incorporated in the numerical model consisted of a density value of 2560 kg/m³, an elastic modulus measured at 34.5 GPa, and a Poisson's ratio equal to 0.20.

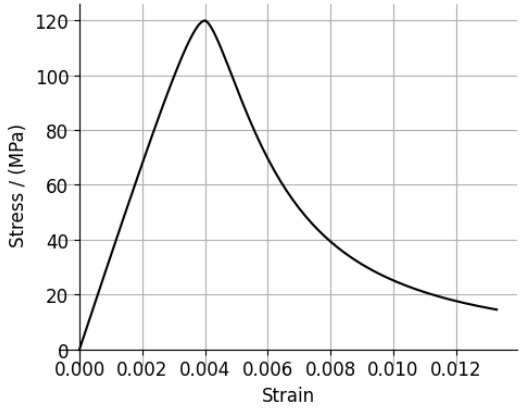

Figure 16: Stress-Strain Response of UHPFRC in Compression

To account for damage evolution, the damage parameter under compression was defined using the formulation proposed by Birtel et al. [32], as given in Equation (2). The damage parameter progression is illustrated in Figure 17,

$$d_c = 1 - \left[\frac{\sigma_c/E_0}{0.2\varepsilon_c^{in} + \sigma_c/E_0}\right] \quad (2)$$

where, σ_c is the stress at an instance, ε_c^{in} is corresponding inelastic strain, and E_0 is the initial elastic modulus.

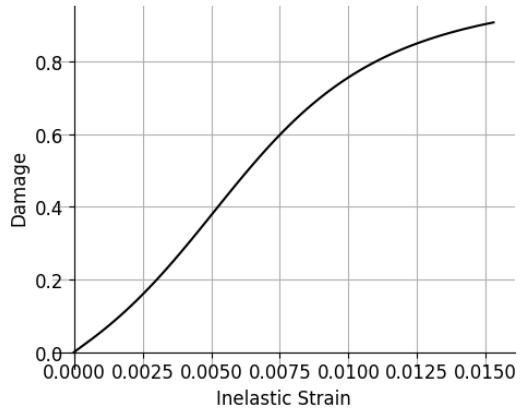

Figure 17: Variation of Damage Parameter for UHPFRC in Compression

The uniaxial tensile behaviour of UHPFRC is notably distinct from that of conventional concrete and is characterized by three distinct phases as linear elastic, strain hardening, and strain softening. In the initial linear elastic phase, stress increases proportionally with strain until initial crack formation. Once the cracking strength is reached, the material enters the strain hardening phase, during which multiple fine cracks develop while fibers in the mix actively involve in bridging the cracks. Upon reaching its tensile strength, the material transitions to the strain softening phase, where localized micro-cracks propagate, leading to a gradual reduction in stress until fracture occurs.

To accurately simulate this behaviour in the FE model, this study employed the AFGC-SETRA [33] recommendations for defining the full tensile stress-strain response, as illustrated in Figure 18. The damage parameter in tension was also defined using Equation (1), and the variation is presented in Figure 19.

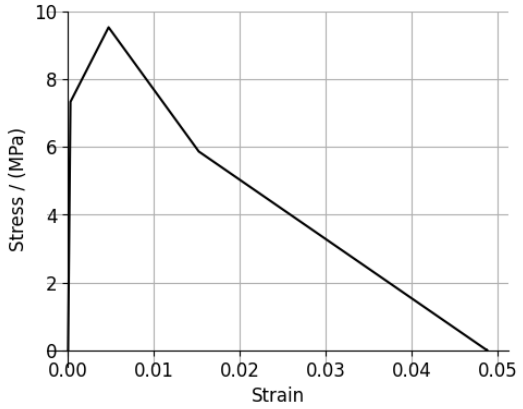

Figure 18: Stress-Strain Response of UHPFRC in Tension

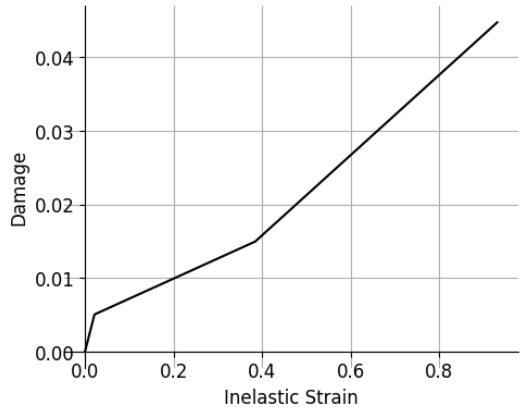

Figure 19: Variation of Damage Parameter of UHPFRC in Tension

6.2.3 Steel

The reinforcement steel was modelled using an elastic-plastic material with isotropic hardening. For the model, the material characteristics were defined as having a density equal to 7800 kg/m³, an elastic modulus valued at 200 GPa, and a Poisson's ratio of 0.3. The experimentally obtained yield and ultimate strength values, presented in Table 2, were incorporated into the numerical model.

6.3 Interface Modelling

Accurate representation of the interface between the RC substrate and the UHPFRC overlay is critical for realistically capturing the structural behavior of retrofitted beams in finite element analysis. While many previous studies have assumed a perfect bond between concrete and UHPFRC, such an approach cannot simulate the relative slip or potential separation between the two material sections. This assumption becomes particularly inadequate when experimental evidence indicates debonding at the interface, as observed in the current study.

The cohesive surface modeling approach employed in this study assumes a linear elastic traction-separation law prior to the initiation of damage, and characterizes failure through the progressive degradation of cohesive stiffness driven by a damage evolution process. In Abaqus, this behaviour is defined with three parts: the linear elastic traction-separation response, the damage initiation criteria,

and the damage evolution zone, as illustrated in Figure 20. The initial phase governs the elastic response of the interface, characterized by normal and shear stiffness components. Once the damage initiation criteria are met, the model transitions into a damage evolution phase, where the cohesive stiffness progressively degrades. This degradation process simulates the gradual loss of load transfer capacity across the interface. The parameters required to define the cohesive behaviour were adopted from the study by Sakr et al. [34].

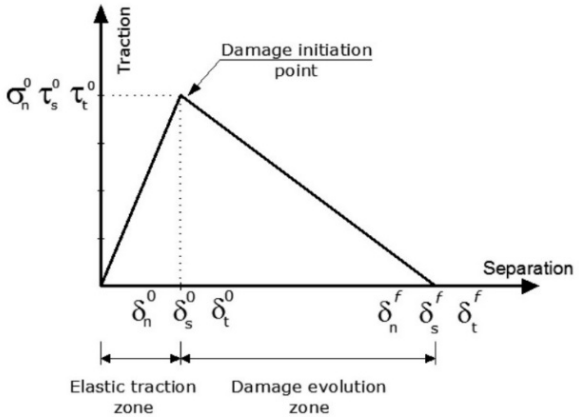

Figure 20: Traction-separation behaviour [35]

6.4 Numerical Validation of Tested Beams

Figure 21 presents a comparison between the load-deflection responses obtained from the FE analysis and those measured experimentally. The numerical predictions closely match the experimental behaviour for both the control beam and retrofitted beams, demonstrating the effectiveness of the developed models. The peak load recorded from the numerical simulation was 202 kN for the control beam and 408 kN for the retrofitted beam, which falls within a 10% deviation from the experimental results. However, the FE models exhibited slightly higher initial stiffness compared to the experimental curves. This discrepancy may be attributed to the idealized material behaviour assumed in the FE analysis.

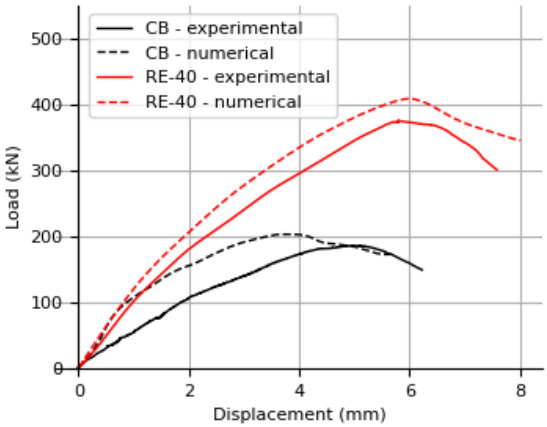

Figure 21: Experimental and Numerical Load-Displacement Relationships

In addition to the load-displacement comparison, the cracking behaviour observed in the FE models closely matched the experimental observations, as illustrated in Figure 22. The prominent diagonal shear crack observed in the control beam during testing was clearly replicated in the numerical model shown in Figure 22 (a), confirming the accurate prediction of the failure mode. Similarly, the flexural crack pattern in the retrofitted beam was effectively captured as depicted in Figure 22 (b). Furthermore, in addition to the flexure cracking behaviour in the composite beam, the shear cracks observed on the RC beam surface of the retrofitted specimen due to delamination of the UHPFRC overlay were also well-represented in the FE model (Figure 22 (c)). Notably, Figure 22 (d) confirms that the cohesive surface interface modelling successfully simulated the debonding failure that occurred experimentally, further validating the robustness of the adopted modelling strategy.

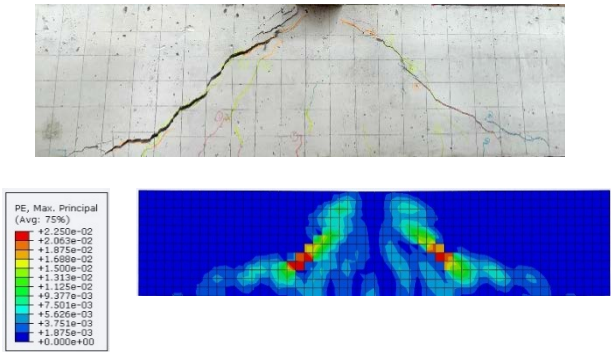

(a) Control Beam

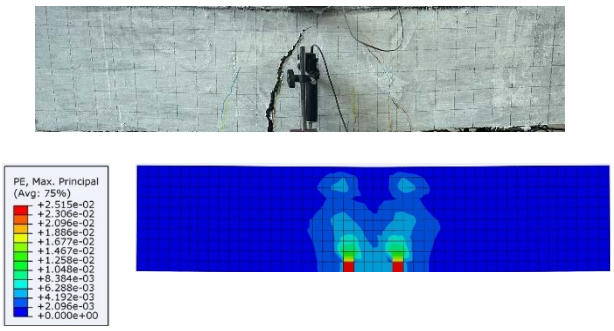

(b) Retrofitted Beam

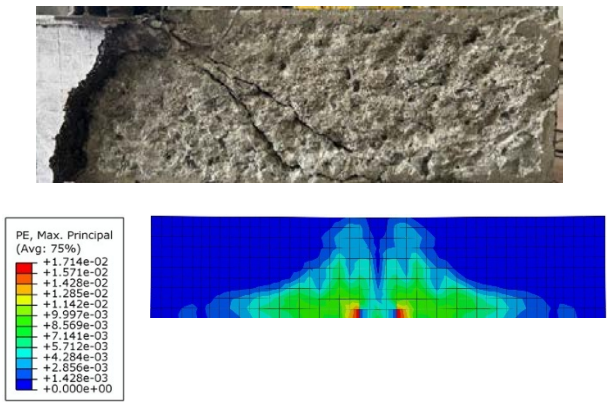

(c) RC Surface of Retrofitted Beam

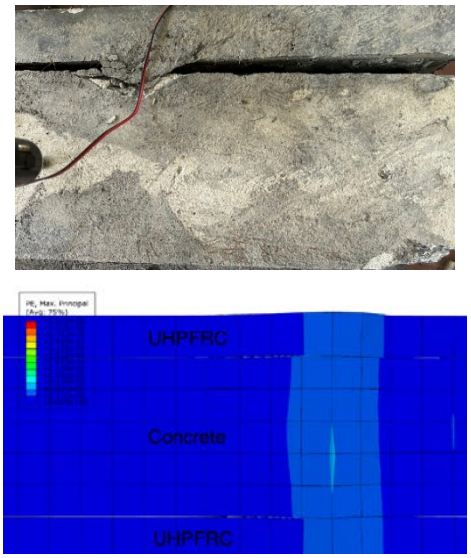

(d) Debonding of the UHPFRC Layer

Figure 22: Failure Behaviour of Beams in Comparison with the FE Model

7. Conclusions

This study focused on experimentally and numerically investigating the effectiveness of UHPFRC retrofitting for enhancing the structural performance of RC deep beams, and the investigation led to several notable conclusions.

1. In this study, a performance-wise and cost-wise optimized UHPFRC mix was developed using locally available materials, achieving a compressive strength of 119.47 MPa.
2. UHPFRC retrofitting significantly improved the load-bearing capacity and deformation characteristics of shear-critical RC deep beams. The brittle shear failure mode of the control beam was successfully transformed into a more favourable flexural failure model by UHPFRC strengthening.
3. The 2-sided 40 mm UHPFRC jacketing configuration resulted in more than a 100% increase in peak load and over a 20% improvement in ultimate midspan deflection compared to the control beam.
4. A numerical investigation was carried out to further enhance the understanding of UHPFRC retrofitted beams. The developed FE models accurately simulated the load-deflection responses of both the control and retrofitted beams, with peak load predictions falling within 10% of the experimental results.
5. Moreover, the numerical models effectively captured the failure modes and crack patterns observed in the experiments, including the diagonal shear cracking in the control beam and the flexural cracks in the retrofitted beam.
6. The cohesive surface-based interface modeling technique successfully replicated the debonding failure observed in the retrofitted beam, demonstrating its effectiveness in accurately modeling interface behaviour.

While the findings are promising, the study does acknowledge some limitations. The experimental investigation included only one retrofitted beam, which limits the breadth of the test data. However, the developed numerical model serves as a valuable tool for conducting further in-depth analysis. Surface preparation was performed using chipping, chosen for its practicality and relevance to local construction practices. Although methods like water jetting may offer superior surface roughness, they are often less feasible in the local context due to higher costs and limited accessibility.

Acknowledgements

This research was conducted as part of an ongoing project on UHPFRC at the University of Peradeniya. The authors gratefully acknowledge Tokyo Cement Company (Lanka) PLC for providing the high-strength Type I OPC (42.5R) cement used in this study.

References

[1] E. Brühwiler and E. Denarié, “Rehabilitation and Strengthening of Concrete Structures Using Ultra-High Performance Fibre Reinforced Concrete,” *Structural Engineering International*, vol. 23, no. 4, pp. 450–457, Nov. 2013, doi: https://doi.org/10.2749/101686613x13627347100437.

[2] D. V. Val and M. G. Stewart, “Reliability Assessment of Ageing Reinforced Concrete Structures—Current Situation and Future Challenges,” *Structural Engineering International*, vol. 19, no. 2, pp. 211–219, May 2009, doi: https://doi.org/10.2749/101686609788220114.

[3] Farshid Jandaghi Alaee and Bhushan Lal Karihaloo, “Retrofitting of Reinforced Concrete Beams with CARDIFRC,” vol. 7, no. 3, pp. 174–186, Aug. 2003, doi: https://doi.org/10.1061/(asce)1090-0268(2003)7:3(174).

[4] G. E. Thermou, S. J. Pantazopoulou, and A. S. Elnashai, “Flexural Behavior of Brittle RC Members Rehabilitated with Concrete Jacketing,” *Journal of Structural Engineering*, vol. 133, no. 10, pp. 1373–1384, Oct. 2007, doi: https://doi.org/10.1061/(asce)0733-9445(2007)133:10(1373).

[5] H. Rodrigues, P. M. Pradhan, A. Furtado, P. Rocha, and N. Vila-Pouca, “Structural Repair and Strengthening of RC Elements with Concrete Jacketing,” *Building Pathology and Rehabilitation*, pp. 181–198, Oct. 2017, doi: https://doi.org/10.1007/978-981-10-5858-5_8.

[6] S. Villar-Salinas, A. Guzmán, and J. Carrillo, “Performance evaluation of structures with reinforced concrete columns retrofitted with steel jacketing,” *Journal of Building Engineering*, vol. 33, p. 101510, Jan. 2021, doi: https://doi.org/10.1016/j.jobe.2020.101510.

[7] Z. J. Wu and J. M. Davies, “Mechanical analysis of a cracked beam reinforced with an external FRP plate,” *Composite Structures*, vol. 62, no. 2, pp. 139–143, Nov. 2003, doi: https://doi.org/10.1016/S0263-8223(03)00108-9.

[8] M. H. Harajli, “Strengthening of Concrete Beams by External Prestressing,” *PCI Journal*, vol. 38, no. 6, pp. 76–88, Nov. 1993, doi: https://doi.org/10.15554/pcij.11011993.76.88.

[9] J. M. de Sena Cruz and J. A. Oliveira de Barros, “Bond between near-surface mounted carbon-fiber-reinforced polymer laminate strips and concrete,” *Journal of Composites for Construction*, vol. 8, no. 6, pp. 519–527, 2004.

[10] S. S. Raval and U. V. Dave, “Effectiveness of Various Methods of Jacketing for RC Beams,” *Procedia Engineering*, vol. 51, pp. 230–239, Jan. 2013, doi: https://doi.org/10.1016/j.proeng.2013.01.032.

[11] N. Islam, M.M. Hoque, Strengthening of Reinforced Concrete Columns by Steel Jacketing : A State of Review, Asian Trans. Eng. 5 (2015) 6–14.

[12] S.-P. Chiew, Q. Sun, and Y. Yu, "Flexural Strength of RC Beams with GFRP Laminates," *Journal of Composites for Construction*, vol. 11, no. 5, pp. 497–506, Oct. 2007, doi: https://doi.org/10.1061/(asce)1090-0268(2007)11:5(497).

[13] W. Wang, J. Liu, F. Agostini, C. A. Davy, F. Skoczylas, and D. Corvez, "Durability of an Ultra High Performance Fiber Reinforced Concrete (UHPFRC) under progressive aging," *Cement and Concrete Research*, vol. 55, pp. 1–13, Jan. 2014, doi: https://doi.org/10.1016/j.cemconres.2013.09.008.

[14] M. Gesoglu, E. Güneyisi, G. F. Muhyaddin, and D. S. Asaad, "Strain hardening ultra-high performance fiber reinforced cementitious composites: Effect of fiber type and concentration," *Composites Part B: Engineering*, vol. 103, pp. 74–83, Oct. 2016, doi: https://doi.org/10.1016/j.compositesb.2016.08.004.

[15] T. E. T. Buttignol, J. L. a. O. Sousa, T. N. Bittencourt, T. E. T. Buttignol, J. L. a. O. Sousa, and T. N. Bittencourt, "Ultra High-Performance Fiber-Reinforced Concrete (UHPFRC): a review of material properties and design procedures," *Revista IBRACON de Estruturas e Materiais*, vol. 10, no. 4, pp. 957–971, Aug. 2017, doi: https://doi.org/10.1590/s1983-41952017000400011.

[16] P. Rossi, Ultra-high performance fibre reinforced concretes UHPFRC an overview, Fifth RILEM Symp. Fibre-Reinforced Concr. - BEFIB' 2000 3036 (2000) 87–100.

[17] Y. Zhu, Y. Zhang, H. H. Hussein, and G. Chen, "Flexural strengthening of reinforced concrete beams or slabs using ultra-high performance concrete (UHPC): A state of the art review," *Engineering Structures*, vol. 205, p. 110035, Feb. 2020, doi: https://doi.org/10.1016/j.engstruct.2019.110035.

[18] A. Ramachandra Murthy, B. L. Karihaloo, and D. S. Priya, "Flexural behavior of RC beams retrofitted with ultra-high strength concrete," *Construction and Building Materials*, vol. 175, pp. 815–824, Jun. 2018, doi: https://doi.org/10.1016/j.conbuildmat.2018.04.174.

[19] H. M. Tanarslan, "Flexural strengthening of RC beams with prefabricated ultra high performance fibre reinforced concrete laminates," *Engineering Structures*, vol. 151, pp. 337–348, Nov. 2017, doi: https://doi.org/10.1016/j.engstruct.2017.08.048.

[20] M. A. Al-Osta, M. N. Isa, M. H. Baluch, and M. K. Rahman, "Flexural behavior of reinforced concrete beams strengthened with ultra-high performance fiber reinforced concrete," *Construction and Building Materials*, vol. 134, pp. 279–296, Mar. 2017, doi: https://doi.org/10.1016/j.conbuildmat.2016.12.094.

[21] A. P. Lampropoulos, S. A. Paschalis, O. T. Tsioulou, and S. E. Dritsos, "Strengthening of reinforced concrete beams using ultra high performance fibre reinforced concrete (UHPFRC)," *Engineering Structures*, vol. 106, pp. 370–384, Jan. 2016, doi: https://doi.org/10.1016/j.engstruct.2015.10.042.

[22] S. Wijesundara, K. Wijesundara, and S. Bandara, "Machine learning approach for predicting the compressive strength of ultra-high performance fiber reinforced concrete (UHPFRC)," *Structures*, vol. 75, p. 108704, May 2025, doi: https://doi.org/10.1016/j.istruc.2025.108704.

[23] Standard Test Method, F. of H.C. Mortar, Standard, A., C1437, Astm C1437 (2009) 15–16. www.astm.org.

[24] C.C. Test, T. Drilled, C. Ag-, Standard Practice for Fabricating and Testing Specimens of Ultra-High iTeh Standards iTeh Standards Document Preview, i (2017) 1–2. https://doi.org/10.1520/C1856.

[25] ASTM C230, Standard Specification for Flow Table for Use in Tests of Hydraulic Cement 1, Annu. B. ASTM Stand. (2010) 4–9.

[26] American Society for Testing and Materials, ASTM C31/C31M -19 Making and Curing Concrete Test Specimens in the Field, ASTM Int. (2019) 1–6. https://doi.org/10.1520/C0031.

[27] C.C. Test, T. Drilled, C.C. Test, B. Statements, ASTM C 39/C 39M – 01. Standard Test Method for Compressive Strength of Cylindrical Concrete Specimens, (2014) 3–9. https://doi.org/10.1520/C0039.

[28] D.J. Carreira, K. Chu, Stress-Strain Relationship for Reinforced Concrete in Tension, (1986) 21–28.

[29] G. H. Mahmud, Z. Yang, and A. M. T. Hassan, "Experimental and numerical studies of size effects of Ultra High Performance Steel Fibre Reinforced Concrete (UHPFRC) beams," *Construction and Building Materials*, vol. 48, pp. 1027–1034, Nov. 2013, doi: https://doi.org/10.1016/j.conbuildmat.2013.07.061.

[30] Z. Lu, Y. Zhao, M. Asce, Empirical Stress-Strain Model for Unconfined High-Strength Concrete under Uniaxial Compression, (2010) 1181–1186.

[31] M. Singh, A. H. Sheikh, M. S. Mohamed Ali, P. Visintin, and M. C. Griffith, "Experimental and numerical study of the flexural behaviour of ultra-high performance fibre reinforced concrete beams," *Construction and Building Materials*, vol. 138, pp. 12–25, May 2017, doi: https://doi.org/10.1016/j.conbuildmat.2017.02.002.

[32] V. Birtel, P. Mark, R. Bochum, Parameterised F inite E lement M odelling of RC B eam S hear F ailure, (2006) 95–108.

[33] J. Resplendino, "Ultra High Performance Concrete: New AFGC Recommendations," Feb. 2013, doi: https://doi.org/10.1002/9781118557839.ch47.

[34] M. A. Sakr, A. A. Sleemah, T. M. Khalifa, and W. N. Mansour, "Shear strengthening of reinforced concrete beams using prefabricated ultra-high performance fiber reinforced concrete plates: Experimental and numerical investigation," *Structural Concrete*, vol. 20, no. 3, pp. 1137–1153, Feb. 2019, doi: https://doi.org/10.1002/suco.201800137.

[35] Hibbitt, Karlsson, and Sorensen, Inc. ABAQUS Theory manual, user manual and example manual, version 6.7. Providence, RI, SIMULIA, 2000.

Numerical Analysis of Web Crippling in Web Rib-stiffened Lipped Channel (WRLC) Beams with Perforations

W K V J B Kulasooriya[1], H M S T Herath[1], and D P P Meddage[2]

Abstract

Cold-formed steel (CFS) sections, especially those with lipped channel profiles are popular in steel construction industry. Thin-walled beams with these sections generally need holes/perforations to facilitate services in the building. These thin-walled sections are generally prone to web-crippling because of their higher slenderness. Therefore, lipped channel beams are provided with ribs in the web to improve stiffness against the applied loads. However, limited research has been conducted on web-crippling resistance of these Web Rib-stiffened Lipped Channel (WRLC) sections. The authors conducted a numerical study using ABAQUS software to evaluate the web-crippling behaviour of WRLC sections under the Internal-Two-Flange (ITF) loading condition. The models were validated using the limited experimental data available in the literature. A parametric study was conducted using the validated model by varying the geometric parameters such as web thickness, hole spacing and web hole ratio. Parametric study showed that reducing web thickness from 2 mm to 1 mm led to a strength reduction of up to 11.5% due to perforations. Thicker sections (.6 mm – 2 mm) showed minimal strength reduction (<1%) even with larger holes and varied spacings. The results were compared with existing empirical design methods and code-based equations. This study provided a comprehensive assessment of how the geometric properties govern the web-crippling load of WRLC sections.

Keywords: Cold-Formed Steel, Perforated Web Stiffened Lipped Channels, ABAQUS, Web Crippling

1. Introduction

Infrastructure development in urban and industrial areas demand for fast, efficient and reliable construction methods [1], [2]. Steel structures have become a key component of modern infrastructure development due to their strength, durability and versatility. For steel structures, Cold-Formed Steel (CFS) has become increasingly popular due to its lightweight nature, cost-effectiveness and ease of manufacturing compared to hot-rolled steel [3]. CFS section refers to a specific shape or profile of steel designed to carry loads and resist forces in structural systems. These sections include C sections, Z sections, hollow sections, hat sections, sigma sections, and Web Rib-stiffened Lipped Channel (WRLC) sections. Each shape offers different benefits for strength, stiffness, and installation.

One major failure mode in CFS sections is web crippling, which is a local failure that occurs when the web of the section is subjected to transverse concentrated loads [4]. The web crippling capacity of various CFS sections has been studied using different approaches including theoretical [4], [5], [6], [7], [8], experimental [9], [10], [11], [12], numerical [13], [14], [15] and more recently data-driven methods such as Machine Learning (ML) [13], [16], [17], [18].

Web crippling capacity becomes especially important when web holes/perforations are present. Pre-punched web perforations are often introduced in CFS sections to allow the passage of service lines such as electrical cables, plumbing, and HVAC ducts. However, these perforations reduce the web crippling capacity of the sections [19]. Early studies investigated the impact of different perforation shapes, including I-sections, Z-sections, circular, square, rectangular, and oval openings [20], [21], [22]. Later Uzzaman et al. [19], [23], [24], [25] conducted both experimental and numerical investigations to study the effect of circular perforations in lipped channel sections.

CFS Web Rib-stiffened Lipped Channel (WRLC) sections are a newer type of CFS sections commonly used in light steel framing and commercially known as “SupaCee”. These sections have a special shape compared to conventional lipped channel sections with curved flange lips and ribs on the web which act as stiffeners. This geometry increases their stiffness and strength such as tensile strength, yield strength making them a cost-effective choice for structural uses like floor joints, girts, roof purlins and bearers [26]. Because of this unique geometry, WRLC sections perform well under different loads such as shear and bending [27], [28], [29]. However, studies have shown that WRLC sections have lower resistance to web crippling capacity compared to standard lipped channel sections under various loading conditions like End Two Flange (ETF), End One Flange (EOF), Interior Two Flange (ITF), and Interior One Flange (IOF) [30]. Adding web perforations under these loading conditions further weakens the WRLC sections web crippling strength [31]. Understanding how WRLC sections behave with and without web perforations is important for efficient member design for web crippling.

1.1. Related Works

Thirunavukkarasu et al. [32] studied the shear capacity of three types of WRLC sections by varying parameters such as overall section depth, flange width, web thickness, yield strength, and web hole ratios. They developed 162 Finite Element (FE) models using ABAQUS software to

[1] W K V J B Kulasooriya and H M S T Herath: Department of Civil Engineering, University of Moratuwa, Sri Lanka. (virajinikulasooriya@gmail.com, sumuduh@uom.lk)
[2]D P P Meddage: School of Engineering Technology, The University of New South Wales, Australia. (p.meddage@unsw.edu.au)

validate experimental results and proposed a new design equation for perforated sections. A web hole ratio of 0.2 was recommended as optimal. Their findings suggest that WRLC sections with web perforations can offer similar or better shear performance compared to conventional lipped channel sections. Thirunavukkarasu et al. [27], explored. the flexural behaviour of plain and perforated WRLC sections with unstiffened flanges. They used 189 FE models to evaluate the impact of different geometric and material parameters. The results showed improved flexural capacity when the web hole ratio exceeded 0.6, and a new design equation was proposed.

Sundararjah et al. [26] examined web crippling of CFS WRLC sections without web perforations under End Two Flange (ETF) and Interior Two Flange (ITF) loading. They conducted 36 experimental tests and validated their FE models using experimental data. The study concluded that WRLC sections have lower web crippling strength than conventional lipped channels. Later, Sundararajah et al. [30] tested 42 CFS WRLC specimens under End One Flange (EOF) and Interior One Flange (IOF) conditions again confirming reduced web crippling capacity in WRLC sections. A design equation based on the Direct Strength Method (DSM) was developed.

More recently, Thirunavukkarasu et al. [33] examined the web crippling capacity of aluminium WRLC sections without web perforations under ETF loading condition through a numerical study. In this study, 24 FE models were developed with varying overall section depths, web thicknesses, corner radius, and bearing lengths. The results demonstrated superior web crippling performance compared to conventional aluminium lipped channel beams. Similarly, Weerasinghe et al. [31] conducted a numerical study on web crippling under ETF loading for CFS WRLC sections with and without web perforations. They analysed 60 FE models with varying web thicknesses, corner radius, bearing lengths, yield strengths, and hole ratios (0.2, 0.4, 0.6). Their results showed that web crippling capacity decreases with larger web holes, and a modified design equation was proposed.

1.2. Research Novelty

Although interest in CFS WRLC sections in growing, research on their web crippling behaviour particularly in the presence of web perforations remains limited. Moreover, few studies have employed numerical modelling to evaluated the web crippling capacity of WRLC sections. Therefore, this study focuses on the numerical investigation of the web crippling behaviour of CFS WRLC sections with unfastened flanges under ITF loading condition. A detailed parametric study was conducted using a validated FE model, incorporating key geometric parameters such as web thickness, yield strength, overall section depth, web hole ratio and bearing length. The results were compared against existing empirical design methods and code-based formulas.

2. Finite Element Modelling

To investigate web crippling performance, a comprehensive finite element model was created for Cold-Formed Steel (CFS) Web Rib-Stiffned Lipped Channel (WRLC) sections featuring unfastened flanges subjected to Interior-Two-Flange (ITF) loading.

The nonlinear Finite Element Analysis (FEA) was conducted using ABAQUS CAE 2020 software [33]. This FE analysis included four major components: the perforated and non-perforated WRCL sections, a load bearing plate, a support bearing plate and the contact interactions among these elements. A slow loading analysis was done using the ABAQUS/Explicit solver for better stability and speed, as the ABAQUS/Implicit solver had convergence issues. Initial geometric imperfections were not considered as they have minor effect on web crippling.[34], [35]. For this FE analysis, a half-model of the full geometry was used considering the symmetry of the beam along vertical direction.

2.1. Section Geometry and Material Properties

The CFS WRLC section lengths were set to greater than $5d_1$, where d_1 is the clear depth of the section, as this is the minimum specimen length required for ITF loading conditions according to AISI S909 [36]. The web perforations in the WRLC sections were positioned at mid-depth of web. The width of the bearing plates was set to B+20 mm, with B is the flange width. The channel sections were modelled using centreline dimensions with a mid-surface shell offset definition. The web perforations in the WRLC sections were positioned at mid of the section depth. Overall section depth (d) is 150 mm.

The material properties for steel were defined with a density of 7850 kg/m³, an elastic modulus of 200 GPa, and a Poisson's ratio of 0.3. An elastic perfectly plastic model with nominal yield strength was used to represent the stress-strain behaviour of selected CFS.

2.2. Mesh Control and Element Types

To ensure both accuracy and computational efficiency, according to Figure 2, a 5 mm × 5 mm mesh was used on the flat areas of the WRLC channel sections. A finer mesh of 1 mm × 5 mm was applied in the corner regions to more accurately capture stress concentrations. For the load bearing plate and support bearing plates, a coarser 10 mm × 10 mm mesh was sufficient due to lower stress sensitivity in those areas. Mesh refinement around the web perforations was enhanced using the medial axis algorithm along with the "minimise mesh transition" feature to improve mesh quality in critical regions. The channel sections were modelled using S4R elements, which are general-purpose, three-dimensional, deformable shell elements. Meanwhile, the loading and bearing plates were modelled as discrete rigid bodies using R3D4 elements.

2.3. Boundary and Loading Conditions

According to Figure 2, boundary conditions were applied using reference points on the load and support bearing plates. To replicate experimental behaviour, all translations of the support bearing plate were fixed it was also restricted from rotating about the Z-axis. The load bearing plate was restricted from moving along the X and Z axes and rotating about the Z axis. A displacement-controlled loading method was implemented by allowing the load bearing plate to move along the Y-axis, with a maximum vertical displacement of 20 mm. Since a half

model was used, symmetry boundary conditions were applied on the XY plane by restricting movement along the Z-axis and rotation about the X and Y axes. Smooth step amplitude curves were used for load application to prevent unwanted inertia effects at the beginning of the simulation.

2.4. Contact Behaviour

The interaction between the channel section and both the load and support bearing plates was defined using surface-to-surface contact modelling. The contact surfaces on the channel section were assigned as slave surfaces, while the bottom of the load bearing plate and the top of the support bearing plate were designated as master surfaces. To limit penetration of the slave surface into the master surface, a "Hard" pressure-overclosure behaviour was used [37]. A friction coefficient of 0.4 was applied to simulate the interaction between the contact surfaces, based on values used in previous studies [15], [34], [38].

2.5. Model Validation

To ensure the accuracy of the parametric study, the developed FE model should be validated using available experimental data. Since no prior experimental results existed for CFS WRLC sections with web perforations, validation was carried out in two phases.

Phase 1: Validation without web perforations

The model was initially validated using experimental data from Sundararajah et al. [26], which examined the web crippling behaviour of CFS WRLC sections without web perforations. The force-displacement curves were compared using the experimental data, the FE results from Sundararajah et al. [26], the FE results from the current study, and the half-model simulation results, as this study employed a half-model approach. The main material properties of the used for the test specimen (ITF-SC15012) were; a yield strength of 571 MPa, Young's modulus of 200,000 MPa, steel density of 7850 kg/m³, and Poisson ratio of 0.3. The geometric dimension of the section used in the simulation are listed in Table 1 and sectional view is shown in the Figure 1.

According to the model validation, both the full and half FE models developed in this study showed strong agreement with the experimental results. Figure 3 presents the comparison of all four force vs. displacement curves, along with the FE predicted failure mode of the selected section. As shown in Table 2, the deviation from the experimental result was 3.1% for the FE model used in the existing study [26], 1.7% for the full FE model and only 0.9% for the half FE model used in the study, demonstrating the accuracy and reliability of the developed models.

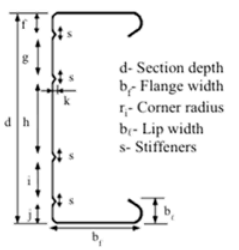

Figure 1: Cross-sectional view of the beam [26]

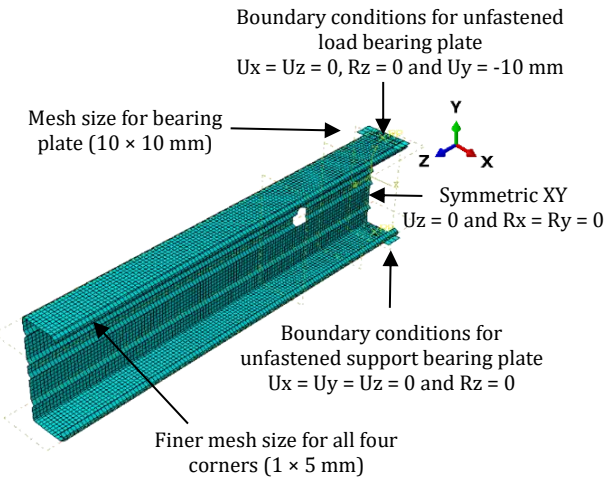

Figure 2: Element type, mesh sizes and boundary conditions used in FE model

Table 1: Dimensions and selected section (ITF-SC15012) [26]

N (mm)	d (mm)	t (mm)	b_f (mm)	r_i (mm)	b_l (mm)	L (mm)
150.0	152.6	1.22	59.6	5.0	19.9	760

Where, N = bearing length, d = overall section depth, t = thickness, b_f = flange width, r_i = corner radius, b_l = lip width, L = specimen length

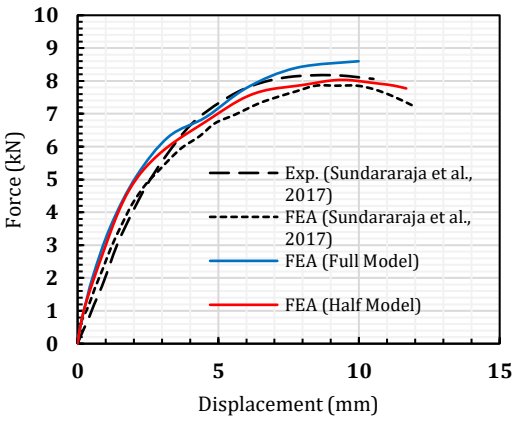

a) Force vs Displacement curve

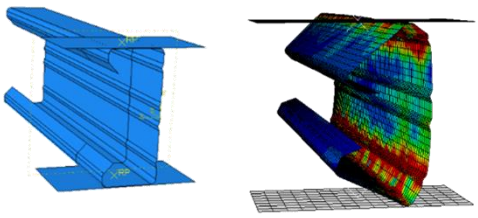

b) Model assembly c) FEA failure mode

Figure 3: Comparison of experimental results and FE results of the ITF-SC15012 section [26] with the FE models from this study for phase 1

Table 2: Comparison of results for phase 1

	Web Crippling Capacity (kN)	Deviation with Exp. Results
Exp. [26]	8.10	-
FEA [26]	7.86	3.1%
FEA (Full Model)	7.96	1.7%
FEA (Half Model)	8.03	0.9%

Phase 2: Validation with web perforations

In the second phase, the model was validated for web-perforated sections using experimental data from Alsanat et al. [39] on CFS aluminium lipped channel sections both with and without perforations. Similar to Phase 1, half-model validation was also performed in this stage. The test specimen (U-ITF-250-3-A0.5) had a yield strength of 224 MPa, Young's modulus of 68,488 MPa, Poisson's ratio of 0.3 and aluminum density 2720 kg/m³. The dimensions of the section used in validation are detailed in Table 3 and Figure 4 shows the cross sectional view.

According to the FE results, a reasonable agreement was observed between the experimental data and the FE model validation conducted in this study. Figure 5 presents the force vs. displacement curves for all four cases, while Table 4 summarizes the web crippling capacities and their deviation values compared to the experimental results.

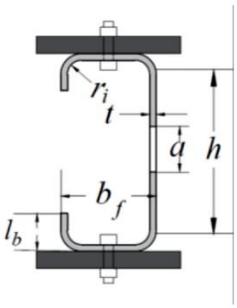

Figure 4: Cross-sectional view of the beam [39]

Table 3: Dimensions and selected section (U-ITF-250-3-A0.5) [39]

N (mm)	d (mm)	t (mm)	b_f (mm)	r_i (mm)	l_b (mm)	L (mm)	a (mm)
100.0	253.9	1.22	77.8	4.8	23.9	1427	120.0

Table 4: Comparison of results for phase 2

	Web crippling capacity (kN)	Deviation with exp. results
Exp. [39]	14.31	-
FEA [39]	14.35	1%
FEA (Full Model)	13.86	3.1%
FEA (Half Model)	13.66	4.5%

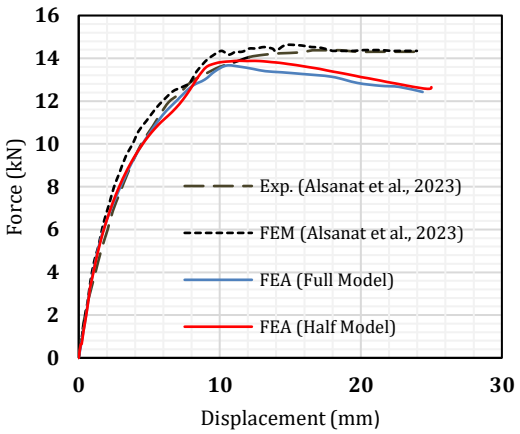

a) Force vs Displacement curve

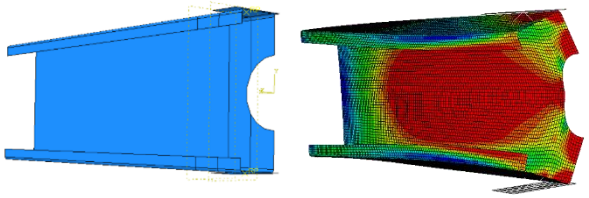

b) Model assembly c) FEA failure mode

Figure 5: Comparison of experimental results and FE results of the U-ITF-250-3-A0.5 section [39] with the FE models from this study for phase 2

3. Parametric Study

The study primarily investigated the influence of key geometric parameters on web crippling performance. These parameters included four different web hole ratios (0, 0.1, 0.2, and 0.4), two hole spacings (300 mm and 450 mm), and three section web thicknesses (1 mm, 1.6 mm, and 2 mm). All models were based on a constant overall section depth of 150 mm, a bearing length of 50 mm, corner radius of 3 mm, flange lip width of 12 mm, flange width of 70 mm and a yield strength of 220 MPa. The dimensions of the ribs (s_1 = 40 mm, s_2 = 20 mm, s_h = 10, s_d = 5 mm) along with the corresponding parameter symbols used in the parametric study are showed in Figure 6. According to the Table 5, total of 21 FE models including 18 perforated beams and 3 solid beams were developed to evaluate the web crippling behaviour of cold-formed steel (CFS) Web Rib-stiffened Lipped Channel (WRLC) under Interior Two Flange (ITF) loading condition with unstiffened flange condition.

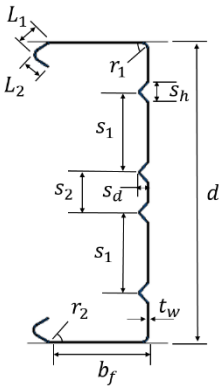

(a) Cross-sectional view

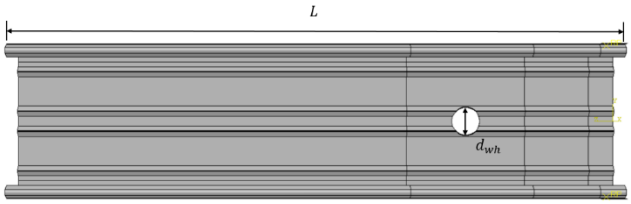

(b) Side view

Figure 6: Geometric properties of the specimen (present study)

The following symbols denote the parameters: d = overall section depth, l_b = bearing length, b_f = flange width, f_y = yield strength, L_1/L_2 = flange lip width, r_1/r_2 = inside corner radius of the flange lips, L = length of the section and d_1 = clear section depth [$d_1 = d - 2(r_1 - t_w)$].

Table 5: Summary of the parametric study

Section	Web hole ratio (D/d_1)	Hole spacing (s) (mm)	web thickness (t_w) (mm)	Total
Web Perforated	0.1,0.2, 0.4	300, 450	1, 1.6, 2	18
Solid	0	-	1, 1.6, 2	3
Total FE Models				21

Based on the available FE results in the Table 6 for CFS WRLC sections with web thicknesses of 1 mm, 1.6 mm and 2 mm, a clear trend in web crippling strength can be observed in relation to web hole ratio and hole spacing.

In 1 mm thick sections, the predicted web crippling strengths at 300 mm hole spacing are 2.02 kN, 1.90 kN, and 1.84 kN for web hole ratios of 0.1, 0.2, and 0.4 respectively. At 450 mm spacing, the corresponding values are 2.02 kN, 1.92 kN, and 1.96 kN. When compared to the solid section (T1H0), which had a web crippling capacity of 2.08 kN, the reductions are more noticeable than in thicker sections. For the 300 mm spacing, the reductions in web crippling capacity are approximately 2.9%, 8.7%, and 11.5% for web hole ratios of 0.1, 0.2, and 0.4 respectively. Meanwhile, for the 450 mm spacing, the reductions are about 2.9%, 7.7%, and 5.8% respectively. These results suggest that 1 mm thick CFS WRLC sections are more vulnerable to the weakening effects of web openings, particularly at closer hole spacing, though increased spacing seems to help reduce this impact slightly.

Table 6: Results of the parametric study

Section	Section name	Hole spacing (mm)	Web thickness (mm)	Web crippling strength values predicted via FEA (kN)			
				0	0.1	0.2	0.4
Web Perforated	T1H300	300	1	-	2.02	1.90	1.84
	T1.6H300	300	1.6	-	4.29	4.29	4.29
	T2H300	300	2	-	6.45	6.44	6.42
	T1H450	450	1	-	2.02	1.92	1.96
	T1.6H450	450	1.6	-	4.30	4.30	4.30
	T2H450	450	2	-	6.45	6.45	6.44
Solid	T1H0	-	1	2.08	-	-	-
	T1.6H0	-	1.6	4.32	-	-	-
	T2H0	-	2	6.50	-	-	-

$$\text{Reduction\%} = \left(\frac{F_{initial} - F}{F_{initial}}\right) \times 100 \qquad \text{eq.1}$$

For the 1.6 mm thick sections, both at 300 mm and 450 mm hole spacing, the predicted web crippling strength remains constant at 4.29–4.30 kN across all three web hole ratios (0.1, 0.2, and 0.4). When compared with the solid section (T1.6H0), which had a web crippling capacity of 4.32 kN, the reduction is minimal. The percentage reduction in web crippling capacity for web hole ratios of 0.2 and 0.4 is approximately 0.7%. This indicates that web perforations had an almost negligible impact on the web crippling strength for this web thickness, suggesting that 1.6 mm thick WRLC sections maintain their web crippling capacity effectively even with moderate perforations and varying hole spacings. The results also suggest that increased spacing (from 300 mm to 450 mm) did not lead to notable differences in strength at this web thickness, highlighting the structural integrity of these sections against web perforations under the tested conditions.

For the 2 mm thick sections, a similar but slightly more varied trend is seen. At 300 mm spacing, the web crippling strength decreased marginally from 6.45 kN (web hole ratio = 0.1) to 6.44 kN (web hole ratio = 0.1) and 6.42 kN (web hole ratio = 0.4). The reductions compared to the solid section are about 0.8%, 0.7% and 0.5%, respectively. For the 450 mm spacing, the values remain almost identical (6.45, 6.45, 6.44 kN), again reflecting very small deviations. This further highlights the observation that thicker WRLC sections (2 mm) are highly resistant to performance degradation due to web perforations. The minimal reduction in web crippling capacity with increasing hole ratios and spacing demonstrates the structural advantage of using thicker sections. The

reductions in web crippling capacity are approximately 0.8% for web hole ratios of 0.1 and 0.2, and around 0.9% for a web hole ratio of 0.4.

According to that, Figure 7 clearly shows the effect of web perforations on web crippling capacity influenced by the web thickness of the WRLC section. The 1 mm thick sections showed the greatest sensitivity to hole size and spacing, with noticeable reductions in strength. On other hand, the 1.6 mm and 2 mm thick sections demonstrated minimal impact, maintaining most of their load-carrying capacity even with increased perforation ratios and varied spacing.

From the parameters, different ratios such as hole spacing to clear section depth (s/d_1), bearing length to clear section depth (l_b/d_1), bearing length to web thickness (l_b/t_w), inside corner radius to web thickness (r_i/t_w), and clear section depth to web thickness (d_1/t_w) were evaluated.

Significant variation was observed in the l_b/t_w, r_i/t_w, and d_1/t_w ratios with increasing web thickness. For the 1 mm web thickness, the values were $l_b/t_w = 50$, $r_i/t_w = 3$, and $d_1/t_w = 142$, indicating relatively high slenderness. As the web thickness increased to 1.6 mm, these ratios decreased to $l_b/t_w = 31.25$, $r_i/t_w = 1.875$, and $d_1/t_w = 88$. Further increase in web thickness to 2 mm resulted in even lower values of $l_b/t_w = 25$, $r_i/t_w = 1.5$, and $d_1/t_w = 70$. These results highlight that as web thickness increases, the l_b/t_w, r_i/t_w, and d_1/t_w ratios decrease significantly. This inverse relationship is critical as it implies reduced relative slenderness and corner radius in thicker members, potentially affecting local buckling and crippling behaviour.

According to that, the d_1/t_w and r_i/t_w ratios exhibit a negative correlation with web crippling strength. As these ratios decrease with increasing web thickness, an improvement in the web's capacity to resist localized crippling may be expected due to reduced slenderness and higher overall stiffness.

The l_b/d_1 and s/d_1 ratios remained relatively stable across all web thicknesses. The l_b/d_1 ratio ranged narrowly from 0.352 to 0.357, while the s/d_1 ratio varied from 2.11 to 3.21. Although these ratios did not show significant variation with web thickness, their influence on web crippling behaviour is still important. A higher l_b/d_1 ratio implies a longer bearing length relative to the web depth, which can enhance load distribution and delay local failure. Similarly, a higher s/d_1 ratio reflects a greater spacing between web openings, which can reduce the interaction effects between adjacent perforations and help maintain structural integrity.

The ratios l_b/t_w, r_i/t_w, and d_1/t_w exhibited a significant decrease of approximately 50% with increasing section web thickness, highlighting their strong sensitivity to web thickness variation and their dominant influence on the web crippling behaviour of CFS WRLC sections. These reductions indicate a substantial decrease in slenderness and curvature-related parameters, which generally contributes to enhanced local stiffness and improved resistance to web crippling. These results of r_i/t_w, and d_1/t_w align well with the findings of previous research conducted on CFS WRLC sections without web perforation [24], [40]. Moreover, influence of d_{wh}/d_1 and l_b/d_1 with earlier studies on the web crippling behaviour of cold-formed steel lipped channel sections with web perforations [19], [23].

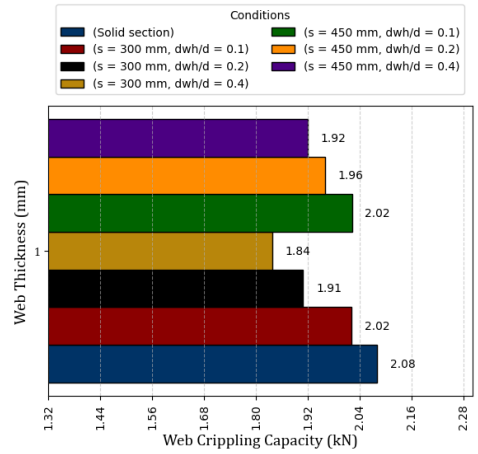

a)

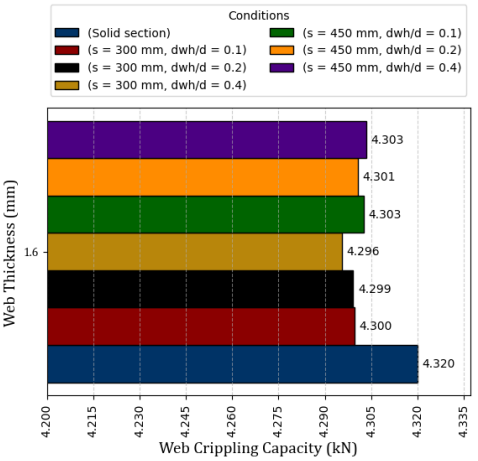

b)

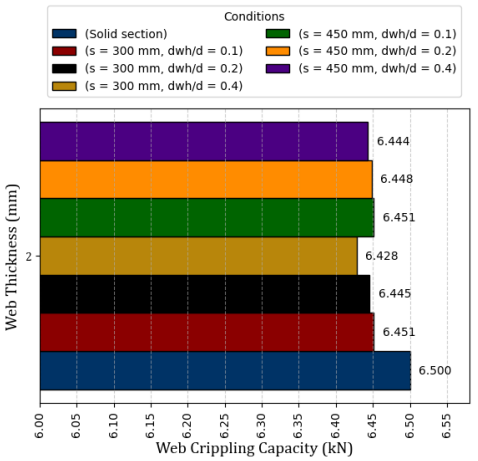

c)

Figure 7: Variation of web crippling resistance along with web thickness

On other hand, the l_b/d_1 and s/d_1 ratios remained nearly constant across all web thicknesses with variations of less than 2%. This minimal change suggests that these ratios were intentionally maintained in the parametric design to isolate the effects of web thickness-dependent parameters. By keeping l_b/d_1 and s/d_1 relatively fixed, the study ensures that the observed changes in web crippling behaviour can be more directly attributed to the variation in section web thickness and the associated geometric ratios that are directly influenced by it.

Including the above discussion section web thickness is a dominant factor in determining web crippling strength. The study clearly shows that thinner sections (1 mm) are significantly more susceptible to performance degradation due to web perforations, with reductions in strength reaching up to 11.5%. In contrast, thicker sections (1.6 mm and 2 mm) exhibit minimal reductions (less than 1%) even with increased web hole ratios and varied hole spacing. Among all the evaluated geometric ratios, l_b/t_w, r_i/t_w, and d_1/t_w demonstrated the most substantial influence on web crippling performance. These ratios decreased significantly by approximately 50% as web thickness increased from 1 mm to 2 mm. This drop corresponds to a reduction in slenderness and curvature effects, which contributes to improved stiffness and enhanced web crippling resistance. Therefore, these three ratios are the most important indicators of a section's vulnerability or resilience to crippling failures in perforated conditions. the l_b/d_1 (bearing length to web depth) and s/d_1 (hole spacing to web depth) ratios remained relatively constant across all web thicknesses.

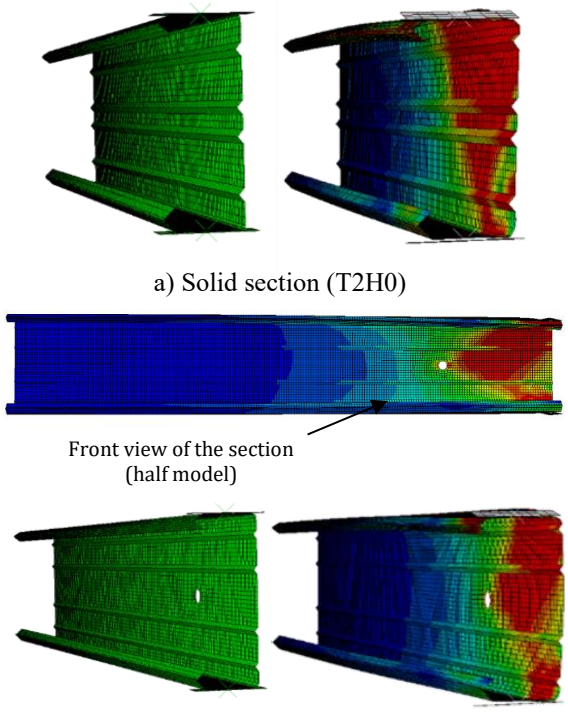

a) Solid section (T2H0)

b) Web perforated section (T1H300)

Figure 8: FEA failure modes

4. Comparison with Existing Design Methods

The three primary design standards used to estimate web crippling behaviour in cold-formed steel (CFS) sections are the Australian/New Zealand Standard (AS/NZS 4600), North American Specification (AISI S100-16), and Eurocode 3 Part 1-3 (EN1993-1-3). Among them, both AS/NZS 4600 and AISI S100-16 adopt the same design equation (eq.2) for evaluating the ultimate web crippling capacity (R_b) of CFS members, whether or not web perforations are present. When web perforations are present, this equation is intended for circular perforations under the flange-unfastened support condition. EN1993-1-3 includes provisions only for solid web sections and does not consider the effects of web perforations. AS/NZS 4600 and AISI S100-16 provide web crippling capacities (R_b) for CFS stiffened flange channel sections. importantly, none of these standards offers specific design guidance for CFS stiffened web channel section such as WRLC sections with or without web perforations. To investigate its accuracy, web crippling capacities from FE and eq.2 in AS/NZS 4600 and AISI S100-16 design standards.

$$R_b = C\, {t_w}^2\, f_y\, \sin\theta \left(1 - C_r \sqrt{\frac{r_i}{t_w}}\right)\left(1 - C_l \sqrt{\frac{l_b}{t_w}}\right)\left(1 - C_w \sqrt{\frac{d_1}{t_w}}\right) \quad \text{eq. 2}$$

where, t_w = web thickness, f_y = yield strength, r_i = inside corner radius, l_b = bearing length, d_1 and d = clear section depth and overall section depth $[d_1 = d - 2(r_i - t_w)]$, θ = angle between web and bearing surface, C = coefficient, C_r = inside corner radius coefficient, C_l = Coefficient of bearing length and C_w = web slenderness coefficient.
Limitations:

$$\frac{d_1}{t_w} \le 200, \frac{l_b}{t_w} \le 210, \frac{l_b}{d_1} \le 1, \frac{r_i}{t_w} \le 3, \theta = 90°$$

4.1 Comparison of the FE results with AS/NZS 4600 and AISI S100-16 Design Standards

To further assess the accuracy of existing design standards in predicting web crippling capacity for CFS WRLC sections with web perforations, a comparative plot was generated using the FE results versus the predicted capacities from the AISI S100-16 and AS/NZS 4600. Figure 9 represent the plots for predicted web crippling capacity values of FEA versus predicted values of AS/NZS 4600 standard and AISI S100-16 design standard respectively. In these plots, a 45° reference line was included to represent perfect agreement between the FEA predictions and code-calculated values.

The results from this comparison clearly reveal that both the AISI S100-16 and AS/NZS 4600 design predictions significantly overestimate the web crippling strength of the tested sections. In the plot, nearly all the data points

corresponding to these two standards lie well above the 45° line and in many cases, are far from it. This indicates a consistent and noticeable deviation from the more accurate FE values. The overestimation is especially pronounced in the case of the AS/NZS 4600 standard, where the predicted values are not only higher but also scattered widely from the FE trend, suggesting a lack of sensitivity in the design equation to changes introduced by web perforations. Similarly, the AISI S100-16 predictions follow a similar pattern of deviation, with their corresponding data points showing no close alignment with the ideal agreement line.

According to Figure 9 the mean of the FEA-to-AS/NZS 4600 capacity ratio was found to be 2.954, indicating that the AS/NZS 4600 standard significantly underestimates the web crippling strength of the tested sections. Furthermore, the coefficient of variation (COV) was calculated as 0.437, variations (scatter) in consistency among the data points. The comparison of results of AISI S100-16 design equation revealed a significant deviation between predicted and actual capacities, with a mean FEA-to-AISI S100-16 ratio of 5.154, indicating that the AISI S100-16 formulation substantially underestimates the web crippling strength across the tested configurations. This level of conservatism suggests that the AISI S100-16 equation may not be well-suited for capturing the complex interaction effects present in perforated WRLC sections. The corresponding coefficient of variation (COV = 0.354) reflects a moderate level of consistency in the underprediction, implying that although the design equation consistently falls short, it does so with relatively low scatter. Nevertheless, the large deviation in mean highlights the potential for non-conservative design if real capacities are not properly accounted for.

These findings suggest that while current design codes may provide conservative estimates for CFS solid web sections, they are not calibrated to account for CFS web stiffened section especially the weakening effects of web perforations.

2.1 Proposed Design Guideline

Based on the limitations and inadequacies observed in current design standards, a modified design guideline was proposed to more accurately predict the web crippling capacities of cold-formed steel (CFS) Web Rib-stiffened Lipped Channel (WRLC) sections with circular web perforations under Interior-Two-Flange (ITF) loading condition. The existing design provisions outlined in AISI S100-16 and AS/NZS 4600 were found to be insufficient for capturing the strength reduction caused by web perforations. To address this, an additional reduction factor was introduced into the existing equation to account for the presence and influence of web perforations. This factor, expressed as $\left[1 - C_a\sqrt{\frac{d_{wh}}{d_1}} + C_n\sqrt{\frac{l_b}{d_1}} + C_s\sqrt{\frac{s}{d_1}}\right]$, modifies the base equation by incorporating three key geometric parameters: hole spacing to clear section depth (s/d_1), bearing length to clear section depth (l_b/d_1), bearing length to web thickness and web hole ratio (d_{wh}/d_1).

The reduction factor reflects how key geometric ratios affect web crippling strength. Larger hole sizes, weaken the web and longer bearing lengths improve strength, so their effect is negative and positive respectively [19], [23]. Greater hole spacing improve strength, so its effect also positive.

$$R_b = C\, {t_w}^2\, f_y \sin\theta \left(1 - C_r\sqrt{\frac{r_i}{t_w}}\right)\left(1 - C_l\sqrt{\frac{l_b}{t_w}}\right)\left(1 - C_w\sqrt{\frac{d_1}{t_w}}\right)\left(1 - C_a\sqrt{\frac{d_{wh}}{d_1}} + C_n\sqrt{\frac{l_b}{d_1}} - C_s\sqrt{\frac{s}{d_1}}\right) \quad \text{eq. 3}$$

where, t_w = web thickness, f_y = yield strength, r_i = inside corner radius, l_b = bearing length, d_1 and d = clear section depth and overall section depth $[d_1 = d - 2(r_i - t_w)]$, θ = angle between web and bearing surface, C = coefficient, C_r = inside corner radius coefficient, C_l = Coefficient of bearing length, C_w = web slenderness coefficient, C_a = coefficient of web hole ratio, C_n = coefficient of bearing length to clear section depth and C_s = coefficient of hole spacing to clear section depth.

All coefficients (C, C_r, C_l, C_w, C_a, C_n and C_s) were optimized to minimize the coefficient of variation (COV) and to have a mean value equal to 1, ensuring the ratio of web crippling values from the proposed design code to the FEA results is maintained. The Generalized Reduced Gradient (GRG) method was used as the nonlinear solving technique for this analysis.

According to the Table 7, the optimization of the proposed web crippling design equation for perforated CFS WRLC sections resulted in a mean ratio of 1.0 and a coefficient of variation (COV) of 0.092. indicating strong agreement between the predicted web crippling capacities and the FE results. A mean value of 1.0 confirms that the proposed equation, with the calibrated coefficients, provides unbiased predictions on average, neither overestimating nor underestimating the web crippling strength. Meanwhile, the COV value of 0.092, which is within acceptable limits for structural design (typically < 0.5), reflects a high level of consistency and reliability in the predictions across the parametric dataset.

Figure 10 shows, the proposed design equation demonstrates strong consistency and excellent agreement in predicting web crippling capacity with FE results. According to figure, the data points closely follow the 45°-line indicating that the predicted values from the design equation accurately match the detailed numerical simulations. This close correlation validates the effectiveness of the proposed reduction factors and coefficient adjustments in capturing the complex behaviour of perforated sections under web crippling. Table 8 presents the predicted web crippling capacities obtained using the proposed design equation alongside the corresponding.

Table 7: Proposed web crippling coefficients for CFS ERLC section under ITF loading condition

	C	C_r	C_l	C_w	C_a	C_n	C_s	Mean	COV
Proposed	0.011	0.49	0.5	0.23	0.12	0.068	0.064	1.00	0.092

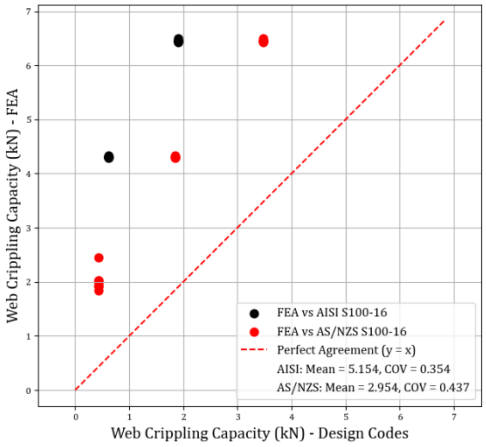

Figure 9: FEA results versus predictions of design standards (SA/NZS 4600 and AISI S100-16)

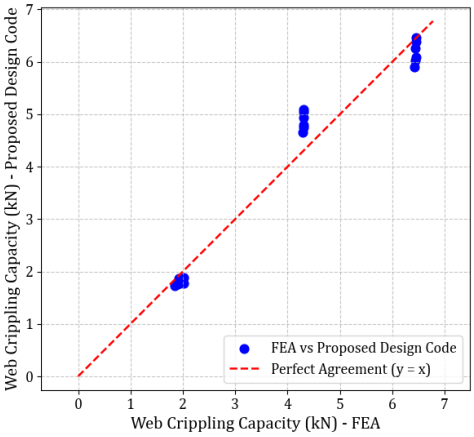

Figure 10: FEA results versus predictions of proposed design equation

This close agreement between these values suggests that the proposed equation (eq. 3) for determine the web crippling capacity with reduction factor equation, incorporating parameters such as web hole ratio, web thickness, and hole spacing, effectively captures the influence of web perforations on web crippling behaviour in CFS WRLC sections

Table 8: Comparison of FEA results and predictions of proposed design equation

	Web crippling capacity (kN)	
	FEA	Proposed design equation
T1H300-S0.1	2.02	1.78
T1H450-S0.1	2.02	1.89
T1.6H300-S0.1	4.29	4.80
T1.6H450-S0.1	4.30	5.08
T2H300-S0.1	6.45	6.09
T2H450-S0.1	6.45	6.45
T1H300-S0.2	1.90	1.76
T1H450-S0.2	1.92	1.86
T1.6H300-S0.2	4.29	4.75
T1.6H450-S0.2	4.30	5.03
T2H300-S0.2	6.44	6.02
T2H450-S0.2	6.45	6.39
T1H300-S0.4	1.84	1.73
T1H450-S0.4	1.96	1.83
T1.6H300-S0.4	4.29	4.65
T1.6H450-S0.4	4.30	4.93
T2H300-S0.4	6.42	5.91
T2H450-S0.4	6.44	6.26

5. Conclusion

This study has presented a numerical investigation on the web crippling behaviour of cold-formed steel (CFS) Web Rib-stiffened Lipped Channel (WRLC) sections with circular web perforations and unfastened flanges under Interior-Two-Flange (ITF) loading condition. A comprehensive parametric analysis was conducted, investigating the influence of various factors such as web hole ratio, hole spacing and web thickness. A total of 21 FE models were created to cover a broad range of conditions. Thinner sections show greater vulnerability, while l_b/t_w, r_i/t_w, and d_1/t_w are key indicators of performance. Section with a 1 mm web thickness experienced up to 11.5% reduction in strength due to web perforations, whereas thicker sections (1.6 mm and 2 mm) showed less than 1% reduction even with larger holes and varied spacings. The geometric ratios l_b/t_w, r_i/t_w, and d_1/t_w are decreasing by approximately 50% as the web thickness increased from 1 mm to 2 mm. The findings were used to assess the effectiveness of current design standards in predicting the web crippling performance of perforated CFS WRLC sections under ITF loading condition. Modification factor were proposed for existing design equation was formulated to better predict the web crippling capacity of web rib-stiffened lipped channel sections with web perforations, achieving a mean ratio of 1.0 and COV of 0.092.

References

[1] J. M. Diaz-Sarachaga, D. Jato-Espino, and D. Castro-Fresno, "Methodology for the development of a new Sustainable Infrastructure Rating System for Developing Countries (SIRSDEC)," *Environmental Science & Policy*, vol. 69, pp. 65–72, Mar. 2017, doi: 10.1016/j.envsci.2016.12.010.

[2] S.-S. Lin, A. Zhou, and S.-L. Shen, "Optimal construction method evaluation for underground infrastructure construction," *Automation in Construction*, vol. 152, p. 104921, Aug. 2023, doi: 10.1016/j.autcon.2023.104921.

[3] I. Rouaz, H. Bouzid, T. Belaid, and M. A. Belkacem, "Comparative Design of an Industrial Building: Cold Formed Steel versus Hot Rolled Steel," *Electronic Journal of Structural Engineering*, vol. 24, no. 2, Art. no. 2, Jun. 2024, doi: 10.56748/ejse.24541.

[4] R. M. Schuster and B. Beshara, "Web crippling data and calibrations of cold formed steel members," 2000, Accessed: May 27, 2025. [Online]. Available: https://scholarsmine.mst.edu/cgi/viewcontent.cgi?article=1009&context=ccfss-aisi-spec

[5] R. A. LaBoube, W. W. Yu, S. U. Deshmukh, and C. A. Uphoff, "Crippling Capacity of Web Elements with Openings," *Journal of Structural Engineering*, vol. 125, no. 2, pp. 137–141, Feb. 1999, doi: 10.1061/(ASCE)0733-9445(1999)125:2(137).

[6] M. Macdonald, M. A. Heiyantuduwa, D. K. Harrison, R. T. Bailey, and J. Rhodes, "Literature review of web crippling behaviour: 2nd Scottish Conference on Postgraduate Research on the Built Environment," *Proceedings of the 2nd Scottish Conference for Postgraduate Researchers of the Built and Natural Environment (PRoBE)*, pp. 473–482, 2005.

[7] M. Z. Khan and A. C. Walker, "Buckling of plates subjected to localized edge loading," 1972.

[8] K. Poologanathan and M. Mahendran, "Web crippling tests of hollow flange channel beams: ETF and ITF load cases," in *Australasian Structural Engineering Conference*, 2014, pp. 1–1. Accessed: May 31, 2025. [Online]. Available: https://eprints.qut.edu.au/70515/

[9] Y. Dai, K. Roy, Z. Fang, G. M. Raftery, and J. B. P. Lim, "Web crippling resistance of cold-formed steel built-up box sections through experimental testing, numerical simulation and deep learning," *Thin-Walled Structures*, vol. 192, p. 111190, 2023, doi: https://doi.org/10.1016/j.tws.2023.111190.

[10] S. Gunalan and M. Mahendran, "Web crippling tests of cold-formed steel channels under two flange load cases," *Journal of Constructional Steel Research*, vol. 110, pp. 1–15, Jul. 2015, doi: 10.1016/j.jcsr.2015.01.018.

[11] L. Sundararajah, M. Mahendran, and P. Keerthan, "Experimental Studies of Lipped Channel Beams Subject to Web Crippling under Two-Flange Load Cases," *Journal of Structural Engineering*, vol. 142, no. 9, p. 04016058, Sep. 2016, doi: 10.1061/(ASCE)ST.1943-541X.0001523.

[12] P. Keerthan, M. Mahendran, and E. Steau, "Experimental study of web crippling behaviour of hollow flange channel beams under two flange load cases," *Thin-Walled Structures*, vol. 85, pp. 207–219, Dec. 2014, doi: 10.1016/j.tws.2014.08.011.

[13] Y. Dai, K. Roy, Z. Fang, G. M. Raftery, and J. B. P. Lim, "Web crippling resistance of cold-formed steel built-up box sections through experimental testing, numerical simulation and deep learning," *Thin-Walled Structures*, vol. 192, p. 111190, Nov. 2023, doi: 10.1016/j.tws.2023.111190.

[14] B. Janarthanan, M. Mahendran, and S. Gunalan, "Numerical modelling of web crippling failures in cold-formed steel unlipped channel sections," *Journal of Constructional Steel Research*, vol. 158, pp. 486–501, Jul. 2019, doi: 10.1016/j.jcsr.2019.04.007.

[15] L. Sundararajah, M. Mahendran, and K. Poologanathan, "Web crippling capacity of cold-formed channel sections with and without longitudinal web stiffeners subject to two flange load cases," in *International Conference on Coupled Instabilities in Metal Structures*, Baltimore, United States, 2016, pp. 1–1. Accessed: May 31, 2025. [Online]. Available: https://eprints.qut.edu.au/98558/

[16] Z. Fang, K. Roy, B. Chen, C.-W. Sham, I. Hajirasouliha, and J. B. P. Lim, "Deep learning-based procedure for structural design of cold-formed steel channel sections with edge-stiffened and un-stiffened holes under axial compression," *Thin-Walled Structures*, vol. 166, p. 108076, Sep. 2021, doi: 10.1016/j.tws.2021.108076.

[17] Y. Karunaratne, S. Dharmawansha, T. Suganiyah, S. Herath, J. B. P. Lim, and D. P. P. Meddage, "Web crippling strength of cold-formed steel lipped channels under interior-two-flange loading: Data-driven modelling with shapley explanations," *Structures*, vol. 78, p. 109241, Aug. 2025, doi: 10.1016/j.istruc.2025.109241.

[18] R. I. Shahin, M. Ahmed, Q. Q. Liang, and S. A. Yehia, "Predicting the web crippling capacity of cold-formed steel lipped channels using hybrid machine learning techniques," *Engineering Structures*, vol. 309, p. 118061, Jun. 2024, doi: 10.1016/j.engstruct.2024.118061.

[19] A. Uzzaman, J. B. Lim, D. Nash, J. Rhodes, and B. Young, "Cold-formed steel sections with web openings subjected to web crippling under two-flange loading conditions—Part II: Parametric study and proposed design equations," *Thin-Walled Structures*, vol. 56, pp. 79–87, 2012.

[20] C. Davis, "The structural behavior of cold-formed steel members with perforated elements," *Doctoral Dissertations*, Jan. 1972, [Online]. Available: https://scholarsmine.mst.edu/doctoral_dissertations/2091

[21] K. Sivakumaran, "Some studies on cold-formed steel sections with web openings," 1988, Accessed: May 23, 2025. [Online]. Available: https://scholarsmine.mst.edu/cgi/viewcontent.cgi?article=1255&context=isccss

[22] K. S. Sivakumaran and K. M. Zielonka, "Web crippling strength of thin-walled steel members with web opening," *Thin-walled structures*, vol. 8, no. 4, pp. 295–319, 1989.

[23] A. Uzzaman, J. B. P. Lim, D. Nash, J. Rhodes, and B. Young, "Cold-formed steel sections with web openings subjected to web crippling under two-flange loading conditions—part I: Tests and finite element analysis," *Thin-Walled Structures*, vol. 56, pp. 38–48, Jul. 2012, doi: 10.1016/j.tws.2012.03.010.

[24] A. Uzzaman, J. B. Lim, D. Nash, J. Rhodes, and B. Young, "Web crippling behaviour of cold-formed steel channel sections with offset web holes subjected to interior-two-flange loading," *Thin-Walled Structures*, vol. 50, no. 1, pp. 76–86, 2012.

[25] A. Uzzaman, J. B. Lim, D. Nash, J. Rhodes, and B. Young, "Effect of offset web holes on web crippling strength of cold-formed steel channel sections under end-two-flange loading condition," *Thin-Walled Structures*, vol. 65, pp. 34–48, 2013.

[26] L. Sundararajah, M. Mahendran, and P. Keerthan, "Web crippling studies of SupaCee sections under two flange load cases," *Engineering Structures*, vol. 153, pp. 582–597, Dec. 2017, doi: 10.1016/j.engstruct.2017.09.058.

[27] K. Thirunavukkarasu *et al.*, "Flexural behaviour and design rules for SupaCee sections with web openings,"

Journal of Building Engineering, vol. 63, p. 105539, Jan. 2023, doi: 10.1016/j.jobe.2022.105539.

[28] K. Thirunavukkarasu *et al.*, "Shear performance of SupaCee sections with openings: Numerical studies," *Journal of Constructional Steel Research*, vol. 190, p. 107142, Mar. 2022, doi: 10.1016/j.jcsr.2022.107142.

[29] C. H. Pham and G. J. Hancock, "Experimental Investigation and Direct Strength Design of High-Strength, Complex C-Sections in Pure Bending," *Journal of Structural Engineering*, vol. 139, no. 11, pp. 1842–1852, Nov. 2013, doi: 10.1061/(ASCE)ST.1943-541X.0000736.

[30] L. Sundararajah, M. Mahendran, and P. Keerthan, "Design of SupaCee Sections Subject to Web Crippling under One-Flange Load Cases," *Journal of Structural Engineering*, vol. 144, no. 12, p. 04018222, Dec. 2018, doi: 10.1061/(ASCE)ST.1943-541X.0002206.

[31] H. Weerasinghe, C. Konthesingha, A. Nanayakkara, and K. Pologanathan, "WEB CRIPPLING BEHAVIOUR OF COLD-FORMED STEEL SUPACEE SECTIONS WITH WEB OPENINGS," Jan. 2023.

[32] K. Thirunavukkarasu *et al.*, "Shear performance of SupaCee sections with openings: Numerical studies," *Journal of Constructional Steel Research*, vol. 190, p. 107142, Mar. 2022, doi: 10.1016/j.jcsr.2022.107142.

[33] M. Smith, "ABAQUS/Standard User's Manual, Version 6.9," 2009, Accessed: Jun. 12, 2025. [Online]. Available: https://research.manchester.ac.uk/en/publications/abaqusstandard-users-manual-version-69

[34] B. Young and G. J. Hancock, "Design of Cold-Formed Channels Subjected to Web Crippling," *Journal of Structural Engineering*, vol. 127, no. 10, pp. 1137–1144, Oct. 2001, doi: 10.1061/(ASCE)0733-9445(2001)127:10(1137).

[35] H. Alsanat, S. Gunalan, P. Keerthan, H. Guan, and K. D. Tsavdaridis, "Web crippling behaviour and design of aluminium lipped channel sections under two flange loading conditions," *Thin-Walled Structures*, vol. 144, p. 106265, Nov. 2019, doi: 10.1016/j.tws.2019.106265.

[36] American Iron and Steel Institute, "Standard Test Method for Determining the Web Crippling Strength of Cold-Formed Steel Beams, 2013 Edition," 2013.

[37] D. Cain, R. LaBoube, and W.-W. Yu, "The effect of flange restraint on web crippling strength of cold-formed steel Z- and I-sections," *CCFSS Library (1939 - present)*, May 1995, [Online]. Available: https://scholarsmine.mst.edu/ccfss-library/105

[38] C. Konthesingha, H. Weerasinghe, A. Nanayakkara, K. Pologanathan, G. Perampalam, and E. Kanthasamy, "Web Crippling Behaviour of Cold-Formed Carbon Steel, Stainless Steel, and Aluminium Lipped Channel Sections with Web Openings," *Buildings*, vol. 12, no. 11, p. 1820, 2022.

[39] H. Alsanat, S. Gunalan, P. Gatheeshgar, M. Alrsai, and K. Pologanathan, "Web crippling investigation of perforated aluminium lipped channels under interior-two-flange loading condition," *Thin-Walled Structures*, vol. 192, p. 111153, Nov. 2023, doi: 10.1016/j.tws.2023.111153.

[40] A. McIntosh, P. Gatheeshgar, K. Pologanathan, S. Gunalan, S. Navaratnam, and C. Higgins, "Web crippling of cold-formed carbon steel, stainless steel, and aluminium channels: Investigation and design," *Journal of Constructional Steel Research*, vol. 179, p. 106538, 2021.

Optimization of UHPFRC-Strengthened Square Bridge Piers for Enhanced Impact Resistance

R Thulakshan[1], N T Vandabona[1], and P L N Fernando[1]

Abstract

The vulnerability of waterway bridges to vessel impacts has spurred interest in intrinsic structural enhancements to improve impact resistance. Ultra-High Performance Fiber Reinforced Concrete (UHPFRC) offers superior strength and energy absorption compared to conventional concrete, although its high cost restricts widespread application. This study investigates the optimization of UHPFRC jacketing for square-shaped bridge piers, aiming to balance structural performance with economical usage of material, using a numerical modelling-based approach. Two jacketing strategies: a conventional full-ring approach and an optimized corner-only method are evaluated through a parametric study that varies the jacket thickness and length. To this end, numerical simulations were conducted using a validated model developed using the advanced finite element software LS-DYNA. The structural performance of the different pier configurations was evaluated in terms of pier displacement, maximum stress, strain energy and damaged areas. The findings reveal that strategically applied UHPFRC in critical regions, particularly pier corners for square shaped piers, can significantly enhance impact resistance and reduce damage level while minimizing material usage. Overall, this research presents an approach for improving the resilience of bridge piers subjected to accidental impact loads.

Keywords: Barge-pier collision, Damage mitigation, Impact loading, Pier displacement, UHPFRC jacketing

1. Introduction

Bridge structures spanning navigable waterways are typically engineered to withstand wind loads, vehicular loads, and seismic excitations. In addition to these forces, bridges, specifically the piers in waterway bridges, are vulnerable to accidental vessel collisions and must be designed to endure the associated collision loads [1]. These collisions can lead to catastrophic structural failures, significant economic losses, and loss of humans' lives. Numerous historical events underscore the severity and importance of ship-bridge or barge-bridge collision incidents.

Recently, a notable tragic event occurred when the Francis Scott Key Bridge in Baltimore, Maryland experienced a catastrophic collapse after being struck by a cargo ship named *Dali*, which had suffered an electrical failure. This collision event caused the complete failure of the bridge structure, leading to six reported fatalities [2]. The collapse of the Francis Scott Key Bridge following the ship collision event is shown in Fig. 1. Such events are not unprecedented and have occurred throughout history. One other notable incident occurred in 1980, when the freighter *MV Summit Venture*, collided with a support pier of the Sunshine Skyway Bridge in the United States. The impact caused a part of the bridge to collapse as shown in Fig. 2., resulting in the tragic loss of 35 lives [1].

These events highlight the persistent risk posed by vessel-bridge collisions, despite the advancement of bridge design standards and maritime safety protocols. The increasing frequency and severity of such incidents have prompted renewed scrutiny of bridge pier design, particularly with regard to impact resistance and residual load capacity following collisions. Conventional reinforced concrete (RC) piers, while widely used for their strength and cost-effectiveness, often exhibit brittle failure modes under high-energy impacts, leading to localized crushing, spalling, and even catastrophic collapse [3]. The limitations of traditional materials and design approaches have driven the search for advanced solutions capable of enhancing the resilience of bridge substructures against accidental loads. Ultra-High-Performance Fiber-Reinforced Concrete (UHPFRC) has emerged as a promising material for both the construction of new bridge piers and the retrofitting of existing ones. UHPFRC offers superior compressive and tensile strength, improved ductility, and exceptional durability compared to conventional concrete, largely due to its dense matrix and high steel fiber content [3, 4]. Recent research demonstrates that UHPFRC jacketing can

Figure 1: Francis Scott Key Bridge collapse after vessel collision [5]

[1] R. Thulakshan, N. T. Vandabona and P. L. N Fernando: Department of Civil Engineering, University of Moratuwa, Moratuwa, Sri Lanka.
(e-mail: thulakshanr.20@uom.lk , vandabonant.24@uom , lakshithaf@uom.lk)

Figure 2: Sunshine Skyway Bridge collapse after vessel collision [6]

significantly enhance the impact resistance of RC piers, reducing deformation and increasing load-bearing capacity during vessel collisions [4]. However, the main drawback of UHPFRC is its high cost, primarily attributed to the use of expensive admixtures and materials.

The study presented in this paper investigates the optimization of UHPFRC-jacketed bridge piers subjected to accidental barge impacts using a numerical modelling-based approach, utilizing the advanced finite element software LS-DYNA. Through this, the study aims to evaluate the effectiveness of UHPFRC as a strengthening material, identify optimal jacketing configurations, and provide practical guidance for enhancing the resilience of bridge structures exposed to maritime hazards. Therefore, by advancing the understanding of impact-resistant design and retrofitting techniques, this research contributes to the development of safer, more robust bridge infrastructure capable of withstanding the growing threat of vessel or barge collisions.

2. Model Geometry and Material Properties

2.1 Barge and Pier Configuration

According to AASHTO, the Jambo Hopper (JH) barge is the most widely used barge type in the US water ways [7]. Therefore, without losing generality, this barge type is employed as the baseline model in the present study. A typical JH barge used in inland waterways in the United States is shown in Fig. 3 and its schematic configuration is shown in Fig. 4. The corresponding barge dimensions are given in Table 1 [7].

In this study, a square pier with a cross-sectional dimension of 3.1 m × 3.1 m and a height of 15 m is considered, following the study by Sha et al. [1]. The pier is modelled as a reinforced concrete column, and the

Figure 3: Typical Jumbo Hopper (JH) barge used in inland waterways [7]

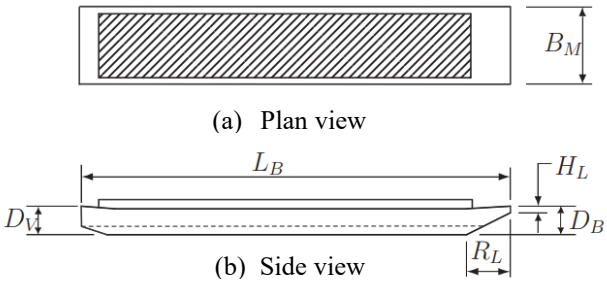

Figure 4: Configuration of the Jumbo Hopper (JH) barge [9]

superstructure weight of 130 tons is applied as an axial nodal load at the top of the pier. Initially, a 0.5 m gap is maintained between the front surface of the barge and the pier to prevent premature contact or penetration. The barge is modelled to collide with the pier at a height of 6.75 m above the foundation level, representing the typical water level during impact scenarios. It is important to note that the analysis does not consider soil-structure interaction effects and hence, the bridge pier is assumed to be fully fixed at the foundation level.

To analyze the effect of deformation and damage in reinforced concrete piers due to barge–pier collisions, this study incorporates detailed nonlinear material models for both concrete and steel in the pier simulation. The pier is modelled with a 50 mm reinforcement cover. Longitudinal steel bars, each 30 mm in diameter, are arranged at 300 mm intervals on all four sides of the pier. Transverse reinforcement is provided by 20 mm diameter stirrups, spaced at 200 mm along the height of the pier [1]. A perfect bond is assumed between steel reinforcement and the surrounding concrete in the modelling process.

Table 1: Barge dimensions used in the present model [7]

Parameter	AASHTO 1991 (ft)	This Study (m)
L_B = Length	195	59.4
B_M = Width	35	10.6
R_L = Bow rake length	20	6
D_B = Depth of bow	13	4
D_V = Depth of vessel	12	3.7
H_L = Head log height	2–3	0.5

2.2 Material Properties

2.2.1. Concrete

LS-DYNA provides various material models to simulate the nonlinear behavior of concrete under dynamic loads. MAT_CONCRETE_DAMAGE_REL3 (MAT_72R3), MAT_WINFRITH_CONCRETE (MAT_084/085), and MAT_CSCM_CONCRETE (MAT_159) are some notable examples [8, 9] Among these, MAT_72R3 and MAT_159 are widely used due to their reliability in modelling the behaviour of concrete under dynamic loads, with a limited number of input parameters, such as unconfined compressive strength and mass density, with other properties being computed through appropriate constitutive models. MAT_CSCM_CONCRETE (MAT_159) is selected in this study to model concrete as

it has been extensively validated in simulating nonlinear and dynamic concrete behaviour under impact loads [10]. Table 2 presents the mix proportions of conventional concrete and UHPFRC, while Table 3 and 5 provide the material properties of conventional concrete and UHPFRC [4], respectively. In the present study, a volume dosage of 1.5% copper-coated smooth steel fibers was considered, and its properties are presented in Table 4. For UHPFRC, the flexural performance is significantly enhanced. As cracks propagate, the specimen remains intact due to the bridging effect of the steel fibers.

Table 2: Mix proportions of concrete and UHPFRC (unit: kg/m^3) [11]

Material	Conventional Concrete	UHPFRC
Cement	551.9	750
Fine Sand	843.1	1030
Coarse Aggregate	745.9	–
Water	282.7	190
Silica Fume	–	225
Nano Particles	–	21.7
Superplasticizer	–	16
Steel Fiber	–	114

Table 3: Material properties of conventional concrete and steel [8]

	Model	Parameter	Meaning	Value
Concrete	*MAT_CSCM _CONCRETE	ρ_c	Mass density	2274.0 kg/m³
		f_c	Uniaxial com. strength	42.0 MPa
		D_{agg}	Maximum agg. Size	10.0 mm
		ε_{uc}	Failure strain	0.1
Longitudinal bars & barge steel (zone 1)	*MAT_PIECEWISE_ LINEAR_PLASTICITY	ρ_{sl}	Mass density	8020.0 kg/m³
		E_{sl}	Elastic modulus	200.0 GPa
		E_{tl}	Tangent modulus	3.0 GPa
		f_{yl}	Yield stress	426.0 MPa
		ε_{ul}	Failure strain	0.25
Stirrup	*MAT_PIECEWISE_ LINEAR_PLASTICITY	ρ_{sh}	Mass density	8020.0 kg/m³
		E_{sh}	Elastic modulus	200.0 GPa
		E_{th}	Tangent modulus	3.0 GPa
		f_{yh}	Yield stress	295.0 MPa
		ε_{uh}	Failure strain	0.25

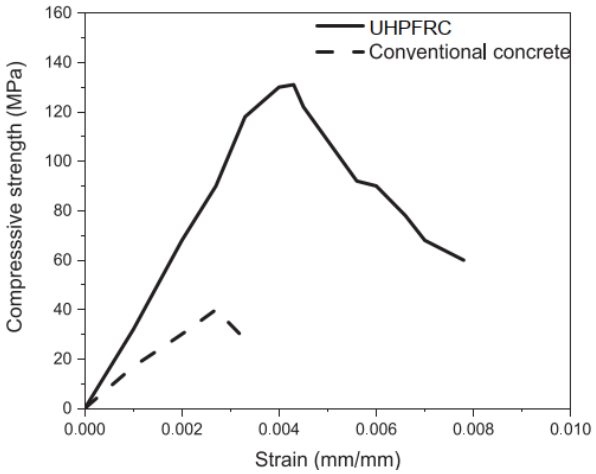

(a)

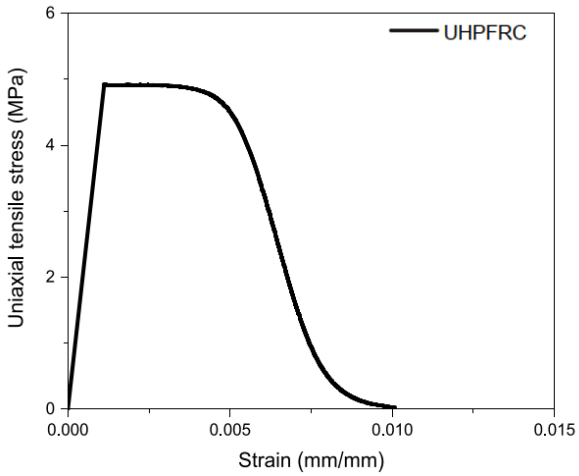

(b)

Figure 5: Uniaxial (a) Compressive and (b) Tensile stress-strain curve [11]

Additionally, Fig. 5(a) and Fig. 5(b) illustrate the uniaxial stress–strain relationships of the UHPFRC material under compressive and tensile loading conditions, respectively.

2.2.2. Reinforcement Steel

The MAT_PIECEWISE_LINEAR_PLASTICITY (MAT_024) model is commonly used for simulating the behavior of reinforcement steel in concrete piers under impact and dynamic loading. This model defines a multi-segment stress-strain curve that closely matches the behavior of steel, including elastic and plastic regions, yield plateau, strain hardening, and failure [9]. It is particularly suited for dynamic loading scenarios, including barge impacts, due to its capability to incorporate strain rate effects and nonlinear material behavior. Table 3 provides the key material parameters of the reinforcement steel [8]. The reinforcement arrangement of the pier model is illustrated in Fig. 6.

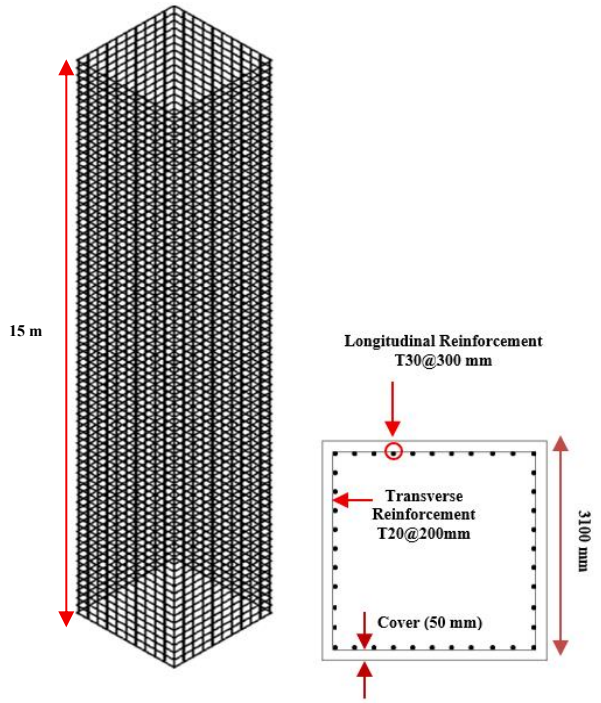

Figure 6: Reinforcement arrangement of the pier

2.2.3. Barge Steel

The barge is divided into two zones based on their deformation response during collision. Fig. 7 illustrates the zoning configuration of the barge and the arrangement of the internal trusses. Zone 1, which is in the impact zone and undergoes significant plastic deformation, is modelled using the MAT_PLASTIC_KINEMATIC (MAT_003) formulation to accurately capture its inelastic behavior. In contrast, Zone 2 experiences negligible deformation and is therefore idealized using the MAT_RIGID (MAT_020) material model to reduce computational cost while preserving mass and inertia. The stress-strain curve of the barge steel is shown in Fig. 8. Other property parameters are tabulated in Table 3. The barge bow consists of a series of internal trusses spaced uniformly at 815 mm intervals. These internal trusses are modelled using beam elements to provide stiffness to the bow structure.

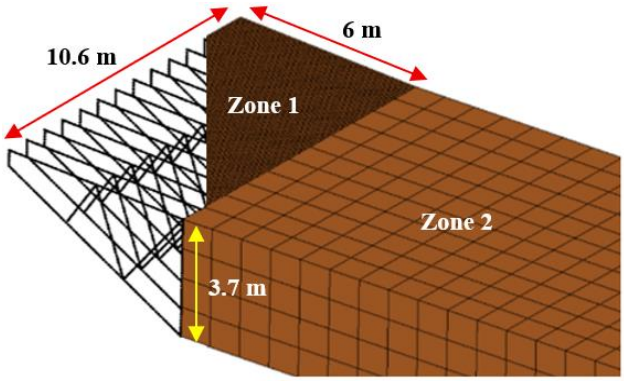

Figure 7: Zoning of the barge in the numerical model

To ensure that the total mass of the barge model matches the actual mass of the real barge, the density of the material in Zone 2 must be adjusted accordingly. This adjustment is made using Eq. (1)

$$\rho_{bs} = \frac{M_b - M_{b1}}{V_{bs}} \quad (1)$$

where ρ_{bs} is the modified density of material in Zone 2 (kg/m^3), M_b is the real barge mass (kg), M_{b1} is the mass of Zone 1 (kg) and V_{bs} is the volume of Zone 2 (m^3). In general, the outer shell of a JH barge is constructed from steel plates with thicknesses ranging from 10 m to 13 mm [7]. Hence, in this study, a plate thickness of 12 mm is adopted [9].

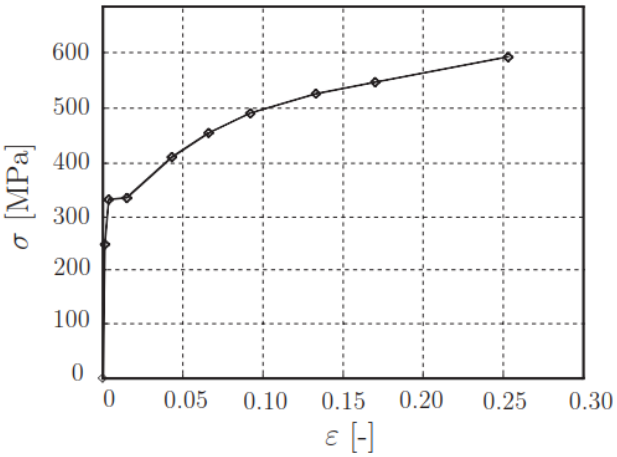

Figure 8: Stress-strain curve of the barge steel [9]

3. Numerical Modelling

3.1 Model Mesh and Validation Study

LS-DYNA employs the central difference scheme among its explicit integration methods. A notable limitation of explicit methods is their conditional stability, which requires the time step to remain below a critical threshold determined by the shortest stress wave propagation time across the element mesh. Since this time increment is directly influenced by the size of the finite element mesh, conducting a mesh convergence study prior to running the simulation is essential.

In the study by Sha et al. [1] , three mesh sizes of 50 mm, 100 mm, and 200 mm were evaluated for the concrete pier. The results indicated that the 200 mm mesh underestimated pier displacement relative to the 100 mm and 50 mm meshes. Although the 50 mm and 100 mm meshes yielded comparable numerical results, the 50 mm mesh incurred a significantly higher computational cost. Since the present study adopts the same full-scale model as that of Sha et al. [1], a minimum element size of 100 mm was employed in this study. The barge bow (Zone 1) was modelled using a mesh size of 100 mm while Zone 2 was meshed with a higher mesh size of 1 m elements to reduce computational cost.

Table 4: Properties of copper-coated micro steel fibre [11]

Fibre type	Diameter D_f (mm)	Length L_f (mm)	Aspect ratio (L_f/D_f)	Density (kg/m^3)	Tensile strength (MPa)	Elastic modulus (GPa)
Smooth fibre	0.2	6	30	7800	> 2850	200

Table 5: Material properties of the UHPFRC [12]

Parameter	Definition	Unit	Value
ρ	Mass density	kg/m³	2600
NH	Hardening initiation	–	1
CH	Hardening rate	–	0
G	Shear modulus	MPa	1.958×10^4
K	Bulk modulus	MPa	2.611×10^4
α	Tri-axial compression surface constant term	MPa	1.502×10^2
θ	Tri-axial compression surface linear term	–	1.462×10^{-1}
λ	Tri-axial compression surface nonlinear term	MPa	1.356×10^2
β	Tri-axial compression surface exponent	MPa^{-1}	3.203×10^{-3}
α_1	Torsion surface constant term	–	1
θ_1	Torsion surface linear term	MPa^{-1}	0
λ_1	Torsion surface nonlinear term	–	0.423
β_1	Torsion surface exponent	MPa^{-1}	1.056×10^{-3}
α_2	Tri-axial extension surface constant term	–	1
θ_2	Tri-axial extension surface linear term	MPa^{-1}	0
λ_2	Tri-axial extension surface nonlinear term	–	0.5
β_2	Tri-axial extension surface exponent	MPa^{-1}	1.056×10^{-3}
R	Cap aspect ratio	–	2.92
X_0	Cap initial location	MPa	4.3×10^2
W	Maximum plastic volume compaction	–	4.257×10^{-3}
D_1	Linear shape parameter	MPa^{-1}	2.825×10^{-10}
D_2	Quadratic shape parameter	MPa^{-1}	3.352×10^{-6}
B	Ductile shape softening parameter	–	100
GFC	Fracture energy in uniaxial stress	MPa·mm	2.061×10^1
D	Brittle shape softening parameter	–	5.0×10^3
GFT	Fracture energy in uniaxial tension	MPa·mm	7.36
GFS	Fracture energy in pure shear stress	MPa·mm	7.36
pwrc	Shear-to-compression transition parameter	–	5
pwrt	Shear-to-tension transition parameter	–	1
pmod	Modify moderate pressure softening parameter	–	0
$\eta_0 c$	Rate effects parameter for uniaxial compressive stress	–	9.927×10^{-4}
Nc	Rate effects power for uniaxial compressive stress	–	0.7817
$\eta_0 t$	Rate effects parameter for uniaxial tensile stress	–	1.336×10^{-4}
Nt	Rate effects power for uniaxial tensile stress	–	0.7087
overc	Maximum overstress allowed in compression	MPa	7.625×10^1
overt	Maximum overstress allowed in tension	MPa	2.0×10^1
Srate	Ratio of effective shear stress to tensile stress fluidity parameters	–	1
repow	Power that increases fracture energy with rate effects	–	0.5
IRATE	Rate effect options	–	1

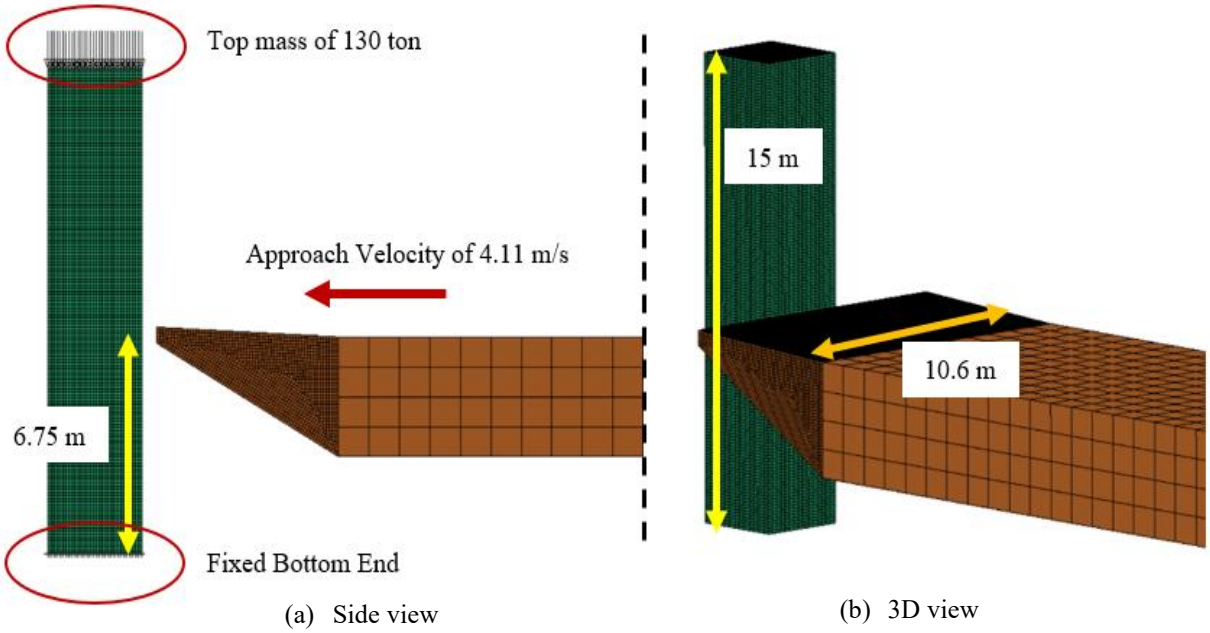

(a) Side view (b) 3D view

Figure 9: Schematic representation of barge and pier arrangement prior to collision

3.2 Model Validation

A validation study for the developed finite element model was conducted by replicating a barge–rigid pier collision scenario from the study by Sha et al. [1]. The comprehensive numerical study by Sha et al. [1], had been validated by referring to several previous numerical and experimental investigations [7, 13, 14]. For the current validation study, a fully loaded barge with a mass of 1723 tons and an approach velocity of 4.11 m/s (14.8 km/h or 8 knots) was considered. Fig. 9 represents the schematic representation of barge and pier arrangement prior to collision. For the validation, the maximum pier displacement and barge bow crush depth were compared, as summarized in Table 6. From Table 6, it can be seen that both the maximum pier displacement and the barge bow crush depth exhibit minor variations from the results in the literature. This is because of the difference in barge bow internal structures in the two models. The barge model adopted in the study by Sha et al. was developed based on a structural drawing of an actual barge. In the present study, certain modifications were implemented for simplicity. For instance, the void spacing between the bow and the rear part of the barge was not considered and was modeled as part of the bow.

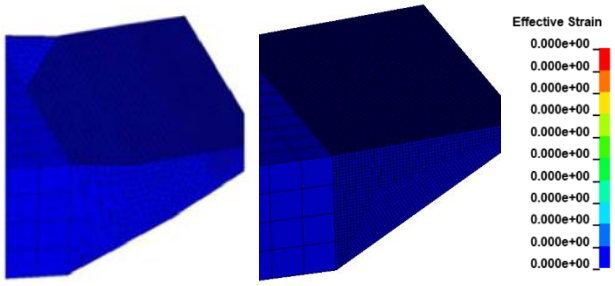

T=0.0 s T=0.0 s

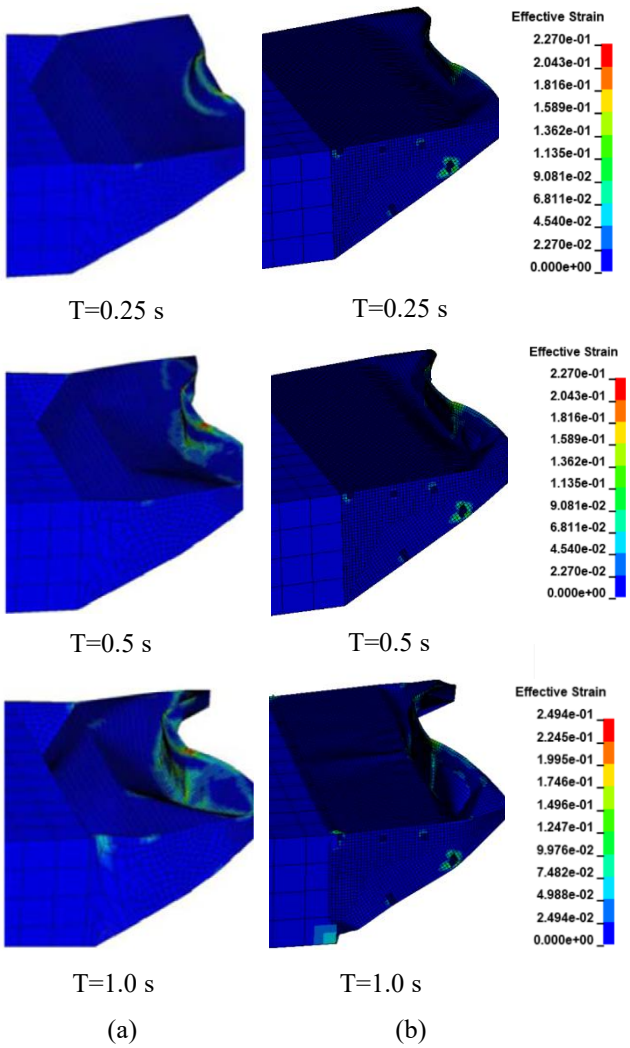

T=0.25 s T=0.25 s

T=0.5 s T=0.5 s

T=1.0 s T=1.0 s

(a) (b)

Figure 10: Damage contour of the barge in the (a) reference study (b) model used in this study

Table 6: Comparison of literature and present models

Model	Maximum Pier Displacement	Barge Bow Crushing Depth
Reference Model	225 mm	2.110 m
Present Model	216 mm	2.184 m
Deviation	4.0%	3.5%

In addition, Fig. 10 presents a comparison of sequential captures of barge deformation patterns at time intervals of 0 s, 0.25 s, 0.5 s, and 1.0 s after the impact. It can be observed that the deformed shape of the barge at these time periods obtained from the numerical model, agrees well with that of the reference study. Both the aforementioned aspects, highlight a good agreement between the numerical model of the present study and the validation study from the published literature [1] and hence, the validated numerical model was used to carry out further investigations.

3.3 Overview of the current study

Previous studies have demonstrated that full-length UHPFRC jackets significantly improve the impact resistance and residual strength of bridge piers but are costly due to the high material price [3, 12]. Therefore, partial strengthening methods can be a feasible option for general applications. Fan et al. [3] identified three critical regions on impact-prone piers: the impact zone and the two ends. Jacketing the impact zone reduces local damage effectively but offers limited protection at the ends. In contrast, end jacketing significantly reduces damage at both ends and helps control overall displacement by stabilizing plastic hinge formation. This targeted confinement enhances ductility, energy dissipation, and shear resistance, reducing the risk of brittle failure under impact [3].

Since water levels in waterways fluctuate, predicting the exact impact point is difficult. Fan et al. [3]compared two equal-volume strengthening strategies: Column-I (impact zone jacketing) and Column-E (end jacketing), under ± 3 m water level variation. Column-E consistently outperformed Column-I in reducing damage and maintaining residual strength, regardless of impact height. Thus, end jacketing offers more reliable impact resistance under uncertain conditions [3]. Hence, an optimized UHPFRC-based strengthening scheme at the ends was proposed for the construction or retrofitting of square-shaped bridge piers, based on a comparative evaluation to that of a conventional technique.

In the case of rectangular or square-shaped piers, the corners act as geometric discontinuities that induce stress concentrations, making them the most vulnerable regions for crack initiation under impact loading conditions [15]. This was the basis for selecting a corner-only jacketing technique (Scheme-2) for investigation. Rectangular jackets are typically limited by their inadequate flexural stiffness, while circular or oval jackets may not be suitable in bridge applications due to space constraints and potential difficulties in integrating them with existing structural and non-structural elements [16]. Therefore, the jacketing in this method adopts a right-angled triangular shape at each corner.

In the present study, two jacketing strategies, referred to as Scheme 1 and Scheme 2, were considered based on the aforementioned information. Scheme-1, which represents the conventional approach, involves applying a continuous external layer of UHPFRC over the pier surface as shown in Fig. 11(a). In contrast, Scheme-2 utilizes UHPFRC at the four corners in the form of right-angled triangular sections, as shown in Fig.11(b), which represents proposed configuration. For both Schemes, various jacketing lengths (l_u) and UHPFRC thickness (t_u) were evaluated. In Scheme-1, the full-length (l_u = 15 m) and partial jackets (l_u = 5 m, 3.5 m, 2 m) were considered with UHPFRC thicknesses of 200 mm, 400 mm, and 600 mm. In Scheme-2, corner jacketing was applied using triangular sections with side lengths (d_u) of 0.75 m, 1.115 m, and 1.55 m for each l_u value mentioned previously. Details of the parametric combinations for Scheme-1 and Scheme-2 are presented in Table 7 and Table 8, respectively. From a construction viewpoint, the UHPFRC jackets can be cast after the curing period of the core to ensure sufficient bond strength [17]. In modelling perfect bonding between the UHPFRC and normal concrete was established using the contact definition CONTACT_TIED_SURFACE_TO_SURFACE algorithm in LS-DYNA.

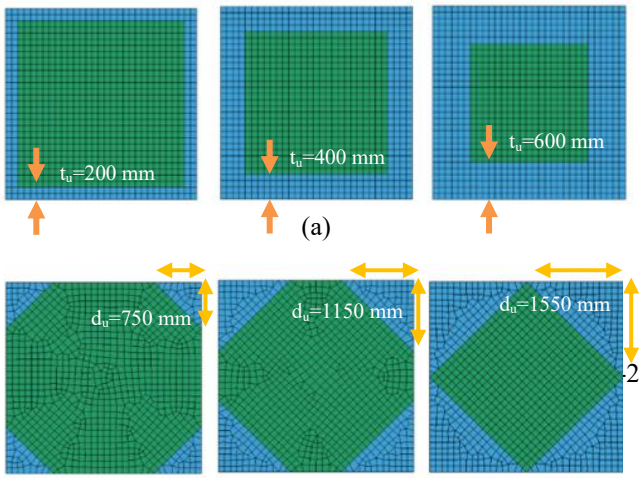

Figure 11: Proposed jacketing techniques (a) Scheme-1 (b) Scheme-2 (note: jacketed area in blue colour)

Table 7: Details of Jacketing for Scheme-1

Jacketing length l_u(m)	Thickness t_u (mm)	UHPFRC Volume (m^3)	Volume ratio V_r (%)
2	200	4.64	3.22
	400	8.64	5.99
	600	12	8.32
3.5	200	8.12	5.63
	400	15.12	10.49
	600	21	14.57
5	200	11.6	8.05
	400	21.6	14.98
	600	30	20.81
Full length	200	34.8	24.14
	400	64.8	44.95
	600	90	62.43

Table 8: Details of Jacketing for Scheme-2

Jacketing length l_u(m)	Side length d_u (m)	UHPFRC Volume (m^3)	Volume ratio V_r (%)
2	0.75	2.25	1.56
	1.15	5.29	3.67
	1.55	9.61	6.67
3.5	0.75	3.94	2.73
	1.15	9.26	6.42
	1.55	16.82	11.67
5	0.75	5.63	3.90
	1.15	13.23	9.17
	1.55	24.03	16.67
Full length	0.75	16.88	11.71
	1.15	39.68	27.52
	1.55	72.08	50.00

4. Results and Discussion

4.1 Comparison of Normal Concrete and UHPFRC

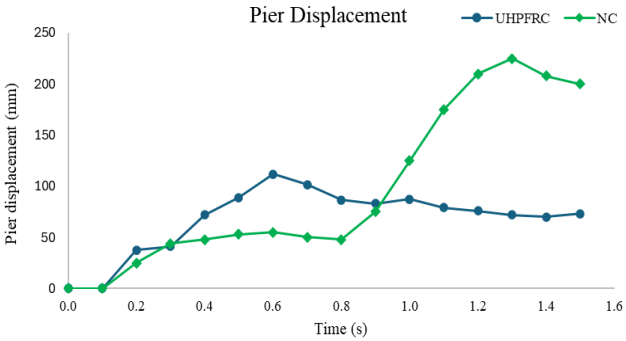

Figure 12: Pier response for impact velocity of 4.11 m/s

The nonlinear behavior of bridge piers subjected to the impact of a fully loaded barge with the mass of 1723 tons traveling at speed of 4.11 m/s (14.8 km/h or 8 knots) was investigated by evaluating displacements at the impact region for piers constructed with conventional concrete and UHPFRC. As illustrated in the displacement time history in Fig. 12, localized damage initiates within the first 0.3 s, driven predominantly by the impact impulse, during which the pier's local response is mostly pronounced. The global structural response becomes significant shortly thereafter. Excessive damage is observed following the peak impact force, primarily due to the limited time available for the pier to respond. The initial force is resisted largely by the pier's inertial capacity, with deformation developing progressively post-impact.

The impact involves a fully loaded barge weighing 1,723 tons traveling at a relatively high velocity of 4.11 m/s, resulting in a substantial impact energy. At the initial stage of contact, significant buckling occurs in the barge bow, as illustrated in Fig. 10, where deformation of the steel components absorbs a considerable portion of the impact energy. Following the interaction between the barge bow and the pier, the barge begins to retreat, and the pier subsequently exhibits oscillatory behavior. For the conventional concrete pier, this oscillatory response is initiated at approximately T = 0.8 s, as evidenced by the displacement–time histories presented in Fig. 12. Minor surface crushing occurs at the initial contact stage, while flexural and shear responses associated with global deformation become more evident at later stages, such as a T = 0.8 s. The conventional concrete pier reaches a peak displacement of approximately 225 mm at 1.3 s, which subsequently decreases. In contrast, the UHPFRC pier demonstrates a peak displacement that is nearly 50% lower, approximately 110 mm at 0.6 s, while also exhibiting noticeable recovery following the impact.

As illustrated in Fig. 12, the UHPFRC pier exhibits greater displacement than the conventional concrete pier during the initial 0.9 s following impact. This initial deflection is attributed to the higher ductility, enhanced energy absorption capacity through deformation, and distinctive material behaviour of UHPFRC under strain rate effects, which enable it to tolerate greater deformation without cracking, unlike the more brittle conventional concrete pier. Furthermore, the increased stiffness and tensile strength of UHPFRC contribute to more rapid dissipation of impact energy, resulting in a faster structural response and ultimately a lower peak displacement. This highlights the superior energy absorption capacity, structural integrity, and damage tolerance of UHPFRC under dynamic collision scenarios.

4.2 Effect of conventional full ring jacketing (Scheme – 1)

Fig.13 presents different jacketing configurations, all with a constant thickness of 200 mm. It shows the damage of the pier corresponding to jacketing lengths of 2 m, 3.5 m, and 5 m, with the total length evenly distributed between the upper and lower parts of the pier. The damage distribution at T = 1.0 s, by which time the maximum damage was found to have been occurred, shows that increasing the jacketing length alone, without altering the thickness, does not lead to a significant improvement in impact resistance, which can be attributed to the localized nature of the damage.

Similarly, the influence of jacketing thickness on impact resistance was investigated by maintaining a constant jacketing length of 3.5 m while varying the thickness. Fig. 14 illustrates damage of the pier corresponding to jacketing thicknesses (t_u) of 200 mm, 400 mm, and 600 mm, respectively. As shown in Fig.14, the damage level at T =1.0 s were compared. Increasing thickness from 200 mm to 400 mm significantly reduces the damaged area, indicating an improvement in impact resistance an improvement in impact resistance. However, a further increase in thickness from 400 mm to 600 mm does not produce a noticeable difference, as both cases exhibit similar levels of damage. This suggests that beyond a certain thickness, additional jacketing may not contribute to further enhancement in performance under impact loading.

In addition to the pier displacement and damage level, the internal strain energy absorbed by the UHPFRC jackets was evaluated for various jacketing length and thickness combinations. The initial kinetic energy (E_B) of the barge was calculated as 14.55 MJ using Eq. (2), where the barge initial velocity V_B and the barge mass M_B are in m/s and Mkg, respectively.

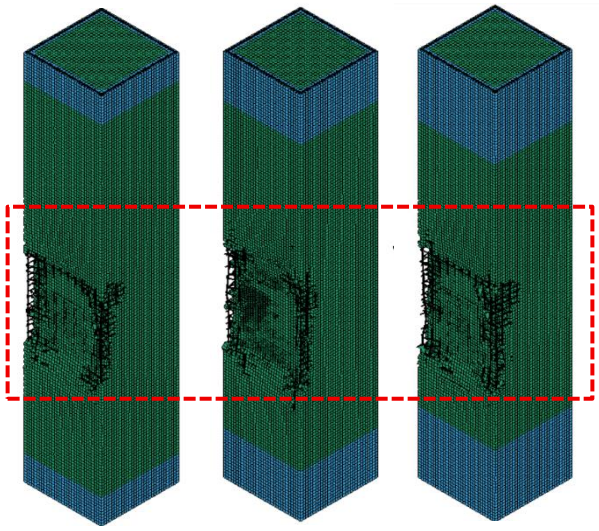

(a) (b) (c)

Figure 13: Damaged level at impact location for jacketing length of (a) 2 m (b) 3.5 m and (c) 5 m

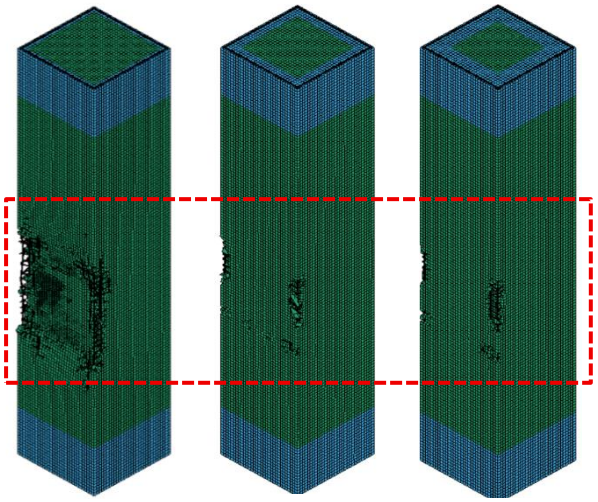

(a) (b) (c)

Figure 14: Damaged level at impact location for jacketing thickness of (a) 200 mm (b) 400 mm and (c) 600 mm

The energy absorbed by the UHPFRC jackets in the form of strain energy at both ends is illustrated in Fig. 15. The results show that, for a pier with a height of 15 m and a cross section of 3.1 m × 3.1 m, a jacketing thickness of approximately 400 mm results in the maximum reduction in collision energy, as indicated by the highest strain energy absorption in the jackets. However, further simulations with a wider range of jacketing combinations are required to determine the optimal configuration more precisely.

$$E_B = \frac{1}{2} M_B V_B^2 \quad (2)$$

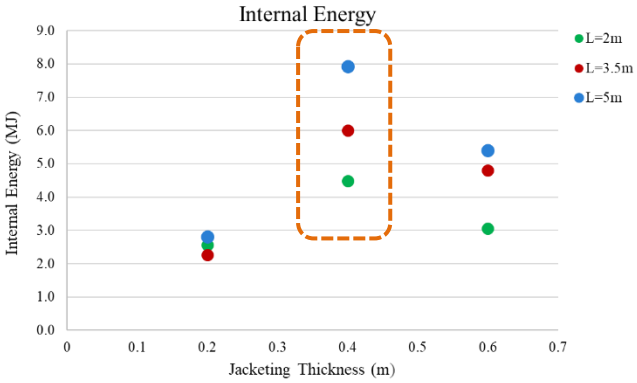

Figure 15: Strain energy observed by the UHPFRC Jackets

4.3 Effect of the proposed corner-only method (Scheme– 2)

In this method, a modified jacketing configuration was proposed, motivated by the observation that sharp-edged piers or columns are more vulnerable to localized stress concentrations during impact loads. To overcome this, triangular-shaped jackets were applied to better protect the corners, where damage is typically most severe. Fig. 16 (a)-(c) illustrates the stress distribution and damage patterns in piers with a constant jacketing length of 3.5 m, while varying the side length of the triangular jacket (d_u) as 0.75 m, 1.15 m, and 1.55 m. As seen in Fig.16 (a), the configuration with d_u = 0.75 m resulted in significant damage near the corners. However, increasing the d_u to 1.15 m and 1.55 m resulted in a noticeable reduction in damage, particularly at the vulnerable edge regions. Although both of these configurations exhibited comparable peak effective stress, the overall damage was further reduced in the case of 1.55 m, indicating improved impact resistance with increased cross-sectional size of the jacketing.

Pier X, with a jacketing length of 3.5 m combined with a triangular cross-section of side length (d_u) 1.55 m, results in a UHPFRC volume ratio of approximately 11.67%, as shown in Table 7. Similarly, Pier Z, with a d_u of 0.75 m applied along the full pier height, yields a comparable volume ratio of 11.71%. As shown in Fig. 17, Pier Z exhibits significantly less damage compared to Pier X despite using a similar amount of UHPFRC, highlighting its improved material efficiency and impact resistance.

4.4 Comparison of the jacketing techniques

Considering both Scheme-1 and Scheme-2, a total of 24 different jacketing configurations were analyzed. Among these, six configurations (three in each scheme) utilized a UHPFRC volume ratio (V_r) within a range of 8% to 12%. For comparison purposes, this specific range was selected, and for each case, the damage level at the impact location and the peak impact stress are presented in Fig.15. The details of those selected piers are summarized in Table 9.

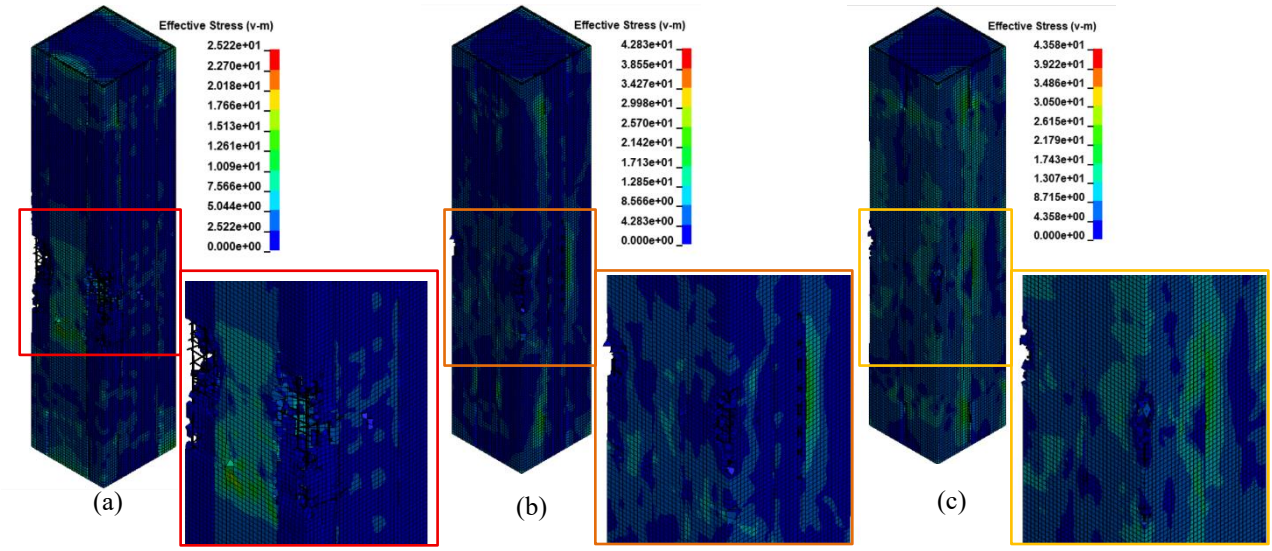

Figure 16: Stress contour and level of damage at the impact location for jacket side length of (a) 0.75 m, (b) 1.15 m, and (c) 1.55 m

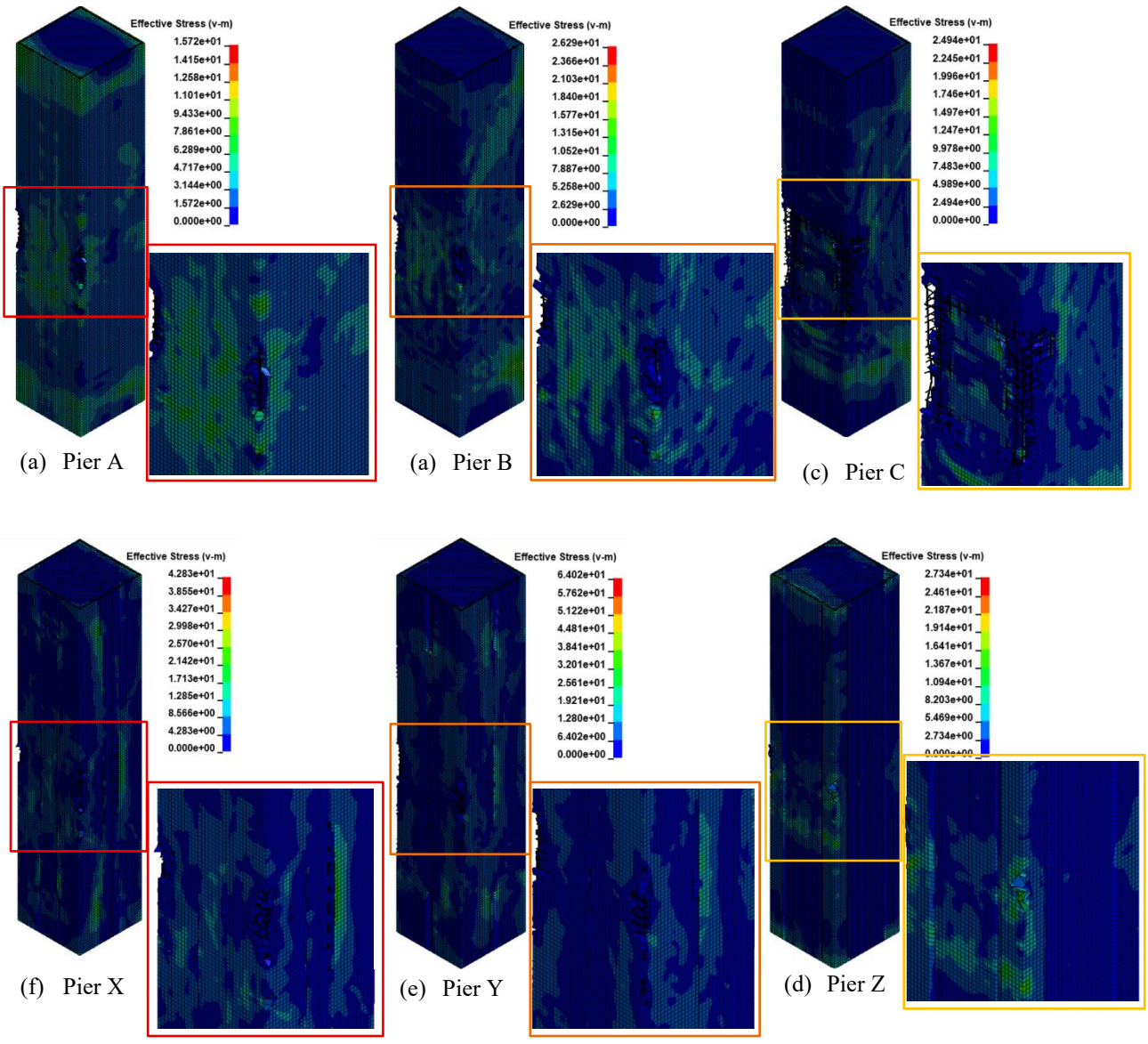

Figure 17: Damage level of various pier configuration which have the V_r in the range of 8 % - 12 %

Table 9: Pier configuration of V_r in the range of 8% -12%

Parameter	Pier Configuration					
	Scheme -1			Scheme -2		
Pier	**A**	**B**	**C**	**X**	**Y**	**Z**
l_u (m)	2	3.5	5	3.5	5	Full
t_u (m)	0.6	0.4	0.2	_	_	_
d_u (m)	_	_	_	1.55	1.15	0.75
V_r (%)	8.32	10.49	8.05	11.67	9.17	11.71

As shown in Fig.17, among the six pier configurations analyzed, Pier Z (d_u = 0.75 m, full-height corner jacketing, V_r = 11.71%) exhibited the least damage, with no reinforcement exposure, outperforming all other configurations. In contrast, Pier C (full perimeter jacketing over 5 m, t_u = 200 mm, V_r = 8.05%) showed the most severe damage at the impact location due to the thinner layer of UHPFRC jacket.

In addition, Piers A, B, X, and Y all showed similar localized failure (slight reinforcement exposure at corners), even though Scheme-1 (A, B) used full-perimeter jacketing and Scheme-2 (X, Y) used corner jacketing. However, the effective stress contours acting on Piers X and Y are relatively higher compared to Piers A and B. This may suggest that when l_u is kept the same (2 m–3.5 m), the method of jacketing (full vs corner) does not significantly alter the damage outcome if the UHPFRC volume is comparable (8%–12%). This may also suggest that geometry and distribution of jacketing play a more dominant role in mitigating localized failure than stress magnitude alone.

5. Conclusions

This study addresses the critical issue of vessel or barge collisions with waterway bridge piers, which is a severe and recurring problem that has been observed globally for several decades. To enhance the impact resistance of vulnerable bridge piers while maintaining cost-effectiveness, optimized strategies were investigated that are applicable to both newly constructed piers and the retrofitting of existing piers. The focus was placed on square-shaped piers, which represent a conventional and widely used form in bridge engineering. Two jacketing approaches were examined: the conventional full-ring jacketing method and the proposed corner-only jacketing technique. The longitudinal and transverse reinforcement configurations were kept unchanged to maintain general applicability. Various combinations of jacketing lengths and thicknesses were analyzed. Based on the results obtained from numerical simulations, several key findings were identified. Those are as follows:

- Under the impact of a fully loaded barge traveling at a maximum velocity of 4.11 m/s (14.8 km/h or 8 knots), the use of UHPFRC for the entire pier results in approximately a 50% reduction in displacement at the impact location (110 mm) compared to a conventional concrete pier (225 mm). However, despite its superior performance, this approach is not considered cost-effective for practical implementation.
- In the conventional full ring jacketing approach (Scheme–1), increasing the jacketing length while maintaining a constant thickness of 200 mm does not significantly improve impact resistance, despite the increased use of UHPFRC material. In contrast, increasing the jacketing thickness while keeping the length constant at 3.5 m proves to be more effective, as it leads to a substantial reduction in damage levels.
- Piers B and C had similar stress levels, yet Pier C exhibited more severe damage, underscoring the importance of thickness in Scheme-1 designs. This may suggest that a thinner jacketing may not provide sufficient confinement or energy absorption during impact.
- Pier Z achieved maximum performance with minimal damage using 11.71% of UHPFRC. This may indicate that well-distributed jacketing over the full pier height is more effective than concentrating material at specific regions (top and bottom).
- By evaluating the impact responses of both Scheme-1 and Scheme-2, it is evident that the use of right-angled triangular corner-only jacketing is more effective than the conventional full-perimeter approach in reducing damage levels during collisions. However, the optimal dimensions of the jacketing are likely to vary depending on the pier geometry, and impact scenario and hence, further research is required to determine these values. To this end, the approach followed in the present study can serve as a helpful reference.

References

[1] Y. Sha and H. Hao, “Nonlinear finite element analysis of barge collision with a single bridge pier,” *Eng Struct*, vol. 41, pp. 63–76, Aug. 2012, doi: 10.1016/j.engstruct.2012.03.026.

[2] D. Rai, "The Truth Behind the Failure of the Francis Scott Key Bridge: Accidental Failure or Design Failure?," *Research Archive*, preprint, 2024.doi: 10.58445/rars.1942.[Online].Available: https://research-archive.org/index.php/rars/preprint/view/1942

[3] W. Fan, D. Shen, X. Huang, and Y. Sun, “Reinforced concrete bridge structures under barge impacts: FE modeling, dynamic behaviors, and UHPFRC-based strengthening,” *Ocean Engineering*, vol. 216, Nov. 2020, doi: 10.1016/j.oceaneng.2020.108116.

[4] G. Gholipour and A. M. Billah, “Dynamic behavior of bridge columns reinforced with shape memory alloy rebar and UHPFRC under lateral impact loads,” *Int J Impact Eng*, vol. 168, Oct. 2022, doi: 10.1016/j.ijimpeng.2022.104297.

[5] "Francis Scott Key Bridge collapse after vessel collision," CNN, Mar. 26, 2024. [Online]. Available: https://www.cnn.com/bridge-collapse-image. [Accessed: 30-April-2024].

[6] "Sunshine Skyway Bridge collapse, May 1980," Tampa Bay Times. [Online]. Available: https://www.tampabay.com/archive/1980/05/09/sunshine-skyway-disaster/. [Accessed: 30-Jul-2002]

[7] P. Yuan, *Modeling, Simulation and Analysis of Multi-Barge Flotillas Impacting Bridge Piers*, Ph.D. dissertation, University of Kentucky, Lexington, KY, 2005.

[8] W. Wang, X. Wang, R. Zhou, and Z. Lu, “A mathematical framework for efficient predictions of dynamic processes of RC piers under barge collisions,” *Case Studies in Construction*

Materials, vol. 19, Dec. 2023, doi: 10.1016/j.cscm.2023.e02460.

[9] W. Wang and G. Morgenthal, “Reliability analyses of RC bridge piers subjected to barge impact using efficient models,” *Eng Struct*, vol. 166, pp. 485–495, Jul. 2018, doi: 10.1016/j.engstruct.2018.03.089.

[10] Y. D. Murray, A. Y. Abu-Odeh, and R. P. Bligh, "Evaluation of LS-DYNA Concrete Material Model 159," FHWA-HRT-05-063, Federal Highway Administration, Turner-Fairbank Highway Research Center, McLean, VA, May 2007.

[11] J. Wei, J. Li, and C. Wu, “An experimental and numerical study of reinforced conventional concrete and ultra-high performance concrete columns under lateral impact loads,” *Eng Struct*, vol. 201, Dec. 2019, doi: 10.1016/j.engstruct.2019.109822.

[12] G. Gholipour and A. M. Billah, “Dynamic behavior of bridge columns reinforced with shape memory alloy rebar and UHPFRC under lateral impact loads,” *Int J Impact Eng*, vol. 168, Oct. 2022, doi: 10.1016/j.ijimpeng.2022.104297.

[13] Consoliza, "Barge Impact Testing of the St. George Island Causeway Bridge: Phase I: Feasibility Study," January 2002.

[14] R. C. Patev, "Full-Scale Barge Impact Experiments," *Transportation Research Circular* 491: Inland Waterway Technical Studies, U.S. Army Corps of Engineers, 1999. [Online]. Available: https://apps.dtic.mil/sti/tr/pdf/ADA425199.pdf. Accessed: July 29, 2025.

[15] Q. Hussain, A. Ruangrassamee, T. Jirawattanasomkul, and D. Zhang, “Stress and strain relations of RC circular, square and rectangular columns externally wrapped with fiber ropes,” *Sci Rep*, vol. 14, no. 1, Dec. 2024, doi: 10.1038/s41598-024-54586-9.

[16] S. Pravin and B. Waghmare, "Materials And Jacketing Technique For Retrofitting of Structures," *International Journal of Advanced Engineering Research and Studies*, vol. 1, no. 1, pp. 15-19, Oct.-Dec. 2011

[17] S. Ali Dadvar, D. Mostofinejad, and H. Bahmani, “Strengthening of RC columns by ultra-high performance fiber reinforced concrete (UHPFRC) jacketing,” *Constr Build Mater*, vol. 235, Feb. 2020, doi: 10.1016/j.conbuildmat.2019.117485.

Review and Modelling of Effects of Corrosion in Dapped End Connections

A. Thananshayan[1], H.G.H. Damruwan[1] and C. Rajapakse[1]

Abstract

This study examines the structural consequences of corrosion in dapped end reinforced concrete connections. These critical regions, frequently encountered in precast concrete systems, are particularly vulnerable to deterioration due to environmental exposure and geometric stress concentrations. The study commences with a comprehensive review of existing literature and experimental investigations concerning the performance of dapped ends under corrosion. Subsequently, numerical modeling was conducted using the VecTor2 software. Corrosion was simulated by reducing the cross-sectional area of the reinforcement through decreases in bar diameter, considering corrosion levels of 5%, 10%, and 15% to represent early to advanced stages of corrosion. Corresponding reductions in mechanical properties, including yield strength, ultimate strength, and ultimate strain, were also incorporated based on degradation equation proposed in the literature. Model validation was performed using experimental results from tests conducted at the University of Rome Tor Vergata. A total of 58 numerical simulations were executed, including 10 validation models, which demonstrated an average load ratio of 0.99 and a coefficient of variation of 8.56% of the remaining simulations, 24 addressed cross- sectional reduction effects, while the other 24 focused on mechanical property degradation. The findings reveal significant reductions in load-carrying capacity and notable changes in failure modes due to corrosion. This study contribu tes to the understanding of the long-term durability of dapped-end regions and provides recommendations for enhancing the design of reinforced concrete structures in corrosive environments.

Keywords: Dapped End Connections, Effects of Corrosion, Re-entrant Corner Crack, Nonlinear finite element model, Uniform Corrosion

1. Introduction

The design of bridges with dapped-ends also referred to as half joints beams involves a localized reduction in the beam's depth at the support zones, as illustrated in Figure 1**.** This design approach gained popularity in the UK during the 1960s and 1970s, resulting in the construction of over 400 concrete bridges with such joints on the current UK Highways England network. Their widespread use was largely due to their compatibility with precast bridge construction methods . Additionally, the design allowed for a reduced overall construction depth while maintaining a level roadway across the bridge deck and support spans[1].

Despite these advantages, half-joint configurations also come with notable drawbacks. A frequently observed issue involves the joint's poor water tightness. In many bridges, inspections reveal that complete water sealing is not achieved, allowing chloride-laden water to penetrate and collect on the lower nibs of the half-joint. This accumulation creates conditions conducive to corrosion, particularly due to the stagnant nature of the trapped moisture[1]. Sri Lankan and tropical coastal environments, the issue is more critical due to high humidity and salinity

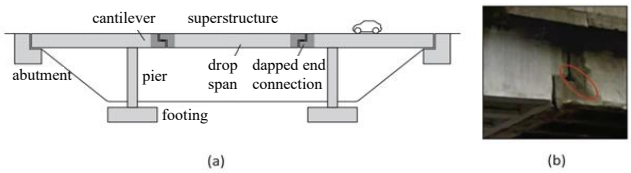

Figure 1: Dapped-end connections in existing bridges: (a) a typical bridge with dapped-end connections; (b) deteriorated connection in Lecco bridge, Italy, prior to its collapse (Google Street view, 2017)

The Figure 2 highlights two major infrastructural failures involving dapped-end connection bridges one in Canada and the other in Italy.

Figure 2 : (a) Concord overpass collapse, Laval, Canada 2006 Overpass collapse; (b) Lecco, Italy 2016

Numerous researchers have undertaken experimental investigations on dapped-end connections with diverse reinforcement configurations, concentrating on the peak load capacity, particularly in the critical re-entrant corner regions. To forecast the structural response, various strut-and-tie models and kinematic models have been formulated to estimate peak loads and crack widths. Experimental studies have also been conducted using both corroded and uncorroded reinforcement bars, from which empirical equations have been derived to quantify the

[1]Ariyarathinam Thananshayan, Damruwan H.G.H and Chathura Rajapakse Department of Civil Engineering, University of Moratuwa, BandaranayakeMawatha,Moratuwa10400,SriLanka. (thananshayanariyaratnam@gmail.com,hasithad@uom.lk,chathura .rajapakse@uo m.lk)

reduction in the mechanical properties of steel attributable to corrosion.

This paper presents a concise review of the relevant literature, followed by the development of nonlinear finite element models utilizing VecTor2. These models incorporate the effects of corrosion by applying previously derived degradation equations.

1.1. Behaviours of dapped end connections

The reinforcement of dapped-end beams is essential for maintaining their structural integrity and performance, particularly due to their vulnerability to stress concentrations and cracking. An orthogonal (Hanger) reinforcement layout is implemented at the bottom of the dapped end to counteract tension forces, while vertical reinforcement is incorporated in the full-depth section to resist shear forces. In the diagonal layout (Figure 3 (a))[2] orthogonal reinforcement is combined with additional reinforcement placed at an angle to intersect the corner crack perpendicularly, thereby providing enhanced resistance against cracking[2]. The orthogonal reinforcement is (Figure 3 (b))[2]combined with additional reinforcement placed at an angle to intersect the corner crack perpendicularly, thereby providing enhanced resistance against cracking

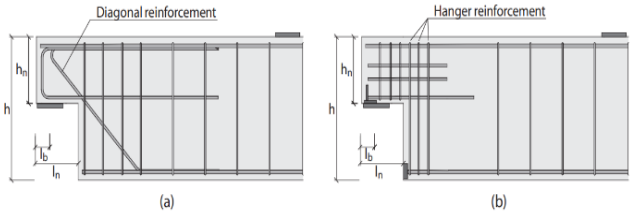

Figure 3 : (a) Diagonal reinforcement layout (b) Orthogonal reinforcement layout

Dapped-end connections can experience various failure modes due to their complex stress distribution and susceptibility to cracking and corrosion. Flexural failures along a re-entrant corner crack (Figure 4 (a)) and shear failures in the dapped-end region (Figure 4 (b)) are two main types. The re-entrant corner failures occur along the inclined corner crack, often referred to as flexural failures because they involve the yielding of the main dapped-end reinforcement, often referred to as flexural failures. Typically occurs in lightly reinforced dapped-end connections. Yielding of reinforcement and widening of corner cracks are indications of this failure[3].

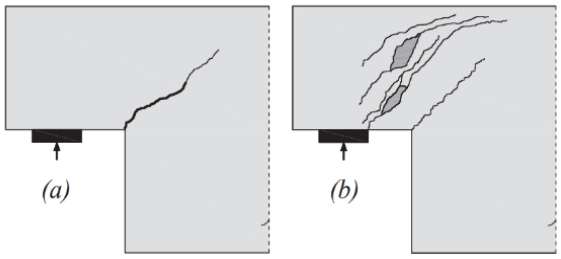

Figure 4 : (a) Flexural failure (b) Shear failure

Shear failures involve the failure of the dapped-end section due to shear forces. This can occur due to inadequate shear reinforcement or poor detailing. Sudden brittle fracture in the dapped-end region is an indication of this failure.

1.2. Corrosion

The dapped end regions are particularly vulnerable to corrosion due to their geometric discontinuities and exposure to adverse environmental conditions. Two prevalent forms of corrosion affecting these areas are uniform corrosion and chloride-induced (pitting) corrosion. Uniform corrosion progresses gradually and uniformly across the reinforcement surface, diminishing the cross-sectional area and resulting in a predictable reduction in strength. Conversely, chloride-induced corrosion, common in coastal or de-icing salt environments, results in localized pitting, which can significantly compromise specific sections of steel bars. The presence of construction joints and minimal concrete cover in dapped ends exacerbates chloride penetration, thereby accelerating corrosion processes. These corrosion mechanisms not only diminish the steel's capacity but also induce cracking and spalling of concrete, severely undermining structural integrity. [4], [5], [6], [7]

Corrosion inhibitors : - High-quality concrete, High pH (Alkalinity) Concrete
Corrosion promoters : - Oxygen, Water, Uneven chemicals, Unintended currents

Notably, large-scale tests conducted at the University of Rome Tor Vergata explored the behaviour of dapped end beams with various reinforcement layouts[8]. These tests highlighted the complex interaction between corbel action and direct shear in deteriorated specimens.

The Figure 5[4] illustrates the corrosion rate with alkalinity level. Chloride-induced corrosion typically occurs in marine environments or areas exposed to de-icing salts, where chloride ions penetrate concrete and disrupt the passive film on steel. In contrast, carbonation-induced corrosion results from the reaction between atmospheric carbon dioxide and the alkaline components of concrete, which lowers the pH and leads to depassivation of the reinforcing steel.

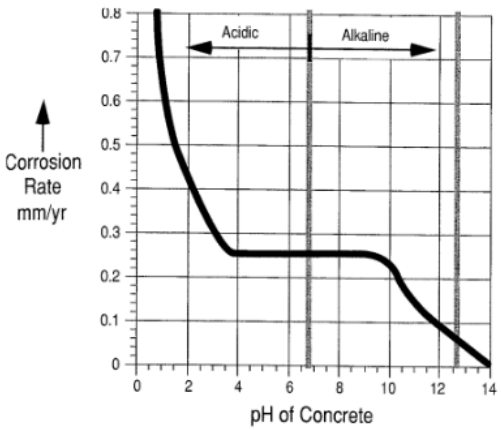

Figure 5 : Relationship between pH of concrete and time

1.3. Experiments with corroded reinforcement bars

Ou et al. investigated the tensile behavior of steel reinforcement subjected to both natural and artificial corrosion. The naturally corroded bars were sourced from a residential building complex located in a marine environment, where long-term chloride exposure had led to varying levels of deterioration. The study covered a wide range of corrosion levels, from 5% to 82% mass loss. Through tensile testing, the research provided detailed insight into how corrosion affects yield strength, ultimate strength, and ductility of reinforcing bars. The findings from this work contributed to the development of empirical degradation equations, which are now commonly used in modelling corroded reinforcement behavior in structural simulations[9].

Léonard et al. [7] investigated the combined mechanical and corrosion effects in reinforced concrete dapped-end connections. While traditional analysis of such disturbed regions (D-regions) relies on strut-and-tie models and finite element methods to understand complex internal force flows, this study built upon the kinematic-based model developed by Rajapakse et al. [10]. That model estimates peak capacity based on the mechanics of the main inclined crack propagating from the re-entrant corner. In addition, this research reviewed experimental studies on corrosion effects in both reinforcement steel and dapped-end connections, and went further by modifying existing degradation equations to better represent corrosion-induced deterioration. The outcome is a more accurate modelling framework that integrates both structural behavior and long-term durability under corrosive environments[7].

Almusallam et al. conducted a pioneering study to examine how corrosion affects the bond strength between steel reinforcement and concrete. Using artificial corrosion techniques, they applied a constant direct current of 0.4 A to induce corrosion in embedded reinforcement bars. The experimental results revealed a nonlinear deterioration pattern: at low corrosion levels, there was a slight increase in bond strength, likely due to rust products enhancing the interlock. However, as corrosion progressed, bond strength dropped sharply falling to nearly one-third of its original value before reaching 10% corrosion. Beyond this point, bond strength continued to decline gradually, reducing to just 10% of its original value by 20% corrosion. This study highlights the critical influence of corrosion on structural performance, particularly in bond-dependent regions like dapped ends[11].

Imperatore et al. carried out experimental research at the University of Rome Tor Vergata to establish degradation relationships for the mechanical properties of steel rebars affected by corrosion. The study focused on artificially corroded bare steel bars, simulating uniform corrosion patterns commonly associated with carbonation-induced deterioration. By analyzing variations in yield strength, ultimate strength, and ductility, the researchers developed empirical models that accurately describe how mechanical performance degrades with increasing corrosion levels. These degradation equations are now widely used for numerical modelling and structural assessment of corroded reinforced concrete members, particularly in service-life evaluations and retrofit design[12].

1.4. Experiments in Dapped-end beams

Rajapakse et al. [10] proposed a kinematic-based analytical model to evaluate failure in existing reinforced concrete dapped-end connections. The model assumes that the main crack initiates at the re-entrant corner and propagates in a manner that divides the dapped-end region into two rigid bodies. These blocks rotate relative to each other about the crack tip, allowing the model to predict the peak load-carrying capacity of the connection. This simplified approach provides insight into the failure mechanism and offers a basis for evaluating the structural integrity of existing deteriorated dapped-end connections.

In a follow-up study, Rajapakse et al. [3] carried out an experimental campaign involving eight large-scale dapped-end beam tests with various reinforcement configurations. The key variables investigated included the amount of dapped-end reinforcement and the ratio of horizontal to vertical reinforcement areas (A_{sh}/A_{sv}). The study found that orthogonal reinforcement layouts did not provide sufficient crack control under service loading conditions. These findings highlight the limitations of conventional reinforcement detailing in dapped-end regions and underline the need for optimized reinforcement strategies to ensure structural performance and crack control.

In their 2024 study, Rajapakse et al. [13] investigated the performance of dapped-end connections with diagonal reinforcement layouts, aiming to improve upon the limitations observed in previous orthogonal reinforcement designs. The research involved eight large-scale experimental tests on specimens designed to replicate bridge dapped ends, incorporating diagonal reinforcement arrangements. The results demonstrate enhanced strength compared to the orthogonal reinforcement configurations. However, crack widths under service loads still exceeded code-prescribed limits (typically around 0.3–0.4 mm), indicating that while diagonal reinforcement improves capacity, serviceability concerns remain. This study emphasizes the need for further refinement in detailing reinforcement to effectively control cracking while maintaining structural strength[13].

In a recent study conducted by Di Carlo et al. [14], the impact of corrosion on the structural performance of Gerber half-joint was experimentally evaluated. The research focused on assessing the degradation in load-carrying capacity due to corrosion-induced damage in reinforced concrete elements commonly used in precast bridge construction. An accelerated electrolytic corrosion process was employed, using a 3% saline solution to simulate aggressive environmental exposure, with a target corrosion level of 15%. Two full-scale specimens were prepared and tested: Specimen G1-C, designed with light reinforcement, and Specimen G2-C, with heavy reinforcement detailing. Following mechanical testing, the reinforcement bars were carefully extracted to quantify the

actual corrosion level, which averaged 13% for G1-C and 14% for G2-C. Notably, the corrosion levels varied across different reinforcement directions, offering insight into the non-uniform nature of corrosion propagation. This study provides valuable experimental data that contributes to the understanding of corrosion effects in dapped-end connections, which are critical zones in precast girder systems.

Desnarck et al. [1] conducted a study to investigate the structural behavior of reinforced concrete (RC) half-joints, focusing on the effects of severe reinforcement loss and anchorage zone cracking. To simulate advanced stages of corrosion without using time-consuming corrosion processes, the researchers mechanically reduced the cross-sectional area of the main reinforcing bars by 50% in a test specimen designated as NS-LR. This approach aimed to replicate the structural implications of significant corrosion damage, particularly in the critical anchorage zone of dapped-end connections. The findings revealed that such localized bar reductions significantly compromised the load-bearing capacity and altered the failure mechanisms of the half-joint. This study highlights the importance of understanding anchorage performance under deteriorated conditions and offers insight into the vulnerability of RC half-joints in aging infrastructure subjected to corrosion-related damage

2. Numerical Analysis

To establish the reliability of the VecTor2 software before applying corrosion effects, a preliminary numerical analysis was carried out. All eight double-end beam specimens (OL1 to OL8) were modelled using data from Rajapakse's experimental study, accurately reproducing the geometry, material properties, boundary conditions, and loading setup. The numerical results were then calibrated by comparing load-deflection responses and failure modes with the experimental data. The models successfully captured the cracking patterns and failure progression, particularly at the re-entrant corner. Although minor deviations were noted due to simplified bond-slip assumptions, the overall results validate VecTor2's suitability for extended simulations involving corroded reinforcements.

2.1. Limitations and modelling assumptions

In this study, the primary focus was given to the crack width and peak load behavior of dapped end connections. These parameters were selected due to their direct relevance to serviceability and ultimate load-carrying capacity, which are critical in evaluating the structural performance of such connections.While other parameters like strain distribution, deflection were not extensively investigated, this decision is justified as dapped ends are highly prone to serviceability failures, especially due to the formation of localized cracks at the re-entrant corner.

These cracks often govern the long-term performance of the connection and occur much earlier than ultimate failure, making crack width control a priority in both design and assessment.

In the present study, the bond between reinforcement and concrete is assumed to be fully intact, i.e., 100%, meaning that bond slip effects (due to corrosion) are not considered. Corrosion levels of 5%, 10%, and 15% are examined to represent increasing stages of reinforcement degradation. These levels correspond to initial and moderate corrosion effects, with 15% representing a (threshold where mechanical properties are significantly compromised.

A uniform cross-sectional area reduction is assumed for the corroded reinforcement, and the change in bar diameter due to corrosion is calculated using the following Equation (1)

$$\boldsymbol{D_{corr} = D\,(1 - X)} \qquad (1)$$

where D is the original bar diameter, X is the corrosion rate (expressed as a decimal), and D_{corr} is the reduced diameter of the corroded bar. This simplified modelling approach allows for consistent representation of corrosion effects across all specimens.

The extent of corrosion along the reinforcement was defined as follows: for horizontal bars, corrosion was applied over 50% of the total length of the dapped end; for vertical bars, it was applied over 50% of the beam height. This modeling strategy allowed for a focused investigation of the degradation mechanisms in the most structurally sensitive areas.

In the corresponding Figure 8 , the green-colored reinforcement represents the corroded vertical bars located at the re-entrant corners, while the brown-colored reinforcement indicates the corroded horizontal bars in the dapped-end region. These color-coded elements visually highlight the localized corrosion zones modeled in the simulation.

2.2. Validation of Reference Modells

Numerical modelling was initiated by validating the experimental test specimens (OL1–OL8) reported by Rajapakse et al. (2022), which served as the baseline model for subsequent simulations incorporating corrosion effects. The Figure 6 and Figure 7 illustrates the test specimen setup and geometry of reinforcement detailing of the test specimens. A total of eight dapped-end connections were constructed as part of four reinforced concrete beams. Each beam featured a rectangular cross-section of 1000 mm × 350 mm, which was reduced to 500 mm × 350 mm at the dapped ends to create the desired half-joint configuration. The dapped-end regions were 650 mm in length, while the overall beam length was 5300 mm. To ensure proper anchorage, the bottom horizontal reinforcement at the dapped ends was provided using hairpin bars. Vertical reinforcement in the dapped-end region consisted of closed stirrups arranged either as two-legged or four-legged configurations, depending on the specimen. The Table 1 shows all 8 specimen's vertical, horizontal reinforcement amount details.

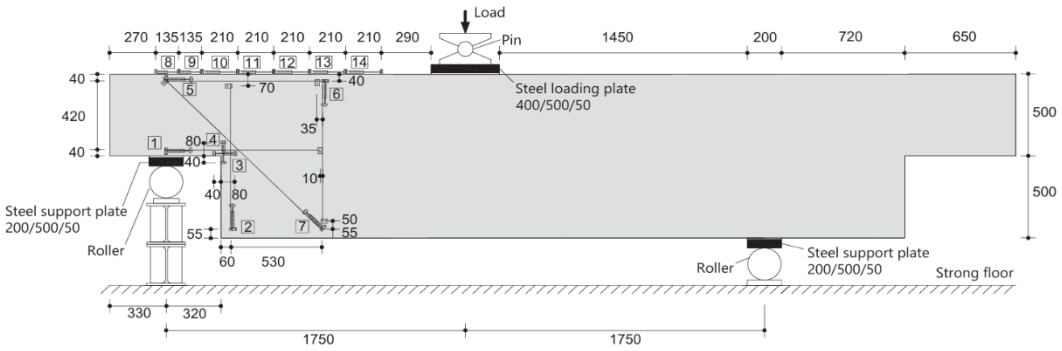

Figure 6: Test setup and instrumentation (dimensions in mm)

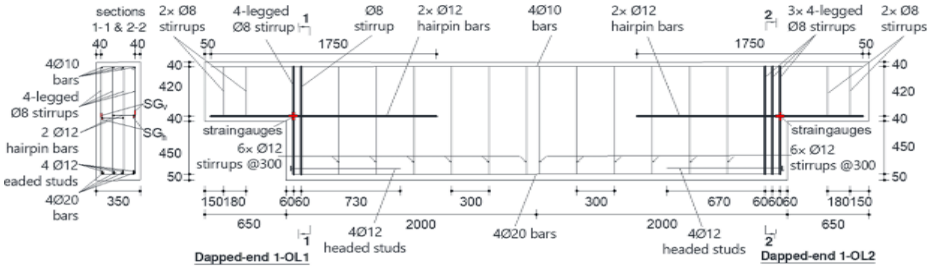

Figure 7: Reinforcements setup of Beam 1

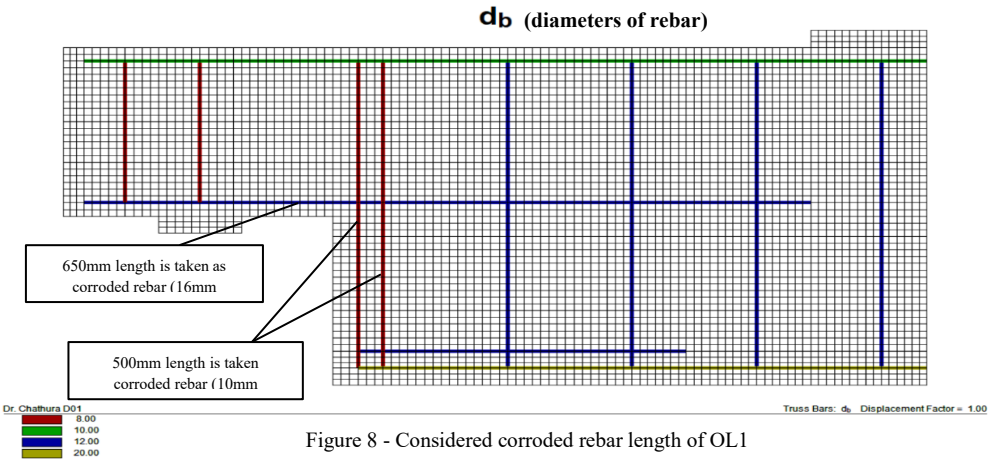

Figure 8 - Considered corroded rebar length of OL1

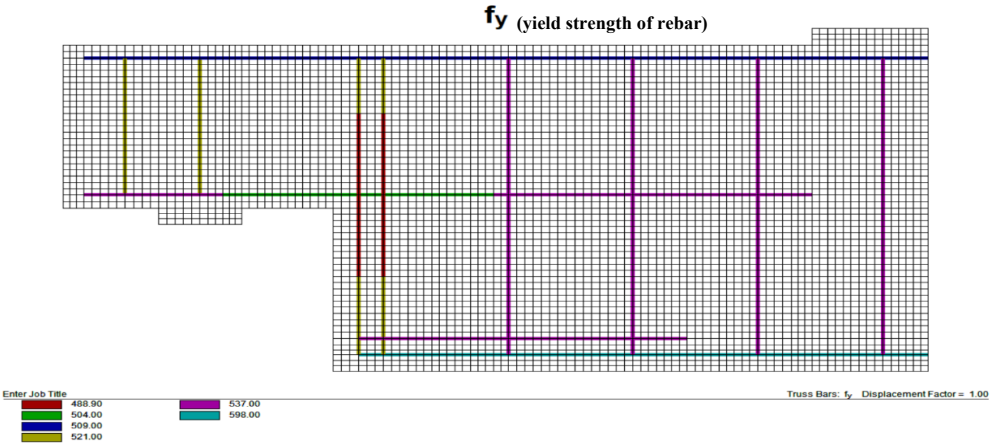

Figure 9: Yield strength values of rebars

Table 1: reinforcement amount details and concrete compressive strength

Specimen	ϕ_h (mm)	A_{sh} (mm²)	ϕ_v (mm)	A_{sv} (mm²)	A_{sh}/A_{sv}	f'_c (MPa)
1-OL1	12	452	8	301	1.50	56.8
1-OL2	12	452	8	603	0.75	56.8
2-OL3	16	804	10	628	1.28	56.4
2-OL4	16	804	10	1099	0.73	56.4
3-OL5	20	1256	12	904	1.39	49.6
3-OL6	20	1256	12	1808	0.70	49.6
4-OL7	25	1964	12	1356	1.45	52.0
4-OL8	25	1964	12	2712	0.72	52.0

ϕ_h = diameter of dapped-end horizontal reinforcement, A_{sh} = total area of dapped-end horizontal reinforcement, ϕ_v = diameter of dapped-end vertical reinforcement, A_{sv} = total area of dapped-end vertical reinforcement, $f'c$ = compressive strength of concrete

The following Figure 10 shows the roller boundary condition applied along one side and at the support in the finite element model

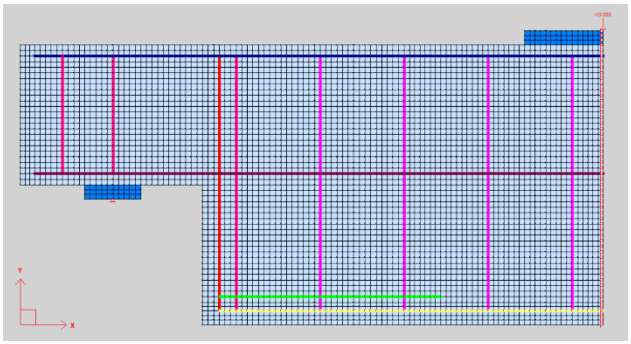

Figure 10 : Restraints and loading method used in the model

The Table 2 presents a comparative analysis of the experimental shear capacities (V_{exp}) and those predicted by the VecTor2 finite element model (V_{FEM}) for all eight tested specimens (OL1–OL8). The results demonstrate a strong correlation between experimental and numerical predictions, with an average V_{exp}/V_{FEM} ratio of 0.99, indicating a high level of accuracy in the VecTor2 model's predictive capability. Additionally, the coefficient variation (COV) of 8.56% reflects a relatively low degree of scatter, further supporting the consistency and reliability of the numerical model in simulating the shear behavior of dapped-end connections.

Table 2 – Experimental and numerical results comparison

Specimen	V_{exp} (kN)	V_{FEM} (kN)	V_{exp} / V_{FEM}
OL1	245	258	0.95
OL2	283	306	0.92
OL3	472	527	0.90
OL4	555	566	0.98
OL5	628	689.67	0.91
OL6	728	661	1.10
OL7	868	850.52	1.02
OL8	995	892.25	1.12
			AVG = 0.99
			COV = 8.56%

Both the experimental and finite element model (FEM) results for specimen OL1 demonstrated consistent trends (Figure 11) in crack development and restraint behavior, particularly during the initial stages of crack formation and at peak load response. This close agreement validates the accuracy of the numerical model in capturing the key structural behaviors observed experimentally.

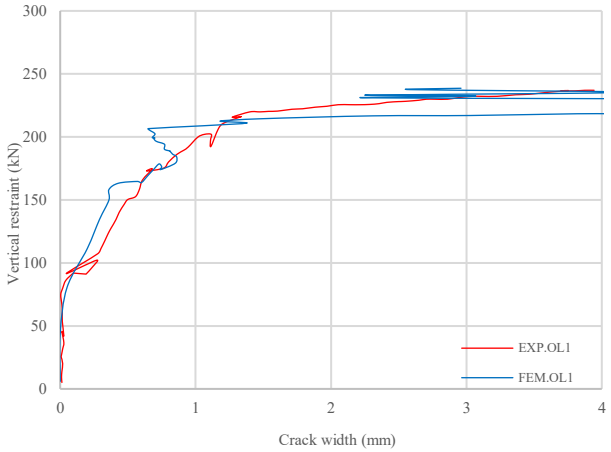

Figure 11 : Crack width at re-entrant corner varies with verticalrestraint

Similarly, the remaining seven dapped-end specimens were also evaluated against their corresponding experimental results (Figure 12). The comparisons, illustrated in the following graphs, demonstrate a strong correlation between the numerical simulations and experimental data, confirming the reliability of the finite element modelling approach across all specimens.

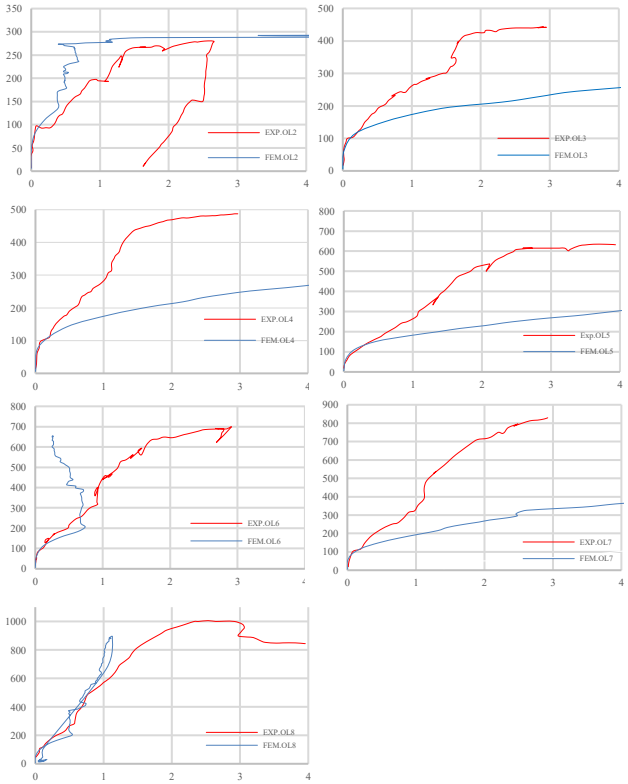

Figure 12 -Crack width at re-entrant corner varies with verticalrestraint for all other 7 simulations

All specimens exhibited almost the same behavior in the early loading stage (~100 kN – 180 kN), with good agreement between experimental and numerical crack widths at the re-entrant corner. Additionally, they reached their yield plateau at nearly the same load level.

To ensure the robustness of the validation, both the corroded and reference specimens from Desnerck et al. were evaluated through numerical simulation. The NS-REF (Normal Strength Reference) and NS-LR (Normal Strength Local Reduction) specimens are central to understanding the performance of reinforced concrete half-joint beams under different deterioration scenarios. The NS-REF specimen serves as the reference, designed and constructed with normal strength concrete (C30/37) and detailed reinforcement (Figure 13)[1] including U-shaped bars, shear stirrups, diagonal bars, longitudinal bars, and vertical shear links in the full-depth section according to best practices established by the strut-and-tie method. [1]

In contrast, the NS-LR specimen is engineered to simulate the local loss of reinforcement capacity typically observed in structures exposed to severe corrosion. This specimen is geometrically identical to NS-REF and initially shares its reinforcement detailing. However, to replicate real-world deterioration, key reinforcing bars at the half-joint nib the critical load transfer region are locally milled down to 50% of their original diameter over a 100mm segment for diagonal bars, the U-bars, and the stir rup closest to the re-entrant corner This localized reduction is consistent with inspection records from existing bridge structures, where section losses of 30–50% are commonly documented. Such simulated damage allows researchers to isolate and evaluate the structural consequences of severe, localized corrosion on half-joint beams by contrasting the performance of NS-LR directly against the undamaged NS-REF specimen.[1]

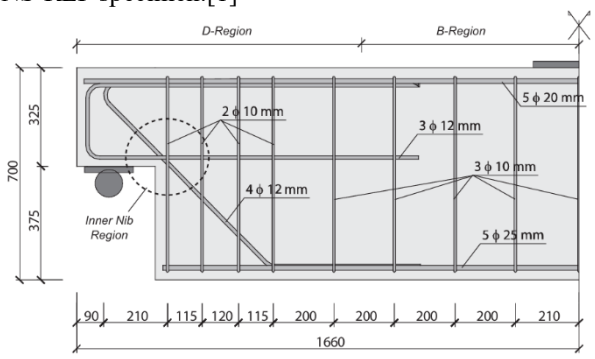

Figure 13 - Geometry and dimensions of experimental half-joint specimens NS-REF and NS-LR

The Figure 14 shows comparison between experimental and numerical simulation values.

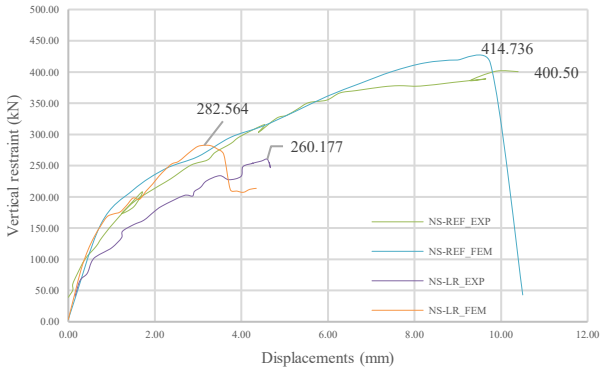

Figure 14 - Failure load vs Deflection curve of NS-REF and NS-LR

2.3.Implementation of Corrosion Effects

The reduced yield strength (f_y), ultimate strength (f_u), and ultimate strain (ε_u) of the reinforcement were obtained using the degradation (Equation (2)) proposed by Ou et al. [9].

$$\begin{aligned} f_{y,corr} &= (1-0.0123X\%)f_y \\ f_{u,corr} &= (1-0.0115X\%)f_u \\ \epsilon_{u,corr} &= (1-0.0125X\%)\epsilon_u \end{aligned} \quad (2)$$

Where X is corrosion rate

The degradation equations proposed by Ou et al. (2016) were incorporated to simulate the mechanical property reduction of corroded reinforcement in the numerical model. These equations, developed based on tensile tests of both naturally and artificially corroded steel bars with corrosion levels ranging from 5% to 82%, account for the reduction in yield strength, ultimate strength, and ultimate strain as a function of mass loss due to corrosion. The observed scatter in ultimate strain, attributed to the irregular distribution of corrosion pits, highlights the importance of incorporating such empirical degradation relationships for accurately capturing the nonlinear behavior of corroded reinforcement. By applying these equations, the model reflects more realistic material properties under different corrosion levels, thereby enhancing the reliability of the simulation results when compared to experimental observations.

The reduced cross-sectional area of the reinforcement was modeled by adjusting the diameter (D) (Equation (1)) of the rebar to account for material loss due to corrosion. Numerical models were simulated for corrosion rates of 5%, 10%, and 15% to evaluate the structural response under varying levels of reinforcement degradation.For all simulations, vertical restraint vs applied displacement graph was ploted. And vertical restraint vs crack width at re-entrant corner.

The following graphs Figure 15 illustrate the results from simulations incorporating reduced mechanical properties due to corrosion. As the amount of reinforcement at the re-entrant corner increases (OL5, OL6, OL7, OL8), the reduction in peak load associated with increasing corrosion levels becomes less pronounced. In contrast, specimens with lower reinforcement (OL1, OL2, OL3, OL4) content exhibit a more significant decline in peak load, indicating a higher sensitivity to corrosion-induced degradation.OL8 exhibits a significant reduction in load-carrying capacity even at a low corrosion level of 5%, while the variations between higher corrosion levels (10% and 15%) remain relatively small. And graphs (Figure 16) present simulation results incorporating reduced mechanical properties and cross-sectional areas over specific lengths of re-entrant vertical and horizontal rebars. A notable observation is the significant variation in structural performance between uncorroded and corroded specimens, even at a corrosion level of just 5%.

3. Results and Discussion

To evaluate the impact of corrosion on the structural behavior of dapped-end reinforced concrete connections, a total of 58 numerical simulations were performed using the VecTor2 software. These included reference specimens, simulations incorporating only mechanical degradation, and those including both mechanical degradation and cross-sectional area loss. The corrosion effects were analyzed at three levels 5%, 10%, and 15% to reflect various stages of deterioration. All models were developed based on experimental geometry and detailing from Rajapakse et al. with material degradation parameters derived from empirical studies.[3], [9]

To ensure the robustness of the validation, additional specimens from Desnerck et al.[1] specifically NS-REF and NS-LR were also simulated. These provided valuable benchmarks for representing both undamaged and severely deteriorated conditions in half-joint structures. The VecTor2 simulations successfully reproduced the reduction in capacity and shift in failure mechanisms observed experimentally, demonstrating that the simplified modeling strategy, which involved geometric bar reduction and mechanical property degradation, can reliably predict structural behavior under corrosion effects.

Across all OL1–OL8 specimens, a consistent decline in peak load capacity was observed with increasing corrosion levels. At 5% corrosion, load reductions ranged from 3.44% to 21.73%, depending on the reinforcement ratio and configuration. At 15% corrosion, the load reduction intensified, reaching up to 42.14% in some specimens, particularly those with lower reinforcement content. This nonlinear deterioration indicates that even relatively modest levels of corrosion can cause substantial reductions in load-bearing performance.

Specimens with higher reinforcement content particularly OL5 to OL8 demonstrated improved resilience, maintaining higher load capacities under corroded conditions. However, the OL8 specimen, despite having the highest reinforcement, still showed a peak load reduction of 25.72% and cross-sectional area loss of 39.5% at 15% corrosion, suggesting that even robust reinforcement detailing cannot fully offset corrosion-induced degradation.

An interesting observation was made with OL6, which exhibited minimal variation in load capacity across the corrosion levels tested. This suggests that OL6 reinforcement layout and material properties may offer an inherent balance between strength and ductility, making it a potentially robust design configuration for use in corrosion-prone environments.

The results also reveal that cross-sectional area loss has a more pronounced impact on load capacity than the degradation of mechanical properties alone. This finding aligns with the conclusions of Desnerck et al.[1], where simulated bar reduction had a direct and severe influence on both anchorage and peak load performance. The nonlinear nature of this deterioration emphasizes the importance of capturing both geometric and material degradation effects when evaluating existing structures or designing for durability. The Table 3 presents the results from all 56 simulations conducted in this study.

Table 3 – Peakload capacity of reference and corroded specimens

	Horizontal			Vertical			Strength reduction		Area reduction	
Specimen	**Fy (MPa)**	**Fu (MPa)**	**Eu(%)**	**Fy (MPa)**	**Fu (MPa)**	**Eu(%)**	**Peak Load (kN)**	**Reduction (%)**	**Peak Load (kN)**	**Redcution (%)**
1-OL1	**537**	**634**	**12.04**	**521**	**644**	**9.82**	**257.4**			
1-OL1_5%	504	598	11.29	489	606	9.2	247.7	3.77	222.1	13.71
1-OL1_10%	471	561	10.54	457	569	8.59	229.3	10.92	185.67	27.87
1-OL1_15%	437	524	7.98	424.87	532	7.97	213.3	17.13	148.94	42.14
1-OL2	**537**	**634**	**12.04**	**521**	**644**	**9.82**	**304.6**			
1-OL2_5%	504	598	11.29	489	606	9.2	291.4	4.33	282.06	7.40
1-OL2_10%	471	561	10.54	457	569	8.59	274.8	9.78	240.39	21.08
1-OL2_15%	437	524	7.98	424.87	532	7.97	257.9	15.33	190.24	37.54
2-OL3	**599**	**703**	**3.03**	**509**	**643**	**9.82**	**527.1**			
2-OL3_5%	562	663	8.69	478	606	10.61	495.5	6.00	457.89	13.13
2-OL3_10%	525	622	8.11	446	569	9.91	473.7	10.13	387.47	26.49
2-OL3_15%	488	581	7.53	415	532	9.19	447.6	15.08	322.04	38.90
2-OL4	**599**	**703**	**3.03**	**509**	**643**	**9.82**	**557.8**			
2-OL4_5%	562	663	8.69	478	606	10.61	536.65	3.79	483.15	13.38
2-OL4_10%	525	622	8.11	446	569	9.91	501.9	10.02	388.63	30.33
2-OL4_15%	488	581	7.53	415	532	9.19	472.6	15.27	260.97	53.21
3-OL5	**598**	**634**	**12.04**	**537**	**634**	**9**	**723.8**			
3-OL5_5%	561	654	8.44	504	598	11.29	698.9	3.44	662.52	8.47
3-OL5_10%	524	614	7.88	470	561	10.54	686.9	5.10	579.23	19.97
3-OL5_15%	488	574	7.31	438	524	9.78	652	9.92	498.95	31.07
3-OL6	**598**	**634**	**12.04**	**537**	**634**	**9**	**655.5**			
3-OL6_5%	561	654	8.44	504	598	11.29	648.4	1.08	624	4.81
3-OL6_10%	524	614	7.88	470	561	10.54	640.5	2.29	603.77	7.89
3-OL6_15%	488	574	7.31	438	524	9.78	632.1	3.57	541.32	17.42
4-OL7	**540**	**647**	**9.98**	**537**	**634**	**12.04**	**845.68**			
4-OL7_5%	507	610	9.36	504	597	11.28	661.9	21.73	635.74	24.82
4-OL7_10%	474	573	8.73	470	561	10.54	671.7	20.57	615.5	27.22
4-OL7_15%	440	535	8.11	438	524	9.78	668.8	20.92	530.01	37.33
4-OL8	**540**	**647**	**9.98**	**537**	**634**	**12.04**	**892.25**			
4-OL8_5%	507	610	9.36	504	597	11.28	708.3	20.62	653.05	26.81
4-OL8_10%	474	573	8.73	470	561	10.54	698.2	21.75	627.21	29.70
4-OL8_15%	440	535	8.11	438	524	9.78	662.8	25.72	539.81	39.50

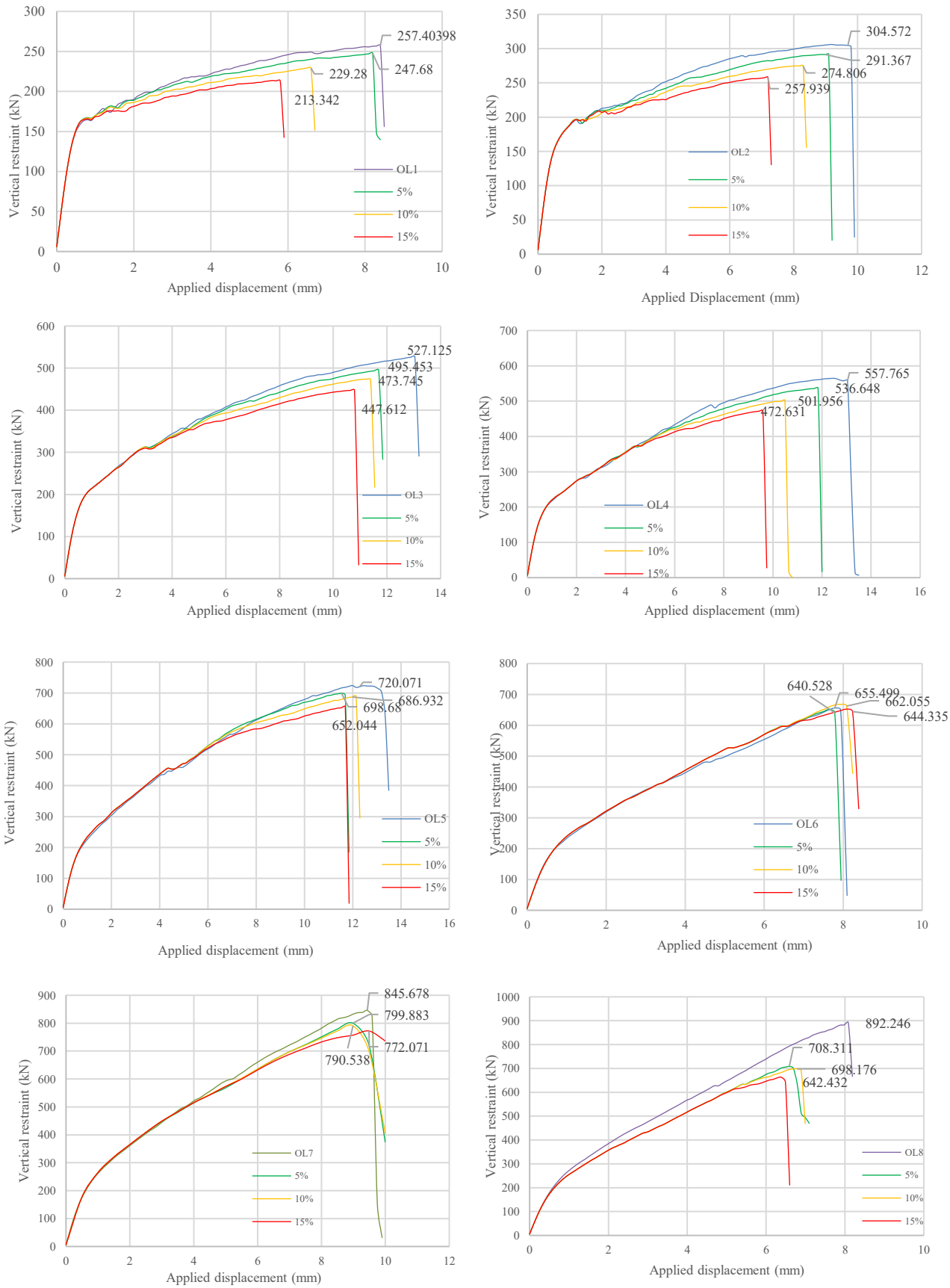

Figure 15 : Peak load comparison between reference specimens and specimens with reduced mechanical properties

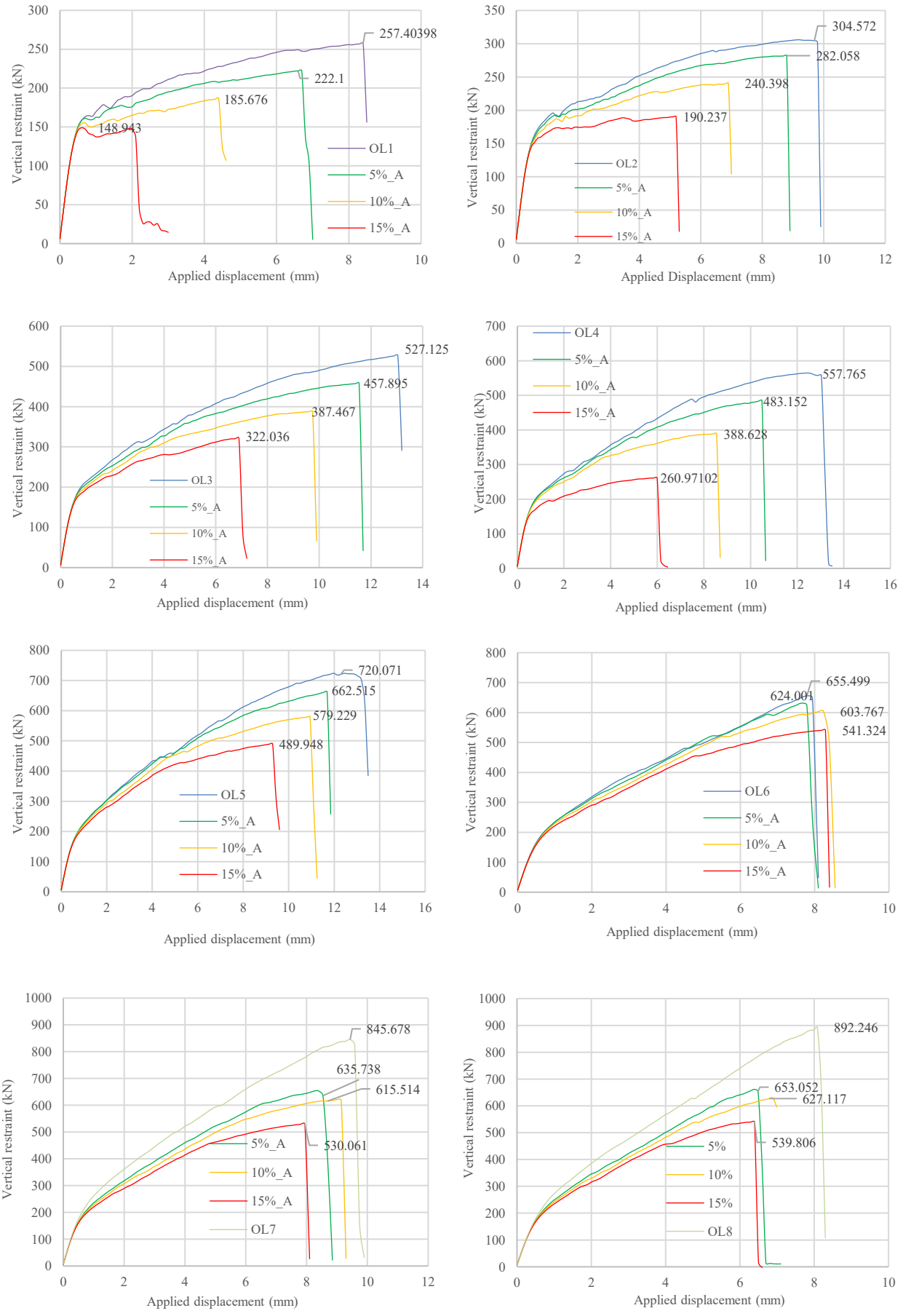

Figure 16 : Peak load comparison between reference specimens and specimens with reduced mechanical properties and cross-sectional area

4. Conclusions

This study comprehensively investigated the structural impact of corrosion on reinforced concrete dapped-end connections using validated nonlinear finite element models developed in VecTor2. The conclusions drawn from the 58 simulations supported by experimental results from Rajapakse et al. and Desnerck et al. are as follows[1], [3]:

- Corrosion significantly compromises load-bearing capacity and alters failure modes in dapped-end connections. Even at moderate corrosion levels (5 - 10%), reductions in peak load of up to 21% were observed. At 15% corrosion, peak load reductions reached as high as 42.14%, accompanied by up to 55% cross-sectional area loss in critical rebars.

- The degradation in structural performance is nonlinear, with cross-sectional area loss contributing more significantly to capacity reduction than mechanical strength degradation alone. This highlights the critical importance of accounting for geometric deterioration when assessing corrosion effects.

- Among the specimens studied, OL1 was the most vulnerable, exhibiting the highest performance loss, while OL6 demonstrated minimal sensitivity to increasing corrosion levels. This suggests that optimized reinforcement configurations can enhance resilience against corrosion-induced degradation.

- Validation against Desnerck et al.'s NS-REF and NS-LR specimens confirmed the model's robustness in capturing both undamaged and corroded behavior, particularly the adverse effects of localized bar reduction and anchorage deterioration.

- The study demonstrates that conventional orthogonal reinforcement layouts may not offer adequate durability under corrosive conditions. Although specimens with higher reinforcement volumes (e.g., OL7, OL8) performed better, they still showed considerable deterioration, indicating that reinforcement detailing alone cannot fully mitigate corrosion effects.

- The findings reinforce the necessity for durability-focused design approaches, such as the use of high-quality concrete, adequate cover, corrosion-resistant reinforcement, and protective detailing—especially in environments exposed to chlorides and moisture.

- Finally, this research highlights the value of numerical models calibrated with experimental data for assessing existing structures and developing retrofitting strategies. These tools are vital for predicting long-term performance and ensuring structural safety in aging infrastructure

References

[1] P. Desnerck, J. M. Lees, and C. T. Morley, “The effect of local reinforcing bar reductions and anchorage zone cracking on the load capacity of RC half-joints,” *Eng Struct*, vol. 152, pp. 865–877, Dec. 2017, doi: 10.1016/j.engstruct.2017.09.021.

[2] P. Desnerck, J. M. Lees, and C. T. Morley, “Impact of the reinforcement layout on the load capacity of reinforced concrete half-joints,” *Eng Struct*, vol. 127, pp. 227–239, Nov. 2016, doi: 10.1016/j.engstruct.2016.08.061.

[3] C. Rajapakse, H. Degée, and B. Mihaylov, “Investigation of shear and flexural failures of dapped-end connections with orthogonal reinforcement,” *Eng Struct*, vol. 260, p. 114233, Jun. 2022, doi: 10.1016/J.ENGSTRUCT.2022.114233.

[4] “Peter H. Emmons - Concrete Repair Maintenance Illustrated_All[1]”.

[5] “Dapped Beams And Corbels: Corrosion Www.Prontubeam.Com.” [Online]. Available: http://www.ideam.es/wp-content/uploads/2017/03/Puente-sobre-el-r%C3%ADo-Guadalfeo.pdf

[6] A. Neville, “Chloride attack of reinforced concrete: an overview,” 1995.

[7] A. : Léonard, L. Promoteur, and B. Mihaylov, “Modelling of Mechanical-Corrosion Interaction in Dapped-End Connections,” 2023. [Online]. Available: https://lib.uliege.behttps://matheo.uliege.be

[8] F. Di Carlo, A. Meda, F. Molaioni, and Z. Rinaldi, “Experimental evaluation of the corrosion influence on the structural response of Gerber half-joints,” *Eng Struct*, vol. 285, Jun. 2023, doi: 10.1016/j.engstruct.2023.116052.

[9] Y. C. Ou, Y. T. T. Susanto, and H. Roh, “Tensile behavior of naturally and artificially corroded steel bars,” *Constr Build Mater*, vol. 103, pp. 93–104, Jan. 2016, doi: 10.1016/j.conbuildmat.2015.10.075.

[10] C. Rajapakse, H. Degée, and B. Mihaylov, “Assessment of Failure along Re-Entrant Corner Cracks in Existing RC Dapped-End Connections,” *Structural Engineering International*, vol. 31, no. 2, pp. 216–226, 2021, doi: 10.1080/10168664.2021.1878975.

[11] A. A. Almusallam, A. S. Al-Gahtani, and A. Rauf Aziz, “Effect of reinforcement corrosion on bond strength,” 1996.

[12] S. Imperatore, Z. Rinaldi, and C. Drago, “Degradation relationships for the mechanical properties of corroded steel rebars,” *Constr Build Mater*, vol. 148, pp. 219–230, Sep. 2017, doi: 10.1016/j.conbuildmat.2017.04.209.

[13] C. Rajapakse, H. Degée, and B. Mihaylov, “Experimental Investigation of Dapped Ends with Diagonal Reinforcement,” *ACI Struct J*, vol. 121, no. 4, Jul. 2024, doi: 10.14359/51740710.

[14] F. Di Carlo, A. Meda, F. Molaioni, and Z. Rinaldi, “Experimental evaluation of the corrosion influence on the structural response of Gerber half-joints,” *Eng Struct*, vol. 285, Jun. 2023, doi: 10.1016/j.engstruct.2023.116052.

Investigating the Possibility of Partially Replacing Cement by Corn Cob Ash and Quicklime in Non-Rectangular Concrete Interlocking Paving Blocks

K R S B Abeywardane[1], A M L N Gunathilaka[1]

Abstract

Usage of supplementary cementitious (SCMs) materials to partially replace cement in concrete products is a global trend in construction industry considering its benefits in financial and sustainable perspectives. Corn or Maize holds a significant position as the second most important cereal crop in Sri Lanka, trailing only behind rice in terms of productions. Corn cob is woody hard core of the corn ear to which the grains are attached. This is discarded as a waste product at the time when processing the harvest to obtain corn seeds. Various previous studies in global context had highlighted the potential of using corn cob ash (CCA) as a SCM and this study was focused on investigating the possibility of partially replacing cement by CCA with Quicklime (QL) in concrete interlocking paving blocks (CPBs) production. A comprehensive experimental study was conducted studying the effect on workability, mechanical and physical properties of CPBs when partially replacing cement by above materials by various proportions. As per results of the study, CPBs produced partially replacing cement up to 15% by CCA (with QL) met the workability, mechanical and physical property requirements specified in standards considered for this study. However, in general, it was noted that the reduction of compressive strength when it increased the partial replacement percentage, even though reductions were insignificant until partial replacement percentage of cement reached 15%. Since usage of the highest replacement percentage is beneficial in financial and sustainable perspectives, the recommended partial replacement percentage of cement in CPB production is 15% CCA and 10% QL.

***Keywords:** Concrete interlocking paving blocks, Corn cob ash, Quicklime, Sustainability, Supplementary cementitious materials*

1. Introduction

Concrete is one of the most extensively used construction materials in the world due its strength, durability and adaptability. Among its many applications, CPBs have gained substantial popularity for pedestrian and vehicular surfaces. Their modular structure offers advantages such as ease of installation, aesthetic pleasing appearance and resistance to cracking due to their segmental configuration. With the growing demand for sustainable urban infrastructure, there is increasing interest in improving the environmental performance of concrete products, especially by reducing reliance on Ordinary Portland Cement. (OPC).

Cement manufacturing is a highly energy intensive process that contributes significantly to environmental degradation. It involves the mining of limestone and other raw materials, followed by high temperature calcination processes that emit large amounts of Carbon Dioxide (CO_2). Globally, cement production is responsible for approximately 5% of total CO_2 emissions, making it one of the largest industrial sources of greenhouse gases. Given this environmental burden, the use of SCMs as partial replacements for cement has become a widely studied strategy for reducing emissions and lowering production costs.

In Sri Lanka, Maize or Corn is the second most important cereal crop after rice. In 2021, Corn cultivation covered 106,757 hectares and produced 472,400 metric tons of yield, with an average productivity of 4.4 metric tons per hectare [1]. The cobs left over after harvesting are considered agricultural waste and are commonly disposed of by land filling or open burning, as shown in Figure 1. This biomass residue can be converted into CCA, which contains pozzolanic components such as Silica (SiO_2), Alumina (Al_2O_3) and Iron Oxide (Fe_2O_3) making it potential SCM.

Figure 1: A dump site of Corn cobs at Pelwahara seed farm

ASTM C125 [2] defines SCMs as inorganic substances that enhances the properties of a cementitious mixture through hydraulic or pozzolanic reactions or both. Meanwhile, ASTM C618 [3] specifies that a material qualifies as a pozzolan if the combined content of SiO_2, Al_2O_3 and Fe_2O_3 is at least 70%. Based on the chemical composition of CCA presented in Table 1, it can be observed that CCA meets the criteria set by ASTM C618 for class N pozzolans. Therefore, CCA shows potential for use as a SCM in concrete production.

K R S B Abeywardane & A.M.L.N Gunathilaka are with Department of Civil Engineering, Open University of Sri Lanka
e-mails: sachinabeywardane@gmail.com & amlgu@gmail.com

Table 1: Reported chemical composition of CCA in previous studies

Reference	[4]	[5]	[6]	[7]
SiO_2 (%)	61.80	67.41	66.38	66.4
Al_2O_3 (%)	6.31	8.39	7.48	7.5
Fe_2O_3 (%)	1.97	4.81	4.44	4.4
CaO (%)	4.01	10.87	11.57	11.6
K_2O (%)	5.81	-	4.92	2.1
MgO (%)	3.24	1.98	2.06	4.9
SO_3 (%)	1.17	1.43	1.07	0.4
Na_2O (%)	0.19	-	0.41	1.1
Burning Temperature	Open burning	Open burning	650 °C	500 °C

Several earlier studies [8,9] have indicated that partially replacing OPC with pozzolanic materials tends to reduce the development of compressive strength at early ages (within the first 14 days) compared to the control sample. This can be expected, as the pozzolanic reaction, which involves the interaction between the pozzolanic material and calcium hydroxide proceeds at a relatively slow rate during the initial curing period. According to Hannesson et al.[10], this is mainly because the early hydration of cement does not generate a sufficient quantity of calcium hydroxide to sustain a significant pozzolanic reaction. To address this issue of reduced early strength, several studies [11-13] have recommended adding a certain amount of hydrated lime when using pozzolanic replacements. Most of these studies suggest incorporating approximately 10% hydrated lime by weight of cement to improve early age strength development.

Accordingly, this study was carried out to investigate the partial replacement of cement with CCA and QL in the production of CPBs, aiming to develop a cost effective and sustainable construction solution. The primary objective of this study was to identify the optimal mix proportions of CCA and QL for cement replacement through comprehensive experimental analysis. The outcomes of this research are especially valuable for developing countries like Sri Lanka, where agriculture waste is abundant and the construction industry continues to seek low cost, ecofriendly alternatives.

2. Methodology

This research study was based on experimental work. The materials and methods were selected with consideration to commonly accepted practices and previous studies, aiming to achieve reliable and consistent results.

2.1 Types of CPBs and Strength Class

SLS 1425: Part 1 [14] the Sri Lankan standard for CPB, defines four different strength classes. For areas with vehicle traffic, the minimum required class is strength class 3. This class needs an average compressive strength of at least 30 N/mm^2. Most CPBs made in Sri Lanka fall under this class, except those used for houses. So, this study is based on CPBs in strength class 3 under SLS 1425: Part 1 [14].

The standard also group CPBs by their shape. There are 2 main types rectangular (R) and non-rectangular (NR). The NR type has three sub types. Among them, NR1 is the most popular type because of its pleasing appearance. The size of NR1 is 220 mm in length, 110 mm in width and 80 mm in thickness. This study choose NR1 for testing. Figure 2 shows the shape of this block.

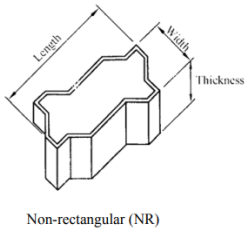

Non-rectangular (NR)

Figure 2: NR type paving block

2.2 Mix design for CPBs

The British Department of Environment (DOE) method was used to develop the mix design for producing CPBs. A previous local study by Baskaran and Gopinath [15] suggested that the DOE method helps to achieve the target compressive strength of CPBs more accurately. First, a control mix was prepared with a target average compressive strength of 30 N/mm^2 and a water cement ratio of 0.54.

As this study focused on identifying the optimum mix by partially replacing cement with CCA and QL, five mix proportions were used for partial replacement of cement as shown in Table 2. The quantities of other ingredients were kept constant. QL was added to enhance the early strength development of the CPBs. QL was kept at constant percentage (10%) by following the same approach as in previously discussed studies [11-13].

Table 2: Alternative mixes with mix proportions

CCA (%)	QL (%)	Cement (kg)	CCA (kg)	QL (kg)	Fine Aggregate (kg)	Coarse Aggregate (kg)
0	0	348.8	0	0	657.3	1226.0
5	10	296.5	17.4	34.9	657.3	1226.0
10	10	279.0	34.9	34.9	657.3	1226.0
15	10	261.6	52.3	34.9	657.3	1226.0
20	10	244.2	69.8	34.9	657.3	1226.0
25	10	226.8	87.2	34.9	657.3	1226.0

2.3 Production of CPBs

The CPBs for this study were produced using an industrial block making machine equipped with a mechanical vibration system. The mix was designed to have a dry consistency with zero slump. OPC, conforming to the local standard SLS 107 [16], was used as the binder. Well graded metals as coarse aggregates and river sand as fine aggregates were used for production of concrete in accordance with BS 812: Part 2: 1995 [17] and BS 882: 1992 [18].

The CCA used in this study was prepared from corn cobs collected from the Pelwehara seed farm, where they had been left to decay. They were sundried to reduce the moisture content as shown in Figure 3(a). The dried corn

cobs were open burned in specially made burn barrels as shown in Figure 3(b) to produce ash. The open burning process estimated to reach temperature range of 400° C – 600°C [4]. The resulting CCA as shown in Figure 3(c) was then grinded in a Los Angeles Abrasion testing machine with steel balls for 60 minutes. This grinding process was done to make it into the powder form to enhance the pozzolanic activity of CCA and to support early strength development in the CPBs. After grinding, only 33.7% of the CCA passed through a 75 micron sieve. Only the portion that passed through this sieve was used in the mix, as the fineness of SCMs significantly affects concrete strength.

(a)

(b)

(c)

Figure 3: Production of CCA from Corn cob waste

2.4 Production of CPBs

The ingredients of concrete mix were proportioned using the weigh batching method as shown in Figure 4(a). Concrete mixes for CPBs production were prepared by manually mixing ingredients as shown in Figure 4(b). The casting of the blocks was carried out using an automated vibratory block making machine as shown in Figure 4(c), following the common industrial practices. After the blocks reached their initial setting time, they were labeled as shown in figure 4(d) and then fully submerged in a water tank for curing.

(a)

(b)

(c)

(d)

Figure 4: Production process of CPBs for the study

3. Results and Discussion

3.1 Workability of Concrete

The slump cone test was done for all mixes. This included the control mix and five mixes with partial replacements. Local standard for CPBs does not specify this test, but it was carried out to check workability. All the mixes showed zero slump, as intended in the mix design. This means that replacing cement with CCA and QL did not affect the workability. Figure 5 shows a photograph taken during the test.

Figure 5: Slump cone test

3.2 Visual Inspection of CPBs

Visual inspection of the CPBs was conducted in accordance with SLS 1425: Part 2 [19]. The inspection included CPBs produced using all alternative mixes. No signs of delamination, cracks, flaking or any other visible defects were observed in any of the CPBs. Furthermore, all CPBs exhibited a uniform color and surface texture, regardless of the mix variation.

3.3 Compressive Strength

Compressive strength tests were conducted on CPBs at 7, 14 and 28 days following SLS 1425: Part 2 [19]. The test setup is shown in Figure 6 and results are summarized in Table 3. Figure 7 shows how the average compressive strength changed over time for each mix. This evaluation focused on how replacement of cement with CCA and QL affected strength development during the curing period.

Figure 6: Compressive strength test for CPBs

Table 3: Compressive strength test results

Sample ID	CCA replacement (%)	QL replacement (%)	Compressive Strength (N/mm^2)					
			7 days		14 days		28 days	
Control Sample	0	0	27.1		29.0		33.4	
			31.5	30.4	31.0	31	32.4	32.9
			32.7		33.0		32.9	
Alt.1	5	10	29.2		30.2		30.8	
			27.1	28.2	28.8	29.1	32.4	32.1
			28.3		28.3		33.1	
Alt.2	10	10	25.7		28.5		33.6	
			29.4	27.3	29.0	28.4	30.1	31.2
			27.1		27.7		29.9	
Alt.3	15	10	23.2		26.0		30.8	
			24.9	24.7	26.7	26.8	29.8	30.3
			26.0		27.8		30.3	
Alt.4	20	10	15.3		20.2		22.1	
			20.9	17.6	18.6	19.4	21.2	22.8
			16.5		19.5		25.1	
Alt.5	25	10	14.2		14.0		17.6	
			13.5	13.6	17.0	15.7	16.5	17.0
			13.0		16.0		17.0	

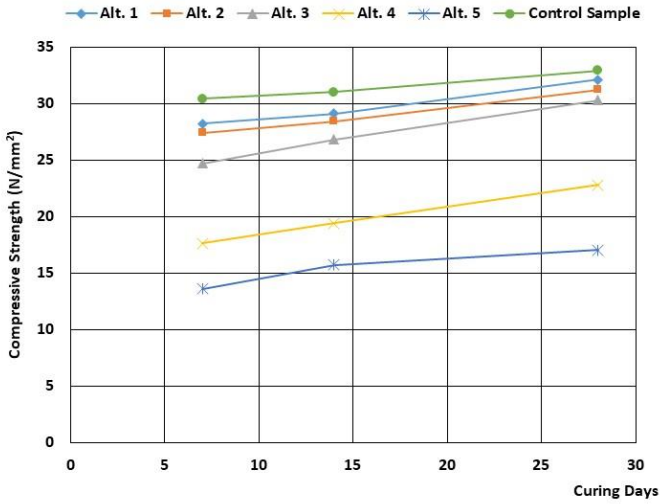

Figure 7: Compressive strength variation during curing days

Table 4: Comparison of 7 and 28 days average compressive strength of alternatives with control sample

Sample ID	Compressive Strength		% of Control Sample	
	7 Days	28 Days	7 Days	28 Days
Control sample	30.4	32.9	100	100
Alt.1	28.2	32.1	92.76	97.57
Alt.2	27.3	31.2	89.80	94.83
Alt.3	24.7	30.3	81.25	92.10
Alt.4	17.6	22.8	57.89	69.30
Alt.5	13.6	17.0	44.74	51.67

The control sample and alternative samples Alt.1 (5% CCA and 10% QL) to Alt.3 (15% CCA and 10% QL) achieved 28 days average strengths above the minimum requirement of 30 N/mm^2.

The control sample recorded compressive strengths of 30.4 MPa at 7 days and 32.9 MPa at 28 days. As shown in Table 4, compressive strength of Alt.1 slightly decreased to 28.2 MPa at 7 days (92.76% of control) and 32.1 MPa at 28 days (97.57%), showing good performance close to the control sample. Alt.2 also maintained relatively high strength, with 27.3 MPa (89.80%) at 7 days and 31.2 MPa (94.83%) at 28 days.

In Alt.3, a noticeable drop was observed at 7 days with 24.7 MPa (81.25%), but the 28-day strength remains high at 30.3 MPa (92.10%). However, beyond 15% replacement, the compressive strength decreases significantly. Alt.4, the strength falls to 17.6 MPa (57.89%) at 7 days and 22.8 MPa (69.30%) at 28 days. The lowest performance was seen at Alt.5, with strengths of 13.6 MPa (44.74%) at 7 days and 17 MPa (51.67%) at 28 days.

Overall, these findings confirm that replacing cement with up to Alt.3 is feasible, as the CPBs still meet the required 28 days target strength of 30 N/mm^2 according to strength class 3 specifications.

3.4 Flexural Strength

While the SLS standard does not include explicit provisions for assessing the flexural strength of CPBs, certain international standards such as IS 15658:2006 (The Indian Standard for CPBs) [20] do specify this test. In practical applications, CPBs are likely to be subjected to flexural stresses due to inconsistencies or irregularities in the supporting base. Therefore, evaluating the flexural strength of CPBs is also considered here. Figure 8(a) illustrates a schematic diagram of the test setup and Figure 8(b) shows a photograph of the actual testing arrangement.

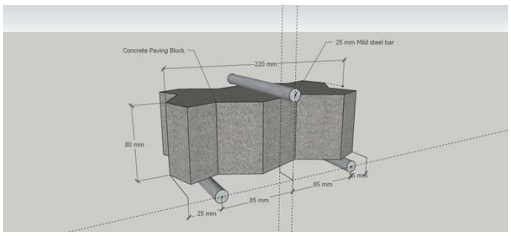

(a)

(b)

Figure 8: Test setup for flexural strength test

In this study, flexural strength tests were carried out on the control sample as well as on samples up to Alt.3 following the procedure outlined in IS 156658:2006 [20]. Figure 9 indicates how flexural strength of the CPBs decreases with the increase of CCA content. However, the average breaking load recorded for Alt.3 was 12.4 kN, which was well above the minimum requirement of 7 kN specified in IS 15658: 2006 [20] for heavy duty and industrial roads.

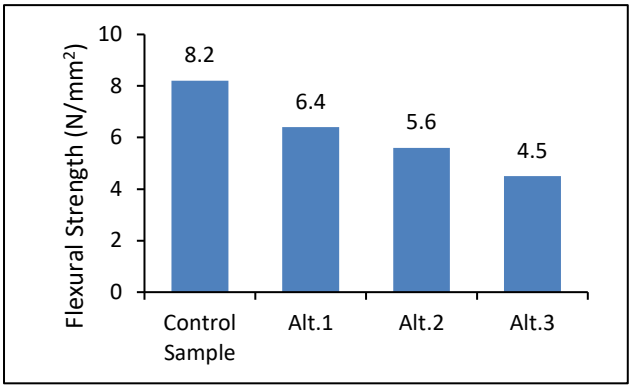

Figure 9: Flexural strength test results

3.5 Water Absorption

Figure 10 presents the water absorption test results for the CPBs. As per the requirements of SLS 1425: Part 1 [14], the water absorption of CPBs must be less than 6% to meet acceptance criteria. The test results indicated that all samples up to Alt.3 complied with this requirement, although a gradual increase in water absorption was observed with higher CCA contents.

The increase in water absorption of CPBs with higher CCA content is associated with changes in the pore structure of the concrete. At moderate CCA replacement levels, CCA help refine the pore system by producing smaller pores, which can be partially filled by pozzolanic reaction products, resulting in a denser microstructure. However, at higher CCA content, the pozzolanic reaction becomes incomplete, leaving some unreacted CCA particles. These unreacted particles create additional voids, increasing the overall porosity of the concrete. This is likely the reason for the observing of rise in water absorption and corresponding reduction in both compressive and flexural strengths with the increase of CCA content.

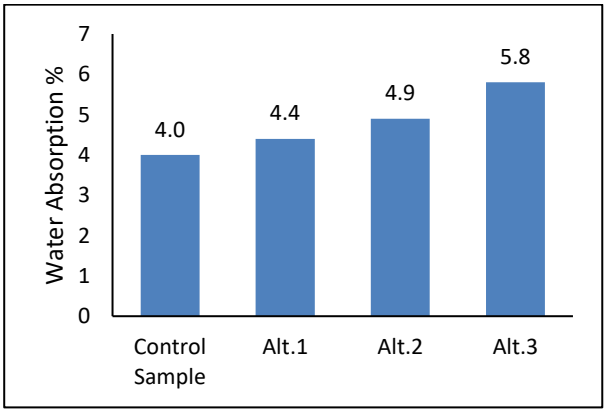

Figure 10: Water absorption test results

3.6 Skid/Slip Resistance

Skid or slip resistance is an important performance characteristic assessed in accordance with the requirements of SLS 1425: Part 2 [19]. Accordingly, tests were conducted on control sample and samples up to Alt.3. The Unpolished Slip Resistance Values (USRV) were measured for both the top and bottom surfaces of the CPBs and are presented in Table 5.

According to the data presented in Table 5, all types of CPBs exhibited a mean USRV greater than 55, which the minimum requirement specified in SLS 1425: Part 1 [14]. It was also observed that the mean USRV increased with the increase of partial cement replacement by CCA.

Table 5: Skid/Slip resistance test results

Sample ID	Side	Mean USRV	USRV for CPBs
Control sample	1st side	67	70
	Opposite side	70	
Alt.1	1st side	85	85
	Opposite side	85	
Alt.2	1st side	85	87
	Opposite side	87	
Alt.3	1st side	85	90
	Opposite side	90	

3.7 Compliance of CPBs with Standards

Table 6 presents a summary of the compliance of both the control samples and alternative samples incorporating CCA and QL with the standards specified for CPBs in SLS 1425: Part 1 [14] and IS 15658:2006 [20]. This was based on a series of tests, including slump test, compressive strength test, flexural strength test, water absorption test and skid /slip resistance test. The results indicated that the control sample and samples of Alt.1, Alt.2 and Alt.3 satisfied the performance requirements specified in both the SLS and IS standards for CPBs.

Table 6: Summary of adherence to the standard requirements

Test	Control sample	Alt.1	Alt.2	Alt.3	Alt.4	Alt.5
Workability of concrete mix	✓	✓	✓	✓	✓	✓
Visual Inspection	✓	✓	✓	✓	✓	✓
Compressive strength ≥ 30 N/mm²	✓	✓	✓	✓	×	×
Flexural strength ≥ 2.5 N/mm²	✓	✓	✓	✓	–	–
Water absorption ≤ 6%	✓	✓	✓	✓	–	–
Skid/Slip resistance ≥ 55	✓	✓	✓	✓	–	–

4. Conclusion

This study focused on the development of non-rectangular type CPBs by partially replacing OPC with CCA and QL in varying proportions to identify the optimum partial replacement percentages. A series of experimental tests were conducted to evaluate key properties including compressive strength, flexural strength, water absorption, skid/slip resistance and workability of concrete. As per results, replacing OPC by CCA and QL under all the considered percentages did not significantly impact workability. However, the increase of CCA percentage with fixed QL percentage of 10% led to reduction in compressive strength and flexural strength, and increase of water absorption and skid/slip resistance of CPBs. These changes other than increase of skid/slip resistance are unfavorable for the expected performances of CPBs. However, the partial replacement of OPC up to 15% CCA and 10% QL satisfied the minimum strength and physical characteristics required for CPBs. Hence, partially replacing OPC by 15% CCA and 10% QL can be identified as the optimum partial replacements percentage as it offered the highest cost saving while complying relevant standard of strength and physical characteristic of CPBs.

Based on basic production cost estimates of CPBs, it can achieve a cost saving of about 5% by adopting the optimum partial replacement percentage presented above (15% CCA and 10% QL). Additionally, it promotes environmental sustainability by effective utilization of agricultural waste.

To ensure long term viability, further studies are recommended especially relevant to durability aspects which were not addressed in this study. Implementing field trials to monitor the performance of paving blocks made with CCA and QL in real world conditions will help validate laboratory findings and confirm their practical applicability.

References

[1] Central Bank of Sri Lanka, *Annual Report – 2021*, pp. 65–67, Apr. 2022.

[2] ASTM International, *Standard Terminology Relating to Concrete and Concrete Aggregates*, ASTM C125-15a, West Conshohocken, PA, 2015.

[3] ASTM International, *Standard Specification for Coal Fly Ash and Raw or Calcined Natural Pozzolan for Use in Concrete*, ASTM C618-15, West Conshohocken, PA, 2015.

[4] S. A. Memon and M. K. Khan, "Ash blended cement composites: Eco-friendly and sustainable option for utilization of corncob ash," *Journal of Cleaner Production*, vol. 175, pp. 442–455, 2018.

[5] K. A. Mujedu, S. A. Adebara, and I. O. Lamidi, "The use of corn cob ash and saw dust ash as cement replacement in concrete works," *International Journal of Engineering Sciences*, vol. 3, no. 4, pp. 22–28, 2014.

[6] D. A. Adesanya and A. A. Raheem, "Development of corn cob ash blended cement," *Construction and Building Materials*, vol. 23, no. 1, pp. 347–352, 2009.

[7] A. Abubakar, A. Mohammed, and D. Samson, "Assessment of embodied energy and carbon IV oxide emission of concrete containing corncob ash," *International Journal of Sustainable and Green Energy*, vol. 10, pp. 76–84, 2021.

[8] M. Mouli and H. Khelafi, "Performance characteristics of lightweight aggregate concrete containing natural pozzolan," *Building and Environment*, vol. 43, no. 1, pp. 31–36, 2008.

[9] S. M. S. Khan, *Production of Sustainable Concrete Using Indigenous Saudi Natural Pozzolan*, Ph.D. dissertation, King Fahd University of Petroleum and Minerals, Saudi Arabia, 2013.

[10] G. Hannesson, K. Kuder, R. Shogren, and D. Lehman, "The influence of high volume of fly ash and slag on the compressive strength of self-consolidating concrete," *Construction and Building Materials*, vol. 30, pp. 161–168, 2012.

[11] G. C. Cordeiro, R. D. Toledo Filho, L. M. Tavares, and E. M. R. Fairbairn, "Pozzolanic activity and filler effect of sugar cane bagasse ash in Portland cement and lime mortars," *Cement and Concrete Composites*, vol. 30, no. 5, pp. 410–418, 2008.

[12] B. H. J. Pushpakumara and G. H. M. J. De Silva, "Characteristics of masonry blocks manufactured with rice husk ash (RHA) and lime," *Engineer: Journal of the Institution of Engineers, Sri Lanka*, vol. 45, no. 3, 2012.

[13] O. S. B. Al-Amoudi, S. Ahmad, M. Maslehuddin, and S. M. Khan, "Lime-activation of natural pozzolan for use as supplementary cementitious material in concrete," *Ain Shams Engineering Journal*, vol. 13, no. 3, p. 101602, 2022.

[14] Sri Lanka Standards Institution, *Specification for Concrete Paving Blocks Part 1: Requirements*, SLS 1425 Part 1:2011.

[15] K. Baskaran and K. Gopinath, "Study on applicability of ACI and DOE mix design methods for paving blocks," *Annual Transactions of the Institution of Engineers, Sri Lanka*, pp. 127–134, 2013.

[16] Sri Lanka Standards Institution, *Ordinary Portland cement*, SLS 107:2015.

[17] British Standards Institution, Testing Aggregates – Part 2: Methods of Determination of Density, BS 812: Part 2:1995.

[18] British Standards Institution, Specification for Aggregates from Natural Sources for Concrete, BS 882:1992.

[19] Sri Lanka Standards Institution, Specification for Concrete Paving Blocks *Part 2: Testing Methods*, SLS 1425 Part 2:2011.

[20] Bureau of Indian Standards, *Precast Concrete Blocks for Paving – Specifications*, IS 15658:2006.

Assessment of Durability of Concrete Carrying Blended Sea Sand and Manufactured Sand

H M S A Koswaththa[1], P R P U B Abeyaratne[1], H A D S Buddika[1], and H D Yapa[1]

Abstract

Sea sand and manufactured sand (M-sand) have emerged as promising substitutes, each possessing unique physical and chemical properties that influence concrete performance. Previous research has indicated that a 50:50 blend of sea sand and M-sand enhances particle size distribution, thereby improving both fresh and hardened properties of concrete. This study focused on evaluating the durability performance of concrete incorporating a 50% sea sand–M-sand blend, in comparison to conventional river sand and unblended sea sand. Durability assessments were conducted using accelerated corrosion testing, rapid chloride permeability, sulfuric acid exposure, and water absorption analysis. The results showed that the blended mix exhibited improved performance in water absorption and accelerated corrosion resistance, chemical exposure, while showing intermediate durability under chloride penetration tests. The findings confirmed that blending of sea sand with M-sand improves concrete durability compared to the use of sea sand alone. This strategy not only enhances the structural performance but also reduces dependence on river sand, promoting environmentally responsible construction in coastal and resource-sensitive regions.

***Keywords:** Sea Sand, Manufactured sand, Concrete, Durability, Sustainability*

1. Introduction

The burgeoning global population and continuous urbanization have significantly increased the demand for concrete, a cornerstone of modern construction, leading to a substantial consumption of its raw materials, particularly freshwater and river sand [1], [2], [3], [4]. This rising demand has traditionally relied heavily on river sand as the fine aggregate [1]. However, its over-extraction has resulted in severe environmental degradation, including riverbank erosion, groundwater depletion, damage to river ecosystems, altered riverbeds, increased salinity intrusion, and flood disasters [5]. Consequently, there is an urgent need to mitigate this predicament and develop sustainable materials for construction [1], [3].

In response to these environmental and resource concerns, alternative fine aggregates such as manufactured sand (M-sand) and offshore sea sand have gained considerable attention [5], [6], [7].

Manufactured sand (M-sand) is produced by crushing rocks and quarry stones, offering an eco-friendly alternative that reduces the environmental impact compared to river sand mining [1], [8]. Sea sand, widely available along coastal regions like Sri Lanka, presents another viable source for fine aggregate, potentially reducing pressure on inland riverbeds and offering advantages such as lower cost and reduced transportation fees for coastal and island constructions [5], [8], [9], [10]

The choice of fine aggregate significantly influences the properties of concrete, including its strength, durability, and workability [1]. Therefore, a comprehensive understanding of how M-sand and sea sand perform in comparison to river sand is imperative for ensuring the sustainability and resilience of concrete structures. The distinct physical properties of manufactured sand and sea sand set them apart from traditional river sand. For sea sand, critical parameters include chloride content and shell content, which can influence steel corrosion in reinforced concrete and the overall strength and durability of the concrete [1], [10], [11], [12]. While chloride can be reduced by washing, some studies note that within certain limits, chloride salts can even enhance the early compressive strength of concrete [10], [13]. On the other hand, for manufactured sand, the angularity index and fine content take precedence as crucial parameters, affecting water demand, workability, strength, and durability [6], [7]. These distinctive properties of M-sand and sea sand have a direct impact on the characteristics of concrete. Nevertheless, it is crucial to note that these properties are contingent on various factors, including the source and processing methods [8], [14].

Previous research has explored blending M-sand with sea sand, with studies indicating that a blend ratio of 50%/50%/can provide an optimum mix ratio when considering the fresh and hardened properties [6], [7]. This approach aims to leverage the contrasting physical properties of these two alternative aggregates to achieve a balanced performance. Despite these reported benefits, a comprehensive understanding of the durability performance of these blended concretes remains less explored. This study, therefore, aimed to bridge this critical knowledge gap by investigating the durability aspect of blended sea sand and manufactured sand concrete and comparing its performance to traditional river sand and 100% sea sand concrete.

[1] H M S A Koswaththa, P R P U B. Abeyaratne, H A D S Buddika, and H D Yapa: Department of Civil Engineering, Faculty of Engineering, University of Peradeniya (anuradhakoswaththa@gmail.com, e18003@eng.pdn.ac.lk, samithbuddika@eng.pdn.ac.lk, hdy@eng.pdn.ac.lk)

2. Methodology

2.1 Materials

Sea sand samples were obtained from the Muthurajawela sea sand yard, where sea sand is washed and sold. M-sand was collected from South Colombo, and river sand was collected from Kandy. The coarse aggregate, used for this study, was a well-graded crushed gneissic material of 20 mm maximum aggregate size. Table 1 presents the physical properties of different aggregate types used in this study.

Blended sea sand and M-sand specimens were compared with two sets of control samples that were produced using river sand (RS) and sea sand (SS).

Table 1: Mix identification and details

Mix ID	Description
SS	Sea sand 100%
RS	River sand 100%
SSMS	Sea sand 50% + M-sand 50%

2.2 Mix design

Two concrete mixes were designed, considering that the water/binder ratio is 0.4 and 0.65, following BS 5328: Part 1: 1997, the target slump was around 120 – 180 mm. A w/c of 0.65 incorporated, suggesting the maximum w/c ratio structural concrete can get and the maximum sand content that can be taken. A 0.4 w/c ratio was used for fresh and hardened property experiments, suggesting maintaining the balance between workability and strength.

A water reducer (superplasticiser) admixture, PLASTOBUILD ES, was used for a 0.4 cement/binder mix design to achieve the required workability while keeping the cement content under the code-specified maximum limit. The cement used was ordinary Portland cement (OPC). A mortar mix of 0.45 w/c was used only for the chemical exposure testing. Table 3 shows the test conducted and the mix design used for specimen preparation. Concrete mixing followed the procedure specified in ASTM C192-98.

Table 2: Mix design details used for the experiments

Component	Concrete mix	Mortar mix
Water/cement ratio	0.65	0.45
Cement content (kg/m^3)	308	555
Water content (kg/m^3)	200	243
Fine aggregate (kg/m^3)	725	1531
Coarse aggregate (kg/m^3)	1183	-
Water reducer (kg/m^3)	-	11
Sand/cement ratio	2.35	2.75

2.3 Accelerated corrosion

The Accelerated Corrosion Test (ACT) methodology, as described by Güneyisi et al. [15], was employed in this study. Concrete cylinders with dimensions of 100 mm diameter and 200 mm height were fabricated, each featuring a 16 mm diameter steel reinforcement bar centrally embedded within the specimen. To prevent crevice corrosion, the steel bar's end was positioned at least 30 mm from the cylinder's bottom and coated with epoxy where it exited the concrete. Following casting, the specimens underwent a 28-day water curing period before the initiation of testing. This study employed a 12V DC power source to induce corrosion. A 5% sodium chloride (NaCl) solution served as the electrolyte, with the liquid level maintained at the specimens' mid-height. In this circuit, the steel bar functioned as the anode (working electrode), and stainless-steel plates placed near the specimen in the solution acted as the cathode (counter electrode). Corrosion current variation over time was continuously monitored and recorded using a data logger. The criterion for identifying the onset of active corrosion and subsequent specimen failure was a sudden and abrupt increase in the measured current, which was observed to coincide with the appearance of surface cracks on the specimen. This rapid evaluation technique aims to shorten the test period to suit practical laboratory conditions.

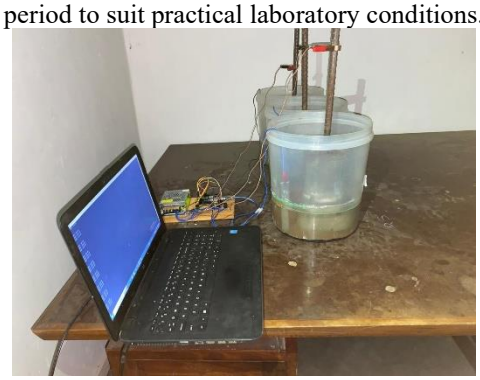

Figure 1: Accelerated corrosion setup and testing

2.4 Chemical Exposure

The chemical resistance of cement mortar incorporating varying shell contents was systematically assessed through controlled exposure to an aggressive sulfuric acid (H_2SO_4) environment. A 1.5% sulfuric acid solution, prepared by diluting concentrated 98% H_2SO_4 with distilled water, served as the testing medium. Following a 28-day standard water curing period to ensure initial hydration and strength development, the prepared mortar cubes were fully submerged in this acid solution. The exposure was maintained at a constant temperature of 22 ± 1°C for predetermined durations of 7, 14, and 28 days. To ensure the consistent aggressive nature of the environment and sustain the concentration of hydrogen ions (H^+) and sulfate ions (SO_4^{2-}), the sulfuric acid solution was completely renewed weekly. Upon the completion of each specified exposure period, the mortar cubes underwent a meticulous visual inspection to identify any macroscopic signs of chemical degradation. Furthermore, uniaxial compressive strength tests were conducted on the exposed cubes to precisely quantify the impact of acid exposure on their fundamental mechanical properties, thereby evaluating the material's structural integrity degradation over time.

2.5 Rapid chloride penetration test

The Rapid Chloride Permeability Test (RCPT) was conducted following ASTM C1202 to evaluate the chloride ion penetration resistance of concrete. Concrete cylinders (100 mm diameter × 200 mm height) were cast, from which two disk-shaped specimens (50 mm thickness, 95–100 mm diameter) were subsequently extracted. All specimens underwent a minimum 28-day water curing under controlled conditions, followed by vacuum saturation to

ensure complete filling of internal voids with water prior to testing. Saturated specimens were then mounted in the RCPT apparatus, with one end immersed in a 3.0% sodium chloride (NaCl) solution and the other in a 0.3 N sodium hydroxide (NaOH) solution. A constant 60 V DC potential was applied across the specimen ends, and the instantaneous current was recorded at 30-minute intervals over a 6-hour period. The total electrical charge (Q), measured in coulombs, passed through each specimen was calculated to quantify its resistance to chloride ion ingress.

2.6 Density, Absorption, and Voids in Hardened Concrete

Density, absorption, and voids in concrete were determined following the ASTM C642-12 standard. Cylindrical concrete specimens, 100 mm in diameter and 50 mm in height, were initially prepared and water-cured for 28 days. Post-curing, specimens were weighed to establish initial mass (Wi), then oven-dried at 100 ± 10°C in 24-hour intervals until consecutive weighings differed by less than 0.5%, recording this as the dry mass (A). Subsequently, the oven-dried specimens were immersed in water at approximately 21°C for a minimum of 48 hours to achieve saturation. The surface water was then wiped off to measure the saturated mass (B). This was followed by boiling the specimens in water at approximately 21°C for 5 hours, natural cooling to 21°C over at least 14 hours, wiping dry, and recording the saturated mass after immersion and boiling (C). The immersed apparent mass (D) was ascertained by weighing the fully submerged specimens in water. Using these recorded masses (A, B, C, D), absorption after immersion and boiling, bulk density (both dry and after immersion), apparent density, and the volume of permeable pore space (voids) were calculated based on the standard's stipulated equations.

3. Results and Discussion

3.1 Accelerated corrosion

In accelerated corrosion testing, the "time to failure" signifies the duration until specimen failure, typically evidenced by a sudden increase in corrosion current. The test method employs an impressed anodic potential to accelerate the electrochemical corrosion process, shortening the observation period to suit laboratory conditions.

Analysis of the results presented in Figure 1 indicates distinct variations in corrosion resistance among the specimens. However, the time difference was not much deviated from one another. The sea sand (SS) specimen exhibited the shortest time to failure at 55.0 days, suggesting a reduced capacity to resist accelerated chloride-induced corrosion compared to the river sand (RS) specimen, which failed at 60.5 days.

Conversely, the blend of sea sand and manufactured sand (SSMS) demonstrated the longest time to failure at 63.0 days. This prolonged resistance implies that the incorporation of manufactured sand effectively enhances the concrete's overall ability to withstand the accelerated corrosion process. Such improvement in corrosion resistance is often linked to beneficial modifications in the concrete's microstructure, such as pore refinement, and potentially increased chloride binding capacity, which collectively restrict the transport of aggressive ions (e.g., chlorides and oxygen) to the embedded steel reinforcement.

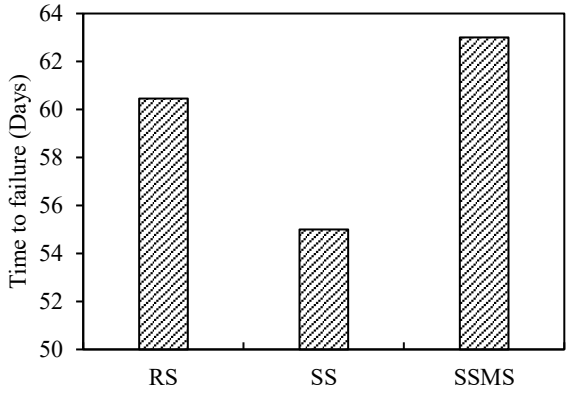

Figure 2: Time to failure under accelerated corrosion testing for SS, RS, and SSMS concrete.

3.2 Chemical Exposure

All specimens showed spalling with the age of acid exposure. Figure 3 shows the physical appearance of all specimens after 7, 14, and 28 days of exposure period. On the surface of the mortar specimens, a white substance was observed, which was inferred to be gypsum. Visual inspection of deteriorated specimens suggested that SS and RS specimens were subjected to severe deterioration compared to MS specimens. When the MS content increases in blended mixtures, less deterioration is observed due to the influence of MS.

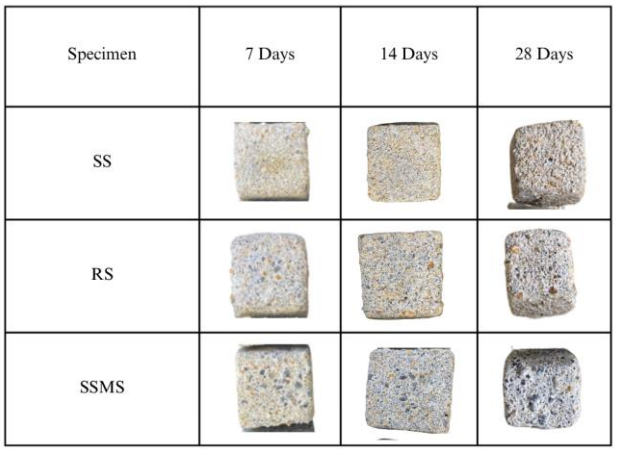

Figure 3: Physical appearance of cement mortar specimens after exposure to sulfuric acid for 7, 14, and 28 days.

Referring to Figure 2, the data illustrate the significant compressive strength degradation of cement mortar specimens (RS, SS, SSMS) subjected to chemical exposure over 28 days. All formulations exhibit a substantial reduction from their initial strengths, indicative of progressive material deterioration. The SS specimen demonstrates the most rapid early-age strength loss, declining from an initial 51.8 MPa to 12.9 MPa at 7 days, representing a 75.1% reduction. The RS specimen follows a similar, albeit slightly less severe, trajectory, with its strength decreasing from 53.0 MPa to 16.0 MPa during the same period. Conversely, the SSMS specimen, despite possessing the lowest initial compressive strength (48.9

MPa), exhibits a comparatively higher strength retention at 7 days, stabilizing at 16.9 MPa. This trend of SSMS outperforming SS and RS in relative strength preservation continues at 14 days, with SSMS at 13.6 MPa, RS at 12.2 MPa, and SS at 11.8 MPa. By 28 days of exposure, all specimens demonstrate profound degradation. The SS specimen records the lowest final compressive strength of 7.1 MPa, closely followed by RS at 7.2 MPa. Notably, the SSMS specimen maintains the highest residual strength at 7.9 MPa after 28 days, indicating slightly higher long-term performance and chemical resistance within this exposure regime, especially considering its lower initial strength. This suggests a differential response of the mortar formulations to the aggressive chemical environment, with the SSMS composition exhibiting more resilient microstructural integrity under prolonged attack.

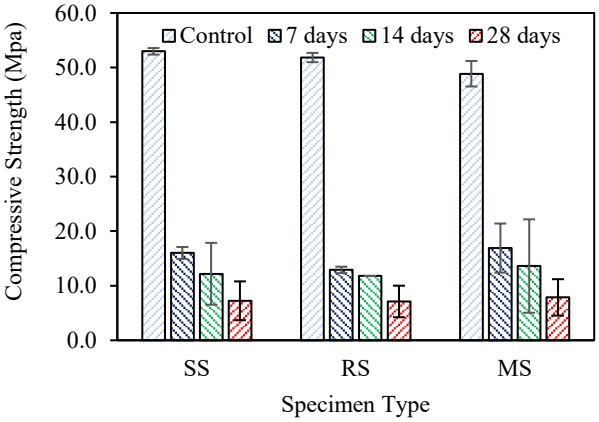

Figure 4: Compressive strength of river sand, sea sand, and sea sand M-sand blended mortar after 7-, 14-, and 28-day chemical exposure for SS, RS, and SSMS concrete.

3.3 Rapid chloride penetration

Chloride ion penetration, a critical factor in the durability of reinforced concrete and the corrosion of steel reinforcement, was evaluated using the Rapid Chloride Permeability Test (RCPT). As presented in Figure 3, concrete made with river sand (RS) exhibited superior resistance, evidenced by the lowest total charge passed (1736.5 Coulombs), categorizing it as having low penetrability. This is attributed to river sand's generally lower chloride content and organic impurities compared to sea sand. In contrast, concrete incorporating sea sand (SS) showed reduced resistance with a higher charge passed (2259.9 Coulombs), falling into the moderate penetrability range. This diminished performance is likely due to the sea sand's higher inherent chloride content, which can influence cement hydration products and pore structure. Sea sand also features a smoother surface texture and may contain shells and organic substances, potentially impairing strength and durability. The 50% sea sand and manufactured sand (SSMS) blend recorded the highest charge passed (2602.35 Coulombs), also within the moderate penetrability category, indicating the lowest resistance among the tested mixes. While manufactured sand (M-sand) typically possesses angular, rougher textures and can densify pore structures, this specific SSMS blend did not enhance chloride impermeability over sea sand alone. This suggests that the combination, possibly due to particle interactions or overall pore structure, adversely affected the blend's ability to resist chloride ingress. Ultimately, river sand concrete provided optimal chloride penetration resistance, underscoring the significant impact of aggregate characteristics and impurities on concrete durability.

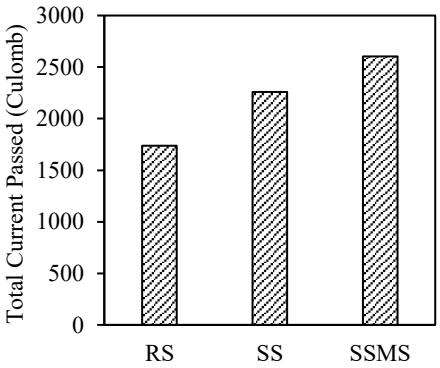

Figure 5: Total current passed through the concrete specimens with for SS, RS, and SSMS concrete.

3.4 Density, Absorption, and Voids in Hardened Concrete

Density

Figure 4 presents bulk density (dry, after immersion, and after immersion and boiling) and apparent density for all specimens. The SSMS blend specimen exhibited the highest dry bulk density (2.42 g/cm³) and apparent density (2.75 g/cm³), indicating the lowest overall porosity among the three mixes. This suggests improved resistance to water and aggressive agent ingress. The SS specimen showed a slightly higher dry bulk density (2.37 g/cm³) than the RS specimen (2.34 g/cm³), implying that SS may have a marginally lower porosity and potentially better durability performance than RS.

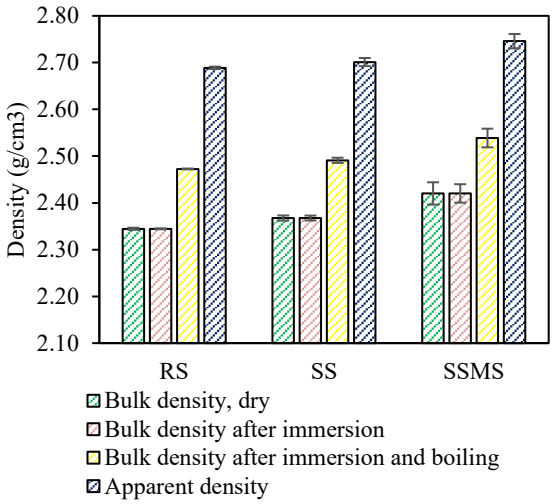

Figure 6: Comparison of dry bulk density, bulk density after immersion, bulk density after immersion and boiling, and apparent density

Water Absorption

Water absorption is a key indicator of concrete's porosity and its vulnerability to deterioration, with lower values generally signifying better durability. As presented in Figure 5, among the three specimens tested, SSMS (Sea Sand and M-sand blend) exhibited the lowest water absorption (4.69% after immersion and 4.90% after immersion with boiling), suggesting the densest microstructure and lowest permeability, likely resulting from optimized particle packing. Sea Sand Concrete (SS) showed intermediate absorption values (5.13% and 5.22%), while River Sand Concrete (RS) had the highest (5.40% and 5.46%), indicating higher porosity and a greater susceptibility to environmental degradation. Overall, the SSMS blend demonstrated superior resistance to water ingress and, by implication, enhanced durability performance.

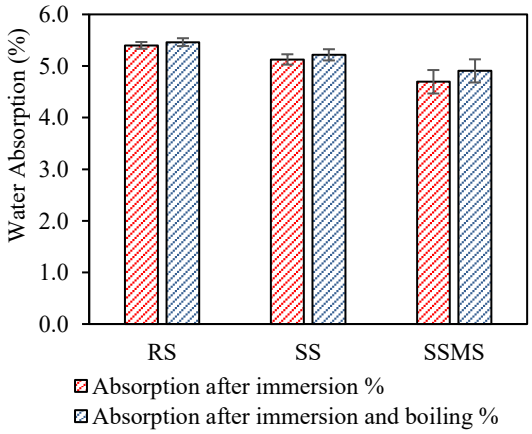

Figure 7: Water absorption percentages after immersion and after immersion with boiling for RS, SS, and SSMS concrete.

Volume of air voids

Volume of air voids results are presented in Figure 6, and river sand concrete (RS) exhibited the highest volume of permeable voids (12.81%), suggesting a more porous structure and lower resistance to chloride ingress, which may compromise durability. Sea Sand Concrete (SS) showed slightly lower void content (12.35%) compared to river sand. The Blended Sea Sand and Manufactured Sand Concrete (SSMS) mix demonstrated the lowest void volume (11.86%), indicating a denser matrix with improved pore structure due to effective particle packing. This aligns with its lower water absorption and highlights SSMS as the most durable mix among the three in aggressive environments.

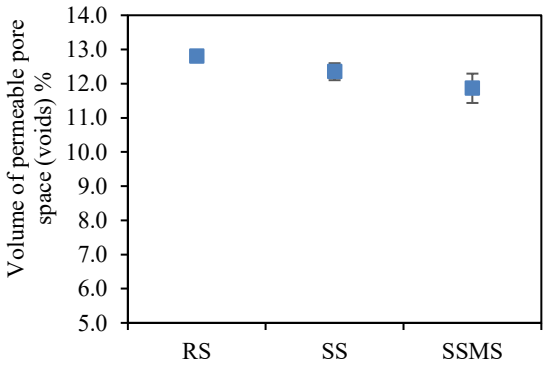

Figure 8: Volume of permeable pore space (void%) for RS, SS, and SSMS concrete

4. Conclusions

Based on the findings of the study, the following conclusions can be made.

Accelerated corrosion results revealed that blending sea sand with M-sand improves the resistance to chloride-induced corrosion compared to the sea sand and river sand mix.

Sulfuric acid exposure tests demonstrated that blended sea sand and M-sand mortar specimens undergo less degradation than those made with river sand or sea sand alone.

The 50% sea sand and 50% M-sand blend achieved the lowest water absorption, highest overall density, and lowest volume of air voids, reflecting a denser and more impermeable concrete matrix compared to mixes containing only sea sand or river sand.

While the Rapid Chloride Penetration Test (RCPT) showed slightly reduced chloride resistance in the blended mix, however total charge passed remained within moderate penetrability limits (2000-4000 coulombs).

Overall, all experiments other than RCPT revealed improved durability performance in blended sea sand M-sand mix compared to control river sand and sea sand specimens. These findings support the idea of using blended sea sand M-sand concrete for the Sri Lankan construction industry, particularly where durability is a concern.

References

[1] Y. Zhao, X. Hu, C. Shi, Z. Zhang, and D. Zhu, "A review on seawater sea-sand concrete: Mixture proportion, hydration, microstructure and properties," *Construction and Building Materials*, vol. 295, p. 123602, 2021.

[2] T. Dhondy, A. Remennikov, and M. N. Shiekh, "Benefits of using sea sand and seawater in concrete: a comprehensive review," *Australian Journal of Structural Engineering*, vol. 20, no. 4, pp. 280–289, 2019.

[3] M. Guo *et al.*, "Characterization of the mechanical properties of eco-friendly concrete made with untreated sea sand and seawater based on statistical analysis," *Construction and building Materials*, vol. 234, p. 117339, 2020.

[4] D. Pan, S. A. Yaseen, K. Chen, D. Niu, C. K. Y. Leung, and Z. Li, "Study of the influence of seawater and sea sand on the mechanical and microstructural properties of concrete," *Journal of Building Engineering*, vol. 42, p. 103006, 2021.

[5] J. Xiao, C. Qiang, A. Nanni, and K. Zhang, "Use of sea-sand and seawater in concrete construction: Current status and future opportunities," *Construction and Building Materials*, vol. 155, pp. 1101–1111, 2017.

[6] A. Branavan, K. M. C. Konthesingha, S. M. A. Nanayakkara, and H. M. R. Premasir, "Optimizing blending of manufactured sand with offshore sand based on physical and virtue characteristics," 2020.

[7] B. Arulmoly, C. Konthesingha, and A. Nanayakkara, "Performance evaluation of cement mortar produced with manufactured sand and offshore sand as alternatives for river sand," *Construction and Building Materials*, vol. 297, p. 123784, 2021.

[8] B. Arulmoly and C. Konthesingha, "Pertinence of alternative fine aggregates for concrete and mortar: A brief review on river sand substitutions," *Australian Journal of Civil Engineering*, vol. 20, no. 2, pp. 272–307, 2022.

[9] R. Mahendran, K. Godwin, T. Gnana Selvan, and M. Murugan, "Experimental study on concrete using sea sand as fine aggregate," *Int. J. Sci. Eng. Res*, vol. 7, pp. 48–52, 2016.

[10] D. A. R. Dolage, M. G. S. Dias, and C. T. Ariyawansa, "Offshore Sand as a Fine Aggregate for Concrete Production," 2013.

[11] U. G. Eziefula, J. C. Ezeh, and B. I. Eziefula, "Properties of seashell aggregate concrete: A review," *Construction and Building Materials*, vol. 192, pp. 287–300, 2018.

[12] R. K. Kularatne, "Suitability of the coastal waters of Sri Lanka for offshore sand mining: a case study on environmental considerations," *Journal of coastal conservation*, vol. 18, no. 3, pp. 227–247, 2014.

[13] K. Katano, N. Takeda, Y. Ishizeki, and K. Iriya, "Properties and application of concrete made with sea water and un-washed sea sand," in *Proceedings of Third International conference on Sustainable Construction Materials and Technologies*, 2013, pp. 1–10.

[14] W. P. S. Dias, G. Seneviratne, and S. M. A. Nanayakkara, "Offshore sand for reinforced concrete," *Construction and Building Materials*, vol. 22, no. 7, pp. 1377–1384, 2008.

[15] E. Güneyisi, M. Gesoğlu, F. Karaboğa, and K. Mermerdaş, "Corrosion behavior of reinforcing steel embedded in chloride contaminated concretes with and without metakaolin," *Composites Part B: Engineering*, vol. 45, no. 1, pp. 1288–1295, 2013.

Feasibility Assessment of Using Recycled Plastic as a Complete Replacement for Coarse Aggregate in Structural Lightweight Concrete

T Abirami[1], C S Bandara[1], H D Yapa[1] and P B R Dissanayake[1]

Abstract

Plastic waste accumulation presents a critical environmental concern. From the recent past, the incorporation of recycled polypropylene plastic coarse aggregates (PPCA) as an alternative to natural coarse aggregates (NCA) in concrete has been emerging as a sustainable solution. This research explored the feasibility of replacing NCA in concrete completely with PPCA. The primary aim was to assess the workability, mechanical performance, and density of such concrete mixes and to determine whether those characteristics can meet the performance benchmarks set for structural lightweight concrete in ASTM C330-05. An experimental study was designed targeting a normal strength concrete mix. The plastic waste used were sorted, cleaned, and shredded into aggregate size ranging from 4 mm to 10 mm. The concrete mix containing 100% PPCA, along with the addition of fly ash, demonstrated satisfactory performance in terms of compressive strength. A slump of 40 mm was recorded, indicating moderate workability. The compressive strengths of 12.49 MPa at 7 days and 19.82 MPa at 28 days were recorded. These results surpassed the minimum 28-day compressive strength requirement set by ASTM C330-05 for lightweight structural concrete. The hardened density of the plastic concrete (PC) was 1675 kg/m³, well below the maximum limit of 1840 kg/m³ defined by the standard. This clearly indicates that the PC qualifies as lightweight concrete in both strength and density categories. PC proves to be a promising material for the applications where dead load reduction is a priority. The findings offer a viable solution for reusing plastic waste in large volumes while also reducing the reliance on non-renewable natural aggregates. The research supports the broader goal of achieving circular economy practices within the construction sector.

***Keywords:** Lightweight concrete, Plastic aggregates, Compressive strength, Cement consumption index, Sustainable construction*

1. Introduction

The excessive generation of plastic waste, particularly polypropylene (PP), has led to significant environmental challenges due to its non-biodegradable nature. Worldwide plastic production has risen significantly, growing from approximately 348 million tons in 2017 to around 400.3 million tons by 2022 [1]. With global production exceeding hundreds of millions of tons annually, effective methods for recycling and reusing plastic waste are critically needed. The construction industry, one of the largest consumers of raw materials and producers of greenhouse gases, has emerged as a viable field for integrating recycled materials to enhance sustainability.

Concrete, the most widely used construction material globally, is traditionally composed of cement, water, and aggregates. Aggregates constitute about 60–75% of concrete volume, with coarse aggregates playing a significant structural role. The expanding global construction activity resulted in the use of 51.7 billion metric tons of natural aggregates in 2018 [2], and this is expected to escalate to 62.9 billion metric tons by 2024 [3]. However, the extraction of natural aggregates is associated with environmental degradation, habitat loss, and depletion of natural resources. Substituting natural coarse aggregates (NCA) with recycled materials like PP coarse aggregates (PPCA) not only helps mitigate the environmental burden but also supports the principles of a circular economy.

PP, a widely used thermoplastic polymer, is commonly found in plastic furniture, electrical appliance, containers, automotive parts, and household items. Due to its non-biodegradable nature and low recycling rates, PP contributes significantly to environmental degradation when disposed of improperly. According to Pavlík [4], PP exhibits a notably low recycling rate, estimated to be around 0.6. In 2017, the pioneering study by Ozbakkaloglu et al. [5] marked the first attempt to incorporate PP coarse aggregates (PPCA) in concrete production. It is important to note that they limited the replacement of NCA with PPCA to a maximum of 30% in both normal and high-strength concrete mixes. Most of the subsequent studies to date also have limited the volumetric replacement level of PPCA to no more than 50% [6, 7, 8, 9, 10]. Based on the available literature, only a few studies have explored replacement levels above 50% [11-21] and out of these, only about nine publications have investigated the complete replacement of NCA with PPCA [13-21]. Purnomo et al., (2019) replaced 100% of NCA with modified PPCA coated with sand and examined the strength properties [13]. They investigated three different plastic concrete (PC) batches with lower water to cement (w/c) ratios of 0.290, 0.287 and 0.256. All other authors likewise employed a w/c ratio of less than 0.4. It showed that none of the past studies have directly incorporated PPCA (without any modifications) in concrete to completely replace the NCA, especially in mixtures with a relatively high w/c ratio. The high w/c ratio means reduced cement content. As the most extensively used construction

T Abirami, C S Bandara, H D Yapa and P B R Dissanayake: Department of Civil Engineering, Faculty of Engineering, University of Peradeniya, Sri Lanka. (e-mail: thuraisingamabirami@gmail.com,csbandara@eng.pdn.ac.lk, hdy@eng.pdn.ac.lk,ranjith@fulbrightmail.org)

material, concrete heavily depends on Portland cement, whose production is a major contributor to CO_2 emissions in the industry [22]. Reducing the cement content in concrete mixtures can significantly lower the environmental footprint while still achieving acceptable performance standards.

Lightweight concrete is beneficial in structural applications where reducing dead load is essential, such as in high-rise buildings and precast elements. Earlier experimental studies have verified that the inclusion of plastic aggregates in concrete results in lower density due to the lightweight nature of plastics [23-25]. However, the mechanical strength is often influenced by the reduced bonding between plastic particles and the cement matrix. Workability is another important aspect affected by plastic inclusion. While certain plastic types may reduce the workability of fresh concrete due to their sharp edges and irregular shapes, modifications to the mix, such as the inclusion of pozzolanic materials like fly ash or silica fume, have been suggested to improve the workability and interfacial transition zone (ITZ). Replacing 20% of cement with fly ash in concrete is widely regarded as an optimal replacement level [26].

This study investigated the strength properties, workability, and density characteristics of PC in which NCA were fully replaced with recycled PPCA to evaluate its suitability as structural lightweight concrete. It aims to validate whether such a concrete mix can meet the ASTM C330-05 standards [27], thus making it suitable for structural use. Further, this study considers relatively high w/c ratio of 0.55 and direct incorporation of shredded plastic waste without any modification. The main additive used is, fly ash which is a supplementary cementitious material as well as a workability enhancer.

2. Materials and Methods

In this section, the materials utilized during the experimental programme and the methods followed are discussed. Figure 1 displays the particle size distribution (gradation) curves of the natural and plastic aggregates.

2.1 Concrete constituents

Conventional concrete constituents such as Portland cement (binder), river sand (natural fine aggregate) with particle size ranging from 0 – 0.45 mm, crushed rock (NCA) having a nominal size limit of 12.5 mm and water were used. The specific gravity of river sand was 2.65, and a fineness modulus was measured as 3.1. The crushed rock exhibited with a specific gravity of 2.85 and a water absorption rate of 0.34%. Additionally, fly ash was used as partial substitution for cement. The class F type fly ash originated from Norochcholai Lakvijaya coal power plant, Puttalam was used.

2.2 Plastic coarse aggregates

The PPCA used in this study were obtained from Plastic and polythene waste recycling center, Gohagoda. Here, initially, the collected plastic wastes were sorted according to various types of plastic resins. Then, they were cleaned and shredded using mechanically operated plastic shredder. Figure 2 shows the recycled crushed PPCA used in this study, which were sorted according to different colours. The maximum nominal size of PPCA was 8 mm and its density was 890 kgm^{-3} and the water absorption capacity is almost zero.

As PPCA was derived from various waste sources, maintaining the same quality was essential. In this study, the plastic waste was processed uniformly by thorough cleaning and only PP-based plastics were selected, including discarded household items such as chairs, basins, and buckets, as well as vehicle spare parts and PP-based electronic waste. These are stable plastic items known for their non-degradable nature.

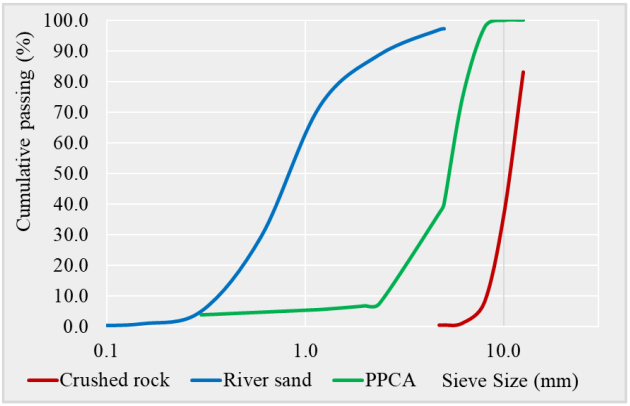

Figure 1: Particle size distribution curves of the natural and plastic aggregates

2.3 Methodology

The methodology of this research study was started with literature review and then, identification of major solid waste in Sri Lanka. The plastic waste and fly ash were found as the major solid wastes. Considering the lightweight aspect of plastic and NCA depletion, it was decided to produce green lightweight plastic concrete by substituting NCA in concrete with PPCA. After the material identification, material collection was done. Then, required material testing, concrete mix design and preliminary casting were carried out. From the preliminary trial and error casting, a mix proportion was finalized. Thereafter, concrete mixing, specimen casting, slump test, compressive strength test and density measurements were performed. The results were analyzed through comparison study and statistical analysis. Eventually, conclusions were made from the results. The major investigations were conducted in terms of compressive strength and density. For each testing a minimum of three specimens were utilized. The detailed procedure is discussed in Section 3.

Figure 2: Crushed plastic aggregates (PPCA)

3. Experimental program

A mix design was performed to produce normal strength concrete using conventional constituents. After several trial-and-error castings, a mix with 28-days cube compressive strength of 45 MPa was obtained. Using this mix one conventional concrete (CC) batch and two PC batches were produced. The ratio of water to cement was maintained at 0.55. Two batches of PC were prepared by completely replacing NCA with PPCA on a volumetric basis. The first mix, named as PP100%, was made without fly ash. The second mix, labeled as PP100%-FA20%, included 20% fly ash as a partial substitution for cement by weight. Table 1 shows the concrete mix proportions used in each batch. The CC batch was used for the comparison study.

Table 1: Concrete mix proportions in kgm^{-3}

Batch	Water	Cement	River sand	NCA	PPCA	Fly ash
CC	216	392.7	886.1	832.1	-	-
PP100%	216	392.7	886.1	-	259.9	-
PP100%-FA20%	216	314.2	886.1	-	259.9	78.6

3.1 Concrete mixing

Initially, all the dry concrete constituents were added in a pan type concrete mixture and mixed until seeing uniform mix. Then, 50% of the water was poured and blended for 3 minutes. After 3 minutes, the rest of the water was poured and blended for another 3 minutes. Afterwards, the mixer was stopped, and the concrete was manually remixed with a trowel for about 2 minutes to ensure uniformity. During mixing, the fine aggregate was dry, while the coarse aggregate was in SSD condition, pre-soaked for 24 hours with surface moisture removed just before mixing.

3.2 Specimen casting

The cubic steel moulds having sizes of 100 mm × 100 mm × 100 mm were cast for compressive strength testing.

Figure 3: Concrete cubes just after casting

A thin coating of oil was applied to the inner surfaces of the steel moulds before casting. Next, freshly mixed concrete was poured in layers, with each layer compacted manually using standard procedures. Finally, the top surface was leveled to ensure a smooth finish (Figure 3). The casted specimens were covered with polythene sheets and allowed for hardening for 24 hours. Then they were unmoulded and kept in the curing tank to allow curing until the day of testing.

3.3 Slump test

To assess the consistency of concrete mixes, slump test was carried out (Figure 4 and Figure 5). After the mixing of concrete, slump test was conducted on the fresh concrete to evaluate its workability, following the ASTM C143-15 standard [28].

Figure 4: Slump of 95 mm for conventional concrete

Figure 5: Slump of 40 mm for PP100%-FA20% concrete

3.4 Compressive strength test

The cube compressive strengths of the cast specimens were determined after 7 and 28 days of curing period conforming to EN 12 390-3 standard [29]. Each test contained three specimens from the same batch. A universal testing apparatus having maximum load capacity of 3000 kN was used.

3.5e Density measurement

Density is a key parameter influencing various physical properties of lightweight concrete, primarily governed by the quantity and density of the lightweight aggregate used [30]. The dry densities of concrete batches after 28-days were measured using ASTM C642-13 standard [31]. Cube specimens with size 100 mm x 100 mm x 100 mm were used for this purpose.

4. Results and Discussion

The results section presents and discusses the experimental findings related to the mechanical performances of lightweight concrete incorporated with 100% recycled PPCA. The performance of the concrete mixtures was evaluated in terms of workability, density, compressive strength, cement consumption index, and structural efficiency with comparisons made to conventional concrete and previous research findings.

4.1 Workability

The workability of freshly mixed concrete and the adhesion between aggregates and cement paste are greatly affected by the physical characteristics of the aggregates such as shape, surface roughness, and texture. As shown in Table 2, the complete replacement of NCA with PPCA reduced the workability of the concrete from 95 mm (CC) to 18 mm (PP100%), due to the uneven shape and sharp edges of PPCA. With the addition of 20% of fly ash, the PP100%-FA20% batch resulted in a slump of 40 mm, which was 122% higher than that of PP100%. It was attributed to the fine and spherical shape of fly ash, compared cement, increased the flowability of concrete [23]. Therefore, PP100%-FA20% batch provides moderate workability for structural lightweight application.

4.2 Compressive strength

The results from compressive strength test of conventional and plastic concrete are shown in Table 2. A compressive strength loss of slightly greater than 50% was observed when 100% of the NCA was replaced with PPCA. The incorporation of 20% of fly ash slightly reduced the strength to reach 19.82 MPa, which was only about 5.7%. This reduction can be negligible when compared to the workability enhancement of 122%. The statistical analysis in the Section 4.9 also shows there is no significant reduction in the strength with the addition of 20% fly ash. Purnomo et al. achieved 28-days compressive strengths of 21.01 MPa, 23.45 MPa, and 26.58 MPa, for cement contents of 482 kgm^{-3}, 529 kgm^{-3} and 558 kgm^{-3}, respectively, when using 100% sand coated PPCA. But current study achieved 19.82 MPa with only 314.2 kgm^{-3} cement content, without any modification to PPCA. Therefore, the composite produced in this study demonstrated better cost-effectiveness than those presented in previous studies.

Table 2: Workability and compressive strength properties of concrete batches

Batch	Slump (mm)	Compressive strength (MPa)	
		7-days	28-days
CC	95	30.33	44.62
PP100%	18	13.12	21.01
PP100%-FA20%	40	12.49	19.82

Figure 6 shows the failure modes of the cube specimens belongs to CC and PP100% batches after compression test. The typical failure cracks observed in the CC batch were barely observed in PC specimens. This was mainly attributed to the high ductility and energy absorption capacity of the PPCA, which helped to reduce the crack propagation and led to a more gradual failure [32].

Figure 6: Failure modes in cube specimens under compressive load for (a) CC, and (b) PP100% batches

4.3 Cement consumption index

Despite the variations across studies and the specific characteristics of materials used, a key technical and economic consideration is the balance between cement consumption and the resulting strength. This is particularly important in the context of lightweight concrete or during the use of lightweight aggregates [22]. The cement-to-strength ratio (kg/MPa) also known as cement consumption index serves as a useful performance indicator for PP-modified concrete, allowing for meaningful comparisons between different studies. Using PPCA, Purnomo et al. obtained consumption indexes of 22.94 kg/MPa, 22.56 kg/MPa, and 20.99 kg/MPa. The current study reported a consumption index of 15.85 kg/MPa, reflecting a more efficient use of cement than that observed in earlier studies.

4.4 Density

The density of PP100%-FA20% concrete and CC were measured as 1674.8 kgm^{-3} and 2394.9 kgm^{-3}, respectively. A 30% reduction in the density was achieved. As observed, the incorporation of recycled PPCA, which possess a relatively low bulk density of 890 kgm^{-3}, led to the noticeable reduction in the overall density of the concrete. According to the past research, concrete is classified as lightweight when its density does not exceed 2000 kgm^{-3}, and the compressive strength is above 17 MPa [33, 34]. Therefore, the PP-modified concrete meets the criteria and supports its suitability for lightweight concrete applications.

4.5 Structural lightweight concrete

The Table 3 shows the various classifications of lightweight concrete as per Neville et al. [34]. The structural lightweight concrete (SLC) must meet specific criteria, including a minimum compressive strength of 17 MPa and a density range between 1400 and 1800 kg/m³ [27, 33, 34]. The PP100%-FA20% concrete produced in this study satisfies these requirements.

Table 3: Lightweight concrete classification

Applications	Standard requirement	
	28-day compressive strength (MPa)	Dry density (kgm^{-3})
Structural concrete	> 17	< 1840
Masonry concrete	7 - 14	500-800
Insulating concrete	0.7 - 7	< 800

4.6 Structural efficiency

The structural efficiency can be measured by the ratio between compressive strength to density [20]. The structural efficiencies of CC and PP100%-FA20% concrete were 18.63 x 10^{-3} $MPa.m^3/kg$ and 11.83 x 10^{-3} $MPa.m^3/kg$, respectively. Here, about 36.5% reduction in the structural efficiency was observed.

4.7 Visual examination

The Figure 7 and 8 show the cut surfaces of the cube specimens belonging to conventional and PP-modified concrete used in this study. These cut surfaces allow visual assessment of aggregates' distribution in the concrete matrix. As the replacement level increases, the number of PPCA particles visible in each cut surface also increases. It was attributed to the volumetric replacement of 12.5 mm nominal size NCA with 8 mm nominal size PPCA. Since, the average size of PPCA were smaller than NCA, a greater number of PPCA is required to occupy the same volume of NCA, leading to more PPCA particles in a given volume. Another observation was that the addition of PPCA led to an increase in the number of pores in the concrete. Major reason for this was that the irregular shapes and poor surface texture of PPCA tended to trap more air during mixing than NCA.

Figure 7: Cut surface of conventional concrete cube specimen (not to scale)

4.8 Bonding

The development of a strong bond is largely determined by the porosity and roughness of the aggregate surface. A textured surface enhances this bond than smooth surface [31]. Although the NCA typically develop a strong bond with the mortar due to their rough and porous surfaces, the PPCA forms a weaker bond due to the smoother, less porous surfaces unless modified or treated. Further, the plastic aggregates are hydrophobic and chemically inert. These factors contributed to the weak ITZ between PPCA and the cement matrix as shown in Figure 9. The major reason for compressive strength reduction as discussed in Section 4.2 was attributed to the weak ITZ.

Table 4: Statistical analysis using Student's t-test

Mix type 1	Mix type 2	Student's t-test results					
		Compressive strength				Density	
		7-days		28-days		28-days	
		p-value	Statistically significant differences	p-value	Statistically significant differences	p-value	Statistically significant differences
CC	PP100%	0.002	Yes	0.0003	Yes	0.0001	Yes
CC	PP100%-FA20%	0.002	Yes	0.0007	Yes	0.0002	Yes
PP100%	PP100%-FA20%	0.055	No	0.0515	No	0.3987	No

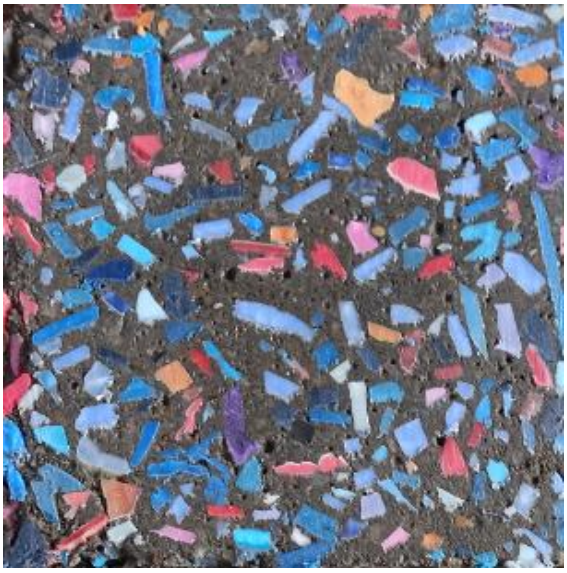

Figure 8: Cut surface of PP-modified concrete cube specimen (not to scale)

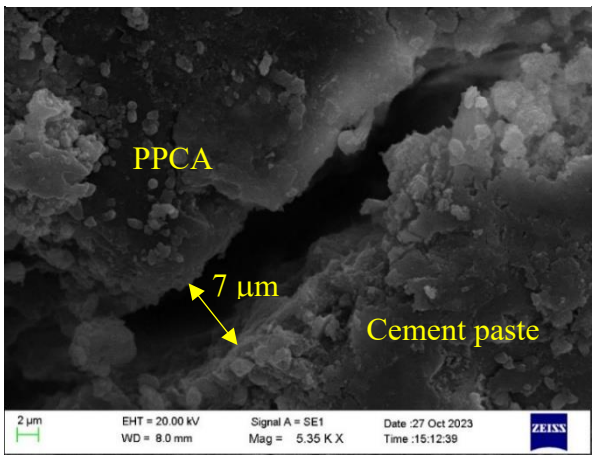

Figure 9: SEM image of ITZ between PPCA and cement paste [23]

4.9 Statistical analysis

The compressive strength and density of the different concrete mixes were statistically analyzed. A standard student's t-test was used to compare the values between groups, with significance assessed at the 95% confidence level ($p < 0.05$). The Excel's Data Analysis Toolpak was employed for the analysis. Here, pairwise comparisons (e.g. CC vs PP100%) were done as shown in Table 4. The statistical output: p-value < 0.05, indicates that the replacement of NCA with PPCA significantly reduced both compressive strength and density. The pairwise comparision confirmed that both 7-day and 28-day compressive strengths of the CC were significantly higher than those of the PC mixes (PP100% and PP100%-FA20%) at a 95% confidence level. Similarly, the densities of CC were significantly greater than the PP100% and PP100%-FA20% mixes. However, no statistically significant difference was observed between PP100% and PP100%-FA20% for strength or density ($p > 0.05$), indicating that the addition of 20% FA had limited influence on the stength reduction.

4.10 Durability aspects

NCAs are known for their long-term durability, demonstrating strong chemical and physical stability that supports the lifespan of concrete structures [34]. In contrast, PPCAs are non-corrosive and chemically stable, but they may experience slow degradation under prolonged exposure to heat or environmental conditions [32]. Nevertheless, its encapsulation within the concrete matrix significantly limits the degradation rate of PP, indicating that, PPCA can offer satisfactory durability performance, compared to NCA [35]. As most concrete structures are designed for 50 - 100 years of service life, the degradation rate of PP within concrete is expected to be minimal during the building's functional lifetime.

5. Conclusions

- The outcomes of this research show the potential of utilizing of waste plastic to produce sustainable concrete with a great lightweight aspect than traditional concrete. This approach not only helps prevent the environmental burdens of waste plastic but also leads to the development of a eco-friendly concrete.
- Further, this study demonstrates that the complete replacement of NCA with recycled PPCA is feasible for producing structural lightweight concrete. The mix achieved satisfactory workability, met the ASTM C330-05 strength and density requirements, and offers promising potential for lightweight structural applications (further investigation needed

for durability properties), particularly where dead load reduction is beneficial. The approach aligns with sustainable development goals and highlights an effective path for large-scale plastic waste reuse.

- The results demonstrated that the PP-modified concrete with 100% PPCA and 20% fly ash yields a 28-days compressive strength of about 20 MPa. Reaching this level of strength in lightweight concrete allows for the use of a relatively low cement content, limited to about 314 kg/m³.
- The incorporation of fly ash in the concrete mix offered the dual benefits of enhancing workability by 122% and reducing cement content by 20% by weight.

Acknowledgements

The financial support from the State Ministry of Skills Development, Vocational Education, Research, and Innovation of the Government of Sri Lanka (MSVRI/RES/03/07-12/2021) is greatly appreciated. Further, the Materials Laboratory at the Department of Civil Engineering, University of Peradeniya facilitated the experimental programme of this research. Special thanks are extended to the laboratory staff members for their support during the experimental work.

References

[1] PlasticsEurope. Plastics - the facts (2023). "Enabling the sustainable future", https://www.plasticseurope.org/

[2] Bekkeri, G. B., Shetty, K. K., & Nayak, G. (2023). "Synthesis of artificial aggregates and their impact on performance of concrete: a review". J Mater Cycles Waste Manag 2023; 25(4): 1988–2011. https://10.1007/s10163-023-01713-9.

[3] Amjad, H., Shah Zeb, M., Khushnood, R. A., et al. (2023). "Impacts of biomimetic self-healing of Lysinibacillus boronitolerans immobilized through recycled fine and coarse brick aggregates in concrete". J Build Eng 2023; 76: 107327. https://10.1016/j.jobe.2023.107327.

[4] Pavlık, Z., Pavlıkova, M., and Zaleska, M. (2019). "Properties of concrete with plastic polypropylene aggregates. Use of Recycled Plastics in Eco-Efficient Concrete".Woodhead Publishing Series in Civil and Structural Engineering, Elsevier, 2019, pp. 189–213. https://10.1016/b978-0-08-102676-2.00009-8.

[5] Ozbakkaloglu, T., Gu, L., and Gholampour, A. (2017). "Short-term mechanical properties of concrete containing recycled polypropylene coarse aggregates under ambient and elevated temperature". J Mater Civ Eng 2017; 29(10): 04017191. https://10.1061/(ASCE)MT.1943-5533.0002046.

[6] Faraj, R. H., Sherwani, A. F. H., and Daraei, A. (2019). "Mechanical, fracture and durability properties of selfcompacting high strength concrete containing recycled polypropylene plastic particles". J Build Eng 2019; 25: 100808. https://10.1016/j.jobe.2019.100808.

[7] Abu-Saleem M., Zhuge, Y., Hassanli, R., et al. (2021). "Evaluation of concrete performance with different types of recycled plastic waste for kerb application". Construct Build Mater 2021; 293: 123477. https://10.1016/j.conbuildmat.2021.123477.

[8] Islam, M. J., and Shahjalal, M. (2021). "Effect of polypropylene plastic on concrete properties as a partial replacement of stone and brick aggregate". Case Stud Constr Mater 2021; 15: e00627. https://10.1016/j.cscm.2021.e00627.

[9] Islam, M. J. (2022). "Comparative study of concrete with polypropylene and polyethylene terephthalate waste plastic as partial replacement of coarse aggregate". Adv Civ Eng 2022; 2022(1): 1–13. https://10.1155/2022/4928065.

[10] Faraj, R. H., Sherwani, A. F. H., Jafer, L. H., & Ibrahimm D. F. (2021). "Rheological behavior and fresh properties of selfcompacting high strength concrete containing recycled PP particles with fly ash and silica fume blended", Journal of Building Engineering. 34, 101667. https://10.1016/j.jobe.2020.101667

[11] Belmokaddem, M., Mahi, A., Senhadji, Y., et al. (2020). "Mechanical and physical properties and morphology of concrete containing plastic waste as aggregate". Construct Build Mater 2020; 257: 119559. https://10.1016/j.conbuildmat.2020.119559

[12] Naveen, D. C., Naresh, K., Keerthi Gowda, B. S., et al. (2022). "Effects of polypropylene waste addition as coarse aggregates in concrete: experimental characterization and statistical analysis". Adv Mater Sci Eng, pp. 1–11. https://10.1155/2022/7886722

[13] Purnomo, H., Putri, R. K., and Perdani, P. (2008). "Splitting tensile strength of lightweight concrete using polypropylene coarse aggregate coated with sand". IOP Conf Ser Mater Sci Eng 2019; 625:012008. https://10.1088/1757-899x/625/1/012008

[14] Purnomo, H, Baskoro, H, & Muslim, F. (2021). "Stress and Strain Behavior of Confined Lightweight Concrete using Sand Coated Polypropylene Coarse Aggregate". *International Journal of Technology, 12(6), 1261-1272.* https://ijtech.eng.ui.ac.id/article/vie0w/5195

[15] Purnomo, H., Chalid, M., Pamudji, G., & Arrifian, T., W. (2022). "Bond–slip relationship between sand-coated polypropylene coarse aggregate concrete and plain rebar", *Materials*, 15(7), 2643. https://www.mdpi.com/1996-1944/15/7/2643

[16] Purnomo, H., Pamudji, G., & Satim, M. (2017). "Influence of uncoated and coated plastic waste coarse aggregates to concrete compressive strength", *MATEC Web of Science*, 101, 01016. https://doi.org/10.1051/matecconf/201710101016

[17] Purnomo, H., Yuandry, A. R., & Tjahjono, E. (2018). "Direct Tensile Strength of Lightweight Concrete using Polypropylene Coarse Aggregate Coated with Sand", *Key Engineering Materials*, Vol. 789, pp. 131-136. https://www.scientific.net/KEM.789.131

[18] Gandjar, P., Bimasena, H., Yuta, P. A., &. Purnomo, H. (2018). "Bond-slip behavior of steel bar embedded in lightweight concrete using sand coated polypropylene coarse aggregate", *Materials Science Forum*, Vol. 929, pp. 103-108. https://www.scientific.net/MSF.929.103

[19] Gandjar, P., Haryanto, Y., Hu, H. T., Asriani, F., & Nugroho, L. (2021). "The flexural behavior of RC beams with sand-coated polypropylene waste coarse aggregate at different w/c ratios", *Advances in Materials,* 10(4). pp. 313-329. https://doi.org/10.12989/amr.2021.10.4.313

[20] Gandjar, P., Satim, M., Chalid, M. (2020). "The influence of river and volcanic sand as coatings on polypropylene waste coarse aggregate towards concrete compressive strength", *Jurnal Teknologi (Sciences & Engineering), 82(4).* https://doi.org/10.11113/jt.v82.14124

[21] Musalamah, S., Purnomo, H., & Handika, N. (2024). "Method for determining fracture energy of a polypropylene coarse lightweight aggregate concrete beam using Digital Image Correlation", *Engineering Proceedings*, 63(1), 19. https://www.mdpi.com/2673-4591/63/1/19

[22] Pelisser, F., Barcelos, A., Santos, D., Peterson, M., & Bernardin, A. M. (2012). "Lightweight concrete production with low Portland cement consumption, Journal of Cleaner Production", 23, 68e74. https://doi:10.1016/j.jclepro.2011.10.010

[23] Abirami, T., Bandara, C. S., Yapa, H. D., Dissanayake, P. B. R., (2024b). "Analysis of engineering performance of concrete comprising recycled crushed plastic waste and fly ash. Journal of Thermoplastic Composite Materials". 0(0). https://doi.org/10.1177/08927057241306430

[24] Abirami, T., Thilakarathna, K. G. D. I. H., Weragama, W. A. R. U., Bandara, C. S., Yapa, H. D., Dissanayake, P. B. R., (2024a). "Mechanical Properties of Green Concrete Containing

Polypropylene Plastic Waste", 517, pp. 117–130. https://doi.org/10.1007/978-981-97-3737-6_10

[25] Islam, M. J., Shahjalal, M. and Haque, N. M. A. (2022). "Mechanical and durability properties of concrete with recycled polypropylene waste plastic as a partial replacement of coarse aggregate. J Build Eng 2022; 54: 104597. https://10.1016/j.jobe.2022.104597

[26] Rumman, R., Kamal, M. R., Manzur, T., Noor, M. A., (2022). "Optimum proportion of fly ash or slag for resisting concrete deterioration due to carbonation and chloride ingress." Structures. Vol. 41, pp. 287-305. https://doi.org/10.1016/j.istruc.2022.04.087

[27] ASTM C330/C330M-05, (2005) "Standard Specification for Lightweight Aggregates for Structural Concrete." West Conshohock-en, ASTM International, 2005.

[28] ASTM C143/C143M-15, (2015) "Standard test method for slump of hydraulic-cement concrete", West Conshohock-en, ASTM International.

[29] European committee for standardization. (2003) Test for hardened concrete – Part 3: compressive strength of test specimens, EN 12 390-3, 2003.

[30] Kan, A., & Demirboğa, R. (2009). A novel material for lightweight concrete production. Cement and Concrete Composites, 31(7), 489–495. https://10.1016/j.cemconcomp.2009.05.002

[31] Standard test method for density, absorption, and voids in hardened concrete. West Conshohock-en, PA: ASTM C642/C642M-13, ASTM International, 2013.

[32] Frigione, M. (2010). Recycling of PET bottles as fine aggregate in concrete. Waste Management, 30(6), 1101–1106. https://doi.org/10.1016/j.wasman.2010.01.014

[33] ACI 213R-2014 (2014). Guide for Structural Lightweight-Aggregate Concrete, American Concrete Institute, Farmington Hills, ISBN:978-0-87031-897-9.

[34] Neville, A. M. and Brooks. (2010). Concrete Technology, New York, USA: Longman Scientific & Technical.

[35] Musa, A. E. S., Ahmed, A., Ahmad, S., Mohamed, K., Al-Fakih, A., & Al-Osta, M. A. (2025). "Properties of concrete incorporating plastic wastes and its applications: A comprehensive review", Journal of Building Engineering, 101, 111843. https://doi.org/10.1016/j.jobe.2025.111843

Study on Methods of Testing Tensile Strength of Concrete

Z R Dole[1], K Baskaran[1]

Abstract

Concrete is a brittle material in nature, having a low tensile strength; hence, indirect methods for testing the tensile strength of concrete are commonly used. This research aims to investigate the applicability of the Modified Direct Tension Test (MDTT) method for determining the tensile strength of concrete using direct axial force, and to compare its performance with that of the Brazilian Splitting Test and Cube Compression Test across different concrete ages and grades. The experimental procedure involved testing concrete grades C2 and C35 at 3, 7, 14, 28, and 56 days. Tensile strength values obtained from both methods are analysed and compared, alongside cube compression test results, to establish correlations between tensile and compressive strengths. The results suggest that the gain patterns of tensile strength versus compressive strength vary with time for both tensile strength testing methods. It was also found out that the novel method provides consistent results, and the specimen modification made to direct the tensile crack at the centre is successful in more than 80% of the cases. Practical applications for the MDTT are identified as Precast concrete evaluation, bridge and tunnel structural performance, and fibre reinforced concrete (FRC) and ultra- high-performance concrete (UHPC) strength and quality assessments. Modifications to be made to the testing apparatus are also discussed.

Keywords: Modified Direct Tension Test; Brazilian Splitting Test; Concrete Tensile Strength; Tensile Strength Development Pattern.

1. Introduction

The mechanical properties of concrete can be divided into tensile strength and compressive strength. Concrete is stronger in compression and weaker in tension due to the brittle behaviour of the material, and it is found that the concrete tensile strength is around 10% of its compressive strength within a given grade. The tensile strength of concrete is an important parameter for the function, durability, and safety of a concrete structure, as cracks often propagate due to the low tensile strength of concrete. These cracks occur due to either static loads or dynamic loads such as live loads or seismic activities like earthquakes, explosives, etc., and cracking of concrete due to tensile stress can be considered as the failure factor of a concrete structure; therefore, important to measure and know the tensile strength of concrete accurately.

The three main methods for testing tensile strength of concrete are the Direct Tension Test, Brazilian Splitting Test, and the Flexural Test. The Direct Tension Test shall be subjected to uniaxial loading and provide the direct tensile strength of concrete. Yet, there are shortcomings of this test due to the setup of the equipment, which may cause secondary bending moments and eccentric loadings on the tested specimens. The Flexural Test or the Modulus of Rupture and the Brazilian Splitting Test are indirect testing methods for the tensile strength of concrete. In the Flexural Test, the 3-point or 4-point bending assemblies are used to determine the tensile strength indirectly, in which the tensile strength on the bending line of the failure plane is measured. The Splitting Test may be conducted on a cubic or cylindrical specimen, where the tensile stress distribution is bound to be at the thin loading plane and has an irregular stress distribution across the cross-section. Also, both these tests provide results that deviate from the true tensile test by some factor. The age's influence on concrete's tensile strength requires more attention.

The main objective of this research is to experimentally investigate the behaviour of tensile strength at early ages of concrete and check the influence of the testing methods using Modified Direct Tension Test (MDTT) as a direct method and the BST as an indirect method. Other specific objectives are listed below.

- Analyse the behaviour of tensile strength of concrete at different ages using the modified Direct Tensile Test and the Brazilian Splitting Test.
- Examine the influence of the two testing methods on the tensile strength of concrete.
- Assess the feasibility and practical applicability of the modified direct tension test method as a substitute.

This research study intended to solely focus on the influence of the early ages of concrete on tensile strength by experimenting with the Direct Tensile Test and the Splitting Test at days 3, 7, 14, 28, and 56. The author intends to experiment with two different grades of concrete, grade C25 and C35. The following limitations of the study were identified.

- The study was limited to laboratory conditions, and the field conditions was not taken into account.
- Also, limited to the Direct Tensile Test and the Brazilian Splitting Test. Flexural tests and other novel methods of tensile testing for concrete were not focused.
- This study did not account for the varying concrete types, admixture types, or aggregate shapes and sizes.

Research studies that attempt to propose relationships between the results obtained by each main testing method and the true tensile strength have varying suggestions. Some of these proposals contradict the Eurocode 2 relationship in which the true tensile strength of concrete is

[1] Z. R. Dole, K. Baskaran: Department of Civil Engineering, University of Moratuwa, Sri Lanka (e-mail: zdolepro@gmail.com)

0.9 times the splitting tensile strength of concrete. The study conducted by Kazemi et al. [1] states that the ratio between the splitting test and flexural strength test against the direct tension test is 1.1 and 1.5, respectively. However, some studies present relationships somewhat closer to the Eurocode 2 relationship when the values obtained by direct tension test are assumed as closest to the uniaxial tensile strength of concrete. Tests carried out by Malarics & Muller [2] suggested a 0.9 conversion rate on splitting tensile test strength values to obtain the uniaxial tensile strength. The computer-aided investigation carried out in Wu et al. [3] observed an overestimation of 5-7% by the splitting tensile test values against the values of the direct tension test. Studies conducted in Mujika [4] and Kazemi et al. [1] emphasize the flexural strength test's drawback in overestimating the true tensile strength value by factors exceeding 1.5. There exist many types of research that favour the Brazilian splitting test over other main testing methods. Min et al. [5] on strain rate dependency on tensile strength testing, Dean et al. [6] on ASTM standard methods of splitting tests, Goaiz et al. [7] on tensile strength variation of SFRC, Choi & Yuan [8] on splitting test and compressive test relationship on Glass Fiber Reinforced Concrete (GFRC) and Polymer Fiber Reinforced Concrete (PFRC) are some studies conducted that favour the splitting test of concrete. Even though the splitting test is an indirect method of measuring the tensile strength of concrete, the overestimation in the values obtained is mostly consistent and has a lower variance in results, the ease of the testing setup and preparation make it a better testing method for building empirical relationships to the true tensile strength.

Novel methods of testing the tensile strength of concrete attempt to overcome the common drawbacks of the main methods, such as gripping issues and asymmetrical forming of tensile stresses in direct tension tests, irregular stress distributions of splitting tests and flexural tests, and crack forming location, etc. Methods such as the cylinder transverse method by Chai et al. [9] to overcome the crack occurrence location issue, and the strut-and-tie methods by Liao et al. [10], Resan et al. [11] show promising results, yet their feasibility in practically implementing these methods for a tensile test check is questionable due to the complicated setups.

Khan [12] and Alhussainy et al. [13] experimented with the direct tensile test with the inclusion of embedded steel rods in the concrete specimen and each adding circular and triangular notches, respectively at the mid-height of the specimens to direct the crack occurrence. The results obtained have been consistent and worth further investigation. Literature on tensile strength gain of early-age concrete suggests that the tensile strength gain pattern differs from the compressive strength gain pattern and contradicts the relationship mentioned in Eurocode 2 [14]. Studies conducted by Ahmed et al. [15], Badarloo et al. [16], and Swaddiwudhipong [17] provide proof of this contradiction.

2. Methodology

The materials used for the concrete mixture were cement, sand as fine aggregates, crushed stone as coarse aggregates, and water as given in Table 1. The cement used for both grades of concrete mixtures was Blended Hydraulic Cement (BHC), which was blended with Portland Fly Ash. The strength of the cement was 42.5 N. The sand volume used as fine aggregates was river sand. Coarse aggregates were obtained as crushed stone gathered from a local rock quarry, which has a minimum passing percentage of 90% through the 20 mm sieve by the time it was delivered from the quarry. Local tap water was used as the water source for the concrete mixture, originating from the Ambathale or Kalatuwawa water treatment plants.

Table 1: Mix Proportions for each grade (in kg/m^3)

	Cement	Water	Fine Aggregates	Coarse Aggregates
Grade 25	355	205	852	1000
Grade 35	400	205	830	975

The sieve analysis for both coarse and fine aggregates was conducted following BS 812, and the selection of sieve sizes and passing percentages was determined in accordance with BS 882: 1992. The percentage of fine aggregates passing through the 600 µm sieve is 42%. The three types of tests conducted on concrete are as follows.

1. Modified Direct Tension Test (MDTT)
2. Brazilian Splitting Test (BST)
3. Cube Compression Test (CCT)

The specimen shape for the Modified Direct Tension Test, as shown in Figure 1, is a 300 mm long rectangular prism consisting of a 100 mm x 100 mm square-shaped cross section. At only two opposite faces in the longitudinal direction of the prism consists of a triangular-shaped notch at midspan to direct the tensile crack towards the midspan, which is 7.5 mm deep and 20 mm long, making the cross-sectional dimensions at midspan 100 mm x 85 mm. The specimen would also consist of two 10 mm diameter rods made out of ribbed bar that is 200 mm in length. 115 mm length of the rod will be submerged into the concrete through the center at each square face end. The submerged end of the rods consists of two 6 mm diameter, 75 mm long rods, each making a right-angle cross. This mechanism of rods would facilitate the pulling action of the concrete prism to create tension and direct the crack at midspan. The mould to replicate this specific shape of the concrete prism was custom prepared using 2 mm thick steel plates. The pouring face of the mould is selected as one of the rectangular faces that is 85 mm in width at the midspan (the long rectangular face that does not contribute as a notch at midspan) The specimen size for the Brazilian Splitting Test (BST) was taken as a cylinder of length 200 mm and 100 mm diameter as specified in the ASTM C496. The specimen sizes for the Cube Compression Test were taken as 100 mm x 100 mm x 100 mm cubes as specified in BS EN 12390-3. Standard, specified-sized moulds for BST and CCT tests were readily available in the laboratory.

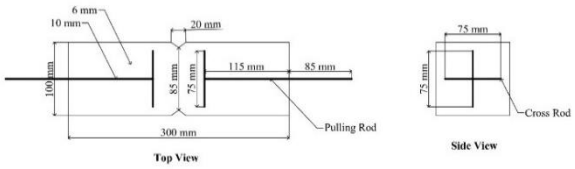

Figure 1: Dimensions of the Specimen for MDTT

For each type of test, two specimens each were cast for a single concrete grade and each concrete age of 3, 7, 14, 28, and 56 days, and the same number of specimens for the next concrete grade. The mixing of the concrete was done in accordance with BS 1881: Part 125: standard for method of mixing and testing concrete in the laboratory, and the drum mixer was used for the mixing of the concrete. The casted specimens were left for hardening for 24 hours and demoulded, where the specimens will be submerged in curing tanks until the test date. Figure 2 show some specimens during the casting phase.

Figure 2: Specimen cast for each MDTT, BST, and CCT tests

The Universal Testing Machine was used to conduct the MDTT, in which the rods inserted at both ends of the concrete prism specimen were used to hold the specimen from the top and bottom. Once the machine starts to pull the rods in the opposite directions, a crack is expected to be generated at the notch location at midspan of the rectangular prism, and the occurrence of this crack generation is considered the failure load. The rate of strain used for this test is 20 mm per minute. The BST and CCT tests were conducted according to ASTM C496 and BS EN 12390-3 standards, respectively. Both types of tests were conducted using the compression testing machine. The loading rate for both tests was 6 kN/s. Figure 3 is a representation of the three types of testing carried out during the experimental work

a) MDTT done using the Universal Testing Machine

b) BST and CCT done using the Compression Testing Machine

Figure 3: Testing done on specimens

3. Results and Discussion

The equations used to derive the tensile strength values from the MDTT and BST methods and the compressive strength values from the CCT are as follows. F denotes the load at failure.

$$\sigma_{MDTT} = \frac{F}{A} \quad (1)$$

Where; σ_{MDTT}: Pulling strength of concrete prism
A: Cross-sectional area of the failure location

$$\sigma_{BST} = \frac{2F}{\pi LD} \quad (2)$$

Where, σ_{BST}: Splitting Tensile strength of concrete
L: Length of the concrete cylinder
D: Diameter of the concrete cylinder

$$\sigma_{CCT} = \frac{F}{w \times l.} \quad (3)$$

Where, σ_{CCT}: Crushing (compressive) strength of the concrete cube
l: Length of the crushing face of the cube
w: Width of the crushing face of the cube

The below given Table 2, Table 3, and Table 4 tabulate the results obtained for MDTT, BST, and CCT, for different samples for the 2 grades examined at different early concrete ages. The result denoted under 14 days for grade 25 concrete in Table 3, represents a specimen that failed due to the failure of the pulling rod, hence, Failure By Bar (FBB).

Figure 4 and Figure 5 represent the variation of tensile strength values obtained from MDTT and BST for concrete grades 25 and 35, and their variation with progression of early ages of concrete. The trendlines drawn for both graphs are based on logarithmic variation to closely fit the progression of the values. In Figure 4, the trendlines drawn for both MDTT and BST are spread closely on top of each other with slight variations. Even though the $R^2 = 0.975$ for MDTT test results, and 0.8963 for BST test results, which represent the spread of the test results obtained, point towards MDTT test results being more consistent with the tensile strength values compared to BST test results. In Figure 5, a similar behaviour on the spread of results can be observed, where the $R^2 = 0.9416$ for MDTT strength values, while $R^2 = 0.8849$ for BST test results further signifying the consistency of results of MDTT over BST tensile strength values for both concrete grades 25 and 35. Another observation is that the trendline for BST falls above the trendline for MDTT up until day 7-10, but crosses and continues to stay below past that. This behaviour is vividly displayed in the concrete grade 35 but not very observable in the grade 25 graph. It can be argued that in the initial week, when concrete strength is low, most of the pulling strength is taken by the pulling rod itself during the MDTT experiments. Once it reaches a certain age where the concrete has gained enough strength, most of the pulling load is taken straight away by the concrete itself without leaving much involvement by the rod. The grade 35 concrete, in these experiments, was strong enough to exploit this behaviour past a certain age, which was not visible in tensile strength results for grade 25 concrete.

Table 2: Results obtained from MDTT

	Grade 25		Grade 35	
Age (Days)	Failure load kN	Stress N/mm^2	Failure load kN	Stress N/mm^2
3	4.55	0.516	9.3	1.087
	4.65	0.533	9.35	1.073
7	9.7	1.166	12.5	1.524
	9.25	1.079	13.55	1.568
14	9.45 (FBB)		16	1.865
	15	1.846	18.75	2.204
28	19.15	2.298	26.75	3.149
	22.05	2.522	26.5	3.048
56	21.15	2.566	27.3	3.209
	25.9	2.978	27	3.210

Table 3: Results obtained from BST

	Grade 25		Grade 35	
Age (Days)	Failure load kN	Stress N/mm^2	Failure load kN	Stress N/mm^2
3	16.3	0.514	25.8	0.817
	13.6	0.430	28	0.891
7	26.2	0.848	52	1.666
	33.4	1.061	46.8	1.501
14	67.6	2.138	65.2	2.067
	53.5	1.689	62.9	2.021
28	87.7	2.796	108.2	3.493
	68.8	2.203	124.6	3.950
56	88.8	2.792	124.6	4.000
	75.1	2.392	101.2	3.228
	89.7	2.773		

Table 4: Results obtained from CCT

	Grade 25		Grade 35	
Age (Days)	Failure load kN	Stress N/mm^2	Failure load kN	Stress N/mm^2
3	60.3	5.906	104.2	10.155
	60.9	5.894	100.1	9.678
7	138.5	13.892	191.4	19.450
	151.5	15.120	156.4	15.609
14	208.5	20.339	297.4	28.961
	225.6	21.941	233.9	23.159
28	230.4	22.770	287.7	28.260
	272.6	26.915	342.0	34.269
56	280.4	27.408	362.5	36.327
	275.6	26.751	350.8	34.909

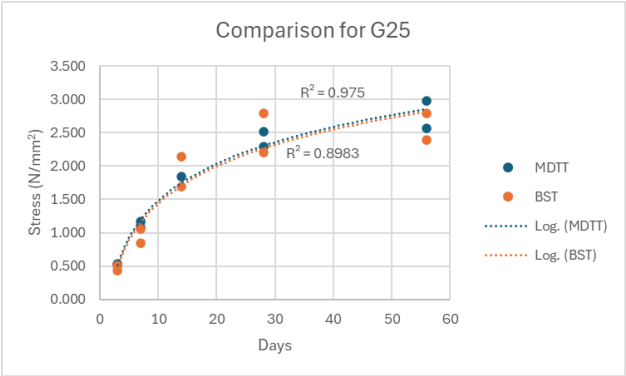

Figure 4: Comparison of Tensile Strength Values from MDTT and BST for Grade 25

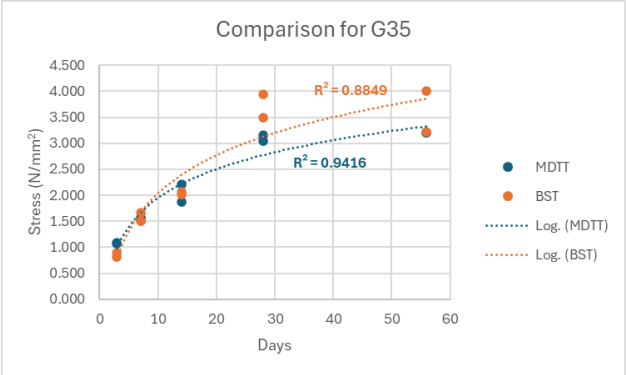

Figure 5: Comparison of Tensile Strength Values from MDTT and BST for Grade 35

Figure 6 showcases the ratios between MDTT and BST tensile strength values for both concrete grades 25 and 35 as the progression of early ages. In almost all cases of grade 25 concrete, the MDTT/BST ratio is above 1.000, meaning that the MDTT tensile strength values represent higher tensile strength than the BST tensile strength values. A vague decline in the ratio can be observed as the age of concrete increases in both concrete grades. In the case of grade 35 concrete, the MDTT ratio is above 1.00 only until day 14. Still, it drops below 1.00 at later ages, signifying the underestimation of tensile strength values obtained using MDTT against BST.

The tensile/compressive strength ratio varies between 1/10 to 1/12 as per Popovics S. (1967). It is expected to validate this conclusion based on the experimental results obtained for MDTT and BST and compare with the separately carried out CCT results. The compressive strength values obtained from CCT is displayed in Figure 7.

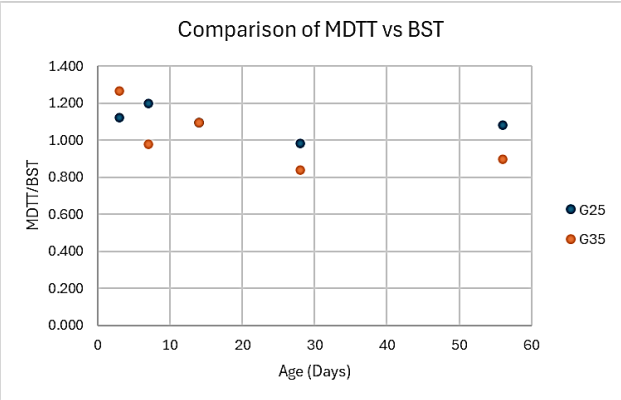

Figure 6: Ratios between MDTT and BST tensile strength value results

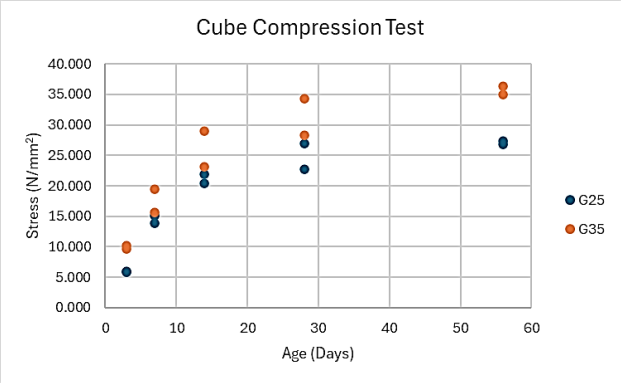

Figure 7: Variation of CCT strength values over age

Figure 8 and Figure 9 represent the ratios of MDTT and BST over CCT strength values, respectively. In Figure 8, the trendline drawn for G25 varies between 0.085 and 0.105, and G35 varies between 0.095 and 0.09 over a 3—to 56-day period. In Figure 8, the red line for G25 varies between 0.09 to 0.11, and for G35 it varies between 0.08 to 0.105. Both the trendlines in Figure 9 maintain a similar gradient in trendlines. The test results for BST imply that the tensile strength value obtained from BST varies with time at a different rate compared to the compression strength of concrete. This observation is noticed again in the MDTT vs CCT for G25 also, but when moved onto G35, the trendline flattened, implying that the test results for MDTT vary at a constant rate with time as the compression strength as the strength grade of the concrete increases.

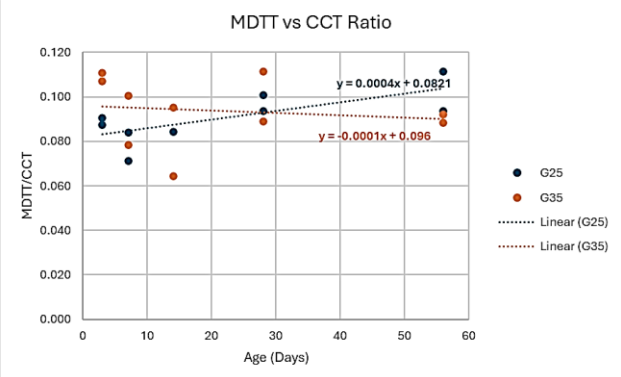

Figure 8: Variation of the MDTT ratio over CCT

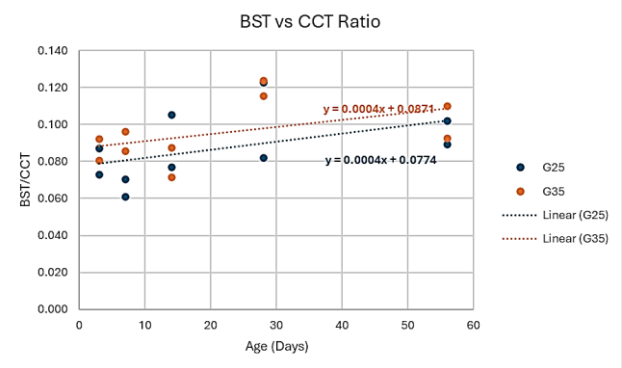

Figure 9: Variation of the BST ratio over CCT

The mode of failure for the specimens prepared for the MDTT was by initial cracking due to tensile action and followed by separation of the specimen from the area of the crack occurrence, which is displayed in Figure 10. Out of the 20 specimens tested for MDTT, 17 of them were separated exactly from the location of the notch at the centre of the specimen, as expected. Although 3 specimens happened to crack and fail away from the notch, recorded as outliers. It was also noticed that in all outliers, the crack occurred above the notch area, lining close to the location of the cross-handle of the upper pulling rod. A quick inspection of the failure pattern of the particular cross-section revealed that the buildup of voids between the cross-handle of the pulling rod and the concrete created a weak cross-section at the surface of the bottom side of the cross-handle. This behavior can be observed in Figure 11.

a) Normal crack location at Notch

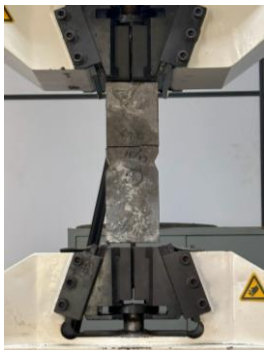

b) Outlier crack location above notch

Figure 10: Failure locations of MDTT Specimens

Figure 11: Failure cross-section of Outliers

As shown in Figure 12, the cylindrical concrete specimens subjected to BST were split along the diameter in the vertical direction in all cases. The surface of the failure plane was homogeneous and regular. The cube concrete specimens underwent CCT, failed mostly due to crushing.

Figure 12: Failure plane of BST specimens

[13] setup of direct tension test done with a similar pulling rod included specimen mechanism concluded that the Normal Strength Concrete, which had an average cylindrical compressive strength of 39 N/mm^2 (Hence around 50 N/mm^2 of cubic compressive strength), had reductions around 10% in the tensile strength values compared to the splitting test values. The recorded tensile strength values using the direct tension test had a ratio of 0.08 against the compressive strength, implying that the ratio between results for the splitting tensile strength test and the compressive strength tests is around 0.09. In this study, both ratios of MDTT vs CCT and BST vs CCT provided a value of around 0.09, hence closely validating the results of the above study. In the case of [12], the test results produced an R^2 value of 0.81, which implies a lesser consistency in test results compared to the test results obtained in this study. Key differences in the specimens of [12] and this study are the increment of submerged depth of pulling rods further into the specimens and including a prismatic notch instead of the circular notch. The Eurocode 2 interpretation of using a simple basic conversion from compressive strength to tensile strength without considering the age of concrete has been challenged by the results obtained using both MDTT and BST test results.

Applications for MDTT

The MDTT can be used to test the tensile strength of concrete, as mentioned in this study, prior to the construction of concrete structures. The application is more ideal for Precast concrete structures where the MDTT setup can be used to determine the tensile strength of the concrete mix that is about to be used for the construction of a particular precast structure. The MDTT method can be applied for structural performance monitoring of bridges and tunnels. A core can be extracted from an existing structure that requires monitoring. The size of the core can be as specified in this study. The obtained core specimen will be shaped at midspan to create a notch, and pulling rods can be inserted into these extracted cores by drilling. Another possible application of MDTT is Fiber-Reinforced Concrete (FRC) & Ultra-High Performance Concrete (UHPC) Validation.

Limitations of MDTT

The proposed MDTT method requires precise alignment during casting and pulling actions to avoid eccentric loading. The MDTT method carried out in this study can be complex to be conducted in a routine site test hence requires the need for improvement to a practical setup. Also, the diameter of the pulling rods must be adequate enough to avoid premature failure in the pulling rods.

4. Conclusions and Recommendations

The following conclusions are being made after conducting the experimental work and the analysis of the results.

- The key issues with the traditional methods for testing tensile strength of concrete have been identified, and a novel method known as MDTT has been introduced, considering past similar setups, and improvements have been made.
- The novel method known as MDTT provides consistent tensile strength results compared to the Brazilian Splitting Test.
- The method used to direct the crack formation to the middle by applying a notch to the specimens in MDTT was found to be a success in more than 80% of the cases in the present study.
- Experimental results from both MDTT and BST suggest that the tensile strength values vary with time at early ages of concrete at a different rate when compared to the compressive strength test results obtained from CCT
- Comparison with past attempts and their results at a similar setup for the MDTT method and improvements made in this study suggest that MDTT can be used as a valid method for testing the tensile strength of concrete.
- Precast concrete quality testing, existing bridge and tunnel performance monitoring, and Fiber-Reinforced Concrete and UHPC quality checking have been identified as some applications where the MDTT method can be incorporated.

The following recommendations can be made to further improve the quality of the MDTT method and validation for practical use in the industry.

- Incorporate the Flexural Strength Test to further broaden the comparison of results to formulate a relationship with MDTT.
- Carry out more test cases for MDTT with a higher number of specimens and a wider range of concrete strength grades to correctly formulate factors and equations for the tensile strength of concrete.
- Check the significance of strain rate in the MDTT method and come up with a value to measure the most optimal results.
- Make attempts to practically try out the applications mentioned in the case study for MDTT.
- Improve the MDTT method in a manner accessible for routine site testing.

References

[1] M. Kazemi, R. Madandoust, and S. Yousefi Moghadam, “Studiu analitic asupra rezistenței la întindere a betonului - Analytical study on tensile strength of concrete,” 2017. [Online]. Available: https://www.researchgate.net/publication/318506827

[2] V. Malarics and H. S. Muller, “Evaluation of the splitting tension test for concrete from a fracture mechanical point of view,” 2010 Korea Concrete Institute, Seoul, Apr. 2010.

[3] Z. Wu, J. Zhang, H. Yu, Q. Wu, and B. Da, “Computer-aided investigation of the tensile behavior of concrete: Relationship between direct and splitting tensile strength,” *Structures*, vol. 55, pp. 453–467, Apr. 2023, doi: 10.1016/j.istruc.2023.06.019.

[4] F. Mujika, “On the difference between flexural moduli obtained by three-point and four-point bending tests,” *Polym Test*, vol. 25, pp. 214–220, Apr. 2006, doi: 10.1016/j.polymertesting.2005.10.006.

[5] F. Min, Z. Yao, and T. Jiang, “Experimental and Numerical Study on Tensile Strength of Concrete under Different Strain Rates,” *The Scientific World Journal*, vol. 2014, pp. 1–11, 2014, doi: 10.1155/2014/173531.

[6] S. W. Dean, C. K. Parker, J. E. Tanner, and J. L. Varela, “Evaluation of ASTM Methods to Determine Splitting Tensile Strength in Concrete, Masonry, and Autoclaved Aerated Concrete,” *J ASTM Int*, vol. 4, no. 2, p. 100446, 2007, doi: 10.1520/jai100446.

[7] H. A. Goaiz, N. A. Farhan, M. N. Sheikh, T. Yu, and M. N. S. Hadi, “Experimental evaluation of tensile strength test methods for steel fibre-reinforced concrete,” *Magazine of Concrete Research*, vol. 71, no. 8, pp. 385–394, 2019, doi: 10.1680/jmacr.17.00516.

[8] Y. Choi and R. L. Yuan, “Experimental relationship between splitting tensile strength and compressive strength of GFRC and PFRC,” *Cem Concr Res*, vol. 35, no. 8, pp. 1587–1591, 2005, doi: 10.1016/j.cemconres.2004.09.010.

[9] Q. Chai, S. Huang, F. Wan, F. Wu, and F. Liu, “A new experimental method to measure and calculate the tensile strength of concrete,” *Front Mater*, vol. 10, 2023, doi: 10.3389/fmats.2023.1216747.

[10] W.-C. Liao, P.-S. Chen, C.-W. Hung, and S. K. Wagh, “An Innovative Test Method for Tensile Strength of Concrete by Applying the Strut-and-Tie Methodology,” *Materials*, vol. 13, no. 12, p. 2776, 2020, doi: 10.3390/ma13122776.

[11] S. F. Resan, S. M. Chassib, S. K. Zemam, and M. J. Madhi, “New approach of concrete tensile strength test,” *Case Studies in Construction Materials*, vol. 12, p. e00347, Apr. 2020, doi: 10.1016/j.cscm.2020.e00347.

[12] M. I. Khan, “Direct tensile strength measurement of concrete,” in *Applied Mechanics and Materials*, 2012, pp. 9–14. doi: 10.4028/www.scientific.net/AMM.117-119.9.

[13] F. Alhussainy, H. A. Hasan, M. N. Sheikh, and M. N. S. Hadi, “A New Method for Direct Tensile Testing of Concrete,” *J Test Eval*, vol. 47, no. 2, p. 20170067, 2018, doi: 10.1520/jte20170067.

[14] B. S. Institution, *Eurocode 2 : design of concrete structures*. British Standards Institution, 2004.

[15] M. Ahmed, J. Mallick, and M. Abul Hasan, “A study of factors affecting the flexural tensile strength of concrete,” *Journal of King Saud University - Engineering Sciences*, vol. 28, no. 2, pp. 147–156, Jul. 2016, doi: 10.1016/j.jksues.2014.04.001.

[16] B. Badarloo, A. Kari, and F. Jafari, “Experimental And Numerical Study To Determine The Relationship Between Tensile Strength And Compressive Strength Of Concrete,” *Civil Engineering Journal*, vol. 4, no. 11, p. 2787, 2018, doi: 10.28991/cej-03091198.

[17] S. Swaddiwudhipong, H.-R. Lu, and T.-H. Wee, “Direct tension test and tensile strain capacity of concrete at early age,” *Cem Concr Res*, vol. 33, pp. 2077–2084, Apr. 2003, doi: 10.1016/s0008-8846(03)00231-x.

Design and application of a small-scale test method for façade fire testing

W V C Fernando[1], R S S Ranasinghe[1] and T G P L Weerasinghe[1]

Abstract

Façades are important for keeping a building safe during a fire. The fire can spread quickly if they fail, causing serious damage to the structure as well as the occupants. Therefore, façade fire testing is necessary for the evaluation of façade fire performance before they are fixed to a building. The rising fire hazards have increased stakeholders' concerns, requiring the adoption of effective fire-safe design practices. International standards offer accurate, full-scale testing procedures, which are challenging to apply in developing countries like Sri Lanka due to high costs, facility constraints, and technical limitations. This study presents a bespoke, small -scale test method for façade fire testing. Adhering to ISO 13785, which demonstrates a mid-scale façade fire test, we scaled down and performed two façade fire tests as case studies. A façade panel configuration with a combustible core was used for the fire test. The panel was prepared mainly using two aluminum sheets, each 4 mm thick, with a 50 mm polyethylene core sandwiched in between. A regular LP gas burner was used to ignite the fire, and 8 thermocouples were positioned on the specimen to record how temperatures changed over time.

To simulate the performance of the small-scale façade fire test we performed, we constructed a numerical model using Fire Dynamics Simulator (FDS) based software. The same conditions were applied to the numerical model,and performance was compared with the case studies. Correlation between the simulation results and experimental data are within acceptable limits. The results of this research will encourage the adaptation of small-scale tests before doing a full-scale test, as it can predict the fire performance of the façade with limited resources. As such, based on such small-scale testing, stakeholders can decide whether the tested panel needs any improvements before the full-scale test.

Keywords: Façades, Fire, Building, Façade fire test, FDS, Numerical model

1. Introduction

Façades have evolved from simple exteriors to stylish, multi-functional elements of modern buildings. Façades are widely used to protect buildings from wind, rain, and sunlight, making them an important part of modern architecture [1]. In a stage of sustainability and innovation, facades are designed to regulate temperature, reduce environmental impact, and protect buildings from outside environments. Additionally, the building's façade is designed for aesthetics and energy efficiency, making it an essential part of green building and zero-carbon efforts [2]. However, as these systems become more complex, the challenges to their safety, especially in the growing number of tall buildings, have increased. Fires involving the façade of buildings represent a significant and modern challenge in fire safety [3]. The façade of a building is particularly vulnerable to damage during a fire [4]. Fire safety measures are typically tracked by appearance, energy efficiency, material selection, and durability. The challenge has been further complicated by the rise of tall buildings, which increases the potential for fire hazards [1]. With evolving architectural trends, there has been increased use of complicated, multi-layered facade systems using new and often combustible materials [1], [5], [6]. They offer aesthetic and thermal performance benefits, but also create fire safety issues, particularly with their potential for fire spread vertically on building facades. More and more global fire disasters, such as the 2017 United Kingdom Grenfell Tower fire [7] highlighted the need for stringent testing of facade fire performance [6]. Such incidents have raised global concern and created a high level of critical need to understand the fire risks associated with building façades [8].

The fire performance of façade systems is greatly influenced by the materials used in their construction and the various factors that affect how these materials behave during a fire. Different materials exhibit different characteristics in terms of flammability, thermal resistance, and structural integrity, and many other factors contribute to the fire performance of the entire façade system [9]. External factors such as wind conditions, fire source type, and compartment openings can also affect fire spread and intensity [10].

Material selection is an important determinant of a façade's response to fire. Non-combustible materials such as stone, concrete, and wrought iron are generally preferred because of their high fire resistance [3]. These features provide stability to the structure and act as a barrier against the spread of flames. Studies have shown that concrete and steel facades exhibit greater thermal resistance compared to combustible materials such as aluminum composite panels (ACP), which have been involved in many high-profile façade fires, including the Grenfell Tower fire [4], [5]. Aluminum panels, especially those with a polyethylene

[1] W.V.C. Fernando, R.S.S. Ranasinghe & T.G.P.L. Weerasinghe: Department of Civil Engineering, University of Moratuwa, Sri Lanka. (e-mail: viranchanuka@gmail.com, rochanasheshan@gmail.com, wwpasindu@gmail.com/ pasinduw@uom.lk)

core, are highly flammable and can contribute to the rapid spread of fire on the exterior of a building.

In addition to material selection and mechanical stability, various external factors can affect façade fire performance. For example, wind conditions can accelerate the spread of façade fires by delivering excess oxygen to the flames and pushing them toward upper stories [11], [12]. The fire source, such as the initial ignition point, is also of critical importance in the rate of fire spread. A fire that starts inside a building can spread through windows or other openings to the façade, causing flames to spread to the building's exterior. Once the fire reaches the façade, combustion products can act as additional fuel, allowing the flames to spread rapidly and vertically [10], [13].

Notable fire incidents such as the 2010 Shanghai Jing'an fire, the 2015 Dubai Address Tower fire, and the 2017 Grenfell Tower fire, which were discussed in the introduction, have been frequently improved by the materials and designs utilized in modern construction, focusing on the urgent need to study fire protection measures. For a long time, the approach to evaluating the performance of façade systems primarily focused on assessing the combustibility of individual materials [4], [8], [13]. However, according to Li et al. [2], such material fire tests are now recognized as inadequate for evaluating façade components, complete façade systems, or their overall reaction to fire. Regulatory bodies worldwide gradually acknowledge the need for up-to-date requirements and codes that mirror the state-of-the-art advancements in façade fire safety. This involves undertaking comprehensive reviews of existing policies and actively searching for input from stakeholders, together with engineers, architects, manufacturers, and fire protection professionals. The intention is to make sure that safety measures remain applicable and effective in the face of evolving production practices and developing technology.

To address this concern, numerous global requirements, which include BS8414, ISO 13785, AS 5113and NFPA 285, advise thorough full-scale façade fire tests as a method of comparing the fire performance of systems before creation [5], [14], [15]. Standards such as ISO 13785-2 [16], BS 8414-1/2 [17] and NFPA 285 [18] have been developed to evaluate the performance of external wall assemblies during fire exposure. These full-scale tests are meant to mimic realistic fire conditions and quantify important parameters like flame spread, heat release, smoke production, and structural behavior. NFPA 285, for instance, employs a two-story test arrangement with an ignition source under controlled conditions placed in a lower compartment to subject fire spread along windows and the facade to testing [18]. These standardized procedures permit a consistent and comprehensive observation of how different facade systems behave against fire exposure.

Despite effectiveness, full-scale fire tests are costly. Full-scale fire testing requires specialized premises, experienced engineers, and substantial financial investment [19]. Many developing countries, including Sri Lanka, thus have serious constraints for adopting these massive-scale methods. The local construction industry does not typically possess the infrastructure to conduct these analyses, thereby leading to over-reliance on foreign test data or highly conservative design approaches [19]. Over-reliance can result in costly overdesigns or inadequately assessed systems that compromise safety. These problems are further compounded by the absence of local standards and the unavailability of technical expertise in fire dynamics [20], [21].

In Sri Lanka, rapid modernization of the construction industry has increased the share of prefabricated cladding panels, new insulation products, and modern methods of construction (MMC) [21]. But regulatory and fire safety practices have fallen behind these developments. New design practices often do not account for the unique fire behavior traits of such new systems. Besides, building envelopes in tropical climates such as Sri Lanka frequently feature ventilated cavities and combustible cladding components with important effects on flame spread behavior [20]. Thus, there is great demand for tools specific to the context that can assess facade fire performance at low test costs and logistical inconvenience of full-scale testing.

One solution in the process is integrating small-scale fire testing with numerical simulation techniques. This approach allows one to conduct understandable and accessible experiments while depending on simulation hardware to extrapolate the results towards predicting full-scale behavior [22]. Small-scale testing may assist in providing relevant performance parameters such as ignition time, flame spread rate, heat release rate, and peak surface temperature. These values may then be plugged into fire codes such as PyroSim, a graphical interface to the Fire Dynamics Simulator (FDS), to simulate fire behavior under different facade designs [22], [23].

PyroSim and FDS offer users the ability to build high-accuracy fire simulations from empirical input. Through explicit specification of material properties, shape, fire source properties, and boundary conditions, researchers can design a virtual facade fire experiment of very high spatial and temporal resolution [23]. They can utilize calibrated simulations, by which experiments provide the reference dataset, as strong predictive tools thereafter. In addition to reducing full-scale test needs, these make it possible to analyze more expansive sets of fire scenarios and design variables for analysis by engineers. This performance-based methodology through simulation is particularly valuable in resource-constrained settings like Sri Lanka, where it is crucial to develop an economically feasible and scientifically valid methodology.

Globally, the fire safety profession is increasingly embracing performance-based design methodologies. These methodologies are founded on measurable performance criteria rather than prescriptive requirements, offering more flexibility in achieving safety objectives [24], [25]This is especially important in skyscraper city complexes, where facades not only need to meet aesthetic and thermal performance standards but also be adequate for fire resistance. Incorporation of fire-safe design into broader urban sustainability objectives is essential to achieving the United Nations' Sustainable Development

Goals (SDGs), particularly Goal 11, to make cities inclusive, safe, resilient, and sustainable [25], [26].

This study aims to develop a simulation-based small-scale test procedure for assessing the fire performance of cladding systems commonly used in mid- and high-rise buildings in Sri Lanka. It offers a locally viable solution, diminishing reliance on foreign test results and conservatism, which can lead to more cost-effective and safer fire safety designs. A standard cladding system will be selected based on material availability and common usage, and a small-scale test rig will simulate realistic fire conditions. Key performance criteria such as ignition delay, flame spread rate, peak temperatures, and structural deformation will be monitored.

These experimental results will then be used to validate a numerical model in PyroSim, which will simulate various fire conditions and material combinations. Simulation outputs will be checked against experimental results to measure the model's predictability. The research will determine if small-scale test-informed simulation models can make good predictions of facade system performance under conditions of large-scale fires, as well as their strengths and weaknesses. Findings will guide how to use the method optimally in Sri Lankan practice to respond to local requirements for fire safety design and remain aligned with global best practices.

1.1. Testing Methodologies and Regulatory Standards

Facade fire safety analysis is necessary in modern building design, particularly because construction nowadays involves complex materials and multi-layer systems. The two principal codes in the United States are the International Building Code (IBC) and the NFPA Building Construction and Safety Code, of which the IBC is the most widely utilized. These codes mandate that the new buildings be constructed to meet some basic performance criteria, like structural stability, weather tightness, aesthetic appeal, energy conservation, and fire safety [27]. Foam plastic insulation, while an excellent energy insulator, presents serious fire risks unless tested and demonstrated to be fire-safe. Their importance took shape in 2017, with the incidence of a horrific fire in London due to flammable outside cladding that killed 71 people and caused several injuries. In this horrific tragedy, the fatal outcome highlighted serious shortcomings in the compliance nature of fire safety. The cladding system in this case presumably did not meet both British and U.S. code specifications [27].

These checks provide an important insight into how numerous façade structures respond to fire, assisting in saving from catastrophic failures and enhancing typical building safety. However, large-scale façade fire test setups, procedures, and acceptance criteria differ across countries, leading to variations in testing standards and safety regulations [28]. Comparison of results from standard fire tests is often challenging, as the same façade specimen may give significantly different results and rates depending on the test standard used, e.g. sample passing NFPA 285 testing in the US. does not require BS 8414-1 testing in the UK [2]. Table 1 showcases a summary of test standards which used in several countries for testing façade fire performance. The summary provides whether those tests are full scale, intermediate scale.

Table 1: Façade Fire Tests

Country	Test Method	Test Scale
USA	NFPA 285(+ ASTM E84)	Full
Canada	ULC S134	Full
France	Lepir II28	Full
Germany	DIN 4102 Part 2029	Full
Sweden	SP Fire 10527	Full
UK	BS 8414-15	Full
EU	EN 1382330	Intermediate
ISO	ISO 13785-231	Full
ISO	ISO 13784-132	Intermediate
ISO	ISO 13784-233	Full/Intermediate
USA	FM 4880(25 ft. and 50.ft)	Full
US	FM 4880	Intermediate

As opposed to the worldwide occurrence of facade fires, the United States has had comparatively few significant external cladding fires since 1990. Yet the few significant ones, mostly in hotels, were caused by non-compliance with NFPA 285 and poor enforcement of fire safety codes [27]. Other nations, including the United Arab Emirates, China, Germany, France, and Russia, have experienced multiple facade fires of global concern, prompting renewed attempts to enhance testing standards and regulatory compliance globally. One of the major challenges is how to address the variations in global construction practices. Anderson et al. [14] reported the development of a harmonized test method for facade systems in the European Union, with a special focus on mounting, fixing, air gaps, material lengths, and structural weaknesses. The exercise began by collating a list of regulatory requirements in member states and identifying those with additional demands in addition to the EN 13501 classification system.

Building on existing standards such as BS 8414 and DIN 4102-20, the project included a system of verification and validation supported by stakeholder endorsement in the form of technical meetings and workshops [29]. The project sought to define a European Union (EU) member state's acceptable classification system while addressing Construction Products Regulation (CPR) requirements. It was focused on enabling a comprehensive assessment of traditional and emerging facade technologies, including glazed and green facades. The project also proposed traditional and new assessment methods based on experimental data and regulatory analysis to reduce duplicate testing burdens on manufacturers.

1.2. Challenges and Approach in developing a small-scale test method

Fire testing is an effective tool for predicting the fire performance of façade systems, but the testing method must ensure consistent conditions and repeatable results [30]. Developing a bespoke test method for façade fire testing poses significant challenges due to the complex

interactions of various factors such as material properties, fire properties, and building structure. Current test methods vary in different countries, and it is difficult to establish a single standard for evaluating façade fire performance. BS 8414 tests are widely used in the UK and NFPA 285 in the US, but they differ in composition, form, and acceptance [2]. That is also an issue to address with a new test method for façade fire testing.

Moreover, another challenge is the cost and time required to conduct large-scale fire tests. Full-scale testing is expensive and needs labor, too. Also, those tests often require several iterations to accurately evaluate the fire performance of the façade system [31]. This has led researchers to explore alternative approaches such as numerical modeling [1], [32]. But even these methods face limitations in terms of model accuracy and statistical resources required for large-scale fire simulations

There has been more use of External Thermal Insulation Composite Systems (ETICS) in terms of material due to its energy efficiency. However, as Cancelliere et al. [30] noted, these systems can pose very severe fire hazards, particularly in the presence of expanded polystyrene (EPS) insulation. Recent fires in Germany on ETICS have initiated large-scale debate and experimental testing focused on their fire performance. Effective fire safety design must incorporate facade performance as part of a holistic risk approach and not as an isolated parameter. The European Commission has, therefore, developed harmonized classification systems for fire performance in line with EN 13501-1, founded on EU and European Free Trade Association (EFTA) member state input to revise the regulations. This has included the development of novel medium-scale test methodologies for determining fire behavior in ETICS systems. These methodologies are seen as being more cost-effective and more realistic than full-scale testing without undermining the validity of the results [30].

In Japan, water-permeable external thermal insulation has gained popularity due to its thermal efficiency and ease of installation. However, fire risks due to combustible materials led to significant revisions in Japan's Building Standard Law in 2000. As per the revisions, any application of combustible materials on the exterior walls of reinforced concrete buildings must be within certified fire-resistant construction systems [33]. Yoshioka et al. [33] also targeted real-case testing for such applications. The Monte Carlo Hotel fire and the TVCC fire in Beijing underscored such incidents, revealing vulnerabilities in facade materials. While current test procedures enabled a fundamental test of heat release and burning behavior, shortcomings in reproducing flame growth and dynamic heating changes indicated a demand for additional refinement in fire test procedures.

Apart from regulatory compliance and material performance, the structural design of facade systems plays a crucial part in fire spread. Jensen [34] indicates that natural vertical airflow within ventilated cavity spaces behind rain-screen panels has the potential to cause rapid and often undetected flame spread. These concealed fires can endanger the stability of the entire facade system with potentially catastrophic effects, like falling debris and embers that endanger adjacent areas. In attic fires, an unchecked flame spread has led to the total loss of blocks of housing. Further, the effectiveness of fire-stopping systems is extremely variable depending on design, exposure, and whether appropriate ventilation is present. Jensen [34] argues that current test standards are not sufficient to evaluate ventilated cavity barrier performance, and the majority of specified systems lack empirical data to support them. This highlights the global need for harmonized, performance-based test methods for the validation of fire-stop technologies and enhanced facade fire resistance.

The harmonization of test standards is an ongoing effort. Anderson et al. [29] state that the European Commission has accomplished a high level of integration of BS 8414-1/2 and DIN 4102-20 tests into a combined testing framework. Hirschler [27] suggests the use of novel evaluation techniques that reduce the number of tests needed by producers. In that system, the manufacturers would conduct one standard test, and results could then be transferred to other standards by utilizing validated equivalency models. The efforts are aimed at reducing redundancy without affecting fire safety assurance. In the US, new changes to the 2021 IBC resolve issues of the application and scope of NFPA 285, additionally reconciling regulatory requirements with real-world fire performance expectations. At the same time, the German project featured by Cancelliere et al. [30] demands fire testing at real installed conditions. Their proposed medium-scale test integrates measurements such as Heat Release Rate (HRR), smoke production, and heat flux to enable precise and repeatable tests. Similarly, Yoshioka et al. [33] recommend that Japan develop a new fire spread testing standard for combustible exterior materials.

To address those issues, several researchers have conducted experimental and numerical studies to evaluate the performance of the façade models based on specific fire resistance standards [19], [35], [36]. For example, Zhou et al. [19], [36], carried out a set of tests to evaluate the combustibility of thermoplastic expanded polystyrene (EPS) façades in line with the JIS A 1310 standard. The ANSI/FM 4880 standard used by Agarwal et al. [35], for Cladding assemblies and were tested for flammability, while Hostikka & Bytskov [37], used numerical simulations to model the ambient temperature of the coating in ISO 13785-2. Additionally, various studies have analyzed the behavior of flames spilling from compartments and impacting façades [14], [38].

These developments reflect the global recognition of the importance of holistic facade fire testing methodologies. As new construction technologies continue to emerge, future testing regimes must achieve a balance between accuracy, reproducibility, and cost-effectiveness. Shared standards and performance-based assessments will be key to ensuring that innovations in building design do not compromise fire safety.

2. Methodology

This study employed a two-part methodology: (1) a small-scale experimental façade fire test designed by adapting the ISO 13785-2 full-scale procedure, and (2) a numerical simulation using PyroSim (FDS interface) to replicate and validate the experimental results. The test

procedure was designed to simulate key aspects of ISO 13785-2, with practical modifications to suit local resource constraints. A test rig, gas burner setup, thermocouple placement strategy, and pre-conditioning procedures were employed to ensure the reliability of the results. Additionally, numerical simulations were performed using the Fire Dynamics Simulator (FDS) to validate experimental observations and explore scalability.

For this study, ISO 13785 is employed as the test standard, with a preference for this instead of regional standards like NFPA 285 or BS 8414. ISO 13785 allows global applicability, especially to developing countries like Sri Lanka, where national fire testing standards are still evolving. The standard is in two parts: ISO 13785-1, which involves intermediate-scale testing (Figure 1), and ISO 13785-2, a full-scale test method. The two-stage approach allows for both cost-effective initial tests and exhaustive examinations at realistic fire conditions. ISO 13785 can be applied to different types of facade materials and systems, and thus it can be used in a wide range of construction scenarios. Its wide range of applicability also encourages manufacturers to meet globally accepted standards, enabling cross-border trade and safety assurance.

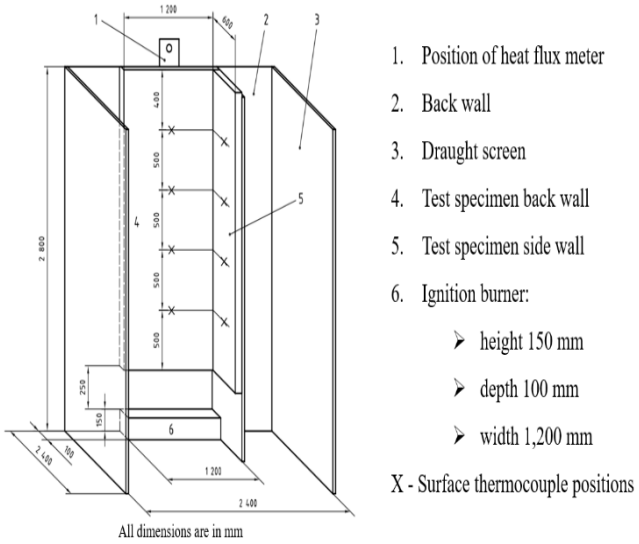

Figure 1: The specimen, support frame, and position of thermocouples according to ISO13785-2:2002.

A custom test rig was constructed to simulate ISO 13785-2 test conditions. A vertical support structure was designed to suspend the facade specimen, and a horizontally mounted propane gas burner was used to provide flame exposure. The arrangement is shown in Figure 2, which presents the schematic layout of the test apparatus. Type-K thermocouples were installed to record temperature at the surface, in the core, and at the back of the specimen. The thermocouple layout is illustrated in Figure 2 by cross icons. A gypsum board screen was also positioned to simulate wind effects and improve flame stability during the test. Although heat flux meters were not available, temperature data and high-resolution video footage were used to monitor flame spread and surface behavior.

Test specimens were conditioned to satisfy ISO 13785-2 specifications. Hygroscopic materials were equilibrated to constant weight and temperature ($23 \pm 2°C$) to reach steady moisture content. Non-hygroscopic materials were also conditioned to eliminate environmental variations. The burner was cleaned, calibrated, and the specimen was properly aligned before testing. Marker lines at equal intervals were drawn to facilitate visual observation of flame spread. Baseline photographs were taken for documentation and later comparison.

The testing began with vertically mounting the specimen on the steel frame. The cameras and thermocouples were activated, and the burner was ignited to supply a constant 20 kW flame to the base of the specimen. Due to local constraints, the burner power output was lowered from the standard 100 kW to 20 kW. Data logging started two minutes before the ignition and was conducted during exposure. The fire behavior was monitored visually and instrumentally, with notes taken on flame spread, surface distortion, smoke production, and cavity ignition. The test was terminated when the fire reached the top of the panel or at 30 minutes, whichever came first. Post-test analysis included visual observation, analysis of temperature data, and photographic documentation of damage and failure modes.

Facade performance was evaluated by a combination of qualitative and quantitative methods. Thermocouple data provided temperature profiles at various depths, from which ignition delay and insulation failure could be established. Visual recordings were made of flame spread rate, smoke performance, and material detachment. These were compared with ISO 13785-2 performance criteria to determine the level of compliance and fire resistance of the system tested. This two-stage analysis method offered both numerical and practical insight into fire performance.

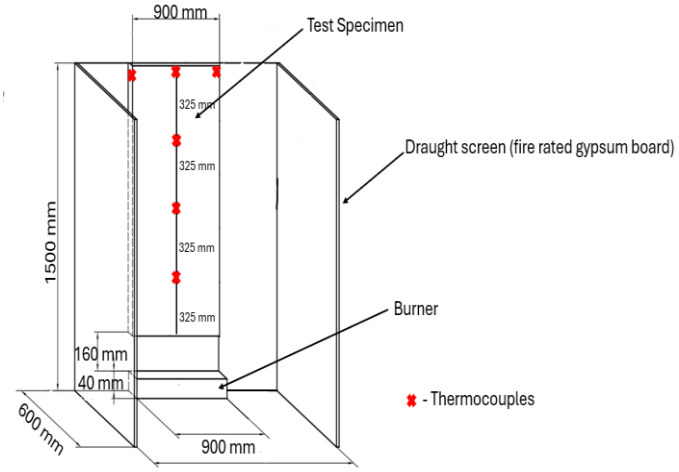

Figure 2: Schematic Diagram of Developed Apparatus

The actual test setup and experimental apparatus are shown in Figures 3 to 5**.** Figure 3 provides a photograph of the fully assembled apparatus. Figure 4 highlights the burner used in the experiment, while Figure 5 shows the façade panel specimen mounted on the support frame before ignition.

Figure 3: Developed Apparatus

Figure 4: Burner

Figure 5: Apparatus with Specimen

There were a few limitations identified in the test process. The use of a 20 kW burner, as opposed to the 100 kW in ISO 13785-2, reduced the severity of fire exposure and may have underestimated the severity of thermal damage. The absence of heat flux meters limited the capability for accurate measurement of radiant heat transfer. In addition, the simplified test fixture lacked side walls, which are necessary to facilitate realistic flame enclosure and lateral spread. Finally, the small sample size and brief duration may have limited observation of long-term effects such as internal smoldering or delayed structural collapse. The modified setup nevertheless provided valuable data on initial fire behavior and validated ISO 13785 as an effective standard for facade fire testing within budgetary limitations.

The test specimen selected in this study was ALUCOPANEL FR, which is a fire-rated aluminum composite panel with widespread use in contemporary facades. The panel consists of two 0.50 mm-thick aluminum sheets laminated to a mineral-filled fire-retardant core. The top layer is finished with polyvinylidene fluoride (PVDF) for corrosion and UV resistance, and the reverse side is finished. The mineral core serves to prevent ignition and reduce flame spread, as well as to impart greater rigidity. ALUCOPANEL FR is well-liked for residential and commercial facades due to its durability, aesthetic flexibility, and certified compliance with international fire regulations

2.1. Numerical Model Development

A three-dimensional numerical model was developed using PyroSim software, which interfaces with the Fire Dynamics Simulator (FDS). The model geometry replicated the experimental test rig, including the façade panel size (1300 mm × 900 mm), burner location, and open-air boundary conditions. The burner was configured to deliver a steady 20 kW heat release rate (HRR), matching the experimental flame source. Material properties such as thermal conductivity, specific heat, and density for the aluminum skins and polyethylene core were input based on manufacturer specifications and literature values. A structured mesh with a uniform grid size of 20 mm was used, with local refinement near the burner and specimen surface. Eight virtual thermocouples were placed at the same locations as in the physical test to extract temperature–time profiles. Radiation and convective heat transfer were modeled using FDS's default radiation solver, and solid-phase combustion was not simulated due to software limitations. The simulation ran for 1800 s, and the output temperature data were compared directly with experimental measurements to assess model accuracy using mean absolute error (MAE) and percentage deviation.

3. Results and Discussion

This research suggests a low-cost technique to evaluate the fire performance of façade systems by small-scale laboratory testing and computational simulation. With the advancement of façade material and design in contemporary buildings, fire safety is an issue of concern. Even though the complete-scale tests NFPA 285 and BS 8414 give detailed assessment standards, they are too costly and require too much infrastructure, and hence impractical in developing situations like Sri Lanka.

The research explores whether smaller-scale testing, governed by ISO 13785-2:2002 with realistic modifications, can replicate the dominant fire behavior of full-scale tests. A test rig was constructed from a vertical steel frame, and the ALUCOPANEL FR specimen (1300 mm × 900 mm) was mounted in position. The conventional 100 kW burner was replaced by a 20 kW burner, and a gypsum-board draught screen was mounted to simulate natural air movement. Thermocouples were installed on the specimen surface, core, and back to measure temperature profiles during the test. Qualitative assessment used visual observations like flame spread markers and video recording.

Before ignition, the sample was preconditioned to 23 ± 2 °C to reach moisture equilibrium. Two minutes before the ignition, data logging began to record baseline temperatures. The burner was operated under controlled conditions for 30 minutes, and temperature measurements were recorded continuously at one- second intervals to achieve the fine characteristics of the thermal response of the sample.

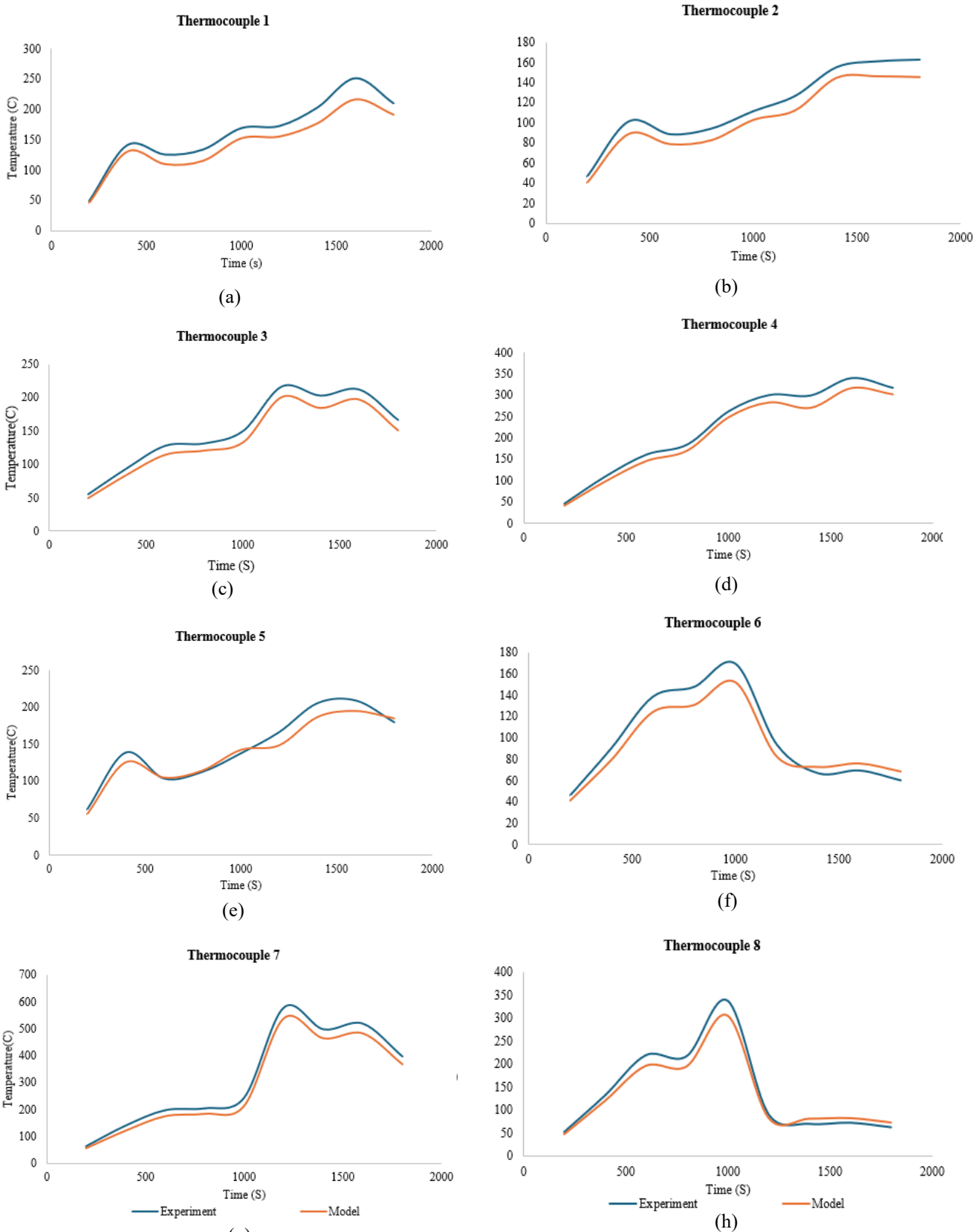

Figure 9: Comparison of Results

Figure 6: Flame Spread during the test

Figure 7: Specimen after the test

Figure 8: Deformation of Panel

Table 2: Accuracy of results

Thermocouple	MAE	Percentage Error
1	17.69	10.55
2	11.78	10.56
3	13.59	9.36
4	21.16	9.42
5	14.92	10.18
6	10.81	10.99
7	24.88	9.03
8	15.30	11.42

Figure 6 shows how the fire spread through the specimen, and Figure 7 indicates what the specimen looked like when the test was concluded. According to Figure 7, the white coloured coating was damaged, but the inner core was still in good condition. Notably, Figure 8 showcases a deformation that occurred.

The comparison of the results by model and the experiment is presented in Figure 9. Thermocouples 1 to 8, which are presented in Figure 1 (a) to (h), were located from the top to the bottom of the specimen. Also, Figure 9(a) shows the upper left-hand side thermocouple, and Figure 9(d) shows the upper right-hand side thermocouple. Both of them, with thermocouples 2 and 3, which are indicated by Figures 9 (b) and (c), show a slightly higher temperature increase. Thermocouples 2 and 3 are located at the top of the middle line of the specimen. When looking at Figures 9 (e) to (h), it can observe an increasing that the temperature values increase as they were located near the burner. Generally, the temperature rises over time in multiple phases before levelling off or dropping, and the model captures this overall pattern quite well. Still, in most cases, especially for thermocouples 1, 3, 4, 5, and 7, the experimental data show slightly higher peak temperatures than the model predicts. For Thermocouples 6 and 8, there are sudden drops in temperature after the peak, which the model the model results exhibit smoothed transitions, indicating a potential limitation in capturing rapid changes. Thermocouple 7 recorded the highest temperature, reaching nearly 600°C, and showed the largest error between model and experiment according to Table 2. The model demonstrated reasonably good agreement with the experimental temperature readings across all eight thermocouples.

Table 2 discusses the accuracy of the models compared to the experiment. Thermocouple 6 had the smallest error, suggesting that the model performed best at that location. Looking at the numbers, the Mean Absolute Error ranged from about 11°C to 25°C, while the Mean Percentage Error stayed between 9% and 11.5%. This shows the model's predictions are quite consistent overall.

The results showed that flame propagation remained limited within the lower half of the test specimen, without any vertical progression reaching the upper end of the test rig. Thermometric records at various levels, like 0.5 m, 1.5 m, and 3.5 m from the burner, were registered below the ISO 13785-2-defined critical temperature of 600 °C. The result indicates that the specimen possessed very high thermal stability along with minimal heat transfer when subjected to fire testing.

No flashover, sustained flaming, flaming droplets, or secondary ignition was observed during the test. The fire performance was controlled and self-extinguishing, with consistent heat release and no sudden thermal rise. Slight deformation was observed in the center of the most exposed panel, resulting from the melting of the polymer core. This kind of behavior is typical for aluminum composite materials under thermal stress and did not influence the structural integrity or lead to rear-face ignition.

Visual inspection and temperature analysis confirmed the material's adherence to the ISO 13785-2 performance criteria. Numerical simulation using PyroSim provided results consistent with the experimental results, replicating the observed trends in temperature and confirming limited flame spread.

Although the analysis focused primarily on temperature data, this approach aligns with ISO 13785-2 standard, which uses temperature thresholds, typically around 600 °C, to assess façade ignition, flame spread, and insulation failure. The placement of eight thermocouples across the specimen allowed for detailed thermal profiling, capturing ignition delay, temperature gradients, and fire resistance behavior. Temperature is a widely accepted and quantifiable indicator of façade fire performance. Therefore, the temperature-based assessment provides a valid and practical means of evaluating the fire performance of the tested system.

Even though direct comparison with full-scale façade fire tests was not possible due to resource constraints, the proposed small-scale method is supported by several relevant studies and international standards that bridge the gap between reduced- and full-scale testing. Notably, ISO 13785 itself includes an intermediate-scale test method (Part 1), which is recognized as a valid and cost-effective approach for preliminary assessment of façade fire behavior before full-scale testing (Part 2). Guillaume et al. (2018) [39] demonstrated that intermediate-scale façade fire tests using ACM panels produced results well aligned with BS 8414 full-scale tests, highlighting the potential of scaled testing to capture key fire performance indicators. Similarly, Li et al. (2022) [2] presented a numerical comparison of ISO, NFPA, and JIS standard test scenarios, supporting the applicability of scaled simulations to reflect realistic façade fire conditions. Furthermore, Schulz et al., in Critical Appraisal of the UK's Regulatory Regime for Combustible Façades, questioned the completeness of BS 8414 by highlighting unaddressed variables such as windows and cavity effects, suggesting that full-scale methods also have limitations. Complementing this, the 2024 Fire Technology article A Taxonomy of UK Reaction-to-Fire Standard Testing [40] emphasized the shift from strict reproducibility toward representative testing methods. Taken together, these sources reinforce that small- and intermediate-scale tests, particularly when paired with simulation, offer valid and practical tools for assessing façade fire performance in early-stage evaluations.

3.1. Limitations

Despite the encouraging results, several limitations should be acknowledged. The experimental setup used a 20 kW burner instead of the 100 kW prescribed in ISO 13785-2, which may have reduced the severity of fire exposure. The test rig lacked sidewalls and full enclosure, limiting realistic flame confinement and lateral spread. In addition, only temperature data was collected due to the absence of heat flux meters and smoke detectors, etc. Furthermore, the numerical model assumed steady-state heat release and did not simulate combustion of the core material in detail. These limitations indicate that while the proposed method is useful for preliminary assessment, further development is needed to enhance its accuracy and alignment with full-scale fire conditions

The experimental work supports the use of small-scale testing as a practical and reliable preliminary step before conducting full-scale façade fire tests. The tested panel system showed reasonable fire-retardant performance under small-scale conditions, indicating that it may be suitable to proceed to full-scale testing. Furthermore, the combination of experimental results and computational analysis strengthens the confidence in using small-scale methods for early-stage assessment.

While the proposed small-scale method has shown promising alignment with simulation results, its validation against full-scale façade fire tests remains a critical next step. Due to local resource limitations, direct full-scale testing could not be conducted. However, the setup was conceptually scaled down from ISO 13785-2, and design principles were preserved to ensure representative thermal behavior. Future research will focus on benchmarking small-scale test results with full-scale test data from standardized procedures such as BS 8414 or ISO 13785-2, either through collaboration or literature-based comparative studies.

4. Conclusion

This research highlights the importance of assessing façade fire performance before installation, especially in regions like Sri Lanka, where full-scale testing is limited by cost and facility constraints. To address this, a small-scale test method was developed, guided by ISO 13785 principles, and applied to a façade panel composed of aluminum sheets and a polyethylene core. Temperature data from 8 thermocouples during the fire test were compared against a numerical model developed using Fire Dynamics Simulator (FDS). The results show that the numerical model accurately reflects the experimental fire behavior, with a Mean Absolute Error (MAE) of approximately 25 and a maximum percentage error of 11.5%. This confirms the success of the small-scale experimental setup and the reliability of the validated simulation model within acceptable error margins.

However, this small-scale test is not intended to replace full-scale testing. Rather, it provides a valuable and affordable preliminary screening method. The next step will involve comparing this validated small-scale model with a simulated full-scale scenario to evaluate how closely the findings align. This progression will help determine the broader applicability of the small-scale method for predicting façade fire behavior and guiding future comparisons with full-scale models. Also, the small-scale test can serve as an effective screening tool to evaluate whether a particular façade panel is suitable to proceed to full-scale testing or whether it requires further improvement or modification beforehand.

References

[1] A. Sharma, T. Zhang, and G. Dwivedi, "Façade Fires in High-Rise Buildings: Challenges and Artificial Intelligence Solutions," in *Sustainable Structures and Buildings*, A. Bahrami, Ed., Cham: Springer International Publishing, 2024, pp. 77–94. doi: 10.1007/978-3-031-46688-5_6.

[2] Y. Li, Z. Wang, and X. Huang, "An exploration of equivalent scenarios for building facade fire standard tests," *Journal of Building Engineering*, vol. 52, p. 104399, Jul. 2022, doi: 10.1016/j.jobe.2022.104399.

[3] F. Lugaresi, P. Kotsovinos, P. Lenk, and G. Rein, "Review of the mechanical failure of non-combustible facade systems in fire," *Construction and Building Materials*, vol. 361, p. 129506, Dec. 2022, doi: 10.1016/j.conbuildmat.2022.129506.

[4] S. T. McKenna *et al.*, "Fire behaviour of modern façade materials – Understanding the Grenfell Tower fire," *Journal of Hazardous Materials*, vol. 368, pp. 115–123, Apr. 2019, doi: 10.1016/j.jhazmat.2018.12.077.

[5] Kate Tq Nguyen, Pasindu Weerasinghe, P. Mendis, and T. Ngo, "Performance of modern building façades in fire: a comprehensive review," *EJSE*, vol. 16, pp. 69–87, Jan. 2016, doi: 10.56748/ejse.16212.

[6] X. Huang, Y. Wang, and E. Guillaume, "Special Issue on Facade Flammability and Fire Engineering," *Fire Technol*, vol. 59, no. 1, pp. 1–3, Jan. 2023, doi: 10.1007/s10694-023-01361-3.

[7] "Civil engineers need to act now on the wider lessons from the Grenfell tower fire tragedy," *Proceedings of the Institution of Civil*

Engineers - Civil Engineering, vol. 174, no. 3, p. 102, Jan. 2021, doi: 10.1680/jcien.2021.174.3.102.
[8] J. Schulz, D. Kent, T. Crimi, J. L. D. Glockling, and T. R. Hull, "A Critical Appraisal of the UK's Regulatory Regime for Combustible Façades," *Fire Technol*, vol. 57, no. 1, pp. 261–290, Jan. 2021, doi: 10.1007/s10694-020-00993-z.
[9] H. T. Nguyen, Y. Abu-Zidan, G. Zhang, and K. T. Q. Nguyen, "Machine learning-based surrogate model for calibrating fire source properties in FDS models of façade fire tests," *Fire Safety Journal*, vol. 130, p. 103591, Jun. 2022, doi: 10.1016/j.firesaf.2022.103591.
[10] P. Wu, W. Xue, T. Wu, M. Hao, R. Zhou, and J. Jiang, "Impact of sliding window opening sizes and crosswinds on combustion characteristics of polyethylene sandwich panels in external venting façade fires," *Safety Science*, vol. 180, p. 106657, Dec. 2024, doi: 10.1016/j.ssci.2024.106657.
[11] Y. Chen, Y. Nie, and J. Zhang, "Acceleration analysis and unsteady mathematical prediction of flame spread over thermal insulation layer in u-shaped building façade fires," *International Journal of Thermal Sciences*, vol. 204, p. 109205, Oct. 2024, doi: 10.1016/j.ijthermalsci.2024.109205.
[12] N. White, M. Delichatsios, M. Ahrens, and A. Kimball, "Fire hazards of exterior wall assemblies containing combustible components," *MATEC Web of Conferences*, vol. 9, p. 02005, 2013, doi: 10.1051/matecconf/20130902005.
[13] J. P. Hidalgo *et al.*, "The Malveira fire test: Full-scale demonstration of fire modes in open-plan compartments," *Fire Safety Journal*, vol. 108, p. 102827, Sep. 2019, doi: 10.1016/j.firesaf.2019.102827.
[14] J. Anderson, L. Boström, R. Jansson McNamee, and B. Milovanović, "Modeling of fire exposure in facade fire testing," *Fire and Materials*, vol. 42, no. 5, pp. 475–483, Aug. 2018, doi: 10.1002/fam.2485.
[15] R. Yang *et al.*, "Fire safety requirements for building integrated photovoltaics (BIPV): A cross-country comparison," *Renewable and Sustainable Energy Reviews*, vol. 173, p. 113112, Mar. 2023, doi: 10.1016/j.rser.2022.113112.
[16] "ISO 13785-2:2002," ISO. Accessed: Jun. 14, 2025. [Online]. Available: https://www.iso.org/standard/22928.html
[17] "BS 8414 Fire performance of external cladding systems." Accessed: Jun. 14, 2025. [Online]. Available: https://www.designingbuildings.co.uk/wiki/BS_8414_Fire_performance_of_external_cladding_systems
[18] "NFPA 285 Standard Development." Accessed: Jun. 14, 2025. [Online]. Available: https://www.nfpa.org/codes-and-standards/nfpa-285-standard-development/285
[19] B. Zhou, H. Yoshioka, T. Noguchi, K. Wang, and X. Huang, "Fire Performance of EPS ETICS Facade: Effect of Test Scale and Masonry Cover," *Fire Technol*, vol. 59, no. 1, pp. 95–116, Jan. 2023, doi: 10.1007/s10694-021-01195-x.
[20] B. Meacham, "Toward a Sociotechnical Systems Framing for Performance-Based Design for Fire Safety," 2022, pp. 1–39. doi: 10.1007/978-3-030-98685-8_1.
[21] B. Meacham, "Fire performance and regulatory considerations with modern methods of construction," *Buildings and Cities*, vol. 3, pp. 464–487, Jul. 2022, doi: 10.5334/bc.201.
[22] "2024.2 PyroSim User Manual | Thunderhead Support." Accessed: Jun. 14, 2025. [Online]. Available: https://support.thunderheadeng.com/docs/pyrosim/2024-2/user-manual/
[23] K. B. McGrattan, R. J. McDermott, C. G. Weinschenk, and G. P. Forney, "Fire Dynamics Simulator, Technical Reference Guide, Sixth Edition," *NIST*, Nov. 2013, Accessed: Jun. 14, 2025. [Online]. Available: https://www.nist.gov/publications/fire-dynamics-simulator-technical-reference-guide-sixth-edition
[24] A. A. Khan, S. Lin, X. Huang, and A. Usmani, "Facade Fire Hazards of Bench-Scale Aluminum Composite Panel with Flame-Retardant Core," *Fire Technol*, vol. 59, no. 1, pp. 5–28, Jan. 2023, doi: 10.1007/s10694-020-01089-4.
[25] "Transforming our world: the 2030 Agenda for Sustainable Development | Department of Economic and Social Affairs." Accessed: Jun. 14, 2025. [Online]. Available: https://sdgs.un.org/2030agenda
[26] "Goal 11 | Department of Economic and Social Affairs." Accessed: Jun. 14, 2025. [Online]. Available: https://sdgs.un.org/goals/goal11
[27] M. M. Hirschler, "Façade requirements in the 2021 edition of the US International Building Code," *Fire and Materials*, vol. 45, no. 5, pp. 586–597, Aug. 2021, doi: 10.1002/fam.2803.
[28] "Facade Fire Hazards of Bench-Scale Aluminum Composite Panel with Flame-Retardant Core | Fire Technology." Accessed: Sep. 29, 2024. [Online]. Available: https://link.springer.com/article/10.1007/s10694-020-01089-4
[29] J. Anderson *et al.*, "European approach to assess the fire performance of façades," *Fire and Materials*, vol. 45, no. 5, pp. 598–608, Aug. 2021, doi: 10.1002/fam.2878.
[30] P. Cancelliere, P. Canzani, S. Sassi, A. Lucchini, S. Messa, and E. Anselmi, "A new test method to determine the fire behavior of façades with etic system," *Fire and Materials*, vol. 45, no. 5, pp. 624–637, Aug. 2021, doi: 10.1002/fam.2886.
[31] R. Stølen, T. Li, T. Wingdahl, and A. Steen-Hansen, "Large- and small-scale fire test of a building integrated photovoltaic (BIPV) façade system," *Fire Safety Journal*, vol. 144, p. 104083, Mar. 2024, doi: 10.1016/j.firesaf.2023.104083.
[32] V. Dréan, B. Girardin, E. Guillaume, and T. Fateh, "Numerical simulation of the fire behaviour of facade equipped with aluminium composite material-based claddings-Model validation at large scale," *Fire and Materials*, vol. 43, no. 8, pp. 981–1002, Dec. 2019, doi: 10.1002/fam.2759.
[33] H. Yoshioka *et al.*, "Study of Test Method for Evaluation of Fire Propagaion along Facade Wall with Exterior Thermal Insulation," *Fire Science and Technology*, vol. 30, pp. 27–44, Jan. 2011, doi: 10.3210/fst.30.27.
[34] G. Jensen, "Fire spread modes and performance of fire stops in vented façade constructions - Overview and standardization of test methods," *MATEC Web of Conferences*, vol. 9, p. 02002, Nov. 2013, doi: 10.1051/matecconf/20130902002.
[35] G. Agarwal, Y. Wang, and S. Dorofeev, "Fire performance evaluation of cladding wall assemblies using the 16-ft high parallel panel test method of ANSI/FM 4880," *Fire and Materials*, vol. 45, no. 5, pp. 609–623, 2021, doi: 10.1002/fam.2852.
[36] B. Zhou, H. Yoshioka, T. Noguchi, K. Wang, and X. Huang, "Upward Fire Spread Rate Over Real-Scale EPS ETICS Façades," *Fire Technol*, vol. 57, no. 4, pp. 2007–2024, Jul. 2021, doi: 10.1007/s10694-021-01103-3.
[37] S. Hostikka and G. Bytskov, "Numerical simulations of the ISO 13785-2 façade fire tests," in *MATEC Web of Conferences*, EDP Sciences, May 2016, p. 03003. doi: 10.1051/matecconf/20164603003.
[38] X. Sun, L. Hu, X. Zhang, F. Ren, Y. Yang, and X. Fang, "Experimental study on flame pulsation behavior of external venting facade fire ejected from opening of a compartment," *Proceedings of the Combustion Institute*, vol. 38, no. 3, pp. 4485–4493, Jan. 2021, doi: 10.1016/j.proci.2020.06.181.
[39] E. Guillaume, T. Fateh, R. Schillinger, R. Chiva, and S. Ukleja, "Study of fire behaviour of facade mock-ups equipped with aluminium composite material-based claddings, using intermediate-scale test method," *Fire and Materials*, vol. 42, no. 5, pp. 561–577, Aug. 2018, doi: 10.1002/fam.2635.
[40] A. Law, G. Spinardi, and L. Bisby, "A Taxonomy of UK Reaction-to-Fire Standard Testing: The Role of Black Boxing of Expertise," *Fire Technol*, vol. 60, no. 3, pp. 1741–1767, May 2024, doi: 10.1007/s10694-024-01547-3.

Review of the Effect of Moss Growth in Structures – Positive and Negative Impacts

L R Irudhiyarajah[1]*, I R Upasiri[1], and A Amarasinghe[1]

Abstract

Mosses are tiny, resilient plants that grow in various habitats and are influenced by factors such as water availability, light exposure, temperature, and substrate composition. Moss growth on building facades and structural surfaces can cause biodeterioration, causing micro-cracking, increased porosity, long-term weakening, and sometimes irreversible damage. However, moss also has potential benefits in sustainable building, such as retaining moisture, controlling temperature, and purifying the air. Moss-based green roofs and facades can enhance thermal performance, mitigate heat island effects, improve air quality, and promote biodiversity. This paper summarizes up-to-date published research articles relevant to moss growth on buildings and structures and the dual function of moss in various environmental exposures. The impact of moss growth depends on moss species, substrate type, and environmental conditions which opens up the door to further studies into much-specified variables as mentioned. Future research should investigate the impact of moss growth on external building walls, particularly within polluted urban environments, where a significant research gap exists. Such studies should address moss's destructive and beneficial effects, examining its interactions with various building substrates and moss species under diverse environmental conditions. The aim should be to enhance understanding of moss's potential contributions to energy efficiency and environmental resilience through methods such as experimental testing, computational modeling, advanced image processing, automated monitoring, and deep learning techniques.

***Keywords:** Moss, biodeterioration, durability, thermal, air purification, image processing, machine learning*

1. Introduction

Mosses are small, resilient, photosynthetic organisms that thrive in various habitats, especially moist environments and also in some cases, even deserts [1, 2]. Their unique developmental processes, structure, and micromorphology allow them to withstand adverse climatic conditions and drought [3]. Mosses lack differentiated tissues but phyllids (leaf-like structures) and a stem, which enables survival in challenging environments [4].

Experimental and in-situ studies have shown that most bryophytes, when well-hydrated, grow optimally between 15°C to 25°C, around 20°C in temperate climates, and up to 30°C in tropical climates. However, temperatures above 30°C are lethal for hydrated bryophytes. When dry, they can survive extreme temperatures ranging from -150°C to +60°C [5, 6].

Mosses attach to surfaces, enabling them to colonize cracks and voids in rocks, soil, and concrete, especially in locations with high humidity, shadow, and poor air circulation [2, 7]. Their ability to colonize surfaces depends on multiple factors. It includes surface and material properties such as porosity, roughness, and moisture retention, as well as environmental conditions like humidity, rainfall, temperature, and sunlight exposure (70,000 - 100,000 lux), with an optimal temperature range of 15–25°C. Additionally, chemical and biological parameters, including pH (preferably 5-5.5), nutrient availability, and microbial interactions, significantly affect the presence and development of moss [2, 8]. Mosses tend to thrive on slightly acidic to neutral surfaces and form biofilms that assist nutrient absorption from the air and colonization [9-11].

Due to their adaptability to various climates and pollution levels, mosses are prevalent in both urban and industrial settings [2]. As a result, they can thrive in tropical to arctic climates. Moss growth is frequent on exterior building walls, which are more exposed to rain, UV radiation, and wind than protected areas, and also applicable to external structures. A study [12] employing embedded sensors and UAVs proved that building facades are particularly vulnerable to such weathering. Mosses commonly colonize exterior elements such as walls, roofs, and pavements, particularly on north-facing, shaded, and moist facades with rough textures, whereas smoother, south-facing facades may exhibit minor biological degradation over the years [2, 13].

The uncontrolled presence of moss on buildings is often viewed as a sign of poor maintenance or a potential structural threat. Moss growth can lead to moisture retention and water accumulation, which in turn causes structural deterioration. This deterioration can be categorized into epilithic and endolithic damage, material degradation, where materials are weakened through mechanisms such as organic acid production and microcracking, and aesthetic degradation (Figure 1). These effects result in the gradual loss of structural integrity, load-bearing capacity, and durability [14, 15], all of which increase maintenance costs and pose health and safety

L.R. Irudhiyarajah*, I.R. Upasiri, Akarshani Amarasinghe
1Faculty of Engineering, University of Sri Jayewadenepura, Sri Lanka.(e-mail:roshildairudhiyarajah@gmail.com, irinduupasiri@sjp.ac.lk,akarshani.amarasinghe@sjp.ac.lk)

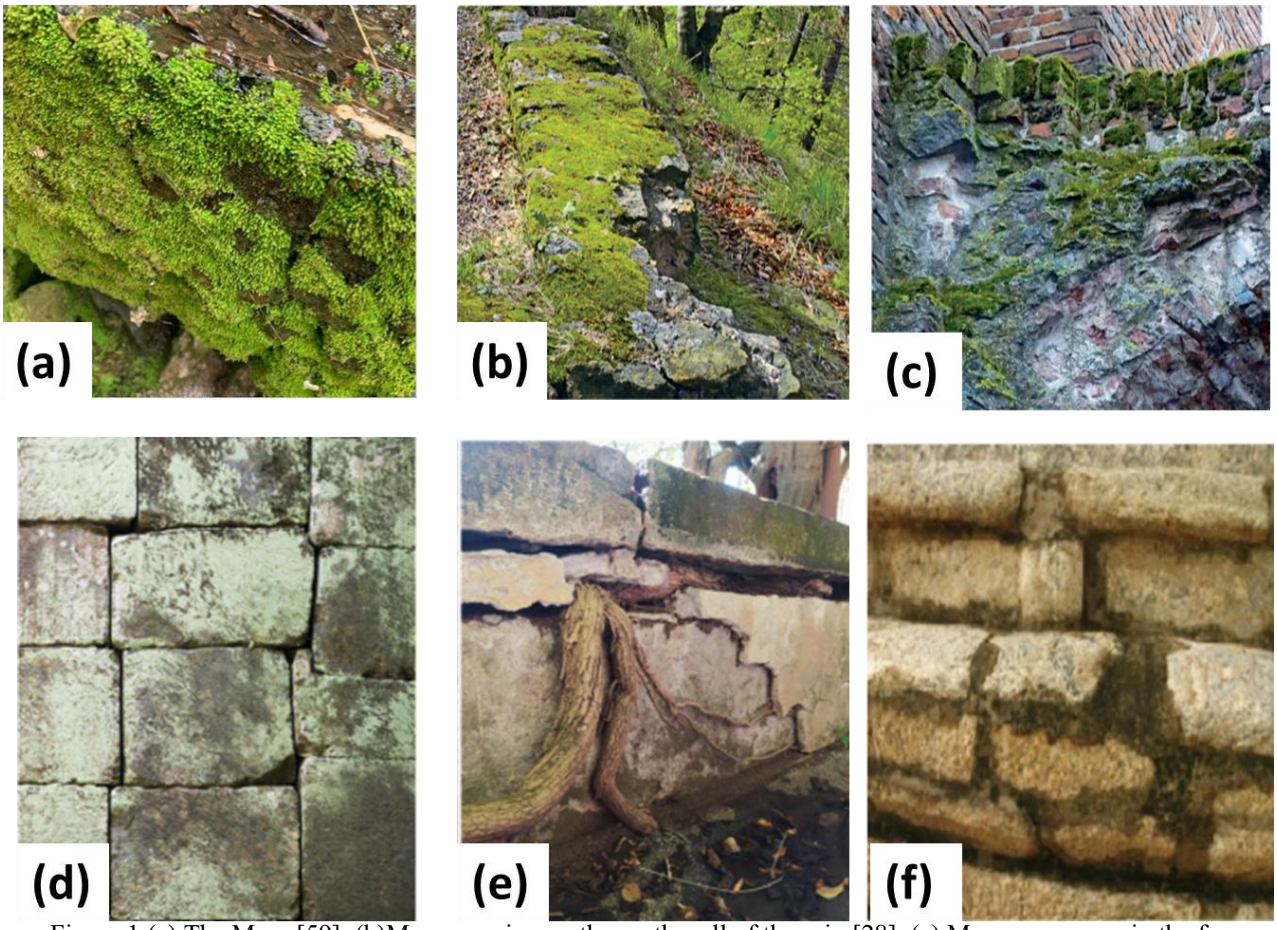

Figure 1:(a) The Moss [59]; (b)Moss growing on the north wall of the ruin [28]; (c) Moss overgrows in the face of the wall [28]; (d) Discoloration caused by moss in the Royal Palace of Portici, Naples, Italy [61]; (e) Cracks caused by moss growth in the Botanical Garden of Portici, Naples, Italy [61]; (f) Moss's growth in Historical structures [71].

risks, including respiratory issues, slippery surfaces, and difficulties in removal due to rapid and continuing growth.

While moss is typically seen as a degrading agent through biological and chemical interactions, recent research has highlighted its potential benefits. These include thermal insulation, noise reduction, mitigation of urban heat island effects, and improved air quality, which act as a natural pollution filter and promote biodiversity. Mosses can also provide partial protection against acid rain and environmental wear, especially when integrated into moss-based concrete systems [5,16-18]. Its rising popularity in green architecture is due to its low maintenance, ecological value, aesthetic appeal, and usefulness in features such as living walls. Moss also supports urban resilience by contributing to stormwater management and energy efficiency [19].

Traditionally, most durability studies focus on the negative impact of moss on historic structures through epilithic and endolithic degradation. However, recent work suggests that moss may play a dual role. Besides contributing to environmental damage, moss may also enhance the performance of modern building elements such as walls, roofs, and facades. This research study addresses a significant gap by investigating the dual impact of moss growth on external walls across various environmental conditions, with a particular focus on polluted urban and marine settings. It highlights how different moss species interact with various walling substrates and investigates the unresolved question of whether moss consistently reduces or potentially enhances material durability. The study aims to present a comprehensive assessment of moss-related degradation and its possible advantages, thereby providing a significant understanding of its influence on building performance.

2. Moss's Growth in Structures

Mosses are herbaceous, non-vascular plants in the Bryophyta class, typically growing between 0.2 and 10 cm tall, with individual leaves ranging from 0.5 to 3 mm [2], [20]. As some of the earliest terrestrial plants, mosses represent the largest group of about 10,000 species, each exhibiting unique characteristics and growth patterns. These are categorized into sub-classes: *Sphagnidae* (sphagnum or peat mosses), *Andreaeidae* (granite or rock mosses), and *Bryidae* (true mosses), which formed around 470 million years ago [21].

According to prior research, mosses are poikilohydric organisms that lack protective tissue to prevent dehydration from sunlight exposure. They are desiccation-tolerant, capable of rehydrating when water becomes available, and can withstand both extreme temperatures and rapid fluctuations [8]. Under favorable conditions and moisture availability, moss tissues can be restored within hours without damage [2]. Mosses absorb water and nutrients through their leaves, using carbon dioxide and

sunlight to produce nutrition [11, 22-23]. Due to their adaptability to various climates, exposed structures are vulnerable to weathering [12].

The moss life cycle begins uniquely with a protonema stage, where spores germinate to form a filamentous or plate-like network of cells optimized for water and nutrient absorption. This protonema then develops into gametophytes, visible green leafy structures, whose development is regulated by plant hormones and environmental conditions. The gametophytes produce rhizoids instead of roots, which anchor the moss to surfaces and aid in moisture absorption. Mosses reproduce both sexually and asexually, via structures known as antheridia and archegonia [24, 25]. As pioneer organisms, mosses are capable of biologically colonizing building materials and structures, regenerating protonema on surfaces such as concrete, brick, or masonry stone. Once established, they propagate through spore dispersal, fragmentation, and moisture-driven growth.

Two primary types of moss are commonly found on structure surfaces: pleurocarpous mosses, also known as carpeting mosses, which are branched, fuzzy, firmly attached, and grow horizontally; and acrocarpous mosses, or cushion mosses, which are unbranched, upright, and grow vertically, as shown in Figure 2 [1, 26]. A study [9] investigating urban epilithic moss populations explored how local environmental factors influence moss species distribution and identified mosses suitable for bio-receptive concrete. Among 137 moss communities observed in Dutch towns, 26 species were identified, with Acrocarpous mosses commonly found in exposed areas and Pleurocarpous mosses thriving in shaded environments, emphasizing the importance of selecting mosses for bio-receptive structures.

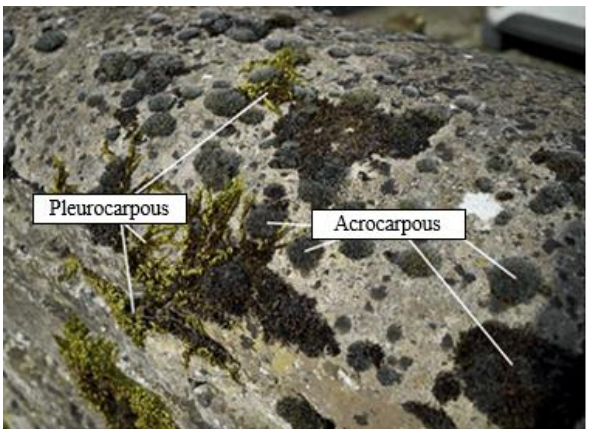

Figure 2: Acrocarpous and Pleurocarpous moss species [26]

The relationship between moss growth and its impact on building surfaces is influenced by multiple factors, including species type, environmental conditions, and the materials used in construction [16]. Accurate identification and evaluation require examining moss species' environmental contexts and substrate materials. For instance, Jang & Viles [26], examined *Brachythecium rutabulum*, a common moss species in temperate and subpolar climates, along with three bryophyte species, *Brinchia apiculatum, Barbula indica,* and *Hyophila involute*, to explore their adaptability to cementitious materials [11]. Murase's [6] study further revealed that moss could be cultivated effectively in a controlled environment within 1-2 months, substantially quicker than its natural growth, which has been utilized in reforestation.

Understanding mosses' biological characteristics, colonization behavior, and environmental preferences is critical for determining how they interact with structures. Depending on the species, orientation, substrate, and environmental exposures, their presence can be beneficial or destructive.

3. Negative Impacts on Moss Growth on Structures

Moss growth on structures causes a chain reaction of negative consequences, beginning with moisture retention and water accumulation, which are fundamental to moss ecology. This moisture accumulation eventually causes material degradation, structural deterioration, and aesthetic degradation. Material degradation and structural deterioration cause reduced durability and structural integrity, respectively. As a consequence, these increase maintenance and repair costs while increasing health and safety issues, particularly owing to slippery surfaces and respiratory problems. These interrelated effects (Figure 3) are especially important for buildings in various regions, as well as for the preservation of structures. Although previous research has investigated moss-related deterioration from microbiological and material science perspectives, a comprehensive knowledge of its long-term effects on structural performance is still lacking.

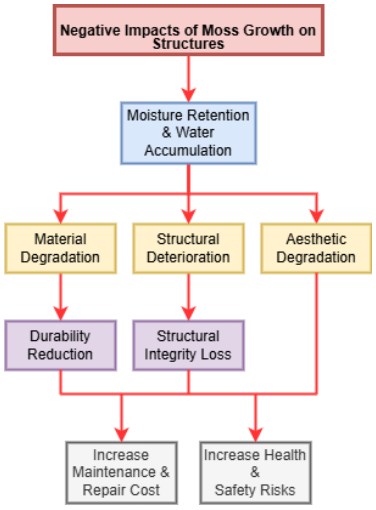

Figure 3: Negative impacts of moss growth on structures

3.1 Moisture Retention, and Water Accumulation

Moss growth significantly contributes to surface moisture retention and water accumulation, particularly on porous and shaded substates. Retained moisture triggers capillary absorption, extends wet cycles, and causes surface-level effects such as efflorescence salt crystallization, and decalcification, particularly in humid conditions. Udawattha [10] has highlighted the importance of intrinsic properties of material properties, such as organic matter content, surface roughness, water

absorption capacity, sorptivity, and capillary action for prolonged moisture retention and moss growth.

Salt crystallization occurs when retained moisture dissolves salts within materials. Upon evaporation, salts recrystallize, generating internal pressures that cause cracking, spalling, and granular disintegration [27]. This is especially destructive in porous and historic materials, and despite numerous studies addressing surface damage, few directly quantify its impact on structural strength. Future work must bridge this gap by linking moss growth, moisture retention, and salt action to mechanical performance across various materials.

Moss colonization can also cause decalcification. Organic acids react with calcium carbonate in heritage masonry, leading to erosion and fissure formation. These processes complicate conservation efforts, as supported by several studies [14, 28-29]. Although these studies provide a solid theoretical understanding, they often lack empirical, quantitative data on moisture impact across different material types, limiting their practical applicability.

3.2 Material Degradation, Structural Deterioration, and Aesthetic Degradation

Moss growth causes persistent moisture retention and water accumulation in structural components, leading to degradation mechanisms that begin at the material surface. This occurs through organic acids, microbial penetration, and continuous moisture, which increases porosity, disrupts particle bonding, and dissolves cementitious components. These processes result in gradual degradation, particularly in cementitious components and historical structures.

According to La Russa and Ruffolo [14], moss initiates both epilithic (surface-level) and endolytic (internal) colonization. Epilithic moss retains moisture and causes surface weathering, while endolytic growth, where microorganisms penetrate the surface, results in internal weakening, micro-cracking, and chemical alteration of materials like sandstone and lime-based mortars.

Karatas & Dal [30] observed that moss and plant growth on Kilit street facades in an Assyrian village increased moisture penetration, which in turn accelerated stone erosion, promoted biological degradation, and triggered structural instability, all of which have an impact on the community's cultural importance. Similarly, Zhang [31] emphasizes that moss growth in Fuzhou's gray brick buildings leads to surface erosion and material weakening due to trapped moisture. This trapped moisture and accumulated water contributes to efflorescence, chemical deterioration, and progressive cracking, ultimately reducing structural integrity and causing irreversible damage as confirmed by machine learning-based techniques. In other case studies, such as Angkor Sandstone Monuments in Cambodia and historical structures in Poland, salt crystallization and microbial colonization are both encouraged by prolonged moisture, which causes material and aesthetic degradation [32, 33].

A Nigerian study [34] on the biodeterioration of external sandcrete/concrete walls revealed that biological growth, including moss and algae, significantly reduced wall durability by promoting moisture retention and surface degradation. Notably, 63% of the affected walls had compressive strengths below 10 N/mm², increasing their risk of failure. The removal of cementitious chemicals (e.g., CaO, SiO_2) by moss further degraded bonding and strength. Surfaces with rough textures (73%) and unpaved surroundings (71%) were more susceptible to deterioration, particularly in structures 10–20 years old.

Non-invasive techniques such as Active Infrared Thermography (IRT) have been introduced to detect early-stage biodeterioration [29]. However, while effective for surface-level diagnosis, IRT is limited in detecting subsurface or microstructural damage. Further, longitudinal studies, such as Popović et al.'s [35] 5-year monitoring of lampenflora in Lazar Cave highlights the role of artificial lighting and human activity in moss persistence, but may not translate well to urban or architectural contexts.

Microbial colonization in early concrete facades revealed how environmental conditions like light, moisture, and nitrogen levels promote biofilm formation involving mosses and cyanobacteria [36]. However, despite highlighting degradation pathways, the study lacks a preventive or analytical framework for material protection. In general, current literature has not comprehensively quantified the rate or severity of moss-related deterioration across climate zones, particularly tropical environments.

Moss growth also has an important effect on the appearance of buildings, particularly heritage and architectural facades, resulting in bio-colonization which can lead to discoloration, uneven surface textures, and stains. Bio-colonization is the process of microorganisms colonizing structures, leading to deterioration and maintenance concerns, reducing their aesthetic appeal. Minerals such as melanin, iron, and manganese can cause black, green, and yellow-brown colors. Carotenoids can also contribute to these colors. Color changes can be caused by environmental factors like as light, temperature, depth, and salinity. The presence of one color could lead to the other, on light-colored material such as stone, mortar, plaster, or concrete [14, 29].

Studies show that discoloration patterns on facades act as an aesthetic indication of chemical and physical degradation. For example, moss on sandstone, limestone, or cement facades can leave black stains from stored moisture and microbial colonization, gradually covering the architectural surfaces [32, 35]. Whereas, according to [31] mosses on gray brick buildings in Fuzhou not only deteriorate the material but also have a substantial influence on the urban aesthetic. Also, permanent ruin in historical structures in Poland was identified due to microbial growth promotion, and aesthetic and material degradation [28]. In a similar study, Eyssautier-Chuine et al. [29] discovered surface discoloration on French limestone monuments due to microbial secretions and organic acid accumulation, particularly in high-humidity locations. This impacts conservation efforts since removing biological stains without causing material loss or microcracking is problematic. In summary, Moss-induced aesthetic damage impacts society's perceptions, preservation decisions, and property values. It is critical to prioritize care strategies for heritage and modern

structures, including proper cleaning, moisture management, and biological growth mitigation techniques.

The current literature lacks consistent methodologies to quantify the individual contribution of biological agents, such as moss, to material degradation in urban environments, which is costly due to modern construction practices, thinner walls, and poor ventilation, necessitating improved moisture control strategies [37]. Also, moss colonization's biological mechanics and visual impacts are restricted by a lack of quantitative data on moss-induced degradation across diverse material types and climatic locations, especially in tropical and coastal areas. The majority of research has focused on particular cases or laboratory conditions, resulting in limited validity. Further, current detection techniques, such as IRT, are limited to surface evaluation and may overlook deeper structural weakening. The aesthetic impact is rarely quantified in terms of cultural value loss or economic value. Additionally, there is a significant gap in linking discoloration patterns with early warning indicators, especially with modern construction materials.

3.3 Structural Integrity and Durability Reduction of Structures

As these material and structural degradation progresses, it reduces mechanical performance. These effects lead to the reduction of structural integrity and long-term durability of elements over time. The following sections discuss deterioration mechanisms, how they impact load-bearing capacity, and how integrity and durability are assessed in moss-affected structures.

Concrete, one of the most frequently utilized materials, is particularly susceptible to moss-related degradation. Moisture retention also has an impact, on boosting hazardous chemicals, increasing water absorption and chloride penetration, and decreasing freeze-thaw resistance [18, 38]. Over time, this reduces the structure's load-bearing capacity and increases the chance of surface disintegration. Safiuddin [39] also reveals frequent concrete deterioration mechanisms, such as cracking, spalling, and moss growth, which are mostly caused by freeze-thaw cycles, water penetration, and deicing chemicals. Similarly, as Karatas and Dal [30] stated that biological corrosion causes technical effects that reduce the strength of elements and structures, leading to slow degradation. However, current research frequently ignores the long-term conflicts between protecting and deteriorating effects.

This biological activity weakens the strength of materials such as concrete, brick, and stone. While these findings are significant, several studies have quantified that the type of moss species and environmental conditions, such as humidity, temperature, and sunlight, could influence the impact [40, 41]. A comprehensive assessment of moss's role in structural durability should take these factors into account, as well as the interaction between biotic (moss species) and abiotic (environmental) influences. For instance, Saeed Bozorgmehr Nia et.al. [15] argue that chemical degradation occurs when moss-produced organic acids react with cementitious components, lowering concrete density and structural integrity. Moss's root-like structure may penetrate concrete, enabling moisture and corrosive agents to seep in. These findings are supported by research indicating how microbial colonization in tropical conditions increases surface porosity and pH levels, resulting in wall collapse and accelerated concrete degradation due to high solar exposure and precipitation [10, 41].

Moss growth, often seen as a sign of aging in buildings, can significantly impact the durability of materials, especially in high-humidity, tropical, or coastal environments, leading to substantial degradation. Durability is a crucial characteristic of construction since it ensures that a material can withstand environmental conditions in which the structure's operation and safety will not deteriorate significantly over time with moss growth [7]. While several studies agree on biodeterioration and structural degradation in the exposed historical structures, they differ in modern building architectures, where no reported damages occurred due to biological growth. However, the evidence is limited to some material durability issues that were not broadly studied.

In contrast, other investigations provide a different perspective. Awais and Khattak [18] found that while the initial compressive strength of moss-infused concrete is slightly lower than that of conventional concrete, it improves over time. This suggests a more complex and less understood relationship between moss growth and material longevity.

Comparative investigations highlight material-specific vulnerabilities. Ferreira et.al, [42] investigates how climatic conditions influence the durability and maintenance of façade claddings, focusing on Ceramic Tiling Systems, Natural Stone Cladding, External Thermal Insulation Composite Systems, and Architectural Concrete Façades; the findings indicate that ETICS deteriorates quickly in humid, salt-exposed environments. The study suggests that moss growth and its biological factors should be examined with environmental exposure conditions, rather than in isolation.

However, some technological solutions, such as using multi-component cement with zeolite enhance the durability of exterior brick masonry, reduce salt efflorescence, and improve mortar characteristics [43]. They suggest that mineral additions and air-entraining admixtures can minimize shrinkage and strengthen masonry. The applicability of these solutions in existing or historical buildings requires further research.

Standard testing is critical for determining wall durability, developing preventative approaches, promoting sustainable building, and extending structural lifespan under various environmental situations. Safiuddin [39] states that ASTM D3273 and D3274 are standard test methods for assessing mold resistance and surface disfigurement in paint films. These tests evaluate the resistance of treated and untreated concretes to microbial growth, such as mold and moss, in an environmental chamber. Similarly, Puertas et al. [44] utilize non-destructive testing methods like ultrasound, thermography, and Ground penetrating radar to detect structural vulnerabilities.

In summary, moss growth affects material durability by physical, chemical, and biological factors, which influence material type, environmental conditions, and maintenance techniques. Predictive durability models frequently lack

moss-specific indicators such as root penetration depth, color intensity, and in-situ moisture patterns. Understanding these interactions is critical for designing adaptable construction solutions, particularly in tropical and coastal areas with high moss spreading.

3.4 Increased Maintenance and Restoration Costs and Health and Safety Risks

All of these negative impacts, such as material degradation, structural deterioration, aesthetic degradation, and a reduction of both durability and structural integrity, ultimately increase maintenance and rectification costs while elevating health and safety risks. This necessitates lead to the creation of preventative and restoration solutions for structures damaged by moss growth. This combined impact is supported by the following literature.

Moss growth on building surfaces can offer serious health and safety risks, particularly in humid and tropical climates. It makes surfaces more slippery to occupants and maintenance workers, particularly on sloping elements such as stairs and roof tiles, and sometimes on vertical walls too. Moreover, fewer have addressed the long-term risks to respiratory health or the indirect consequences on building maintenance expenses resulting from increasing safety regulations. The Institute of Medicine (IOM) analyzed studies on indoor moisture and reported that these conditions raise health risks in households by 30-50%. The findings emphasize the substantial connection between indoor environmental conditions and negative health outcomes, emphasizing the need for improved moisture management in buildings [45]. Future studies should employ a multidisciplinary approach, combining material science, public health, and architectural safety, to detect risks and propose safer exterior design characteristics for high-traffic or public buildings.

The presence of moss growth on exterior structures increases maintenance and restoration costs due to biological colonization, which retains moisture against the surface, causing material, structural, and aesthetic degradation. Regular cleaning is required to preserve functional and aesthetic functions, but it may deteriorate surface finishes and raise labor and material costs. Specialized conservation techniques may be required in heritage or culturally significant structures to prevent damage to original architectural materials. Continuous moisture caused by moss growth can result in secondary issues such as staining, surface deposits, and microbial buildup. Although these effects are initially visual, they often require specialized maintenance or restoration, especially in heritage structures. Unchecked growth may reduce the service life of exterior components, highlighting the importance of timely preventative interventions to control long-term costs.

Furthermore, moss growth-induced discoloration, which is typically uneven and dependent on climatic conditions such as shade, rainfall, and surface porosity, greatly reduces the aesthetic appeal of architectural features. This might have a detrimental impact on the public's perception of the maintenance of historical or public structures. In severe circumstances, such discoloration may trigger inaccurate restoration activities, such as repainting or resurfacing entire wall portions, therefore compromising the structure's historical identity [28, 30].

Proactive detection and management measures must mitigate moss-induced harm. Buildings have to tolerate harsh weather conditions to retain structural integrity and safeguard interior areas, avoiding complications such as water penetration, structural instability, and poor indoor air quality [22, 46-47].

Moss impacts materials based on species characteristics, substrate adaptability, and environmental conditions. To prevent the biological degradation of walls across construction phases, Nnaji [34] suggests strategies such as employing wall rendering, biocide-infused paints, zinc oxide (0.5%) coatings, decreasing the water-cement ratio, and adding additional materials such as fly ash, silica fume, and slag. Adequate drainage and paving are also highlighted. These procedures are intended to mitigate the harmful effects of moss and biological growth on the durability of exterior sandcrete/concrete walls.

Karatas and Dal [30] suggest surface cleaning using low-pressure water and air for dirt and discolored stone surfaces, mechanical dry cleaning for soft limestone, biological control using herbicides, and mechanical techniques. They recommend hydraulic lime-based joints and anti-corrosion coatings to enhance structural protection. Ferreria et al. [42] propose ceramic tiling or natural stone cladding, avoiding ETICS in high-humidity or coastal environments, applying hydrophobic sealants and biocide-infused coatings, and adjusting the façade design for optimal durability. Notably, facades that face east have a longer life. Timely inspection and treatment of degradation in exterior structures is critical for structural integrity and long-term occupant safety.

Several studies recommend mechanical cleaning and chemical treatment procedures such as blasting, sandblasting, pressure washing, dry ice blasting, biocide sprays, zeolite coatings, UV radiation, and temperature and humidity management, which may all remove growths from surfaces, some limitations exist [30, 34]. However, recent heritage conservation studies pointed out the potential damage to ancient façade caused by poorly governed abrasive cleaning procedures. Although Biocide treatments can be effective, they often have negative impacts on environmental concerns and require several applications on large-scale buildings, leading to substantial maintenance costs, emphasizing the need for long-term, less disruptive preventative approaches.

Similarly, as Karatas and Dal [30] further emphasized, corrective measures include removing defective repairs, repairing structural cracks (up to 0.5 cm) with binder mortar injection or sewing (for larger cracks), replacing lost stability stones with original ones, preserving deformations up to 5 cm, and replacing non-original elements such as PVC-based windows and iron doors with historically accurate materials. According to Udawattha et.al. [10], high-porosity materials are more vulnerable to moss growth, water absorption, and faster deterioration. However, research on improving porosity without affecting water vapor ability of material is limited, highlighting the need for further studies to balance durability and environmental adaptation to reduce moss spread and sustain vapor transmission.

Despite detailed records of moss-related deterioration, significant research gaps exist in linking moss growth characteristics to material porosity and moisture retention, particularly under tropical climate dynamics, and lack incorporated design and maintenance strategies for compromising climate versatility, aesthetic preservation, and public safety.

Figure 4 highlights the negative effects of moss growth on building structures and its research gaps, including moisture retention, material degradation, structural deterioration, aesthetic degradation, structural integrity, and durability reduction, as well as increased maintenance costs, and health and safety risks.

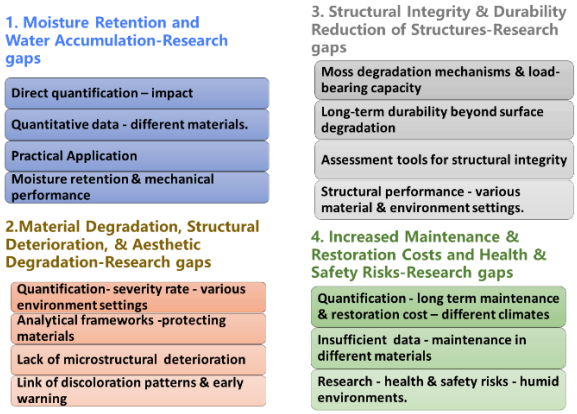

Figure 4: Overview of the negative impacts of moss growth on structural surfaces

4. Positive Impacts on Moss Growth on Structures

Mosses are gaining popularity in architecture due to their environmental and functional benefits. They retain moisture, provide thermal insulation, reduce noise, and enhance energy efficiency. Mosses also act as natural pollution filters, absorbing pollutants and dust, improving air quality and decreasing urban heat island effects. Their porous nature improves stormwater management and flood risk. As well as they also offer resistance to chemicals and surface protection against acid rain and contribute to climate resilience, sustainability, and functional design innovation. Figure 5 illustrates the interconnected benefits in contemporary architecture, contributed by moss growth in structures, as follows.

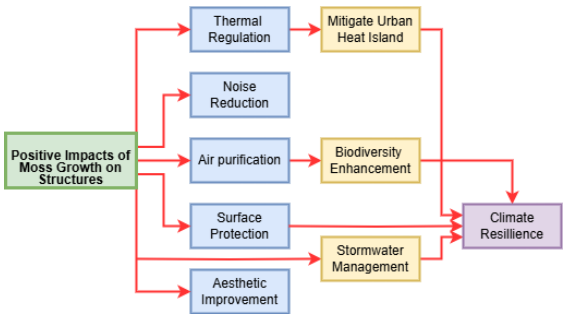

Figure 5: Positive impacts of moss growth on structures

4.1 Thermal Regulation and Heat Island Mitigation through Moss Integration

Moss-based insulation is useful for humid climates and green roofs for improved heat dissipation and environmental sustainability [48]. One study investigates moss-based green roofs' thermal and humidity regulation effects in Dubai's urban environment. Four plant species were studied: *Polytrichum Commune, Thuidium Kanedae, Anomobryum Filiforme,* and *Kentucky Bluegrass*. *Polytrichum Commune* revealed surface temperature by 2.58°C to 3.81°C, while relative humidity increased from 48.0% to 93.3%, with strong cooling potential, whereas *Thuidium Kanedae* and *Anomobryum Filiforme* showed moderate reductions, while *Kentucky Bluegrass* remained steady but showed significant cooling above 30°C [49].

Similarly, another study by Cruz de Carvalho et.al [50] examines moss-based green roofs in the Mediterranean region, where high temperatures, radiation, and limited water availability present challenges. Mosses can dry out and rehydrate, making them ideal for non-irrigated green roofs because they are identified as poikilohydric, Moreover, the presence of moss plays a crucial part in maintaining CO_2 neutrality in the atmosphere [51]. As Fedorik and some researchers [13, 16, 50] argued, Peat and Sphagnum moss insulation materials have similar thermal conductivity values to conventional insulation, ranging from 0.033 to 0.044 W/(m·K) at 10°C. These materials have high porosity, resistance to water vapor diffusion ranging from 2.3 to 3.9, and a specific heat capacity of 1280-1490 J/(kg·K). These properties make them ideal for humid climates and are particularly effective when combined with green roofs to improve heat dissipation and environmental sustainability.

The Urban Heat Island effect (UHI), a major urban climate problem, is affected by solar energy surface management. Conventional building materials transfer 92% of the absorbed energy into convective heat, whereas vegetation converts a considerable part into latent heat. According to studies, moss demonstrated the most efficient thermal behavior among tested vegetation types, converting 50% of radiation into latent heat with the lowest albedo (0.07), based on a comparative analysis of the thermal behavior of common urban building materials and vegetation and their consequences for the UHI effect [52]. Cuce et al. [53] highlight the use of moss in green infrastructure, particularly in façades and roofs, to mitigate solar gain and UHI effects in dense urban areas.

Trkulja et al. [54] conducted experimental research on the environmental performance of Vertical greenery systems (VGS), demonstrating that VGS can significantly enhance energy efficiency and thermal regulation in buildings. Their findings showed that VGS installations can lead to annual energy savings of up to 8%, reduce CO_2 emissions by 2.7 kg/m² per year, and improve air purification. The study also estimated that the capital investment for implementing thermal measures in VGS could be recouped within 8 years. Additionally, VGS was shown to regulate heat movement through dense vegetation, offer protection from winter winds, and decrease heating and cooling demands. The study indicates that vegetation-based systems like moss and VGS can significantly enhance thermal efficiency and sustainability in urban building design.

Additionally, the study emphasized the importance of plant variety and substrate composition in regulating temperature [53]. According to the study by Awais and Khattak et al. [19], moss concrete is an eco-friendly urban construction solution that reduces the UHI effect by reducing temperature extremes. While evidence of moss's cooling effect has been demonstrated in the lab and the outdoors, its efficiency depends on substrate moisture, species selection, and long-term survival. Mosses have an important function in CO_2 absorption and thermal buffering but are often neglected owing to cost constraints. They should be included in sustainable construction strategies [51].

While previous investigations on moss-based systems indicate clear benefits in thermal insulation and energy efficiency, current research remains limited in scope. Most studies are location-specific or experimental, often conducted under controlled conditions, which restricts their applicability to varied climate zones or building types. Although moss species have shown the ability to regulate surface temperature and humidity, especially in harsh environments [49], large-scale field studies and long-term performance evaluations that consider variables such as biodegradation, age, and climate fluctuation are lacking. Some studies suggest that Peat and Sphagnum moss may offer insulation characteristics comparable to conventional materials [55] and highlight their potential for cooling and CO_2 neutrality. However, quantitative evidence on energy savings in urban environments or comparisons with standard insulation systems is insufficient. These limitations are particularly significant for tropical regions like Sri Lanka, where the real-world effectiveness of moss as a passive cooling component remains underexplored.

Research gaps also include a lack of investigation into moss–material interactions specific to local walling types and minimal data on thermal performance across vertical surfaces exposed to solar radiation. Additionally, the absence of standardized evaluation methods and modeling techniques complicates consistent assessment of moss-induced temperature reductions and thermal efficiency across building applications.

4.2 Noise reduction

Beyond thermal benefits, moss-based systems also offer acoustic insulation. Zechmeister et al. [5] highlighted maintenance issues. Moss walls have been demonstrated to suppress ambient noise by up to 10 dBA, offering better interior applications; however, this value is likely ideal and requires real-world validation. Whereas, Sleinus et al. [56] created bio-composites from Sphagnum moss, flax, and vermiculite, displaying enhanced acoustic absorption and environmental advantages while emphasizing the conflicts between material control and ecological function.

Jakubovskis et al. [13] highlight the biophilic design potential of moss-bio receptive concrete, emphasizing its passive sound dampening and aesthetic benefits while pointing out a lack of broad field data and long-term ecological integration responses. In addition to this Jakubovskis et al. [57] developed bio-colonized concrete panels that promote moss growth, exhibiting the potential for noise reduction. Compared to green walls, living walls absorb energy from sound waves, which helps minimize noise, ultimately offering a comfortable building environment.

In summary, moss-based systems have the potential for controlling acoustic sound, but future research should focus on long-term performance, maintenance, and the conversion of laboratory results into reliable, field-validated building solutions.

4.3 Promoting Biodiversity and Ecological Value through Improving Air Quality

Mosses have become biofilters that capture particular matter (PM) and heavy metals while enhancing urban air quality through their participation in building envelopes, but realistic expansion and species optimization remain major challenges. Mosses also act as a natural air purifier [18]. Especially, an experimental approach called “Fine dust collection capacity of a moss greening system for the building envelope” has revealed that moss captures fine particulate matter (PM_x; x-different fractions of PM) from the air, which consists of Al, Ti, Si, Ca, Na, and K, thereby improving urban air quality. Perini et al. [3] found that moss species, including *Homalothecium sericeum, Barbula unguiculata,* and *Grimmia pulvinata* can trap up to 45,580 particles per mm^2 (PM_x collection capacity), which improves air quality.

Additionally, moss-covered surfaces can absorb harmful pollutants like nitrogen oxides (NO_x) and heavy metals such as mercury, reducing air contamination in urban environments and mining areas [9, 17]. Karklina et al. [58] used lab simulations to examine three moss species: *Dicranum scoparium, Plagiomnium affine,* and *Hypnum cupressiforme* in a control shrub for PM absorption. Mosses, specifically *Hypnum cupressiforme* and *Plagiomnium affine*, can effectively absorb $PM_{2.5}$ and PM_{10} with average efficiencies of 41% for $PM_{2.5}$ and 47% for PM_{10}, where *Plagiomnium affine* exhibited the biggest difference (51.45% for PM_{10} and 41.63% for $PM_{2.5}$) under laboratory conditions. This suggests that they could be a lightweight and low-maintenance alternative to vascular plants in green infrastructures. Igbar et al. [59] used moss (*Dicranum scoparium*) as a biomonitor on the University of Lagos campus walls and found high levels of Zn, Pb, and Cd that exceeded local and UNEP rules and regulations, proving its role as a passive heavy metal filter.

Moss-covered surfaces in urban environments not only enhance air quality as a Natural pollution filter but also boost biodiversity and ecological value by providing better microhabitats for many different organisms, resulting in a more reliable and diverse urban environment.

Recent research studies suggested the presence of moss on building elements or materials may offer both environmental and economic benefits. For example, moss can regulate moisture levels and protect the wall surface from weathering, offering potential benefits [47]. Furthermore, they provide a cost-effective, low-maintenance green envelope, such as building exterior (facades, roofs, and windows) for large-scale urban and industrial building applications due to their low substrate, water, and nutrient requirements, low irrigation for passage of the water, as well as their high desiccation tolerance [13, 16].

X. Li et al. [48] have developed a green 3D printing protocol for innovative applications of moss, combining aerogel and hydrogel with a hydrothermal nano-modification process. This method offers space-saving, durable, and convenient growth, with effective thermal insulation, antimicrobial properties, and excellent adsorption of methanal and $PM_{2.5}$, surpassing traditional 3D-printed products. However, uncertainties remain regarding these technologies' capacity for growth and durability beyond laboratory conditions.

Though mosses have demonstrated their ability as natural pollution filters and ecological boosters, there are research gaps regarding their scalability and real-world applications. While laboratory experiments demonstrated that they are effective in trapping PM and heavy metals, little is known about their long-term performance in dynamic urban environments. Furthermore, species selection and optimization for certain climates, surface types, and pollution levels have not been thoroughly investigated. There is also no specific evidence that improving air quality leads to measurable increases in urban biodiversity. While mosses are believed to enhance microhabitats, further research is needed to determine their effect on flora and fauna. Despite being low-maintenance, their long-term durability, recovery ability, and maintenance requirements for building envelopes are poorly understood. Addressing these gaps is essential to sustainable urban design.

4.4 Surface Durability, Chemical Resistance, and Stormwater Management

Mosses, when integrated into construction materials or surfaces, can shield structures from environmental damage, acid rain, and surface deterioration. Ervik et al. [60] discovered that moss on old asbestos cement roofs works as a stabilizing layer, trapping and binding weathered asbestos fibers, decreasing fiber mobilization into the air and runoff, and protecting the surface from rain impact and chemical exposure. Furthermore, Moss mats, when applied to modular green walls or bio-receptive concrete, provide a natural barrier against UV radiation and acid rain. They absorb moisture without structural penetration, reducing direct water contact with the underlying material and potentially reducing freeze-thaw damage. Additionally, Cozzolino et al. [61] found that mosses, despite their biodeterioration capacity, are less aggressive than vascular plants and may prevent colonization by destructive species when stable, indicating a potential sacrificial or shielding role. Thus, when employed effectively, mosses can provide passive protection against environmental stresses and chemical attacks by serving as a green interface layer between contaminants and built construction.

Vegetation and permeable surfaces assist stormwater management by absorbing rainwater [19], lowering runoff, and minimizing flooding. Green roofs may retain up to 80% of the annual rainfall [62], although this value likely reflects optimal performance conditions and can vary depending on vegetation type and local climate. Cascone [63] claims that green roof substrates, particularly those containing moss or shallow-rooted species, efficiently absorb stormwater, delay peak flow, and mitigate urban floods when paired with built drainage layers. This highlights moss's functional potential, especially in engineered systems where weight constraints limit the use of deeper substrates. Supporting this, Burszta-Adamiak et al.'s [64] pilot research on urban green roof constructions found that *Ceratodon purpureus* effectively established and retained water at a maximum weight of 7.0 $kg \cdot m^2$, making it suitable for lightweight and large green roofs. Rocha et al. [65] further discovered that moss-dominated beds on Lisbon green roofs increase rainfall retention during Mediterranean storm conditions, but might require pre-treatment for increased contaminants in water quality runoff. While this underscores moss's hydrological buffering capacity, it also raises practical concerns about runoff quality, which may require supplementary filtration systems in reuse-focused installations.

4.5 Aesthetic Appeal and Climate Resilience in Sustainable Design

Mosses add particular visual qualities to building surfaces, including textural diversity, adaptive coloring, and a biophilic character that corresponds with sustainable design concepts. Veeger et al. [9] investigated the aesthetic adaptation of urban moss communities to bio-receptive concrete, revealing that species such as *Tortula muralis* and *Grimmia pulvinata* provide changing textures and colors, integrating moss into a living architectural feature. Nasr et al. [62] emphasized the significance of green walls in sustainable architecture, noting their ability to improve environmental performance and enhance architectural interest, and suggested the use of moss attributes. Radić et al. [66] discovered that vertical greenery systems (VGS), particularly mosses in modular structures, produce a uniform and calm aesthetic suitable for both ancient and modern environments. Out of 400 participants, 118 strongly agreed and 185 agreed that VGSs are appealing. Moss-integrated VGS not only enhances visual appeal but also significantly contributes to climate resilience. Integrating living vegetation into facades improves the aesthetic and promotes sustainable urban architecture

However, long-term maintenance needs, particularly in harsh urban environments, remain under-researched. Furthermore, the integration of moss in VGS and moss-based concrete in sustainable construction lacks comprehensive long-term performance assessments. Further investigations are required to evaluate mechanical strength, resistance to weathering, and microbial interactions under diverse climatic conditions.

Figure 6 presents the summary of the positive impacts of moss growth on various factors, including thermal regulation, UHI mitigation, noise reduction, air purification, promoting biodiversity and ecological value, surface protection, stormwater management, and aesthetic enhancement. These effects are supported by research studies demonstrating its effectiveness in improving energy efficiency and creating climate resilience in sustainable design and architecture.

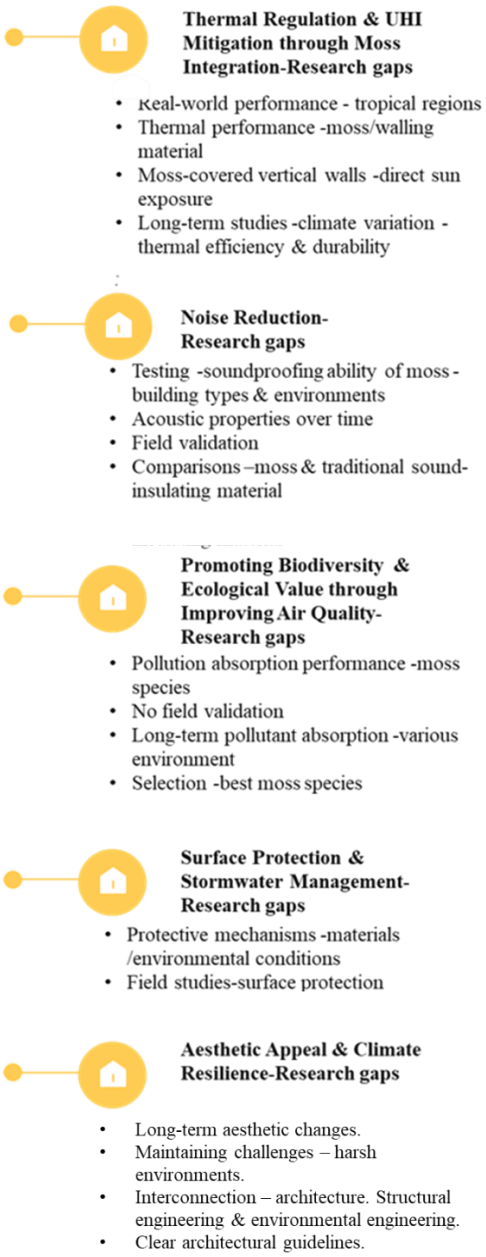

Figure 6: Overview of the positive impacts of moss growth on structural surfaces

5. State-of-the-Art Research on Moss Growth Identification in Structures

Despite the experimental studies mentioned in sections 3 and 4 on moss growth, recent studies expanded on numerical modeling, Image processing, and artificial intelligence to assess the performance and impacts of moss growth on building facades and structures. An interdisciplinary approach, incorporating laboratory testing, field data, and computational simulation, has helped further comprehend the mechanisms of moss degradation in exterior wall systems.

For example, Finite element models (FEM) have been utilized to simulate the impact of moss on structural behavior. Puertas et.al [44] used FEM and XFEM surrogate modeling to assess damage progression and crack formation in the Tower of Muhammad at the Alhambra (Granada, Spain), confirming existing structural pathologies and demonstrating accelerometers' effectiveness for real-time monitoring. Their study underscored that continuous assessment is crucial, and suggested Bayesian model updating and aging degradation models for improved predictive accuracy for sustainable management and preservation of historical structures. Similarly, Yasui et.al [67] applied FEM to simulate temperature control in moss-covered ceramics. Revealing that water evaporation (2452-2380 kJ/kg), has decreasing surface temperatures, confirming that moisture retention has a direct impact on temperature regulation in moss-based materials.

Though laboratory testing and numerical models are vital for understanding moss growth on building materials, they often require time and resources. Beyond FEM, Automated monitoring and intelligent techniques, such as hyperspectral imaging, digital image correlation, and machine learning-based classification, improve the accuracy and speed of performance evaluations. Dias et al. [68] explored advanced technologies for automating building facade inspections, highlighting their potential to improve visual assessment, collect data, and reduce diagnostic uncertainty in building maintenance. Similarly, Guedes et.al [12] demonstrated the mutually beneficial qualities of RGB, thermal, and multispectral sensors on UAVs to identify façade pathologies by detecting cracks, moisture, coating detachment, and moss. Finding that RGB sensors were most effective for crack detection, thermal imaging for subsurface moisture issues, and multispectral sensors detected biological growth but not fine structural cracks.

Numerous researchers have used machine learning and deep learning approaches for automated moss identification and severity assessments. Also, Zhang et.al [31] applied the YOLOv8 machine learning model in Fuzhou, China, to detect efflorescence and plant growth in gray brick buildings, which leads to surface erosion and material weakening, and irreversible facade damage. Similarly, the study by Mishra and colleagues investigates the application of two AI techniques, ChatGPT and YOLOv5, to detect and characterize surface degradation in ancient structures. ChatGPT, which is developed for natural language activities, showed potential in reporting observable damage using appropriate prompts and cues without prior training, whereas YOLOv5 demonstrated accurate visual detection, highlighting the complementary responsibilities of each of these tools [69].

Ramani et al [70] present a 97% accuracy rate for detecting and classifying moss and crack damage in stone monuments using a deep learning model, incorporating Luminance and Gray-Level Co-occurrence Matrices (GLCM) for data analysis and a Multi-Layer Neural Network for classification, combining GLCM and luminance images using K-means clustering. Also, their study classified moss degradation into four categories based on RGB values: no obvious damage, slight damage, moderate damage, and severe damage. The RGB values range from [91 93 100] to [250 250 250], indicating no obvious damage. Values between [90 120 40] and [160 195 95] indicate slight damage, values between [40 50 30] and [60 88 52] suggest moderate damage, and values between [10 10 10] and [67 78 96] define severe damage. Perumal

& Venkatachalam's, [71] work validated the effectiveness of using K-means clustering and Canny edge detection, enhancing early detection and enabling targeted conservation strategies.

Additionally, Ushada and Murse [6] developed an Artificial Neural Network (ANN) model to control moss growth by analyzing temperature variables. The model achieved high prediction accuracy with less than 10% error, as temperature changes significantly influenced moss growth, and essential growth factors, such as specific leaf and ground area per plant, were identified as 1.498 m^2/kg and 28 mm^2, respectively, for *Rhacomitrium canescens*, showcasing the potential for growth control in building envelopes.

Current methods for monitoring moss growth on building facades have limitations in uniformity, scalability, and predictive integration. Many models rely solely on RGB data, excluding hyperspectral, thermal, or multispectral inputs. Standardized RGB limits across different walling materials limit the generalizability of moss severity classification. Temporal analysis is often lacking, limiting understanding of moss growth and its long-term impact. Future research should develop hybrid models combining numerical simulations with multisource image data, real-time monitoring systems, and automated classification algorithms for early detection, severity grading, and predictive maintenance planning in modern and heritage buildings.

Figure 7 illustrates current approaches for identifying and analyzing moss growth on buildings and structures, incorporating numerical modeling, image processing, and artificial intelligence.

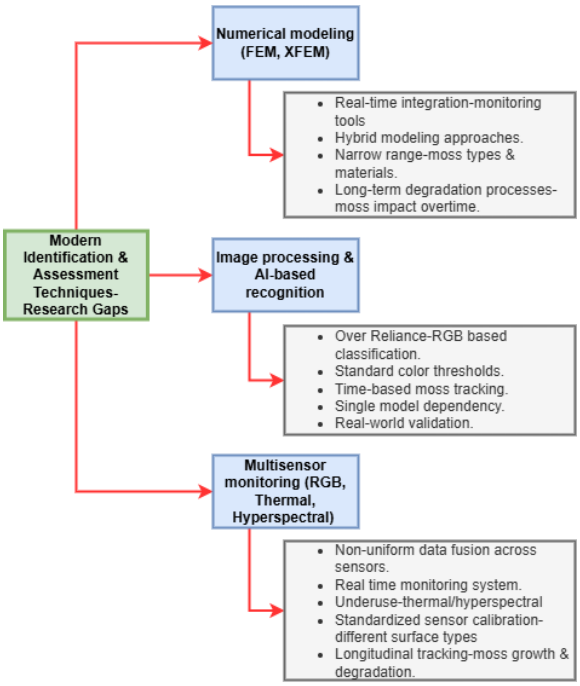

Figure 7: Overview of research gaps in current approaches to identification and analysis of moss growth

6. Concluding Remarks

Mosses, non-vascular plants in the Bryophyta class, are the largest group of 10,000 species, developed around 470 million years ago. They are poikilohydric, rehydrating, desiccation-tolerant, and able to withstand extreme temperatures. Its optimal temperatures range from 15-25°C. Moss can grow faster (1-2 months) in controlled environments than natural growth, which thrives on high moisture, shade, and low air circulation surfaces. Two common types of moss that can thrive on building surfaces are Pleurocarpous mosses, which grow horizontally along surfaces, and acrocarpous mosses, which grow upright. Mosses have a distinctive life cycle, beginning with protonema, evolving into gametophytes, reproducing asexually or sexually, colonizing building materials, regenerating protonema, and spreading through spore dispersal. Colonization is influenced by surface properties, pH range, nutrients, and microbial interactions. Mosses, due to their adaptability to climates and pollution levels, are ideal for urban and industrial environments, especially popular in areas exposed to weathering like rain, wind, and ultraviolet radiation.

Moss growth on structures has negative impacts, starting with moisture retention and water accumulation, which in turn lead to material degradation, structural deterioration, and aesthetic degradation. These effects further compromise structural integrity and durability, leading to increased maintenance and restoration costs and health and safety risks. Studies have shown that Epilithic colonization of mosses on surfaces causes moisture retention, discoloration, and surface weathering. On the other hand, Endolytic colonization occurs when microorganisms penetrate the surface, causing internal weakening, micro-cracks, and chemical alteration. As reported in previous studies, moss growth, originating from epilithic forms, develops into root-like structures and microbial interactions, causing irreversible structural degradation not only in historical structures but also in mortars, plasters, and concrete, which is leading to increased porosity, salt crystallization, and decalcification. Moss growth in building elements has protective effects, but oxalic acid may contribute to concrete erosion. Chemical degradation occurs when moss-produced organic acids react with cementitious components, lowering concrete density and structural integrity. Moisture retention increases hazardous chemicals, water absorption, chloride penetration, and freeze-thaw resistance.

However, Moss in architecture provides environmental and economic benefits to sustainable construction practices. Mosses enhance environmental performance by improving thermal insulation, regulating surface temperature, mitigating the urban heat island effect, and enhancing acoustic properties. They also improve environmental quality through carbon sequestration and air purification, and they contribute to biodiversity and ecological value. Additionally, mosses aid in storm management, enhance surface durability, and protect against acid rain and environmental wear. Mosses are increasingly used in design as a living material that promotes energy efficiency, biophilic practices, and green infrastructure, thereby demonstrating their potential as a passive, low-maintenance component in creating sustainable, climate-resilient built environments.

The relationship between moss growth and its effects is complex and varies based on species, environmental

conditions, and building materials, making studying relevant species crucial.

So, moss growth on building facades is assessed using various techniques, such as laboratory testing, computer modeling, FEM analysis, automated monitoring (3D laser scanning, infrared thermography, photogrammetry, digital image processing), and deep learning models in the past. Finite element simulations, image-based techniques, and machine learning have enhanced damage progression evaluation, real-time monitoring, and moss detection accuracy, while deep learning algorithms have improved severity classification and detection. However, hybrid models, combining multi-source imaging data, predictive analytics, and real-time monitoring, are crucial for early detection, conservation planning, and sustainable structural maintenance, despite challenges in generalizability and data standardization. More research is needed for reliability and to predict the impacts of various materials and moss types along with environmental conditions.

Future research should integrate biological understanding, material science, and digital technologies to address moss growth and its impact on durability. Including temporal data, environmental parameters, and multisource imaging (e.g., RGB, thermal, and hyperspectral) can improve early detection, classification, and long-term monitoring. Standardized severity grading systems and hybrid models incorporating artificial intelligence, real-time sensing, and numerical simulations can provide scalable, accurate assessments.

Construction and building technology advancements present major possibilities for low-maintenance, energy-efficient, and climate-resilient exterior designs. These include passive cooling systems and moss-covered facades that regulate surface temperature. Predictive maintenance frameworks provide cost-effective preservation solutions, particularly for historic structures. An integrated moss-based system promotes sustainable design by limiting degradation and guaranteeing long-term environmental performance. Importantly, Future studies should determine the marginal level at which moss's ecological and thermal advantages convey the potential for structural degradation. This will assist the industry in balancing bio-integration and durability by offering recommendations on appropriate moss coverage, material reliability, and exposure conditions. This knowledge will assist designers and engineers make informed decisions about using moss in architectural systems, preventing undesirable consequences such as moisture retention, biological corrosion, surface erosion, or any other degradation. Researchers collaborate with structural engineering, environmental engineering, computer engineering, data analytics, and architectural design to build strong, resilient, and environmentally adaptable constructed environments.

References

[1] H. Govndapyari, Sanavar, Y. M. Bahuguna, and P. L. Uniyal, “Habitat Preference in Pleurocarpus Mosses of Imphal District, Manipur, India,” *Evansia*, vol. 31, no. 3, pp. 99–108, Sep. 2014, doi: 10.1639/079.031.0305.

[2] P. Julinova and D. Beckovsky, “Perspectives of moss species in urban ecosystems and vertical living-architecture: A review,” in *Advances in Engineering Materials, Structures and Systems: Innovations, Mechanics and Applications - Proceedings of the 7th International Conference on Structural Engineering, Mechanics and Computation, 2019*, CRC Press/Balkema, 2019, pp. 2370–2375. doi: 10.1201/9780429426506-408.

[3] K. Perini, P. Castellari, M. Calbi, S. Prandi, and E. Roccotiello, “Fine dust collection capacity of a moss greening system for the building envelope: An experimental approach,” *Build Environ*, vol. 267, Jan. 2025, doi: 10.1016/j.buildenv.2024.112203.

[4] W. Lin, Y. Wang, Y. Coudert, and D. Kierzkowski, “Leaf Morphogenesis: Insights From the Moss Physcomitrium patens,” Sep. 23, 2021, *Frontiers Media S.A.* doi: 10.3389/fpls.2021.736212.

[5] H. G. Zechmeister, L. Möslinger, A. Korjenic, E. Streit, A. Sulejmanovski, P. Frank, and E. Hummel, “Viability of Living Moss for Indoor Green Walls: A Study on Temperature, Humidity, and Irrigation,” *Sustainability*, vol. 15, no. 21, p. 15625, Nov. 2023, doi: 10.3390/su152115625.

[6] M. Ushada and H. Murase, “Identification of a Moss Growth System using an Artificial Neural Network Model,” *Biosyst Eng*, vol. 94, no. 2, pp. 179–189, Jun. 2006, doi: 10.1016/j.biosystemseng.2006.03.001.

[7] M. Chemrouk and N. Attari, “Durability of Concrete with Particular Reference to High Performance Concrete,” Sep. 2003.

[8] A. Adessi, R. De Philippis, and F. Rossi, “Drought-tolerant cyanobacteria and mosses as biotechnological tools to attain land degradation neutrality,” *Web Ecol*, vol. 21, no. 1, pp. 65–78, Apr. 2021, doi: 10.5194/we-21-65-2021.

[9] M. Veeger, E. M. Veenendaal, J. Limpens, M. Ottelé, and H. M. Jonkers, “Moss species for bioreceptive concrete: A survey of epilithic urban moss communities and their dynamics,” *Ecol Eng*, vol. 212, Feb. 2025, doi: 10.1016/j.ecoleng.2024.107502.

[10] C. Udawattha, H. Galkanda, I. S. Ariyarathne, G. Y. Jayasinghe, and R. Halwatura, “Mold growth and moss growth on tropical walls,” *Build Environ*, vol. 137, pp. 268–279, Jun. 2018, doi: 10.1016/j.buildenv.2018.04.018.

[11] I. Chairunnisa and D. Susanto, “Living material as a building façade: The effect of moss growth toward mechanical performance on pre-vegetated concrete panels,” *International Journal of Technology*, vol. 9, no. 6, pp. 1266–1275, Dec. 2018, doi: 10.14716/ijtech.v9i6.2445.

[12] J. V. F. Guedes, G. de S. Meira, E. de S. Bias, B. Pitanga, and V. Lisboa, “Performance of Sensors Embedded in UAVs for the Analysis and Identification of Pathologies in Building Façades,” *Buildings*, vol. 15, no. 6, Mar. 2025, doi: 10.3390/buildings15060875.

[13] R. Jakubovskis, “Biophilic Facades: The Potentiality of Bioreceptive Concrete,” Nov. 12, 2024. doi: 10.20944/preprints202411.0678.v1.

[14] M. F. La Russa and S. A. Ruffolo, “Mortars and plasters - How to characterize mortar and plaster degradation,” Oct. 01, 2021, *Springer Science and Business Media Deutschland GmbH*. doi: 10.1007/s12520-021-01405-1.

[15] Saeed Bozorgmehr Nia, “Assessing the Durability of Coastal High-Performance Concrete (HPC) Structures Exposed to Biodegradables such as Algae and Moss,” *JournalofCivilEngineeringandMaterialsApplication*, vol. 7, no. 2, pp. 121–129, Jun. 2023.

[16] K. Perini, P. Castellari, A. Giachetta, C. Turcato, and E. Roccotiello, “Experiencing innovative biomaterials for

buildings: Potentialities of mosses," *Build Environ*, vol. 172, Apr. 2020, doi: 10.1016/j.buildenv.2020.106708.
[17] F. Meloni, S. Calabrese, O.Vaselli, F.Capecchiacci, F. Ciani, L. Brusca, S. Bellomo, W. D'Alessandro, K. Daskalopoulou, S. Venturi, B. Nisi, D. Rappuoli, F. Tassi, and J. Cabassi, "Active Moss Biomonitoring of Mercury in the Mine-Polluted Area of Abbadia San Salvatore (Mt. Amiata, Central Italy)," *Toxics*, vol. 13, no. 1, Jan. 2025, doi: 10.3390/toxics13010002.
[18] M. Awais and S. U. Khattak, "Exploring the Potential of Moss Concrete as an Eco-Friendly Solution to Mitigate Urban Heat Island Effect," 2023.
[19] A. Almusaed, A. Almssad, A. Alasadi, I. Yitmen, and S. Al-Samaraee, "Assessing the Role and Efficiency of Thermal Insulation by the 'BIO-GREEN PANEL' in Enhancing Sustainability in a Built Environment," *Sustainability (Switzerland)*, vol. 15, no. 13, Jul. 2023, doi: 10.3390/su151310418.
[20] B. Goffinet, "Systematics of the Bryophyta (mosses): From molecules to a revised classification," 2004. [Online]. Available: https://www.researchgate.net/publication/233986259
[21] D. Jayanthi, S. J. Meghana, H. G. Rao, and S. Shravya, "Cyanobacterial symbiosis with bryophytes," in *Microbial Symbionts: Functions and Molecular Interactions on Host*, Elsevier, 2022, pp. 15–27. doi: 10.1016/B978-0-323-99334-0.00023-2.
[22] E. Korol and N. Shushunova, "Innovative Device Technology of Green Roof Systems," *IOP Conf Ser Mater Sci Eng*, vol. 1079, no. 3, p. 032099, Mar. 2021, doi: 10.1088/1757-899x/1079/3/032099.
[23] M. Wesołowska and M. Laska, "Thermomodernization of buildings with the utilization of green walls," 2019, doi: 10.1051/e3sconf/2019.
[24] X. Liu, P. Zhou, X. Li, and D. Zhang, "Propagation of desert moss Syntrichia caninervis in peat pellet: a method for rapidly obtaining large numbers of cloned gametophytes," *Plant Methods*, vol. 17, no. 1, Dec. 2021, doi: 10.1186/s13007-021-00740-7.
[25] D. P. Biswal and K. C. S. Panigrahi, "Red Light and Glucose Enhance Cytokinin-Mediated Bud Initial Formation in Physcomitrium patens," *Plants*, vol. 11, no. 5, Mar. 2022, doi: 10.3390/plants11050707.
[26] K. Jang and H. Viles, "Moisture Interactions Between Mosses and Their Underlying Stone Substrates," *Studies in Conservation*, vol. 67, no. 8, pp. 532–544, 2022, doi: 10.1080/00393630.2021.1892430.
[27] J. M. P. Q. Delgado, A. S. Guimarães, V. P. De Freitas, I. Antepara, V. Kočí, and R. Černý, "Salt Damage and Rising Damp Treatment in Building Structures," 2016, *Hindawi Limited*. doi: 10.1155/2016/1280894.
[28] M. Trochonowicz, B. Klimek, and D. Lisiecki, "Biological corrosion and vegetation in the aspect of permanent ruin," *Budownictwo i Architektura*, vol. 17, no. 4, pp. 017–026, Feb. 2019, doi: 10.24358/bud-arch_18_174_02.
[29] S. Eyssautier-Chuine, K. Mouhoubi, F. Reffuveille, J.-L. Bodnar, and J.-L. Bodnar Thermographic, "Thermographic imaging for early detection of biocolonization on buildings," vol. 2020, no. 8, Mar. 2020, doi: 10.1080/09613218.2020.1730740ï.
[30] L. Karatas and M. Dal, "Investigating the Geoenvironmental and Climatic Impacts on the Facades of Historical Houses in Killit (Dereiçi) Village, Mardin," *Mimarlık Bilimleri ve Uygulamaları Dergisi (MBUD)*, Dec. 2023, doi: 10.30785/mbud.1319556.
[31] L. Zhang, Y. Chen, L. Zheng, B. Yas, J. Zhang, A. Xie, and S. Lou, "Investigating the Surface Damage to Fuzhou's Ancient Houses (Gu-Cuo) Using a Non-Destructive Testing Method Constructed via Machine Learning," *Coatings*, vol. 14, no. 11, Nov. 2024, doi: 10.3390/coatings14111466.
[32] J. Li, M. Deng, L. Gao, S. Yen, Y. Katayama, and J. D. Gu, "The active microbes and biochemical processes contributing to deterioration of Angkor sandstone monuments under the tropical climate in Cambodia – A review," Jan. 01, 2021, *Elsevier Masson s.r.l.* doi: 10.1016/j.culher.2020.10.010.
[33] M. Ljaljević Grbić, I. Dimkić, Z. Savković, M. Stupar, A. Knežević, A. Jelikić, and N. Unković, "Mycobiome Diversity of the Cave Church of Sts. Peter and Paul in Serbia—Risk Assessment Implication for the Conservation of Rare Cavern Habitat Housing a Peculiar Fresco Painting," *Journal of Fungi*, vol. 8, no. 12, Dec. 2022, doi: 10.3390/jof8121263.
[34] C. C. Nnaji, U. H. Amadi, and R. Molokwu, "Investigative study of biodeterioration of external sandcrete/concrete walls in Nigeria," *Research Journal of Environmental Toxicology*, vol. 10, no. 2, pp. 88–99, 2016, doi: 10.3923/rjet.2016.88.99.
[35] S. S. Popović, N. V. Nikolić, M. N. Pećić, A. A. Anđelković, and G. V. S. Simić, "First Report on a 5-Year Monitoring of Lampenflora in a Famous Show Cave in Serbia," *Geoheritage*, vol. 15, no. 1, Mar. 2023, doi: 10.1007/s12371-022-00771-z.
[36] W. Xiong, Y. Tao, P. Wang, K. Wu, and L. Chen, "Impact of Environmental Factors on the Formation and Development of Biological Soil Crusts in Lime Concrete Materials of Building Facades," *Applied Sciences (Switzerland)*, vol. 12, no. 6, Mar. 2022, doi: 10.3390/app12062974.
[37] J. Lin and D. Scott, "Assessment of Significances of Building Failure Induced by Foundation Failure, Façade Failure and Moisture Problem," 2006.
[38] W. P. S. Dias, "Factors Influencing the Service Life of Buildings," 2013.
[39] M. Safiuddin, "Concrete damage in field conditions and protective sealer and coating systems," *Coatings*, vol. 7, no. 7, Jul. 2017, doi: 10.3390/coatings7070090.
[40] F. Lucas, L. Adelard, F. Garde, and H. Boyer, "Study of moisture in buildings for hot humid climates," 2002.
[41] M. Sanchez-Silva, A. M. Asce, D. V Rosowsky, and M. Asce, "Biodeterioration of Construction Materials: State of the Art and Future Challenges," pp. 352–365, 2008, doi: 10.1061/ASCE0899-1561200820:5352.
[42] C. Ferreira, J. Barrelas, A. Silva, J. de Brito, I. S. Dias, and I. Flores-Colen, "Impact of environmental exposure conditions on the maintenance of facades' claddings," *Buildings*, vol. 11, no. 4, Apr. 2021, doi: 10.3390/buildings11040138.
[43] T. Kropyvnytska, R. Semeniv, and H. Ivashchyshyn, "Increase of brick masonry durability for external walls of buildings and structures," 2017.
[44] E. Puertas, F. Ávila, E. García-Macías, and R. Gallego, "Preventive Preservation of Rammed Earth Historical Heritage Through Continuous Monitoring, Architectural Inspections, and Data Fusion," *Buildings*, vol. 14, no. 10, p. 3294, Oct. 2024, doi: 10.3390/buildings14103294.
[45] W. J. Fisk, Q. Lei-Gomez, and M. J. Mendell, "Meta-analyses of the associations of respiratory health effects with dampness and mold in homes," *Indoor Air*, vol. 17, no. 4, pp. 284–296, 2007, doi: 10.1111/j.1600-0668.2007.00475.x.
[46] M. C. Phillipson, R. Emmanuel, and P. H. Baker, "The durability of building materials under a changing climate," *Wiley Interdiscip Rev Clim Change*, vol. 7, no. 4, pp. 590–599, Jul. 2016, doi: 10.1002/wcc.398.

[47] K. J. Beasley, “Building Facade Failure Risk Assessment,” *Journal of Performance of Constructed Facilities*, vol. 28, no. 5, Oct. 2014, doi: 10.1061/(asce)cf.1943-5509.0000651.

[48] X. Li, R. Wu, J. Wang, and J. Huang, “Green 3D printing: Portable, wearable, and antibacterial photosynthetic material for the crowded world,” *AIP Adv*, vol. 14, no. 12, Dec. 2024, doi: 10.1063/5.0244875.

[49] C. Jung, J. Awad, M. A. Ismail, and A. H. Chohan, “Enhancing Urban Sustainability through Green Roofs: A Thermal Performance Evaluation in Dubai,” *Future Cities and Environment*, vol. 9, no. 1, 2023, doi: 10.5334/fce.206.

[50] R. Cruz de Carvalho, Z. Varela, T. A. do Paço, and C. Branquinho, “Selecting Potential Moss Species for Green Roofs in the Mediterranean Basin,” *Urban Science*, vol. 3, no. 2, Jun. 2019, doi: 10.3390/urbansci3020057.

[51] D. B. Pinto and J. Castro-Gomes, “Waste subtracts and nutrients as ingredients for vegetation growth in construction materials – A review,” Oct. 01, 2022, *Elsevier Ltd*. doi: 10.1016/j.clet.2022.100548.

[52] E. (Eva) Stache, B. (Bart) Schilperoort, M. (Marc) Ottelé, and H. M. (Henk) Jonkers, “Comparative analysis in thermal behaviour of common urban building materials and vegetation and consequences for urban heat island effect,” Apr. 01, 2022, *Elsevier Ltd*. doi: 10.1016/j.buildenv.2021.108489.

[53] P. M. Cuce, E. Cuce, and M. Santamouris, “Towards Sustainable and Climate-Resilient Cities: Mitigating Urban Heat Islands Through Green Infrastructure,” *Sustainability (Switzerland)*, vol. 17, no. 3, Feb. 2025, doi: 10.3390/su17031303.

[54] T. Trkulja, M. Radujković, and M. Nikolić-Topalović, “Vertical greenery system: a model for improving energy efficiency of buildings,” *Gradjevinar*, vol. 74, no. 8, pp. 561–571, 2022, doi: 10.14256/JCE.3370.2021.

[55] F. Fedorik, J. Zach, M. Lehto, H. Kymäläinen, R. Kuisma, M. Jallinoja, K. Illikainen, and S. Alitalo, “Hygrothermal properties of advanced bio-based insulation materials,” *Energy Build*, vol. 253, Dec. 2021, doi: 10.1016/j.enbuild.2021.111528.

[56] D. Sleinus, M. Sinka, A. Korjakins, V. Obuka, V. Nikolajeva, R. Brencis, and E. Savicka, “Properties of Sound Absorption Composite Materials Developed Using Flax Fiber, Sphagnum Moss, Vermiculite, and Sapropel,” *Materials*, vol. 16, no. 3, Feb. 2023, doi: 10.3390/ma16031060.

[57] R. Jakubovskis, J. Malaiškienė, and V. Gribniak, “Bio-colonization layered concrete panel for greening vertical surfaces: A field study,” *Case Studies in Construction Materials*, vol. 19, Dec. 2023, doi: 10.1016/j.cscm.2023.e02394.

[58] J. Karklina, E. Karklins, L. Abele, J. B. Renard, and L. Strazdina, “Atmospheric Pollution Particulate Matter Absorption Efficiency by Bryophytes in Laboratory Conditions,” *Atmosphere (Basel)*, vol. 16, no. 4, Apr. 2025, doi: 10.3390/atmos16040479.

[59] A. D. Igbar, O. D. Amusa, A. J. Ihejimba, and O. T. Ogundipe, “Biomonitoring of heavy metals pollution in the university of Lagos, Akoka campus environment using the moss *Dicranium scorparium* Hedw,” *Science World Journal*, vol. 18, no. 3, pp. 445–451, Oct. 2023, doi: 10.4314/swj.v18i3.18.

[60] T. Ervik, S. Eriksen Hammer, and P. Graff, “Mobilization of asbestos fibers by weathering of a corrugated asbestos cement roof,” *J Occup Environ Hyg*, vol. 18, no. 3, pp. 110–117, 2021, doi: 10.1080/15459624.2020.1867730.

[61] A. Cozzolino, P. Adamo, G. Bonanomi, and R. Motti, “The Role of Lichens, Mosses, and Vascular Plants in the Biodeterioration of Historic Buildings: A Review,” Dec. 01, 2022, *MDPI*. doi: 10.3390/plants11243429.

[62] Y. Nasr, H. El Zakhem, A. E. A. Hamami, M. El Bachawati, and R. Belarbi, “Comprehensive Assessment of the Impact of Green Roofs and Walls on Building Energy Performance: A Scientific Review,” Oct. 01, 2024, *Multidisciplinary Digital Publishing Institute (MDPI)*. doi: 10.3390/en17205160.

[63] S. Cascone, “Green roof design: State of the art on technology and materials,” Jun. 01, 2019, *MDPI*. doi: 10.3390/su11113020.

[64] E. Burszta-Adamiak, E. Fudali, J. Łomotowski, and K. Kolasińska, “A pilot study on improve the functioning of extensive green roofs in city centers using mosses,” *Scientific Review Engineering and Environmental Sciences*, vol. 28, no. 1, pp. 118–130, 2019, doi: 10.22630/PNIKS.2019.28.1.11.

[65] B. Rocha, T. Paço, A. Luz, P. Palha, S. Milliken, B. Kotzen, C. Branquinho, P. Pinho, and R. de Carvalho, “Are biocrusts and xerophytic vegetation a viable green roof typology in a mediterranean climate? A comparison between differently vegetated green roofs in water runoff and water quality,” *Water (Switzerland)*, vol. 13, no. 1, Jan. 2021, doi: 10.3390/w13010094.

[66] M. Radić, M. B. Dodig, and T. Auer, “Green facades and living walls-A review establishing the classification of construction types and mapping the benefits,” Sep. 01, 2019, *MDPI*. doi: 10.3390/su11174579.

[67] K. Yasui, A. Tanaka, K. Ito, M. Fujisaki, and H. Kinoshita, “Experimental and numerical analyses of temperature-reducing-effect by heat of water evaporation on a moss-greening ceramic utilizing waste silica,” *Materials*, vol. 11, no. 9, Aug. 2018, doi: 10.3390/ma11091548.

[68] I. S. Dias, I. Flores-Colen, and A. Silva, “Critical analysis about emerging technologies for Building’s façade inspection,” *Buildings*, vol. 11, no. 2, pp. 1–19, Feb. 2021, doi: 10.3390/buildings11020053.

[69] M. Mishra, K. Zhang, C. Mea, L. Barazzetti, F. Fassi, F. Fiorillo, and M. Previtali, “Deep Learning-Based AI-Assisted Visual Inspection Systems for Historic Buildings and their Comparative Performance with ChatGPT-4O,” in *International Archives of the Photogrammetry, Remote Sensing and Spatial Information Sciences - ISPRS Archives*, International Society for Photogrammetry and Remote Sensing, Dec. 2024, pp. 327–334. doi: 10.5194/isprs-archives-XLVIII-2-W8-2024-327-2024.

[70] P. Ramani, V. Reji, V. S. Kumar, G. Murali, and A. S. Kurhade, “Deep Learning-Based Detection and Classification of Moss and Crack Damage in Rock Structures for Geo-Mechanical Preservation,” *Journal of Mines, Metals and Fuels*, pp. 783–798, Mar. 2025, doi: 10.18311/jmmf/2025/47760.

[71] R. Perumal and S. B. Venkatachalam, “Non invasive detection of moss and crack in monuments using image processing techniques,” May 01, 2021, *Springer Science and Business Media Deutschland GmbH*. doi: 10.1007/s12652-020-02006-x.

Soil Engineering Based Characterization of Ceramic Clays in Sri Lanka

B G N M S Kumara[1,*], H G S Mayuranga[1], A G Jayasinghe[2], and G I P De Silva[3]

Abstract

The use of commonly available clay materials for production of bricks, tiles, and pottery in Sri Lanka has roots stretching back over three millennia. However, in recent times concerns are growing over material scarcity and waste management. In this context, this study was carried out with the intension of economizing the production process by introducing systematic characterization of Sri Lankan ceramic clays to produce bricks, roofing tiles and terra cotta floor tiles. The specific objectives were to investigate the relationship between composition and the engineering properties of fired clay over a range of firing temperature, and to investigate the variations of the above relationship brought about by addition of grog. Given that waste generation is a significant problem in the production process, use of grog in the production process offers an avenue for minimizing waste. It may also be evaluated against the hypothesis that the use of grog enhances mechanical and durability properties of ceramic products. For this purpose, the study used red clay from Mahiyangana area and kaolin from Hebarawa area with grog as raw materials and determined mix proportions that optimized compressive strength, water absorption, dry and firing shrinkage at different firing temperatures that varied from 700°C to 1000°C. When tested without grog, the highest compressive strength (of 13.8 MPa) and least dry and firing shrinkage (of 6.7% and 8.3%) were obtained for the 1:1 ratio of red clay to kaolin fired at 800°C. This optimum mix of red clay and kaolin was then modified with 5%, 10%, and 15% grog additions to evaluate the performance with grog. The addition of 5% grog and firing at 800°C enhanced compressive strength to 14.59 MPa and reduced water absorption. This study demonstrates that it is possible to produce building products to meet the relevant standards while making use of waste materials.

***Keywords:** Ceramic clay, Compressive strength, Firing temperature, Grog, Shrinkage*

1. Introduction

Ceramic products that are the backbone of human civilization are still a major part of today's building industry because of their robustness, versatility, and eco-friendliness [1,2]. Bricks, roof tiles and terra cotta floor tiles are found to be valuable both structurally as well as aesthetically [3,4]. In the Sri Lankan context, the ceramics industry has relied on natural reserves of clay particularly red clay from Mahiyangana and kaolin clay from Hebarawa that have been core inputs in manufacturing high-quality ceramics.

Nowadays, Sri Lankan ceramics industry is confronted with various challenges that undermine its development and sustainability. The most fundamental challenge is the depletion of high-grade reserves of clay, which precludes long-term access to the most critical raw materials. Accompanying this challenge is growing concern regarding the environmental impacts of waste production and wasteful use of natural resources [5,6]. These concerns are compounded by a perceived shortage of systematic, engineering-based research that conscientiously probes the behavior of indigenous clays under alternating thermal and compositional conditions.

Although red clay and kaolin clay are optimally utilized and appreciated, a vast empirical knowledge gap still exists in their performance characteristics. Specifically, not many technical facts about how their characteristics such as strength, shrinkage, and water absorption change with variations in mix proportions, firing temperatures, and grog percentage have been documented [7,8]. A crushed clay material that has been pre-fired which known as grog is typically added to ceramic formulations to control shrinkage and enhance mechanical strength, but its effect on Sri Lankan ceramic products based on clay has been under investigated [9]. This limited amount of information limits the industry to take full advantage of production methods and produce environmentally friendly, high-performance ceramic products.

To bridge this gap, the present research undertakes a detailed characterization of Sri Lankan ceramic clays examining their behavior when fired individually and in mixtures between 700°C and 1000°C. The study also evaluates the overall influence of the addition of 5%, 10%, and 15% grog on main performance parameters such as compressive strength, dimensional stability (shrinkage), and water absorption [2].

Through providing a scientific basis for the laboratory observation of the material properties of kaolin and red clays, this study assists process optimization in the production of ceramics. This allows for the development of optimized production methods that are able to enhance product quality to the highest levels, reduce waste and promote efficiency in the utilization of raw materials. Finally, the research meaningfully contributes to the field of soil mechanics and material engineering, and promotes more environmentally friendly industrial operations in Sri Lanka's ceramics industry [7].

[1]Department of Civil and Environmental Engineering, University of Ruhuna, Galle, Sri Lanka. (e-mail: nikinimadu87@gmail.com, sushan.m@cee.ruh.ac.lk)
[2]Department of Civil Engineering, The Open University of Sri Lanka (e-mail: anjay@ou.ac.lk)
[3]Department of Materials Science and Engineering, University of Moratuwa. (e-mail:indikagip@uom.lk)

Grog has broad application in worldwide ceramic manufacturing. However, under controlled laboratory conditions, the impact of grog on Sri Lankan ceramics, particularly Mahiyangana red clay and Hebarawa kaolin, is not satisfactorily established. The objective of this research is to bridge this knowledge gap by determining the impact of addition of grog and firing temperatures on critical material properties such as mechanical strength, dimensional shrinkage, and water absorption. Currently, there is a deficiency of comprehensive, region-specific engineering characterizations of such clays in the literature. Besides, previous studies have yet to identify optimal grog levels and firing regimes that would facilitate sustainable manufacturing practices and lead to better functional performance of ceramic products in Sri Lanka.

2.Literature Review

Numerous studies have investigated the effects of grog and various waste materials on the properties of ceramic products. De Silva and Mallwattha (2018) [9] and De Silva et al. (2022) [4] reported that incorporating ceramic sludge and rice husk ash improved durability and thermal performance in clay-based roofing tiles. Dubale et al. (2024) [10] demonstrated that recycling demolition tile waste enhanced the strength of fired bricks at an industrial scale. Vieira and Amaral (2017) [8] and Vieira and Monteiro (2006) [2] examined how grog content and particle size affect shrinkage and mechanical behavior in heavy clay ceramics. However, these studies largely focus on non-Sri Lankan clays and do not reflect the mineralogical or geotechnical characteristics of tropical soils. Grog is a pre-fired ceramic material that is ground into an aggregate form and incorporated into ceramic mixtures. Its addition is widely reported to improve dimensional stability and reduce shrinkage during firing, although this may sometimes result in a decrease in mechanical strength [11]. Grog modifies the clay matrix by reducing its plasticity, thereby limiting excessive deformation during sintering [12].

Globally, several researchers have evaluated optimal firing regimes and grog content in diverse clay matrices, often identifying the 700–1000°C range as effective for balancing strength and durability [13]. Particle size distribution and mineralogical composition of grog also significantly influence porosity and mechanical outcomes [14]. Yet, most such investigations rely on temperate-region clays or industrial byproducts that differ considerably from Sri Lanka's clay resources [15,16]. There is a distinct lack of research contextualizing grog-clay mixtures using Sri Lankan raw materials with their specific plasticity and mineral profiles. This study addresses that gap through standardized geotechnical and material characterization of local clays, coupled with firing experiments, to generate regionally relevant data for improving ceramic production in Sri Lanka.

3. Methodology

This research adopts a systematic, laboratory-based experimental approach to investigate the macro-engineering characteristics of Sri Lankan ceramic clays with respect to their suitability for brick, roof tile, and floor tile production. The method includes geotechnical testing, controlled firing laboratory experiments and performance testing under a variety of material compositions and thermal conditions. The techniques aim to identify the optimal clay proportioning ratios, assess the effect of grog percentage and quantify main properties such as compressive strength, shrinkage, and water absorption. Figure 1 illustrates the sequence of procedures followed in the experimental protocol.

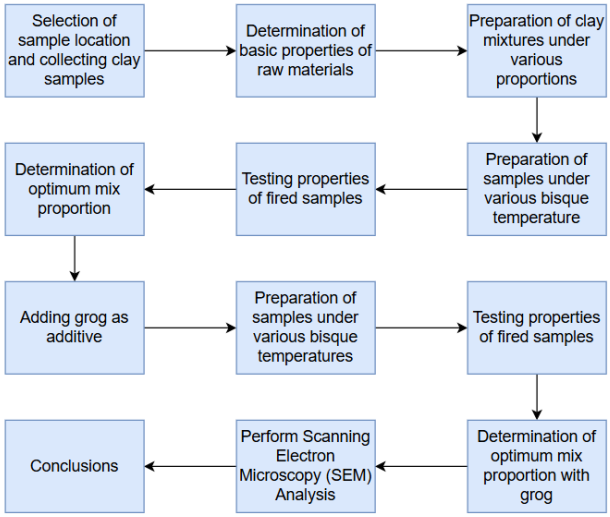

Figure 1: Flow chart of the methodology

3.1 Selection of Sampling Locations and Collection of Clay Samples

The research initiated with identification of the two significant clay sources from Sri Lanka where Mahiyangana tile factory red clay (7°20'39.5"N, 80°59'34.0"E) and the kaolin clay of Hebarawa area (7°31'11.7"N, 80°58'43.8"E), as shown in Fig. 2 and Fig. 3. They were selected by the virtue of their well-documented use for ceramic production and the distinct geotechnical properties of each type of clay Mahiyangana red clay plastic and iron-rich and Hebarawa kaolin finer and more resistant to heat.

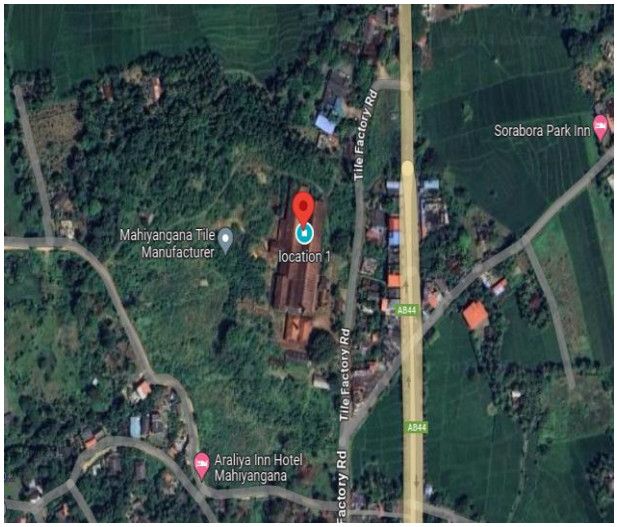

Figure 2: Mahiyangana tile factory land

Figure 3: Hebarawa site location

Clay samples were collected from multiple points within each site to capture natural variability in texture and composition. Sampling was carried out below the surface layer to avoid contamination. The materials were sealed in airtight containers to retain natural moisture content and prevent external contamination prior to laboratory testing [6].

3.2 Determination of Properties of Raw Materials

The physical and mechanical properties of the raw clays were evaluated through a series of standardized tests as shown in Table 1 [3].

Table 1: Conducted tests for determining the properties of raw material

Laboratory experiments	Engineering parameter/s	Standards
Specific Gravity Test	Specific gravity	ASTM D854
Sieve Analysis Test	Particle size distribution Fine content	ASTM C136 ASTM C114
Hydrometer Test	Particle size distribution of fine soil particles	ASTM D7928
Atterberg Limit Test	Liquid Limit (LL) Plastic Limit (PL) Plasticity Index (PI)	ASTM D4318
Moisture Content Test	Natural moisture content	ASTM D2216

3.3 Preparation of Samples Under Various Mix Proportions

For the clay mixtures preparation, red clay and kaolin were blended at eleven compositions ranging from 0% red clay and 100% kaolin to 100% red clay and 0% kaolin, at 10% increments. All compositions were blended with 20% by weight water to provide a workable plastic consistency [4]. This water level gave good workability for shaping and drying dimensional stability. The composition range selected permitted the full investigation of the influence of red clay to kaolin clay ratio on significant ceramic properties such as shrinkage, strength, and water absorption. All mixtures were thoroughly mixed to give particle size distribution uniformity and repeatable performance when tested. The available raw materials used in this process are illustrated in Fig. 4.


(a) (b)

Figure 4: Raw materials: (a) Red clay, (b) Kaolin clay

Sample preparation was in accordance with ASTM C773. Water absorption and compressive strength were measured by testing cylindrical samples of 38 mm diameter and 76 mm height, as shown in Fig. 5. Dry and firing shrinkage tests were conducted using prismatic samples of 100 mm × 25 mm × 15 mm. The results of the tests are presented by Fig. 6. All the samples were accurately cast to ensure dimension keeping and uniformity, and subsequently passed a controlled drying process prior to being fired [17].


Figure 5: Samples for check compressive strength and water absorption tests


Figure 6: Samples for check dry shrinkage and firing shrinkage

3.4 Firing Process

After sample preparation, the samples were allowed to dry in the air for a week under room conditions, as shown in Fig. 7. The process allowed for slow evaporation of excess water to avoid potential cracking or deformation during firing later on. After the drying period was over, the samples were checked to inspect if they were dry enough and ready to be further analyzed.

Figure 7: Samples after air drying

Following air drying, the samples were oven dried for one hour in order to get rid of any excess moisture. This was critical to prevent cracking when firing by providing complete dryness. Upon oven removal, the well-dried samples were now ready to be fired in bisque.

Firing was done in a muffle furnace, as shown in Fig. 8. Two-hour firing of the samples was carried out at 800°C and 1000°C [7]. Visual color changes were observed during firing, indicating thermal transformation of the clay. Bisque firing enhanced the strength of the material and stabilized the samples for testing.

Figure 8: Firing process

3.5 Testing Properties of Fired Samples

3.5.1 Dry Shrinkage

Dry shrinkage was also conducted to measure the dimensional change as a result of the evaporation of moisture when air-dried. The readings were taken before and after drying to find out the percent shrinkage. The test is important in analyzing the way the clay is going to act when being dried, where formulations to minimize cracking and dimensional instability in the final product can be determined.

3.5.2 Firing Shrinkage

Firing shrinkage was determined by measuring samples before and after firing, as shown in Fig. 9. Shrinkage results from particle fusion and densification at high temperatures. The test provides critical data regarding the sintering volumetric changes, which can be utilized to project final product sizes and ensure consistency in the production of ceramics.

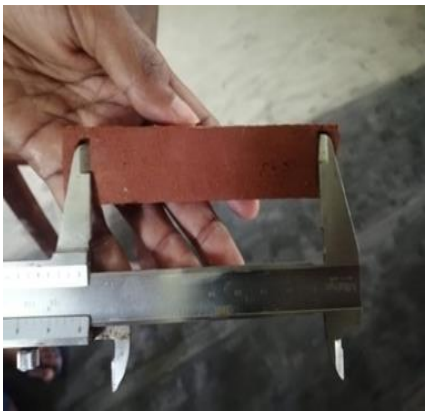

Figure 9: Testing firing shrinkage

3.5.3 Water Absorption

Water absorption tests were also carried out to determine the water absorption capacity of the fired samples. The samples were initially oven-dried, followed by immersion in water for 24 hours in accordance with ASTM D570, and weighed again to determine the percentage of water absorbed. The test is crucial in deciding on the durability of the material because excess water absorption leads to structural failure in the long term. Lower values of absorption indicate higher density and improved resistance to water, hence such compositions are better suited for use in moist or outdoor environments.

3.5.4 Compressive Strength

Compressive strength was tested on a calibrated compression test machine in Fig. 10. The load was applied at a constant rate until failure, and the maximum load sustained by the sample was recorded. This test is fundamental for determining the load-carrying capacity of the ceramic material. Higher compressive strength values indicate better mechanical properties, making the material suitable for use in bricks and roofing tiles.

Figure 10: Compressive strength check

3.6 Adding grog as Additive

Grog is a powder yielded from pre-firing grinding of clay which is illustrated in Fig. 11 and is added to clay bodies to change their properties. In the current research, grog was added to the optimal quantity of clay at three

different weight percentages of 5%, 10%, and 15%. To achieve uniform distribution within the clay matrix, grog particles of less than 0.425 mm were used, as determined through sieve analysis. This was the selected particle size to optimize mechanical strength while minimizing drying shrinkage. The research focused on evaluating the effect of varying proportions of grog on key properties such as compressive strength and water absorption [2].

Figure 11: Crushed pre-fired clay (grog)

3.7 Preparation of Samples with Grog Under Various Bisque Temperatures

Samples prepared with grog were fired at four different temperatures of bisque of 700°C, 800°C, 900°C and 1000°C. It was taken to maintain each temperature to evaluate the effects of different levels of heat on the material's properties. These different firing temperatures enabled us to determine the optimal thermal conditions for increasing strength and durability. Observing the samples at all temperatures provided information on the impact of heat on such significant properties as shrinkage, density and other significant properties of the grog-clay mixtures.

3.8 Testing Properties of Grog Added Fired Samples

After firing, the grog-added samples were tested to determine various material properties. Measurements of dry shrinkage and firing shrinkage revealed how grog is effective in reducing overall dimensional change during drying and firing. Density tests examined the fired bodies' density, and water absorption tests measured porosity quantitatively, the latter having a significant effect on durability and resistance to water. Compressive strength tests examined load-carrying capacity of the samples at varying grog content. The above tests enabled better understanding of the impact of grog ratio and firing temperature on strength, durability, and quality of the fired ceramic products.

3.9 Perform Scanning Electron Microscopy (SEM) Analysis

SEM analysis was carried out to study the surface morphology and microstructural features of the clay samples. SEM images were captured at appropriate magnifications in the high vacuum state with the help of a scanning electron microscope. This analysis provided detailed insights into particle bonding, porosity, and the distribution of grog within the clay matrix.

4. Results and Discussion

4.1 Properties of Raw Materials

A series of laboratory experiments were conducted to determine the fundamental physical properties of the red clay and kaolin clay samples. These included tests for specific gravity, Atterberg limits (liquid limit, plastic limit, and plasticity index), particle size distribution through sieve analysis and hydrometer test. The results obtained from these tests are summarized in Table 2.

Table 2: Properties of raw materials

Laboratory Experiment	Properties	Red Clay	Kaolin Clay
Specific Gravity Test	Specific Gravity	2.28	2.45
Atterberg Limit Tests	Liquid Limit (%)	41.28	57.62
	Plasticity Limit (%)	29.67	39.89
	Plasticity Index (%)	11.61	17.73
Hydrometer Test	Fines Content (%)	68.55	72.51
Sieve Analysis	Sand Content (%)	31.45	27.36
	Gravel Content (%)	0	0.13

The index properties of red and kaolin clays were assessed to determine their suitability for ceramic applications. Specific gravity values suggest a higher mineral density in kaolin. Atterberg limits indicate that kaolin exhibits higher plasticity, supporting a broader workable moisture range. Particle size distribution data confirm both soils are predominantly fine-grained, with kaolin having slightly more sand content, potentially enhancing packing characteristics during forming.

Based on the USCS, red clay is classified as Lean Clay CL indicating low plasticity and moderate workability. Kaolin clay with a higher liquid limit and PI is classified as Elastic Silt MH reflecting high plasticity and greater moisture sensitivity. These classifications are consistent with the observed fines content and Atterberg parameters validating their differential behavior during processing and firing.

4.2 Determination of Optimum Mix Proportion

This part discusses the effect of red clay and kaolin ratio variation on significant ceramic properties such as shrinkage, strength, and water absorption. Establishing the best ratio offers dimensional stability, mechanical strength, and moisture resistance in the final product.

4.2.1 Variation of Dry Shrinkage

Dry shrinkage is a basic parameter of dimensional stability in ceramic processing and is mostly governed by the plasticity of the clay, mineral content, and particle size distribution. Red Clay which exhibits medium plasticity and is lean in nature shows controlled shrinkage characteristics. Kaolin Clay having smaller particle size and higher plasticity index shows higher capillary tension on loss of moisture resulting in higher shrinkage. Examination of these properties under controlled mixing

helps in establishing an optimum mixture for minimizing deformation and cracking due to drying.

According to Fig 12, dry shrinkage begins at 8.6% for 100% red clay, steadily decreases to a low of 6.7% at 50% red clay and then jumps to 10.3% at 100% kaolin. This trend maintains red clay's ability to stabilize shrinkage because greater amounts of kaolin increase dimensional contraction from its finer texture and higher water holding capacity. 50:50 is the most dimensionally stable ratio, most appropriate for minimizing drying defects and obtaining better pre-firing quality in ceramic items.

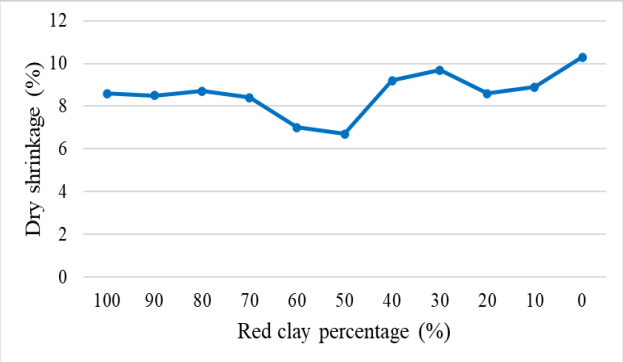

Figure 12: Variation of dry shrinkage with mix proportion

4.2.2 *Variation of Firing Shrinkage*

As shown in Fig. 13, dry shrinkage follows the same trend as firing shrinkage with the lowest value of 8.2% achieved by 60% red clay at 800°C. Firing shrinkage increases continuously with higher content of kaolin to a maximum of 10.4% at 0% red clay. This is attributed to the sintering characteristic of kaolin which possesses finer particle size and higher plasticity and thus denser and more firing shrinkage. Red clay, being the opposite, offers better thermal stability due to its coarse grain structure and low vitrification potential. Results indicate that the red-to-kaolin ratio of approximately 60:40 offers the best dimension control upon firing, minimizing warping or cracking.

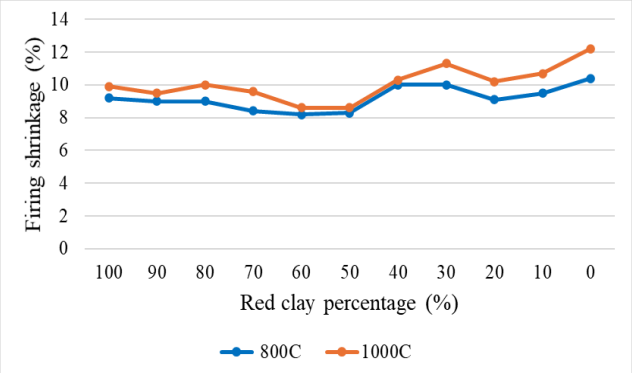

Figure 13: Variation of firing shrinkage with mix proportion

4.2.3 *Variation of Compression Strength*

Fig. 14 illustrates the compressive strength as a function of clay mix proportion. Highest strength of 13.80 MPa is at 50% red clay, indicating an optimal blend between red clay binding ability and kaolin structural strength. With a reduction in red clay, strength reduces significantly to 8.44 MPa at 0% red clay. This decrease is most likely due to the lower plasticity and lower green body strength of kaolin, both of which compromise particle bonding at firing. The results indicate that optimal mechanical performance in ceramic products is achieved with a 50%–60% red clay content which is in the zone of minimum shrinkage and maximum density.

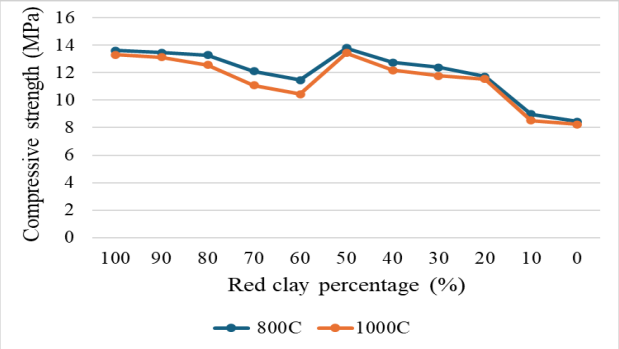

Figure 14: Variation of compressive strength with mix proportion

4.2.4 *Variation of Water Absorption*

From Fig. 15, the water absorption follows a decreasing trend with the reduction of red clay content having the maximum value of 13.43% at 100% red clay and minimum value of 9.76% at 10% red clay. The reason for the high absorption of red clay-rich samples is that it possesses a relatively porous microstructure as well as higher plasticity, which supports the retention of moisture during firing. As kaolin content increases, the denser packing and finer mineral structure reduce porosity thereby lowering water absorption. However, excessively low red clay content compromises strength, as can be seen in Fig. 16. Therefore, the results show that while kaolin enhances water resistance an optimum red clay content must be maintained to guarantee overall product strength.

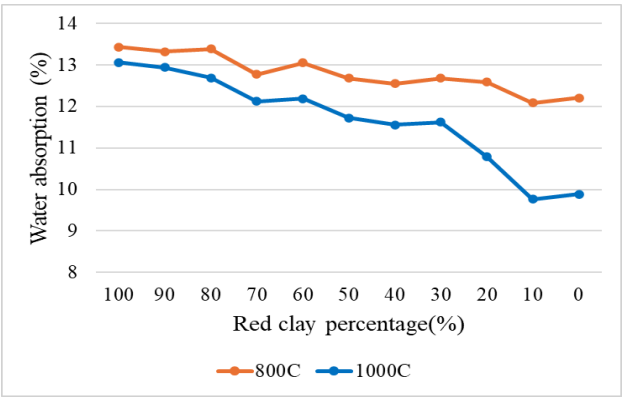

Figure 15: Variation of water absorption with mix proportion

4.3 *Determination of Optimum Mix Proportion with Grog*

The action of grog as an additive is also analyzed to shrinkage control and mechanical enhancement. Different percentages of grog are tested out to establish the ideal percentage that will minimize defects without influencing strength.

4.3.1 *Variation of Dry Shrinkage with Grog*

It is observed from Fig. 16 that the addition of grog influences the dry shrinkage characteristics of the clay mixture significantly. The control sample without grog has a minimum shrinkage of 6.7% which confirms its dense and cohesive character. Quite unexpectedly, the 5% addition of grog increases shrinkage to a high 9.5% possibly due to disruption of the microstructure and reduced plastic bonding. However, further additions of 10% and 15% grog reduce shrinkage slightly to 8.6% and 9.1% respectively. This means that while small amounts of grog interfere with particle packing and create voids, the higher amounts tend towards dimensional stabilization by the creation of a stiffer granular skeleton that inhibits shrinkage on drying.

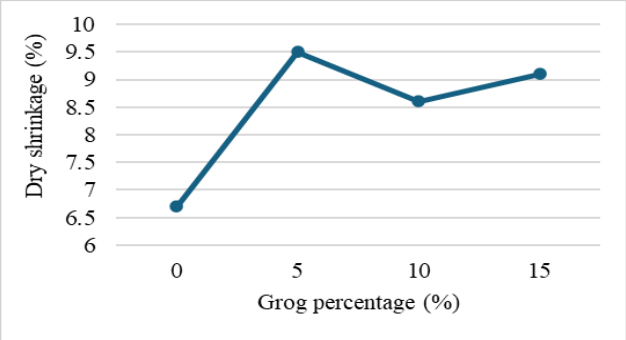

Figure 16: Variation of dry shrinkage with grog

4.3.2 *Variation of Firing Shrinkage with Grog*

Fig. 17 shows that firing shrinkage trends upwards with reducing grog content reaching a maximum of 11.5% at 5% grog and 1000°C. The initial increment is caused by increased sintering activity and particle rearrangement, as the fine clay matrix dictates behavior at low grog content. As grog percentage increases above 5%, shrinkage begins to fall, as grog particles being pre-fired and inert to resist further densification. This limits the extent of matrix consolidation and helps in dimension control at high temperature. The evidence confirms the role of grog as a stabilizer in thermally reactive ceramic systems, especially at high temperatures of firing.

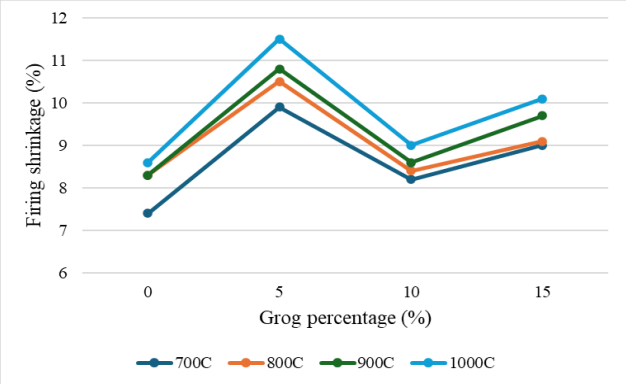

Figure 17: Variation of firing shrinkage with grog

4.3.3 *Variation of Compressive Strength with Grog*

Compressive strength results were presented in Fig. 18, indicate that 5% grog content achieves the optimum strength of 14.59 MPa at 800°C which is superior to the rest of the grog contents. The development of strength at this level indicates an optimum level of balance between matrix quality and internal stress relief as grog improves resistance to shrinkage cracking. When the grog content exceeds 5%, strength losses occur due to increased porosity and reduced matrix cohesion, as inert grog particles replace the binding clay phase. Furthermore, the fact that all samples achieved optimum strength at 800 °C confirms this temperature as the ideal firing point, where sintering is effective without over-firing or pore coalescence [10].

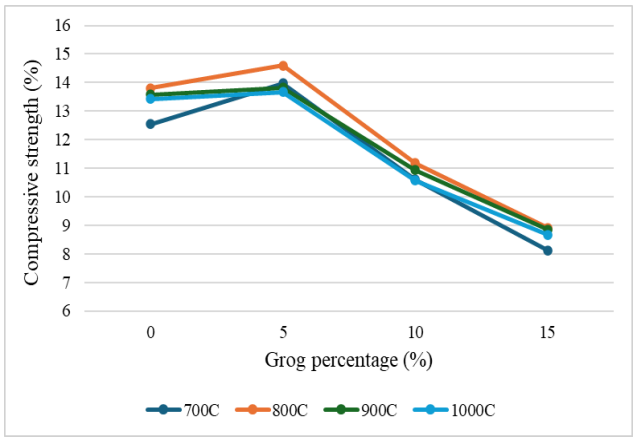

Figure 18: Variation of compressive strength with grog

4.3.4 *Variation of Water Absorption with Grog*

As seen from Fig. 19, water absorption decreased with the increase in firing temperature for all grog levels indicating better densification through vitrification. The lowest absorption value, 9.71%, was achieved for 5% grog at 1000°C, indicating an optimal balance between particle packing and matrix sintering. Nevertheless, at 10% and 15% grog, water intake increased immensely due to the inert nature of grog bringing in additional interconnecting pores, reducing overall compactness. This means that while structure is improved by minor levels of grog, significant levels produce higher porosity and penetration of moisture.

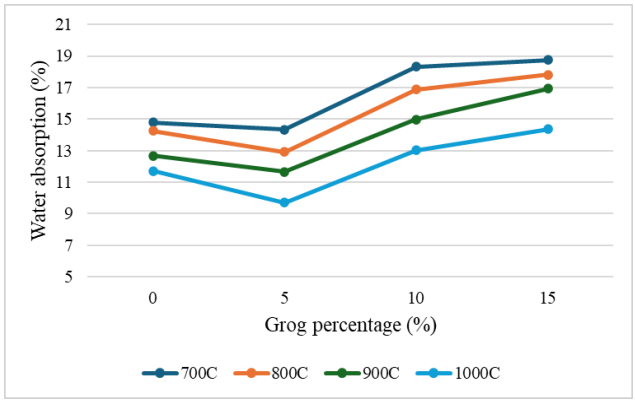

Figure 19: Variation of water absorption with grog

4.4 *Properties Variation with Temperature*

This section summarizes the effects of firing temperature on shrinkage, strength, and water absorption using various levels of grog. Analyzing temperature-dependent

characteristics is significant in establishing optimal firing conditions and required ceramic performance.

4.4.1 Variation of Firing Shrinkage with Temperature

Fig. 20 illustrates that firing shrinkage is a function of rising temperature for all percentages of grog. For instance, 0% grog indicates a rise from 7.4% at 700°C to 8.6% at 1000°C, but 5% grog has values of 9.9% to 11.5% owing to higher particle fusion in the fine matrix. But 10% grog has relatively lower shrinkage (8.2% to 9%) and 15% grog has an equally stabilized range (9% to 10.1%). These results confirm that grog additions, especially greater than 5%, reduce the extent and range of thermal shrinkage by inhibiting densification of the clay matrix and acting as a shrinkage-resistant filler [18].

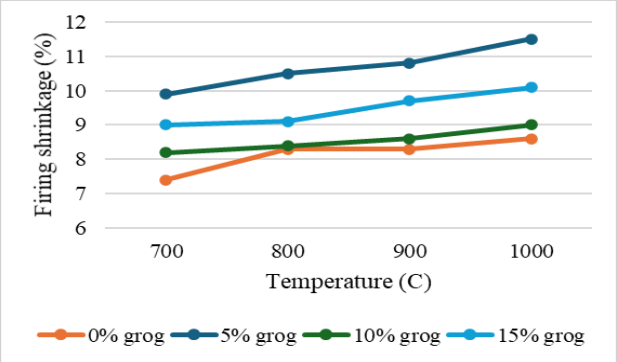

Figure 20: Variation of firing shrinkage with temperature

4.4.2 Variation of Compressive Strength with Temperature

From Fig. 21, compressive strength with increasing firing temperature up to 800°C and above levels off or slightly decreases. The maximum strength of 14.59 MPa was achieved at 800°C by 5% grog which shows this composition delivers optimum densification and matrix continuity. At temperatures over 800°C, the strength drop is attributed to over-firing factors such as pore coalescence or microcracking. Higher concentrations of grog (10% and 15%) always resulted in lower strengths due to the increased porosity and decreased cohesive bonding within the matrix. Hence, 5% grog fired at 800°C gives the optimal condition to maximize mechanical performance.

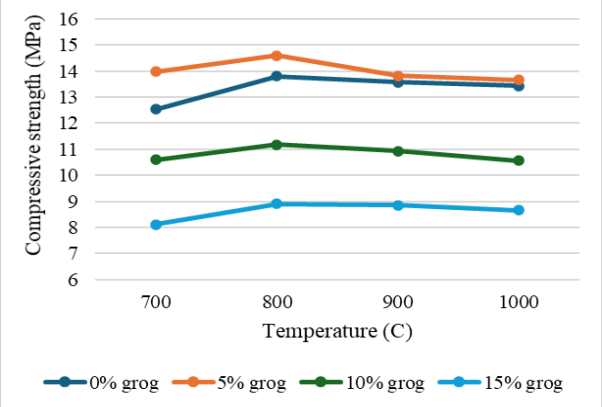

Figure 21: Variation of compressive strength with temperature

4.4.3 Variation of Water Absorption with Temperature

Fig. 22 shows a declining trend in water absorption for each grog level at higher firing temperatures inferring rising vitrification. The minimum water absorption of 9.71% at 1000°C with 5% grog confirms maximum strength levels and shows densification of the matrix to be successful. The 10% and 15% grog samples had higher water absorption at all temperatures, further inferring that excessive grog increases pore continuity and reduces moisture resistance. It highlights the importance of restricting grog content when attacking low-porosity, water-resistant ceramics.

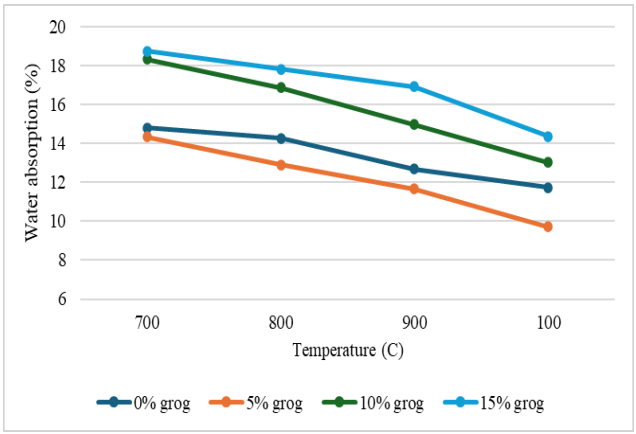

Figure 22: Variation of water absorption with temperature

The maximum compressive strength of 14.59 MPa was obtained at a firing temperature of 800°C with 5% grog content, aligning with previous studies which improved mechanical performance at intermediate grog levels [2]. This enhancement is attributed to efficient particle packing and increased matrix continuity. The optimized particle size distribution, combined with the fine grain structure of kaolin-rich Sri Lankan clays, promotes uniformity. These factors facilitate effective sintering densification, resulting in a structurally coherent and mechanically stronger products.

In addition, a 50:50 mixture of red clay to kaolin containing 10% grog and fired at 800°C had compressive strength of 13.80 MPa. This is within the expected performance range of 12–15 MPa for grog-modified ceramic materials in Southeast Asia [11,19]. This composition also displayed favorable shrinkage characteristics with 6.7% dry shrinkage and 8.3% firing shrinkage, indicating good dimensional stability. This is in line with the inherent mineralogical properties of Sri Lankan clays, namely their kaolinite rich nature and fine particle grading, responsible for structural strength during drying as well as firing phases [20,21].

4.5 Statistical Analysis and Interpretation

A two-way ANOVA was conducted to examine the effect of grog content and firing temperature on compressive strength. The analysis revealed statistically significant main effects for both variables, with $p < 0.001$ for grog content and $p = 0.0125$ for firing temperature. The effect of grog content was particularly significant, as indicated by an F-value > 218, and in line with its highly significant contribution to regulating mechanical

performance. Interestingly, the interaction effect between temperature and grog was statistically nonsignificant ($p = 0.755$), such that every factor has an individual contribution to the development of strength without synergistic dependence.

These statistical findings complement the physical inferences based on the experimental evidence. The higher compressive strength at the intermediate grog levels is consistent with Vieira et al. (2006)[2], who emphasized the positive effect of grog as promoting a denser packing structure and increased matrix cohesion. When accompanied by fine-grained, sintering-reactive kaolin clay, addition of grog results in development of a stable and homogenous microstructure capable of withstanding mechanical stress well even at moderate firing temperatures.

Further, the observed improvement in compressive strength and shrinkage performance for 50:50 red clay–kaolin blend with 10% grog strongly reflects the synergistic influence between clay mineralogy and ideal grog content. These results suggest that a viable grog addition range of 5–10%, when combined with a firing temperature range of 800–1000°C, provides a good balance between densification, mechanical strength, and dimensional stability. These results are of helpful guidance for the preparation of high-performance products using locally sourced raw materials.

4.6 Microstructural Characterization through Scanning Electron Microscopy (SEM)

As indicated in Fig. 23 and Fig. 24, the scanning electron micrographs offer valuable insights into the microstructural evolution of the ceramic products as influenced by variations in grog content and firing temperature.

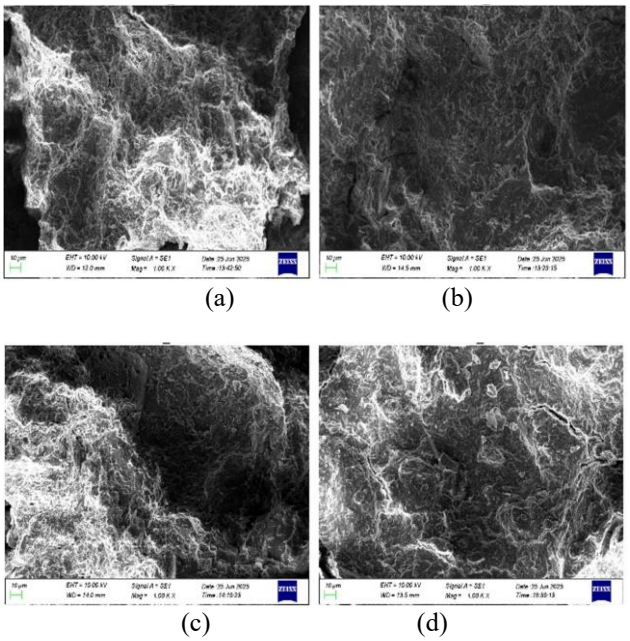

(a) (b) (c) (d)

Figure 23: Interpretation of SEM Images at 800^0C. (a) 0% grog; (b) 5% grog; (c) 10% grog (d) 15% grog. (Magnification: 1,000×)

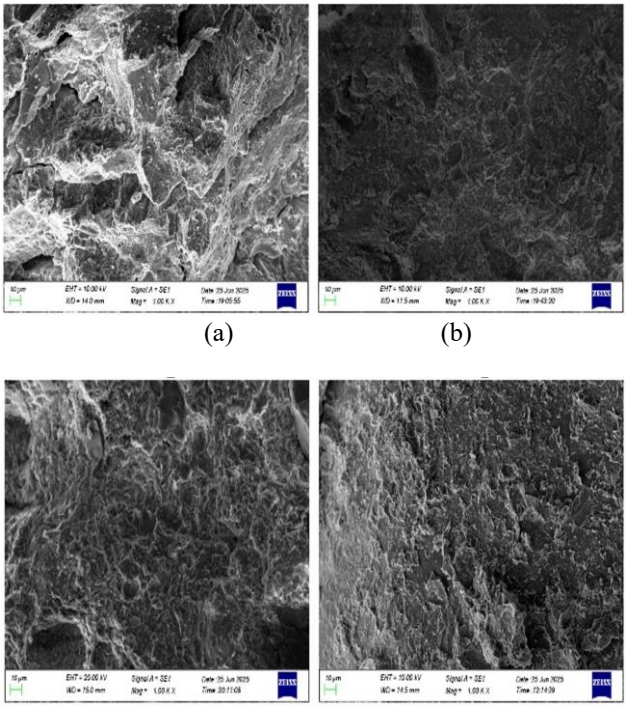

(a) (b) (c) (d)

Figure 24: Interpretation of SEM Images at 1000^0C. (a) 0% grog; (b) 5% grog; (c) 10% grog (d) 15% grog. (Magnification: 1,000×)

All the samples exhibit coarse grain morphology and porosity at 800°C. Incompletely defined boundaries, loosely organized grains, and incomplete sintering are typical in the microstructure. As grog content increases from 0% to 15%, the matrix is heterogeneously structured. Grog particles add inert inclusions that elevate intergranular voids and potential crack propagation paths. At 15% grog, the structure is very porous, indicating poor bonding.

Conversely, 1000°C-fired samples have enhanced sintering and particle bonding. Micrographs show smooth surface morphology, tight grain packing, and reduced open porosity. The 0% grog shows densification with fewer open voids, which signifies vitrification. 5% and 10% grog samples at this temperature are dense with enhanced integration of grog. In particular, the 10% grog sample reflects a perfect cohesion, well-distributed particles, minimal crack density, and visible grain fusion, implying enhanced microstructural reinforcement. But 15% grog introduces minor agglomeration and vitrified residue, signaling a point of no return after which grog fragments homogeneity.

These observations align with established literature. Increased firing temperatures enhance sintering kinetics, grain growth, reduced porosity, and enhanced densification [22]. Grog increases shrinkage and thermal resistance but must be properly optimized. According to Kingery et al. (1976) [23], too much grog introduces structural discontinuities if poorly bonded. Further, Johari et al., 2010 (2018) [24] mentioned that a firing temperature of 1000°C or higher is necessary to achieve proper bonding between the grog and the matrix.

5. Conclusion

The current research was carried out on systematic macro-characterization of Sri Lankan ceramic clays, i.e., Mahiyangana red clay and Hebarawa kaolin, for maximum composition, grog content, and firing conditions for brick, roof tiles, and terracotta products. By analyzing principal properties compressive strength, shrinkage, and water absorption, the research established the most effective formulations for industrial use based on international standards. The findings assist in maintaining ceramic production by providing maximum local material utilization while minimizing effects on the environment. The key conclusions are:

- A red clay to kaolin clay proportion of 50:50 resulted in the best compromise between mechanical strength (13.80 MPa at 800°C) and stability of dimensions (6.7% dry shrinkage, 8.3% firing shrinkage), being comparable to other compositions.
- 5% grog enhanced compressive strength (14.59 MPa), but increased percentages (10–15%) increased porosity and water absorption, showing a trade-off between reinforcement and durability.
- 800°C firing maximized strength and shrinkage, but 1000°C decreased water absorption but slightly decreased the matrix strength, showing the necessity of proper thermal control.
- The optimum mix met ASTM C62-17 standards (water absorption <17%), confirming its suitability for harsh-weather construction work.

These results offer actionable suggestions to Sri Lankan producers to produce high-performance ceramics using available raw materials in the country, reducing reliance on imported additives.

6. Recommendations and Future Directions

To build on this study and address open questions, future studies must include advanced material science techniques and applied scalability assessments. The following are recommended paths to improve ceramic manufacturing processes and extend application scopes:

- Test industrial waste materials (ceramic sludge, granite dust) or natural products for their ability to enhance thermal resistance, reduce shrinkage, or lower firing temperatures.
- Explore energy-saving methods like two-stage firing or microwave sintering to ensure maximum efficiency without compromising quality.
- Subject products to lasting durability testing (acid rain exposure, freeze-thaw test) to demonstrate actual use performance and longevity.
- Evaluate the carbon footprint and cost-benefit analysis of optimized blends to achieve sustainable manufacturing according to the principles of circular economy.

By addressing such gaps, follow-up research can further develop Sri Lanka's ceramic industry to be competitive within the local market and also in the global market with a thrust of sustainability.

Acknowledgement

Authors would like to thank all the academic and non-academic staffs of Department of Civil and Environmental Engineering of the Faculty of Engineering, University of Ruhuna for giving all the facilities and guidance to successfully conduct this research study.

References

[1] M. Dondi, M. Marsigli and I. Venturi, "Microstructure and mechanical properties of clay bricks: Comparison between fast firing and traditional firing," *British Ceramic Transactions*, vol. 98, no. 1, pp. 12–18, 1999.

[2] C.M. Vieira and S.N. Monteiro, "Effect of the particle size of the grog on the properties and microstructure of bricks," *Materials Science Forum*, vols. 530–531, pp. 438–443, 2006.

[3] J. Bhattarai *et al.*, "Study on the physical and mechanical properties of ancient clay brick samples of Kathmandu Valley, Nepal," *Tribhuvan University Journal*, vol. 32, no. 2, pp. 1–18, 2018.

[4] S. De Silva *et al.*, "Engineering properties and microstructure of a sustainable roof tile manufactured with waste rice husk ash and ceramic sludge addition," *Case Studies in Construction Materials*, vol. 17, 2022.

[5] M.M. Jordán *et al.*, "Firing transformations of cretaceous clays used in the manufacturing of ceramic tiles," *Applied Clay Science*, vol. 14, no. 4, pp. 225–234, 1999.

[6] C.-H. Weng, D.-F. Lin and P.-C. Chiang, "Utilization of sludge as brick materials," *Advances in Environmental Research*, vol. 7, no. 3, pp. 679–685, 2003.

[7] N. Sandra, "Influence of firing temperature on the mechanical properties of bricks," *International Journal of GEOMATE*, vol. 26, no. 117, 2024.

[8] C.M. Vieira and L.F. Amaral, "Recycling of grog by addition into heavy clay ceramic manufacturing," *Ceramic Engineering and Science Proceedings*, pp. 159–166, 2017.

[9] S. De Silva and M.P.D.P. Mallwattha, "Strength, durability, thermal and run-off properties of fired clay roof tiles incorporated with ceramic sludge," *Construction and Building Materials*, vol. 179, pp. 390–399, 2018.

[10] M. Dubale, M.V. Vasić, G. Goel and A.S. Kalamdhad, "The recycling of demolition roof tile waste as a resource in the manufacturing of fired bricks: A scale-up to the industry," *Construction and Building Materials*, vol. 398, Article 131851, 2024. doi:10.1016/j.conbuildmat.2023.131851.

[11] R.A. Mohamed and A.A. Abbas, "The role of grog in improving fired clay brick characteristics," *International Journal of Civil Engineering and Technology*, vol. 7, no. 4, pp. 424–431, 2016.

[12] C.H. Tsai, S.J. Wu and C.Y. Lin, "Effect of grog addition on sintering behavior and dimensional stability of ceramic bodies," *Ceramics International*, vol. 43, no. 12, pp. 9014–9020, 2017.

[13] L. Hernandez and F. Garcia, "Optimization of grog content in structural ceramics using local clays," *Journal of Materials Research and Technology*, vol. 8, no. 4, pp. 3862–3870, 2019.

[14] P. Jones and D. Martin, "Effect of grog particle size and distribution on microstructure and strength of fired clay ceramics," *Ceramics International*, vol. 41, no. 6, pp. 7725–7732, 2015.

[15] D.L. Perera, A.D. Samarasinghe and M. Hettiarachchi, "Characterization of Sri Lankan clays for ceramic applications: A comparative study," *Sri Lankan Journal of Applied Earth Sciences*, vol. 2, no. 1, pp. 15–24, 2021.

[16] T.S. Samarawickrama and R.A.L.H. Gunasekara, "Mineralogical influence on the thermal performance of clay blends in Sri Lanka,"

Journal of the National Science Foundation of Sri Lanka, vol. 47, no. 2, pp. 203–211, 2019.

[17] K.N. Sundari, Subari and B.D. Erlangga, "Characterization of Buleleng clay and improvement of its ceramic properties," *National Research and Innovation Agency*, Denpasar and Bandung, Indonesia, 2024.

[18] E. Tsega, "Effects of firing time and temperature on physical properties of fired clay bricks," *American Journal of Civil Engineering*, vol. 5, no. 1, p. 21, 2017.

[19] M.A. Rahman, M.N. Islam and M.M. Hossain, "Effect of grog addition and firing temperature on the properties of ceramic bricks," *Construction and Building Materials*, vol. 205, pp. 541–548, 2019.

[20] W.S. Fernando, P.R.D. Perera and A.D. Silva, "Geotechnical and mineralogical characterization of ceramic clays in Sri Lanka," *Journal of the Geological Society of Sri Lanka*, vol. 19, no. 1, pp. 45–53, 2017.

[21] Y.S. Kim, H.J. Park and D.S. Lee, "Evaluation of firing temperature effects on the mechanical performance of clay bricks containing recycled grog," *Journal of Asian Ceramic Societies*, vol. 6, no. 3, pp. 312–319, 2018.

[22] M.W. Barsoum, *Fundamentals of Ceramics*, CRC Press, Boca Raton, FL, 1st ed., 603 pp., 2002.

[23] W.D. Kingery, H.K. Bowen and D.R. Uhlmann, *Introduction to Ceramics*, 2nd ed., Wiley, New York, 1976.

[24] I. Johari, S. Said, B. Hisham, A. Bakar and Z.A. Ahmad, "Effect of the change of firing temperature on microstructure and physical properties of clay bricks from Beruas (Malaysia)," *Science of Sintering*, vol. 42, no. 2, pp. 245–254, 2010.

Annex 01

The impact of the M7.7 Mandalay earthquake on high-rise buildings with long natural periods in Bangkok

Pennung Warnitchai

Professor of Structural Engineering
Asian Institute of Technology (AIT)

Director of Earthquake Research Center of Thailand (EARTH)

Tectonic Map and Active Faults of SouthEast Asia

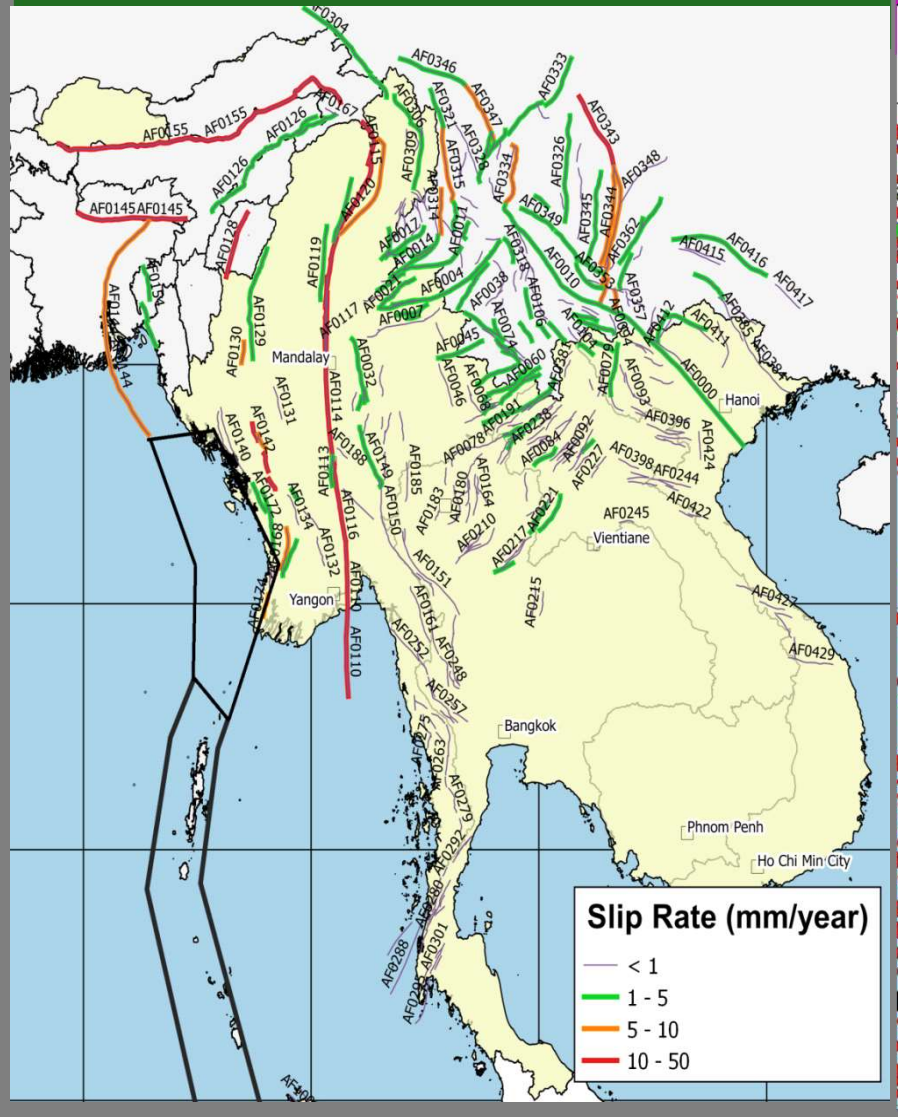

Seismicity Map of SouthEast Asia (1905-2014)

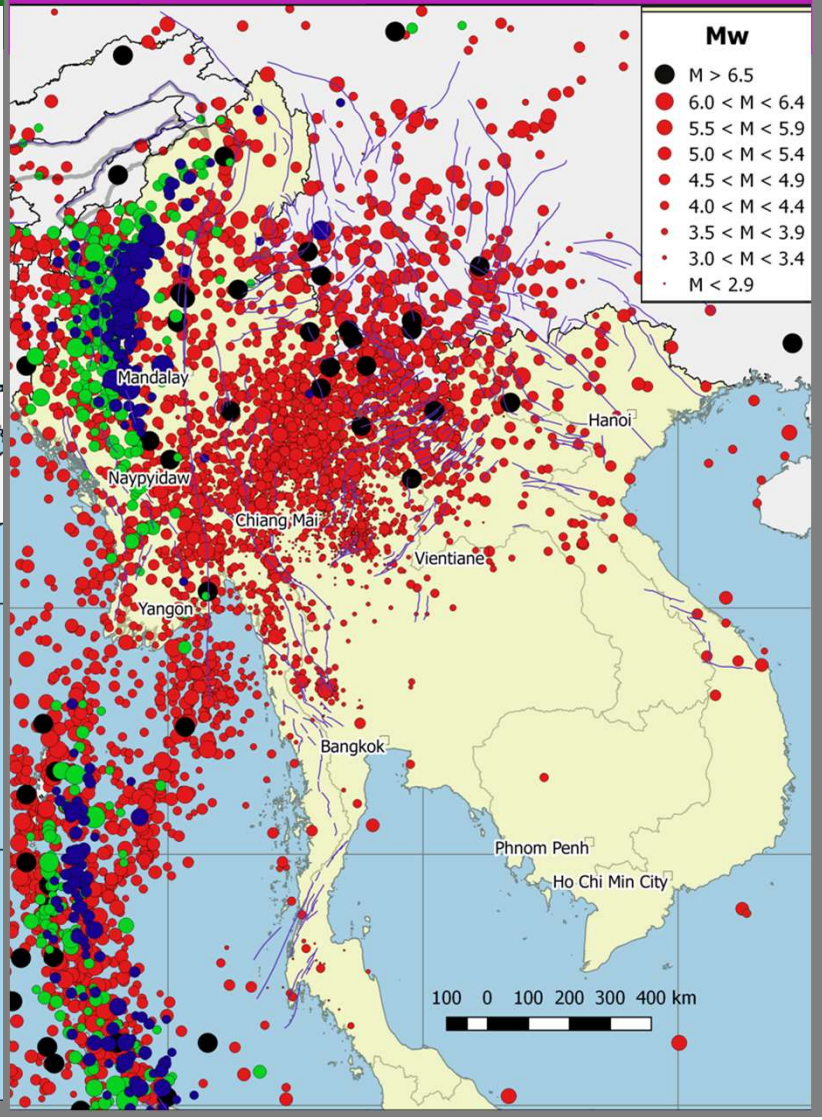

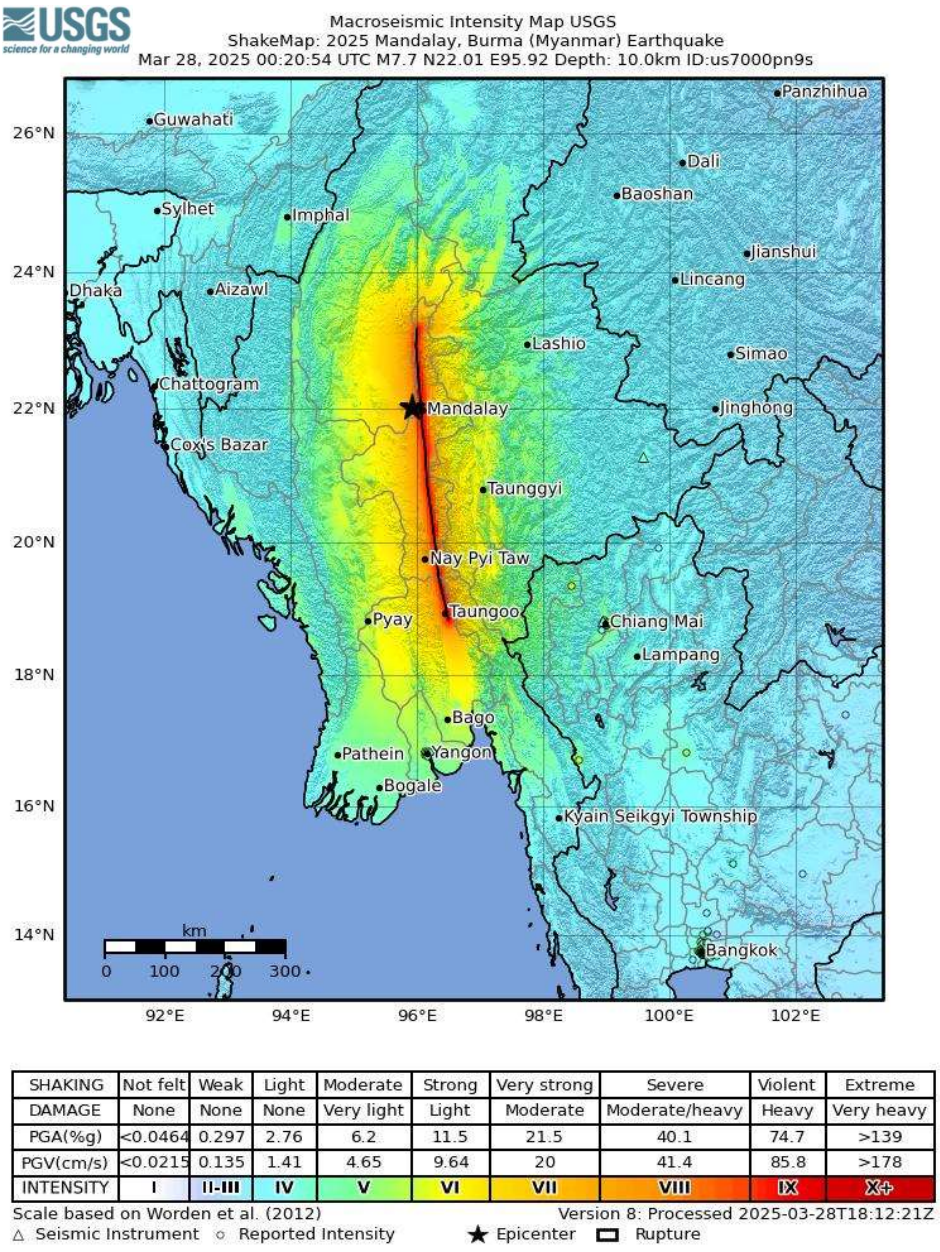

SHAKING	Not felt	Weak	Light	Moderate	Strong	Very strong	Severe	Violent	Extreme
DAMAGE	None	None	None	Very light	Light	Moderate	Moderate/heavy	Heavy	Very heavy
PGA(%g)	<0.0464	0.297	2.76	6.2	11.5	21.5	40.1	74.7	>139
PGV(cm/s)	<0.0215	0.135	1.41	4.65	9.64	20	41.4	85.8	>178
INTENSITY	I	II-III	IV	V	VI	VII	VIII	IX	X+

Scale based on Worden et al. (2012)
Version 8: Processed 2025-03-28T18:12:21Z
△ Seismic Instrument ○ Reported Intensity ★ Epicenter ▭ Rupture

M 7.7 - 2025 Mandalay, Burma (Myanmar) Earthquake

2025-03-28 06:20:54 (UTC)
22.013°N 95.922°E
10.0 km depth

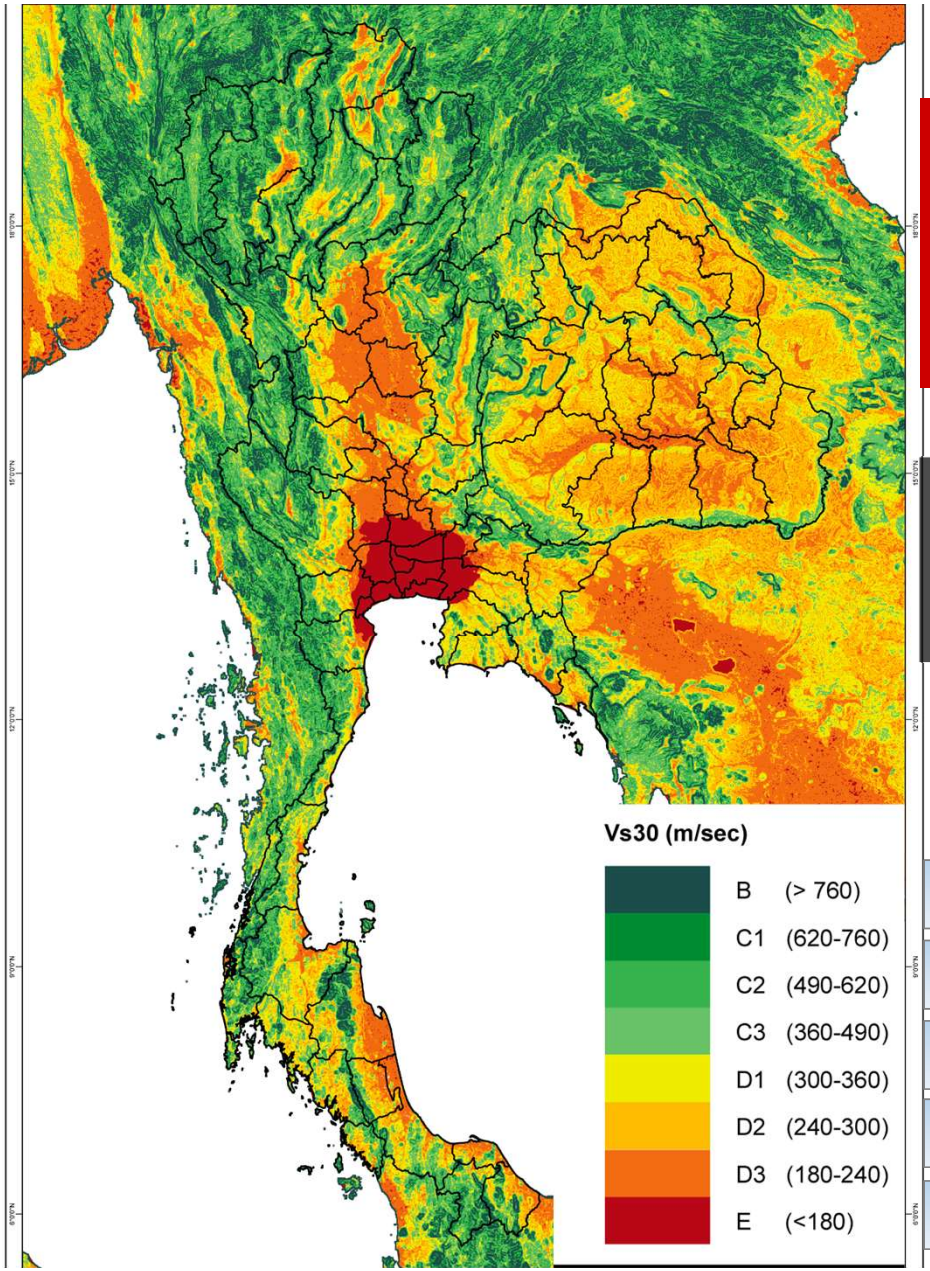

Map showing Soil (Site) Conditions in Thailand

(derived from digital elevation data—SRTM30 and boreholes data)

Bangkok and neighboring provinces are located inside a large soil basin.

Rock (No Amplification)

Very Stiff Soil

Stiff Soil (Moderate Amplification)

Moderately Soft Soil

Very Soft Soil (High Amplification)

Depth to Basement Rock in Bangkok Basin

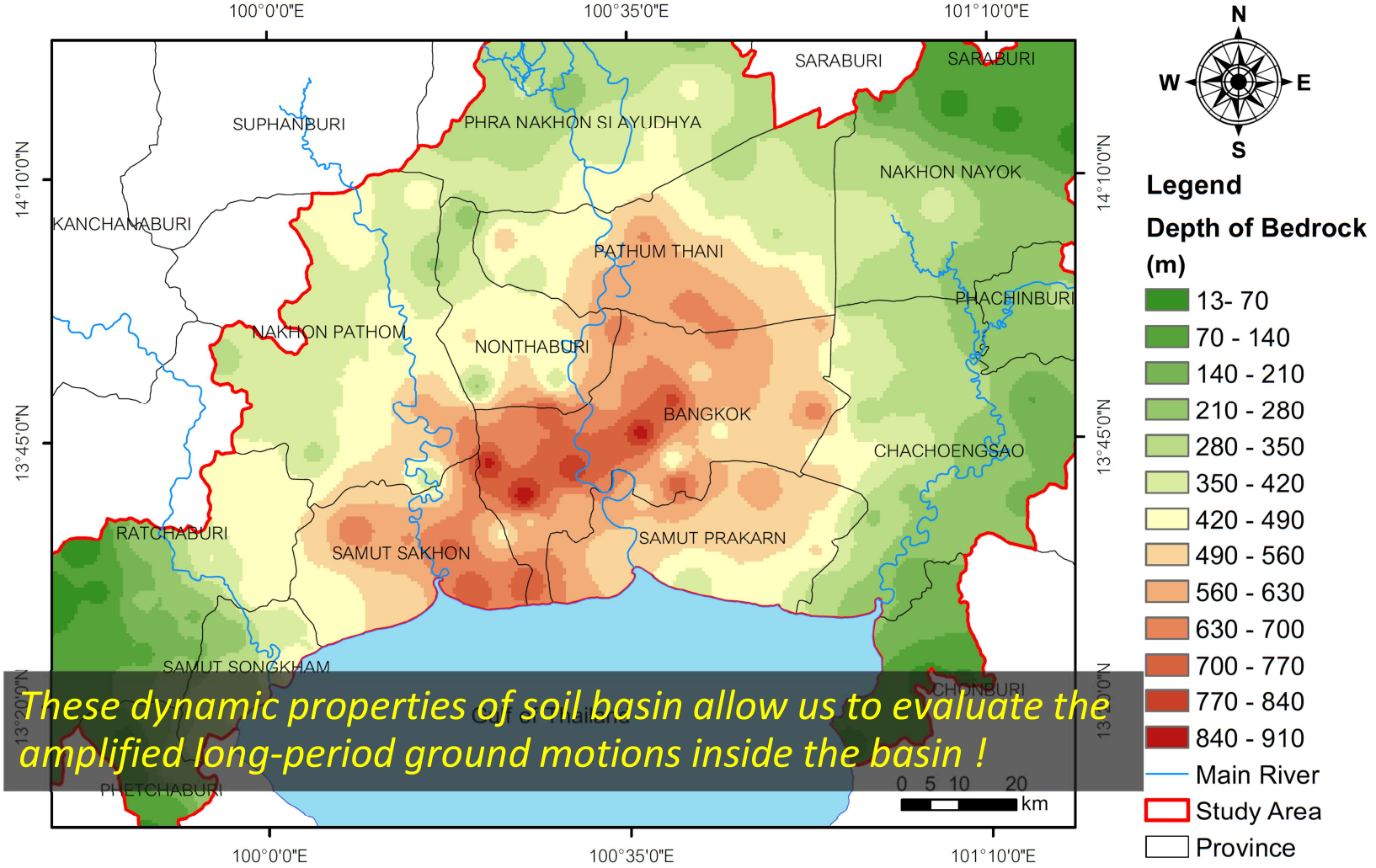

These dynamic properties of soil basin allow us to evaluate the amplified long-period ground motions inside the basin !

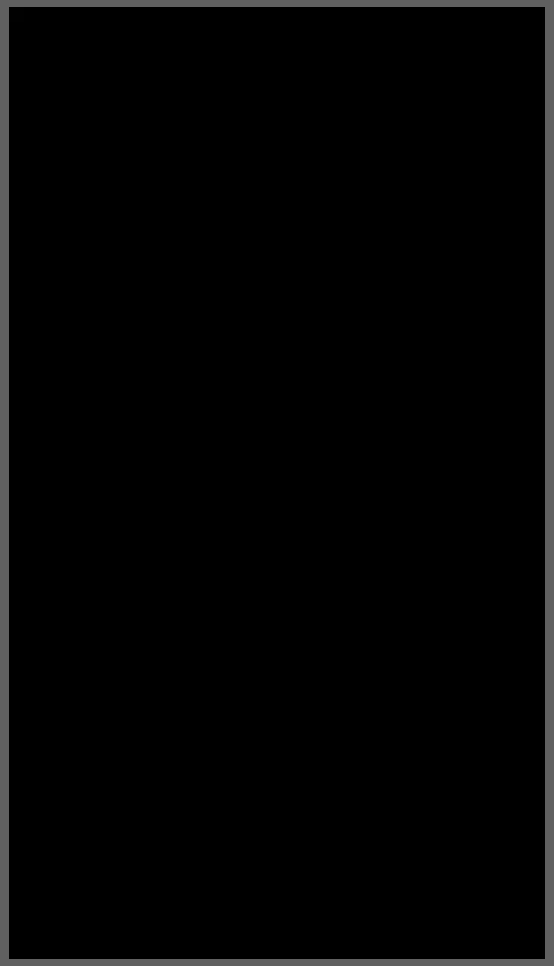

Resonance Effect

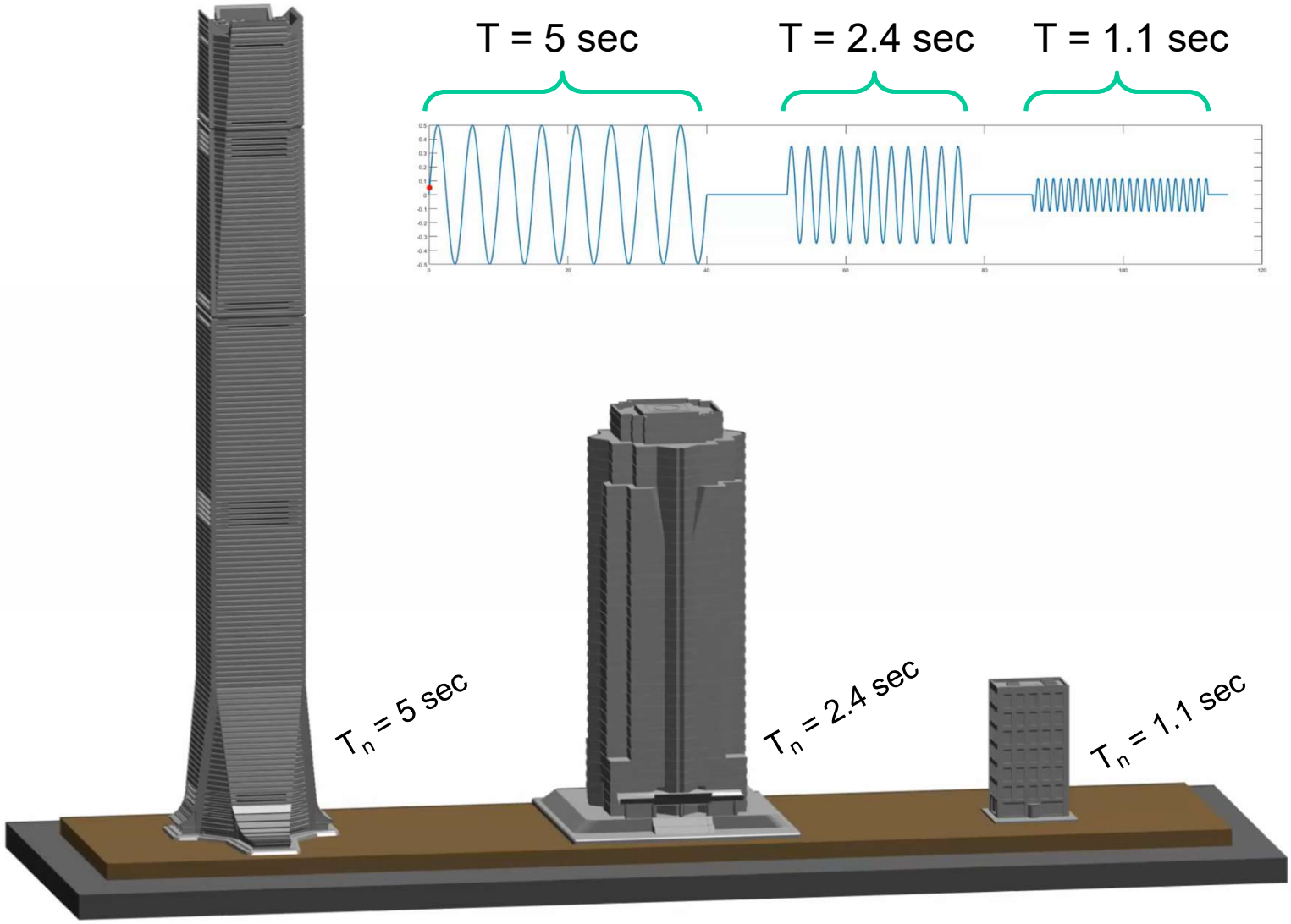

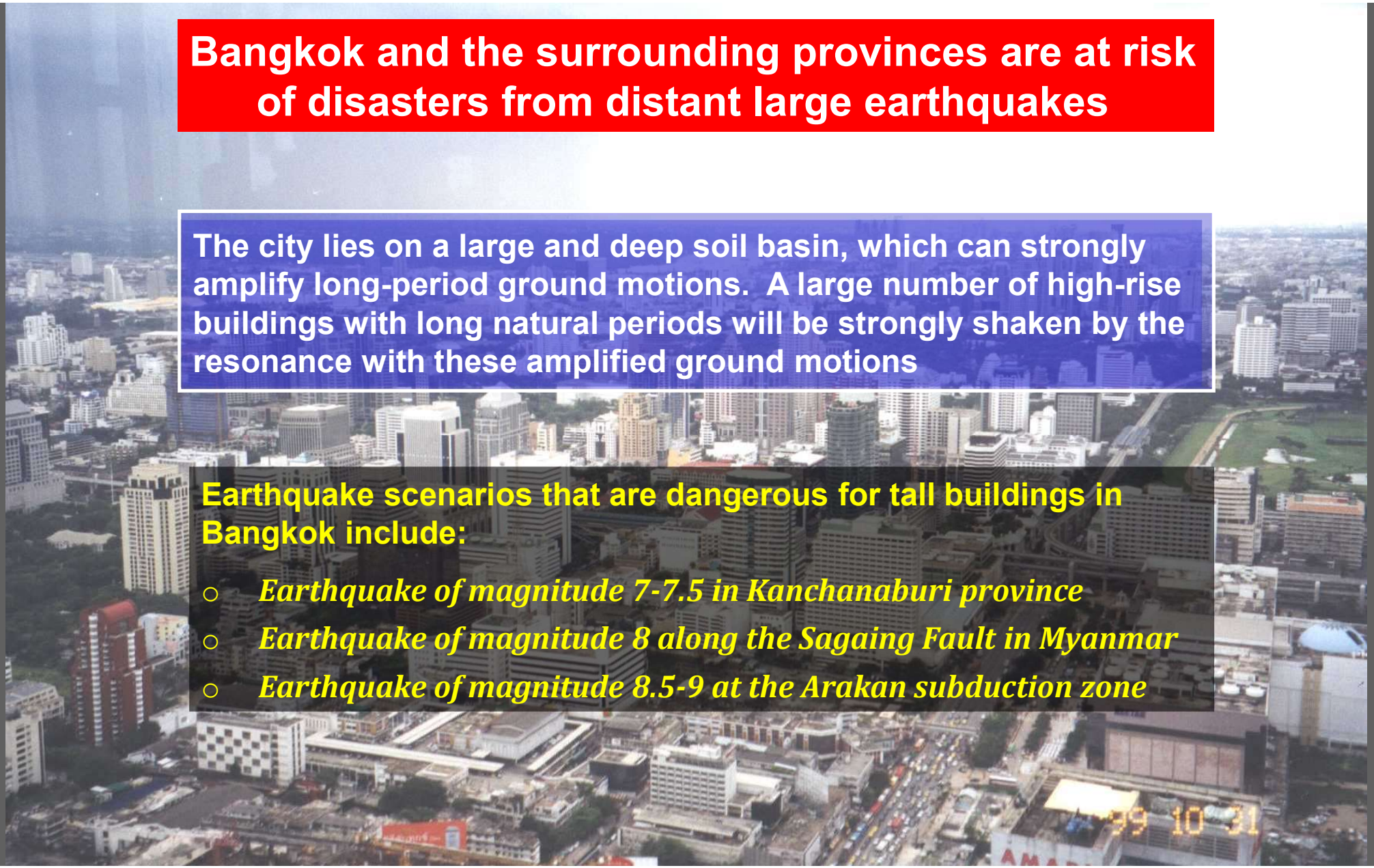

Bangkok and the surrounding provinces are at risk of disasters from distant large earthquakes

The city lies on a large and deep soil basin, which can strongly amplify long-period ground motions. A large number of high-rise buildings with long natural periods will be strongly shaken by the resonance with these amplified ground motions

Earthquake scenarios that are dangerous for tall buildings in Bangkok include:

- *Earthquake of magnitude 7-7.5 in Kanchanaburi province*
- *Earthquake of magnitude 8 along the Sagaing Fault in Myanmar*
- *Earthquake of magnitude 8.5-9 at the Arakan subduction zone*

With the 2007 amendment to the Earthquake related ministerial regulations, the control area for earthquake-resistant design was extended to Bangkok and the surrounding provinces.

กฎกระทรวง

กำหนดการรับน้ำหนัก ความต้านทาน ความคงทนของอาคาร
และพื้นดินที่รองรับอาคารในการต้านทานแรงสั่นสะเทือนของแผ่นดินไหว
พ.ศ. ๒๕๕๐

อาศัยอำนาจตามความในมาตรา ๕ (๓) แห่งพระราชบัญญัติควบคุมอาคาร พ.ศ. ๒๕๒๒ และมาตรา ๘ (๓) แห่งพระราชบัญญัติควบคุมอาคาร พ.ศ. ๒๕๒๒ ซึ่งแก้ไขเพิ่มเติมโดยพระราชบัญญัติควบคุมอาคาร (ฉบับที่ ๓) พ.ศ. ๒๕๔๓ อันเป็นกฎหมายที่มีบทบัญญัติบางประการเกี่ยวกับการจำกัดสิทธิและเสรีภาพของบุคคล ซึ่งมาตรา ๒๙ ประกอบกับมาตรา

“บริเวณที่ ๑” หมายความว่า พื้นที่หรือบริเวณที่เป็นดินอ่อนมากที่อาจได้รับผลกระทบจากแผ่นดินไหวระยะไกล ได้แก่ กรุงเทพมหานคร จังหวัดนนทบุรี จังหวัดปทุมธานี จังหวัดสมุทรปราการ และจังหวัดสมุทรสาคร

“บริเวณเฝ้าระวัง” หมายความว่า พื้นที่หรือบริเวณที่อาจได้รับผลกระทบจากแผ่นดินไหว ได้แก่ จังหวัดกระบี่ จังหวัดชุมพร จังหวัดพังงา จังหวัดภูเก็ต จังหวัดระนอง จังหวัดสงขลา และจังหวัดสุราษฎร์ธานี

“บริเวณที่ ๑” หมายความว่า พื้นที่หรือบริเวณที่เป็นดินอ่อนมากที่อาจได้รับผลกระทบจากแผ่นดินไหวระยะไกล ได้แก่ กรุงเทพมหานคร จังหวัดนนทบุรี จังหวัดปทุมธานี จังหวัดสมุทรปราการ และจังหวัดสมุทรสาคร

“บริเวณที่ ๑” หมายความว่า พื้นที่หรือบริเวณที่เป็นดินอ่อนมากที่อาจได้รับผลกระทบจากแผ่นดินไหวระยะไกล ได้แก่ กรุงเทพมหานคร จังหวัดนนทบุรี จังหวัดปทุมธานี จังหวัดสมุทรปราการ และจังหวัดสมุทรสาคร

“บริเวณที่ ๒” หมายความว่า พื้นที่หรือบริเวณที่อยู่ใกล้รอยเลื่อนที่อาจได้รับผลกระทบจากแผ่นดินไหว ได้แก่ จังหวัดกาญจนบุรี จังหวัดเชียงราย จังหวัดเชียงใหม่ จังหวัดตาก จังหวัดน่าน จังหวัดพะเยา จังหวัดแพร่ จังหวัดแม่ฮ่องสอน จังหวัดลำปาง และจังหวัดลำพูน

(๑) บริเวณเฝ้าระวังและบริเวณที่ ๑

(ก) อาคารที่จำเป็นต่อความเป็นอยู่ของสาธารณชน เช่น สถานพยาบาลที่รับผู้ป่วยไว้ค้างคืน สถานีดับเพลิง อาคารศูนย์บรรเทาสาธารณภัย อาคารศูนย์สื่อสาร หอบังคับการบิน โรงไฟฟ้า โรงผลิตและเก็บน้ำประปา

(ข) อาคารเก็บวัตถุอันตราย เช่น วัตถุระเบิด วัตถุไวไฟ วัตถุมีพิษ วัตถุกัมมันตรังสี หรือวัตถุที่ระเบิดได้

(ค) อาคารสาธารณะที่มีผู้ใช้อาคารได้ตั้งแต่สามร้อยคนขึ้นไป ได้แก่ โรงมหรสพ หอประชุม หอศิลป์ พิพิธภัณฑสถาน หอสมุด ศาสนสถาน สนามกีฬา อัฒจันทร์ ตลาด ห้างสรรพสินค้า ศูนย์การค้า สถานีรถ และโรงแรม

(ง) สถานศึกษาที่รับนักเรียนหรือนักศึกษาได้ตั้งแต่สองร้อยห้าสิบคนขึ้นไป

(จ) สถานรับเลี้ยงเด็กอ่อนที่รับเด็กอ่อนได้ตั้งแต่ห้าสิบคนขึ้นไป

(ฉ) อาคารที่มีผู้ใช้อาคารได้ตั้งแต่ห้าพันคนขึ้นไป

สิบเมตรขึ้นไป

ัวฝายมีความสูง

บาลที่รับผู้ป่วยไว้

ค้างคืน สถานีดับเพลิง อาคารศูนย์บรรเทาสาธารณภัย อาคารศูนย์สื่อสาร หอบังคับการบิน โรงไฟฟ้า โรงผลิตและเก็บน้ำประปา

(ข) อาคารเก็บวัตถุอันตราย เช่น วัตถุระเบิด วัตถุไวไฟ วัตถุมีพิษ วัตถุกัมมันตรังสี หรือวัตถุที่ระเบิดได้

(ค) อาคารสาธารณะ ได้แก่ โรงมหรสพ หอประชุม หอศิลป์ พิพิธภัณฑสถาน หอสมุด ศาสนสถาน สนามกีฬา อัฒจันทร์ ตลาด ห้างสรรพสินค้า ศูนย์การค้า สถานีรถ โรงแรม สถานบริการ และอาคารจอดรถ

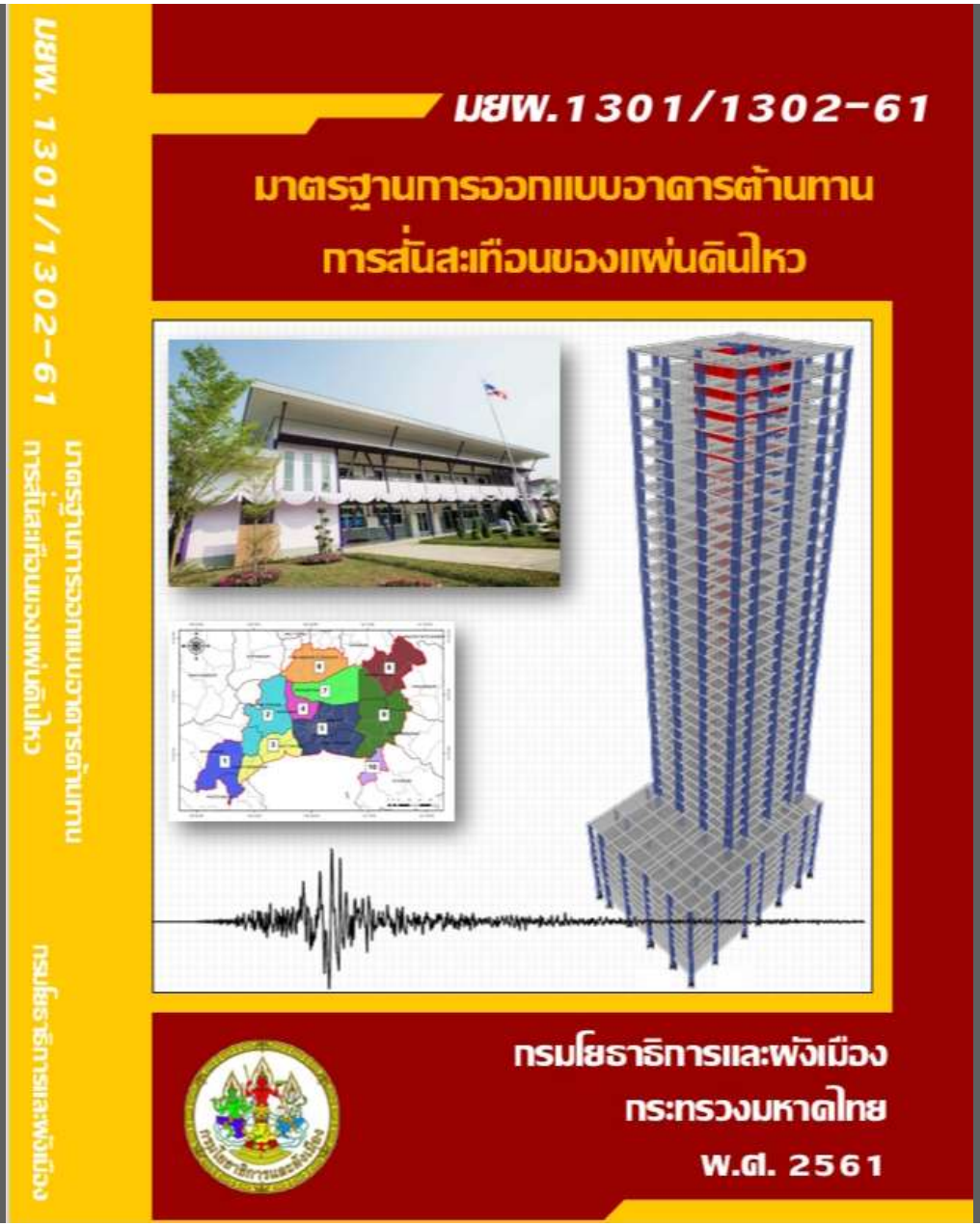

National Standard DPT 1301/1302-61: Seismic Resistant Design of Buildings and Structures

Issued by Department of Public Works and Town & Country Planning, Ministry of Interior (2019)

The new design spectra for Bangkok and the surrounding provinces have already been included in DPT1301/1302-61.

New Design Spectra for Bangkok and surrounding provinces

Earthquake induced force in the Building

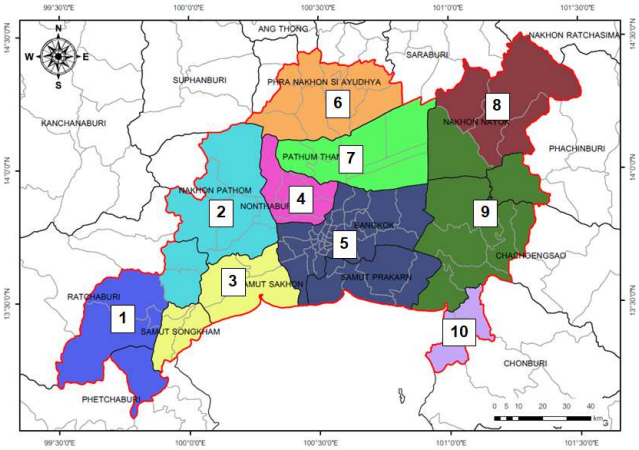

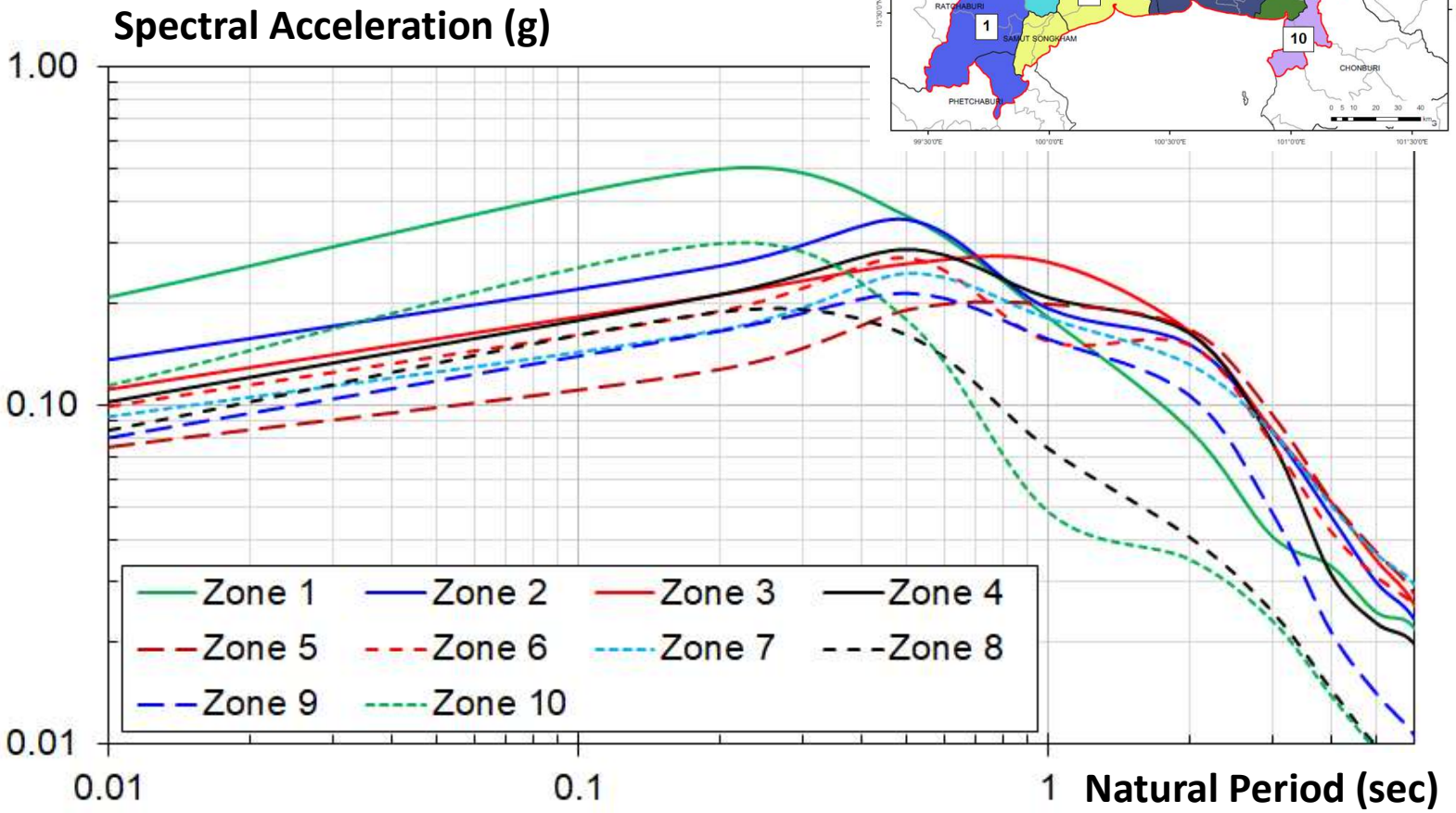

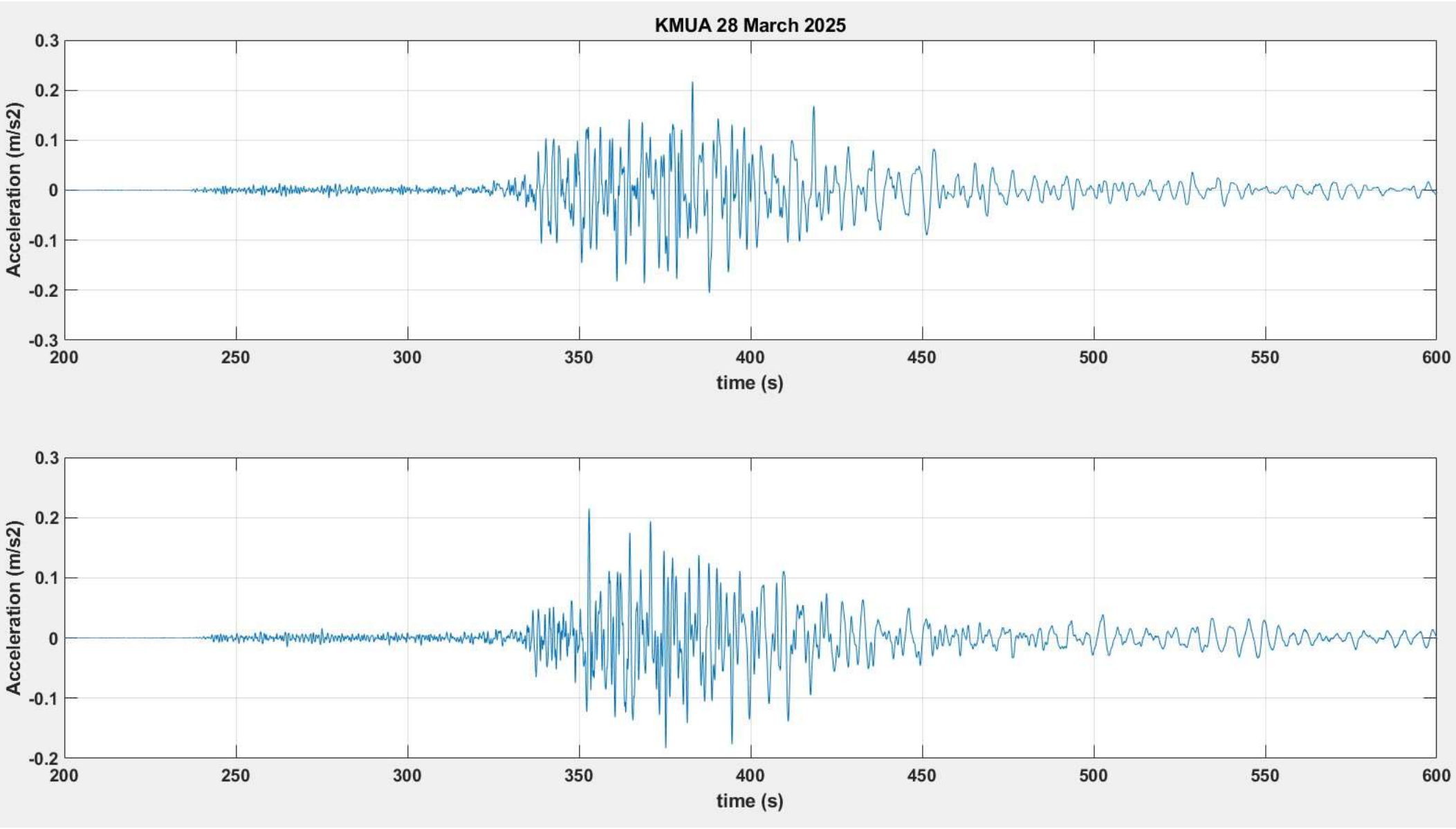
KMUA 28 March 2025
Acceleration (m/s2)
0.3
0.2
0.1
0
-0.1
-0.2
-0.3
200
250
300
350
400
450
500
550
600
time (s)
Acceleration (m/s2)
0.3
0.2
0.1
0
-0.1
-0.2
200
250
300
350
400
450
500
550
600
time (s)

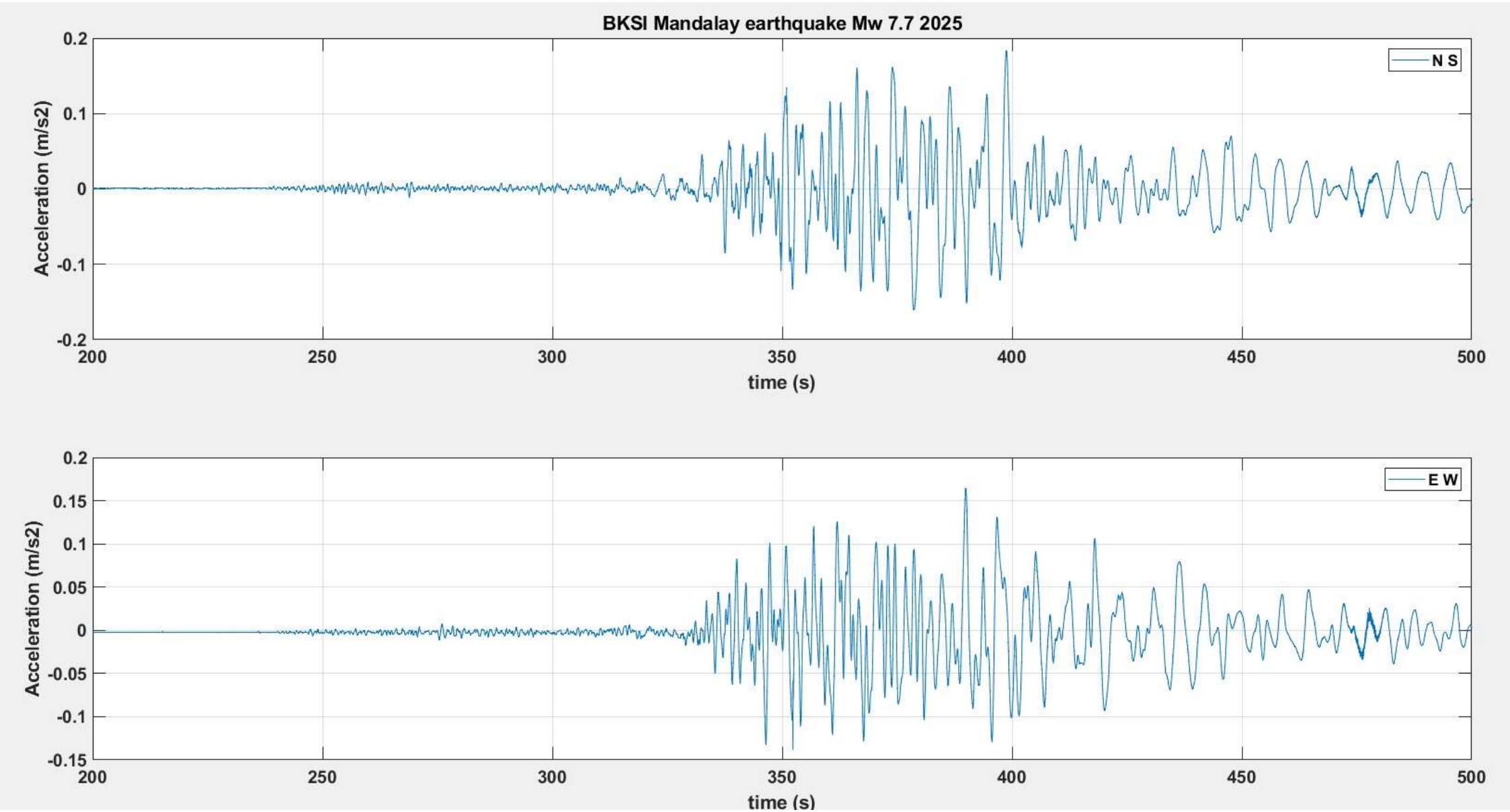
BKSI Mandalay earthquake Mw 7.7 2025
N S
Acceleration (m/s2)
time (s)
E W
Acceleration (m/s2)
time (s)

EQ induced force in the Building

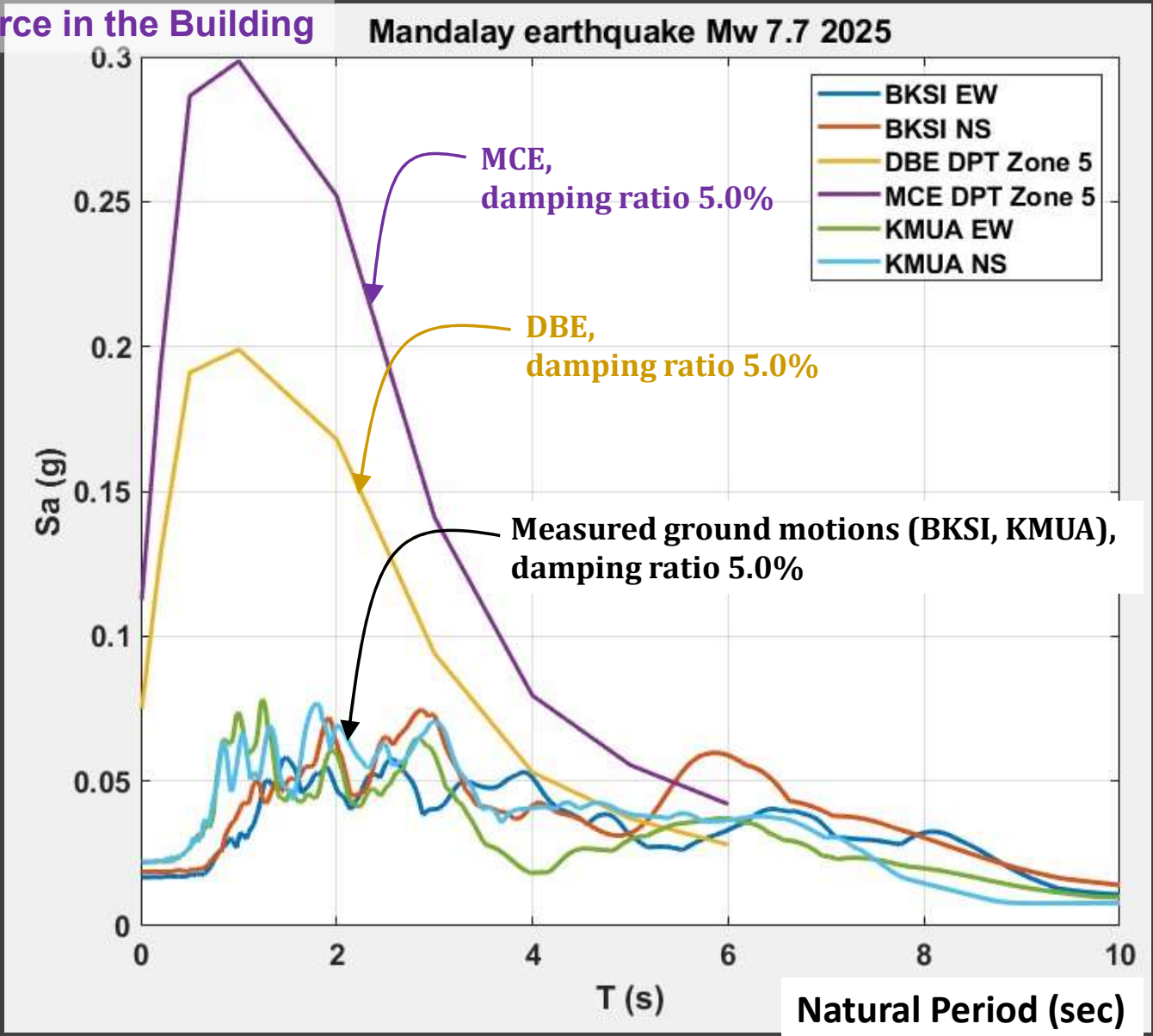

Thailand Structural Engineers Association
TSEA
สมาคมวิศวกรโครงสร้างแห่งประเทศไทย

Summary of Damages

Total Collapse – 1 Bldg (SAO bldg. during construction)

Structural damages – Approx. more than 10 Bldgs

Non-structural damages – Approx. Several 100 Bldgs

All buildings in Bangkok, except collapsed SAO bldg, are safe from the earthquake with varying of damages but no reported injuries or death, except the collapsed SAO bldg with around 100 labors death or missing.

Slight to Moderate Damage to Non-Structural Masonry Walls

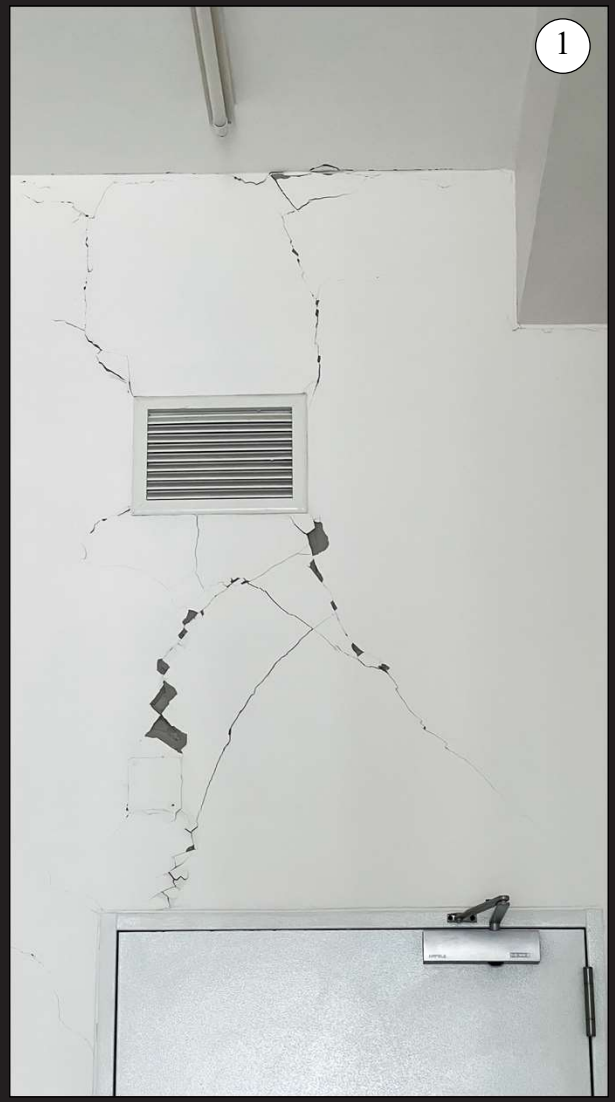

Severe Damage to Non-Structural Masonry Walls–ผนังอิฐก่อร้าวทะลุสองฝั่ง

Significant Structural Damage (25-story, Rajavithi Hospital)

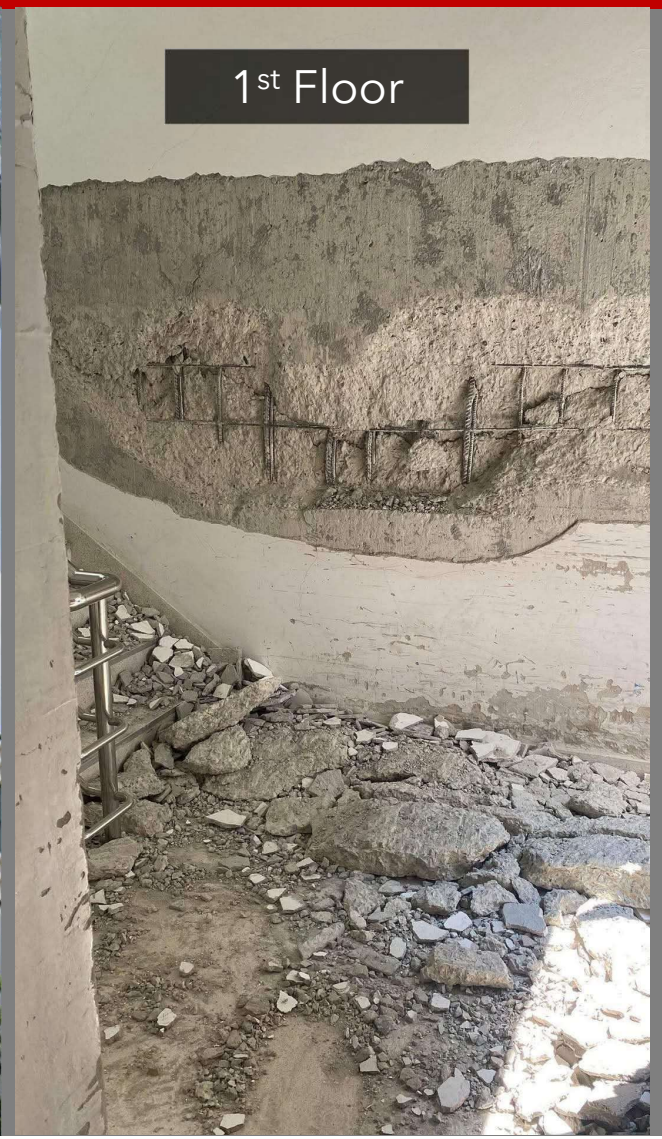

Significant Structural Damage (25-story, Rajavithi Hospital)

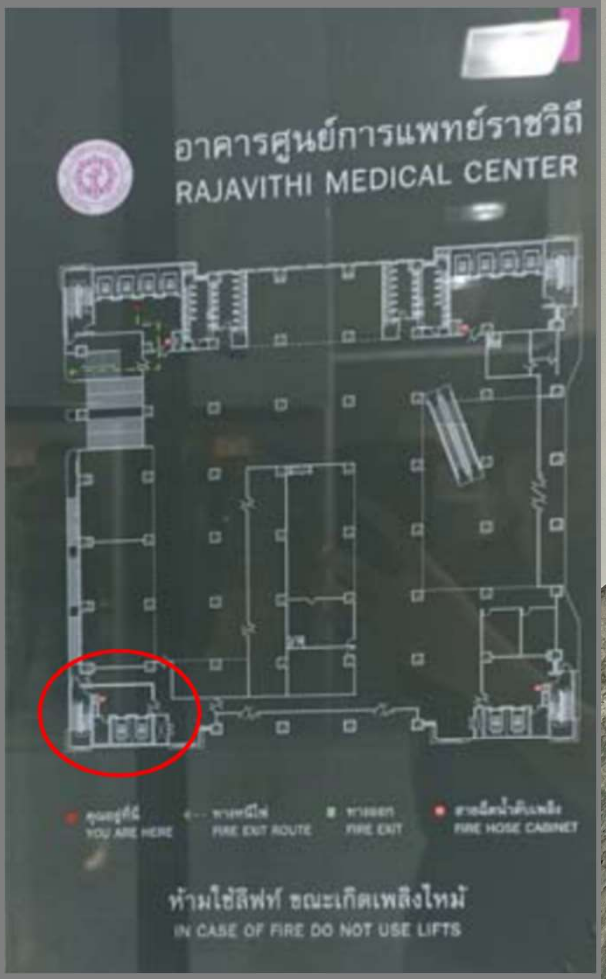

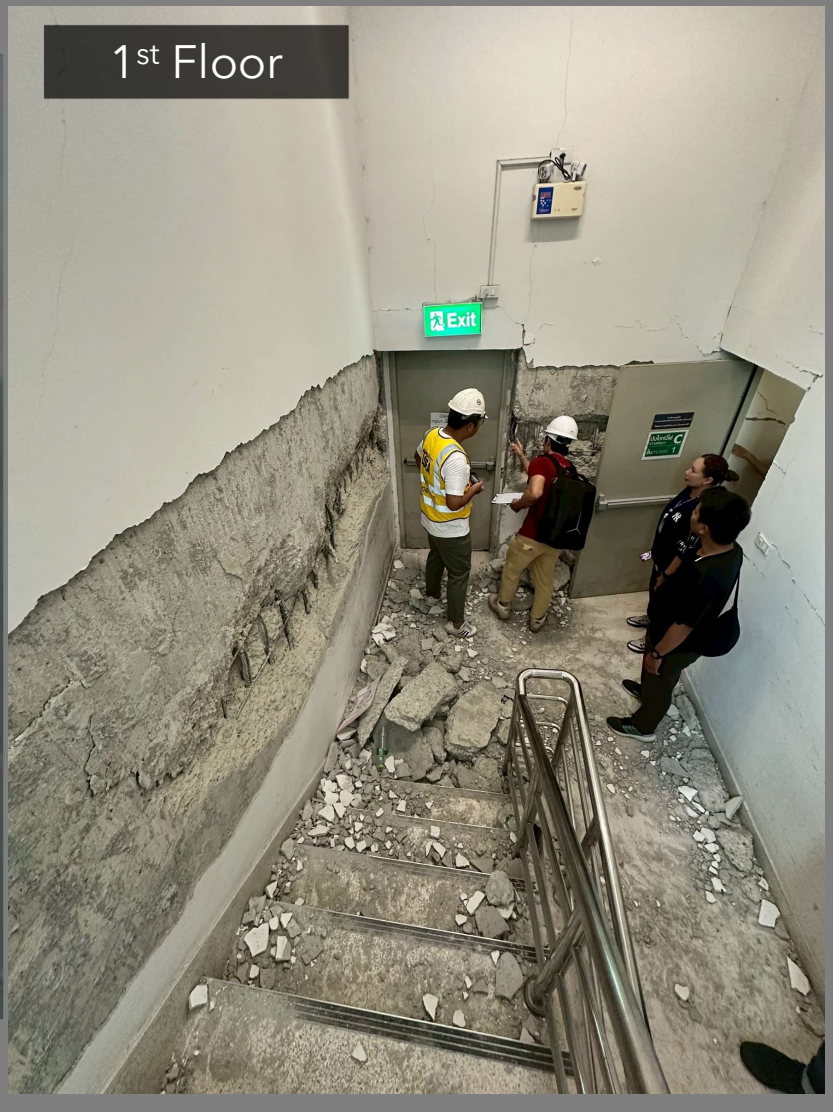

Significant Structural Damage (Building in Bangkok)

$$\text{Roof Drift Ratio} = \frac{\Delta}{H}$$

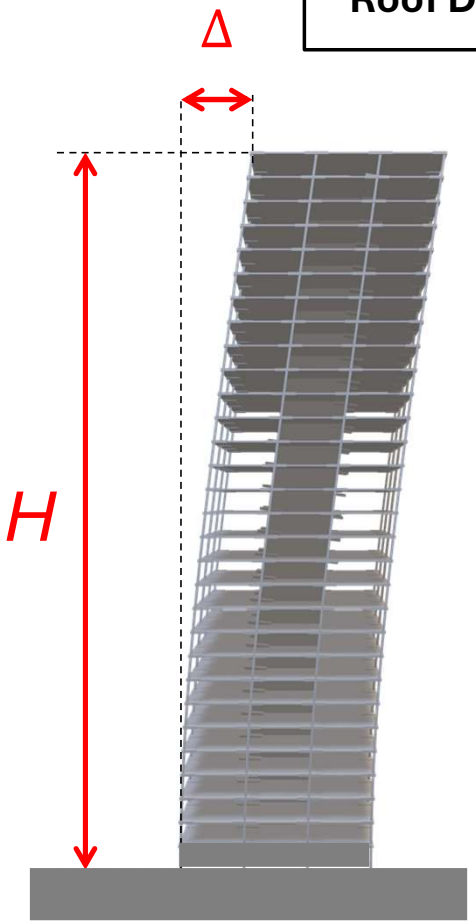

$$\text{Inter-Story Drift Ratio} = \frac{\delta}{h}$$

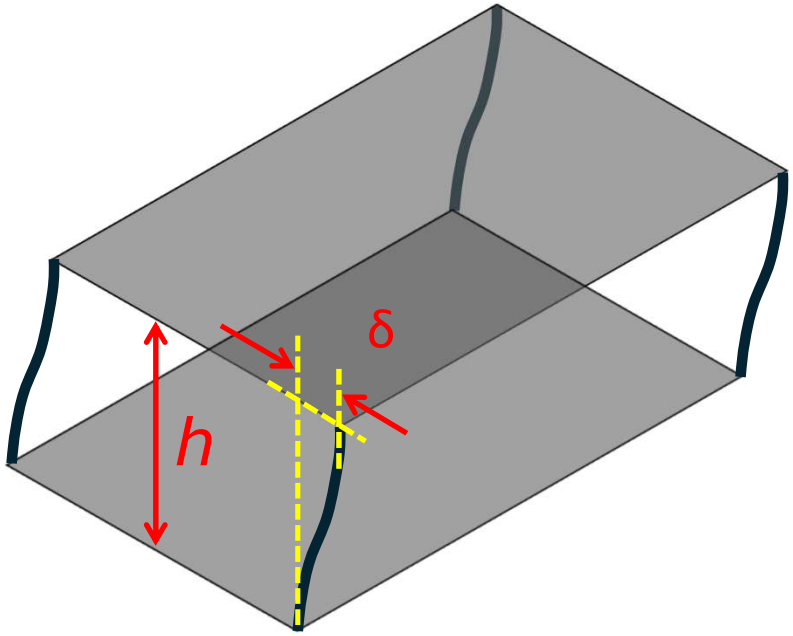

Roof Drift Ratio

Station: Department of Public Works and Town & Country Planning (PWSA)

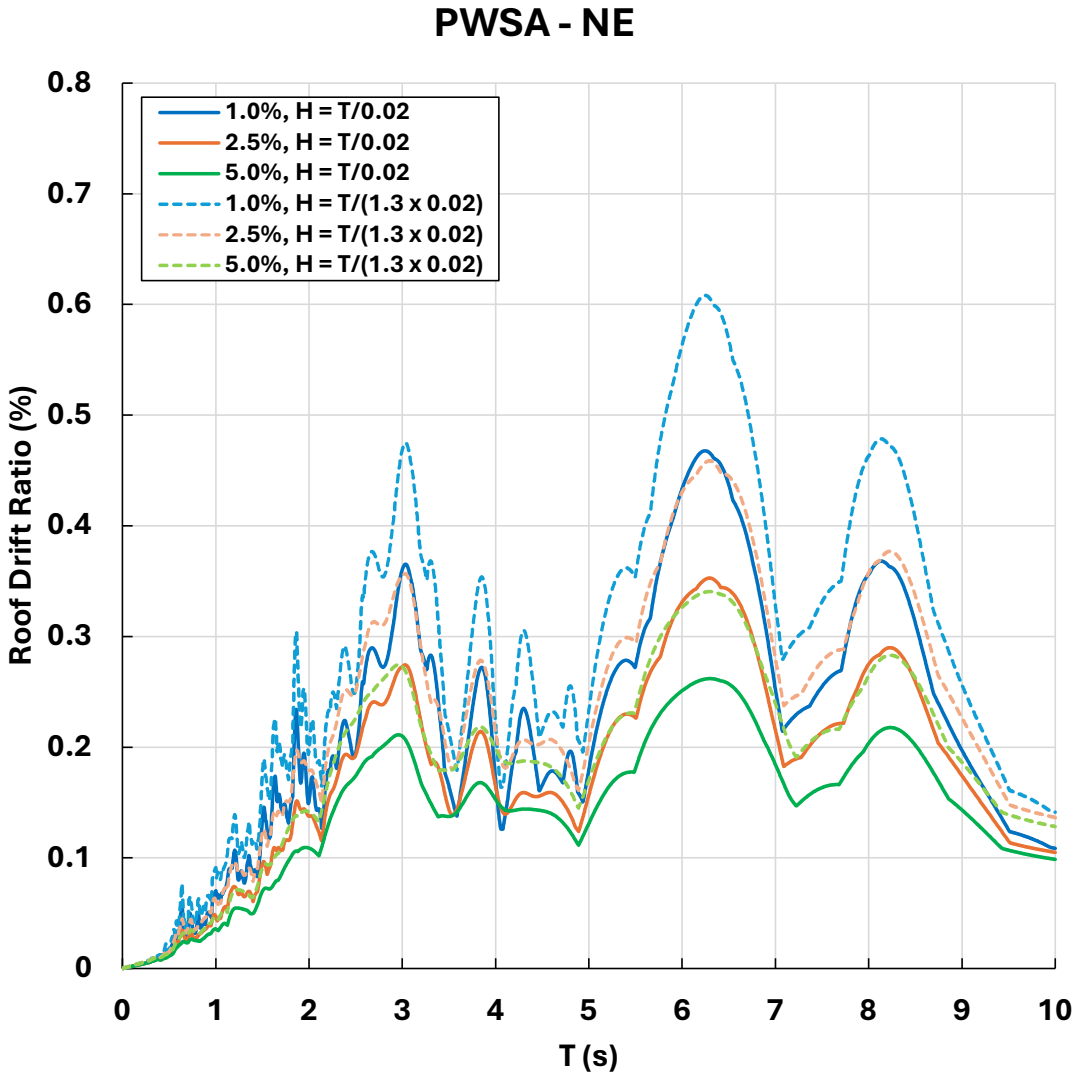

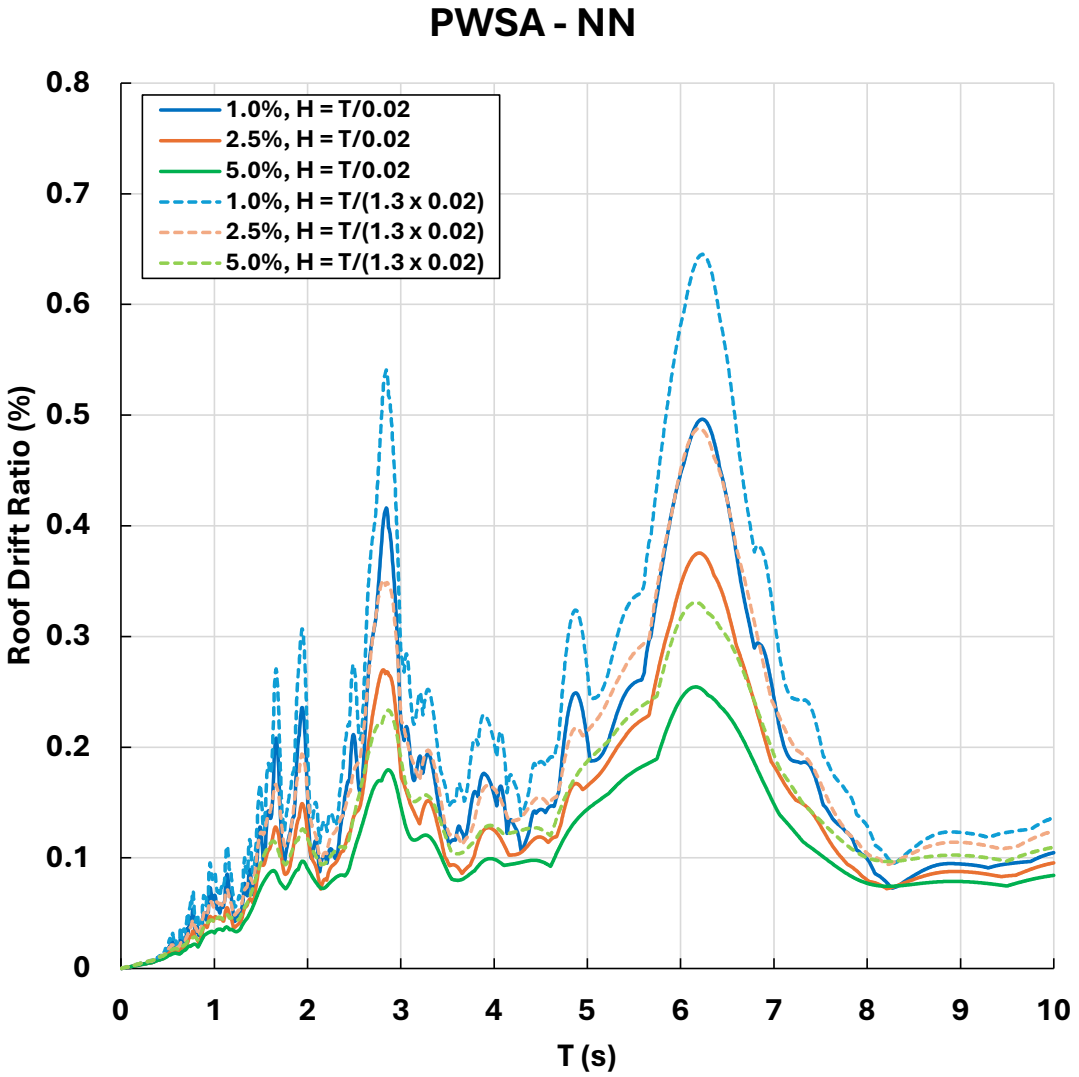

Damped Free Vibration

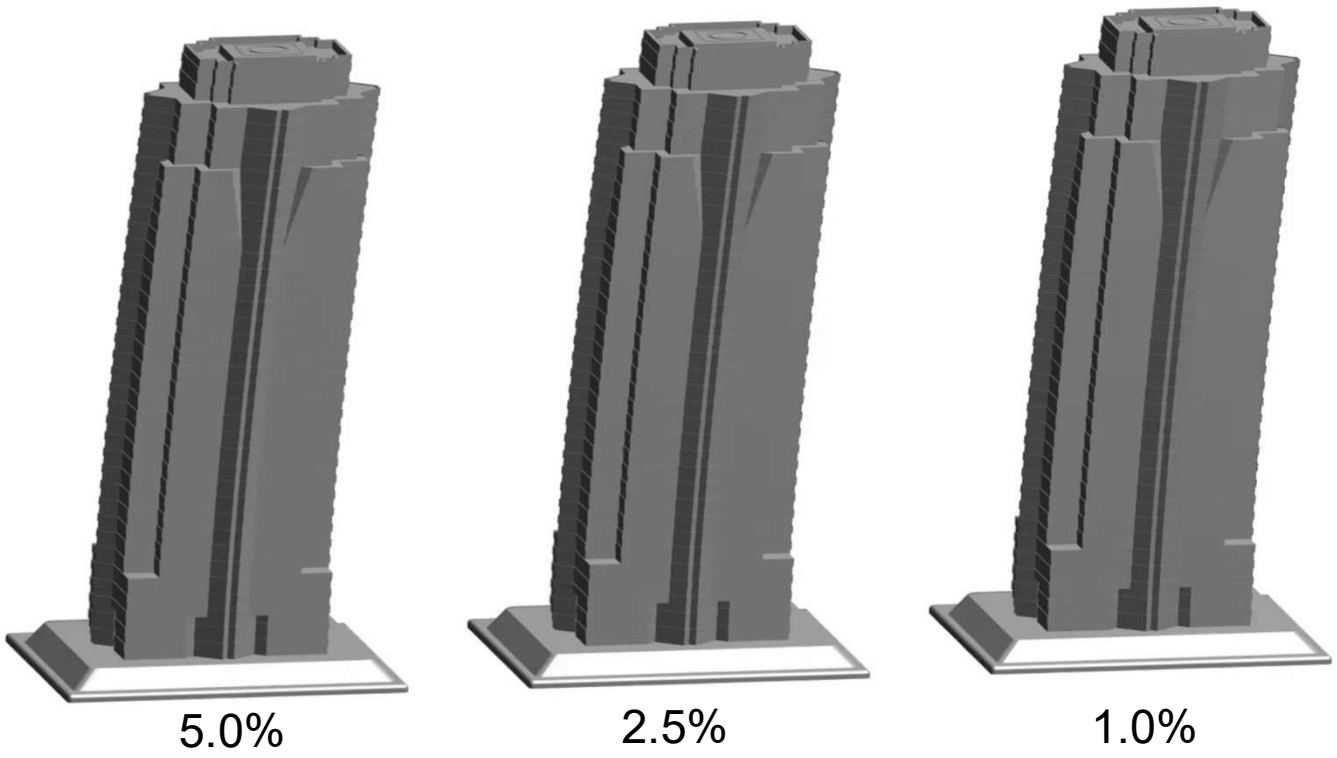

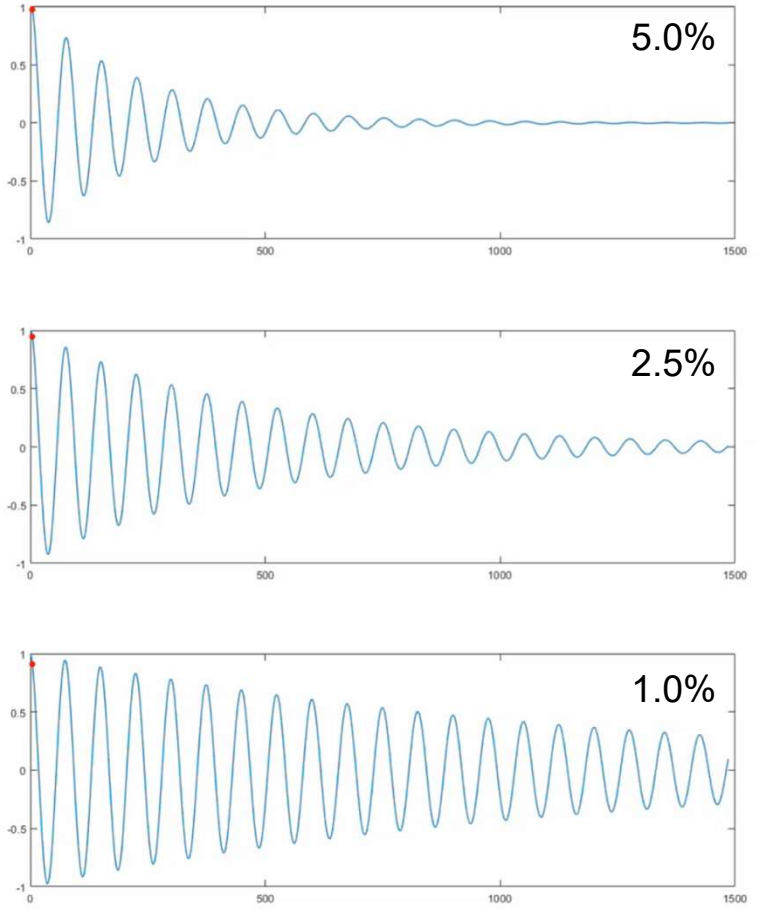

Harmonic Shaking

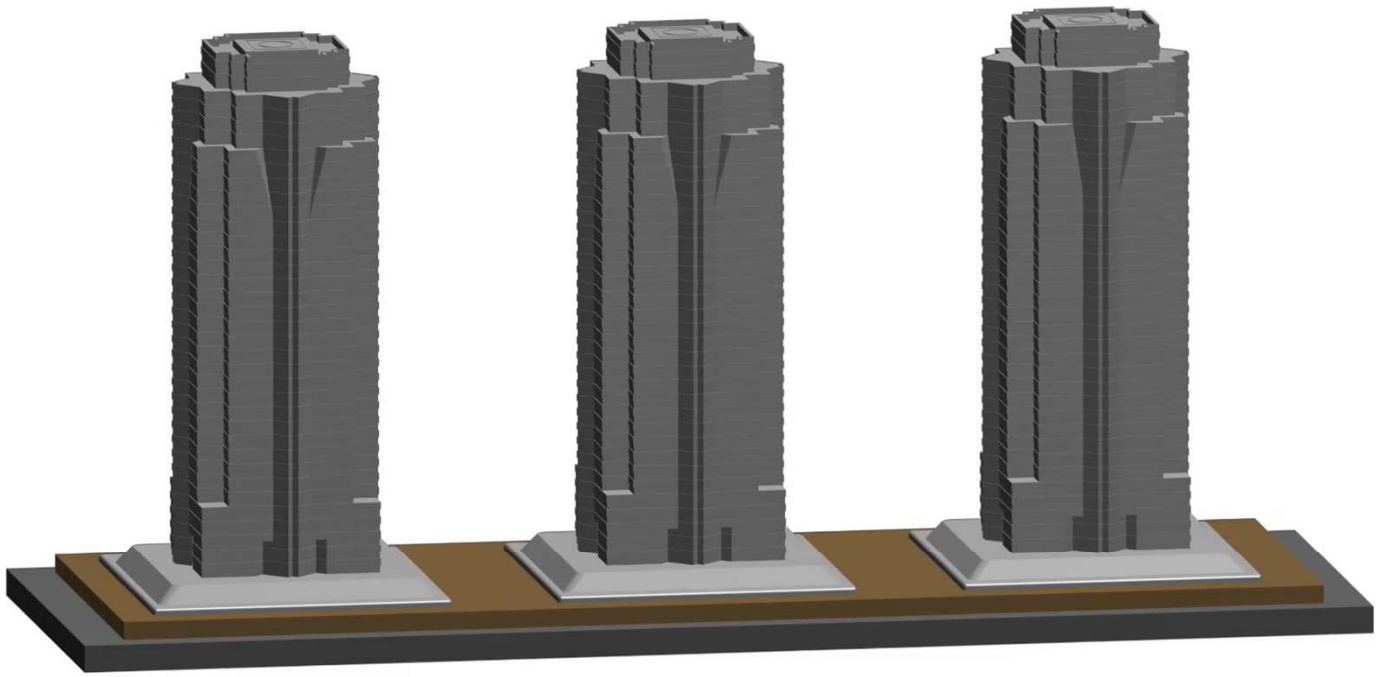

5.0% 2.5% 1.0%

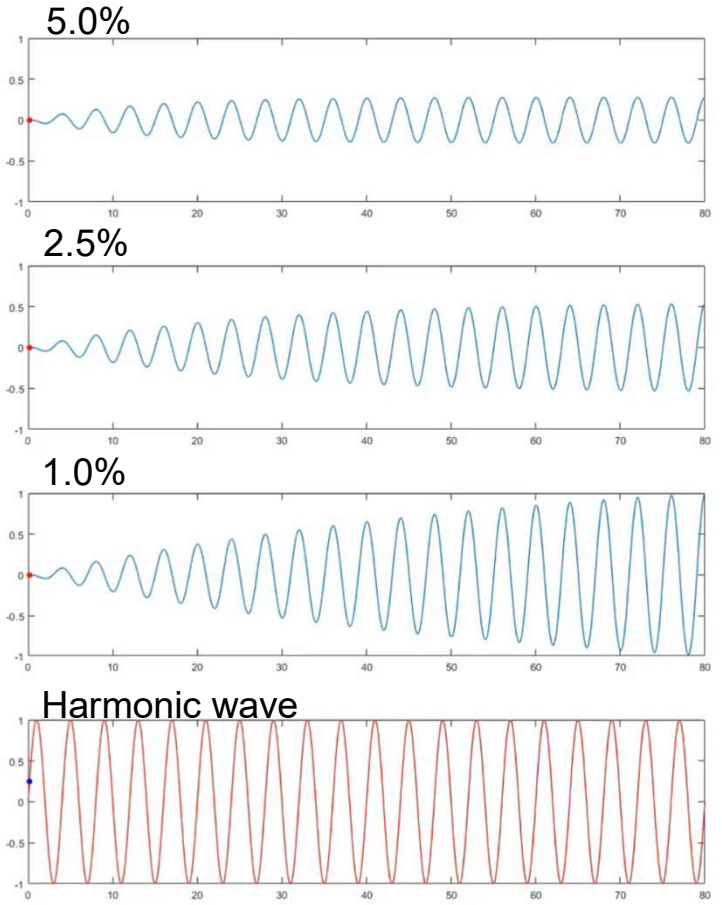

Roof Drift Ratio

Station: Department of Public Works and Town & Country Planning (PWSA)

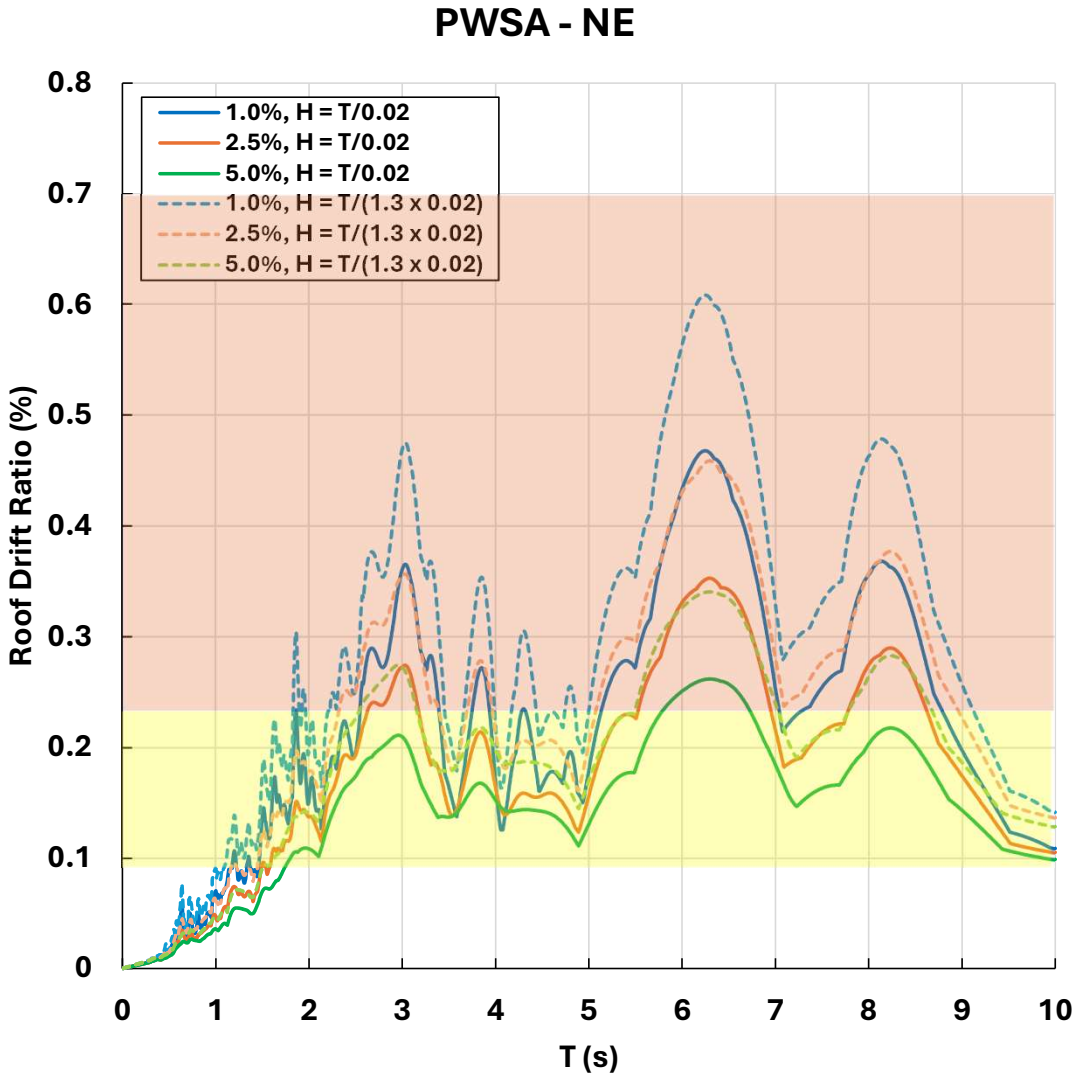

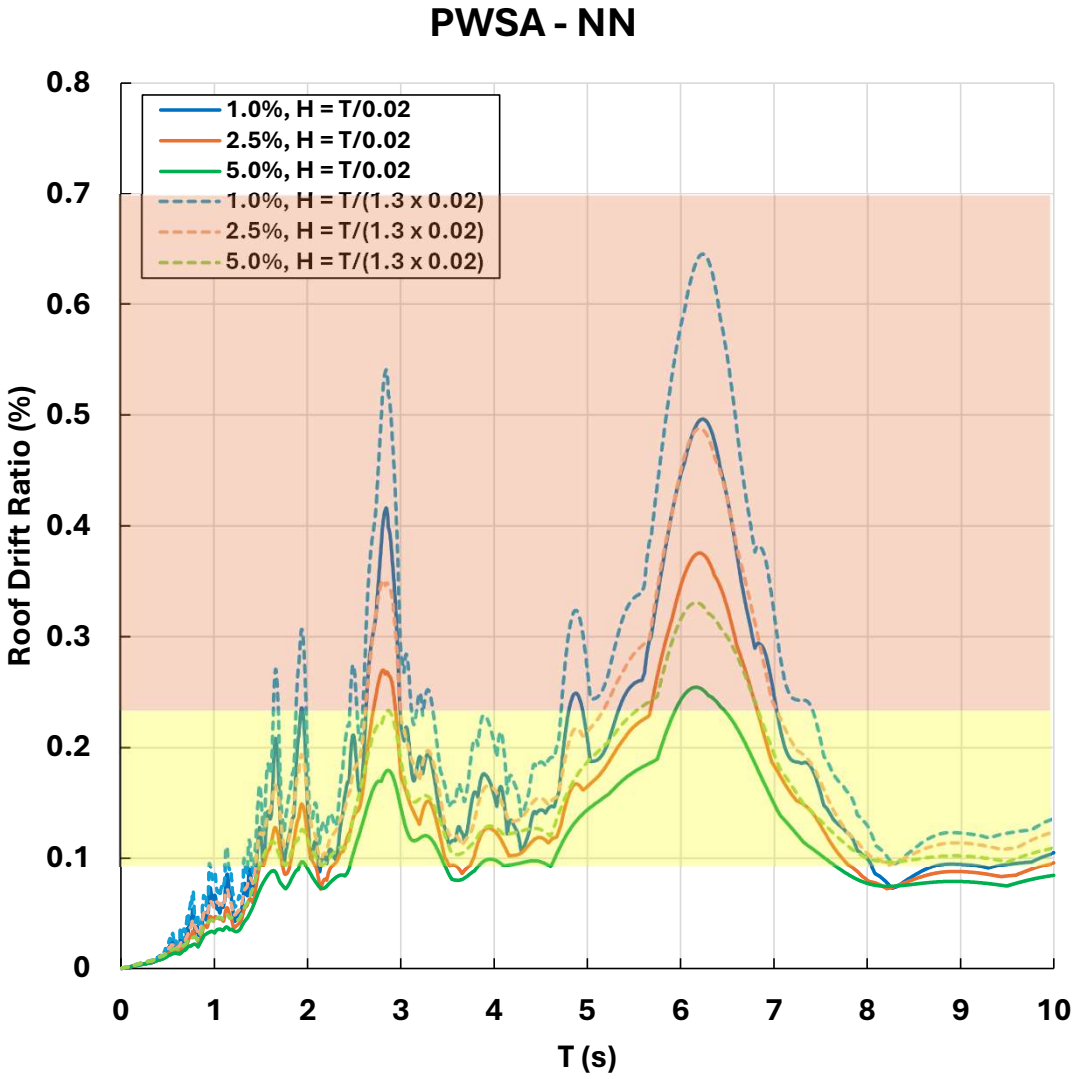

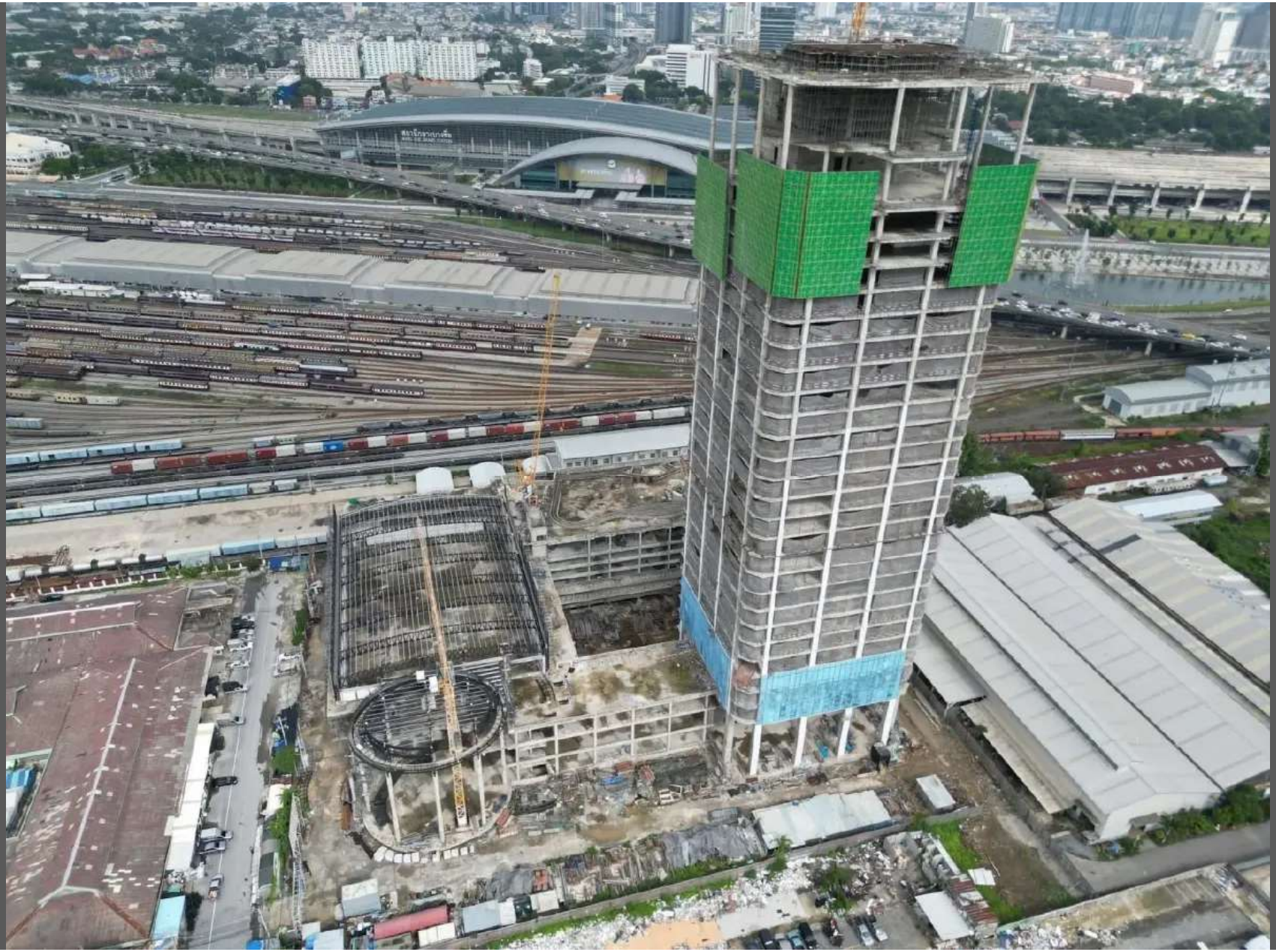

Building model

	Linear Static	Modal		
Model	Base Reaction (Ton)	Period (s)		
		Mode 1	Mode 2	Mode 3
Linear-elastic	53725.51	2.883 UX	2.272 UY	2.050 RZ

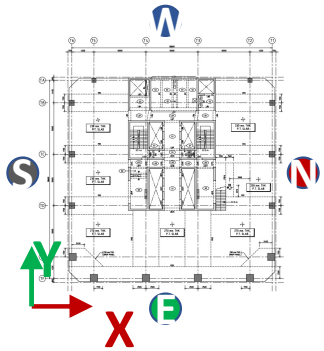

KMUTT's Model

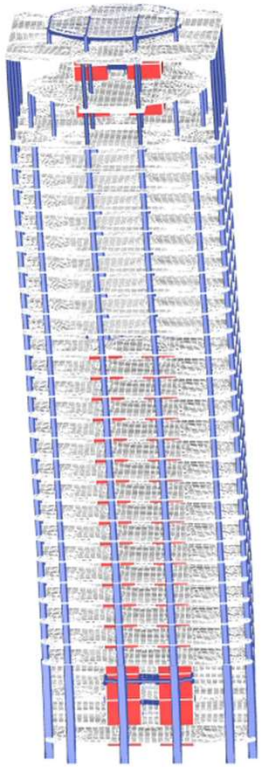

Mode 1 X

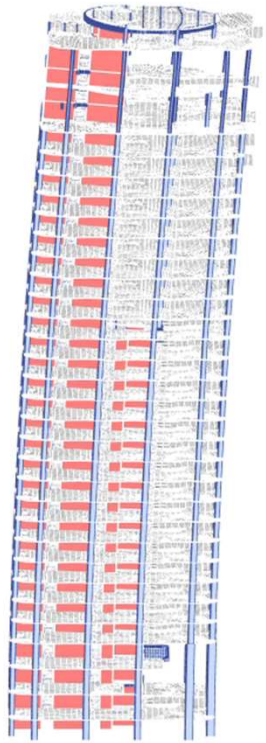

Mode 2 Y

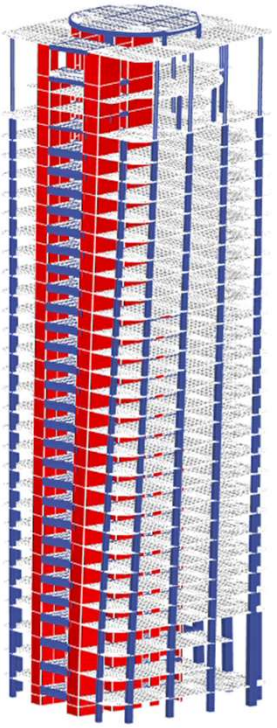

Mode 3 Z

Roof Drift Ratio

Station: Queen Sirikit National Convention Center (BKSI)

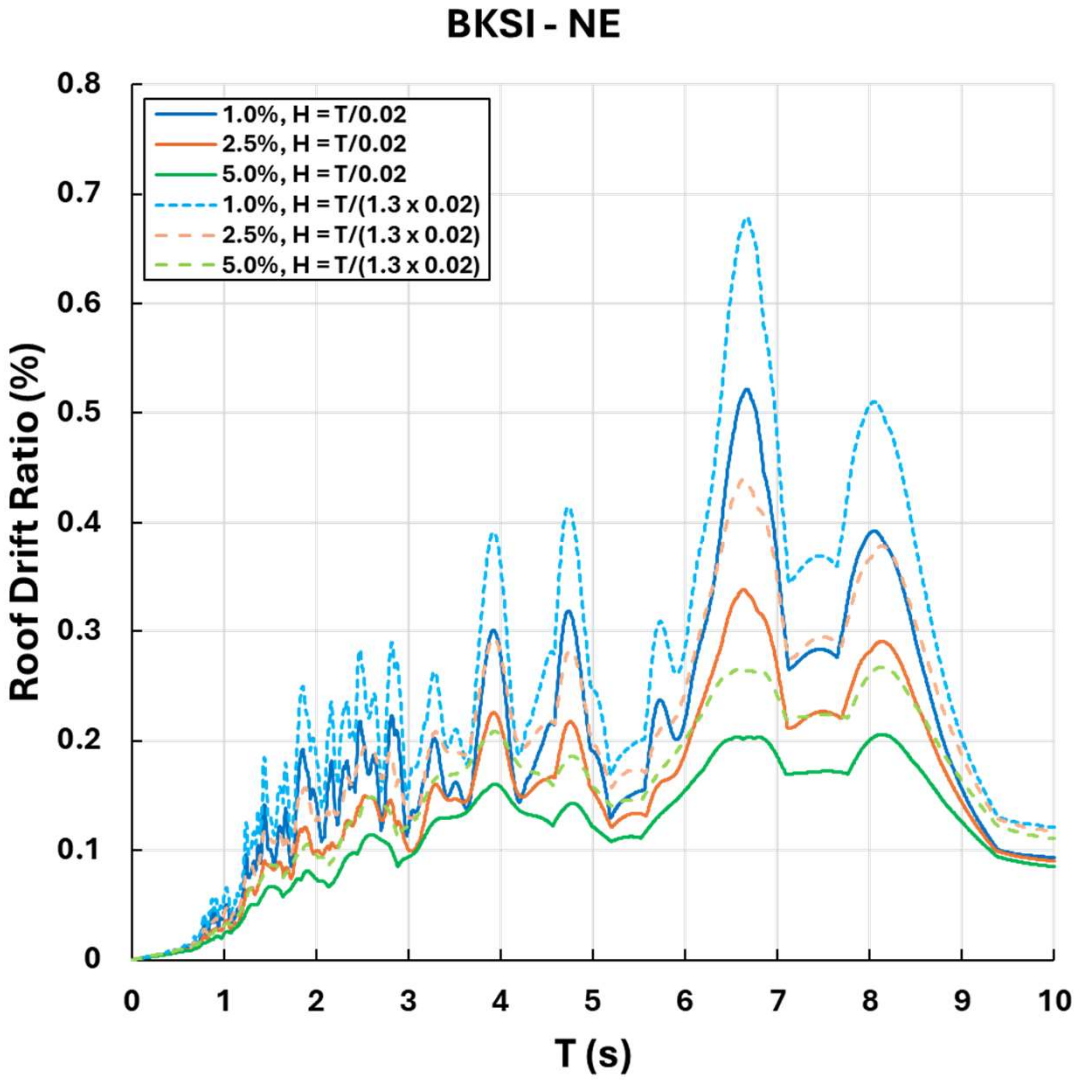

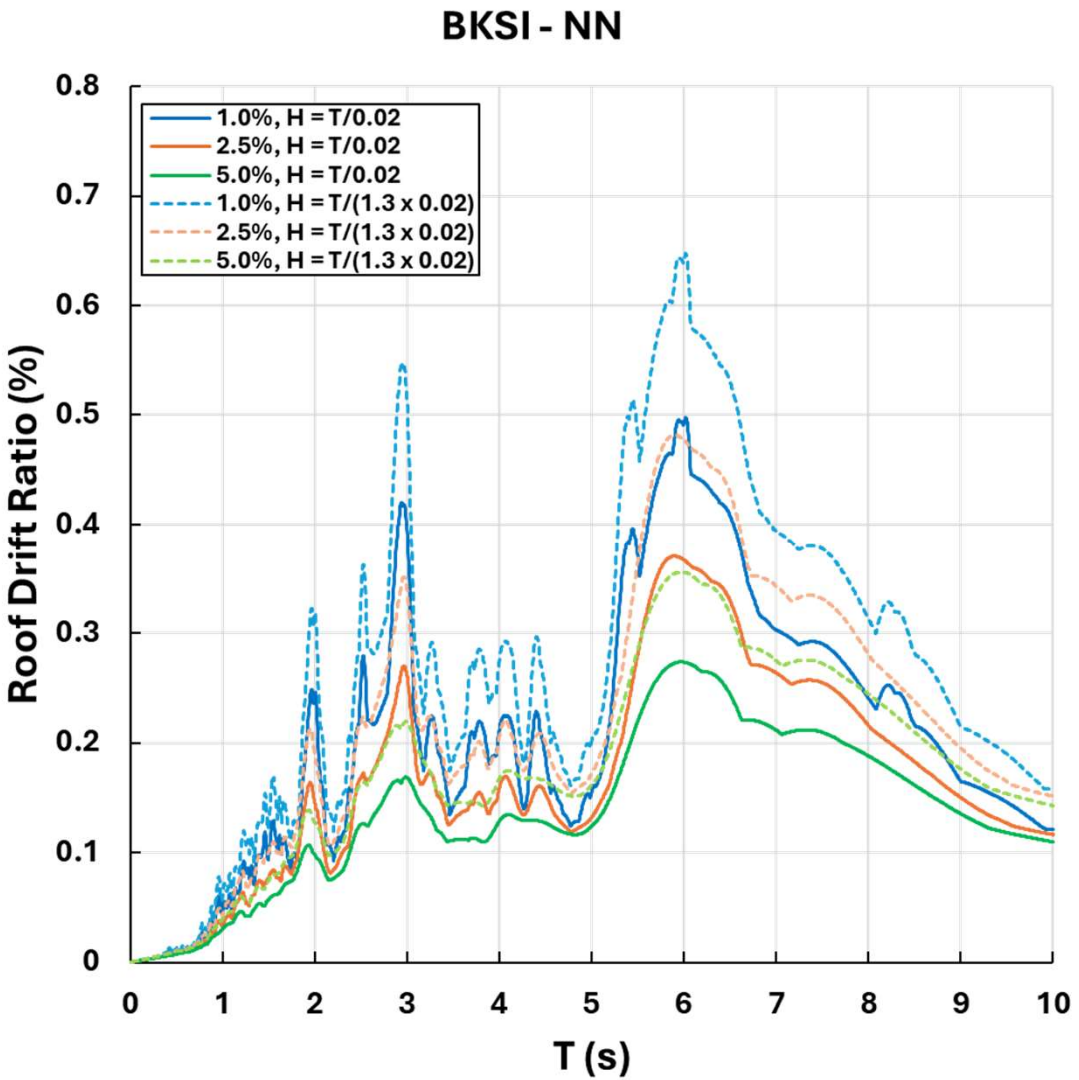

Roof Drift Ratio

Station: King Mongkut's University of Technology Thonburi (KMUA)

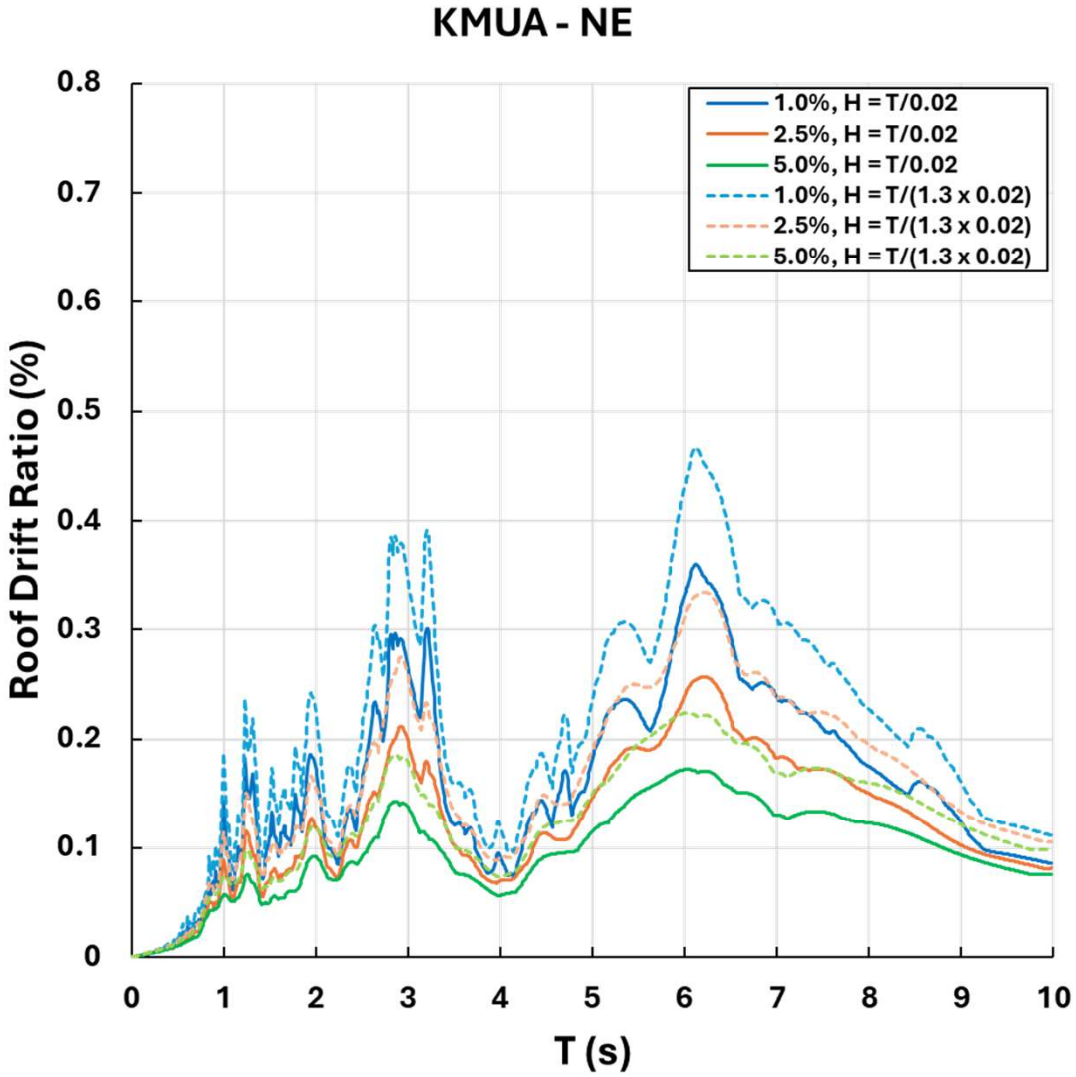

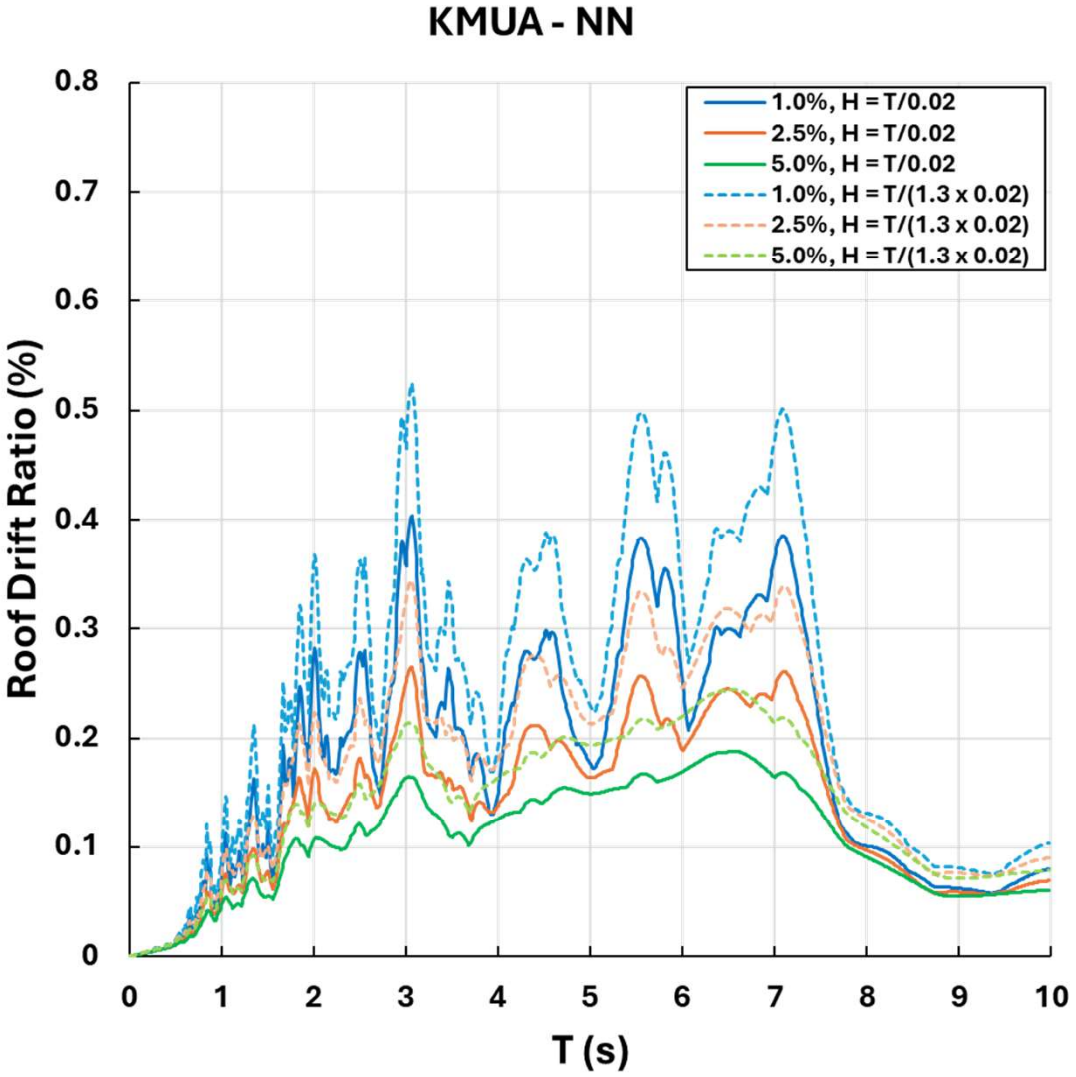

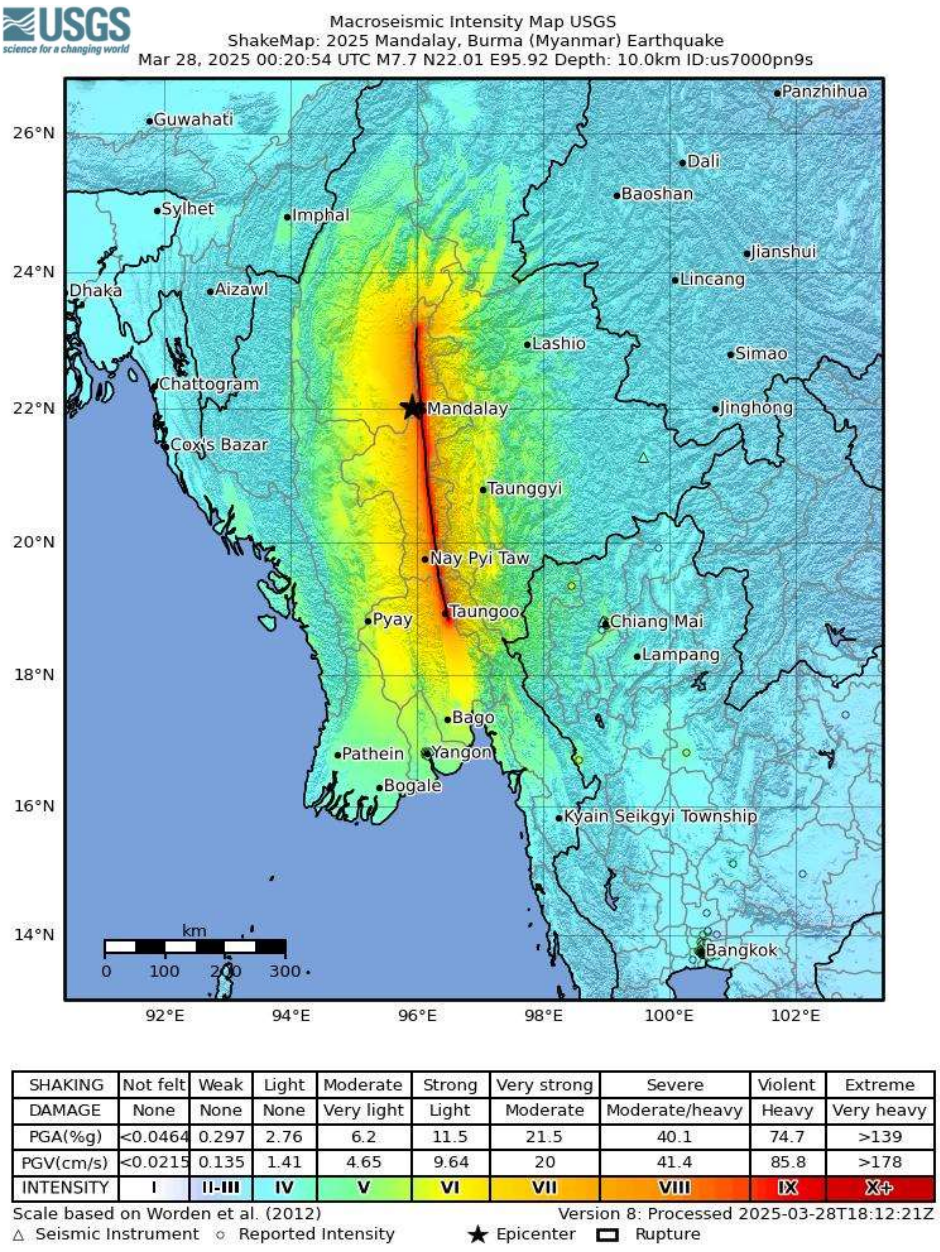

SHAKING	Not felt	Weak	Light	Moderate	Strong	Very strong	Severe	Violent	Extreme
DAMAGE	None	None	None	Very light	Light	Moderate	Moderate/heavy	Heavy	Very heavy
PGA(%g)	<0.0464	0.297	2.76	6.2	11.5	21.5	40.1	74.7	>139
PGV(cm/s)	<0.0215	0.135	1.41	4.65	9.64	20	41.4	85.8	>178
INTENSITY	I	II-III	IV	V	VI	VII	VIII	IX	X+

Scale based on Worden et al. (2012)
Version 8: Processed 2025-03-28T18:12:21Z
△ Seismic Instrument ○ Reported Intensity ★ Epicenter ▭ Rupture

M 7.7 - 2025 Mandalay, Burma (Myanmar) Earthquake

2025-03-28 06:20:54 (UTC)
22.013°N 95.922°E
10.0 km depth

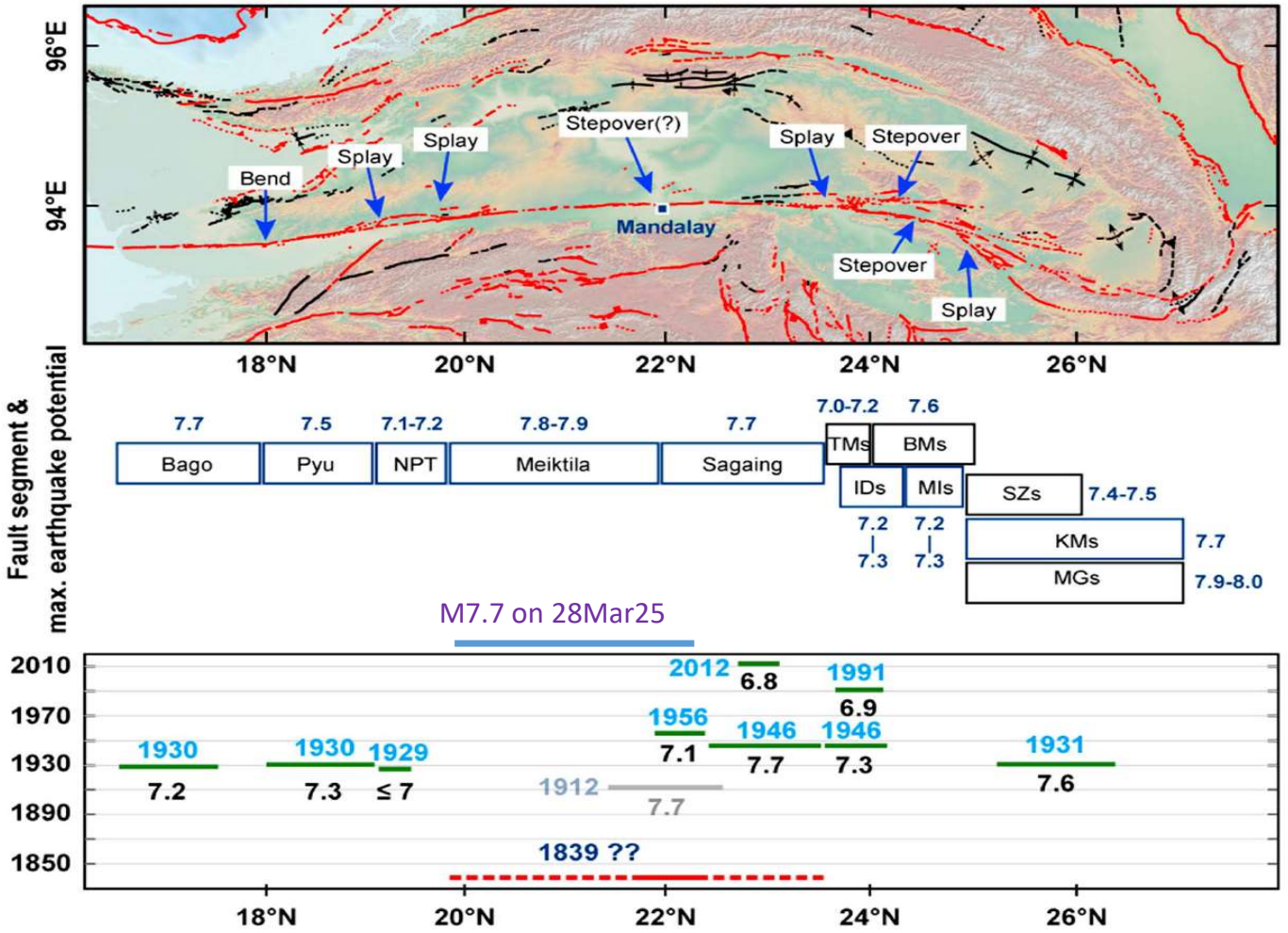

Figure 22. Map and chart of potential maximum earthquake magnitudes (M_w) associated with named segments of the Sagaing fault. Blue arrows show the boundaries of fault segments. Ruptures of the past century appear in the lower box. Green lines are the proposed rupture patches along the Sagaing fault since the beginning of the twentieth century; gray line shows the proposed rupture section along the Kyaukkyan fault, parallel to the Sagaing fault. Red line marks the possible rupture patch of the 1839 earthquake, inferred from historical data. BMs = Ban Mauk segment; TMs = Tawma segment; IDs = In Daw segment; MIs = Mawlu segment; SZs = Shaduzup segment; KMs = Kamaing segment; MGs = Mogang segment.

Roof Drift Ratio

Station: Department of Public Works and Town & Country Planning (PWSA)

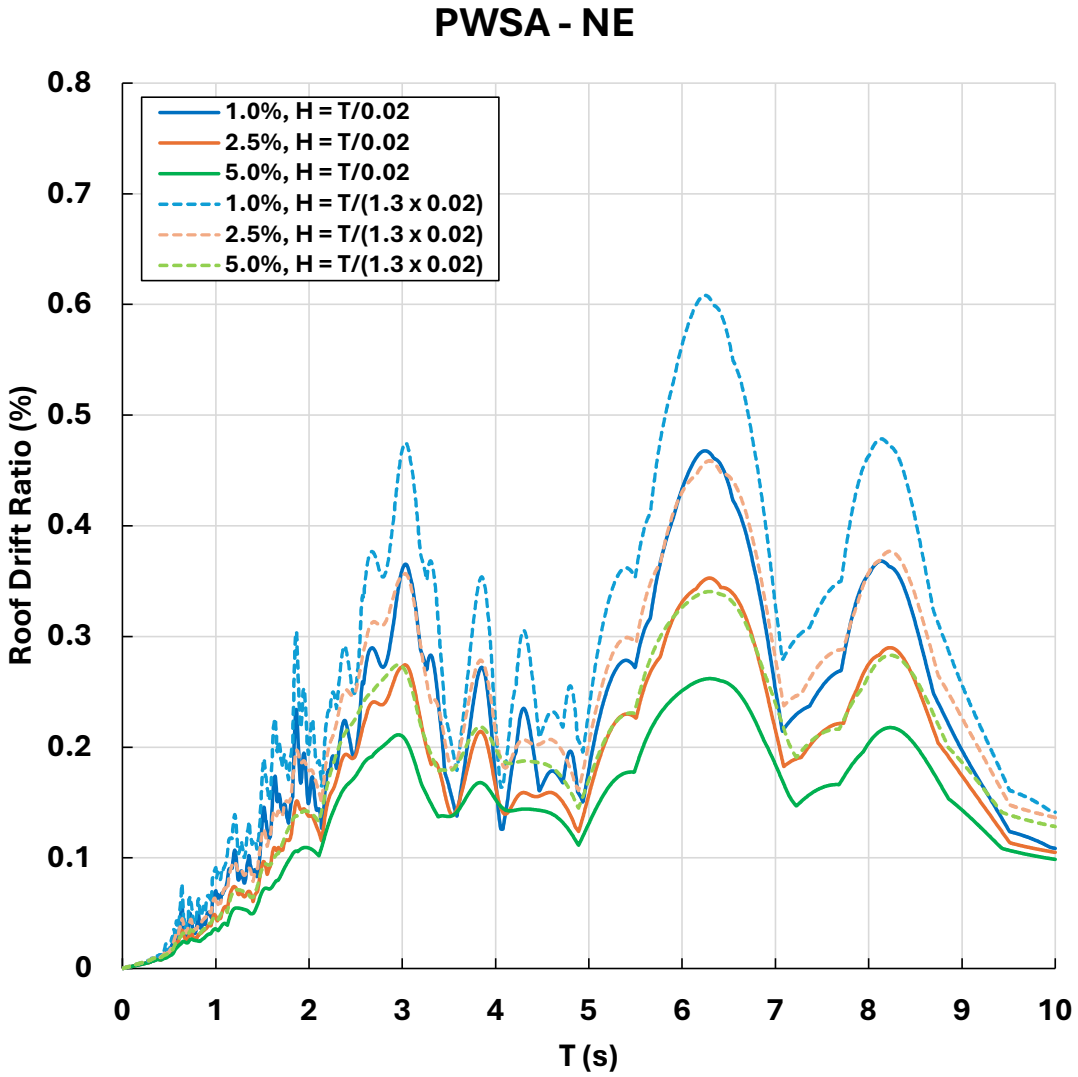

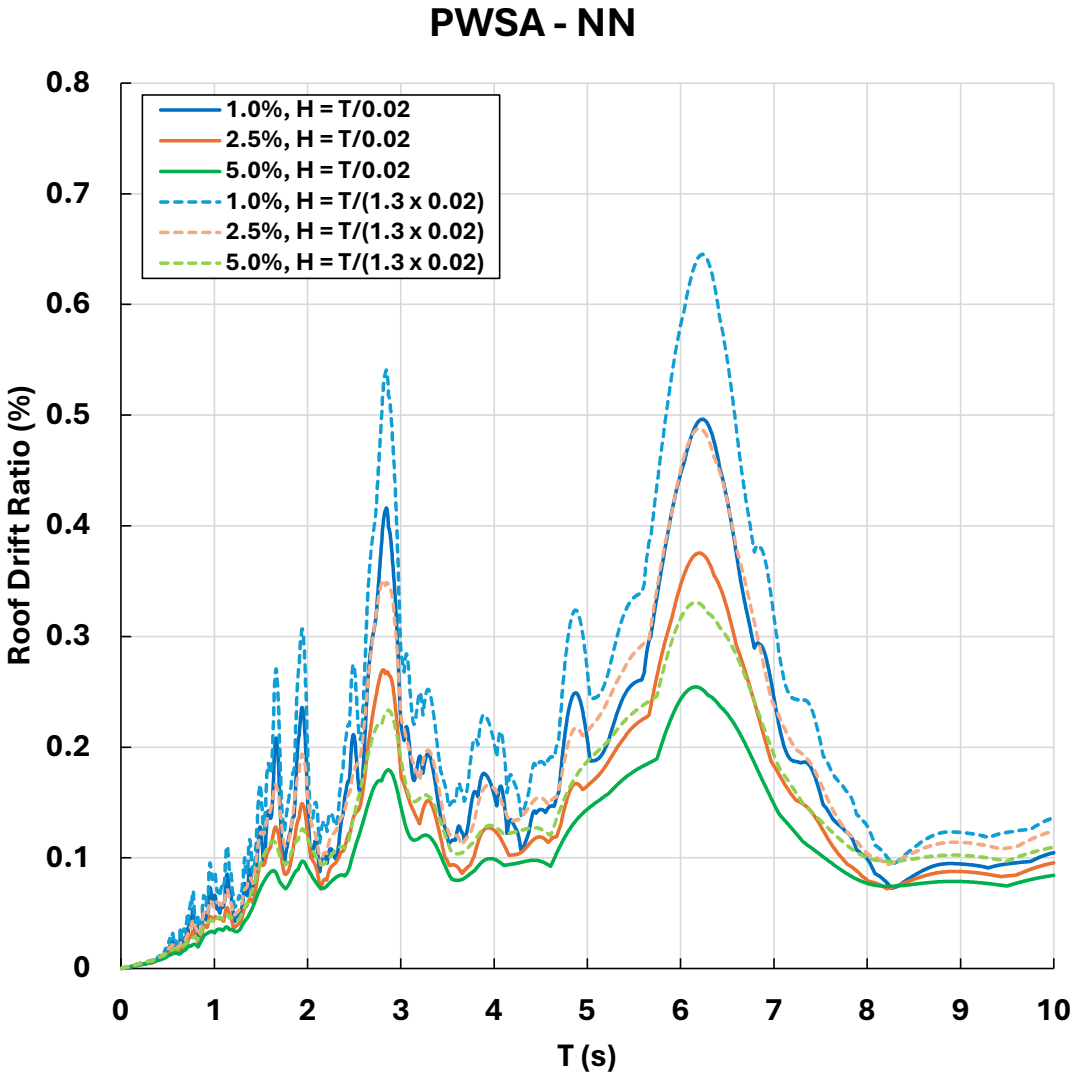

Typical Tall Buildings in Thailand

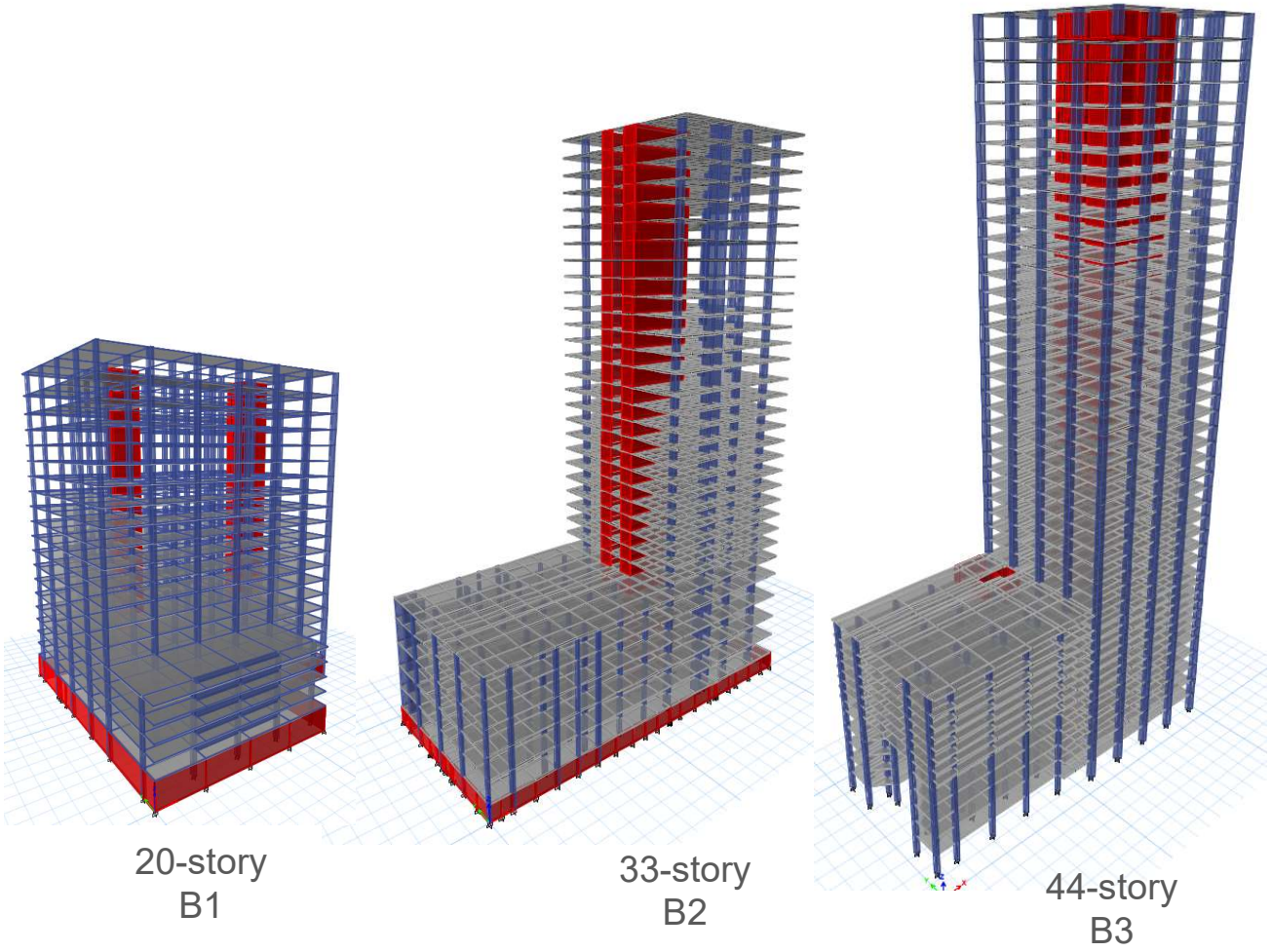

20-story
B1

33-story
B2

44-story
B3

- ***RC slab-column frames carry gravity loads***
- ***RC walls & cores resist lateral loads***
- ***Masonry infill walls extensively used***
- ***Possess irregular features commonly found in typical tall buildings, e.g. podium and non-symmetrical arrangement of RC walls, etc.***

Ductile Structural Walls

A basic requirement for walls to be ductile: ***a flexural plastic hinge zone should be formed at the base of the wall, and brittle failure mechanisms should not be permitted to occur****.*

This is achieved by establishing a desirable hierarchy in the failure mechanics using ***capacity design procedures*** *and by appropriate detailing of the potential plastic hinge region.*

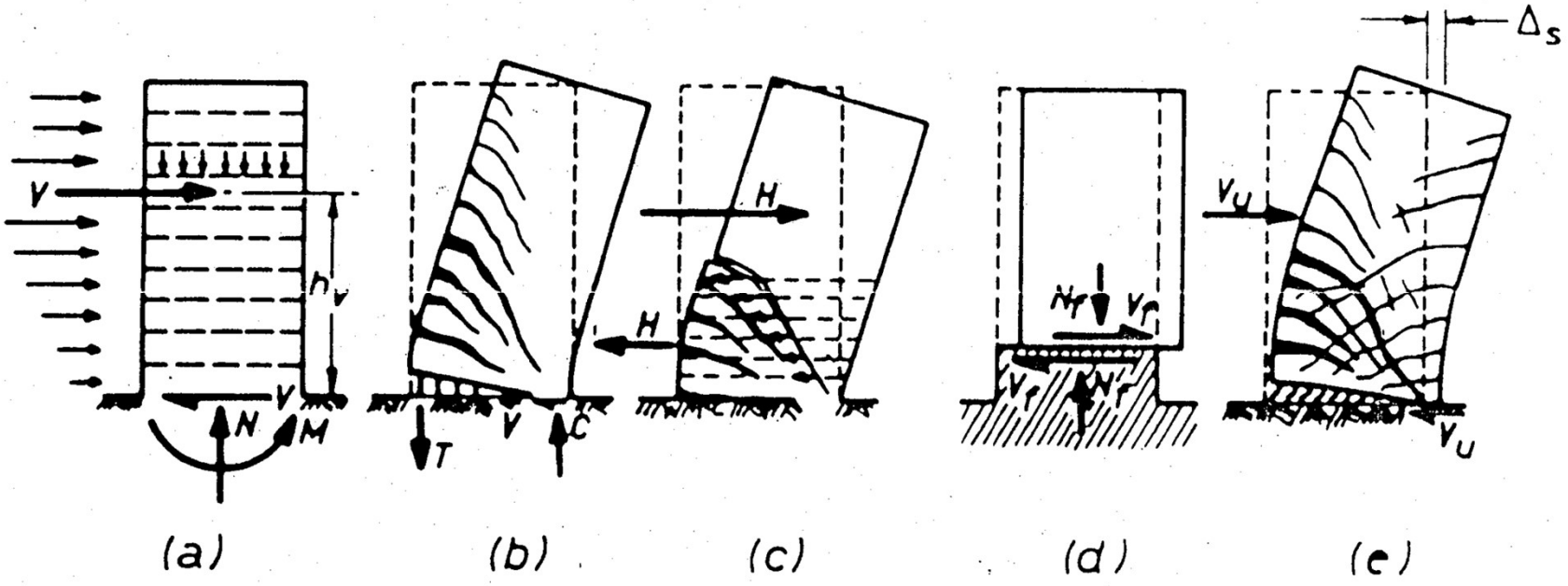

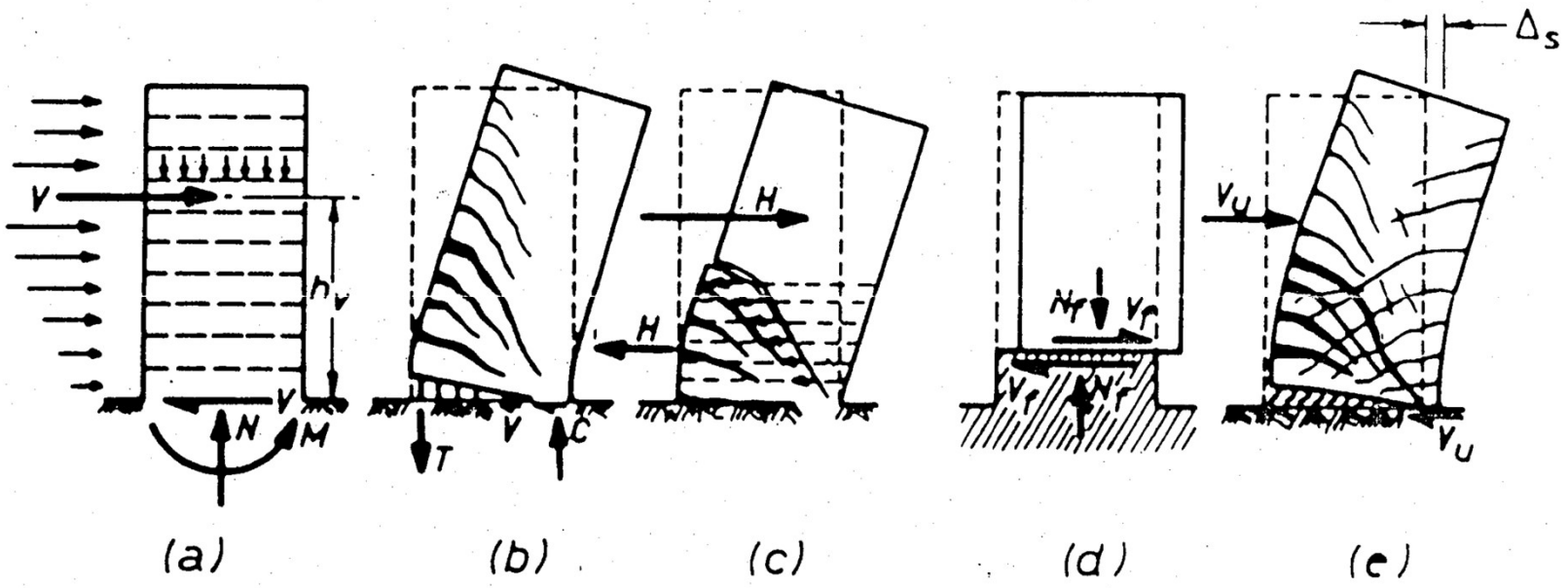

Brittle Failure modes in RC walls *to be prevented are:*

- *Diagonal tension failure (c) caused by shear,*
- *Diagonal compression failure caused by shear,*
- *Instability of thin walled sections,*
- *Instability of the principal compression reinforcement,*
- *Sliding shear along construction joints (d),*
- *Shear or bond failure along lapped splices or anchorages (b).*

The Cyclic Behavior of A 44-Story Building with **Ductile Structural Walls**

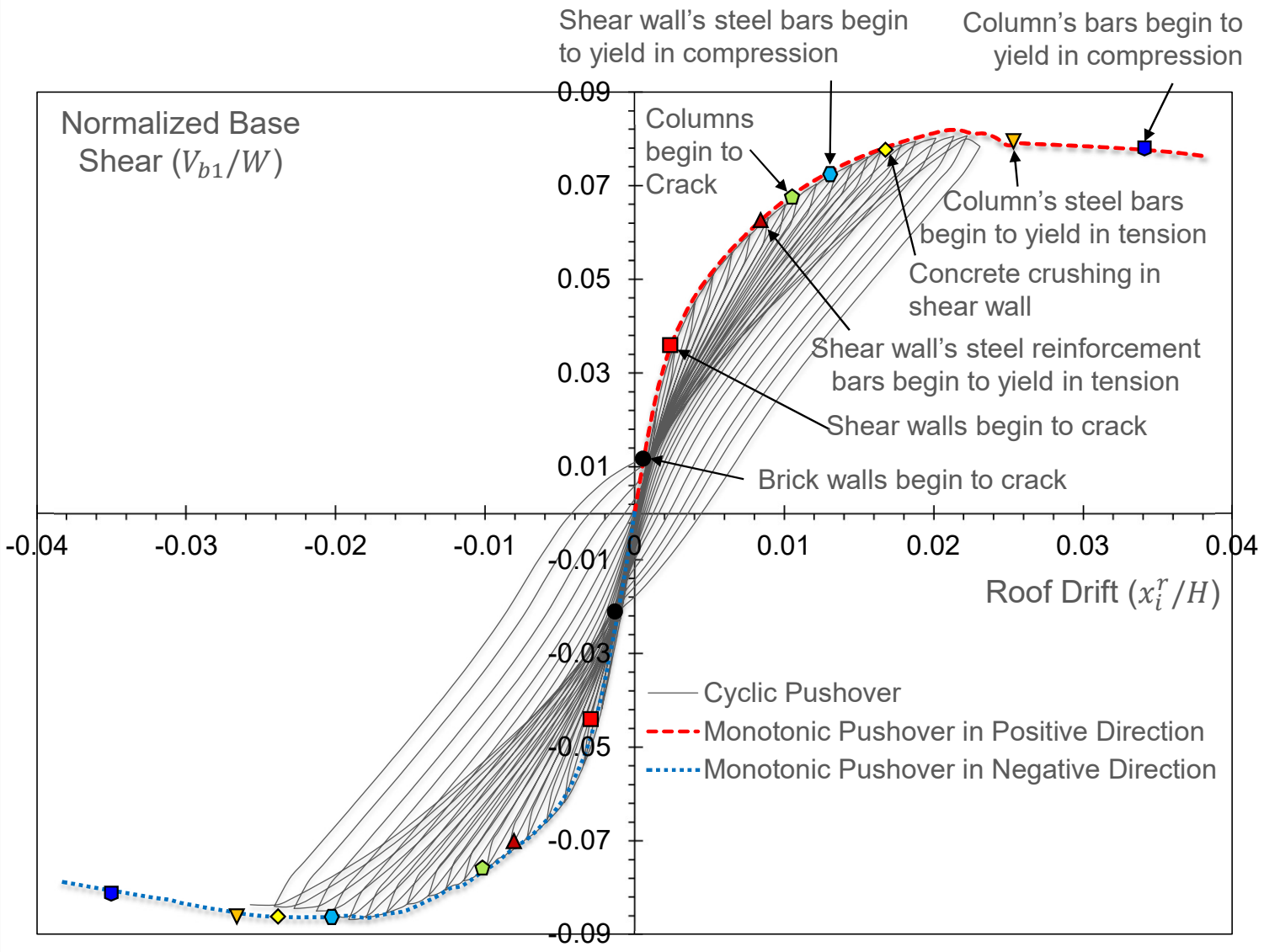

Roof Drift Ratio

Station: Department of Public Works and Town & Country Planning (PWSA)

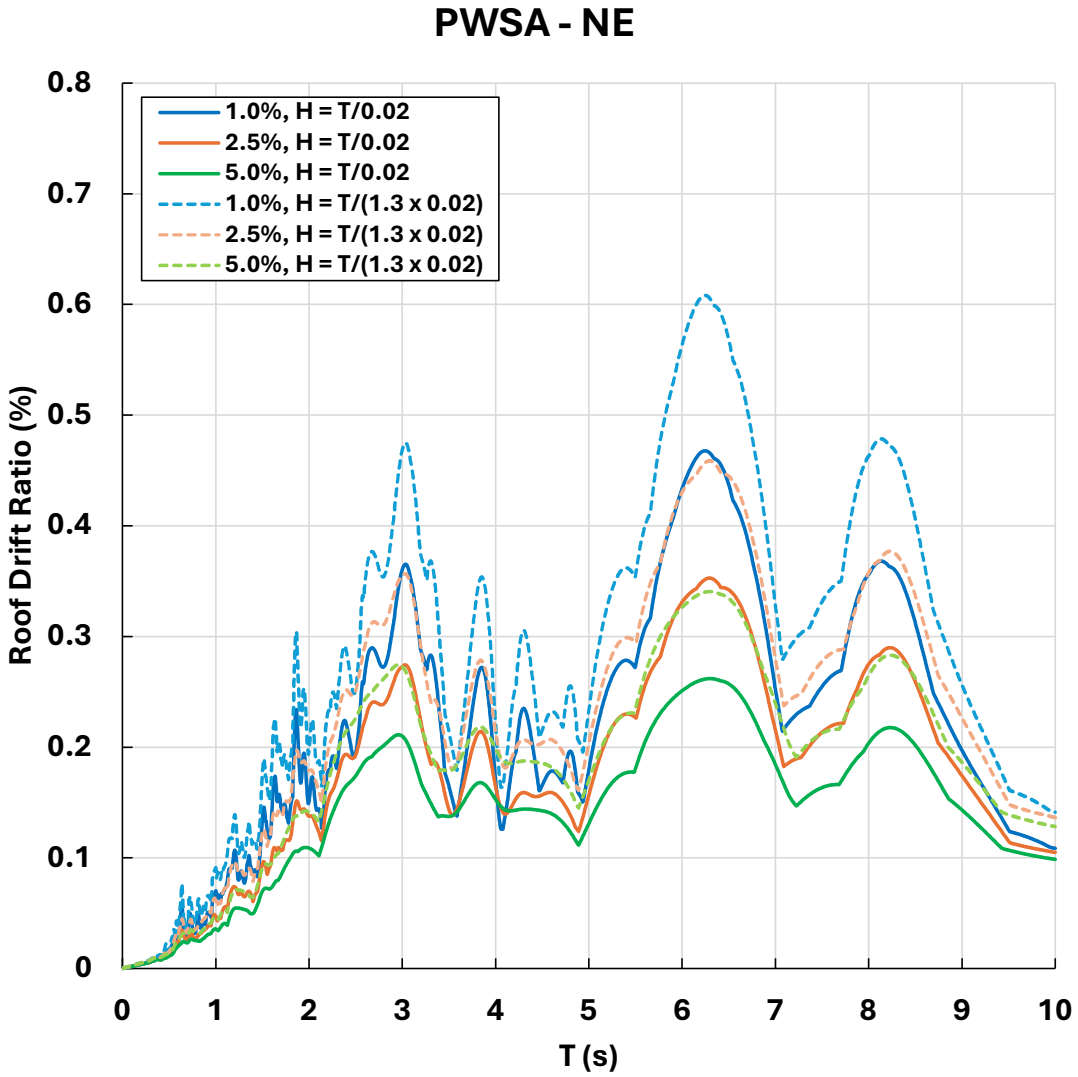

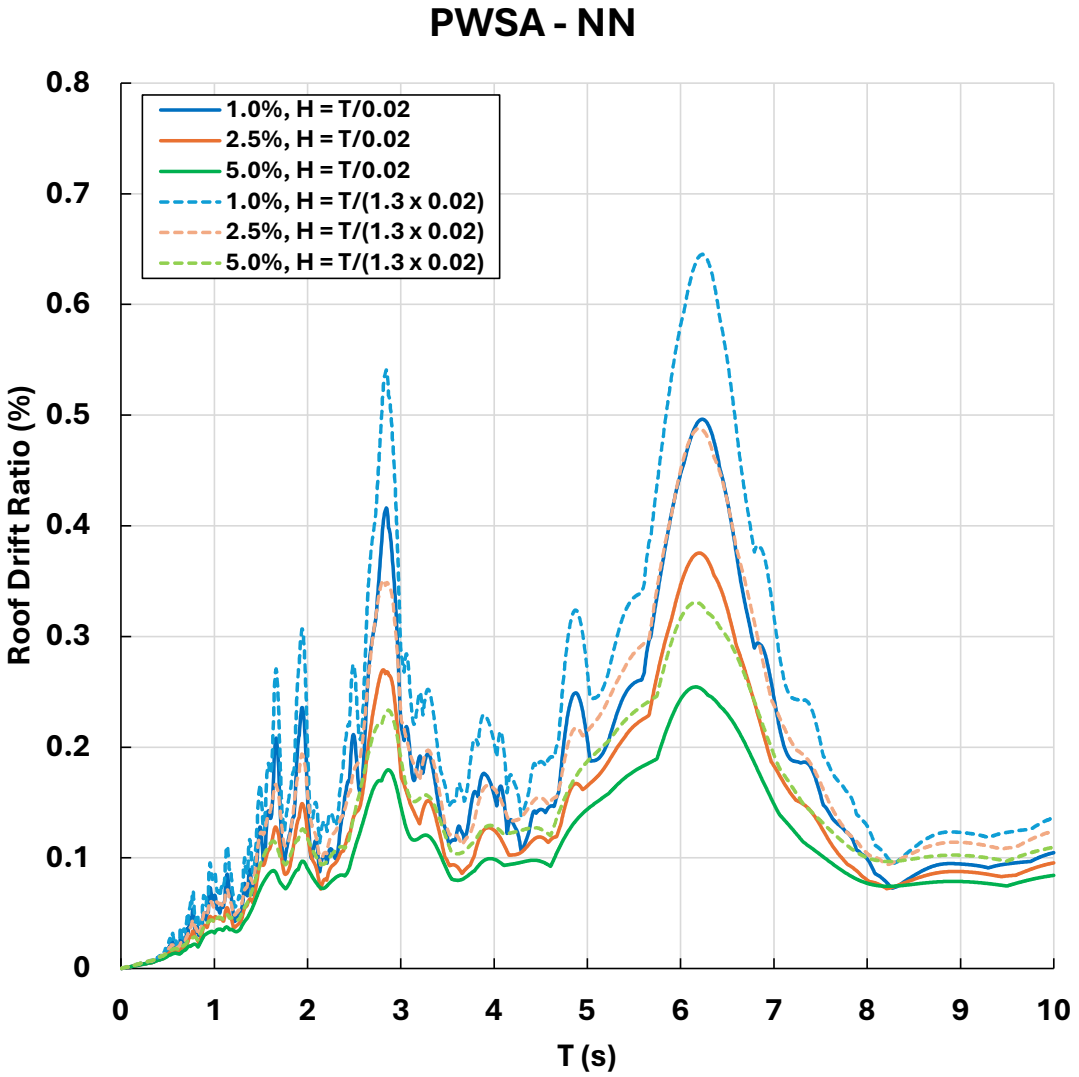

Fluid Viscous Damper (FVD) for building vibration control

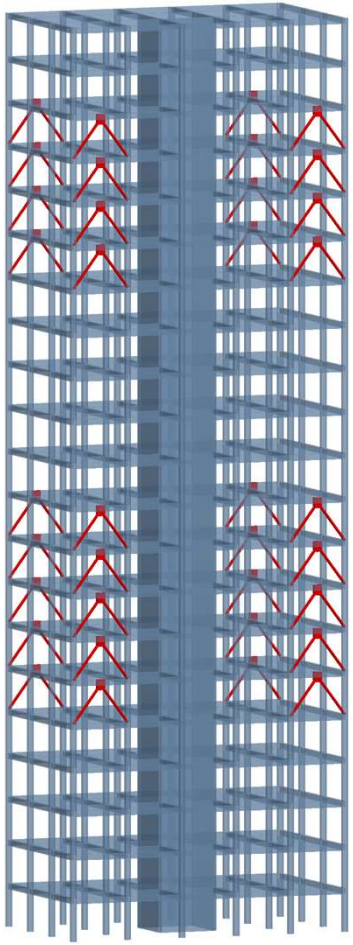

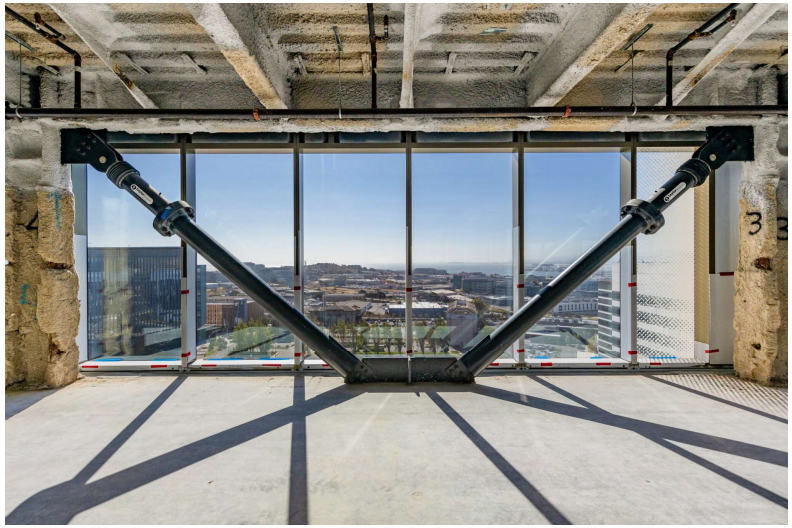

https://www.linkedin.com/posts/ncsea_fluid-viscous-dampers-effectively-dissipate-activity-7146470330536968192-SYJS/

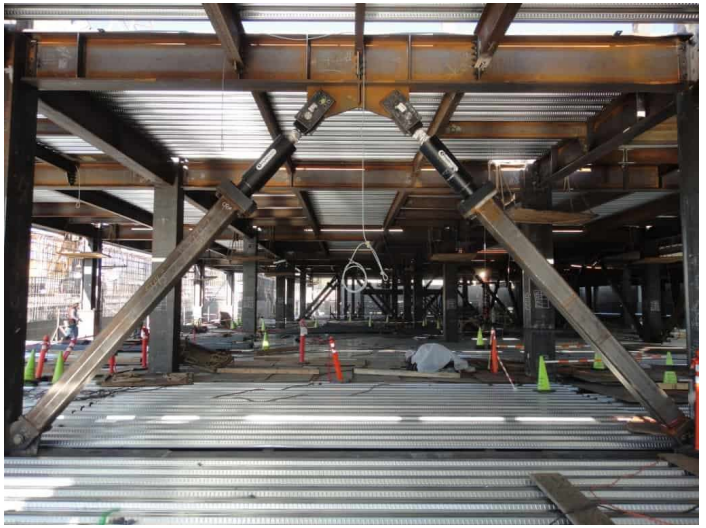

https://doi.org/10.3390/buildings15020260

https://ana.ir/en/news/1973/iran-among-nine-countries-holding-viscous-fluid-damper-technology

https://ryanrakhmats.wordpress.com/2018/04/22/fluid-viscous-damper-fvd/

Structural Health Monitoring of A Hospital Building in Chiang Rai

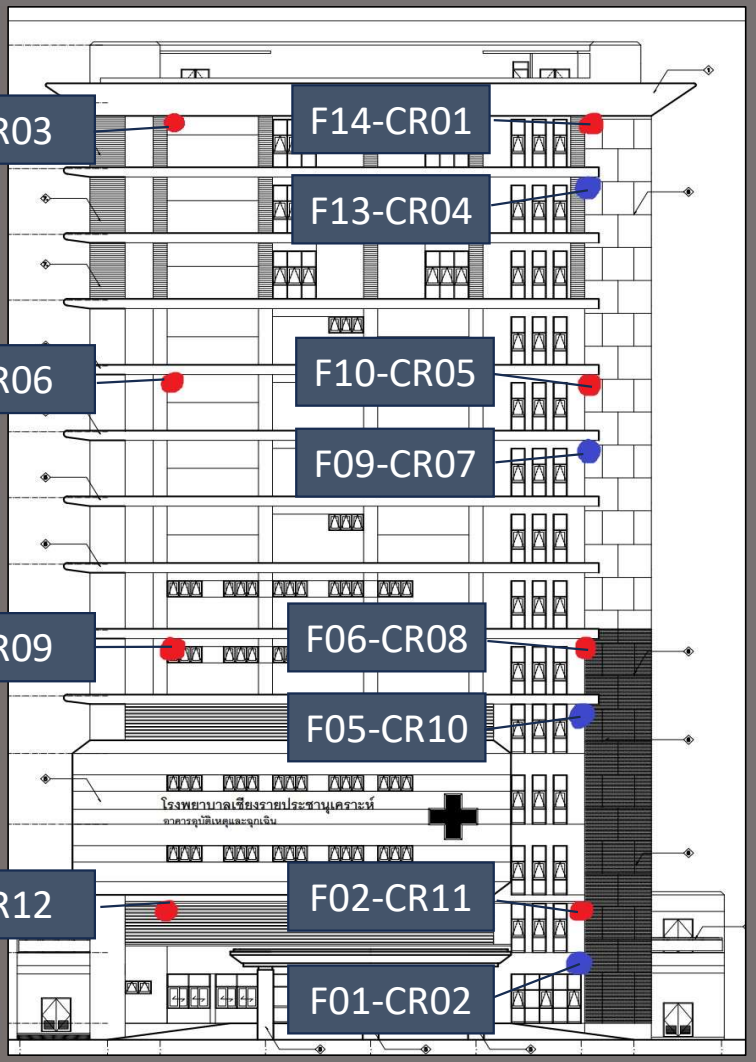

Testing the SHM system & Identify Building Dynamic Properties by Human Excitation

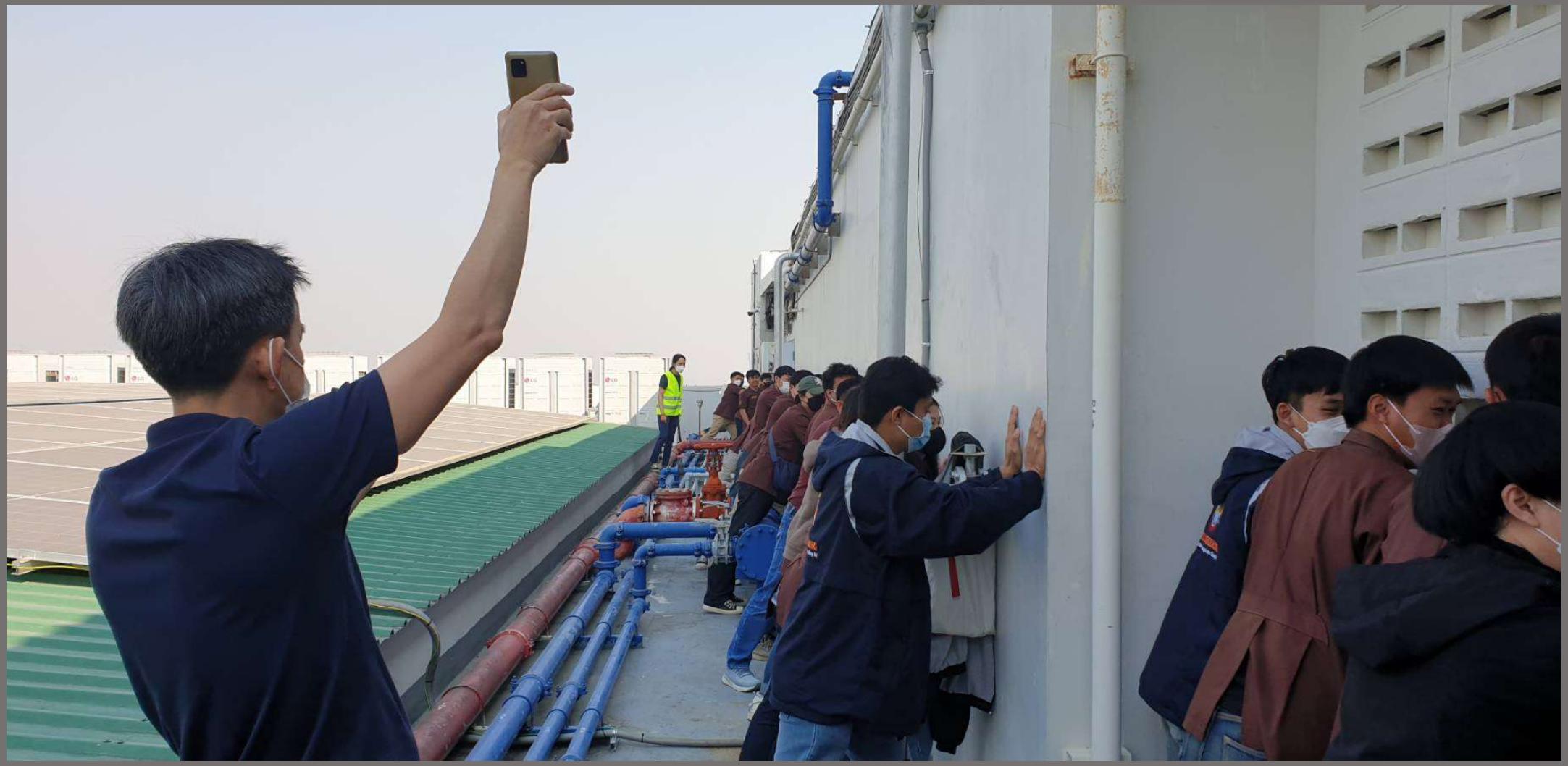

3D Mode Shape (Updated FEM Model)

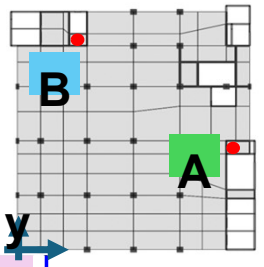

1X

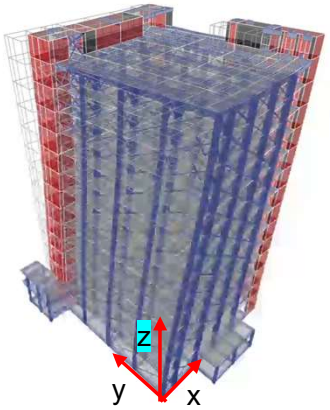

f_{FEM} = 0.868 Hz
$f_{HumanEx}$ = 0.933 Hz

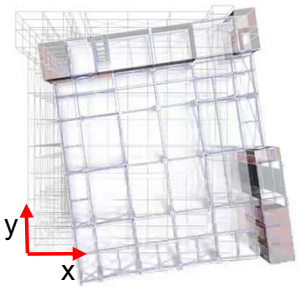

1Y

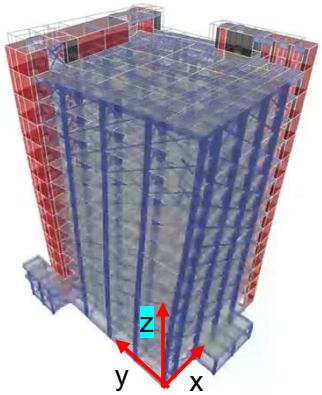

f_{FEM} = 0.933 Hz
$f_{HumanEx}$ = 0.946 Hz

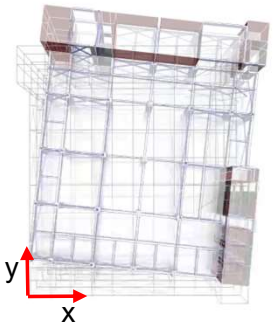

1R

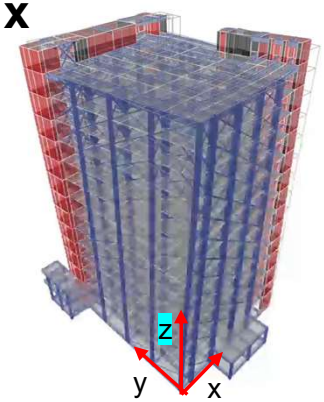

f_{FEM} = 1.386 Hz
$f_{HumanEx}$ = 1.332 Hz

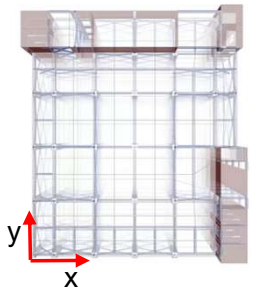

Sensor: B A B A B A

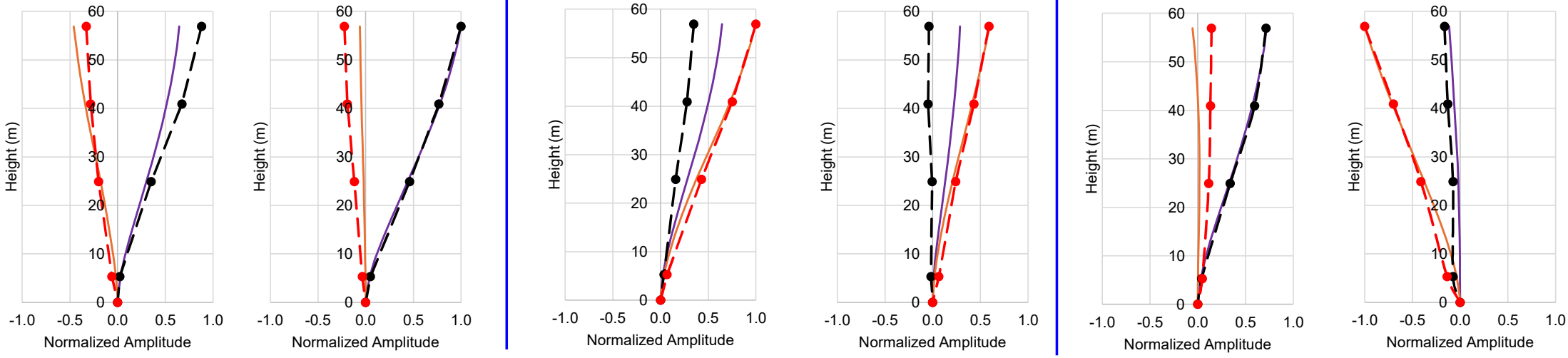

3D Mode Shape (Updated FEM Model)

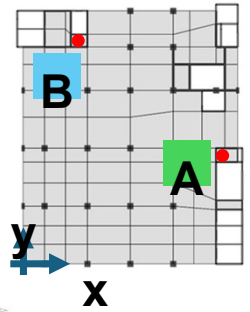

2X

f_{FEM} = 2.877 Hz
$f_{HumanEx}$ = 2.863 Hz

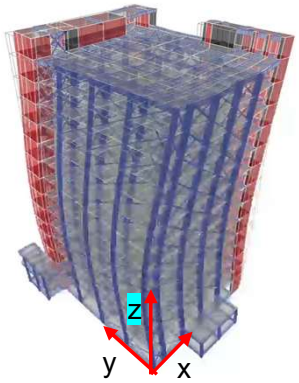

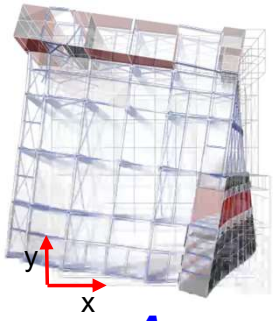

Sensor: B

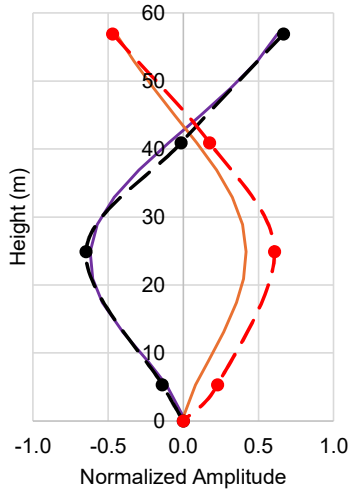

A

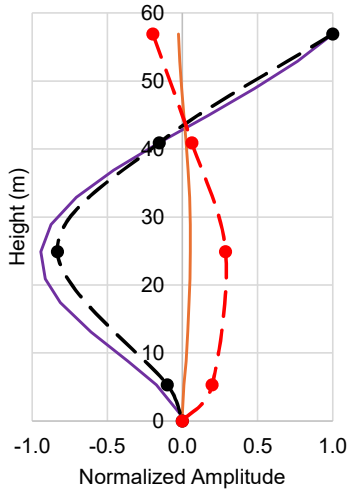

2Y

f_{FEM} = 3.207 Hz
$f_{HumanEx}$ = 3.084 Hz

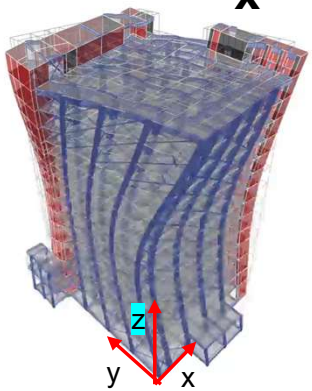

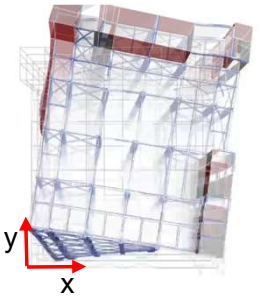

B

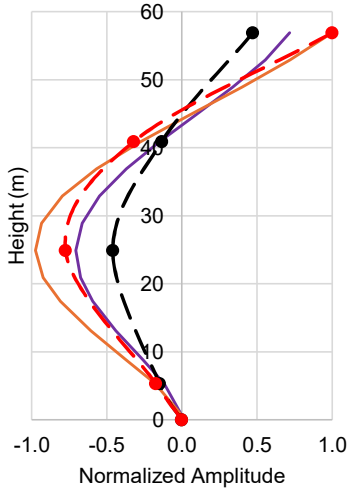

A

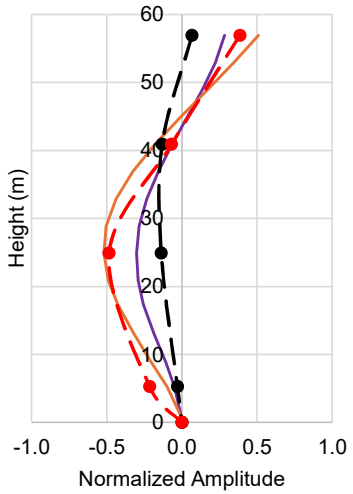

Visualization of Demand-to-Capacity Ratio of Structural Members in 3D Building Model

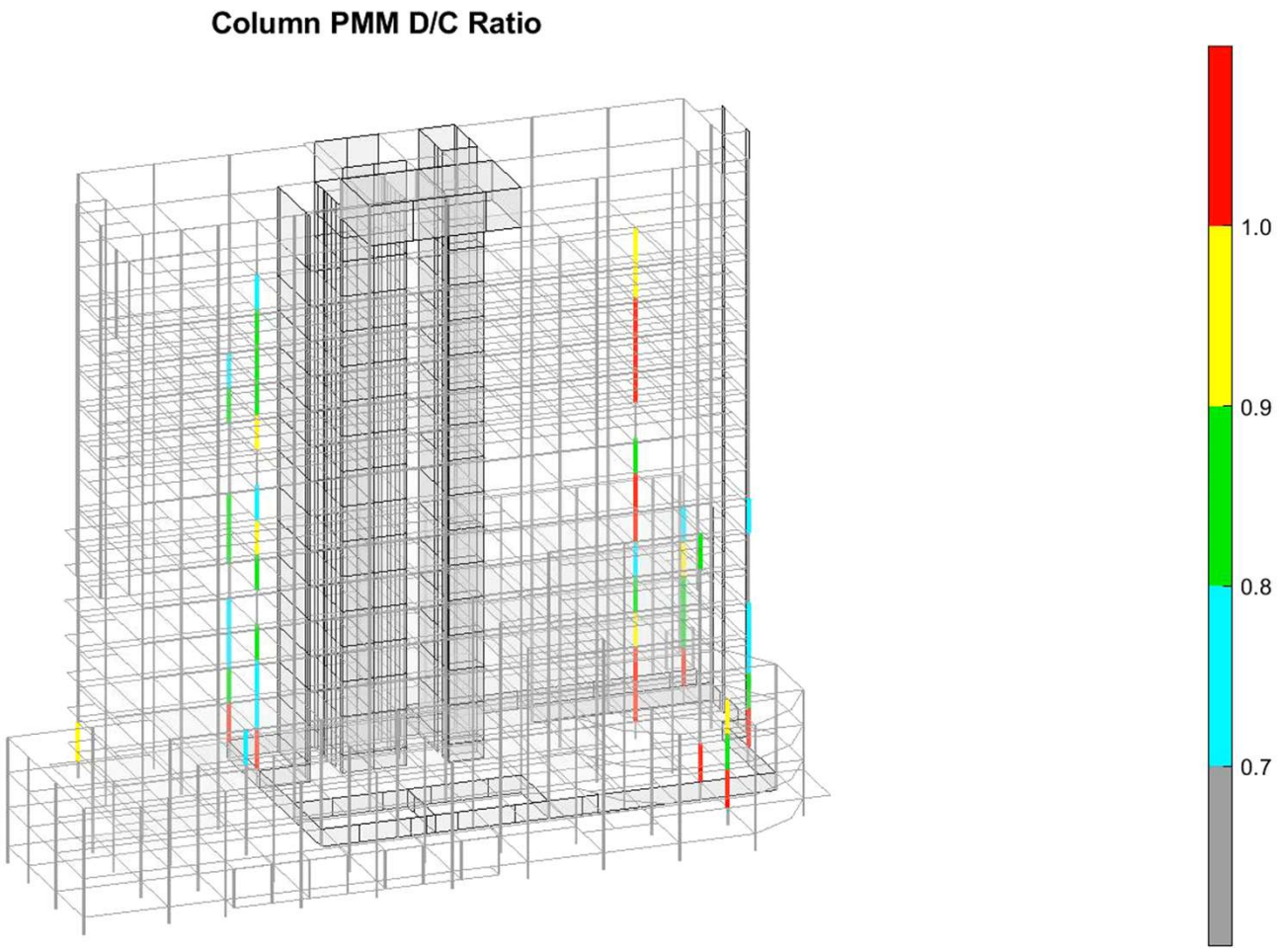

Proceedings of Annual Sessions 2025
Published by .....

SSESL
Society of Structural Engineers, Sri Lanka (SSESL)

Room No. 222, 2nd Floor,
Institution of Engineers Building,
120/15, Wijerama Mawatha,
(via Vidya Mawatha)
Colombo 00700, Sri Lanka

94 11 2698726
ssesl@sltnet.lk
www.ssesl.lk